Matematisk-fysiske Meddelelser
udgivet af
Det Kongelige Danske Videnskabernes Selskab
Bind **35**, nr. 1

Mat. Fys. Medd. Dan. Vid. Selsk. **35**, no. 1 (1966)

DISTRIBUTION OF OCTUPOLE OSCILLATOR STRENGTH IN EVEN-EVEN SPHERICAL NUCLEI FROM Ni TO Pb

BY

C. J. VEJE

København 1966
Kommissionær: Munksgaard

Synopsis

The distribution of the octupole oscillator strength, arising from one-phonon excitations of density variation modes in even-even spherical nuclei, is analysed on the basis of an interaction consisting of pairing + octupole-octupole force.

Special attention is paid to the isospin structure of the states.

It is found that, in many cases, two or three lines of comparable strength occur in the low-energy spectrum ($\lesssim$ 5 MeV).

The experimental evidence on energy and transition probability, which is available almost only for the very lowest state, can be accounted for reasonably well by a strength constant for the octupole-octupole force which varies smoothly with the atomic number.

PRINTED IN DENMARK
BIANCO LUNOS BOGTRYKKERI A-S

CONTENTS

	Page
1. Introduction	5
2. The Hamiltonian	6
The short-range part of the interaction	6
The long-range part of the interaction	8
3. The excitations	10
The isospin of the excitation	12
The isospin dependence of the long-race force	15
4. Reduced transition probabilities	16
Inelastic scattering	18
Charge exchange scattering	19
Scattering via isobaric analogues and stripping	20
Sum rules	22
5. Octupole coupling in simple examples	24
6. Effects of shell structure	27
7. Examples of the isospin structure of the excited states	37
8. The possible existence of strong $\tau \simeq 1$ lines	40
9. Modification in the spectra, when $\varkappa_1 \neq 0$ is introduced	41
10. Simultaneous adjustment of $\varkappa_0$ and $\varkappa_1$	43
11. Influence of $\varkappa_1$ on inelastic scattering	45
12. The collective character of the states	46
13. The renormalization procedure	48
14. The parameters	49
15. The calculation and the results	51
Comparison with the calculation by Gillet et al.	83
16. Concluding remarks	85
The fitting of the octupole force constant	85
The general distribution of oscillator strength	86
The low energy part of the spectrum	87
The isospin properties	88
Acknowledgements	88
References	89

1. Introduction

In recent years, a theory has been developed which gives a description of the density variation modes of nuclear vibrations in terms of single-particle excitations. This represents an improvement upon older, more phenomenological theories, not only by relating the collective and the single-particle aspects, but also by comprising in the same picture all degrees of collectiveness of the spectrum.

In a quantal system like a nucleus, density variations occur due to transitions of one or more particles between different states. When a particle is excited (a particle-hole pair created out of the ground state), the corresponding fluctuations in the nuclear field affect the motion of the other particles and tends to generate other particle-hole excitations.

Thus, because of the interaction between the particles through the field, the randomly distributed fluctuations from different single-particle excitations come in phase, and a more or less collective movement of the particles, a vibration, arises.

The octupole vibrations which we shall study are known from experiment to be less collective than the quadrupole ones. They should be more intimately connected to the details in the single-particle level scheme, and the oscillator strength in the low energy part of the spectrum might be spread over several levels.

The lowest octupole excitation has been studied by YOSHIDA (ref. 1) in a few cases.

In the present work we shall extend the investigation of the octupole excitation of lowest energy to a wider region of the periodic table. This gives information about the way in which the coupling constant for the effective force must vary with the atomic number in order to reproduce the observed energies. We are also going to study the excitations of higher energy and the whole energy distribution of the oscillator strength. It may be mentioned here that from the calculation two rather strong lines appear frequently in the low-energy region (2–5 MeV).

Since the isospin character of the vibrational states has been discussed only briefly before, we pay special attention to this problem and the relation to the isospin dependence of the field producing force (the long-range component).

2. The Hamiltonian

The "microscopic" description of collective excitations of a many-body system was introduced in nuclear physics by several authors, and we meet it under different names (method of linearized equations, random phase approximation, Sawada method, Baranger method, quasi-boson approximation, generalized Tamm-Dancoff method) (refs. 2 and 6). It has been used by several investigators, e.g., by YOSHIDA (ref. 1) in the study of quadrupole and octupole vibrations in some cases of spherical nuclei, by BÈS, by MARSHALEK, and by SOLOVIEV et al. for deformed nuclei (ref. 3), and by KISSLINGER and SORENSEN for quadrupole oscillations in a wide region of the periodic table (ref. 4). Since the theory has been presented repeatedly, we shall only mention here as much as is needed for introducing definitions and notations (which are almost the same as that used by YOSHIDA (ref. 1)). We consider spherical even-even nuclei. The particles are supposed to move in a shell-model potential, interacting by a short-range and a long-range force. Thus, the Hamiltonian is

$$H = H(\text{shell mod.}) + H(\text{short range}) + H(\text{long range}). \tag{2.1}$$

The short-range part of the interaction

The short-range part of the interaction is represented by a pairing force (ref. 5). Only that part of the pairing which influences the particles in the partly filled shells is taken into account, and pairing between neutrons and protons is not included.

The pairing + shell-model part of the Hamiltonian is

$$\left.\begin{aligned} & H(\text{shell model}) + H(\text{short range}) \\ & = \sum_{jmt_0} \varepsilon(j,t_0)a^+(j,m,t_0)a(j,m,t_0) \\ & - \tfrac{1}{4} G(t_0) \sum_{\substack{j',m',\\ j,m,t_0}} a^+(j',m',t_0)a^+(j',-m',t_0)a(j,-m,t_0)a(j,m,t_0) \\ & \times (-1)^{j'-m'-j+m}. \end{aligned}\right\} \tag{2.2}$$

Here, t_0 is the z component (or the $\nu = 0$ spherical tensor component) of the isospin of the particle with the convention

$$t_0 = \left\{ \begin{array}{l} \frac{1}{2} \text{ for protons} \\ -\frac{1}{2} \text{ for neutrons,} \end{array} \right\} \quad (2.3)$$

$\varepsilon(j, t_0)$ is the shell-model single-particle energy, $a^+(j, m, t_0)$ and $a(j, m, t_0)$ are creation and annihilation operators for a particle in the state j, m, t_0 (j represents all quantum numbers necessary to specify the state, with the exception of t_0 and the magnetic quantum number m). The force constant in the pairing $G(t_0)$, and the number of particles n in the partly filled shell are inserted into the BCS equations (2.4) and (2.5) which are solved for protons and neutrons separately with respect to the quantities $\lambda(t_0)$ and $\Delta(t_0)$:

$$\sum_j \frac{j + \frac{1}{2}}{E(j, t_0)} = \frac{2}{G(t_0)}, \quad (2.4)$$

$$\sum_j v^2(j, t_0) \times (2j + 1) = n, \quad (2.5)$$

where

$$E(j, t_0) = \left((\varepsilon(j, t_0) - \lambda(t_0))^2 + \Delta^2(t_0) \right)^{1/2}, \quad (2.6)$$

$$v^2(j, t_0) = \tfrac{1}{2} \left(1 - \frac{\varepsilon(j, t_0) - \lambda(t_0)}{E(j, t_0)} \right). \quad (2.7)$$

Here, $E(j, t_0)$ is the quasiparticle energy, $\lambda(t_0)$ the chemical potential or Fermi energy, $\Delta(t_0)$ the gap, $v^2(j, t_0)$ is the probability for the shell-model level jmt_0 to be filled. The probability for it to be empty is

$$u^2(j, t_0) = 1 - v^2(j, t_0). \quad (2.8)$$

The index t_0 is often omitted below.

Since the octupole oscillations involve mainly single-particle transitions between different shells, the pairing has less influence than for the quadrupoles. It has been checked that uncertainty in the pairing strength constant G is less significant than uncertainties in other parameters. Thus, in almost all cases (cf. sect. 14) we have used a standard value for G/A (A is the atomic number).

The long-range part of the interaction

We shall simulate the interaction between the particles through the octupole part of the nuclear field by an effective force of attractive long-range octupole-octupole type, working between all nucleons. Expressed in terms of creation and annihilation operators it takes the form

$$\left.\begin{aligned} & H\,(\text{long range}) \\ &= -\tfrac{1}{2}\sum_{\substack{\mu \\ j's \\ m's \\ t_0's}} (-1)^{3-\mu} \langle t_0'(1)\, t_0'(2) \,|\, \varkappa\big(\vec{t}(1), \vec{t}(2)\big) \,|\, t_0(1)\, t_0(2)\rangle \\ &\times \langle j_1' m_1' \,|\, i^3 Y_{3\mu} \left(\frac{r}{a}\right)^3 |\, j_1 m_1\rangle \langle j_2' m_2' \,|\, i^3 Y_{3-\mu} \left(\frac{r}{a}\right)^3 |\, j_2 m_2\rangle \\ &\times a^+\big(j_1, m_1', t_0'(1)\big)\, a^+\big(j_2', m_2', t_0'(2)\big) \\ &\times a\big(j_2, m_2, t_0(2)\big)\, a\big(j_1, m_1, t_0(1)\big), \end{aligned}\right\} \tag{2.9}$$

where the quantity

$$a = \left(\frac{\hbar}{M\omega_0}\right)^{1/2}, \tag{2.10}$$

M being the nucleon mass and ω_0 the frequency of the harmonic oscillator used in the shell-model potential. (For further details, see below). In the force constant $\varkappa$ we have introduced the isospin of the nucleons $\vec{t}(1)$ and $\vec{t}(2)$.

Assuming the interaction to be invariant under rotations in isospin space, we can write $\varkappa$ in the form

$$\left.\begin{aligned} \varkappa &= \varkappa_0 + \varkappa_1 \,.\, 4\vec{t}(1) \,.\, \vec{t}(2) \\ &= \varkappa_0 + \varkappa_1 \sum_{\nu} 2\, t_\nu(1)\, 2\, t_{-\nu}(2)(-1)^\nu, \end{aligned}\right\} \tag{2.11}$$

where $t_\nu(1)$ and $t_\nu(2)$ are spherical components of the isospins of the particles. Thus, $\varkappa_0$ represents the isoscalar or $\tau = 0$ component of the force, and $\varkappa_1$ the isovector or $\tau = 1$ part. In the following section we come back to the relative magnitude and sign of $\varkappa_1$ and $\varkappa_0$.

Below we concentrate on that part of the field which acts on protons or neutrons, but does not change neutrons into protons, or vice versa. In that case, only the $\nu = 0$ part of the force is working and thus it is the only part which is considered in the treatment below. The $\nu \neq 0$ components are

relevant when exciting vibrations in the neighbouring odd-odd nuclei (cf. sect. 4).

Since the force is introduced to describe the variations in the field, we shall only take into account the field-producing part of the interaction (i.e. the annihilation matrix element in the particle-hole interaction).

The radial dependence in the field is not very well established. Our choice is made mainly for the sake of simplicity, and further investigations would be of great interest.

We shall primarily study the low-lying, strong excitations, which are supposed to be connected to vibrations of the nuclear surface. With our expression for the radial matrix element the surface region obtains a heavy weight. It may be that contributions to the field interaction from single-particle transitions $j \to j'$, involving changes in the principal quantum number of the harmonic oscillator $|\Delta N| = 3$, are not properly weighted in our picture. For instance, particles with a tail far outside the nucleus probably give rise to much smaller polarization of the core than supposed by the r^3 dependence which attributes a great influence to the outermost part of the wave function. A better dependence might be obtained, e.g., by using the radial derivative of a Saxon-Wood potential. The effect should be especially significant for the resulting high-energy modes, whereas the low-energy modes should be less affected. For our choice of force it appears that, for single-particle transitions with $\Delta N = 1$, the radial matrix elements are all of the same order of magnitude, even when squared. (The smallest values are obtained when the change in the number of radial nodes is maximal).

This means that the radial part of the interaction does not give rise to strong cancellation of any of the contributions from the single-particle transitions of low energy. For the $\Delta N = 3$ terms the square of the radial matrix element is fluctuating more strongly, sometimes being quite small when a great change in the number of radial nodes is involved. Roughly speaking, the squares of the $\Delta N = 3$ radial matrix elements are half as large as the $\Delta N = 1$ terms. The angular part of the matrix element is very sensitive to whether spin flip is involved or not. E.g., the square of the reduced matrix element is about 20 times larger for $j_1, j_1' = 7/2, 13/2$ than for $j_1, j_1' = 9/2, 13/2$.

It may finally be mentioned that it is still an unresolved problem whether the isospin independent ($\tau = 0$) field and the isospin dependent field ($\tau = 1$) are of the same radial structure. (For a definition of τ, see sections 3 and4). You might suggest that for the $\tau = 1$ modes volume phenomena play a greater role compared to surface phenomena than for $\tau = 0$ modes and, thus, that the radial dependence of the $\tau = 1$ field is slower than for the $\tau = 0$ field.

3. The excitations

For the total Hamiltonian H (2.1) the quasi-boson approximation is used. We describe the excitation as a superposition of two-quasiparticle creations and annihilations and write the excitation operator $B^+(\alpha)$ in the form

$$\left.\begin{aligned} B^+(\alpha) = \sum_{\substack{j_1 j_2 \\ m_1 m_2 \\ t_0}} \{ & p(\alpha, j_1, j_2, t_0) \langle j_1 m_1 j_2 m_2 | 3\mu \rangle \alpha^+(j_1, m_1, t_0) \alpha^+(j_2, m_2, t_0) \\ & + (-)^\mu q(\alpha, j_1, j_2, t_0) \langle j_1 m_1 j_2 m_2 | 3 - \mu \rangle \alpha(j_2, m_2, t_0) \alpha(j_1, m_1, t_0) \}, \end{aligned}\right\} \quad (3.1)$$

where the quasiparticle creation and annihilation operators are given by

$$\alpha^+(j, m, t_0) = u(j, t_0) a^+(j, m, t_0) - (-1)^{j-m} v(j, t_0) a(j, -m, t_0), \quad (3.2)$$

$$\alpha(j, m, t_0) = u(j, t_0) a(j, m, t_0) - (-1)^{j-m} v(j, t_0) a^+(j, -m, t_0). \quad (3.3)$$

This means that the two-quasiparticle excitations (each having energy $E(j_1) + E(j_2)$), are considered to be elementary oscillators which are coupled by the long-range part of the force. In the expression for $B^+(\alpha)$, j_1 and j_2 run over all possible proton and neutron states, but each pair should only be taken once, i.e. if $j_1 j_2 t_0$ is included, $j_2 j_1 t_0$ should not be.

Now, $B^+(\alpha)$ working on the ground state $|0\rangle$, gives the excited state $|\alpha\rangle$ with energy $\hbar\omega_\alpha$

$$|\alpha\rangle = B^+(\alpha)|0\rangle \quad (3.4)$$

and $B(\alpha)|0\rangle = 0$, where $B(\alpha)$ is the hermitian conjugate to $B^+(\alpha)$. We further have

$$[H, B^+(\alpha)] = \hbar\omega_\alpha B^+(\alpha) \quad (3.5)$$

which, on inserting (3.1), gives the expressions (12.1) and (12.2) for $p(\alpha, j_1 j_2 t_0)$ and $q(\alpha, j_1 j_2 t_0)$ used in sect. 12.

The orthonormality of the states gives (taking as above in eq. (3.1) each pair $j_1 j_2$ only once)

$$\sum_{j_1 j_2 t_0} \{ p(\alpha, j_1, j_2, t_0) p(\alpha', j_1, j_2, t_0) - q(\alpha, j_1, j_2, t_0) q(\alpha', j_1, j_2, t_0) \} = \delta_{\alpha\alpha'}. \quad (3.6)$$

Following the common procedure (ref. 6) we end up by eq. (3.7) the solutions $\hbar\omega$ of which are the resulting energies

$$\left(\frac{\varkappa_p}{7} S^p - 1\right)\left(\frac{\varkappa_n}{7} S^n - 1\right) - \frac{\varkappa_{np}^2}{49} S^p S^n = 0 \tag{3.7}$$

or

$$4\frac{\varkappa_0 \varkappa_1}{49} S^p S^n - \frac{\varkappa_0 + \varkappa_1}{7}(S^p + S^n) + 1 = 0. \tag{3.8}$$

Here,

$$S^p = \sum_{jj'}^{p} \frac{\langle l'j' \| i^3 Y_3 \left(\frac{r}{a}\right)^3 \| lj \rangle^2 \big(u(j)v(j') + v(j)u(j')\big)^2 \big(E(j) + E(j')\big)}{\big(E(j) + E(j')\big)^2 - (\hbar\omega)^2}, \tag{3.9}$$

where the sum runs over all possible proton states j and j', which may be coupled to spin and parity 3^-. The analogous neutron quantity is denoted by S^n.

The first term in the numerator in S^p is an ordinary reduced matrix element

$$\left.\begin{aligned} \langle l'j' \| i^3 Y_3 \left(\frac{r}{a}\right)^3 \| lj \rangle &= (4\pi)^{-1/2} i^{l-l'+3} (-1)^{j-1/2} \\ \times \tfrac{1}{2}\big(1 + (-1)^{l'+l-3}\big) \langle j' j \tfrac{1}{2} -\tfrac{1}{2} \mid 30 \rangle &\langle l'j' \mid \left(\frac{r}{a}\right)^3 \mid lj \rangle \\ \times \big((2j+1)(2j'+1)\big)^{1/2}&. \end{aligned}\right\} \tag{3.10}$$

In ref. 1 YOSHIDA presents a table showing the matrix elements of $\left(\frac{r}{a}\right)^3$, using harmonic oscillator wave functions. The quantities $\varkappa_p$, $\varkappa_n$ and $\varkappa_{np}$ are the octupole-octupole force constants for the proton-proton, neutron-neutron and neutron-proton force, respectively. For these we have used the expressions (2.11):

$$\varkappa_n = \varkappa_p = \varkappa_0 + \varkappa_1, \tag{3.11}$$

$$\varkappa_{np} = \varkappa_0 - \varkappa_1. \tag{3.12}$$

If $\varkappa_1 = 0$, the equation (3.8) for the determination of $\hbar\omega$ reduces to

$$S^p + S^n = \frac{7}{\varkappa_0} \tag{3.13}$$

which is the usual secular equation, and $\varkappa_0 = 0$ gives

$$S^p + S^n = \frac{7}{\varkappa_1}. \tag{3.14}$$

The analogue to this equation has been discussed for dipoles (ref. 7) for which the opposite sign convention has been used in general.

In order to provide an idea of the variation of the force constant $\varkappa$ with A we may use a simple scaling argument.

If we assume the matrix elements to represent an interaction with a range short compared to the nuclear radius, the interaction matrix elements are inversely proportional to the nuclear volume, i.e. $\sim 1/A$. Since each of the factors $(r_1/a)^3$ and $(r_2/a)^3$ varies proportional to $A^{1/2}$, we expect $\varkappa$ to be proportional to A^{-2}.

In our treatment we look apart from couplings to other modes, although such effects may sometimes be of importance. Thus, the resulting states of excitation energies more than some few MeV appear in regions with large level density. In such a situation the present calculation is only expected to give the gross structure of the 3^- distribution.

For the low-lying states, the most important couplings may be those to modes which involve large amplitudes. Thus the couplings to the strongly collective quadrupole vibrations of very low energy are expected to be of special significance.

In deformed nuclei, we know that this coupling causes a splitting of octupole modes with different K values. In the present calculation the most interesting modification of the results which this effect may cause may be that the strength of the strong octupole line, which in the following calculation is often found in the 4–5 MeV region, may be spread over several states, which may be imagined as arising from the coupling of a 3^- phonon to one or more 2^+ phonons.

The isospin of the excitation

In this section we are going to discuss briefly the isospin properties of the excitations, which properties so far have been neglected.

In the same way as the excitation in ordinary space can be described by the spherical tensor quantum numbers λ, μ ($\lambda = 3$ in our case), it may in isospin space be characterized by analogous quantities τ, ν, where τ must be either 0 or 1 in the present treatment. The excitation operator $B^+(\tau, \nu; \lambda, \mu)$ may e.g. be of the type

$$M(\tau = 0;\ \lambda = 3, \mu) = \sum_i \tfrac{1}{2} r_i^3 Y_{3\mu}(i) \tag{3.15}$$

or

$$M(\tau = 1, \nu;\ \lambda = 3, \mu) = \sum_i r_i^3 Y_{3\mu} t_\nu(i), \tag{3.16}$$

where i runs over all particles in the nucleus (cf. sect. 4). We shall use the matrix elements of the M operators between the ground state and the excited states to describe the isospin structure of the excitations, as further explained in sect. 4.

The matrix elements of $M(\tau = 1, \nu = 1; 3, \mu)$ are non-vanishing only when the excitation involves creation of a neutron hole, proton pair, i.e. when it leads to another nucleus. Such an excitation may be realized by a (p, n) scattering on the nucleus. In the same way τ, $\nu = 1, -1$ leads to the excitations of a neighbouring nucleus $Z, A \rightarrow Z-1, A$, e.g. by an (n, p) process. Such excitations and their relevance to the present treatment are discussed briefly in sect. 4. The $\tau = 0$ or $\tau, \nu = 1,0$ excitations give rise to states in the target nucleus and, as we shall see below, these two excitations are in general mixed, although the strong low-lying states to a good approximation are $\tau = 0$.

As pointed out by LANE and SOPER (ref. 8) and later utilized and explained in greater detail, e.g., by SLIV (ref. 10) and by BOHR and MOTTELSON (ref. BM), the isospin T of a state in a heavy nucleus is in many respects a very well-conserved quantity. Therefore we must ensure that the states which we find have good (T, T_0). (T_0 is the third component of T).

As long as we only apply $\tau = 0$ excitation operators to the ground state, for which

$$(T, T_0) = (T_1, -T_1) = \left(\frac{N-Z}{2}, \frac{Z-N}{2}\right), \tag{3.17}$$

there is no problem: we reach a state with the same T, while $\tau, \nu = 1,0$ operators may give rise to some mixture of $T = T_1$ and $T = T_1 + 1$. The $T_1 + 1$ part of the excitation is contained in the isobaric analogue to an excitation of low energy in the neighbouring nucleus with $T_0 = -T_1 - 1$. It has quite another structure than the T_1 states in the same energy region and is only mixed weakly with them (ref. 9).

To illustrate the relation to our calculation let us, for simplicity, assume sharp Fermi surfaces for protons and neutrons. Let $\varepsilon(F, n)$ and $\varepsilon(F, p)$ be the Fermi energies for neutrons and protons, respectively. Let us consider a particle-hole excitation for which the particle (i.e. a proton) is created in a state (j_1, m_1) such that $\varepsilon(j_1, m_1) < \varepsilon(F, n)$ or the hole (i.e. a neutron hole) is created in a state (j_2, m_2) such that $\varepsilon(j_2, m_2) > \varepsilon(F, p)$.

In this case T_- acting on the state gives zero. We cannot further align the state in isospin space and, hence, $T = T_1$.

For our purpose this means that, for single-particle transitions inside partly filled shells and for part of the transitions from one shell to the next, there is no possibility for isospin impurities.

It should be stressed that this does not mean that the excitation is pure $\tau = 0$, since $\tau = 1$ and $T = T_1$ are able to couple to T_1.

For the transitions of higher energy, T is not automatically conserved. Let us consider a definite particle-hole excitation (j_1, j_2) and let $A^+(\tau = 1, \nu = 0)$ create the particle-hole pair, coupled to $(\tau = 1, \nu = 0; \lambda = 3, \mu)$. The resulting state with good quantum numbers $(T, T_0) = (T_1, -T_1)$ is then formed by coupling of the ground state $T = T_1$ and $\tau = 1$:

$$\left.\begin{aligned} &\{A^+(\tau = 1)\,|\,T_1>\}_{(T_1,1)\,T_1,-T_1} \\ &= <10\,T_1 - T_1\,|\,T_1 - T_1>\, A^+(\tau = 1,\ \nu = 0)\,|\,T_1 - T_1> \\ &+ <1 - 1\,T_1 - T_1 + 1\,|\,T_1 - T_1>\, A^+(\tau = 1,\ \nu = -1)\,|\,T_1 - T_1 + 1> \end{aligned}\right\} \tag{3.18}$$

$$\left.\begin{aligned} &= \sqrt{\frac{T_1}{T_1+1}}\, A^+(\tau = 1,\ \nu = 0)\,|\,T_1 - T_1> \\ &- \sqrt{\frac{1}{T_1+1}}\, A^+(\tau = 1,\ \nu = -1)\,|\,T_1 - T_1 + 1> \end{aligned}\right\} \tag{3.19}$$

$$\sim A^+(\tau = 1,\ \nu = 0)\,|\,T_1 - T_1> \quad \text{for} \quad T_1 >> 1. \tag{3.20}$$

The state is thus a superposition of an excitation, based on the ground state $|\,T_1 - T_1\rangle$, and an excitation based on $|\,T_1 - T_1 + 1\rangle$, which is the isobaric analogue to the ground state. In the following we neglect the last part. The justification for this procedure is, partly, that for the states of low energy which we are most interested in, the effect should be very small and, partly, the assumption of $T_1 \rangle\rangle 1$, which should be well satisfied, except for the lightest nuclei considered.

When the Fermi surface is smeared out, i.e. when our elementary modes are two-quasiparticle excitations instead of particle-hole excitations, the discussion which was given above contains a slight oversimplification. This is due to the fact that the quasiparticles do not have a definite z component of the isospin in the way we have defined them. Thus, the elementary modes involving the creation of a proton-neutron quasiparticle pair are mixtures of $\nu = \pm 1$.

It shall finally be stressed that in general it is not allowed to treat the

coupling in isospin space between the vibration and the ground state of a heavy nucleus in the weak coupling limit. This means that it is not possible to consider the excitation operator as a definite entity, the isospin of which is coupled to that of the ground state by simple vector coupling, or which may be rotated in isospace without complications.

It is e.g. easy to find a ($\tau = 1$, $\nu = 1$) particle-hole excitation, for which the ($\tau = 1$, $\nu = 0$) partner gives zero when acting on the ground state of a heavy nucleus. This happens whenever the particle or the hole is placed in a level (j,m) which is occupied by neutrons but empty for the protons.

The isospin dependence of the long-range force

The isospin dependence of the long-range force is contained in the isovector component $\varkappa_1$ of which little information is available. It is expected to be negative (to have opposite sign of $\varkappa_0$), since this will push the $\tau = 1$ excitations upwards in energy, as is the case for the giant dipole. (For further details, see sect. 5). This means that the *nn* and *pp* force should be somewhat weaker than the *np* force, or even have opposite sign, if $\varkappa_0 < |\varkappa_1|$.

An estimate of the magnitude of $\varkappa_1$ may be obtained by assuming that the oscillating field has the same isospin dependence as the central nuclear field for which the dependence manifests itself, e.g., in the semi-empirical mass formula and in the real part of the optical potential (ref. 50). This gives

$$\varkappa_1/\varkappa_0 \simeq -1/2. \tag{3.21}$$

A similar result is obtained by assuming that the two-body force responsible for the interaction is approximately of Serber type. Such estimates have been discussed by Bohr and Mottelsen (ref. BM).

A determination of $\varkappa_1$ on the basis of a fit to the experimentally determined energies is not possible. This is analogous to the situation for quadrupole vibrations where even many more data are available (ref. KSII). This difficulty is caused by the fact that all the experimental information concerns the low-energy states, and for these the $\tau = 1$ part of the force has only little effect in comparison to the $\tau = 0$ part, and also compared to other parameters, as e.g. the single-particle energies which are not very well known. (We shall see below that a more detailed investigation of the 2–5 MeV part of the spectra, using inelastic scattering with different projectiles and comparing results for different states and for different nuclei, may be one of the best tools for determining $\varkappa_1$, but still a large uncertainty is expected). On the other hand, we are able to obtain a fairly correct picture of the strong lines in the low-energy spectrum without detailed information on $\varkappa_1$, and therefore

we have simply used an isospin independent octupole-octupole force in our general calculations in sect. 15.

By this choice the lines of $\tau = 1$ type are poorly determined but, as we shall see for $\varkappa_1 = -0.5\varkappa_0$, there is no strong tendency to build up very great, individual $\tau = 1$ lines.

A discussion of the influence of $\varkappa_1$ and some examples of spectra, calculated with $\varkappa_1 = -0.5\varkappa_0$ and $\varkappa_1 = -2\varkappa_0$, are presented in sections 5 and 9. For the strong lines of low energy it is possible to give simple rules for the changes in energies and reduced transition probabilities resulting from a finite $\varkappa_1$.

4. Reduced transition probabilities

The coherence and isospin properties of the excitations can be described in terms of the matrix elements of the multipole operators $M(\tau = 0;\ \lambda = 3, \mu)$ and $M(\tau = 1, \nu;\ \lambda = 3, \mu)$ which were given above ((3.15) and (3.16)).

In our treatment only the $\nu = 0$ component of $M(\tau = 1)$ is relevant.

Taking the square of the reduced matrix element from the ground state to the state in question (labelled 3^-, α), we obtain two new quantities, namely the reduced transition probabilities

$$\left.\begin{aligned} B_0 &\equiv B(\tau = 0;\ 0 \to 3-, \alpha) \\ &\equiv |\langle 3-, \alpha || M(\tau = 0;\ \lambda = 3, \mu) || 0 \rangle|^2, \end{aligned}\right\} \tag{4.1}$$

and

$$\left.\begin{aligned} B_1 &\equiv B(\tau = 1,\ \nu = 0;\ 0 \to 3-, \alpha) \\ &\equiv |\langle 3-, \alpha || M(\tau = 1,\ \nu = 0;\ \lambda = 3, \mu) || 0 \rangle|^2. \end{aligned}\right\} \tag{4.2}$$

In the same way, the ordinary electric transition operator

$$M(E3, \mu) = \sum_i r_i^3 Y_{3\mu}(i)\, e\left(\tfrac{1}{2} + t_0(i)\right) \tag{4.3}$$

gives rise to

$$B \equiv B(E3;\ 0 \to 3-, \alpha) \equiv |\langle 3-, \alpha || M(E3, \mu) || 0 \rangle|^2. \tag{4.4}$$

We see that

$$M(E3, \mu) = e\big(M(\tau = 0;\ \lambda = 3, \mu) + M(\tau = 1,\ \nu = 0;\ \lambda = 3, \mu)\big). \tag{4.5}$$

If for an excitation B_1 vanishes, we shall call it pure $\tau = 0$, whereas $B_0 = 0$ for a pure $\tau = 1$ excitation.

The expressions for B_0 and B_1 can be obtained as special cases from the general formula for B. This has been calculated by KS II under certain conditions. Following their derivation it is easy to get a generalized expression

$$\left.\begin{aligned} B = a^6 \Big\{ & |S^n\Big(1-\frac{\varkappa_n}{7}S^n\Big)|^{1/2} S^p e_p + \operatorname{sign}\Big(\varkappa_{np} S^p\Big(1-\frac{\varkappa_n}{7}S^n\Big)\Big) \\ & \times |S^p\Big(1-\frac{\varkappa_p}{7}S^p\Big)|^{1/2} S^n e_n \Big\}^2 \Big/ \Big\{ |S^n\Big(1-\frac{\varkappa_n}{7}S^n\Big)| \times S'^p \\ & + |S^p\Big(1-\frac{\varkappa_n}{7}S^p\Big)| S'^n \Big\}. \end{aligned}\right\} \quad (4.6)$$

Here,

$$\operatorname{sign}\{x\} = \frac{x}{|x|} \quad (4.7)$$

and S'^p is the derivative of S^p with respect to $\hbar\omega$, the energy of the excited state:

$$\left.\begin{aligned} S'^p = \frac{\partial S^p}{\partial(\hbar\omega)} = \sum_{jj'}^{p} \Big\{ & \frac{2\hbar\omega\, |\langle l'j' || i^3 Y_3 \Big(\frac{r}{a}\Big)^3 || lj\rangle|^2}{\big((E(j)+E(j'))^2 - (\hbar\omega)^2\big)^2} \\ & \times \big(E(j)+E(j')\big)\big(u(j)v(j') + v(j)u(j')\big)^2 \Big\}, \end{aligned}\right\} \quad (4.8)$$

S'^n being the analogous neutron quantity.

The quantities e_n and e_p are the effective charges of neutrons and protons, respectively.

Since we are taking all single-particle transitions into account, the effective charges for an $E3$ transition are the bare charges $e_p = e$ and $e_n = 0$. The expression for B_0, the $\tau = 0$ part of B, is obtained when using $e_p = e_n = 1/2$ in (4.6) while B_1 appears when $e_p = -e_n = 1/2$.

The following relation applies to the three quantities

$$B = e^2\big(\sqrt{B_0} \pm \sqrt{B_1}\big)^2, \quad (4.9)$$

where the minus sign should be used if

$$|S^p\Big(1-\frac{\varkappa_n}{7}S^n\Big)| < |S^n\Big(1-\frac{\varkappa_n}{7}S^p\Big)| \quad (4.10)$$

which, due to the neutron excess, often is the case.

If $\varkappa_1 = 0$ (but $\varkappa_0 \neq 0$) we obtain the simpler expressions

$$B = a^6 e^2 \frac{S^{p2}}{S'^p + S'^n}, \tag{4.11}$$

$$B_0 = a^6 \frac{(S^p + S^n)^2}{4(S'^p + S'^n)}, \tag{4.12}$$

$$B_1 = a^6 \frac{(S^p - S^n)^2}{4(S'^p + S'^n)}. \tag{4.13}$$

If $\varkappa_0 = 0$ and $\varkappa_1 \neq 0$ we get the same formula for B, whereas the expressions for B_0 and B_1 are interchanged because of the sign in the numerator in the general formula (4.6). For an arbitrary $\varkappa_0$, $\varkappa_1$ mixture the sign is sometimes positive, sometimes negative. For the strong states of low energy it is found to be positive in the calculations below.

Inelastic scattering

While B is connected to electromagnetic excitations, B_0 and B_1 are the relevant quantities in inelastic nucleon scattering.

When a particle passes through the nucleus, its motion is changed by the nuclear field and it interacts with the nucleons in a complicated manner.

In a simplified picture we may assume, however, that inside the nucleus the nucleons in a projectile interact with the nuclear field in very much the same way as the other nucleons do, and thus that the interaction essentially is of the form

$$\left.\begin{aligned} &\sum_{j,\mu} \{\varkappa_0 r_j^3 Y^*_{3\mu}(j) M(\tau = 0;\ \lambda = 3, \mu) \\ &+ 2\varkappa_1 \sum_{\nu} r_j^3 Y^*_{3\mu}(j)\, t^*_\nu M(\tau = 1, \nu;\ \lambda = 3, \mu)\}, \end{aligned}\right\} \tag{4.14}$$

where we sum over the nucleons j in the projectile. The $\tau = 1$, $\nu = \pm 1$ terms govern the charge exchange reactions considered below. For inelastic scattering without charge exchange the reduced transition probability will be proportional to

$$\left(\varkappa_0 \sqrt{B_0} \pm \varkappa_1 \sqrt{B_1} \frac{\sum_j 2t_0(j)}{k}\right)^2 \tag{4.15}$$

or

$$B_0\left(1 + b\sum_j \frac{2t_0(j)}{k}\right)^2, \tag{4.16}$$

where

$$b = \pm\frac{\varkappa_1}{\varkappa_0}\sqrt{\frac{B_1}{B_0}} \tag{4.17}$$

and k is the number of nucleons in the projectile. The plus sign should be used if $B_0 < B$ and the minus sign if $B_0 > B$. We note that we here have utilized the assumption of the simple isospin dependence of the interaction (4.14), whereas the precise dependence on the radial coordinate of the projectile nucleons is of minor importance.

Here, as in the following, we neglect the electromagnetic part of the excitation when we consider inelastic nucleon scattering.

The numerical value of the factor $\sum_j \frac{2t_0(j)}{k}$ in (4.16) is maximal when the projectile contains only one kind of nucleons, i.e. when $k = 1$. If the projectile contains both protons and neutrons, the B_1 part is somewhat washed away, and (4.16) comes closer to B_0.

The expression is simplified if either the total isospin of the projectile is zero, as for α-particles and deuterons, or if the relevant nuclear field with which it interacts is isospin independent ($\varkappa_1 = 0$). Then we get B_0. This means that we are exciting just the $\tau = 0$ part of the vibration.

If the excitation is either pure $\tau = 0$ or $\tau = 1$, only one of the terms survives, but in practice this situation is never reached (cf. sections 7 and 9).

One of the more interesting features in the expression is the interference between the two terms. Even when the state is fairly pure in τ character, i.e. $B_0 \gg B_1$ or $B_1 \gg B_0$, this interference gives rise to considerable variations in the relative cross sections, using projectiles with different isospin (cf. sect. 11).

Since the experimental material contains mainly measurements of B, and since the underlying theory for electromagnetic processes is more reliable than the theory of direct reactions, we will preferably discuss this quantity. However, we note that inelastic scattering, using different particles, may give in the future most valuable information on the structure of the excitations.

Charge exchange scattering

In the preceding section, we have discussed the inelastic processes connected to $\tau = 0$ and $\tau = 1$, $\nu = 0$ excitations. Now, whereas the $\tau = 0$ part

of the interaction only gives rise to scattering, the $\tau = 1$ part may flip the isospin of an incoming nucleon, i.e. give rise to charge exchange reactions, involving excitations of $\tau = 1$, $\nu = \pm 1$ character. Let us consider a (p,n) process.

We use again the simplified expression (4.14) for the interaction between the incoming particle and the nucleus. For the $\tau = 1$ part the ratio between the nuclear matrix elements for isospin flip to non-isospin flip of the nucleon is given by

$$\left.\begin{aligned} &\frac{\langle T_1 - T_1 + 1, \beta | M(\tau = 1,\ \nu = 1) | T_1 - T_1 \rangle}{\langle T_1 - T_1, \beta | M(\tau = 1,\ \nu = 0) | T_1 - T_1 \rangle} \\ &= \frac{\langle T_1 - T_1 11 | T_1 - T_1 + 1 \rangle \langle T_1 || M(\tau = 1) || T_1 \rangle}{\langle T_1 - T_1 10 | T_1 - T_1 \rangle \langle T_1 || M((\tau = 1 || T_1 \rangle} \\ &= \sqrt{\frac{1}{T_1}}, \end{aligned}\right\} \tag{4.18}$$

$| T_1 - T_1 + 1, \beta \rangle$ being a state in an odd-odd nucleus which is the isobaric analogue to the vibration $| T_1 - T_1, \beta \rangle$ in the target. Thus, by studying the relative probabilities for exciting low-energy states in the target and analogues in the odd-odd nucleus by protons we are able to learn something about the isospin dependence in the interaction between projectile and target.

Scattering via isobaric analogues and stripping

Without going into details we shall briefly sketch how we can obtain information on the structure of the octupole vibrations from stripping experiments and from inelastic proton scattering via isobaric analogue states (states with $T \neq -T_z$). For the sake of simplicity we only consider the last type of experiments. The generalization to stripping is straightforward.

When bombarding a nucleus, say (N_1, Z_1) which has $(T, T_0) = (T_1, -T_1)$, with protons, we are able to form various states $| N_1, Z_1 + 1, \beta \rangle$ with $(T, T_0) = (T_1 + \frac{1}{2}, -T_1 + \frac{1}{2})$ in the compound nucleus $(N_1, Z_1 + 1)$, which are isobaric analogues to states $| N_1 + 1, Z_1, \beta >$ with $(T, T_0) = (T_1 + \frac{1}{2}, -T_1 - \frac{1}{2})$ of low excitation energy in the nucleus $(N, Z) = (N_1 + 1, Z_1)$. The reaction amplitude for the entrance channel is proportional to

$$\langle N_1, Z_1 + 1, \beta | a^+ (\text{proton}) | N_1, Z_1, \text{ ground state} \rangle \tag{4.19}$$

in analogy to

$$\langle N_1 + 1, Z_1, \beta | a^+ (\text{neutron}) | N_1, Z_1, \text{ ground state} \rangle, \tag{4.20}$$

the square of which is a spectroscopic factor for a (d,p) process leading from the target ground state to the low excited state β in the nucleus $(N,Z) = (N_1+1, Z_1)$. Now, the compound state may decay by proton emission to some state in the target. In the decay the amplitude is determined by

$$\langle N_1, Z_1, \gamma \,|\, a\,(\text{proton}) \,|\, N_1, Z_1+1, \beta \rangle, \tag{4.21}$$

which (if β is not the analogue to the ground state) corresponds to a pick-up spectroscopic factor for neutron pick-up from an excited state in the target (N_1+1, Z_1) to a state γ in the final nucleus (N_1, Z_1).

One possibility of learning something about the structure of the octupole oscillations is thus to bombard an even Z odd N target with protons to form a 3^- isobaric analogue state in the compound nucleus. When this state decays through the different proton channels, this "pick-up" process provides information on the occupation of the different single-particle states in the 3^- oscillation.

As a simplified example, let the final state in the target be a single quasiparticle (j',m') + a quasiparticle vacuum, which is assumed to be the same as that in the compound nucleus, and let the emitted proton have quantum numbers j, m. The channel state is

$$\sim \sum_{\substack{m \\ m'}} a^+(j,m,t_0 = \tfrac{1}{2})\alpha^+(j',m',t_0' = -\tfrac{1}{2})\langle jmj'm' \,|\, 3\mu \rangle |\, 0 \rangle \tag{4.22}$$

and the decaying state is the isobaric analogue to

$$B^+(3,\mu,\alpha)\,|\,0'> \tag{4.23}$$

(a one-phonon state with $\lambda = 3$, μ). By $|\,0\rangle$ and $|\,0'\rangle$ we denote the relevant phonon vacua. The overlap is

$$\sim u(j,m)p(\alpha,j,j'), \tag{4.24}$$

where $p(\alpha,j,j')$ is the amplitude for the j,j' two-quasiparticle excitation in the oscillation α.

When obtaining this result we have neglected the overall reduction factor $2T+1$ which appears in the transition probability for proton decay of an isobaric analogue state. This factor is easily understood, since we imagine that the isobaric analogue state can be formed by applying the isospin raising operator T_+ to the low-energy state in the $(N+1, Z)$ nucleus, i.e. by transforming a neutron into a proton. However, there are $2T+1$ excess neutrons which can be transformed. Thus, the particle with quantum numbers j,m only has the probability $(2T+1)^{-1}$ of having $t_0 = 1/2$ in the decaying analogue state.

Another possibility to learn something about the structure of the octupole oscillations is to study inelastic proton scattering from an even-even target via an isobaric analogue state in the compound system to a 3^- oscillation in the target. In a naive approach we think of using preferably isobaric states which are known (or expected) only to contain to a very small amount a component of a single particle coupled to a 3^- state. In a decay of the analogue state in which a proton is emitted, leaving a hole together with the "last odd particle", we may thus directly gain information on the probability that the target 3^- state contains just this specific particle-hole component.

Let us therefore assume, for simplicity, that the compound state is just the analogue to a single quasiparticle + a quasiparticle vacuum, which is the same as for the target. Let again j, m be the quantum numbers for the emitted particle and j', m' those for the odd nucleon.

The channel state is

$$\sum_{m,\mu} a^+(j,m,t_0 = \tfrac{1}{2}) B^+(3,\mu,\alpha) \langle jm3\mu | j'm' \rangle |0> \tag{4.25}$$

and the decaying state the isobaric analogue to

$$\simeq \alpha^+(j',m',t_0' = -\tfrac{1}{2}) |0'>. \tag{4.26}$$

The overlap is

$$\simeq v(j,m) p(j,j',\alpha) \sqrt{\frac{7}{2j'+1}} . (-1)^{j-j'}. \tag{4.27}$$

Again a reduction factor $(2T+1)^{-1}$ is introduced in the decay probability, when the isospin structure of the states is taken into account.

The major difference between the quadrupole and the octupole vibrations is that, whereas the first ones are in general built up by many two-quasiparticle excitations of roughly the same energy and thus with amplitudes of comparable magnitude, the octupoles are often (cf. sect. 12) formed by some few unperturbed modes. For these modes the amplitudes are rather large (of the order of magnitude of unity) and thus more easy to measure.

Sum rules

In the analysis of transition strengths for multipole excitations the sum rules for reduced transition probabilities play a significant role.

The energy weighted sum of B values is given by the formula (ref. BM).

$$\sum_f (E_f - E_i) B(E3;\ i \to f) = \frac{147\hbar^2}{8\pi M} e^2 \sum_p \langle i | r_p^4 | i \rangle . \tag{4.28}$$

In the first sum we start from a state i, e.g. the ground state, and sum over all states f, which can be reached by an $E3$ excitation. E_f and E_i are the two relevant energies. The last sum runs over all protons p.

From the derivation one immediately generalizes to get the corresponding sums for B_0 and B_1 for the excitations from the ground state:

$$\left.\begin{aligned} &\sum_\alpha (E_\alpha - E_0) B(\tau = 0;\ 0 \to 3-, \alpha) \\ &= \sum_\alpha (E_\alpha - E_0) B(\tau = 1,\ \nu = 0;\ 0 \to 3-, \alpha) \\ &= \frac{147\hbar^2}{8\pi M} \left\{ \tfrac{1}{4} \sum_p \langle r_p^4 \rangle + \tfrac{1}{4} \sum_n \langle r_n^4 \rangle \right\} . \end{aligned}\right\} \tag{4.29}$$

Here, p denotes protons, n neutrons. The index α runs over all available 3^- states in the nucleus. The expectation values of r^4 should be evaluated in the ground state. These expressions are slightly model dependent. In the derivation it is supposed that the multipole operator and the Hamiltonian commute, except for the kinetic energy part. This implies that the shell-model potential is velocity independent and that it is permissible to neglect exchange effects. This is consistent with our approximations when we only consider the $\nu = 0$ excitations. Then we may use an octupole-octupole force which contains only the factor

$$\varkappa_0 + 4\varkappa_1 t_0(i)\, t_0(j) \tag{4.30}$$

which commutes with $M(\tau = 1, \nu = 0)$ as well as with $M(\tau = 0)$.

The single contributions to the sums ((4.28) and (4.29)) and the total sums we call oscillator strengths and total oscillator strengths, respectively. If the protons and neutrons contribute with equal amounts to the sums, then the total B oscillator strength is twice the B_0 strength.

Due to the neutron excess, the contribution from the neutrons is actually often twice as high as that from the protons, which means that the total B strength is 4/3 of the B_0 strength. This is partly due to an oversimplification in our treatment, because we use the same frequency in the harmonic oscillator potential for protons and neutrons. Thus, the protons are kept closer to the nuclear centre, and $\sum_p \langle r_p^4 \rangle$ is too small. A better treatment would be to use, e.g., Saxon-Wood potentials for protons and neutrons.

When making the transformation from the unperturbed two-quasiparticle excitations to the resulting excitations, the total oscillator strengths are unchanged. This is a purely mathematical statement.

Thus the magnitude of the total B,B_0 and B_1 strengths may be calculated, e.g., in a simple model of non-interacting particles in a pure harmonic oscillator potential.

When using a model in which the levels closest to the Fermi energy λ are chosen empirically, as we do below, we introduce an element of inconsistency, due to the fact that we are not sure that these levels can be calculated with the help of any velocity independent potential. It is also immediately seen that, when pushing levels around in a somewhat arbitrary way, the total oscillator strengths cannot be expected to be constant. Since, however, this pushing concerns mainly levels near the Fermi level and some of them move up and others move down, the effect is actually very small (at most some few percent).

Sometimes the so-called isospin zero part of the total B oscillator strength is considered (ref. 11). This quantity is Z/A times the total strength and in our treatment it has not any very distinct meaning.

5. Octupole coupling in simple examples

Before discussing the spectra of real nuclei it may be instructive to consider the simple case of one proton line and one neutron line coupled by the octupole force.

To obtain a measure for the strength of the excitations it is convenient to define

$$F^p = \tfrac{1}{2}\sum_{j_1 j_2}^{p} |\langle l_2 j_2 || i^3 Y_3 \left(\frac{r}{a}\right)^3 || l_1 j_1 \rangle|^2 \big(u(j_1)v(j_2) + v(j_1)u(j_2)\big)^2 \qquad (5.1)$$

summing over all the proton states j_1 and j_2. The analogous neutron quantity is F^n. The factor $\frac{1}{2}$ is chosen because each term in the sum appears twice.

When the two lines are of equal energy and strength ($F^p = F^n$) the resulting spectrum consists of a pure $\tau = 0$ mode and a pure $\tau = 1$ mode. For the first one, energy and strength are determined only by $\varkappa_0$, the $\tau = 0$ part of the force, and for the second one only by $\varkappa_1$ (fig. 1).

When $F^p \neq F^n$, but the two lines remain in the same position, the resulting modes become of mixed isospin character, but still the low-energy mode

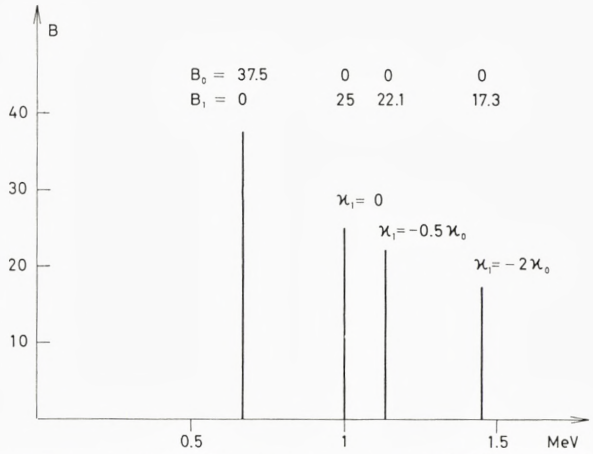

Fig. 1. Position of the two resulting lines for constant $\varkappa_0$ and different values of $\varkappa_1$, when the unperturbed spectrum consists of a protron line $F^p = 50$, and a neutron line $F^n = 50$, both placed at 1 MeV. The line of lowest energy is independent af $\varkappa_1$. B, B_0 and B_1 are given in arbitrary units, obtained when $a = 1$ (cf. equation (4.6)).

is mainly $\tau = 0$, determined by $\varkappa_0$, and the high-energy mode mainly $\tau = 1$, determined by $\varkappa_1$ (fig. 2). This is correct, even if there is rather strong asymmetry in the unperturbed spectrum.

When $\varkappa_0$ is constant and $-\varkappa_1$ increases, the low state becomes purer with respect to isospin. This may be considered in two ways.

1) When $\varkappa_1$ is introduced, it sucks some of the $\tau = 1$ part from the low excitation, which then becomes purer. Thus B_1 decreases while B and B_0 approach each other.
2) When $\varkappa_1$ is introduced, $\varkappa_n$ and $\varkappa_p$ are diminished whereas the proton-neutron force becomes stronger. If, e.g., the state is preferably built up by neutron excitations ($F^n > F^p$), they lose influence and more proton excitations are mixed in. Thus, B increases while B_0 decreases. (The strong component of the excitation is weakened).

It is interesting to note that even when $\varkappa_1 = -2\varkappa_0$ (the *nn* and *pp* forces are repulsive) there is a low-energy collective state. The reason is, that now $\varkappa_{np} = 3\varkappa_0$, i.e. the neutron-proton force is strongly attractive. For the high-lying mode the energy goes up when $-\varkappa_1$ and thus $\varkappa_{np}$ increases, since it becomes more difficult to separate neutrons from protons. From the sum rules it follows immediately that when $F^p \neq F^n$ the two resulting modes cannot at the

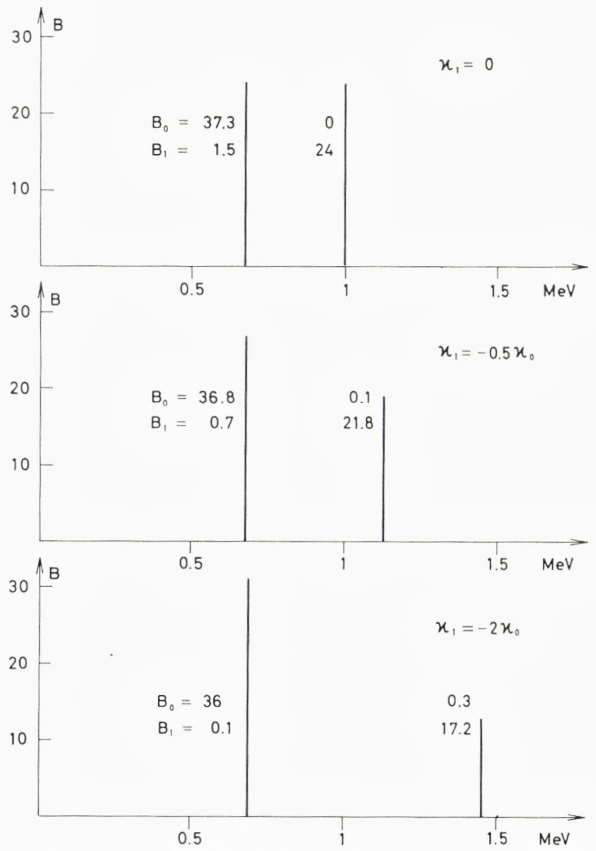

Fig. 2. Spectra for constant $\varkappa_0$ and different values of $\varkappa_1$, when the unperturbed spectrum is $F^p = 40$ in 1 MeV and $F^n = 60$ in 1 MeV. Again $a = 1$ (see fig. 1).

When $\varkappa_1 = -0.5$ times the $\varkappa_0$ value from the figure, but $\varkappa_0 = 0$, a line with $B = B_0 = 24$, $B_1 = 0$ appears in 1 MeV and another one with $B = 14.1$, $B_0 = 0.9$ and $B_1 = 22.1$ in 1.14 MeV.

same time be of pure isospin type. When $\varkappa_1$ is introduced, the low-energy mode becomes of $\tau \simeq 0$ type, but then the high-energy mode must be of mixed isospin character, i.e. $B_0 \neq 0$.

Let us now proceed to the other possibility for asymmetry in the unperturbed spectrum, viz. the case where $F^n = F^p$ but the two lines have different energies (fig. 3). The variations in B are easily understood, when it is remembered that if $\varkappa_1$ is introduced, e.g. more of the high-energy unperturbed mode is mixed into the resulting state of lowest energy. It is obvious that when the forces are so strong that the distance between the two resulting

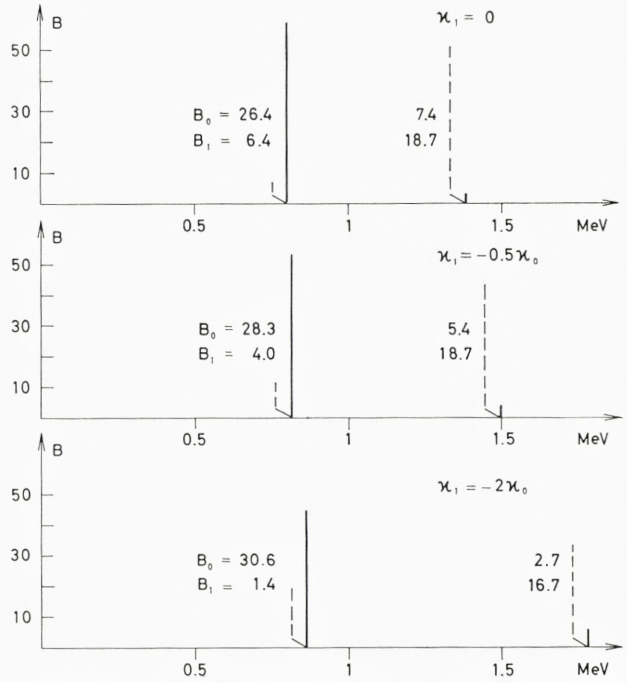

Fig. 3. Spectra for constant $\varkappa_0$ and different values of $\varkappa_1$, when the unperturbed spectrum is $F^p = 50$ in 1 MeV and $F^n = 50$ in 1.5 MeV. When F^p and F^n are interchanged, B gets the values indicated by dashed lines, while B_0 and B_1 are unaffected. Again $a = 1$ (see fig. 1).

modes is much greater than the distance between the unperturbed lines, we are again close to the symmetric case of fig. 1, but we learn that the situation with rather pure modes is reached much earlier.

6. Effects of shell structure

In order to obtain qualitative insight into the manner in which the shell structure affects the resulting spectrum we shall in this section, in some simple examples, study the energy distribution of B oscillator strength, using an isospin independent octupole force.

Let us first consider a system of non-interacting particles in a pure harmonic oscillator potential.

By 3^- excitations a particle can be raised either one or three shells, giving one group of excitations at an energy $\hbar\omega_0$ and another one at $3\hbar\omega_0$.

To find the oscillator strength distribution on these two groups we define, for the proton excitations (cf. (5.1))

$$F_1^p = \tfrac{1}{2} \sum_{|\Delta N = 1|} |\langle l_2 j_2 || Y_3 \left(\frac{a}{r}\right)^3 i^3 || l_1 j_1 \rangle|^2 \big(u(j_1) v(j_2) + v(j_1) u(j_2)\big)^2, \quad (6.1)$$

$$F_2^p = \tfrac{1}{2} \sum_{|\Delta N = 3|} |\langle l_2 j_2 || Y_3 \left(\frac{a}{r}\right)^3 i^3 || l_1 j_1 \rangle|^2 \big(u(j_1) v(j_2) + v(j_1) u(j_2)\big)^2, \quad (6.2)$$

where ΔN is the change in principal quantum number from j_1 to j_2.

Analogous quantities F_1^n and F_2^n are defined for neutrons. Apart from a trivial factor, F_1^p is simply the sum of the B values for all the transitions to the states of excitation energy $\hbar\omega_0$, i.e.

$$\sum_{\alpha(\Delta N = 1)} B(E3;\ 0 \to 3-, \alpha) = e^2 a^6 F_1^p. \quad (6.3)$$

It is easy to calculate F_1^p, and F_2^p can then be found from the energy weighted sum of B values (4.28).

For the lightest nuclei $F_1^p = 0$, since a $3\hbar\omega_0$ transition is needed to form a 3^- state. In the limit of very heavy nuclei $F_1^p \simeq F_2^p$.

For $Z = 20$ we get $F_1^p/F_2^p = 70\,\%$, for $Z = 40$ we obtain $76\,\%$ and for $Z = 70$ the ratio is $82\,\%$. This means that in a very large Z interval the sum of B values for excitations of energy $\hbar\omega_0$ is approximately 3/4 of the sum of B values for $3\hbar\omega_0$ excitations. The $\Delta N = 1$ excitations contribute about $20\,\%$ to the total B oscillator strength.

When we introduce an isospin-independent octupole-octupole force between the nucleons, the neutron and proton excitations at $\hbar\omega_0$ couple and give an unshifted line at $\hbar\omega_0$ and a line with lower energy, as explained in the preceding section (cf. fig. 1). The same is the case for the neutron and proton excitations at $3\hbar\omega_0$, and finally there is a coupling between the lines in the two energy regions. This is illustrated by fig. 4. The $\varkappa$ value is taken from the detailed calculation below, where it is fitted by the experimental data. We see that the introduction of the octupole force does not push the lines very far down, and the oscillator strength, placed on the low lines, is almost unchanged. This result is, however, very sensitive to the strength of the octupole force. If $\varkappa$ is increased by about $35\,\%$, the low line comes down to zero energy, i.e. the spherical shape becomes unstable in this model.

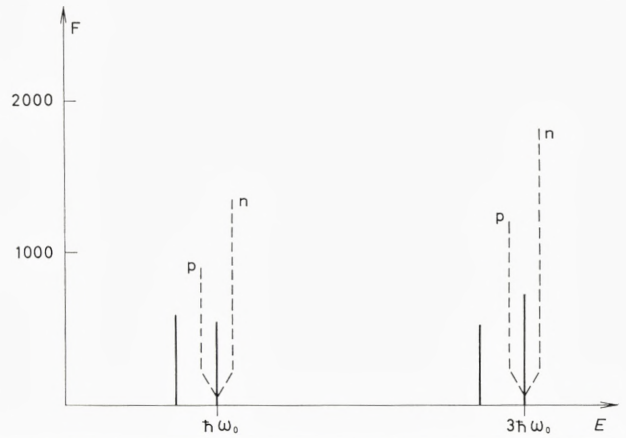

Fig. 4. Resulting spectrum for a simple model of the nucleus $A,Z = 90,40$, when $\varkappa_1 = 0$ and $\varkappa_0 \neq 0$. The unperturbed lines are dashed, the resulting ones fully drawn. The proton and neutron lines are denoted by p and n, respectively. The unperturbed lines are concentrated in $\hbar\omega_0$ (= 9.15 MeV) for $\Delta N = 1$ and in $3\hbar\omega_0$ for $\Delta N = 3$, and they are represented by their strength F, introduced in the text ((5.1) and (6.1)). For the resulting states $F = \frac{(S^p)^2}{S'}$, where $S' = S'^p + S'^n$. The value for $\varkappa_0$ has been taken from the detailed calculation (sect. 15). If S is 35% smaller, i.e. if $\varkappa_0$ is 35% greater, the spherical shape becomes unstable. In the unperturbed spectrum the $\Delta N = 1$ lines contribute with 20% to the total B oscillator strength. The two resulting lines of lowest energy contribute with 21.5%, the lowest one alone with 9.5%.

The spectrum is independent of the atom number A under the following conditions: 1) The slow change in the ratio F_1^p/F_2^p with A is neglected, 2) The ratio between neutrons and protons is kept constant, 3) The coupling constant $\varkappa$ varies like A^{-2}. This $\varkappa$ variation was suggested in section 2 by a simple scaling argument.

The deviation of the actual central nuclear field from that of a harmonic oscillator has important effects on the octupole spectra. Thus, the broadening of the shells leads to a smearing out of the oscillator strengths in the $\hbar\omega_0$ and the $3\hbar\omega_0$ regions.

Of special significance for the low-energy spectra is the spin-orbit splitting which pushes levels down to the shells below. This means that inside the partly filled shell there are transitions (a weak and a strong one, depending on whether spin flip is involved or not) the energies of which are prevented from going to zero essentially only by the pairing gap. The effect begins to be of importance with the $4g_{9/2}$ level around $A = 80$. It is illustrated by a simple model in fig. 5. For the first excited state $S(= S^p + S^n)$ and thus the energy is largely determined by the low-energy unperturbed line, but B receives very substantial contributions from the higher lines.

For a more detailed study of the effect of the spread in the single-particle spectrum we go on to fig. 6. In fig. 6a all the low-energy single-particle

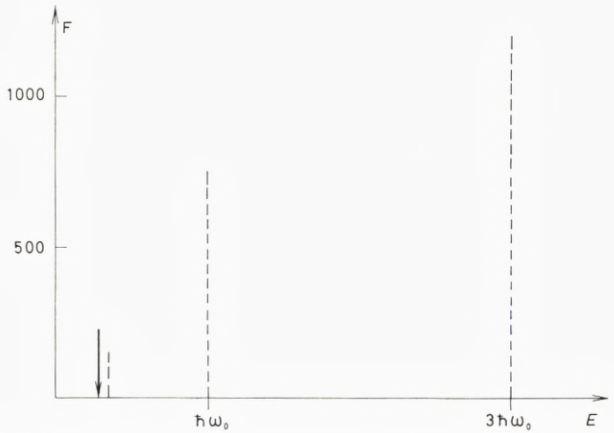

Fig. 5. Illustration of the influence of the strong transition inside the partly filled shell to the lowest resulting line for the nucleus $A,Z = 90,40$. The strengths F_1^p and F_2^p are placed in $\hbar\omega_0$ and $3\hbar\omega_0$, respectively, with the exception that the strong $3p_{3/2} - 4g_{9/2}$ line is placed at the expected position 3.27 MeV $\simeq 1/3\hbar\omega_0$ (shown by dashed lines). The situation here is especially favourable to the low energy transition, since for this one the $u\ v$ factor in the numerator in S is almost equal to unity. (The transition goes from an almost filled to an almost empty level). In the detailed calculation (sect. 15), the collective mode of lowest energy occurs at 2.61 MeV (shown by an arrow). If we use this energy in the model, $S_1^p = 434$ and $S_2^p = 90$. The contribution to S^p from the lowest-lying unperturbed line is 254. We can illustrate the influence of the higher-lying unperturbed lines on B in the following way. Let us first calculate B by taking only S^p and S'^p from the transition of lowest energy into account, subsequently by including all the $\Delta N = 1$ lines, and finally by also including the $\Delta N = 3$ lines (keeping E fixed). In this case, the ratio of B values is 1 : 2.9 : 4.2. In the detailed calculation $S_1^p = 537$, which is more than found above, because of the influence of the broadening of the shells. The quantity S_2^p should be changed less. Using the value from above, $S_2^p/S_1^p \sim 90/537 \sim 17\,\%$, which should be a reasonable value.

transitions are placed as in a preliminary calculation, roughly equal to that in sect. 15. All the high-energy transitions are placed at $3\hbar\omega_0$. As a standard nucleus Sn^{116} is chosen.

Fig. 6b shows the picture when the octupole force is introduced. In the low-energy region two strong lines appear, one governed primarily by the transitions inside partly filled shells, and another one by the transitions between neighbouring shells. From table 1 it appears that these two lines contain about $10\,\%$ of the total B oscillator strength, i.e. the same amount as the line of the lowest energy in the simple harmonic oscillator picture in fig. 4.

In the medium region around $\hbar\omega_0$ many weak lines show up. In total they contain $23\,\%$ of the B oscillator strength, which is $5\,\%$ more than when $\varkappa_0 = 0$.

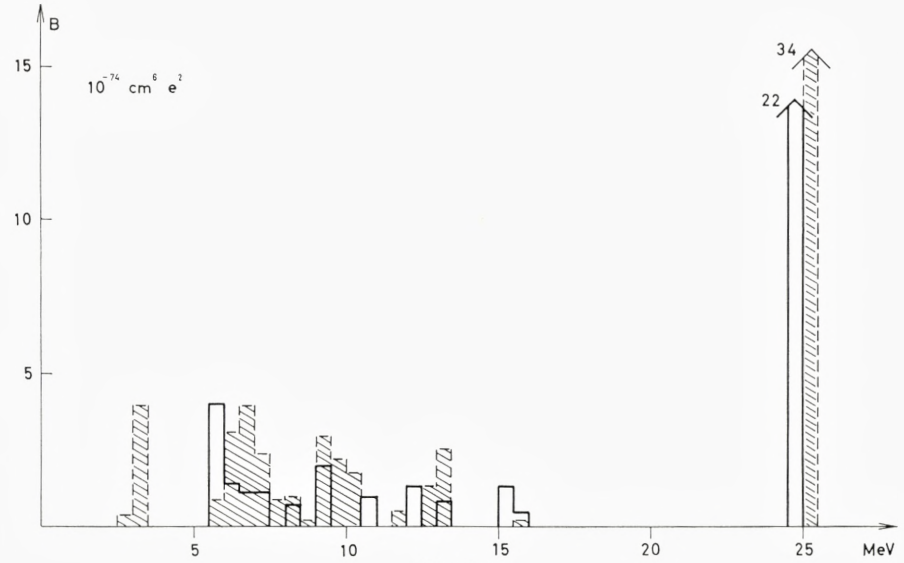

Fig. 6a.

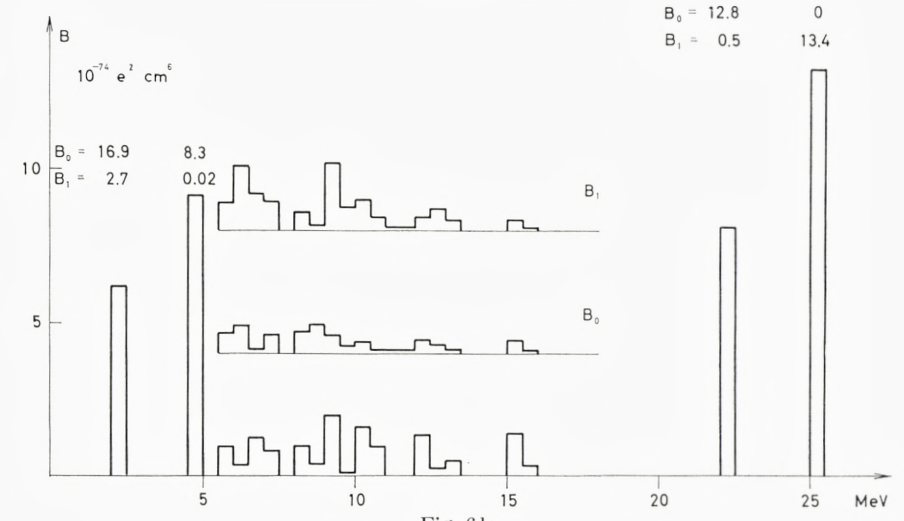

Fig. 6b.

Fig. 6. Histogram of the energy distribution of B values for Sn^{116}.

a) The unperturbed spectrum with the proton lines fully drawn and the neutron ones dashed. The $\Delta N = 3$ levels are concentrated in $3\hbar\omega_0$. The position of the $\Delta N = 1$ levels comes from a preliminary calculation and is somewhat different from the values used in section 15. The B value in a) is calculated with an effective charge e on all nucleons.

b) The spectrum when the isospin independent octupole force is introduced ($S = 0.578 \times A^{5/3}$, which corresponds closely to $S_1 = 0.45 \times A^{5/3}$ used below). For the medium region around $\hbar\omega_0$, histograms of B_0 and B_1 are inserted. For the strong lines above and below this energy region, B_0 and B_1 are written above the lines. B_1 and B_0 are in units of 10^{-74} cm^6.

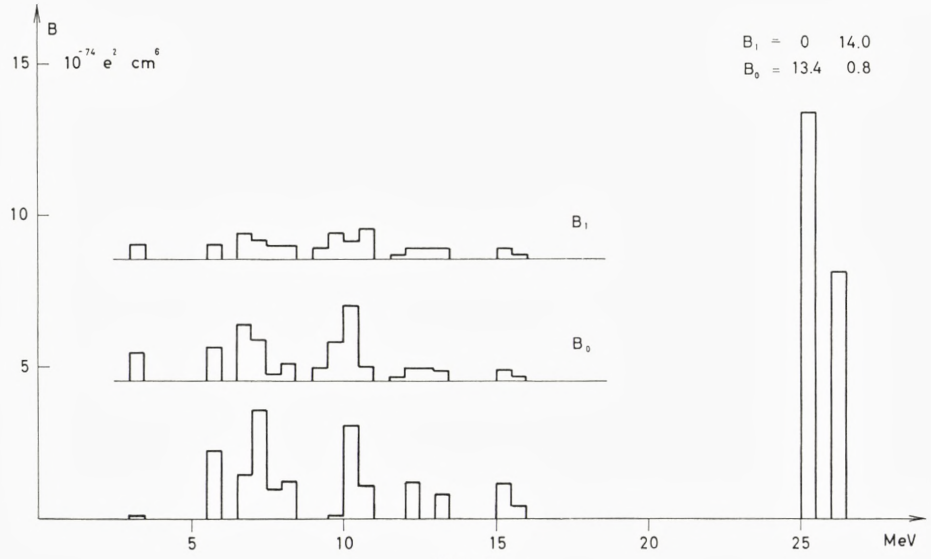

Fig. 6 c.

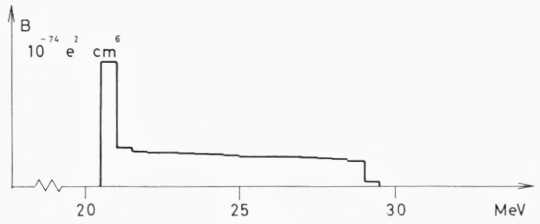

Fig. 6 d.

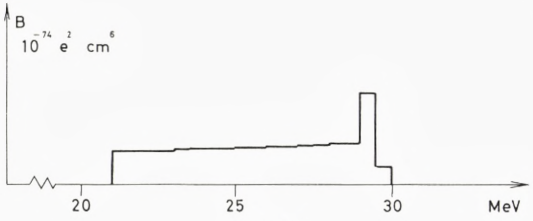

Fig. 6 e.

Fig. 6. Histogram of the energy distribution of B values for Sn^{116}.

c) B, B_0 and B_1 for $\varkappa_1 = -$ half the $\varkappa_0$ value from b) and $\varkappa_0 = 0$.

d) The spectrum in the $3\hbar\omega_0$ region when F_2 is smeared out between 2.5 $\hbar\omega_0$ and 3.5 $\hbar\omega_0$ and $\varkappa_0$ is the same as in b). (For computational reasons the region of proton F_2 lines is pushed down 0.2 MeV compared to the neutron F_2 region).

e) The change from d), when $\varkappa_1$ like in c) and $\varkappa_0 = 0$.

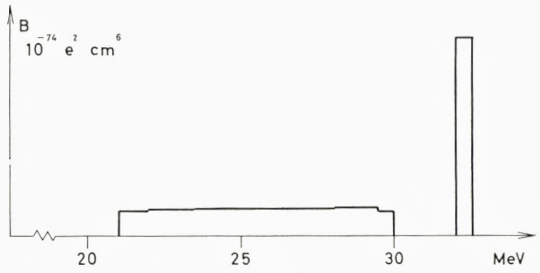

Fig. 6 f.

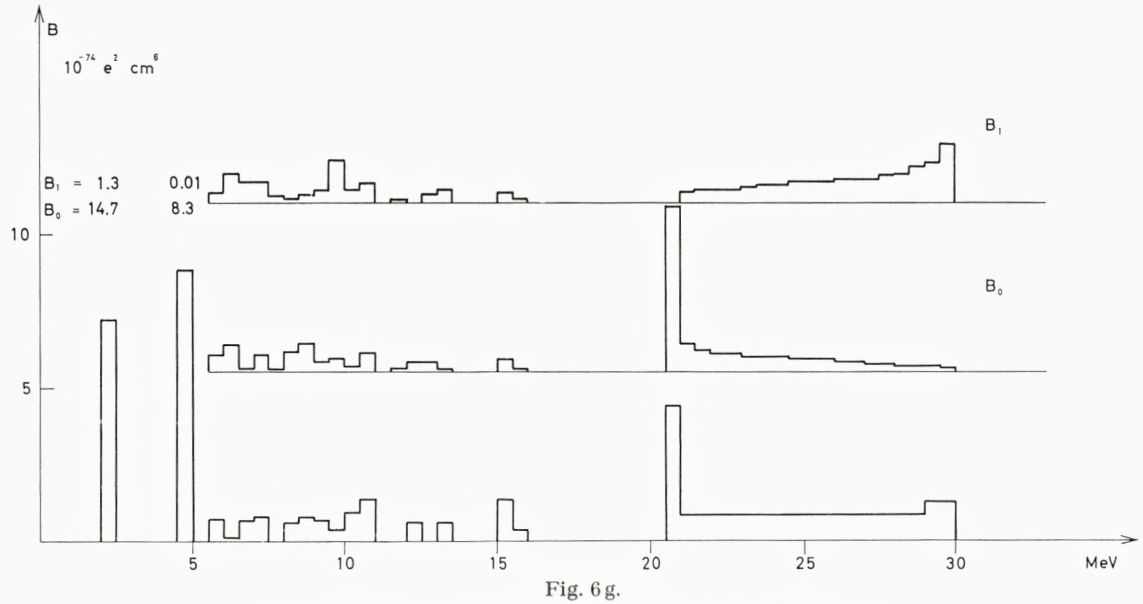

Fig. 6 g.

Fig. 6. Histogram of the energy distribution of B values for Sn^{116}.

f) The change from d), when $\varkappa_0 = 0$ and $\varkappa_1$ four times stronger than in c).

g) Histograms of B, B_0 and B_1 when $\varkappa_0$ has the same value as in b) and $\varkappa_1 = -0.5\,\varkappa_0$. The unperturbed spectrum is for F_1 the same as in a) and for F_2 the same as in d).

Finally, we get two high-energy, strong lines. They are not realistic but appear because of the concentration of the F_2 transitions at $3\hbar\omega_0$.

To get some insight into the way in which smearing out of the $3\hbar\omega_0$ transitions affects the picture we consider a crude model, the main results of which are shown in figs. 6 d, e and f (figs. 6 e and 6 *f* are discussed in sect. 8). The unperturbed $3\hbar\omega_0$ lines are distributed with constant density between $2.5\hbar\omega_0$ and $3.5\hbar\omega_0$. This change in the model from above affects the lines only slightly in the $\hbar\omega_0$ domain, and therefore they are not shown.

TABLE 1. Contributions (here called relative oscillator strengths) to the energy-weighted sum of B, B_0 and B_1 for the two low-lying strong levels in the resulting spectrum of Sn^{116} from the model of fig. 6 and for the two high-lying levels which occur when F_2 is concentrated at $3\hbar\omega_0$.

The data are given for a pure $\varkappa_0$ force (denoted $\varkappa_0$) (the force from fig. 6 b), for a mixed force with same $\varkappa_0$ and $\varkappa_1 = -0.5\,\varkappa_0$ (denoted $\varkappa_0+\varkappa_1$) (the force from fig. 6 g), for this value of $\varkappa_1$ and $\varkappa_0 = 0$ (denoted $\varkappa_1$) (force from fig. 6 c), and for $\varkappa_1$ four times greater and still $\varkappa_0 = 0$ (denoted $4\varkappa_1$). Finally, "none" means the sum fractions from the unperturbed spectrum, i.e. when $\varkappa_0 = \varkappa_1 = 0$.

levels	force	rel. B osc. str.	rel. B_0 osc. str.	rel. B_1 osc. str.
two low-energy strong levels	$\varkappa_0$	7 %	17 %	1 %
	$\varkappa_0+\varkappa_1$	8 %	17 %	$^1/_2$ %
two high-energy levels	$\varkappa_0$	67 %	64 %	80 %
	$\varkappa_1$	72 %	80 %	83 %
	$4\varkappa_1$	77 %	79 %	91 %
	$\varkappa_0+\varkappa_1$	67 %	64 %	83 %
	none	72 %	79 %	79 %

As was to be expected, the oscillator strength is pushed somewhat to the low-energy end of the region, where stronger lines are built up, while a great part is left as a rather constant background (fig. 6 d).

We note that the force is not able to form a very strong line in the gap between F_1 and F_2. This is partly due to a cancellation effect; the contributions to S from F_1 and F_2 have opposite signs. Attempts to press a greater part of the oscillator strength down from the $3\hbar\omega_0$ region does not result in the formation of a strong line in the gap, but makes the strength go further down to the $\hbar\omega_0$ region. If only the $3\hbar\omega_0$ unperturbed lines are included in the Sn spectrum, the $\varkappa_0$ value from fig. 6 d is just strong enough to place the resulting state of lowest energy at the edge of the F_2 region. When $\varkappa_0$ is made twice as large, the state comes down from 20.61 MeV to 17.95 MeV and the contribution to the total B oscillator strength increases from 21 % to 32 %. If $\varkappa_0$ is once more multiplied by two, we are very near unstability of the spherical shape of this fictive nucleus. The state appears at 7.63 MeV, but only contains 38 % of the B oscillator strength and 62 % are still left in the $3\hbar\omega_0$ region.

From the discussion above we expect the spectrum in a nucleus to consist of some few, strong lines of low energy (2–5 MeV) and many weak ones distributed rather uniformly in the $\hbar\omega_0$ and $3\hbar\omega_0$ regions.

When going from nucleus to nucleus the qualitative picture of the spec-

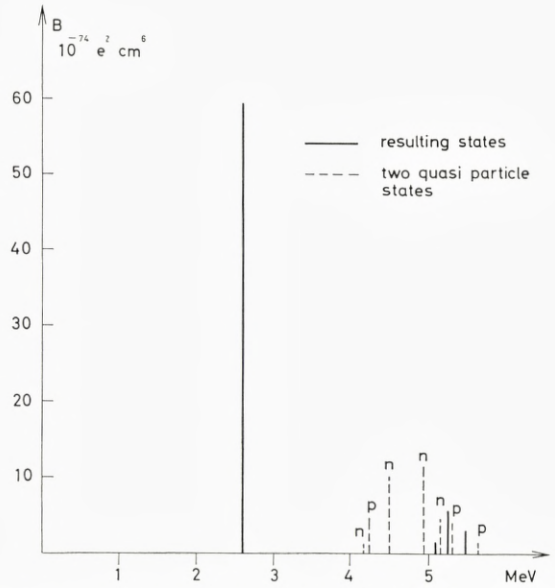

Fig. 7. The B values in the low-energy spectrum in $A,Z = 208,82$. Resulting lines fully drawn, unperturbed dashed. p and n denote proton and neutron two-quasiparticle excitations, respectively. The B values in the unperturbed spectrum are calculated by giving all particles effective charge e. Note that the proton lines of highest energy indicate the start of the "continuum" of states in the $\hbar\omega_0$ region.

The single-particle levels come from a preliminary calculation, using the same neutron levels as in case 9a and KSII proton levels (cf. sect. 15):

$g_{7/2}$: 0, $d_{5/2}$: 0.8, $h_{11/2}$: 2.1, $d_{3/2}$: 2.6 and $s_{1/2}$ 2.95 MeV. In this calculation $c_0 = 0.413$.

trum in these two regions should vary rather slowly, the variations being essentially brought about by the changes in intershell distances and the broadening of the shells.

The low-energy, strong states are expected to vary much more quickly in position and B value, since they are very dependent on the energy and the number of particles available for the transitions inside the partly filled shells. This is the reason why we concentrate on this part of the spectrum in the detailed investigation below.

The fine structure in the low-energy part of the unperturbed spectrum has a strong influence on the distribution of the oscillator strength among the very lowest-lying resulting states. We shall give some characteristic examples in concluding this survey of the qualitative features of the spectrum. The examples are chosen from the numerical calculation in sect. 15.

The general, well-known trend is that the level of lowest energy has a

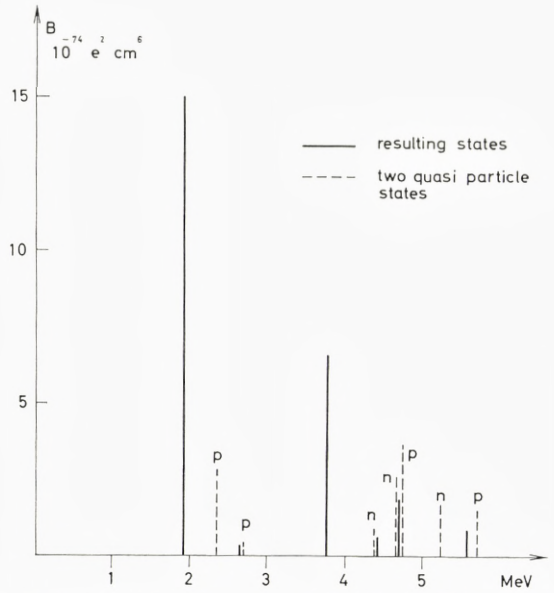

Fig. 8. The B values in the low-energy spectrum in $A,Z = 142,60$ (case 8a in section 15). Same notation as in fig. 7.

small $S' = S'^{p} + S'^{n}$ and thus a great B, whereas the opposite is true for the following ones.

An example is given by the double magic Pb^{208}, for which the lowest part of the spectrum is shown in fig. 7. In this and the following figures only the 6–10 lowest states are included. It should be kept in mind that the unperturbed lines of greatest energy in the figures are just the lowest ones of the numerous states forming almost a continuum up to 10–15 MeV, as shown in fig. 6.

For a non-magic nucleus the single-particle transitions inside partly filled shells in general all have energies well below the intershell transitions. This gives rise to a gap in which a collective state may appear, and thus the oscillator strength in the low-energy part of the resulting spectrum is in general split into two or more parts. Figs. 8 and 9 refer to a neutron-magic and a non-magic nucleus.

A special fine structure effect in the very lowest end of the spectrum is seen when the lowest unperturbed transition is weak (due to the uv factor or because spin flip is involved). This is illustrated by fig. 10.

Table 2 gives the contributions to the total B and B_0 oscillator strengths for the lowest states. We see that the strength in the low part of the spec-

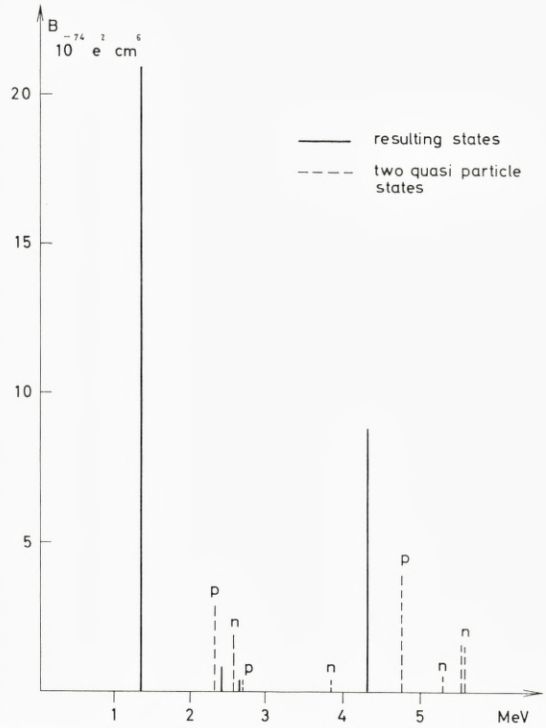

Fig. 9. The B values in $A,Z = 148,60$ (case 8a in sect. 15). Same notation as in fig. 7.

trum, is fairly constant, although it may be distributed in different ways among the lowest states. In $A,Z = 142,60$ the lowest level is moderately collective (closed neutron shell) and in $A,Z = 148,60$ it is very collective. (We note that the increase in B and decrease in E just compensate each other).

For the next nucleus in the table the lowest state is especially weak, while for $A,Z = 90,40$ the collective state is fairly high in energy and largely governed by the strong proton transition across the closed $Z = 40$ subshell. This gives rise to an especially great contribution to the B strength.

7. Examples of the isospin structure of the excited states

In this section we shall give examples of the isospin structure, i.e. the relative magnitude of B, B_0 and B_1, for the excited states which we find below, using the $\varkappa_0$ force. To start with the strong low-energy lines we see

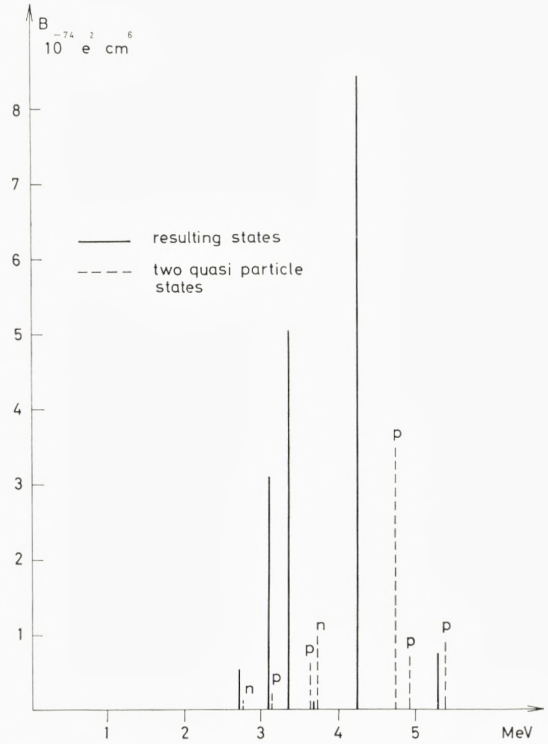

Fig. 10. The B values in $A,Z = 132,54$ (case 7b in section 15). Same notation as in fig. 7.

from tables 3 and 4 that B_0 is of the order of or greater than B, and $B_1 \ll B$. This means that the lines, as was to be expected, are fairly pure $\tau = 0$. This is the case even for single closed shell nuclei, where you might expect a greater $\tau = 1$ mixing.

The tables teach us further that even small $\tau = 1$ impurities are able to change the ratio of B_0 to B so that it differs considerably from unity. Because of the neutron excess, S^n for the lowest level is in general greater than S^p, and thus $B_0 \geq B$. Since for this level B_0 is never much smaller than B, it follows from the considerations in section 4 that it contains a greater part of the B_0 oscillator strength than of the B strength (see also table 2).

The levels in the $\hbar\omega_0$ region (fig. 6b), which although individually weak contain in total an appreciable part of the B oscillator strength, are very often of mixed $\tau = 0$ and $\tau = 1$ type ($B_0 \simeq B_1$). However, τ is less significant here. In the $3\hbar\omega_0$ region of fig. 6b we get a rather pure $\tau = 0$ state and a pure $\tau = 1$ state, due to the fact that we have concentrated

TABLE 2. Row I gives for some nuclei the relative contribution to the total B oscillator strength from the resulting level of lowest energy, and row II the contributions from the five states of lowest energy.

Rows III and IV give the same quantities for the B_0 strength.

The contributions to the B_1 strength are always very small.

A,Z	142,60 case 8a	148,60 case8a	132,54 case 7b	90,40 case 3
I	2.5 %	2.5 %	$^1/_4$ %	5 %
II	6 %	5.5 %	7 %	8 %
III	5 %	8 %	$^1/_2$ %	7 %
IV	16 %	16 %	13 %	13 %

TABLE 3. E (in MeV), B (in $e^2\,10^4\,f^6$), B_0 and B_1 (in $10^4\,f^6$) for all the lowest lying resulting states for some nuclei, when a pure isospin-independent force is used. The data come from the general calculation in sect. 15, with the exception that for $A,Z = 120,50$ the proton transition $4g_{9/2} - 5h_{11/2}$ was placed 0.8 MeV higher.

$A,Z = 90,40$				$A,Z = 120,50$			
E	B	B_0	B_1	E	B	B_0	B_1
2.61	8.4	6.3	0.2	2.51	7.0	21	3.6
3.77	0.4	0.4	10^{-6}	3.31	5×10^{-2}	0.1	10^{-2}
4.23	1.7	2.2	0.04	4.48	6.2	7.6	8×10^{-2}
4.73	0.2	0.4	0.07	5.14	0.1	4×10^{-2}	10^{-2}
4.80	0.5	0.2	0.07	5.29	2.4	0.4	0.8
5.07	7×10^{-3}	0.8	0.7	5.65	5×10^{-2}	0.2	5×10^{-2}

$A,Z = 142,60$				$A,Z = 148,60$			
E	B	B_0	B_1	E	B	B_0	B_1
1.92	15	16	3×10^{-2}	1.36	21	46	4.8
2.65	0.4	0.5	9×10^{-3}	2.41	0.9	0.4	2.6
3.77	6.6	20	3.4	2.67	0.4	2×10^{-2}	0.2
4.44	0.6	0.5	10^{-2}	3.83	0.2	0.6	0.1
4.70	1.9	5×10^{-2}	1.3	4.30	8.8	12	0.2
5.12	3×10^{-3}	1.5	1.6	5.18	10^{-2}	4.2	3.8
5.56	0.8	3.2	0.7	5.35	0.1	1.7	1.0
				5.58	10^{-2}	5×10^{-2}	10^{-2}

TABLE 4. B_1/B_0 for the two strongest lines in the low-energy spectrum of some nuclei from case 8 a (see detailed calculation in sect. 15).

A,Z	138,56	140,58	142,58	142,60	144,60	146,60	148,60
lowest level.....	0.03	0.01	0.10	0.002	0.04	0.08	0.10
next, strong level ...	0.18	0.17	0.10	0.17	0.10	0.04	0.02

all the $3\hbar\omega_0$ transition strength on a single neutron and a single proton line. In a real case we would expect the $3\hbar\omega_0$ region to look somewhat like the $\hbar\omega_0$ one.

If F_2 is smeared out in the same way as in fig. 6d, a rather strong $\tau = 0$ state is formed at the low end and B_0 falls off when we go upwards, whereas B_1 is constant in the region. This result is, however, dependent on the model. Variations in the relative and absolute density of neutron and proton states may influence the picture considerably.

8. The possible existence of strong $\tau \simeq 1$ lines

As seen in sect. 5, we can in the case in which we use an isospin independent force primarily expect to treat the $\tau \simeq 0$ states correctly while the $\tau \simeq 1$ states are mainly determined by the magnitude of $\varkappa_1$. To get information on the distribution of the B_1 oscillator strength and the possible existence of strong $\tau \simeq 1$ states we therefore, in this section, study the spectrum of our standard nucleus Sn^{116} (fig. 6) when a pure $\varkappa_1$ force is used.

When F_2 is concentrated in $3\hbar\omega_0$, a strong $\tau \simeq 1$ line and a $\tau = 0$ line are formed in the high-energy end of the spectrum (fig. 6c). If $\varkappa_1$ is made four times stronger, the line of highest energy appears at 30.68 MeV with $(B, B_0, B_1) = (8.3, 0.6, 13.2)$. The influence of the $\Delta N = 1$ lines is very small. If they were left out, the $\tau = 0$ line would be unchanged, the $\tau \simeq 1$ line would be 10–15 % weaker. The oscillator strengths from table 1 show the expected variations. If the $3\hbar\omega_0$ lines are smeared out between $2.5\hbar\omega_0$ and $3.5\hbar\omega_0$ the oscillator strengths are practically unchanged, but the tendency to forming a distinct high-lying $\tau \simeq 1$ state is considerably weakened, as seen from figs. 6, e and f, especially if $\varkappa_1 = -0.5\varkappa_0$.

Of particular interest is the problem whether strong $\tau \simeq 1$ lines could be expected in the lower energy part of the spectrum. It is striking that in the present model no such lines appear in the gap between the $\Delta N = 1$ and the $\Delta N = 3$ excitations, not even when $\varkappa_1 = -2\varkappa_0$. This is due to

the same cancellation effect as considered in sect. 6 in connection with the investigation of the possible existence of states in the gap below the $3\hbar\omega_0$ region (for pure $\varkappa_0$ force), but the effect is even stronger here, since the density of the oscillator strength in the high-energy end of the unperturbed spectrum in the $\hbar\omega_0$ region is small, i.e. the levels are weaker and are more widely spread. We will study this point again below, using a $\varkappa_0+\varkappa_1$ force.

In the $\hbar\omega_0$ region many weak states, often of mixed isospin character, appear and even in the lowest part, where the nuclei show more individual trends, a study of some nuclei of different types has revealed no tendency to formation of stronger $\tau = 1$ states. We are led to conclude that, with the models and $\varkappa_1$ values which we have used, there is no pronounced tendency towards building up individual very strong $\tau = 1$ levels. Even in the $\Delta N = 3$ region the B_1 oscillator strength is expected to be smeared out over a broad energy interval, unless $\varkappa_1$ is very strong.

As mentioned above, the interaction matrix elements for the $\Delta N = 3$ transitions are less reliable than for $\Delta N = 1$, and this may give rise to modifications.

9. Modifications in the spectra, when $\varkappa_1 \neq 0$ is introduced

On the basis of the discussion of the simple examples in section 5 and the cases of pure $\varkappa_0$ and pure $\varkappa_1$ force (sects. 6 and 8) it is easy to understand the qualitative effects of an octupole coupling which contains both isoscalar and isovector components. An example is given in fig. 6g.

In the $3\hbar\omega_0$ region of the spectrum the B_0 oscillator strength is pushed downwards, B_1 upwards.

A concentration of B, coming from $\tau \simeq 0$ levels is formed in the low energy end and a concentration of B, coming from $\tau \simeq 1$ levels is formed at the high end. However, the tendency for forming a distinct, high-lying $\tau \simeq 1$ line is only weak. When $\varkappa_1 = -2\varkappa_0$, this is no longer correct. A line with $B = 7.74$, $B_1 = 10.72$ (same units as in fig. 6) is formed at 31.95 MeV, containing 32 % of the total B oscillator strength and 77 % of the B_1 strength. This is rather near to the results for a pure $\varkappa_1$ force. We note that this concentration is only reached when we use a $\varkappa_1$ value, which is very large compared to the tentative theroretical estimates. Table 1 gives relative oscillator strengths for different $\varkappa_1$ values in a spectrum in which F_2 is concentrated in $3\hbar\omega_0$. If F_2 is smeared out, the figures for B, B_0 and B_1 are practically unchanged in the $3\hbar\omega_0$ region.

TABLE 5. E, B and B_0 for some selected resulting states as discussed in the text. Units as in table 3. The data are given for pure $\varkappa_0$ force, for $\varkappa_0 + \varkappa_1$, where $\varkappa_1 = -\frac{1}{2}\varkappa_0$, and for $\varkappa_0 + \varkappa_1$ force with $\varkappa_1 = -2\varkappa_0$. The magnitude of $\varkappa_0$ is the same in all three cases.

The results for Sn^{116} are due to the same calculation as in table 3.

	$\varkappa_1 = 0$	$\varkappa_1 = -\frac{1}{2}\varkappa_0$	$\varkappa_1 = -2\varkappa_0$	Nucleus (A,Z)
E	2.26	2.45	2.65	116,50
B	5.7	6.8	8.0	lowest excited state
B_0.....	16	14	12	
E	2.61	2.63	2.66	90,40
B	8.4	8.0	7.6	lowest excited state
B_0.....	6.3	6.5	6.8	
E	1.36	1.50	1.61	148,60
B	21.0	21.5	21.6	lowest excited state
B_0.....	45.8	35.0	27.1	
E	4.65	4.65	4.66	116,50
B	9.0	8.7	8.5	next strong state
B_0.....	8.2	8.3	8.2	
E	4.30	4.31	4.32	148,60
B	8.8	9.2	9.6	next strong state
B_0.....	12.0	11	11	
E	4.70	4.75	4.79	142,60
B	1.9	1.1	0.5	
B_0.....	0.05	0.1	0.2	

In the medium region around $\hbar\omega_0$, the states are weaker since some $\tau = 0$ strength is sucked down by $\varkappa_0$ and some $\tau = 1$ strength upwards by $\varkappa_1$. If only the F_1 lines are included in the unperturbed spectrum, a calculation using the same values of $\varkappa_0$ and $\varkappa_1$ as in fig. 6g gives the perhaps somewhat surprising result that no strong $\tau \sim 1$ line is formed above the F_1 lines. This reminds us of what happened when only F_2 was included. In sect. 6 we saw that then a rather strong force $\varkappa_0$ was needed to suck a greater part of the oscillator strength out of the unperturbed lines.

In the low-energy spectrum, the presence of $\varkappa_1$ tends to decrease B_1, and this may have considerable influence on B and B_0. A quantitative insight requires a more detailed study. For the resulting state of lowest energy the changes depend on 1) the relative magnitude of S^p and S^n, 2) whether the near-lying unperturbed modes are neutron or proton excitations. When $S^n > S^p, \varkappa_1$ tends to mix more proton motion into the state, B

increases and B_0 goes down (see the data for $A,Z = 116,50$ in table 5). The opposite trend is observed when $S^p > S^n$ (e.g. $A,Z = 90,40$). It may be noted that only few cases exist where $S^n < S^p (B_0 < B)$ for the lowest state.

Some modification arises from the low-lying modes. An example is $A,Z = 148,60$ (table 5). Here, $S^n > S^p$, and thus B increases when $\varkappa_1$ is introduced, but only very little, since the lowest and strongest unperturbed transition inside the partly filled shells is a proton one (fig. 9), the role of which is weakened by $\varkappa_1$.

In all the above mentioned cases $\varkappa_1$ makes the state less collective in the sense that E is increased. In $A,Z = 142,60$ we find an example where $B_0 \sim B$ (the neutron excess and the closing of the neutron shell neutralize each other). Then E,B and B_0 are almost independent of whether $\varkappa_1 = 0$, $\varkappa_1 = -0.5\varkappa_0$ or $\varkappa_1 = -2\varkappa_0$ (table 6).

For the next strong excitation in the low-energy part of the spectra the rules from above may be used, but it may happen that B and B_0 both move up or move down, when $\varkappa_1$ is introduced. For the weaker levels one should be more careful by using simple arguments, since there is a strong dependence on the nearest unperturbed modes. Finally, table 5 gives an example (from $A,Z = 142,60$) of a line which is mainly of $\tau = 1$ character. (The line comes between a proton and a near-lying neutron mode). When the $\tau = 1$ part of the excitation is shifted to higher energy, B decreases strongly.

10. Simultaneous adjustment of $\varkappa_0$ and $\varkappa_1$

When fitting the experimental energies by an isospin independent octupole-octupole force we make of course a systematic error. In this section we shall sketch briefly how our results would have been changed if a fit to experimental energies had been made by some general $\varkappa_0,\varkappa_1$ mixture.

When, for the lowest state, B and B_0 are different as, e.g., for $A,Z = 116,50$ we see from table 6 that we are able to make very great variations in B and B_0, by keeping the energy fixed and varying $\varkappa_0$ and $\varkappa_1$ simultaneously. This is not possible, however, when $B_0 \simeq B$ as is the case for the next, strong state in $A,Z = 116,50$ or for the lowest excitation in $A,Z = 142,60$. For the energies we obtain the result that states with great difference between B and B_0 move upwards relative to the states for which B and B_0 are equal, when $\varkappa_1$ is introduced. An example is given in fig. 11. By applying these simple rules it is easy to predict the variations and we have not gone further into a systematic study.

TABLE 6. E, B, B_0, B_1 and b in the same units as in table 3 for the two strongest, low-energy lines in some selected nuclei for different values of $\varkappa_1$. For $\varkappa_1 \neq 0$ we have chosen $\varkappa_0$ to give the lowest-lying resulting state approximately the same energy as when $\varkappa_1 = 0$.

$A,Z = 88,38$ case 4a			
$\varkappa_1 = 0$ $c_0 = 0.48$	E	2.74	4.63
	B	6.2	1.4
	B_0	4.9	3.7
	B_1	0.07	0.5
	b	0	0
$\varkappa_1 = -0.5\,\varkappa_0$ $c_0 = 0.48$	E	2.75	4.70
	B	6.0	1.9
	B_0	5.1	3.4
	B_1	0.03	0.2
	b	0.04	0.13
$\varkappa_1 = -2\varkappa_0$ $c_0 = 0.48$	E	2.77	4.76
	B	5.8	2.4
	B_0	5.3	3.1
	B_1	0.01	0.05
	b	−0.08	0.25

$A,Z = 142,60$ case 8a			
$\varkappa_1 = 0$ $c_0 = 0.45$	E	1.92	3.77
	B	15	6.6
	B_0	16	20
	B_1	0.03	3.4
	b	0	0
$\varkappa_1 = -0.5\,\varkappa_0$ $c_0 = 0.45$	E	1.92	3.89
	B	15	8.5
	B_0	16	16
	B_1	0.01	1.3
	b	0.02	0.14
$\varkappa_1 = -2\varkappa_0$ $c_0 = 0.45$	E	1.92	4.00
	B	15	9.9
	B_0	15	13
	B_1	0.003	0.3
	b	0.03	0.28

$A,Z = 116,50$ case 6			
$\varkappa_1 = 0$ $c_0 = 0.45$	E	2.20	4.23
	B	6.9	7.5
	B_0	18	4.6
	B_1	2.5	0.4
	b	0	0
$\varkappa_1 = -0.5\varkappa_0$ $c_0 = 0.43$	E	2.18	4.20
	B	11	6.6
	B_0	20	4.7
	B_1	1.3	0.2
	b	0.13	−0.09
$\varkappa_1 = -2\varkappa_0$ $c_0 = 0.41$	E	2.16	4.17
	B	17	5.5
	B_0	22	4.6
	B_1	0.4	0.04
	b	0.24	−0.18

$A,Z = 112,48$ case 5b			
$\varkappa_1 = 0$ $c_0 = 0.45$	E	2.15	3.82
	B	9.1	6.3
	B_0	17	1.8
	B_1	1.1	1.4
	b	0	0
$\varkappa_1 = -0.5\varkappa_0$ $c_0 = 0.435$	E	2.14	3.93
	B	12	4.5
	B_0	18	1.6
	B_1	0.5	0.7
	b	0.09	−0.33
$\varkappa_1 = -2\varkappa_0$ $c_0 = 0.42$	E	2.13	4.04
	B	15	2.1
	B_0	18	1.1
	B_1	0.1	0.1
	b	0.17	−0.72

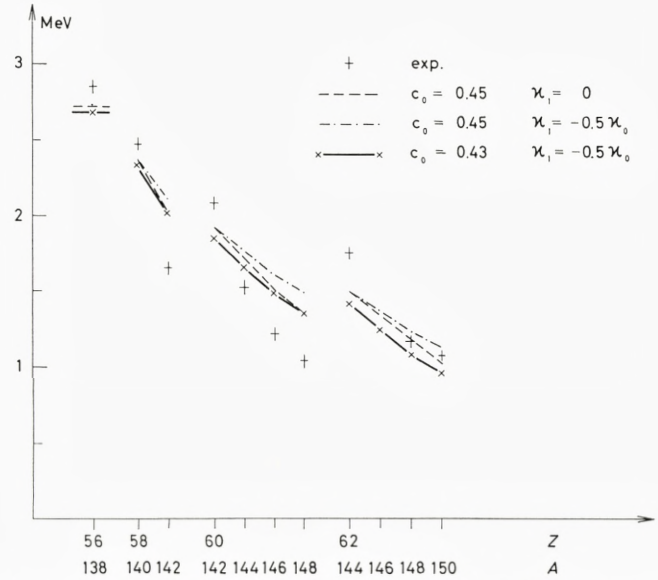

Fig. 11. Experimentally and theoretically determined values of the lowest resulting energy in nuclei in case 8a from section 15. The theoretical values are calculated for different $\varkappa_0$ and $\varkappa_1$. c_0 is defined by $S_1 = 7/\varkappa_0 = c_0 \times A^{5/3}$ where $\varkappa_0$ is the effective force constant as discussed in sections 13 and 14. A is the atomic number.

Only one comment is left. As will be discussed below, it is almost always possible for $\varkappa_1 = 0$ to use a smoothly varying $\varkappa_0$ in different regions of the periodic table. An exception is e.g. the nucleus $A,Z = 90,40$, for which a somewhat smaller $\varkappa_0$ is needed to reproduce the experimental energy. As seen above, the theoretically determined energy is practically unchanged when $\varkappa_1 \neq 0$ is introduced (since $B \lesssim B_0$). Thus, $\varkappa_1 \neq 0$ cannot provide a greater $\varkappa_0$.

11. Influence of $\varkappa_1$ on inelastic scattering

In the preceding sections we have discussed the influence of $\varkappa_1$ on B and B_0 which two quantities are relevant in Coulomb excitations and in the scattering of isospin-zero particles, respectively.

For some few examples, table 6 gives the quantity b, defined in sect. 4, especially connected to scattering, e.g. of protons or neutrons.

For $\varkappa_1 = 0$, b vanishes, but already for $\varkappa_1 = -0.5\varkappa_0$, in some cases it is so large that it should influence the relative cross section considerably. E.g. for $|b| = 0.1$, the relative cross section for inelastic proton and α

particle scattering should differ by 20 %. From a comparison of the results in the table with those from the detailed calculation (tables 21 to 36) it is easily seen where the greatest effects are expected.

12. The collective character of the states

The amount of collectiveness in the excitation can be demonstrated, e.g., by comparing B with the single-particle estimate $B_{\text{s.p.}}$ (table 7). It may be

TABLE 7. The ratio for some selected nuclei of the predicted B value (from the detailed calculation) to the single-particle value, using for this last one the estimate $B_{\text{s.p.}} = 0.416\ A^2\ e^2\ 10^{-78}\ \text{cm}^6$.

case	1	2a	3a	5a	6	7a	7b	7c
A,Z	60,28	88,38	96,42	110,48	116,50	124,52	124,52	124,52
$B/B_{\text{s.p.}}$	16	24	23	14	12	6	3	17

case	8a	8a	8c	8c	9a
A,Z	140,58	150,62	140,58	150,62	208,82
$B/B_{\text{s.p.}}$	13	35	20	45	33

mentioned that, when the single-particle transition of lowest energy goes from an almost filled to an almost empty level, every one of the particles gives a contribution to B, which thus may be large without any coupling between the excitations. More detailed information on the states is obtained from a study of the relative magnitude of the amplitudes for different two-quasiparticle creations and annihilations in the resulting excitation $p(\alpha,j_1,j_2)$ and $q(\alpha,j_1,j_2)$ introduced in sect. 3.

If $\varkappa_1 = 0$ but $\varkappa_0 \neq 0$ they are given by (ref. 1)

$$p(\alpha,j_1,j_2) = \frac{1}{(S'(\hbar\omega_\alpha))^{1/2}} \frac{\langle j_2 || i^3 Y_3 \left(\frac{r}{a}\right)^3 || j_1 \rangle (u_{j_1} v_{j_2} + v_{j_1} u_{j_2})}{E(j_1) + E(j_2) - \hbar\omega_\alpha}, \qquad (12.1)$$

$$q(\alpha,j_1,j_2) = \frac{1}{(S'(\hbar\omega_\alpha))^{1/2}} \frac{\langle j_2 || i^3 Y_3 \left(\frac{r}{a}\right)^3 || j_1 \rangle (u_{j_1} v_{j_2} + v_{j_1} u_{j_2})}{E(j_1) + E(j_2) + \hbar\omega_\alpha}, \qquad (12.2)$$

where $\hbar\omega_\alpha$ is the energy of the state, and

$$S'(\hbar\omega_\alpha) = S'^{p}(\hbar\omega_\alpha) + S'^{n}(\hbar\omega_\alpha). \tag{12.3}$$

When $\hbar\omega_\alpha$ is not very near to the energy of any of the unperturbed modes, many of these contribute to the state with comparable amplitudes. Because of the denominators the amplitudes for quasiparticle annihilation are much smaller than for quasiparticle creation, unless $E(j_1) + E(j_2) \gg \hbar\omega_\alpha$. This condition is fulfilled when the level is pushed far down from the unperturbed

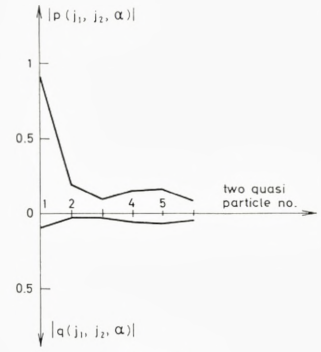

Fig. 12a.

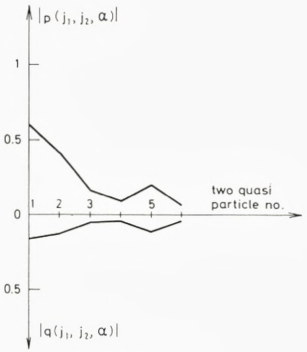

Fig. 12b.

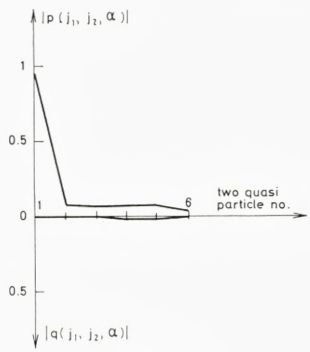

Fig. 12c.

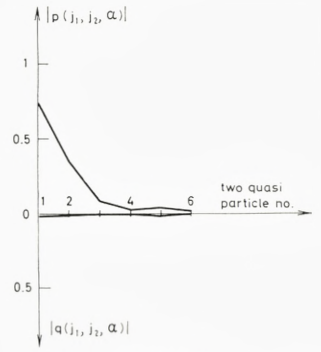

Fig. 12d.

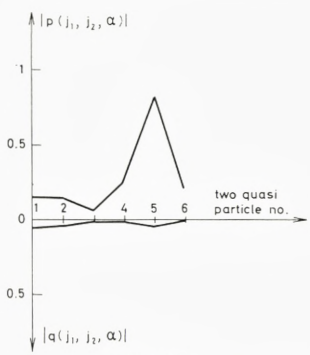

Fig. 12e.

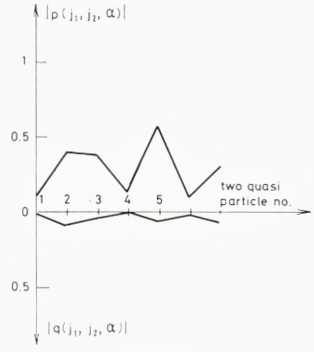

Fig. 12f.

Fig. 12. The numerical value of the two-quasiparticle amplitudes $p(\alpha, j_1, j_2)$ and $q(\alpha, j_1, j_2)$ (p up q down) from the 6 or 7 unperturbed lines of lowest energy
a) to the lowest lying collective level in $A,Z = 142,60$ (case 8a).
b) to the lowest lying collective level in $A,Z = 148,60$ (case 8a).
c) to the lowest lying collective level in $A,Z = 132,54$ (case 7b).
d) to the second resulting level in $A,Z = 148,60$ (case 8).
e) to the fifth resulting level in $A,Z = 148,60$ (case 8a).
f) to the third resulting level in $A,Z = 116,50$ (case 6, a preliminary calculation).

energies towards zero, or when considering contributions from higher lying transitions.

For the state of lowest energy the amplitude $p(\alpha,j_1,j_2)$ has the same sign as the reduced matrix element times the uv factor. This means that it has the same sign as the annihilation term in the two-quasiparticle interaction (ref. BM). In this sense there is a special coherence in the lowest state. This coherence is also demonstrated by the fact that all contributions to B have the same sign, S^p only contains positive terms.

For the other states the denominator in $p(\alpha,j_1,j_2)$ is negative for contributions from unperturbed modes at lower energy and positive for contributions from unperturbed modes at higher energy.

Then, some cancellation effect arises (cf. the discussion in sects. 6 and 8 of the vanishing of the lines in the gap between the $\Delta N = 1$ and the $\Delta N = 3$ transitions).

In fig. 12 the numerical values of the amplitudes for the lowest resulting state are given for a medium collective (a), a strongly collective (b), and a weakly collective case (c). For (c) the nearest unperturbed mode dominates completely. In (a) $p^2 - q^2$ from the lowest unperturbed excitation is $\simeq 85\,\%$, while in (b) the contribution from the six lowest ones is about $54\,\%$. Thus, $46\,\%$ is left for contributions from the remaining part of the levels in the unperturbed spectrum. In (d) and (e) we consider the 2^{nd} and the 5^{th} resulting state from the same nucleus as in (b). (d) is a rather weak state where $S_p < 0$ because it lies just above a strong proton line. (e) is the second, strong state in the spectrum. Another example of this kind is (f).

13. The renormalization procedure

As mentioned above all the single-particle transitions in principle are taken into account when the resulting energies and transition probabilities are calculated. Thus, no concept of effective charge is introduced.

The contributions from the $\Delta N = 3$ excitations are evaluated in the simple harmonic oscillator model. Such an approximative treatment may be justified by the fact that S_2, the $\Delta N = 3$ part of S, always plays a minor role in comparison to that of S_1. When going to the highest end of the periodic table this changes somewhat, but still in ^{208}Pb $S_1 > 2S_2$, although the double closed shells allow no transitions of very low energy in S_1.

When performing the calculation we found it convenient to work with a renormalized force constant $\varkappa_{\text{eff}}$ defined by

$$\frac{7}{\varkappa_{\text{eff}}} = S_1 (= S - S_2). \tag{13.1}$$

The resulting energies are thus obtained as the solutions to this equation, neglecting the energy variation of S_2. This should be a good approximation, when the low-energy states are considered.

To calculate B we added to S_1^p the quantity $S_2^p = 0.05\, A^{5/3}$ which value was found to be a good approximation from $^{16}0$ to ^{208}Pb.

For $S' = S^{p'} + S^{n'}$ we simply used S_1' since the difference is very small and of no importance, when the uncertainties in the treatment are remembered. In the calculation of B_1 and B_0 we used values of S_2, quoted in sect. 14.

14. The parameters

The nuclei which we have considered are divided into regions (cases) as shown below. In each of these regions G was chosen as $20/A_0$ where A_0 is some representative atomic number in the region. This standard value is pretty near to that which has been used before in spherical nuclei (refs. 4 and 12).

An exception is made for the region $28 \leq Z \leq 50$. Here, KISSLINGER and SORENSEN (ref. 12) have found that G_p (G for protons) should be $26/A$ to give the right quasiparticle energies. We have made calculations for both values of G_p and find the best results with the high one. (For further details: see below).

The shell-model levels $\varepsilon(j)$ have been taken from ref. (13) except for the partly filled shells for which the level separations were obtained from KS I and KS II or from stripping and pick-up experiments (for details, see below). Since one of the weakest points in the treatment is the poor knowledge of the exact value of $\varepsilon(j)$s, we have in several cases made calculations with different level schemes.

In our treatment we have looked apart from short range neutron-proton interactions. Experimentally it is found that sometimes there are rather strong shifts in the single-particle levels, e.g., so that the neutron level with $j = l - \frac{1}{2}$ moves down in energy when the lower spin-orbit partner is filled by the protons (ref. 14). By using a simple δ-function force it has been possible to describe this effect (ref. 15), but the explanations are still rather tentative, and a survey including satisfactory quantitative predictions over

a wider region of the periodic table does not exist. In some cases where experiments indicate the existence of this effect, it is taken into account.

Since many parts of the residual interaction are not explicitely included in our Hamiltonian, we should not be surprised to see how the theoretically or experimentally determined effective locations of the levels change from region to region of the periodic table.

There is little direct evidence concerning the separation of levels in different shells. In our calculation the distance from the "center of gravity" of the partly filled shell to the centers of gravity in the shells above and below have been chosen to be approximately the same as in the simple shell-model calculation (ref. 13), but sometimes, when the shell is almost filled or almost empty, we have tried to reproduce approximately the distances corresponding to the strongest, low energy transitions across the shells. It is clear that the uncertainty here suggests to take the energies and B values of the states in the 3–5 MeV region as even more tentative and preliminary results than those for the resulting state of lowest energy.

In the determination of the $\varkappa$ variation we started by estimating S_2/A from the simple harmonic oscillator model, giving points on a line 0.027 A within 5 %. The experimental energies were inserted in S_1 to give some experimental value of the effective force constant (13.1). Smoothe curves were drawn for $7/\varkappa_{\text{eff}}A = S_1/A$ and $7/\varkappa A = S/A$. As we could perhaps have expected, none of these curves could be fitted by a simple power dependence of A, but to a good approximation $7/\varkappa_{\text{eff}}$ could in the different regions of the periodic table be given by a variation like $A^{5/3}$. Then all the calculations were run again, using

$$\frac{7}{\varkappa_{\text{eff}}} = S_1 = c_0 \frac{A^{5/3}}{\text{MeV}}. \tag{14.1}$$

The details are discussed in section 15. In most cases $c_0 = 0.45$ was chosen. This value corresponds to a force constant, given by

$$\frac{7}{\varkappa} = 0.45 \frac{A^{5/3}}{\text{MeV}} + 0.027 \frac{A^2}{\text{MeV}} \tag{14.2}$$

(cf. equation (13.1)).

Since S_2 varies somewhat more strongly with A than S does, $S_1 = S - S_2$ was a little lower in the heaviest nuclei ($c_0 = 0.404$ for Pb).

For the lighter nuclei the situation was unclear, but S_1 may have a variation like A^2.

The $A^{5/3}$ variation of $\varkappa$ is somewhat slower than expected from the simple scaling argument in sect. 2. Whether this points to a real effect is difficult to say, in view of uncertainties in S_2 due to the meager knowledge of the high lying unperturbed modes, and in view of uncertainties in S_1 which is strongly influenced by the two-quasiparticle excitations of lowest energy.

15. The calculation and the results

In our treatment we shall neglect the pairing interaction between neutrons and protons. Thus, it is essential that there is a reasonably large distance between their Fermi levels; therefore we have not considered nuclei with $28 < Z < 40$ when $28 < N < 40$, whereas we have investigated nuclei with Z and N at each side of the subshell at 40 and nuclei, where the proton shell between 50 and 82 is almost empty and the same neutron shell is almost filled.

For each value of N and Z and for the possible, different level schemes the BCS equations (2.4) and (2.5) were solved and the values for $u(j)$, $v(j)$ and $E(j)$ inserted into the eigenvalue equation for $\hbar\omega_\alpha$ (3.13). For some of the nuclei λ and Δ are given in tables 8 to 19. The distances from some levels in the partly filled shell to a level in the shell above and the shell below is given in table 20.

TABLE 8. λ and Δ for case 1.

	$N = 30$	$N = 32$	$N = 34$	$N = 36$
λ	−0.32	0.131	0.594	1.079
Δ	0.810	1.048	1.152	1.142

TABLE 9. λ and Δ for case 2 a.

	$Z = 30$	$Z = 32$	$Z = 34$	$Z = 36$	$Z = 38$
λ	−0.560	−0.125	0.339	0.842	1.457
Δ	0.89	1.153	1.270	1.107	1.018

	$N = 40$	$N = 42$	$N = 44$	$N = 46$	$N = 48$
λ	2.670	3.138	3.496	3.818	4.123
Δ	0.650	0.833	0.884	0.828	0.650

TABLE 10. λ and Δ for protons from case 2 b.

$N = 40$:	$Z = 30$	$Z = 32$	$Z = 34$
λ	− 0.645	− 0.205	0.257
Δ	0.991	1.303	1.467

$N = 42$:	$Z = 32$	$Z = 34$	$Z = 36$
λ	− 0.263	0.178	0.667
Δ	1.215	0.972	0.958

$N = 44$:	$Z = 32$	$Z = 34$	$Z = 36$
λ	− 0.349	0.082	0.570
Δ	1.168	1.289	1.306

$N = 46$:	$Z = 32$	$Z = 34$	$Z = 36$	$Z = 38$
λ	− 0.429	− 0.013	0.465	1.111
Δ	1.082	1.182	1.169	1.093

$N = 48$:	$Z = 34$	$Z = 36$	$Z = 38$
λ	− 0.116	0.364	1.060
Δ	1.114	1.082	0.963

$N = 50$:	$Z = 36$	$Z = 38$
λ	0.259	1.017
Δ	0.955	0.760

TABLE 11. λ and Δ for cases 3 a and 4 a.

	$Z = 38$	$Z = 40$	$Z = 42$	$Z = 44$
λ	1.435	2.293	2.858	3.286
Δ	0.848	0.835	0.996	1.039

TABLE 11 (continued).

$Z = 40$:	$N = 52$	$N = 54$	$N = 56$
λ.....	−0.227	0.132	0.766
Δ	0.518	0.617	0.569

$Z = 42$:	$N = 52$	$N = 54$	$N = 56$	$N = 58$
λ.....	−0.242	0.119	0.685	1.189
Δ	0.534	0.653	0.687	0.968

$Z = 44$:	$N = 52$	$N = 54$	$N = 56$	$N = 58$	$N = 60$
λ.....	−0.244	0.097	0.577	1.010	1.317
Δ	0.521	0.651	0.727	0.940	1.095

TABLE 12. λ and Δ for case 5 a.

	$Z = 46$	$Z = 48$	$N = 56$	$N = 58$	$N = 60$	$N = 62$	$N = 64$	$N = 66$	$N = 68$
λ.....	3.586	3.868	0.171	0.501	0.850	1.215	1.655	2.062	2.364
Δ	0.749	0.591	0.759	0.799	0.838	0.836	0.841	0.947	1.032

TABLE 13. λ and Δ for neutrons from case 5 c.

	$N = 56$	$N = 58$	$N = 60$	$N = 62$	$N = 64$	$N = 66$	$N = 68$
λ.....	−0.093	0.150	0.415	0.726	1.131	1.529	1.833
Δ	0.898	0.957	0.971	0.942	0.914	0.988	1.057

TABLE 14. λ and Δ for neutrons from case 6.

	$N = 64$	$N = 66$	$N = 68$	$N = 70$	$N = 72$	$N = 74$
λ.....	1.199	1.700	2.012	2.277	2.520	2.746
Δ	0.606	0.756	0.854	0.901	0.912	0.889

TABLE 15. λ and Δ for case 7 a.

	$Z = 52$	$Z = 54$	$Z = 56$	$Z = 58$
λ	0.241	0.425	0.616	0.818
Δ	0.504	0.674	0.774	0.828

	$N = 68$	$N = 70$	$N = 72$	$N = 74$	$N = 76$	$N = 78$	$N = 80$
λ	1.548	1.740	1.930	2.120	2.313	2.507	2.704
Δ	1.051	1.032	0.992	0.928	0.835	0.706	0.516

TABLE 16. λ and Δ for protons from case 7 b.

	$Z = 52$	$Z = 54$	$Z = 56$	$Z = 58$
λ	-0.310	-0.095	0.143	0.414
Δ	0.438	0.569	0.631	0.657

TABLE 17. λ and Δ for neutrons from case 7 c.

	$N = 68$	$N = 70$	$N = 72$	$N = 74$	$N = 76$	$N = 78$	$N = 80$
λ	2.040	2.290	2.519	2.731	2.931	3.122	3.307
Δ	0.745	0.797	0.815	0.800	0.749	0.655	0.491

TABLE 18. λ and Δ for case 8 a.

	$Z = 56$	$Z = 58$	$Z = 60$	$Z = 62$	$N = 84$	$N = 86$	$N = 88$
λ	0.154	0.421	0.704	0.985	-0.469	-0.275	-0.006
Δ	0.530	0.538	0.549	0.514	0.533	0.733	0.877

TABLE 19. λ and Δ for case 9 b.

	$Z = 76$	$Z = 78$	$Z = 80$
λ	2.709	3.055	3.283
Δ	0.139	0.233	0.152

	$N = 114$	$N = 116$	$N = 118$	$N = 120$	$N = 122$	$N = 124$
λ	1.546	1.716	1.887	2.056	2.227	2.444
Δ	0.721	0.665	0.604	0.529	0.425	0.256

TABLE 20. The energy difference between some level in the partly filled shells and a level in the shell above or below.

case	levels	energy (MeV)
1, protons and neutrons	$3f_{7/2} - 3p_{3/2}$	2.6
	$4g_{9/2} - 4g_{7/2}$	3.88
2a, protons	$2d_{3/2} - 3f_{5/2}$	7.5
	$4g_{9/2} - 4g_{7/2}$	2.4
2a, neutrons	$2d_{3/2} - 3f_{5/2}$	7.5
	$4g_{9/2} - 4g_{7/2}$	2.2
3, protons	$2d_{3/2} - 3f_{5/2}$	7.5
	$4g_{9/2} - 4g_{7/2}$	2.4
3, neutrons	$4g_{9/2} - 4d_{5/2}$	2.9
	$5h_{11/2} - 5f_{7/2}$	5.4
5b, protons	$3f_{7/2} - 3f_{5/2}$	2.9
	$4g_{9/2} - 4g_{7/2}$	2.4
5b, neutrons	$4g_{9/2} - 4d_{5/2}$	3.6
	$4s_{1/2} - 5f_{7/2}$	4.9
6, neutrons	$4g_{9/2} - 4d_{5/2}$	3.4
	$5h_{11/2} - 5f_{7/2}$	3.6
7a, protons	$4g_{9/2} - 4d_{5/2}$	3.0
	$4s_{1/2} - 5f_{7/2}$	4.44
7a, neutrons	$4g_{9/2} - 4g_{7/2}$	3.2
	$4s_{1/2} - 5f_{7/2}$	5.7
8a, protons	$5h_{11/2} - 5f_{7/2}$	5.4
	$4g_{9/2} - 4g_{7/2}$	2.2
8a, neutrons	$5p_{1/2} - 6g_{9/2}$	2.3
	$4s_{1/2} - 5f_{7/2}$	4.67
9b, protons	$4s_{1/2} - 5h_{9/2}$	4.26
	$4g_{9/2} - 4g_{7/2}$	2.1
9b, neutrons	$5p_{1/2} - 6g_{9/2}$	3.6
	$4s_{1/2} - 5f_{7/2}$	4.95

The number of terms in S_1 was between 54 and 96, greatest in the heaviest nuclei.

The calculation was performed on a GIER computing machine with programs written in ALGOL.

In general the ten lowest resulting energies have been calculated. In tables 21 to 36 we report all those which seem to be of interest with special emphasis on those excitations which have significant values of B or B_0. In figures 13 to 20 we give the energy of the lowest mode and compare with the experimental data. When experimental B values are available, we also give the theoretical results.

A very large part of the experimental information comes from an article by HANSEN and NATHAN (ref. 16). The B values, given by these authors, were derived from inelastic α scattering experiments, assuming pure Coulomb excitation. However, it appears that owing to the fact that the energy of the α particles comes near to the Coulomb barrier, penetration becomes important, and the real B values are smaller by a factor two or three in most cases (an exception seems to be the $A \sim 145$ region, cf. ref. 48). Therefore only the energies from ref. 16 are given below.

Case 1: $Z = 28$.

In this region the proton shell is closed, and the situation could be expected to be somewhat similar to *Sn* where a strong line appears just below the energy of the proton transitions between the shells. Such a line is only seen for the heaviest isotopes.

For neutron number = 30, the neutron fermi energy lies below the lowest level in the partly filled shell, the neutron transitions are rather high in energy, and most of the available oscillator strength is concentrated on one level. The calculations were done with the KS II neutron levels: $f_{5/2}$:0, $p_{3/2}$:0, $p_{1/2}$:3 and $g_{9/2}$:4 MeV and with the KS I levels 0.78, 0, 1.56 and 4.52 MeV. Since COHEN, FULMER and MCCARTHY found good experimental agreement with the last level scheme (ref. 17) we only report the results which have been obtained when using this scheme. For the KS II single particle energies there is an accidental degeneracy which can give rise to special phenomena in the figures. Apart from this, the results from the two calculations are not very different.

In recent (d,t) experiments, the results of which were published when our calculation was finished, FULMER and DALHNICK (ref. 18) find good agreement with KS I, only the $p_{1/2}$ level should perhaps come at 1.12 MeV.

Since the proton shell is closed, the lowest resulting states are essentially governed by the strong neutron transition $p_{3/2} - g_{9/2}$ and the weak $f_{5/2} - g_{9/2}$ transition. The proton transitions coming up from the (sd)-shell are rather weak and not very low energetic. The most important proton excitation is $f_{7/2} - g_{9/2}$ which is of medium strength. If we change the intershell distance $f_{7/2} - p_{3/2}$ from 2.6 MeV, the value we have used, to 4 MeV, as supposed by

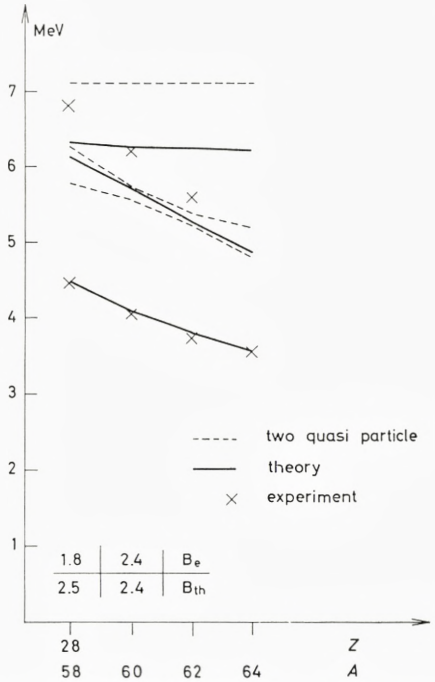

Fig. 13. The lowest-lying theoretical and experimental energies and B values for the Ni group (case 1), $c_0 = 0.39$. The dashed lines indicate the two-quasiparticle energies. The experimental data are taken from different authors (ref. 34).

KS II, the B value in $A,Z = 58,28$ is diminished by a factor of 2, whereas in 64,28 it goes down by a factor $\frac{4}{3}$. The energy is 0.5 MeV greater in the lightest nucleus, 0.1 in the heaviest one. This great influence, especially on the B values, is not very surprising, since mainly the protons contribute here. The $\tau = 0$ part of B is less affected.

The best fit to the energies was reached by $c_0 = 0.39$, for which the energies are plotted in fig. 13. This value does not lie on the smooth curve for S_1 discussed in sect. 14, and therefore another calculation was run, using $c_0 = 0.435$. In table 21 the lowest energy is given for $c_0 = 0.435$ and energies for all the stronger lines for $c_0 = 0.39$.

The theory indicates the existence of one or two higher-lying excitations of appreciable strength and in some cases such levels are found, but the agreement between theory and experiment is poor, perhaps because of uncertainties in the shell-model levels.

The B values of the lowest level are rather well reproduced by theory. We note that when we extend the $f_{7/2} - p_{3/2}$ distance towards the KS II value,

TABLE 21. The first row gives energy, B and B_0 for the state of lowest excitation energy for case 1, $c_0 = 0.435$. The following rows contain data for the most strongly excited, low-lying states in case 1, when $c_0 = 0.39$.
For units, see caption to table 3.

A,Z:	58,28			60,28			62,28			64,28		
E, B, B_0:	4.84	1.8	2.5	4.46	1.7	2.9	4.19	1.6	3.3	3.95	1.5	3.5
	4.47	2.5	3.3	4.07	2.4	3.9	3.82	2.3	4.4	3.57	2.3	4.8
	6.13	0.6	0.3	6.25	1.2	0.6	6.26	1.4	0.8	6.21	1.5	1.0
	6.31	0.2	0.1	7.30	0.2	3×10^{-2}	7.33	0.2	4×10^{-2}	7.33	0.2	5×10^{-2}
	7.24	0.2	10^{-2}									

B passes the experimental figure. As it was to be expected, $S^p < S^n$ for the lowest level and $B_0 > B$ as discussed before. When the number of neutrons increases, the lowest resulting level is pressed down, away from the lowest proton mode; B decreases and B_0 goes up.

Note added in proof: A new investigation of the Ni spectra has recently been planned in Paris. Partly inspired by this experiment we have performed two more calculations to see how the results are changed when other single particle shell model level schemes are used: (b) proton levels $f_{7/2}$: -3, $p_{3/2}$:0, $f_{5/2}$:0.8, $p_{1/2}$:2.2 and $g_{9/2}$:3.0 MeV, neutron levels $f_{7/2}$: -4, $p_{3/2}$:0, $f_{5/2}$:0.77, $p_{1/2}$:1.12 and $g_{9/2}$:4.0 MeV, $G_n = 24/A$. (c): The $g_{9/2}$ neutron level placed at 3 MeV, the other levels unchanged from (b). $G_n = 24/A$. In both cases $c_0 = 0.39$. The results are presented in tables 21 b and 21 c.

TABLE 21 b. Energy, B and B_0 (in same units as in table 3) for the strongest, low energy excitations in case 1 b, when $c_0 = 0.39$.

A,Z:	58,28			60,28			62,28			64,28		
E, B, B_0:	4.57	3.3	3.1	4.31	3.3	3.9	4.04	3.2	4.7	3.77	3.2	5.4
	6.55	0.006	0.2	6.23	0.1	0.06	6.04	0.4	0.003	5.92	0.6	0.01
	7.40	0.2	0.09	7.35	0.3	0.2	7.33	0.3	0.3	7.25	0.3	0.5
	7.95	0.1	0.4	8.00	0.2	0.4	7.94	0.1	0.5	7.73	10^{-3}	0.3

TABLE 21 c. Energy, B and B_0 (in the same units as in table 3) for the strongest, low energy excitations in case 1 c, when $c_0 = 0.39$.

A,Z:	58,28			60,28			62,28			64,28		
E, B, B_0:	4.34	3.1	3.3	4.03	3.0	4.0	3.78	2.9	4.6	3.61	2.9	5.2
	6.12	0.2	0.01	5.91	0.4	10^{-2}	5.84	0.7	0.05	5.79	0.8	0.1
	7.15	0.2	0.4	7.25	0.3	0.4	7.28	0.3	0.4	7.27	0.3	0.5
							7.79	0.01	0.4	7.79	0.2	0.5

Case 2: $28 < Z < 40$; $40 \leq N \leq 50$

Here rather many neutrons (or rather neutron holes) are available in the unfilled shell for the lighter isotopes whereas there are only few protons. The B values are low in the beginning and increase with increasing atomic number. There is some tendency for giving a line in the gap above the transitions inside partly filled shells, but the stronger proton transitions between the shells are rather high in energy and do not contribute much to the low-energy spectrum.

Calculations were made for (a) the KS I proton levels $f_{5/2} = 0$, $p_{3/2} = 0.6$, $p_{1/2} = 1.8$ and $g_{9/2} = 3.4$ MeV and $G_p = 26/A$. Neutron levels from KS II: $f_{5/2} = 0$, $p_{3/2} = 0.3$, $p_{1/2} = 2.5$ and $g_{9/2} = 3.6$ MeV. (b) neutron levels like in (a), proton levels which are almost equal to the KS II ones: $p_{3/2}$:0, $p_{1/2}$:1.8, $g_{9/2}$:2.8 and $f_{5/2}$: $-0.6 + (50 - N) \times 0.1$ MeV where N is the neutron number, $G_p = 26/A$. In both cases $c_0 = 0.45$ was used. The lowest proton and neutron two-quasiparticle excitations are the weak $f_{5/2} - g_{9/2}$ and the strong $p_{3/2} - g_{9/2}$ transition. When going from (a) to (b) the $p_{3/2}\, g_{9/2}$ distance which represents the strong proton transition inside the shell is constant, and thus the (a) and (b) results are rather similar. The differences arise from the fact that in (b) the $f_{5/2}$ proton level is placed above $p_{3/2}$ and is populated less for the lower values of the neutron number. Therefore the strong $p_{3/2} - g_{9/2}$ transition has the greatest uv factor in (b), and B is larger. In tables 22 and 23 we give the results for cases (a) and (b). The lowest level was discussed above. For the second level, given in table 22, S^n is small, because we have just passed a neutron excitation. Thus in most cases $B > B_0$.

Some of the lines of higher energy are rather mixed in isospin character ($B_0 \simeq B_1 >> B$), indicating that the line is primarily due to neutron excitations. The experimental material is very meager. For the lighter nuclei Darcey gives energies below the theoretically predicted values and with slower variation.

For $A,Z = 88,38$ the energy is rather well reproduced by the (a) calculation, but B is too small by 30 % (see also the results from case 3).

Case 3: $Z = 40, 42$; $50 \leq N \leq 82$. ($A,Z = 88,38$ is also included).

In this region, we start with a relative large lowest energy in $A,Z = 90,40$, having a closed neutron shell and closed proton subshell, but B is large since the transition across the proton subshell is strong. When more neutrons enter, the energy goes down. The quantity B is almost constant and is spread a little over the lowest levels.

We used the KS I proton levels (as in case 2a), and neutron levels based on stripping experiments (ref. 19) $d_{5/2}$:0, $s_{1/2}$:1.7, $g_{7/2}$:2.6, $d_{3/2}$:2.7 and

TABLE 22. Energy, B and B_0 for the low-energy, stronger levels in case 2 a, $c_0 = 0.45$. Same units as in table 3.

A,Z:	70,30			72,32			74,32		
E, B, B_0:	2.54	1.4	4.4	2.51	2.0	5.0	2.84	2.0	5.2
	5.05	0.5	0.4	4.75	1.1	0.5	4.78	1.0	0.4
	5.28	0.7	0.7	5.63	0.2	0.8	5.67	0.3	1.0

A,Z:	76,32			78,32			74,34		
E, B, B_0:	3.13	2.1	5.2	3.29	1.9	4.9	2.42	3.2	6.1
	4.79	0.8	0.3	4.22	0.3	0.5	4.41	0.3	0.3
	5.62	0.3	1.1	5.46	0.1	0.9	5.60	0.4	1.1
							6.35	0.5	0.3

A,Z:	76,34			78,34			80,34		
E, B, B_0:	2.72	3.3	6.3	3.01	3.4	6.2	3.17	3.2	5.9
	4.44	1.2	0.2	4.43	0.7	0.2	4.17	0.6	0.4
	5.65	0.6	1.3	5.59	0.5	1.5	4.53	0.6	0.04
							5.42	0.3	1.3

A,Z:	82,34			78,36			80,36		
E, B, B_0:	3.19	2.7	5.4	2.44	5.7	7.8	2.67	5.7	7.4
	4.16	1.5	1.2	3.92	0.6	10^{-4}	5.46	1.3	1.8
	5.18	0.07	0.9	5.51	1.4	1.7			

A,Z:	82,36			84,36			86,36		
E, B, B_0:	2.82	5.6	7.1	2.89	5.2	6.8	2.85	4.6	6.5
	5.31	0.9	1.7	3.87	0.5	0.2	3.73	1.1	0.3
				4.58	0.03	0.6	4.69	0.2	1.7
				5.11	0.3	1.0	6.00	0.5	0.3
				6.13	0.7	0.2			

A,Z:	84,38			86,38			88,38		
E, B, B_0:	2.46	8.0	8.2	2.54	7.6	7.9	2.55	7.1	7.8
	5.14	1.6	1.6	4.53	0.3	1.1	4.59	0.7	2.3
				4.94	0.5	0.8	5.50	0.6	0.06
				5.77	0.5	0.02			

TABLE 23. Energy, B and B_0 for the level of lowest excitation energy in case 2 b, $c_0 = 0.45$. The following levels are rather weak and not very different from case 2 a. Same units as in table 3.

A,Z:	70,30			72,32			74,32		
E, B, B_0:	2.41	2.1	5.2	2.33	3.1	6.2	2.65	3.2	6.2
A,Z:	76,32			78,32			74,34		
E, B, B_0:	2.97	3.0	6.0	3.16	2.7	5.5	2.25	4.4	7.2
A,Z:	76,34			78,34			80,34		
E, B, B_0:	2.54	4.5	7.2	2.82	4.4	6.9	3.00	4.1	6.4
A,Z:	82.34			78,36			80,36		
E, B, B_0:	3.08	3.5	5.8	2.41	6.1	8.2	2.64	6.1	7.8
A,Z:	82,36			84.36			86,36		
E, B, B_0:	2.75	5.9	7.2	2.81	5.4	6.7	2.77	4.8	6.4
A,Z:	84.38			86,38			88,38		
E, B, B_0:	2.51	7.6	7.9	2.49	7.3	7.4	2.37	7.0	7.1

$h_{11/2}$: 2.8 MeV. Two calculations were run. a) $G_p = 26/A$ and b) $G_p = 20/A$. The neutron single-particle energies might be somewhat uncertain. There is some indication of a rather strong movement of the $g_{7/2}$ neutron level (ref. 20). Therefore this level is lowered by 0.4 MeV in $Z = 42$.

When neutrons are added to $N = 50$, the strong neutron transition $d_{5/2} - h_{11/2}$ is populated and goes rapidly down in energy. At $N = 56$ there is a minimum for the collective energy. After that the transition goes up, and the weak $g_{7/2} - h_{11/2}$ transition becomes the lowest one. The proton excitations have higher energy, and the uv factor in the numerator in S goes down (to 0.7) with increasing Z. To fit the experimental energy, $c_0 = 0.48$ was needed, which is greater than in the neighbouring cases. In fig. 15 the results are given for $Z = 40$ when using $c_0 = 0.45$. From the previous discussion we remember that we are not able to fit the energies with a lower c_0 value, if $\varkappa_1 < 0$ is introduced.

For $Z = 40$ the lowest level of the lightest nuclei has $S^p > S^n$ and thus

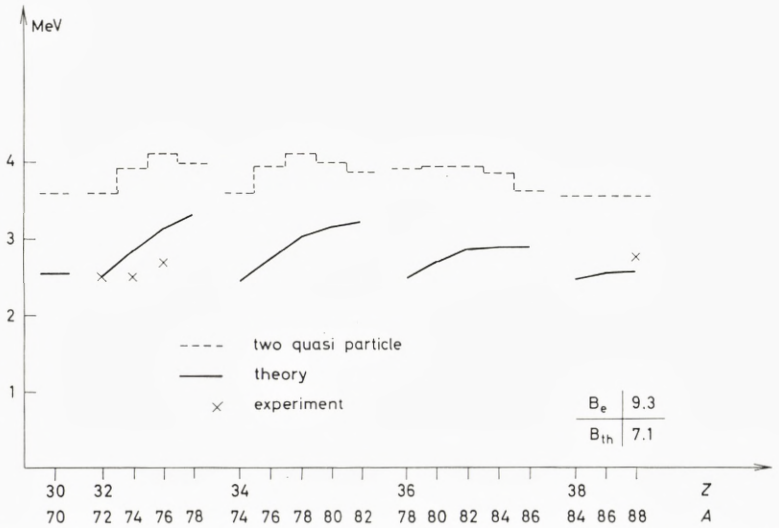

Fig. 14. The lowest-lying theoretical and experimental energies and B values for case 2a. The experimental data for $A,Z = 88,38$ are due to HELM (ref. 35). The other ones come from an experiment by W. DARCEY (ref. 36).

TABLE 24. Energy, B and B_0 for the low-energy, stronger excitations in cases 3a and 4a, $c_0 = 0.45$. Same units as in table 3.

A,Z:	88,38			90,40			92,40		
E, B, B_0:	2.74	6.2	4.9	2.61	8.4	6.3	2.37	9.1	9.3
	4.63	1.4	3.7	4.23	1.7	2.2	4.36	1.8	1.3
	4.80	1.5	2.7	4.80	0.5	0.2	5.19	0.3	1.3
				5.06	7×10^{-3}	0.8			

A,Z:	94,40			96,40			92,42		
E, B, B_0:	2.03	9.3	13	1.62	9.8	17	2.93	9.2	7.1
	3.31	0.7	0.02	3.21	1.5	0.07	4.06	0.9	1.0
	4.40	1.9	1.1	4.41	1.9	1.1	4.28	0.8	1.0
	5.24	0.4	1.1	5.27	0.6	1.5	4.80	0.6	1.0
							5.07	0.01	0.9

A,Z:	94,42			96,42			98,42		
E, B, B_0:	2.63	9.0	9.7	2.26	8.6	12	1.92	8.7	15
	4.12	0.6	0.3	3.54	1.4	0.07	3.49	2.1	0.3
	4.36	1.4	1.0	4.12	0.6	0.2	4.13	0.5	0.2
	5.19	0.3	1.4	4.39	1.6	0.9	4.40	1.7	0.9
				5.26	0.7	1.5	5.29	0.8	1.7

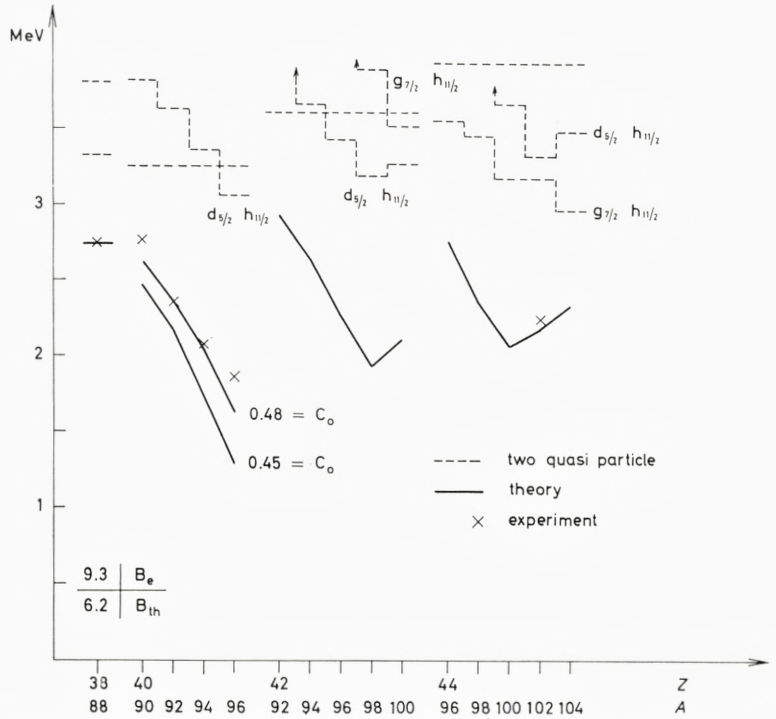

Fig. 15. Energies and B values for cases 3 and 4, where $d_{5/2}\ h_{11/2}$ and $g_{7/2}\ h_{11/2}$ denote the energy of the two-low lying neutron quasiparticle excitations. The theoretical energies are calculated with $c_0 = 0.48$. For $Z = 40$ the results for $c_0 = 0.45$ are shown. The experimental energies are due to HANSEN and NATHAN (ref. 16). For $A,Z = 88,38$ see caption to fig. 14.

TABLE 24 (continued).

A,Z:	100,42			96,44			98,44		
E, B, B_0:	2.11	8.8	15	2.76	8.1	9.7	2.36	7.6	12
	3.55	1.5	0.06	3.75	2.2	0.5	3.74	3.1	0.8
	4.43	1.7	0.8	4.29	1.6	1.1	4.31	1.8	1.1
	4.77	5.6	0.3	5.00	0.3	0.5	5.02	0.4	0.6
	5.37	1.4	1.6				5.44	10^{-5}	0.6

A,Z:	100,44			102,44			104,44		
E, B, B_0:	2.06	7.6	14	2.17	7.7	14	2.32	7.5	14
	3.75	3.0	0.8	3.79	2.9	0.6	3.82	2.4	0.4
	4.33	2.0	1.1	4.36	2.1	1.0	4.38	2.2	0.9
	4.72	0.5	0.4	4.73	0.6	0.4	4.74	0.7	0.4
	5.03	0.6	0.6	5.05	0.7	0.6	5.06	0.9	0.6

TABLE 25. Energy, B and B_0 for the lowest excitation, case 3 b and 4 b, $c_0 = 0.45$. Same units as in table 3.

A,Z:	88,38			90,40			92,40		
E, B, B_0:	2.26	6.0	4.4	2.10	9.9	7.0	1.92	11	10
A,Z:	96,40			96,40			92.42		
E, B, B_0:	1.64	13	15	1.28	15	21	2.29	9.3	6.5
A,Z:	94,42			96,42			98,42		
E, B, B_0:	2.12	11	9.5	1.87	12	13	1.60	12	17
A,Z:	100,42			96,44			98,44		
E, B, B_0:	1.77	12	17	2.48	9.6	9.7	2.17	9.5	12
A,Z:	100,44			102,44			104,44		
E, B, B_0:	1.91	9.5	15	2.02	9.5	15	2.16	9.4	15

$B_0 > B$. This is changed when the neutron number grows, and for some nuclei $B_0 \sim 2B$. The smaller G_p in case b results in smaller collective energy but causes no major changes in B. We note that the theory predicts the existence of some higher-lying collective states.

Case 4: $Z = 44$.

The levels are the same as in case 3, only the neutron $g_{7/2}$ is lowered still further and the splitting in the neutron states changes a bit because of the variation in A.

The neutron levels are: $d_{5/2}$: 0, $s_{1/2}$: 1.6, $g_{7/2}$: 1.8, $d_{3/2}$: 2.6 and $h_{11/2}$: 2.7 MeV. For the discussion, see case 3.

Case 5: $Z = 46$ and 48.

When passing on to this region there are still fewer proton holes in the partly filled shell, and the available oscillator strength is not concentratedon the lowest excitation. A number of level schemes was studied. We shall only mention three:

a) the same proton levels as in case 3 a.
$G_p = 26/A$.

Neutron levels experimentally found by CUJEC (ref. 21) in stripping experiments in *Pd* $g_{7/2}$:0, $d_{5/2}$:1, $s_{1/2}$:2.5, $h_{11/2}$:2.9 and $d_{3/2}$:3.1 MeV.

b) same proton levels as in a) $G_p = \frac{26}{A}$.
KS I neutron levels:
$d_{5/2}$:0, $g_{7/2}$:0.22, $s_{1/2}$:1.9, $d_{3/2}$:2.2, and $h_{11/2}$:2.8 MeV.

c) proton levels like in a) $G_p = \frac{26}{A}$, neutron levels from a tentative interpretation of a (d,p) and (d,t) experiment in Cd by ROSNER (ref. 45).
$d_{5/2}$:0, $g_{7/2}$:0.2, $h_{11/2}$:2.25, $s_{1/2}$:2.25 and $d_{3/2}$:2.85 MeV.
This scheme is in fair agreement with the experimental (d,p) results, obtained by SILVA and GORDON (ref. 46) who find $g_{7/2}$ to be placed less than 0.4 MeV above $d_{5/2}$. KS II assumes this distance to be more than 1 MeV.

In a) there is a rather strong variation in the lowest neutron two-quasiparticle energies. The transition $d_{5/2} - h_{11/2}$ has the lowest energy, which varies much as λ passes $d_{5/2}$. In addition, the uv factor varies from 0.4 to 1. This causes a rapid variation in the resulting energy. This variation is not found in b) or c), since here the $d_{5/2} - h_{11/2}$ uv factor only varies from 0.6 to 0.9 and the two-quasiparticle energy changes more slowly. The lowest unperturbed energy appears about 0.5 MeV lower in c) than in b). The

TABLE 26. Energy, B and B_0 for the low-energy, stronger excitations in case 5 a, $c_0 = 0.45$. Same units as in table 3.

A,Z:	102,46			104,46			106,46		
E, B, B_0:	2.95	11	11	2.71	8.6	10	2.29	7.1	11
	4.11	1.7	0.5	3.71	2.8	0.7	3.66	4.3	1.5
	5.25	0.2	1.3	4.07	1.9	0.9	4.07	2.0	1.0
				5.28	0.3	1.2	5.30	0.4	1.2

A,Z:	108,46			110,46			106,48		
E, B, B_0:	1.86	7.0	13	1.60	7.4	16	2.73	8.9	11
	3.65	4.9	1.8	3.65	5.1	2.0	3.76	4.7	1.4
	4.07	2.2	1.1	4.07	2.3	1.2	5.23	0.5	1.2
	5.31	0.5	1.1	5.33	0.5	1.1			

TABLE 26 (continued).

A,Z:	108,48			110,48			112,48		
E, B, B_0:	2.33	7.2	11	1.19	7.0	13	1.65	7.2	15
	3.71	6.5	2.3	3.70	7.4	2.9	3.70	7.8	3.2
	5.25	0.5	1.1	5.25	0.6	1.0	5.48	0.2	1.0

A,Z:	114,48			116,48					
E, B, B_0:	1.77	7.5	16	1.99	7.6	16			
	3.46	1.7	1.2	3.62	4.2	2.3			
	3.75	6.8	2.6	3.83	4.0	1.2			
	5.51	0.5	1.1	5.53	0.7	1.0			

TABLE 27. Energy, B and B_0 for the low-energy, strong excitations in case 5 b, $c_0 = 0.45$. Same units as in table 3.

A,Z:	102,46			104,46			106,46		
E, B, B_0:	2.67	11	13	2.53	11	14	2.38	10	15
	4.16	2.1	0.4	3.82	1.1	0.03	3.79	1.8	0.2
				4.14	2.3	0.5	4.13	2.5	0.7

A,Z:	108,46			110,46			106,48		
E, B, B_0:	2.22	9.5	16	2.10	9.1	17	2.57	11	14
	3.76	2.6	0.5	3.74	3.3	0.8	3.95	3.4	0.4
	4.12	2.6	0.9	4.11	2.6	1.0			

A,Z:	108,48			110,48			112,48		
E, B, B_0:	2.42	10	15	2.27	9.6	16	2.15	9.1	17
	3.90	4.5	0.8	3.85	5.5	1.3	3.82	6.2	1.7

A,Z:	114,48			116,48					
E, B, B_0:	2.22	9.7	18	2.35	10	19			
	3.85	5.9	1.6	3.89	5.3	1.3			

TABLE 28. Energy, B and B_0 for the low-energy, stronger excitations in case 5 c, $c_0 = 0.45$. Same units as in table 3.

A,Z:	102,46			104,46			106,46		
E, B, B_0:	2.38	9.6	13	2.20	9.1	14	2.03	8.8	15
	3.72	2.8	0.6	3.71	3.4	0.8	3.70	3.9	1.1
	4.08	2.0	0.8	4.08	2.2	0.9	4.09	2.3	1.0

TABLE 28 (continued).

A,Z:	108,46			110,46			106,48		
E, B, B_0:	1.88	8.4	16	1.82	8.1	16	2.25	9.2	14
	3.68	4.5	1.4	3.68	4.8	1.7	3.78	5.7	1.6
	4.09	2.4	1.1	4.09	2.5	1.2			

A,Z:	108,48			110,48			112,48		
E, B, B_0:	2.08	8.8	15	1.94	8.4	16	1.88	8.1	16
	3.76	6.5	2.0	3.75	7.2	2.5	3.74	7.6	2.8

A,Z:	114,48			116,48					
E, B, B_0:	2.06	8.1	16	2.31	8.4	16			
	3.77	7.3	2.6	3.81	6.7	2.2			

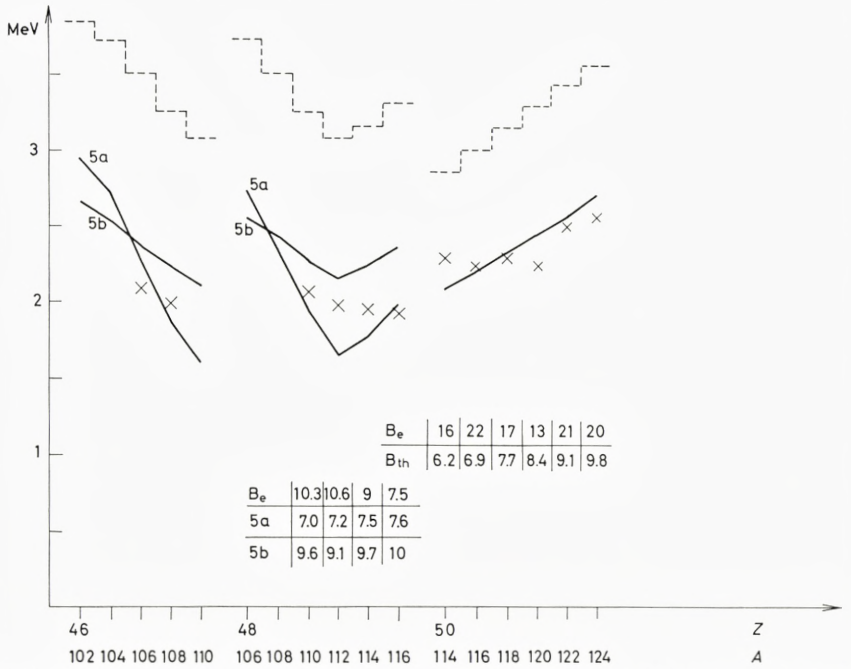

Fig. 16. Theoretically and experimentally determined energies and B values for cases 5a and 5b and for case 6. In 5, the quasiparticle energies are from case a. For cases 5, experimental data are available from HANSEN and NATHAN (ref. 16), from M. SAKAI et al. (ref. 37), and from MCGOWAN et al. (ref. 38). The experimental values for case 6 come from LEMBERG et al. (ref. 39).

Experiments by HANSEN and NATHAN for the nuclei in case 6 give the same energies except for Sn^{120} where they find an energy of perhaps 2.40 MeV. Their B values are a factor of 3 greater than the experimental ones given in the figure.

proton Fermi energy is higher than the energy of the levels in the partly filled shell. The lowest proton transition becomes high in energy and the uv factor is only 0.5 for $Z = 46$ and 0.25 for $Z = 48$. This means that the transitions from $p_{1/2}$ and $g_{9/2}$ to the next shell become important. The result is a strong, higher-lying 3^- state, for which $B > B_0$ while $B < B_0$ for the resulting level of lowest energy.

When comparing the results with the experimental data it is seen that none of the level schemes, which we tried, could give the correct trend in the energies and B values. Still, something seems to be missing to give the right variation with A. Therefore, further experimental studies of the location of the single-particle levels would be interesting.

Case 6: $Z = 50$.

The *Sn* region has been discussed above, especially in relation to fig. 6. We have seen how the closed proton shell gives rise to a higher-lying strong line.

Since the proton shell is closed, we used for the proton single-particle levels the Nilsson values (ref. 13) with the exception that $5h_{11/2}$ was placed in the middle of the 50–82 shell, just as in case 7 and as in the Mottelson-Nilsson paper (ref. 13). The energies are the following:

$3f_{7/2}$: −2.1, $3p_{3/2}$:0, $3f_{5/2}$:0.7, $3p_{1/2}$:1.4,
$4g_{9/2}$:3.7, $4d_{5/2}$:7.1, $4g_{7/2}$:7.4, $4s_{1/2}$:9.1,
$4d_{3/2}$:9.2 and $5h_{11/2}$:8.4 MeV.

The neutron levels were taken from KS I:

$d_{5/2}$:0, $g_{7/2}$:0.22, $s_{1/2}$:1.9, $d_{3/2}$:2.2, $h_{11/2}$:2.8 MeV.

Calculations have also been performed for another neutron level scheme, proposed by Cohen and Price on the basis of a stripping experiment (ref. 22). Since, however, they give a poorer fit to experimental energies, and since after publication the measurements have been reinterpreted (ref. 23) so that the level scheme comes much closer to KS I, the results of this calculation are not reported.

The two neutron transitions in the partly filled shell are the weak $g_{7/2} - h_{11/2}$ and the strong $d_{5/2} - h_{11/2}$, which lies a little higher. The energies of both transitions go up and the uv factor down, when A increases.

The transitions from the closed proton shell give rise to the second strong line. The line of lowest energy has $B_0/B \simeq 2.5$ due to the small S^p because of the closed shell, whereas the higher lying strong line has $B_0/B < 1$.

TABLE 29. Energy, B and B_0 for the low-energy, stronger excitations in case 6, $c_0 = 0.45$. Same units as in table 3.

A,Z:	114,50			116,50			118,50		
E, B, B_0:	2.11	6.2	15	2.20	6.9	18	2.31	7.7	20
	4.24	7.8	4.5	4.23	7.5	4.6	4.22	6.9	4.6
	5.44	1.4	2.9	5.31	0.5	2.4	5.14	0.02	1.6
							5.57	1.4	1.0

A,Z:	120,50			122,50			124,50		
E, B, B_0:	2.43	8.4	22	2.56	9.1	24	2.70	9.8	26
	4.20	6.2	4.5	4.19	5.3	4.2	4.18	4.2	3.5
	5.01	0.05	1.0	5.44	0.8	1.9	5.34	0.4	1.9
	5.52	1.3	1.6						

Some of the levels of higher energy have very different values of B_0 and B. In some cases $B \ll B_0$ because the line is a rather pure neutron one.

The energies are in good agreement with the results of LEMBERG et al. and of HANSEN and NATHAN (see fig. 16), but the B values are smaller by a factor 2 or more than the Lemberg ones.

It is noteworthy that this large discrepancy appears just in *Sn* where, as mentioned above, B_0/B is extraordinarily great and thus the introduction of an isospin dependence in the octupole-octupole force will have especially large effects on B. However, we see from tables 5 and 6 that an unexpected large value of $-\varkappa_1/\varkappa_0$ is needed to reproduce the experimental B value completely.

It is rather unsatisfactory that the proton single-particle levels come just from a simple shell-model calculation. Because of the uncertainty in the position of the proton $5h_{11/2}$ level we have performed a calculation with the energy of this level increased by 0.8 MeV. Some results are given in tables 3 and 5. The shift in the $5h_{11/2}$ single-particle energy causes considerable changes, especially for the higher-lying, strong excitation, since the $4g_{9/2} - 5h_{11/2}$ proton transition (energy 4.7 MeV) is one of the strongest ones in the low-energy spectrum.

Preliminary results from inelastic α scattering by FARAGGI et al. (ref. 24) indicate the possible existence of a second, strong 3^- state around 5 MeV in A,Z = 122,50 and 124,50, the intensity being however much lower than when exciting the lowest octupole state.

It is interesting to note that from the calculation B should be roughly equal for the higher lying state and for the lower lying one, while B_0, which is the relevant quantity in α scattering, should be much smaller. Recently,

ALLAN et al. (ref. 25) have by means of inelastic proton scattering found a possibly collective level in $A,Z = 116,50$ and $118,50$ around 3.9 MeV with unknown spin and parity. For the heavier *Sn* isotopes this level has disappeared, at least in the region below 4.7 MeV. It would be interesting to study the possible relationship between this state and the states found by FARAGGI et al.

Case 7: $50 < Z < 82$, $50 < N \leq 82$.

As mentioned in connection with fig. 10, there are here only few protons and few neutron holes in the partly filled shells and the oscillator strength in the low-energy spectrum is spread over several levels. Three level schemes were used, viz.

a) protons: $g_{7/2}$:0.8, $d_{5/2}$:0.8, $h_{11/2}$:2.4, $d_{3/2}$:3.13 and $s_{1/2}$:3.36 MeV; neutrons: $d_{5/2}$:0, $g_{7/2}$:1, $h_{11/2}$:1.66, $s_{1/2}$:2.1 and $d_{3/2}$:2.37 MeV.
b) same level scheme as in a), but the proton $g_{7/2}$ is lowered to 0 MeV.
c) protons like in a), neutrons like in case 6.

The proton levels in a) were chosen on the basis of a suggestion by KISSLINGER (ref. 26) and are almost identical to the KS II levels. The neutron levels in a) come from a stripping experiment in the $N = 82$ region (ref. 27). There is rough agreement between this neutron level scheme and single-particle energies, found by JOLLY in (d,p) and (d,t) experiments in *Tl* (ref. 47).

In case b) we only changed the position of the proton $g_{7/2}$ level in order to investigate how this modifies the picture. The two level schemes a) and c) are really different, and we report in detail the results for both with the aim to demonstrate the influence of changing the single-particle parameters.

The main difference between the "a-neutron levels" found by experiment in the end of the region and the *c* levels, which fitted the quasiparticle energies nicely in *Sn*, is that $h_{11/2}$ in the last case is placed at the top of the shell, so that the neutron transitions from $d_{5/2}$ and $g_{7/2}$ are allowed by the uv factor, whereas in the first case $h_{11/2}$ as well as $d_{5/2}$ and $g_{7/2}$ are almost

TABLE 30. Energy, B and B_0 for the low-energy, stronger excitations in case 7 a, $c_0 = 0.45$. Same units as in table 3.

A,Z:	120,52			122,52			124,52		
E, B, B_0:	1.93	7.3	14	2.09	5.7	11	2.24	4.2	7.7
	2.36	2.1	3.2	2.47	3.1	5.1	2.58	4.8	6.5
	4.19	7.8	5.8	4.23	8.3	6.0	4.24	8.7	6.3
	5.31	1.8	0.7	5.32	1.7	0.6	5.12	0.2	1.5
							5.35	1.3	0.2

TABLE 30 (continued).

A,Z:	126,52			128,52			130,52		
E, B, B_0:	2.39	3.2	5.5	2.54	3.0	4.8	2.68	4.8	6.1
	2.68	5.4	6.3	2.76	4.9	4.8	2.81	2.5	2.0
	3.15	0.2	1.8	3.31	0.8	3.5	3.52	1.9	5.1
	4.24	8.9	6.7	4.24	9.1	7.4	4.21	8.9	8.1
	5.20	1.0	2.1	5.22	1.4	2.4	5.20	1.3	2.8

A,Z:	124,54			126,54			128,54		
E, B, B_0:	2.01	9.7	15	2.16	8.8	12	2.30	8.6	11
	2.41	2.8	2.9	2.48	3.5	3.2	2.56	3.2	2.5
	4.35	7.6	5.9	4.37	8.0	6.2	3.17	0.1	1.9
	5.53	1.9	1.0	5.53	1.8	0.9	4.37	8.3	6.6
							5.55	1.4	0.5

A,Z:	130,54			132,54			134,54		
E, B, B_0:	2.42	9.5	11	2.49	10	11	2.52	11	11
	2.65	1.6	0.9	3.56	1.0	3.5	3.81	1.7	4.4
	3.35	0.5	2.8	4.33	8.7	8.5	4.28	8.4	9.8
	4.36	8.5	7.3	5.40	1.4	4.0	5.33	0.8	4.6
	5.40	1.3	3.2						

A,Z:	136,54			130,56			132,56		
E, B, B_0:	2.53	11	11	2.15	13	15	2.24	14	13
	4.12	10	17	2.52	1.2	0.5	3.37	0.3	2.6
	5.19	0.1	3.7	3.17	0.1	2.0	4.46	8.2	7.3
	6.08	0.2	2.1	4.71	7.9	6.5	5.52	0.5	3.0
				5.75	2.0	1.6	5.76	1.4	1.0

A,Z:	134,56			136,56			138,56		
E, B, B_0:	2.29	14	13	2.32	14	13	2.32	14	13
	3.58	0.6	2.9	3.83	1.0	3.1	4.24	9.5	16
	4.43	8.4	8.5	4.37	8.5	10	5.26	3×10^{-3}	3.4
	5.56	1.2	5.4	5.44	0.5	5.5	5.82	1.4	0.4
							6.13	0.01	1.7

TABLE 30 (continued).

A,Z:	136,58			138,58			140,58		
E, B, B_0:	2.11	16	15	2.13	16	15	2.13	17	15
	3.59	0.5	2.7	3.84	0.7	2.6	4.33	9.3	16
	4.51	8.3	8.5	4.45	8.5	11	5.29	3×10^{-3}	3.0
	5.66	0.8	5.9	5.51	0.3	5.5	5.98	1.5	2.0
				6.04	1.1	0.5			

TABLE 31. Energy, B and B_0 for the lowest line in case 7 b, $c_0 = 0.45$. Same units as in table 3.

A,Z:	120,52			122,52			124,52		
E, B, B_0:	2.00	4.8	11	2.15	3.1	7.3	2.29	1.9	4.5

A,Z:	126,52			128,52			130,52		
E, B, B_0:	2.43	1.2	2.7	2.58	0.8	1.7	2.74	0.5	1.1

A,Z:	124,54			126,54			128,54		
E, B, B_0:	2.16	3.1	6.9	2.30	1.9	4.3	2.43	1.2	2.7

A,Z:	130,54			132,54			134,54		
E, B, B_0:	2.58	0.8	1.7	2.74	0.5	1.2	2.93	0.5	1.0

A,Z:	136,54			130,56			132,56		
E, B, B_0:	3.08	3.0	3.4	2.42	1.8	2.5	2.57	1.4	2.5

A,Z:	134,56			136,56			138,56		
E, B, B_0:	2.73	1.6	2.5	2.88	5.0	5.6	2.90	5.6	5.8

A,Z:	136,58			138,58			140,58		
E, B, B_0:	2.53	9.7	9.5	2.56	9.9	9.3	2.56	10	9.8

TABLE 32. Energy, B and B_0 for the low-energy, stronger excitations in case 7 c, $c_0 = 0.45$. Same units as in table 3.

A,Z:	120,52			122,52			124,52		
E, B, B_0:	2.12	11	20	2.26	11	20	2.41	11	18
	4.26	7.4	4.7	4.28	7.4	4.6	3.12	0.05	1.8
	5.09	0.1	1.5	5.15	0.5	1.9	4.30	7.4	4.6
	5.40	1.3	0.01				5.19	0.9	2.1

A,Z:	126,52			128,52			130,52		
E, B, B_0:	2.54	11	16	2.64	9.5	13	2.71	8.3	10
	3.21	0.6	3.8	3.34	1.7	6.4	3.51	3.0	8.4
	4.31	7.3	4.6	4.31	7.1	4.7	4.30	6.7	4.8
	5.21	1.2	2.3	5.21	1.3	2.5	5.20	1.2	2.9
				5.72	5×10^{-4}	2.1	5.71	3×10^{-3}	2.1

A,Z:	124,54			126,54			128,54		
E, B, B_0:	2.09	15	21	2.21	14	19	2.32	14	17
	3.05	0.01	1.2	3.14	0.05	2.4	3.26	0.4	3.9
	4.39	7.0	4.8	4.41	7.1	4.9	4.42	7.1	5.0
	5.25	0.1	2.0	5.33	0.6	2.7	5.38	1.0	3.2
	5.60	1.4	0.1						

A,Z:	130,54			132,54			134,54		
E, B, B_0:	2.40	13	15	2.47	12	13	2.52	11	11
	3.41	1.0	5.3	3.58	1.7	6.1	3.77	1.9	5.1
	4.41	7.1	5.3	4.40	7.0	5.7	3.88	1.2	2.8
	5.39	1.3	3.6	5.38	1.2	4.1	4.36	6.7	6.4
							5.34	0.9	4.7

A,Z:	136,54			130,56			132,56		
E, B, B_0:	2.55	10	9.8	2.12	16	18	2.20	15	16
	4.17	10	16	3.29	0.4	4.0	3.44	0.8	4.8
	5.27	0.4	4.8	4.50	7.0	5.2	4.50	7.1	5.6
	5.81	0.1	1.2	5.50	0.6	3.7	5.54	1.0	4.8
				5.84	1.0	0.07			

TABLE 32 (continued).

A,Z:	134,56			136,56			138,56		
E, B, B_0:	2.27	15	14	2.31	14	13	2.35	13	12
	3.62	1.1	4.8	3.80	0.8	2.7	4.29	9.7	15
	3.74	1.1	1.4	3.90	1.3	3.5	5.36	0.2	5.2
	4.48	7.1	6.3	4.44	7.2	7.5	5.67	0.5	1.0
	5.52	1.0	5.4	5.46	0.6	5.6			

A,Z:	136,58			138,58			140,58		
E, B, B_0:	2.07	17	16	2.12	17	15	2.16	16	14
	3.63	0.9	4.0	3.81	0.5	1.8	4.38	9.4	15
	3.75	0.4	1.7	3.91	1.1	3.6	5.41	0.08	4.9
	4.54	7.2	6.6	4.50	7.4	8.1	5.71	0.4	2.2
	5.61	0.6	5.8	5.52	0.3	5.5			
				5.83	0.5	1.8			

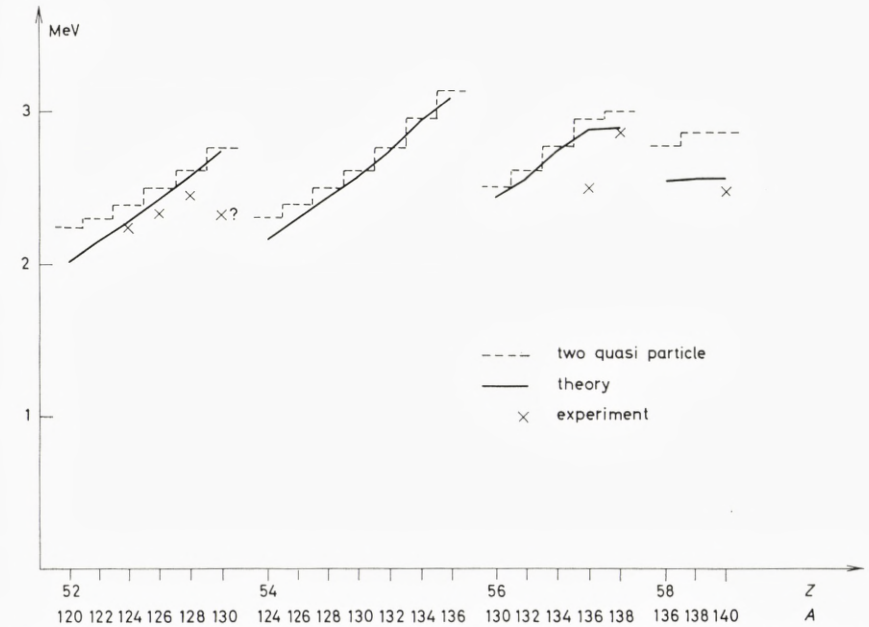

Fig. 17. Energies for case 7b. The experimental points are due to HANSEN and NATHAN (ref. 16). Recent experiments (ref. 40) indicate a possible existence of 3^- states in the following nuclei:
$A,Z = 130,56 : E = 1.80$ MeV, $A,Z = 132,56 : E = 2.06$ MeV,
$A,Z = 134,56 : E = 2.37$ MeV.

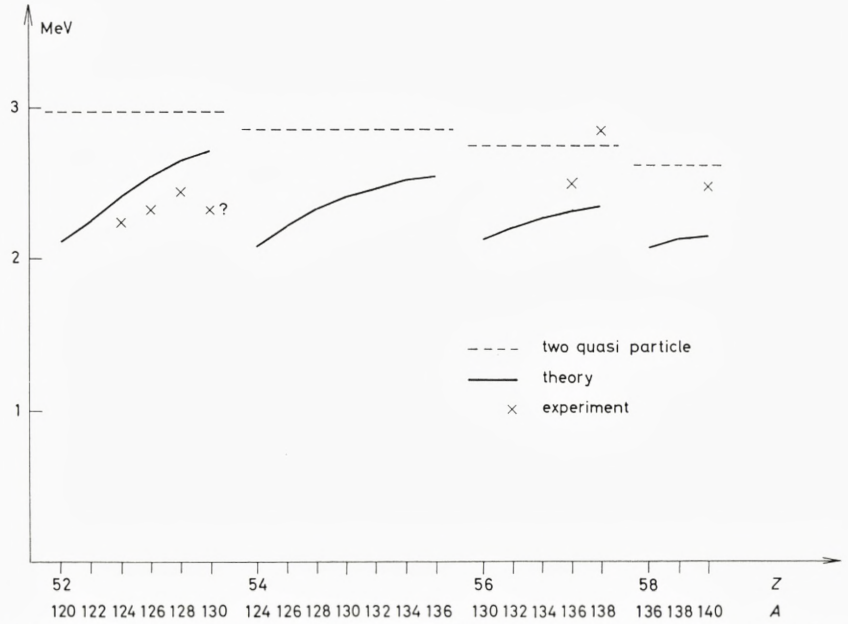

Fig. 18. Energies for case 7c. When comparing this and fig. 17 we see that now the lowest lying proton transition comes below the neutron ones. As discussed in the text, this causes great changes.

filled. Therefore, all the transitions inside partly filled shells are rather weak in case a) for Z just above 50. In case b) this is even more pronounced, since here the strong proton transition $d_{5/2}$–$h_{11/2}$ has a very small uv factor (both levels are almost empty). As seen from fig. 17, the lowest resulting state in b) almost sticks to the two-quasiparticle energy.

The trend in the B values follows from the above mentioned facts. In a) the oscillator strength in the lowest part of the spectrum is spread over more levels, and in b) the lowest line is especially weak, as seen from fig. 10. Following, in table 31, the isotopes with $Z = 56$ for case b), we see a bump in the B values at $A = 136$. The reason is that the lowest neutron two-quasiparticle energy here is increased so much that it comes pretty near to the lowest proton excitation, and thus S^p goes up.

In c) the resulting state of lowest energy is always the strongest one. For the following states there is often an appreciable difference between B and B_0. Still, for the strong ones, $B_0 > 3B_1$.

The experimental results by HANSEN and NATHAN (giving $B = 45$ for $A,Z = 124,52$ and $128,52$) might perhaps be taken as an indication that the

c) levels are most reliable at least in the beginning of the region, but the experimental information is very incomplete. Recent experiments by GERSCHEL et al. (see caption to fig. 17), indicate a possible existence of 3^- states, which show a more rapid energy variation than the theoretically calculated ones. A confirmation of the results would be very interesting.

We note that we are here in a region, where some of the nuclei might be fairly near to (or even have) non-spherical equilibrium shape (ref. 28). This will of course influence the spectra.

Case 8: $50 < Z < 82$, $82 \leqslant N$

(below the region of stable quadrupole deformation).

Here, relatively few particles are available in the partly filled shells, and above the lowest resulting state a strong octupole excitation is formed, largely governed by the intershell transitions, as shown in figs. 8 and 9. We report the results arising from three different level schemes:

a) protons: $g_{7/2}$:0, $d_{5/2}$:0.8, $h_{11/2}$:2.4, $d_{3/2}$:3.13, $s_{1/2}$:3.36; neutrons: $f_{7/2}$:0, $p_{3/2}$:0.83, $i_{13/2}$:1.36, $f_{5/2}$:1.88, $h_{9/2}$:1.9, $p_{1/2}$:2.25 MeV.
b) the neutron level $i_{13/2}$ changed to 0.75 MeV.
c) neutron levels as in a). The proton level $h_{11/2}$ changed to 3.2 MeV.

The proton levels come from a modification of a suggestion by KISSLINGER for $A \simeq 200$ and are almost identical to the KS II levels. In case c) we studied the influence of placing the proton level $h_{11/2}$ between $d_{3/2}$ and $s_{1/2}$, where the neutron $h_{11/2}$ lies in case 5. The neutron levels are due to COHEN, FULMER and MCCARTHY (ref. 27). They do not find the $i_{13/2}$ level, which in a) and b) is placed in two different positions.

The second position reproduces the $f_{7/2} - i_{13/2}$ distance in KS II. On the other hand, they use values which are greatly deviating from ours, especially by placing the $h_{9/2}$ level 0.72 MeV below $f_{7/2}$. For the three cases $c_0 = 0.45$, $c_0 = 0.47$ and $c_0 = 0.41$, respectively, were used (see comment below).

Another calculation was run, using the proton levels from case a) and neutron levels, partly based on a suggestion by KISSLINGER: $f_{7/2}$:0, $h_{9/2}$:0.2, $i_{13/2}$:1.5, $p_{3/2}$:1.75, $f_{5/2}$:2.3, $p_{1/2}$:2.9 MeV. The results from this calculation are the same as those from case a) for $N = 82$. For the greater Ns the energies are just a little higher; they are not reported.

For case a) the lowest proton transitions are the weak $g_{7/2} - h_{11/2}$ and the strong (for $Z > 56$ lower lying) $d_{5/2} - h_{11/2}$, the uv factor of which changes

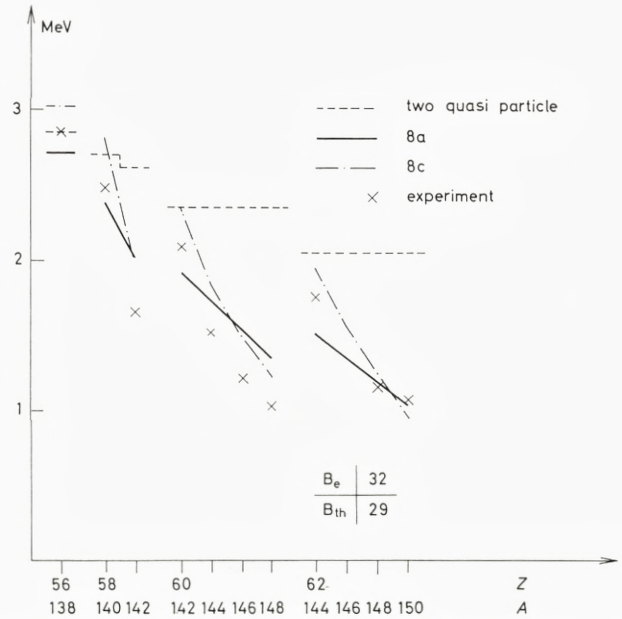

Fig. 19. Energies for case 8a with $c_0 = 0.45$ and for case 8c with $c_0 = 0.41$. "Two-quasiparticle" refers to the lowest lying two-quasiparticle energy in case 8a. The experimental points are due to HANSEN and NATHAN (ref. 16) and E. VEJE (ref. 48) (the B value).

from 0.2 at $Z = 56$ to 0.8 at $Z = 62$. The neutron transitions are the weak $i_{13/2} - h_{11/2}$ with a small uv factor and the strong $f_{7/2} - i_{13/2}$ with a uv factor varying from 0 to 0.72.

Figs. 8 and 9 illustrate how the picture changes when going away from the closed neutron shell. The most remarkable feature is the drop in the energies, caused by the increasing strength of the low-energy neutron lines, which lie above the proton two-quasiparticle excitation of lowest energy.

In case c) the proton quasiparticle energies are increased. This gives the neutron variation a greater influence, but causes an overestimate of the high energies. Changing two protons into two neutrons, i.e. going from $A,Z = 142,58$ to 142,60 or from 148,60 to 148,62 gives experimentally, like in case c), that the energy of the lowest 3^- state goes up, whereas the opposite is true for a). In this sense b) is a little better than a).

For the excitation of lowest energy the neutron excess gives rise to $B_0 > B$, i.e. $S^n > S^p$, even when the neutron shell is closed. The contributions from S_2 are partly responsible for this. For $A,Z = 142,60$ S_1^p is somewhat greater than S_1^n.

TABLE 33. Energy, B and B_0 for the low-energy, stronger excitations in case 8 a, $c_0 = 0.45$. Same units as in table 3.

A,Z:	138,56			140,58			142,58		
E, B, B_0:	2.72	7.8	11	2.38	11	14	2.02	11	23
	2.97	2.6	4.3	3.71	6.7	19	2.67	1.7	0.1
	3.67	5.6	17	4.69	1.8	0.03	3.98	7.8	16
	4.69	1.8	0.02	5.70	0.01	1.8	5.24	0.1	1.8
	5.66	0.03	2.4	5.83	0.03	1.7			

A,Z:	142,60			144,60			146,60		
E, B, B_0:	1.92	15	16	1.72	17	26	1.52	19	36
	3.77	6.6	20	4.03	7.6	16	4.06	1.2	2.5
	4.70	1.9	0.05	5.26	0.03	1.7	4.22	7.5	12
	5.12	0.01	1.5	5.61	0.9	1.8	5.10	0.01	1.9
	5.56	0.8	3.2						

A,Z:	148,60			144.62			146,62		
E, B, B_0:	1.36	21	46	1.51	21	21	1.35	25	32
	4.30	8.8	12	3.81	6.8	20	2.44	0.04	2.7
	5.18	0.01	4.2	4.70	1.8	0.05	4.06	7.7	16
	5.35	0.1	1.7	5.12	3×10^{-3}	1.5	5.71	0.4	3.0
				5.63	0.5	4.7	5.80	0.5	2.3

A,Z:	148,62			150,62		
E, B, B_0:	1.19	29	44	1.04	33	57
	2.34	0.03	2.6	2.29	0.2	2.4
	4.07	0.8	1.8	4.32	8.9	12
	4.24	7.9	12	5.19	0.01	4.2
	5.85	1.0	3.6	5.36	0.01	2.1

Above the transitions inside the partly filled shells there is a rather strong line for which B is only a fraction of B_0 in the neutron magic nuclei. (The transition is governed largely by the neutron transitions).

When we had finished our above mentioned calculations, a new neutron level scheme became available, based on a tentative and preliminary interpretation of some experimental results due to YANG et al. (ref. 29):

$$f_{7/2}:0,\ p_{3/2}:1.2,\ h_{9/2}:1.7,\ f_{5/2}:1.9 \text{ and } i_{13/2}:2.0 \text{ MeV}.$$

TABLE 34. The first row gives E, B and B_0 for the lowest excited state from case 8 b, $c_0 = 0.47$, and the second row those for the same state in case 8 c, $c_0 = 0.41$. Same units as in table 3.

A,Z:	138,56			140,58			142,58		
E, B, B_0:	2.74	6.4	9.2	2.41	9.9	12	1.84	7.2	19
	3.03	17	35	2.82	17	29	1.99	11	29

A,Z:	142,60			144,60			146,60		
E, B, B_0:	1.96	13	15	1.66	14	24	1.45	15	33
	2.37	20	29	1.84	17	37	1.49	21	50

A,Z:	148,60			144,62			146,62		
E, B, B_0:	1.32	17	42	1.56	19	19	1.36	22	30
	1.23	25	66	1.95	27	33	1.57	28	47

A,Z:	148,62			150,62					
E, B, B_0:	1.18	25	41	1.06	28	52			
	1.24	33	65	0.97	41	90			

They did not see the $p_{1/2}$ level which we then placed at 2.3 MeV. The precise location of this level should have only a very small influence on the resulting spectrum.

When using this level scheme and the a) protons, the energy for the lowest state was changed by less than 0.1 MeV, the variation with neutron number N being a little slower than in a). The B values were increased by 10–20 %. For the higher lying strong, resulting states the changes were rather small. The main difference from a) to this case is that c_0 was changed from 0.45 to 0.43 to obtain the best energy fit.

Another calculation was performed with the Yang et al. data and protons from case c). When c_0 is chosen to fit the lowest resulting energy in A,Z = 150,62, (c_0 = 0.393), the agreement with experiment becomes poorer than in c) (less steep variation of energy), especially for the Z = 60 nuclei. B is increased by 10–20 %.

As seen above, in this region we have had some difficulties in fitting $\varkappa$. By just a small change in c_0 we are able to bring the lowest resulting state in A,Z = 150,62 down to zero energy. This warns us to be suspicious on the validity of our simple treatment. It is a well-known trend from the

quadrupole case that, when the resulting state is pressed far down from the lowest two-quasiparticle mode, the simple quasi-boson treatment breaks down. Anharmonicity effects and the Pauli principle should possibly have been taken into account. For the octupoles the situation should in general be better (the excitations are not so collective), one of the exceptions perhaps being just the nuclei below the rare-earth deformed region. It should be further stressed that the approximation of neglecting coupling between quadrupole and octupole vibrations might be especially bad here, near the domain of stable quadrupole deformation, where the 2^+ vibrations are very strong and of low energy.

Case 9: $Z \leq 82$, $N \leq 126$,
(above the region of stable quadrupole deformation).

In this final case only few proton and neutron holes in the partly filled shells are available. A higher lying state is formed, stronger than the lowest resulting mode.

Two level schemes were used:

a) neutron levels suggested by KISSLINGER (ref. 26) (almost identical to KS II) $h_{9/2}$:0, $f_{7/2}$:0.2, $i_{13/2}$:0.92, $p_{3/2}$:1.65, $f_{5/2}$:1.98, $p_{1/2}$:2.55 MeV; proton levels from calculations on Pb^{208} by GILLET et al. (ref. 30) $g_{7/2}$:0, $d_{5/2}$:1.69, $h_{11/2}$: 2.34, $d_{3/2}$:3.83, $s_{1/2}$:4.18 MeV.

b) same neutron levels, proton levels from a recent experiment by NATHAN (ref. 31) $g_{7/2}$:0, $d_{5/2}$:1.73, $h_{11/2}$:2.06, $d_{3/2}$:3.05 and $s_{1/2}$:3.40 MeV.

The single-particle energies in the neutron shell above the partly filled shell are taken from a report on stripping experiments (ref. 32).

The proton energies above the partly filled shell are the values used by GILLET et al. (refs. 33 and 30). The other single-particle energies come from the simple shell-model calculations (ref. 13) as explained before. The a) calculation was performed especially with the aim to compare it with the calculation by GILLET et al. (ref. 30).

The neutron single-particle energies are not exactly equal to the Gillet ones, but the differences are so small that it might be reasonable not to take them into account.

The transitions inside the partly filled shells are for the protons the weak $g_{7/2}\, h_{11/2}$ and the strong $d_{5/2}\, h_{11/2}$ transition and for the neutrons the weak $h_{9/2}\, i_{13/2}$ and the strong $f_{7/2}\, i_{13/2}$ transition, but all the contributing levels are almost filled. This is especially pronounced for the protons where the uv factor is very near to zero.

TABLE 35. Energy, B and B_0 for the low-energy, stronger excitations in case 9 a, $c_0 = 0.413$. Same units as in table 3.

A,Z:	192,76			192,78			194,78		
E, B, B_0:	2.49	3.0	15	2.21	4.7	20	2.48	4.2	18
	4.53	13	51	4.45	20	38	4.31	21	50
	5.55	5.9	16	5.05	1.7	15	5.54	5.1	13

A,Z:	196,78			198,78			196,80		
E, B, B_0:	2.76	4.4	18	3.03	5.6	23	2.47	6.1	21
	4.10	20	57	3.88	19	60	4.08	28	50
	5.38	3.4	12	5.18	1.5	8.1	5.69	1.0	10

A,Z:	198,80			200,80			202,80		
E, B, B_0:	2.74	6.6	22	3.00	9.4	31	3.19	21	67
	3.93	28	58	3.75	24	59	3.60	7.9	22
	5.34	3.9	9.1	5.18	1.8	8.1	3.66	4.7	12

A,Z:	204,80			202,82			204,82		
E, B, B_0:	3.13	34	112	2.96	16	43	3.10	33	88
				3.65	29	58	3.57	9.8	21
				5.87	1.8	11	5.77	1.1	10

A,Z:	206,82			208,82					
E, B, B_0:	3.01	45	125	2.79	49	147			

The greatest role is played by the strong transitions between the shells, giving a rather low-lying and strong octupole state in the doubly magic Pb^{208} (fig. 7).

For the lower A values, there is a strong higher-lying 3^-, whereas the lowest one is rather weak and near to the two-quasiparticle energy. Because of the neutron excess and the weakness of the proton transitions inside the partly filled shell, B for the lowest state is smaller than B_0.

One more calculation was run, using the a) neutron levels and proton levels from KS II:

$$g_{7/2}{:}0,\ d_{5/2}{:}0.8,\ h_{11/2}{:}2.1,\ d_{3/2}{:}2.6 \text{ and } s_{1/2}{:}2.95 \text{ MeV}.$$

TABLE 36. Energy, B and B_0 for the low-energy, stronger excitations in case 9 b, $c_0 = 0.404$. Same units as in table 3.

A,Z:	192,76			192,78			194,78		
E, B, B_0:	1.64	0.9	1.2	2.16	7.5	25	2.32	4.2	9.6
	2.47	4.0	18	4.38	26	48	2.48	2.9	14
	4.41	18	58	5.04	1.2	11	4.22	25	56
	5.46	2.0	3.2	5.63	5.4	7.3	5.50	6.1	12
	5.52	4.3	10	5.79	0.8	3.0			

A,Z:	196,78			198,78			196,80		
E, B, B_0:	2.34	2.3	4.0	2.34	2.1	3.6	2.43	8.7	27
	2.74	5.3	21	3.00	8.0	30	4.00	33	57
	3.99	23	60	3.78	21	61	5.40	4.5	4.6
	5.34	4.1	11	5.16	1.7	7.7	5.67	0.9	6.9
	5.86	2.8	3.6	5.68	4.3	4.7			

A,Z:	198,80			200,80			202,80		
E, B, B_0:	2.69	9.9	28	2.77	2.9	6.4	2.77	3.0	6.8
	3.84	31	63	2.96	12	37	3.10	28	82
	5.30	4.8	9.1	3.67	25	58	3.57	8.3	21
				5.15	2.4	8.0	3.65	1.6	3.7
							4.98	0.7	5.2

A,Z:	204,80			202,82			204,82		
E, B, B_0:	2.76	6.5	17	2.90	24	59	2.98	44	109
	3.01	34	109	3.57	28	53	3.54	8.0	16
	4.62	4.0	0.4	5.02	4.6	3.8	4.93	2.3	4.7
	5.39	4.2	5.3	5.80	2.9	8.5	5.72	1.8	9.2

A,Z:	206,82			208,82					
E, B, B_0:	2.85	53	140	2.62	58	165			
	4.59	4.2	0.1	4.56	4.3	0.4			
	4.80	0.3	3.3	5.08	2.4	1.1			
	5.44	1.5	3.5	5.46	1.9	2.5			
	5.68	0.8	5.2						

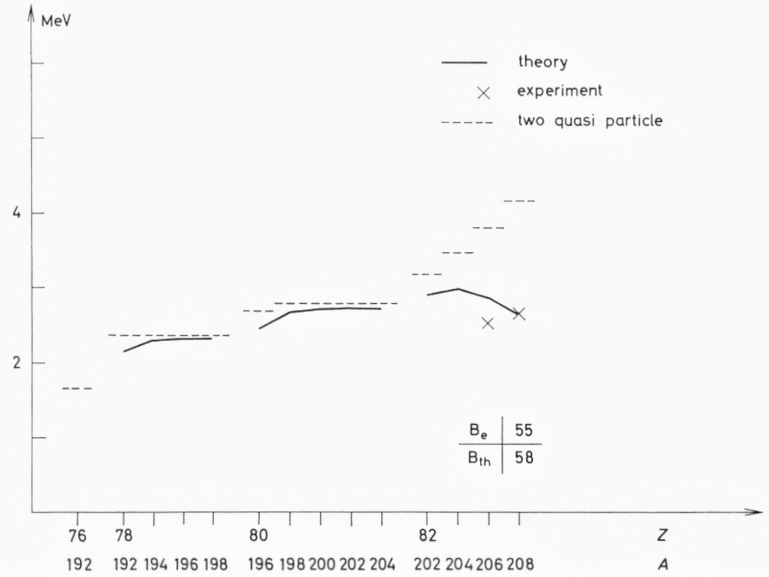

Fig. 20. The lowest lying energy, B value and two-quasiparticle energy for the nuclei in case 9b, where $c_0 = 0.404$. The experimental values come from ref. 41 and ref. 49.

Although the proton energies are quite different from those above, the resulting states are only affected little, especially the state of lowest energy. The quantity c_0 was 0.413 in a) and 0.404 in b). The results are given in tables 35 and 36.

In Pb^{208} the agreement between theory and experiment is quite satisfactory, but it must be remembered that c_0 is chosen lower than in the other cases.

If $\varkappa_1 < 0$ is used B will exceed the experimental value since $B_0 > B$.

Comparison with the calculation by GILLET et al.

As mentioned above, we are able to compare our results with those obtained by GILLET et al. (ref. 30) in Pb^{208} when using a spin and isospin dependent force in which the radial dependence is of Gaussian type in the distance between the two nucleons. In table 37 and table 38 we quote the amplitudes p and q for quasiparticle pair creation and annihilation, respectively, from the lowest neutron and proton modes to the lowest resulting state. It is remarkable that all the amplitudes except those for the neutron $5f_{5/2}$ $6s_{1/2}$ quasiparticle excitation have the same sign for the two quite different forces.

TABLE 37. For GILLET's calculation (ref. 30) and for the calculation from case 9 a, the table gives E, $p = p(\alpha, j_1, j_2)$ and $q = q(\alpha, j_1, j_2)$ for the lowest neutron particle-hole excitations, contributing to the first octupole excitation in Pb^{208}. E is the energy for the relevant particle-hole excitation.

Since there is some difference between GILLET's phase convention (ref. 42) and ours, the sign for our amplitudes p and q in this table is changed to be in agreement with GILLET's choice of phase.

transition	GILLET			this calculation		
	E	p	q	E	p	q
$5f_{5/2}$–$6g_{9/2}$	4.01	0.19	0.03	4.17	0.21	0.04
$5p_{3/2}$–$6g_{9/2}$	4.34	−0.42	−0.07	4.50	−0.50	−0.12
$5f_{5/2}$–$6i_{11/2}$	4.80	0.39	0.07	4.94	0.41	0.12
$5p_{1/2}$–$6d_{5/2}$	5.02	0.08	0.02	5.16	0.23	0.07
$5f_{5/2}$–$6d_{5/2}$	5.59	0.06	0.02	5.73	0.11	0.04
$5f_{7/2}$–$6g_{9/2}$	5.78	−0.20	−0.06	5.95	−0.09	−0.03
$5p_{3/2}$–$6d_{5/2}$	5.92	−0.05	−0.02	6.06	−0.15	−0.06
$5f_{5/2}$–$6s_{1/2}$	6.04	−0.08	−0.04	6.20	0.12	0.04
$5p_{1/2}$–$6g_{7/2}$	6.14	0.17	0.04	6.07	0.20	0.07
$5f_{5/2}$–$6g_{7/2}$	6.71	0.13	0.05	6.64	0.15	0.06
$5d_{3/2}$–$6f_{5/2}$	6.93	0.05	0.02	6.69	0.11	0.04

TABLE 38. E, p and q for the lowest proton particle-hole excitations contributing to the first octupole state in Pb^{208}. For further explanation, see caption to table 37.

transition	GILLET			this calculation	
	E	p	q	p	q
$4d_{3/2}$–$5h_{9/2}$	4.61	−0.47	−0.08	−0.33	−0.08
$4s_{1/2}$–$5f_{7/2}$	5.16	0.37	0.08	0.22	0.07
$4d_{3/2}$–$5f_{7/2}$	5.51	−0.15	−0.04	−0.11	−0.03
$4d_{5/2}$–$5h_{9/2}$	6.75	−0.07	−0.02	−0.06	−0.02
$4d_{3/2}$–$5p_{3/2}$	7.26	−0.13	−0.05	−0.09	−0.04
$4s_{1/2}$–$5f_{5/2}$	7.56	−0.15	−0.06	−0.10	−0.04
$4d_{5/2}$–$5f_{7/2}$	7.65	0.14	0.06	0.10	0.05
$5h_{11/2}$–$6i_{13/2}$	7.72	−0.17	−0.07	−0.17	−0.08
$4d_{3/2}$–$5f_{5/2}$	7.91	−0.10	−0.04	−0.08	−0.04

Concerning their magnitudes, there is also a quite strong correlation. The most interesting feature is that the Gillet neutron amplitudes in general are a little smaller than our amplitudes, whereas the proton ones are about 50 % greater.

This is consistent with the result that GILLET et al. reach 60 % of the experimental B value (which is only known $\pm$ 30 %, ref. 41) without using any renormalization of the charge. If we took only the $\Delta N = 1$ transitions into account (keeping the resulting energy constant) B would go down with a factor of two.

A stronger influence from the proton excitations on the lowest resulting level is obtained when an isospin dependent force is introduced. Thus, when $\varkappa_1 = -0.5\varkappa_0$ is used and $\varkappa_0$ is changed to give approximately the same energy as when $\varkappa_1 = 0$, the B value is increased by 50 %, which means that it becomes greater than the experimental value. ($c_0 = 0.38$, $\varkappa_1 = -0.5\varkappa_0$ gives $E = 2.83$ MeV, $B = 72$.)

16. Concluding remarks

The most striking feature we meet when we start the numerical calculations is the very great sensitivity of the results to the energies of the shell-model levels inside the partly filled shells, and the incomplete and partly contradictory information which is available concerning these energies.

It looks as if one may sometimes take different shell-model level schemes for all of which it is possible to argue reasonably well, and obtain very different quantitative pictures for the lowest part of the resulting spectrum, especially for the B values. This should be kept in mind, when our conclusions are studied.

When the number of experimental results increases, and when more modes of excitation are to be described from the same quasiparticle energies, we may get a better insight into the variation of $\varepsilon(j)$, and then also into the precise validity of the theory.

The fitting of the octupole force constant

For simplicity reasons a major part of the calculation was made, using an isospin independent octupole force constant.

In general it has been possible to fit the experimental energies of the lowest resulting excitation reasonably well with a smoothly varying $\varkappa$. In the *Ni* region we had to use a value which was a few percent larger, and in *Zr* a value which was a few percent smaller. Although difficult to say definitely (cf. sect. 14) there seems to be some tendency for a weaker $\varkappa$ variation with A than obtained by a simple scaling argument (cf. sect. 2).

This might be taken as an indication that the surface region of the nucleus should have a stronger weight than assumed by our simple Hamiltonian.

The magnitude and variation of $\varkappa$ are in general agreement with the parameters used by SOLOVIEV et al. (ref. 3), although some details are different. E.g. they take only part of the single-particle levels into account. When more and more levels are included, their $\varkappa$ value approaches our value (ref. 43).

They also use another (slower) A variation inside each of the two regions of deformed nuclei around $A \sim 180$ and $A \sim 240$, whereas the variation from the first region to the second is approximately the same as our overall variation.

From the calculations on quadrupole vibrations (ref. KS II) it is well known that when the lowest resulting energy is pressed far down from the lowest two-quasiparticle excitation, the fitting of $\varkappa$ becomes very difficult. Even a small change in $\varkappa$ may bring the resulting energy down to zero.

This indicates that the simple quasiboson approximation breaks down. When the state is very collective, the Pauli principle and various anharmonicities should presumably have been taken into account (ref. 44).

Since the octupole vibrations are only moderately collective, the simple theory should work better for these than for the quadrupoles.

An exception is perhaps the nuclei just below the deformed rare-earth region where the nuclei seem to be able to undergo octupole deformation rather easily. However, there is in this case a great uncertainty in the single-particle energies, and a definite conclusion is difficult.

The general distribution of oscillator strength

From the calculation it appears that the octupole-octupole force sucks $5-10\,\%$ of the total B oscillator strength down and places it on some few, strong lines in the lowest part of the spectrum. While B for these lines varies quickly, $B \times E$ shows a much slower variation.

The rest of the oscillator strength is distributed in the $\hbar\omega_0$ and $3\hbar\omega_0$ regions. In the present model it will not be concentrated to any high degree at some few levels but is spread rather smoothly over large energy intervals. One of the more interesting results is that very strong lines just below or above the $3\hbar\omega_0$ region can hardly be expected, but it should be stressed that we have used a crude model and parameters which are not very well

known. There is especially poor knowledge about the energy distribution of the unperturbed excitations in the $3\hbar\omega_0$ region.

The influence of the shell structure is clearly seen. E.g. the low-energy part of the oscillator strength in the typical case is split into two parts because of an energy gap in the unperturbed spectrum. This gap appears just above the two-quasiparticle excitations inside partly filled shells.

It is worthwhile to note that the octupole excitation of lowest energy in some sense only represents a fine structure in the resulting spectrum, although it has been the subject of almost all theoretical and experimental investigations and is the most easily observed. The fine structure occurs because the spin-orbit splitting pushes a level down, so that some particles outside the core may change orbit almost without change in energy and make large octupole moments. An essential part of the oscillator strength is left on higher levels.

The low energy part of the spectrum

From the calculation it is seen that the energy of the lowest resulting state very intimately follows the variations in energy and strength of the very lowest two-quasiparticle modes. By studying the single-particle level scheme and the filling of the levels it is possible in a very simple way to understand the variations in position and strength of the strong excitations of low energy.

The few measured B values are reproduced by the calculation, in general within $30\,\%$.

This is the best we could expect from the simple theory.

We may stress that the calculation has been performed without introducing any effective charge. If the $3\hbar\omega_0$ unperturbed transitions were not included, the B values would be about a factor of two smaller. Some uncertainty is introduced in B by simply using harmonic oscillator values for the strength and energy of the high-lying transitions.

There is some indication that the theory systematically underestimates the B value and it is not difficult to find possible reasons for this. One is that an isospin independent octupole force is used. We have seen how in almost all cases introduction of an isovector component leads to an increase in the resulting B value. We have not gone into a systematic study but may mention that in the *Sn* region where the discrepancies between theory and experiment for the B values are especially great, introduction of $\varkappa_1 \neq 0$ will have an especially large effect. Another possible reason is the systema-

tic error due to the use of the same harmonic oscillator potential for protons and neutrons. Thus, because of the neutron excess, the protons are kept too close to the nuclear centre and contribute too little to the transition moments. Finally, it is a more trivial possibility that a somewhat stronger pairing force should have been used. This would give higher two-quasi-particle energies. To reproduce the experimental energies a stronger octupole-octupole force should be used, the state would be more collective, i.e. B greater.

The isospin properties

In the calculation it has been found that the low-energy strong excitations to a good degree are of $\tau = 0$ type, although $\tau = 1$ impurities may give rise to interesting effects, e.g. so that the "strength" of the excitation depends of whether it is measured with the help of inelastic scattering of protons,or with α scattering or with Coulomb excitation. For the models which we have used, and for $\varkappa_1$ values from a tentative theoretical estimate, there is no strong tendency towards concentrating the $\tau = 1$ oscillator strength on a single level.

When using a pure $\varkappa_0$ force we make a systematic error, which however should be small, when the energies of the strong excitations of low energy are considered. For B there may be a more significant change when $\varkappa_1$ is introduced, as mentioned above.

It is very difficult to determine the strength of the $\tau = 1$ part of the long-range force. One possibility might be to study the ratio of isospin flip to non-isospin flip in the excitation of 3^- states by inelastic nucleon scattering. Another one is to study relative cross sections for inelastic scattering processes, using particles with different isospins and exciting different 3^- levels in the same nucleus.

It should be less rewarding to study, e.g., the lowest 3^- state in neighbouring nuclei, since the change in isospin character with a change in the atomic number is not very rapid.

Acknowledgements

The author is indebted to many guests and members of the staff of the Niels Bohr Institute, University of Copenhagen, for valuable comments and discussions. He especially wants to thank Drs. O. Nathan and O. Hansen

for stimulating discussions on the experimental aspects, professors L. KISSLINGER and V. GILLET for comments on the energies of the single-particle levels, and professor S. YOSHIDA for the explanation of some points in his calculation of quadrupole and octupole vibrations (ref. 1).

Also remarks from mag. scient. J. P. BONDORF are much appreciated. Primarily, however, the author feels very indebted to professor A. BOHR for his kind interest and many valuable discussions and suggestions concerning this work.

References

1. S. YOSHIDA: Nucl. Phys. **38**, 380 (1962).
2. M. KOBAYASI and T. MARUMORI: Progr. Theor. Phys. **23**, 387 (1960);
   R. ARVIEU and M. VENERONI: Compt. Rend. **250**, 992, 2155 (1960);
   A. BOHR and B. MOTTELSEN: Lectures on Nuclear Structure and Energy Spectra, to be published; in the following called BM.
3. V. G. SOLOVIEV: Phys. Lett. **6**, 126 (1963).
   V. G. SOLOVIEV, P. VOGEL and A. A. KORNEICHUK: Preprint, Dubna 1964;
   LU YANG, V. G. SOLOVIEV, P. VOGEL and A. A. KORNEICHUK: Preprint, Dubna 1964;
   D. BÉS: Nucl. Phys. **49**, 544 (1963);
   E. R. MARSHALEK: Thesis, UCRL 10046 (1962);
   E. R. MARSHALEK and O. RASMUSSEN: Nucl. Phys. **43**, 438 (1963); cf. also ref. 6.
4. L. KISSLINGER and R. A. SORENSEN: Revs. Mod. Phys. **35**, 853 (1963); in the following called KS II.
5. S. T. BELYAEV: Mat. Fys. Medd. Dan. Vid. Selsk. **31**, no. 11 (1959).
6. For a presentation of the theory and the approximations involved, see, e.g., A. M. LANE: Nuclear Theory, Benjamin, New York 1964, or BM or KS II.
7. See, e.g., G. E. BROWN: Lectures on Many-Body Problems, Nordita 1962, or G. E. BROWN: Unified Theory of Nuclear Models, North Holland Publishing Company, Amsterdam 1964.
8. A. M. LANE and J. M. SOPER: Phys. Lett. **1**, 28 (1962).
9. D. ROBSON: Phys. Rev. **137**, B 535 (1965).
10. L. A. SLIV: Private communication.
11. O. NATHAN and S. G. NILSSON: Collective Nuclear Motion and the Unified Model; in Alpha, Beta and Gamma Ray Spectroscopy, Ed. Kai Siegbahn, North Holland Publishing Company, Amsterdam 1965.
12. L. S. KISSLINGER and R. A. SORENSEN: Mat. Fys. Medd. Dan. Vid. Selsk. **32**, no. 9 (1960); in the following called KS I.

13. S. G. Nilsson: Mat. Fys. Medd. Dan. Vid. Selsk. **29**, no. 16 (1955);
B. Mottelson and S. G. Nilsson: Mat. Fys. Skr. Dan. Vid. Selsk. **1**, no. 8 (1959).
14. B. L. Cohen: Phys. Rev. **127**, 597 (1962).
15. L. Silverberg: Arkiv för Fysik **20**, 341 (1962) and private communication.
16. O. Hansen and O. Nathan: Nucl. Phys. **42**, 197 (1963).
17. B. L. Cohen, R. A. Fulmer, and A. L. McCarthy: Phys. Rev. **126**, 698 (1962).
18. R. H. Fulmer and W. W. Dalhnik: Nuclear Structure Studies in the Ni Isotopes with (d, t) reactions, preprint, March 1965.
19. B. L. Cohen: Phys. Rev. **125**, 1358 (1962).
20. B. L. Cohen: Phys. Rev. **127**, 597 (1962).
21. B. Cujec: Phys. Rev. **131**, 735 (1963).
22. B. L. Cohen and R. E. Price: Phys. Rev. **121**, 1441 (1961).
23. B. Cujec: Private communication.
24. H. Faraggi et al.: Phys. Lett. **13**, 244 (1964);
H. Faraggi: Private communication.
25. D. L. Allan et al.: Nucl. Phys. **66**, 481 (1965).
26. L. Kisslinger: Private communication.
27. R. A. Fulmer: A. L. McCarthy and B. L. Cohen: Phys. Rev. **128**, 1302 (1962). They do not see the $d_{5/2}$ level but expect it to at least 0.6 MeV below $g_{9/2}$.
28. E. Marshalek, L. W. Person and R. K. Sheline: Revs. Mod. Phys. **35**, 108 (1963).
29. F. C. Yang, P. R. Christensen, B. Herskind and R. Borchers: Private communication.
A later interpretation of the experimental data gives the following single-particle energies: $f_{7/2}$: 0, $p_{3/2}$: 0.89, $i_{13/2}$: 1.38, $p_{1/2}$: 1.61, $f_{5/2}$: 1.91 and $h_{9/2}$: 2.00 MeV.
30. V. Gillet, A. Sanderson and A. Green: Phys. Lett. **11**, 44 (1964).
31. S. Hinds et al.: Phys. Lett. **17**, 302 (1965).
32. B. L. Cohen and Paresh Mukherjee: Phys. Rev. **127**, 1284 (1962).
33. V. Gillet: Private communication.
34. M. Crut et al.: Nucl. Phys. **17**, 665 (1960);
H. W. Broek: Phys. Rev. **130**, 1914 (1963);
K. Matsuda: Nucl. Phys. **33**, 536 (1962);
H. Crannel et al.: Phys. Rev. **123**, 923 (1961);
cf. also the references in ref. 1 and ref. 11.
35. R. H. Helm: Phys. Rev. **104**, 1466 (1956).
36. W. Darcey: Private communication and Proceedings of the Paris Conference 1964, Centre National de la Recherche Scientifique, Paris 1965.
37. M. Sakai et al.: Phys. Lett. **8**, 197 (1964).
38. F. K. McGowan, R. L. Robinson, P. H. Stelson and J. L. C. Ford: Nucl. Phys. **66**, 97 (1965).
39. D. Alkazov, J. P. Gangrinskij, J. K. Lemberg, J. I. Udralov: Tibilsi Conference, Februar 1964.
40. R. A. Ricci: Private communication;
G. Gerschel et al.: Proceedings of the Paris Conference 1964, Centre National de la Recherche Scientifique, Paris 1965.
41. H. Crannel et al.: Phys. Rev. **123**, 923 (1961).

42. V. Gillet and N. Vinh Mau: Nucl. Phys. **54**, 321 (1964).
43. P. Vogel: Private communication.
44. K. Ikeda, T. Udagawa and H. Yamamura: preprint;
B. Sørensen: Thesis, Copenhagen 1965.
45. B. Rosner: Phys. Rev. **136**, B 664 (1964).
46. R. L. Silva and G. E. Gordon: Phys. Rev. **136**, B 618 (1964).
47. R. K. Jolly: Phys. Rev. **136**, B 683 (1964).
48. E. Veje: to be published.
49. Landolt Börnstein, Zahlenwerte und Funktionen, Neue Serie, Springer Verlag, Berlin 1961.
50. See, e.g., A. M. Lane: Nucl. Phys. **35**, 676 (1962).

Indleveret til Selskabet den 24. november 1965.
Færdig fra trykkeriet den 8. august 1966.

Matematisk-fysiske Meddelelser
udgivet af
Det Kongelige Danske Videnskabernes Selskab
Bind **35,** nr. 2

Mat. Fys. Medd. Dan. Vid. Selsk. **35,** no. 2 (1966)

A STUDY OF ENERGY LEVELS IN ODD-MASS YTTERBIUM ISOTOPES BY MEANS OF (*d*,*p*) AND (*d*,*t*) REACTIONS

BY

D. G. BURKE, B. ZEIDMAN, B. ELBEK,
B. HERSKIND, AND M. OLESEN

København 1966
Kommissionær: Munksgaard

CONTENTS

		Page
1.	Introduction	3
2.	Theoretical Considerations	5
3.	Experimental Procedure and Results	7
4.	Interpretation of the Spectra	14
	A. The $1/2-[521]$ orbital	18
	B. The $5/2-[512]$ orbital	24
	C. The $1/2-[510]$ orbital	25
	D. The $3/2-[512]$ orbital	28
	E. The $7/2+[633]$ orbital	30
	F. The $7/2-[514]$ orbital	31
	G. The $9/2+[624]$ orbital	32
	H. The $3/2-[521]$ orbital	32
	I. The $5/2-]523]$ orbital	33
	J. The $5/2+[642]$ orbital	34
	K. Vibrational States	36
5.	Determination of Δ from the U^2 and V^2	46
6.	Comparison of Intensities with Predicted Values	48
7.	Summary	52

Synopsis

The results of an experimental study of (d,p) and (d,t) reactions with 12 Mev deuterons on targets of Yb^{168}, Yb^{170}, Yb^{172}, Yb^{174} and Yb^{176} are reported. A magnetic spectrograph was used to analyze the reaction products with an overall energy resolution of $\sim 0.1\,\%$. The observed populations of the low-lying states in the final odd nuclei are in general agreement with predictions based on the stripping theory for deformed nuclei, made by the use of the Nilsson wave functions and single-particle cross sections obtained from a distorted wave Born approximation calculation.

The relative populations of the various members of a rotational band based on an intrinsic state are highly characteristic of the state, and change only slightly from one nucleus to another. This property permits the unambiguous assignment of all the low-lying orbitals, except those with very weak cross sections, without the necessity of measuring angular distributions.

Many previously unknown levels have been found in the present work, and approximately fifty of them have been classified in terms of the Nilsson model. In addition, some speculations concerning vibrational states have been made. The use of the complementary reactions is shown to be a useful technique for determining the hole or particle character of the states. The filling of the orbitals as a function of mass number is in good agreement with pairing theory predictions, and indicates that the pairing energy parameter, Δ, is 0.80 ± 0.15 Mev.

PRINTED IN DENMARK
BIANCO LUNOS BOGTRYKKERI A-S

1. Introduction

The amount of experimental information concerning the excited states of deformed odd nuclei has increased considerably in recent years together with an improvement of the theoretical description of these states. The low-lying states can be described remarkably well as collective rotations based on single-particle orbitals in a deformed potential[1,2]. Some success has also been obtained in interpreting certain states at higher excitation as collective vibrations based on the single-particle levels. These collective states can be considered to be the result of a correlated motion of many particles where, in the limiting case, the amplitude of each single-particle component is small compared to the total. However, in actual fact, collective vibrational states often exhibit properties which indicate that one or two single-particle components may constitute appreciable fractions of the total amplitude. In order to understand the properties of these states, it would be useful to have a knowledge of the systematics of intrinsic states and the composition of the collective states in this region.

As a result of the various different modes of excitation the energy spectrum of a heavy deformed nucleus can be very complex. For the experimental study of such spectra, it is advantageous to make use of nuclear reactions with a high degree of selectivity in the nature of the states populated. Thus, it is well known that reactions involving the transfer of a single nucleon between projectile and target are especially suited for the determination of the various single-particle components of a state which, in principle, can be determined from the reaction cross sections.

In the past, (d,t) and (d,p) reactions have been used to study low-lying levels in several nuclei which have a spherical equilibrium shape[3,4]. The two reactions serve as complementary spectroscopic tools in that the stripping process favours the population of particle states whereas the pick-up process favours the population of hole states. A number of deformed nuclei have also been studied by means of the (d,p) reaction[5,6,7] and it has been

shown that the probabilities for populating the various members of rotational bands can be predicted quite well, using the stripping theory of SATCHLER[8] with the nuclear wave functions of NILSSON[1] and the intrinsic-particle cross section given by a distorted wave Born approximation (DWBA) calculation[9]. It is not a priori expected that such is the case, since all three basic parts of the analysis do not have a sound theoretical footing. In the form used, the Satchler stripping theory is valid only insofar as the reaction proceeds by a one step process. For the deformed nuclei, the presence of a large number of low-lying easily excited rotational levels provides a region where the two-step process of excitation and stripping may be important. It will be shown however, in an unambiguous case, that this mechanism is not of primary importance. The use of Nilsson wave functions based upon a harmonic oscillator potential is justified by the success achieved using these wave functions. More realistic wave functions would be obtained from calculations in a deformed Woods-Saxon well, but the qualitative features of the wave functions must be retained, i.e. large components of the wave function must remain large, small components remain small. DWBA calculations that have been used to date assume a zero-range interaction and spherical nuclei. It would be desirable to have coupled channel calculations that treat finite-range, non-locality and spin-orbit coupling in a deformed system while utilizing optical model parameters obtained from an extensive series of experiments and analysis. The complexity of this problem places it beyond the current range of detailed calculation. It has been shown, however, that the zero-range calculation provides good qualitative relationships among the cross sections for different l-values and Q-values, provided reasonable optical model parameters are used[5, 6]. If sufficient information is available, this feature makes it possible to extract detailed absolute information once the procedure has been calibrated. This has been done in the present study. Information was available prior to analysis for several low-lying intrinsic bands. This information was used in an empirical analysis of some of the data from both (d,p) and (d,t) reactions and the results were compared with those obtained with the procedures outlined above. Cross-checks and consistency between the two methods of analysis together with consistency in the results obtained from the analysis of all the data show that the procedures are reliable. We can therefore state that despite the theoretical objections that can be raised, the procedures used yield meaningful identifications and spectroscopic factors. In the discussion to follow, it is therefore tacitly assumed that use of the Satchler stripping theory, Nilsson wave functions and representative zero-range DWBA calcu-

lations is justified and may be utilized as a framework within which to analyze the data.

The present work is part of an investigation of the energy levels in the ytterbium nuclei by means of the (d,p) and (d,t) reactions. The analysis of the results for the even-even final nuclei will appear as a separate report[10]. In order to examine the systematic behaviour of the intrinsic states and their filling near the Fermi surface it is helpful to carry out experiments on a series of isotopes. Therefore, targets enriched in each of the stable isotopes of ytterbium were used. The ytterbium series, where there are seven stable isotopes (five even-even and two odd), was chosen because there is very little variation in nuclear deformation[11]. Also, the vibrational states in the heavier ytterbium nuclei are at higher excitation energies than in other rare earths[10, 12]. Thus, it is expected that they will have less interaction with the low-lying intrinsic states populated by the stripping and pick-up processes, making possible the observation of relatively pure single-particle states over a greater interval of excitation.

2. Theoretical Considerations

From the work of SATCHLER[8] it is seen that the differential cross section for a (d,p) reaction between a target nucleus with spin I_i and a final state with spin I_f can be written

$$\frac{d\sigma}{d\omega} = \frac{2I_f + 1}{2I_i + 1} \sum_l S_l \varphi_l(\theta), \tag{1}$$

where $\varphi_l(\theta)$ is the single-particle reaction cross section for angular momentum transfer l at the angle θ. This quantity can be obtained by means of a distorted wave Born approximation (DWBA) calculation.

The spectroscopic factor, S_l, is determined by the nuclear structure only, and is thus independent of angle θ, Q-value, etc. If one uses the Nilsson wave functions[1], the value of S_l for a transition to a rotational state in a deformed nucleus is

$$S_l = \sum_j \theta_{jl}^2, \tag{2}$$

where

$$\theta_{jl} = g \sqrt{\frac{2I_i + 1}{2I_f + 1}} \langle I_i j \pm K_i \mp \Delta K | I_f K_f \rangle C_{jl} \langle \varphi_i | \varphi_f \rangle. \tag{3}$$

The C_{jl} values are characteristic of the orbital into which the neutron is stripped and are related to the Nilsson coefficients $a_{l\Lambda}$ by means of the Clebsch-Gordon transformation

$$C_{jl} = \sum_{\Lambda} a_{l\Lambda} \langle l\tfrac{1}{2}\Lambda\Sigma | j\Omega \rangle, \tag{4}$$

where the quantities Λ, Σ, K and Ω are the same as those used by NILSSON. K_i and K_f are the spin components parallel to the symmetry axis in the initial and final nucleus, respectively. ΔK is the K value of the orbital into which the neutron is stripped. $\langle \varphi_i | _f \varphi \rangle$ is the overlap integral for the initial and final states and is expected to be nearly unity if the nuclear deformation does not vary greatly. The factor g is equal to $\sqrt{2}$ if $K_i = 0$ or $K_f = 0$ but otherwise is equal to unity.

In general, the reaction cross section to a given state can have contributions from several different l-values. However, for an even-even target nucleus where j is necessarily equal to I_f the expression simplifies to

$$\frac{d\sigma}{d\omega} = 2C_{jl}^2 \varphi_l. \tag{5}$$

In this case it is therefore much easier to compare the theoretical and experimental results, and it is for this reason that the experiments pertaining to levels in odd nuclei are discussed first. It is then possible to use empirical values of $C_{jl}^2 \varphi_l$ to make better predictions for the population of states in even-even nuclei.

The above discussion neglects the partial filling of levels caused by the pairing force and assumes that $U^2 = 1$, where U^2 is the probability that the state into which the neutron is stripped is empty in the target nucleus. Therefore, expression (5) should be changed to read

$$\frac{d\sigma}{d\omega} = 2C_{jl}^2 \varphi_l U^2. \tag{6}$$

All the expressions (1)–(6) are valid also for the (d,t) reaction, provided an appropriate φ_l is used and U^2 is changed to V^2, where $U^2 + V^2 = 1$. The C_{jl} coefficients in this case pertain to the state from which the neutron is removed.

3. Experimental Procedure and Results

The 12-Mev deuteron beam used in these experiments was produced by the Niels Bohr Institute Tandem Accelerator. The reaction products were analyzed in a single gap, broad range, magnetic spectrograph[13]. Targets of Yb, isotopically enriched in the desired mass number, were prepared by vacuum evaporation onto carbon backings from a tantalum crucible heated by electron bombardment[14]. The enriched samples were obtained in the form of Yb_2O_3 from the Stable Isotopes Division of the Oak Ridge National Laboratory and the isotopic compositions estimated by the supplier are shown in Table 1. Before evaporation, the oxides were reduced by lanthanum to ytterbium metal. The target thickness was between 50 $\mu g/cm^2$ and 150 $\mu g/cm^2$. The Yb^{168} target was not prepared in the above manner, because of the low natural abundance of this isotope (0.2 %). For this target, a sample enriched to $\sim 10\%$ Yb^{168}, obtained from Oak Ridge, was subjected to further enrichment in the University of Aarhus isotope separator, and simultaneously deposited on a carbon backing by the technique developed by Skilbreid[15]. The final enrichment is estimated to be ~ 99 % and the thickness was ~ 40 $\mu g/cm^2$.

The beam defining slits and the entrance aperture of the spectrograph were set to give an energy resolution of approximately 0.1 %. The solid angle of the spectrograph varies slightly with plate position and this dependence was determined by placing a ThB alpha source in the target position and, using different magnetic field strengths, making short exposures of known duration at various positions on the plate. The mean value of the solid angle was $\sim 5 \times 10^{-4}$ steradians for the slit settings used in these experiments.

Table 1. Isotopic Composition of the Yb Targets.

Target Mass	Isotopic Abundance						
	168	170	171	172	173	174	176
168	> 99	—	—	—	—	—	—
170	< 0.1	85.4	5.42	3.66	1.93	2.86	0.75
171	< 0.02	0.27	95.96	2.03	0.63	0.91	0.20
172	< 0.01	0.05	0.75	97.15	1.01	0.87	0.19
173	< 0.05	0.05	0.44	2.33	92.6	4.3	0.38
174	< 0.01	0.02	0.08	0.20	0.52	98.97	0.22
176	< 0.01	0.03	0.16	0.29	0.29	1.45	97.77

With a deuteron energy af 12 Mev and the mass differences encountered in this region of the periodic table, the ground-state triton group always had a greater magnetic rigidity than the elastic deuterons. The excitation energy in the triton spectrum, at which the elastic deuteron peak appeared, increased from ~1 Mev with a Yb^{168} target to ~3 Mev with a Yb^{176} target. The magnetic rigidity of the ground state proton group was always less than that of the elastic deuterons and therefore these groups appeared at an excitation of several Mev in the inelastic deuteron spectrum. For these experiments, an absorbing foil of aluminium, 27 mg/cm^2 thick, was placed over the region of the photographic plates where the deuterons were expected, in order to prevent tritons from appearing in the deuteron spectra. Aluminium foils from 100 mg/cm^2 to 154 mg/cm^2 thick were placed over the plates where the protons were expected in order to stop deuterons, tritons and alpha particles. These foils also served the purpose of reducing the proton energy such that the desired proton tracks were denser and thus easier to count. No absorbing foil was used over the plates where the triton groups were expected. The plate-holder was loaded with five photographic plates, 20.3 cm long × 5.1 cm wide, placed end to end. The plates were manufactured by Ilford and had a Type K2 emulsion with a thickness of 25 microns. In this manner it was possible to record simultaneously the proton, triton and inelastic deuteron spectra from a target, although in practice some information from at least one of these spectra was often lost due to the cracks where the plates were joined.

Beam currents from 100 nA to 600 nA were used and the total charge for each exposure was measured with a Faraday cup and current integrator. In the analysis of the data, peak intensities were determined relative to the intensity of the elastic deuteron peak. However, on the long exposures required, the track density in the elastic peak was so great that counting was impossible. Therefore, a short exposure, planned to give a reasonable number of tracks in the elastic peak, was made immediately before and/or after the long exposure. The relative intensities of the short and long exposures were determined from the charges measured by the beam current integrator.

In order to convert these relative intensities into absolute cross sections for the proton and triton groups, separate experiments were performed to measure the absolute cross section for elastic deuteron scattering. Two separate approaches were tried. In one case, an Yb target was placed in a scattering chamber where a solid-state counter was used as a detector. The angular distribution of the elastic peak was measured for 12 Mev deuterons.

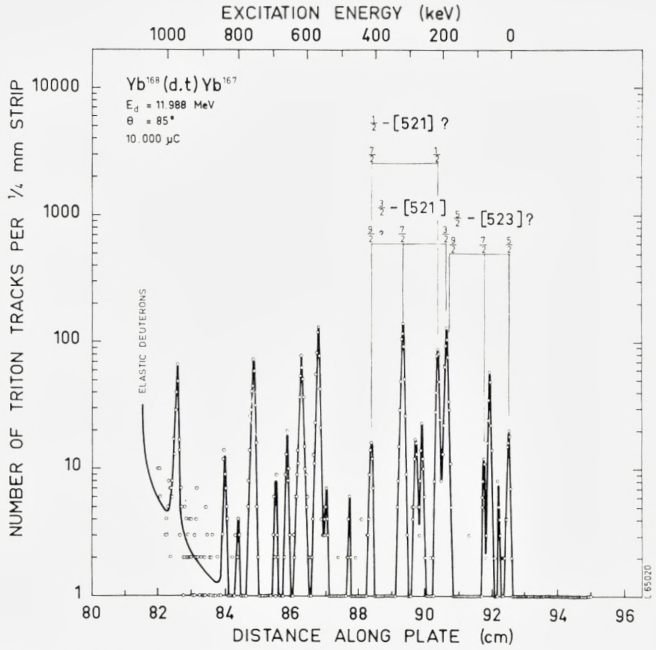

Figure 1. Triton spectrum for the reaction $Yb^{168}(d,t)Yb^{167}$ at $\theta = 85°$.

If one assumes that the cross section for small angle scattering approaches the Rutherford cross section, these data can be normalized to absolute values without a knowledge of target thickness, detector solid angle, etc. For the second method, the same experimental arrangement was used and the relative intensities of elastic deuterons were measured at several angles for beam energies of 5 Mev and 12 Mev. By assuming that the 5 Mev elastic scattering cross section is equal to the Rutherford cross section, the absolute value for the 12 Mev elastic scattering cross section is obtained. The two methods gave results which agreed within 10 %, and the estimated uncertainty in the results is ~15 %. This procedure was carried out for targets of several different Yb isotopes, but any differences in the elastic scattering cross sections for the different masses were smaller than the experimental uncertainties. Therefore, in the analysis of the data, the same elastic scattering cross section was assumed for all masses of ytterbium. The values used were 460 mb/sr, 60 mb/sr and 13 mb/sr for scattering angles of 60°, 90° and 125°, respectively. No attempt has been made to measure angular distributions of the reaction products. For most reactions, spectra have been obtained at two, and sometimes three, of the angles stated above, in

TABLE 2. Levels Populated in Yb^{167}.

Energy	Previously Known Energy	Nilsson Assignment	$d\sigma/d\Omega$ (d,t)*				
			$\theta = 56°$	$\theta = 60°$	$\theta = 85°$	$\theta = 90°$	$\theta = 125°$
0	0	5/2 5/2 − [523]	9	~ 5	13		
30			5	~ 4	~ 3		
59			15	17	34	28	
79		7/2 5/2 − [523]	~ 2	~ 3	7		
187		9/2 5/2 − [523] + 3/2 3/2 − [521]	49	45	90	96	78
212		1/2 1/2 − [521] ?	42	52	62	55	40
258			12	10	12	19	
277			4	6	12		
316		7/2 3/2 − [521]	50	64	98	124	89
408		9/2 3/2 − [521] + 7/2 1/2 − [521] ?	~ 7		12		~ 22
477					2		
545					~ 4		
566			~ 40	44	89	82	
601			~ 4				
614			~ 26	30	~ 60	62	
660				9	10		
692					~ 4		
752			~ 22	21	52	47	
801					~ 2		
835				5	~ 8	~ 10	
966				24	~ 33	28	

* Due to the fact that the areas of the Yb^{168} targets were small, greater difficulties were encountered in normalizing intensities to the elastic scattering cross sections. Hence the uncertainties on relative values from different angles can be as great as 20 %, as compared with 10 % for the other Yb targets.

order to help isolate impurity peaks by means of their different kinematic shift of energy with angle.

The photographic plates were scanned by counting the tracks in strips, $^1/_4$ mm wide, using microscopes with specially constructed stages. For the determination of energies the peak positions were defined to be the positions of one-third maximum height on the high energy sides of the peaks. The calculation of output energies and Q-values was performed on a GIER digital computer. Energy calibration of the spectrograph was carried out using the 6.0498 Mev and 8.7864 Mev alpha particle groups from an active deposit of ThB placed in the target position.

The proton and triton spectra obtained for the different targets at $\theta = 90°$ are shown in Figures 1–10. For the case of the Yb^{168} target, the spectra from

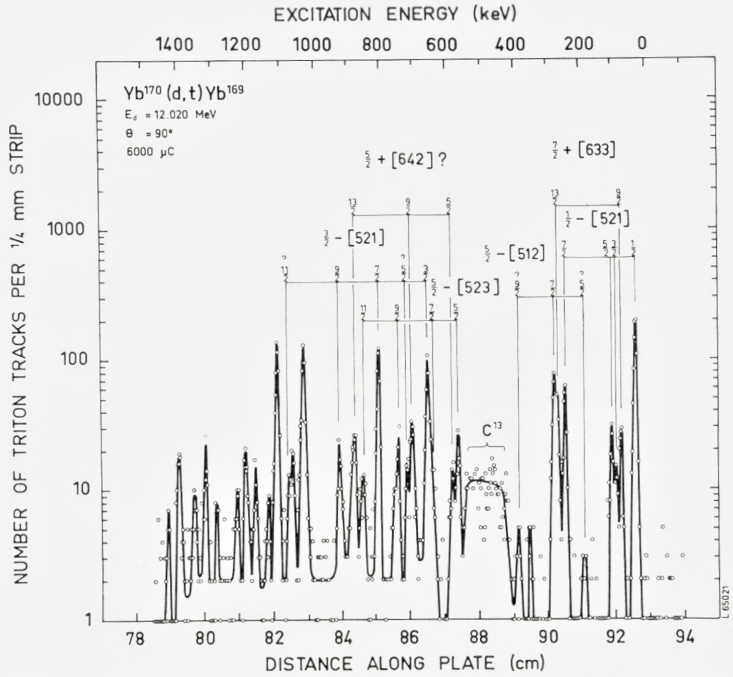

Figure 2. Triton spectrum for the reaction $Yb^{170}(d,t)Yb^{169}$ at $\theta = 90°$.

an experiment at $\theta = 85°$ are shown, because the reaction products from C^{13} in the target backing obscure important regions of the spectra at $\theta = 90°$. The excitation energies and cross sections for the various levels observed are given in Tables 2–7. The energies quoted in the first column of Tables 2–7 are the averages of the values obtained from the various exposures. The uncertainties in excitation energies are less than 2 or 3 kev for low-lying states and less than 5 or 6 kev for states at ~1.5 Mev excitation. The level assignments given in the third columns of these tables are discussed in the next section.

The cross sections in Tables 2–7 have been corrected for variation of the solid angle of the spectrograph with radius and for the contributions of isotopic impurities in the elastic peaks used for normalization. In the course of this work, a number of exposures have been repeated, and the intensities of the strong peaks were found to be reproducible to within 10 %. In view of this, and the possible variation in the elastic cross sections with mass, the uncertainty in relative intensities from different target masses is estimated to be not greater than ~15 %. The absolute intensities are also subject to

TABLE 3. Levels Populated in Yb^{169}.

Average (Weighted) Energy	Previously Known Energy	Nilsson Assignment	$\frac{d\sigma}{d\Omega}(d,t)\frac{\mu b}{sr}$		$\frac{d\sigma}{d\Omega}(d,p)\frac{\mu b}{sr}$		
			$\theta = 60°$	$\theta = 90°$	$\theta = 56°$	$\theta = 60°$	$\theta = 85°$
0	0	7/2 7/2 + [633]		not seen	~ 1		
24	24	1/2 1/2 − [521]	162	155	238	~ 230	115
70	71	9/2 7/2 + [633]	12	22	~ 13		14
84	87	3/2 1/2 − [521]	30	8	63	C^{13*}	49
98	100	5/2 1/2 − [521]		26			
	157	11/2 7/2 + [633]					~ 1 ?
192	191.5	5/2 5/2 − [512]			Si^{28*}	8	4
244	244	7/2 1/2 − [521]	32	48	99		72
266	265	9/2 1/2 − [521]	46	26	300	Si^{28*}	228
		13/2 7/2 + [633]					
277	278.5	7/2 5/2 − [512]		65			
390	388	9/2 5/2 − [512]			7	7	7
487	488	11/2 1/2 − [521]			3		4
523	522	11/2 5/2 − [512]			5	6	4
569	570.5	5/2 5/2 − [523]	9	20	5		4
584		5/2 5/2 + [642]		11			
647	647	7/2 5/2 − [523]	69	~ 13	53	43	~ 10
657		3/2 3/2 − [521]		80			~ 17
704		9/2 5/2 + [642]	23	30	9	~ 6	10
718		5/2 3/2 − [521]		~ 12		~ 9	
747	746	9/2 5/2 − [523]	6	~ 22	~ 6	9	11
805		7/2 3/2 − [521] + K = 1/2 γ-vib	56	100	43	42	36
849		3/2 1/2 γ-vib	~ 3	~ 15	236	178	145
	871	11/2 5/2 − [523]	8	31			
877		13/2 5/2 + [642]			~ 9	~ 6	~ 4
911		5/2 1/2 γ-vib			70	47	49
925		9/2 3/2 − [521] ?	6	22			
959					76	48	37
996		7/2 1/2 γ-vib			21	Si^{28*}	19
1030			55	110	19		
1064			6	17	~ 18	~ 14	
1074				8	~ 8	~ 14	
1106			54	105	44	23	
1134				8	8		

(*continued*)

TABLE 3 (continued).

Average (Weighted) Energy	Previously Known Energy	Nilsson Assignment	$\frac{d\sigma}{d\Omega}(d,t)\frac{\mu b}{sr}$		$\frac{d\sigma}{d\Omega}(d,p)\frac{\mu b}{sr}$		
			$\theta = 60°$	$\theta = 90°$	$\theta = 56°$	$\theta = 60°$	$\theta = 85°$
1170				~ 6	11		
1182					~ 2	10	
1198			~ 6	21	9		
1225				11	13	14	
1285				~ 9	173	120	
1317				18	~ 20	18	
1351				~ 14	171	111	
1395			~ 7	20	68	58	
~ 1421				5	~ 4	7	
1459				16	~ 61	29	
1473					~ 40	23	
1526					73	46	
1553					~ 88	56	
1567					~ 21		
1607					~ 50		
1640					238		
1688					334		
1733					~ 61		
1767					~ 150		

* This section of the plate was obscured by reactions from the element indicated.

the error in the determination of the elastic scattering cross section and thus may have an error as large as 20–25 %. The smaller peaks have larger errors, not only because of poorer statistics (in these experiments, a total count of 100 tracks usually corresponds to about 10–20 microbarns per steradian), but also because of the danger of an impurity peak being included in the count. In the present work, isotopic impurities are not a serious problem in this respect because the spectra of all the stable species of Yb have been measured. Thus, where necessary, the contribution to a spectrum from this source can be easily subtracted. The C^{13} in the carbon of the target backings often resulted in "peaks" in the spectra, as can be seen in several of the figures. The protons and tritons from this impurity are also easy to identify because they always occur at the same energy and the "peaks" are broader. The extra broadness is due to the fact that the energy of outcoming particles has a greater variation with angle for a light target nucleus

than for a heavy one. As the slit at the entrance to the magnetic field region of the spectrograph usually subtended an angle of several degrees at the target, an appreciable energy spread can result for a light target nucleus. It should also be noted that another difficulty arises with the data in Tables 2–7. It often happens that peaks are found in the (d,t) and (d,p) spectra corresponding to the same excitation energy within the uncertainty of the measurements. However, due to the high density of levels, there is a possibility that more than one level is present. Thus, although both (d,p) and (d,t) cross sections may be quoted for such a level, it may be that they correspond to two different "unresolved" states.

The ground-state Q-values for the reactions studied are given in Table 8. For completeness, the data from odd targets have also been included. Columns 4 and 5 show the neutron separation energies calculated from the (d,t) and (d,p) Q-values and the last column shows the neutron separation energies obtained from the tables of MATTAUCH et al.[16]. The uncertainty on the present Q-value measurements is of the order of 12 kev.

4. Interpretation of the Spectra

The predicted intensity for the various states in a rotational band based on a Nilsson state can be calculated from expression (6). As the quantities U^2 and V^2 are not well known initially, it is not easy to predict accurately the absolute cross sections for levels near the ground state. However, since the value of V^2 is the same for all members in a rotational band, the relative intensities of the states within the band are preserved.

Representative values of the quantity φ_l are shown in Figure 11, plotted in a manner which shows the dependence on l and the Q-value. These values have been obtained from a DWBA calculation of SATCHLER[17] who has used reasonable values of the optical-model parameters*). There is evidence[6] that the angular distributions and absolute values calculated for the (d,p) process agree with experiment, but no such tests of the (d,t) calculations have been made. Table 9 shows the predicted differential (d,t) cross sections for some of the Nilsson orbitals found in this mass

* Optical-model parameters used in the calculations were as follows:

		V	W	r_0	a	r_0'	a'	W_D	r_c
(d,p)	Deuteron potential	86		1.15	0.87	1.37	0.7	12	1.25
	Proton potential	55		1.25	0.65	1.25	0.47	15	1.25
(d,t)	Deuteron potential	103	0	1.15	0.81	1.34	0.68	52	1.3
	Triton potential	100	14	1.07	0.854	1.7	0.73	0	1.4

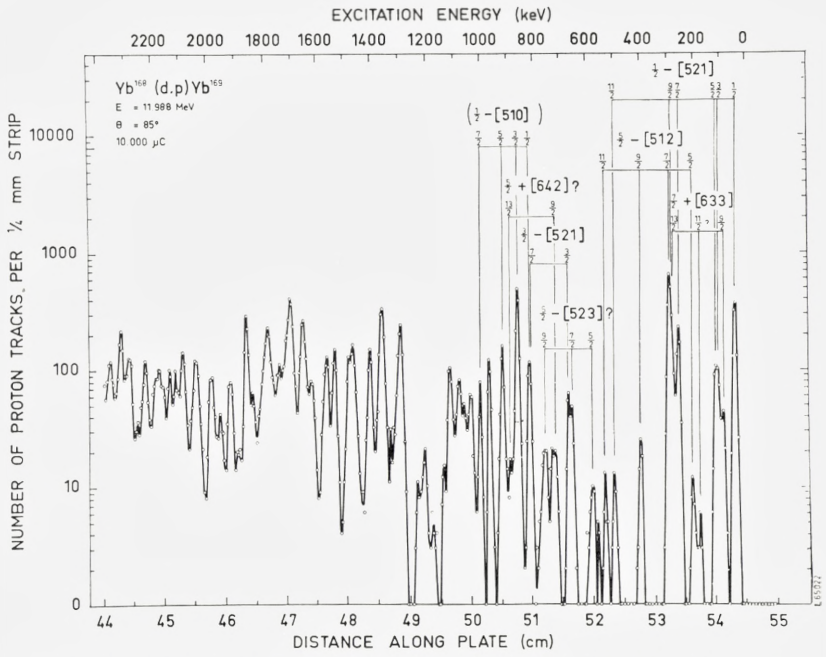

Figure 3. Proton spectrum for the reaction $Yb^{168}(d,p)Yb^{169}$ at $\theta = 85°$.

region. These values were calculated using expression (6) with $\theta = 90°$, $Q = 0$, $V^2 = 1$. The C_{jl}^2 were calculated from Nilsson's wave functions[1,6] for a deformation of $\eta = 6$, and the φ_l were obtained from Figure 11. The dependence of φ_l on the l-value for the (d,p) reaction is similar to that for the (d,t) reaction so the ratios of intensities within a band are not widely different in the two processes. (This is not true, of course, when the target nucleus is odd, where the simplified expression (6) is not valid.)

In the spectra of Figures 1–10 it is seen that many of the states corresponding to the observed proton and triton groups have been classified in terms of the Nilsson model. All the reasons for the choice of each assignment will not be discussed in detail. The decisions have been based largely on the fact that each Nilsson orbital has a characteristic distribution of intensity amongst the various members of its rotational band and that this distribution is similar for all nuclei. Other properties of the bands, such as moments of inertia, decoupling parameter (for $K = 1/2$ bands), systematics of excitation energy with neutron number, etc. were also considered. In the case of orbitals which originate from shell-model states of relatively small angular momenta, the members of the band with low spin values tend to have large

TABLE 4. Levels Populated in Yb^{171}.

Average (Weighted) Energy	Previously Known Energy	Nilsson Assignment	$\frac{d\sigma}{d\Omega}(d,t)\frac{\mu b}{sr}$		$\frac{d\sigma}{d\Omega}(d,p)\frac{\mu b}{sr}$	
			$\theta = 60°$	$\theta = 90°$	$\theta = 60°$	$\theta = 90°$
0	0	1/2 1/2 − [521]	480	340	167	68
72	66.73	3/2 1/2 − [521]	95	82	42	34
	75.88	5/2 1/2 − [521]				
121	122.4	5/2 5/2 − [512]		4.3	~ 14	~ 7.4
168	167.6	9/2 7/2 + [633]	28	38	12	10.3
208	208.0	7/2 5/2 − [512]	115	127	208	160
230	230.5	7/2 1/2 − [521]	103	110	66	45
~ 250	247	9/2 1/2 − [521]		~ 11		
318	317.3	9/2 5/2 − [512] + Yb^{172}		4.4	~ 6**	~ 6**
369		13/2 7/2 + [633]	18	48	11	25
449		11/2 5/2 − [512]		2.8	~ 8	~ 4.8
486		11/2 1/2 − [521]		4.6	~ 2.5	~ 5.3
838	835.0	7/2 7/2 − [514] + ?	14	22	51	38
~ 867	862			16		
876					~ 3	~ 4
902		3/2 3/2 − [521]*	104	117		
906					21	~ 12
945	948.3	9/2 7/2 − [514] + 1/2 1/2 − [510]*			44	50
971			~ 42	72		
~ 987						
995		3/2 1/2 − [510]*			298	198
1026			~ 46	62	32	~ 34
~ 1038						
1052		5/2 1/2 − [510]*			71	86
1079		7/2 3/2 − [521]*	~ 46	78	18	26
~ 1113					~ 4	~ 5
1118			~ 17	36		
1144		7/2 1/2 − [510]*			30	31
1188			~ 8	14		
1204					8	21
~ 1244				1		
1254		9/2 1/2 − [510]*			~ 6	9
1280				11		
1290					~ 31	~ 21
~ 1300				~ 6		
1320				15		
1328					144	93
1348			~ 41	72		

(continued)

TABLE 4 (continued).

Average (Weighted) Energy	Previously Known Energy	Nilsson Assignment	$\frac{d\sigma}{d\Omega}(d,t)\frac{\mu b}{sr}$		$\frac{d\sigma}{d\Omega}(d,p)\frac{\mu b}{sr}$	
			$\theta = 60°$	$\theta = 90°$	$\theta = 60°$	$\theta = 90°$
~ 1356					~ 28	~ 28
1387				~ 4		
1395					208	141
1402				~ 5		
1432				20	~ 36	~ 29
1460				27		
1486				28	250	175
1518			72	125		
1524					75	45
1559				~ 2		
1588					~ 23	32
1599				8		
1627					292	141
1638				20		
1662				19		
1671					358	174
1715				5		
1730					210	
1765					68	
1771				32		

* These states are thought to be γ-vibrations which contain large fractions of the single-particle states indicated. See text.

** After subtraction of $\sim 6\,\mu b/sr$ due to isotopic impurity in the target.

values of C_{jl}^2 and thus strong cross sections. In these cases it is easy to make an unambiguous assignment of the observed peaks. However, orbitals originating from shell-model states of high angular momentum tend to have large values of C_{jl}^2 for the high spin states only. As the cross section decreases rapidly with increasing l-value, the net result is that the total population of such bands is more than an order of magnitude weaker than for the strongest ones. This situation is found in the present work for some of the Nilsson orbitals which come from the $i_{13/2}$ shell-model state. In addition, these bands usually have only about two states for which C_{jl}^2 is not vanishingly small, and hence only two members of the band are populated strongly enough to be observed. This makes the identification less certain than when several members are populated, especially if one of the two weak peaks is obscured by stronger groups.

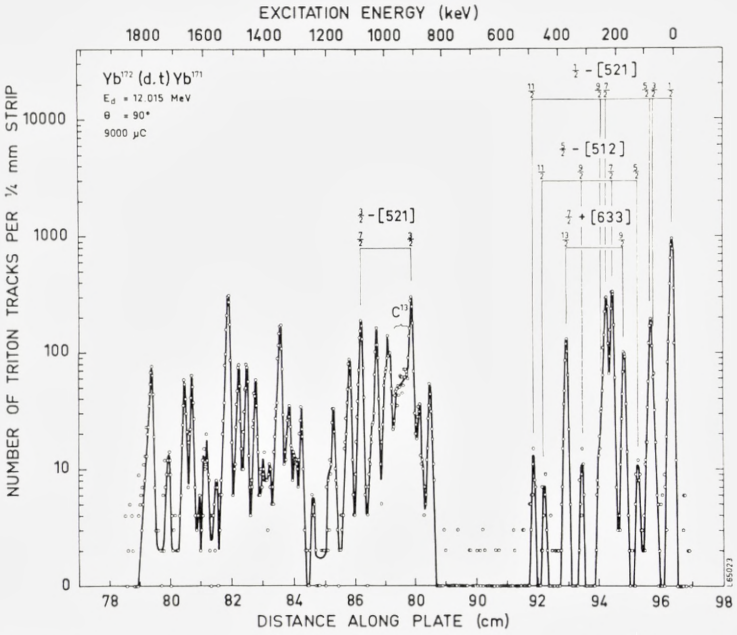

Figure 4. Triton spectrum for the reaction $Yb^{172}(d,t)Yb^{171}$ at $\theta = 90°$.

Level schemes for the Yb^{167}, Yb^{169}, Yb^{171}, Yb^{173} and Yb^{175} are given in Figures 12–16 where the assigned states are separated into rotational bands. No level scheme is given for Yb^{177} as the results are essentially the same as those of VERGNES and SHELINE[6]. The excitation energy of the band head of each Nilsson state is shown plotted against the neutron number in Figure 17. Points plotted at negative energies in this diagram indicate that the orbital is a hole state, as determined from relative (d,p) and (d,t) cross sections and systematics.

In view of the similarity of the spectrum of a given band in one nucleus to that of the same band in the other nuclei, it seems reasonable to consider one orbital at a time, discussing its properties in the different isotopes. The bands which have the largest cross sections will be considered first.

A – *The* $1/2-[521]^*$ *Orbital*

This orbital is known to be the ground state of Yb^{171} and it has a characteristic level spacing due to its decoupling parameter $a \approx 0.87$**. It occurs at an excitation energy of 24 kev in Yb^{169} and a similar level spacing is

* The notation used here is $K\pi[Nn_z\Lambda]$. When a particular member in a rotational band is referred to, the quantum numbers used are $IK\pi[Nn_z\Lambda]$.

** For previously known levels, see references 18–20.

TABLE 5. Levels Populated in Yb^{173}.

Average (Weighted) Energy	Previously Known Energy	Nilsson Assignment	$\frac{d\sigma}{d\Omega}(d,t)\frac{\mu b}{sr}$		$\frac{d\sigma}{d\Omega}(d,p)\frac{\mu b}{sr}$	
			$\theta = 60°$	$\theta = 90°$	$\theta = 90°$	$\theta = 125°$
0	0	5/2 5/2 − [512]	19	20	8	~ 2
79	78.7	7/2 5/2 − [512]	440	450	165	64
179	179.6	9/2 5/2 − [512]	~ 3	1	7	4
301		11/2 5/2 − [512]	~ 4	12	~ 7	4
398	399	1/2 1/2 − [521]	630	475	54	15
~ 410	413.3	9/2 7/2 + [633]				
~ 462		3/2 1/2 − [521]	120	30	9	~ 5
478		5/2 1/2 − [521]		80	15	
600		13/2 7/2 + [633] + ?	~ 25	58	35	~ 15
620		7/2 1/2 − [521] + ?	109	130	63	21
630	636	7/2 7/2 − [514] + ?				
655		9/2 1/2 − [521]	~ 3	12		
743		9/2 7/2 − [514]	~ 2	9	45	12
875		11/2 1/2 − [521]		8		
890					~ 9	4
1031		1/2 1/2 − [510]			~ 12	~ 2
1073		3/2 1/2 − [510]	11	19	370	145
1120		5/2 1/2 − [510]	5	12	190	76
1168			3	26	~ 4	
1221		7/2 1/2 − [510]			93	40
1224		3/2 3/2 − [521]	94	112		
1306		9/2 1/2 − [510]			16	~ 15
1324			12	12		
1340		3/2 3/2 − [512]			127	36
1354		7/2 3/2 − [521]	60	88		
1404		5/2 3/2 − [512]	5	9.6	209	78
1440			28	58		
1445					~ 15	
1496		7/2 3/2 − [512]			114	41
1582			17	27		
1605		9/2 3/2 − [512] + ?		18	22	~ 28
1625				17		
1665				11	430	168
1714			5	24	252	130
1735				12	112	~ 50
1765			~ 2	~ 25	78	~ 48
1790					99	
1815				14		
1855				170		
1878				45		

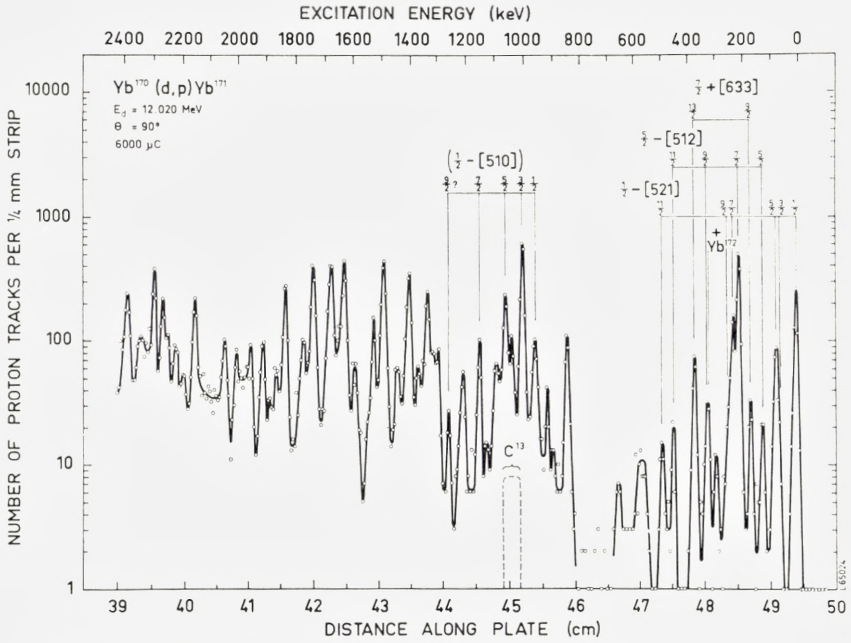

Figure 5. Proton spectrum for the reaction $Yb^{170}(d,p)Yb^{171}$ at $\theta = 90°$.

observed. The first two members of the band have also been found in Yb^{173} where the band head energy is 399 kev[21].

From Table 9 it appears that all states up to a spin of 11/2 should be populated in the present work. This is seen to be the case in Yb^{171} where, however, the 3/2 and 5/2 states are not resolved from each other and the peak due to the 9/2 level shows as a shoulder on the side of that due to the 7/2 state. The level energies are in good agreement with those previously reported. The 11/2 member had not been observed before, but its energy fits nicely into the sequence.

A similar intensity pattern is found in Yb^{169} except that some of the weaker groups were not seen. The 3/2 and 5/2 states are resolved in the (d,t) spectrum but the group due to the 9/2 level is hidden by a larger peak. That of the 11/2 state is obscured by the C^{13} "peak" in Figure 2, but can be seen in Figure 3. It is noted that the ground state of Yb^{169} is the 7/2 + [633] orbital. As the 7/2 member of this band has an extremely small value of C^2_{jl} it is not seen in this work. Hence, the 1/2 1/2 − [521] state at 24 kev excitation is the first level for which a triton or proton group is actually seen. For all levels in Yb^{169}, energies have been measured relative to the

TABLE 6. Levels Populated in Yb^{175}.

Average (Weighted) Energy	Previously Known Energy	Nilsson Assignment	$\frac{d\sigma}{d\Omega}(d,t)\frac{\mu b}{sr}$		$\frac{d\sigma}{d\Omega}(d,p)\frac{\mu b}{sr}$	
			$\theta = 60°$	$\theta = 90°$	$\theta = 90°$	$\theta = 125°$
0	0	7/2 7/2 − [514]	14	13	~ 15	~ 3
101		9/2 7/2 − [514]	43	59	~ 35	15
225		11/2 7/2 − [514]		~ 3		
260		9/2 9/2 + [624]		12		
511*		1/2 1/2 − [510]	} 30	50	64	30
516		13/2 9/2 + [624]				
552		3/2 1/2 − [510]	120	84	390	105
600		5/2 1/2 − [510]	43	45	176	56
633		5/2 5/2 − [512]	< 34	~ 26	~ 7	~ 4
694		7/2 1/2 − [510]	< 12	~ 11	79	29
723		7/2 5/2 − [512]	540	500	93	29
773		9/2 1/2 − [510] + ?		~ 3	22	11
809		3/2 3/2 − [512]	18	14	106	24
837		9/2 5/2 − [512]		~ 7		
868		5/2 3/2 − [512]	48	35	233	82
913		1/2 1/2 − [521]	630	400	~ 22	~ 7
954		7/2 3/2 − [512]	~ 10	16	115	33
~ 977		11/2 5/2 − [512]	} 125	~ 12		
~ 984		3/2 1/2 − [521]		~ 26		
1004		5/2 1/2 − [521]		86	~ 7	
1061		9/2 3/2 − [512] + ?	~ 8	~ 8	~ 20	~ 3
1088		9/2 7/2 + [633] + ?	~ 45	42	~ 17	
1166		7/2 1/2 − [521]	108	108		
1196		9/2 1/2 − [521]	~ 5	~ 14		
1300			~ 6	~ 10	~ 9	
1336		13/2 7/2 + [633]	} 25	38		
1360				~ 10	755	215
1420			~ 8	~ 8	377	147
1460		11/2 1/2 − [521] + ?		~ 5	228	77
1616		3/2 3/2 − [521]	104	90		13
1677		5/2 3/2 − [521]	20	22		
1745			~ 5	~ 8		
1765		7/2 3/2 − [521]	54	71		

* Energy estimated from level spacings of other members of this band.

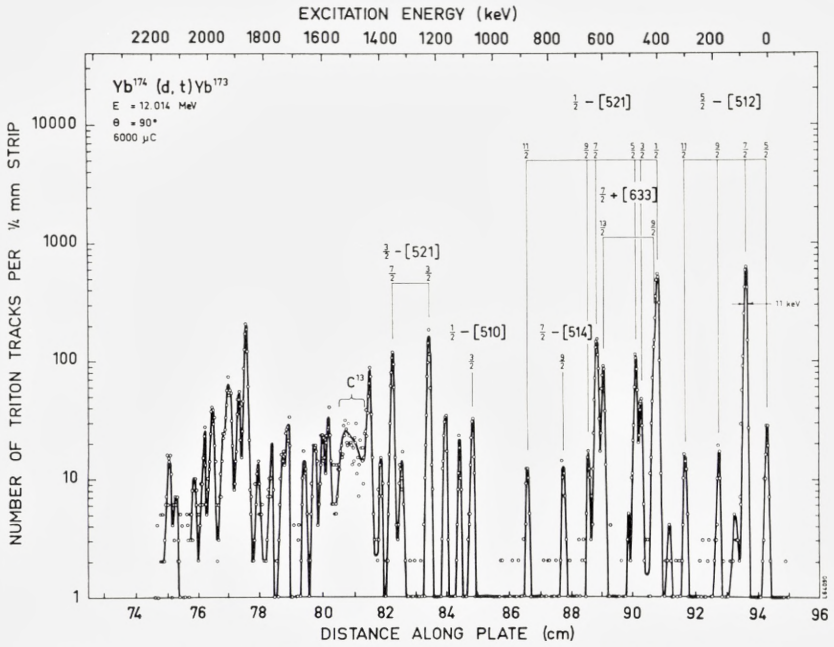

Figure 6. Triton spectrum for the reaction $Yb^{174}(d,t)Yb^{173}$ at $\theta = 90°$.

1/2 1/2−[521] group and then increased by 24 kev to yield excitation energies above the ground state.

In Yb^{173} and Yb^{175}, all six members of this band are clearly seen in the (d,t) process. A comparison of the observed relative (d,t) intensities with predicted values is given in Table 10. For each nucleus, there are two columns. The left shows the relative cross section at $\theta = 90°$ normalized to 100 for the 1/2 1/2−[521] state. The right column shows the values of C_{jl}^2 obtained from the relative intensities, using values of φ_l from Figure 11. The values of C_{lj}^2 given have been normalized such that their sum is equal to unity. For the case of Yb^{169} it was not possible to normalize in this manner as two of the weak peaks were not seen. In this case, the value of C_{jl}^2 for the spin 1/2 member was set equal to that of the same state in Yb^{171}.

Values for the decoupling parameter and inertial parameter, $\hbar^2/2\Im$, obtained from the energy spacings of the levels, are given in Table 11 where the data for all bands are summarized. The observed dependence of these quantities on the neutron number for the 1/2−[521] orbital fits quite well into a plot such as that given by Sheline et al.[22].

TABLE 7. Levels Populated in Yb^{177}.

Average Energy	Previously Known Energy	Nilsson Assignment	$\frac{d\sigma}{d\Omega}(d,p)\frac{\mu b}{sr}$	
			$\theta = 90°$	$\theta = 125°$
0	0	9/2 9/2+[624]	Obscured	~ 1
111	109	7/2 7/2−[514]	~ 2	
124	123		~ 1	
222	220	9/2 7/2−[514]	12	5
268	265	13/2 9/2+[624]	35	15
306	306	Yb^{174} impurity	6	~ 1
335	333	1/2 1/2−[510]	9	
379	379	3/2 1/2−[510]	305	89
424	426	5/2 1/2−[510]	148	46
530	527	7/2 1/2−[510]	59	26
615	614	9/2 1/2−[510]	14	8
708	709	3/2 3/2−[512]	168	51
774	773	5/2 3/2−[512]	218	68
822			~ 14	
867	868	7/2 3/2−[512]	112	33
976	976	9/2 3/2−[512]	15	9
1050			7	
1104			11	
1124			5	
1173			5	
1222	1226	7/2 7/2−[503]	346	121
1362	1365	3/2 3/2−[501]	740	235
1447	1449	5/2 3/2−[501]	172	
1496			70	
1564	1567	7/2 3/2−[501]	14	

The absolute intensities of the triton and proton groups are dependent on V^2, the probability that the state is filled in the target nucleus. In Figure 18, the (d,p) and (d,t) cross sections for the 1/2 1/2−[521] state at $\theta = 90°$ are shown as a function of target mass. As the absolute cross section is dependent on the Q-value, the (d,t) data have all been adjusted to the corresponding values for $Q = -1.5$ Mev with the aid of the Q-value dependence from Figure 11. Similarly, the (d,p) cross sections have been corrected to the values they would be for $Q = 4.0$ Mev. The data are interpreted as being an indication of the filling of the 1/2−[521] state in the various isotopes. In the heavier targets, the (d,p) cross section becomes small and the (d,t) cross section tends to become constant. This means that the state is nearly

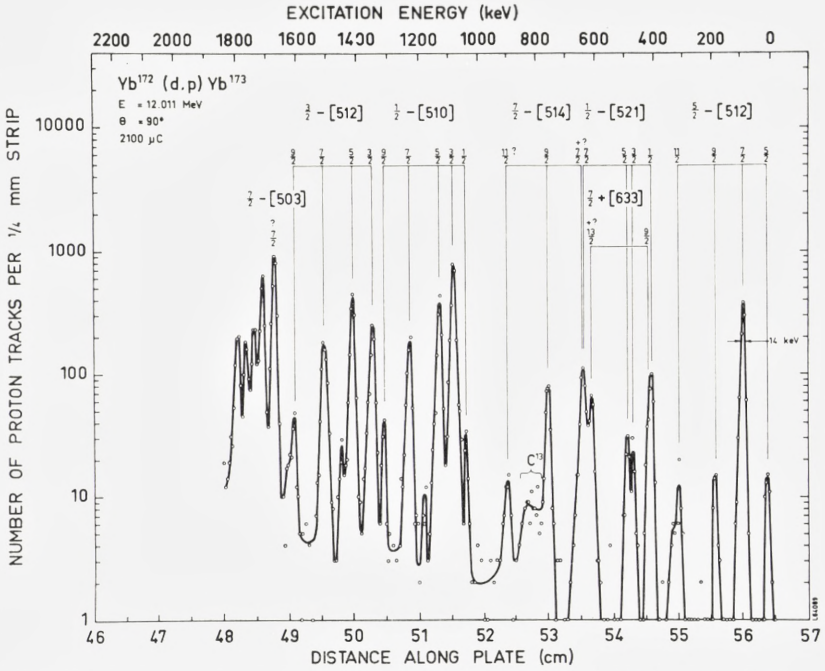

Figure 7. Proton spectrum for the reaction $Yb^{172}(d,p)Yb^{173}$ at $\theta = 90°$.

filled in these isotopes, as would be expected since it is the ground state of Yb^{171}. Below mass 171, the cross section for (d,t) becomes small, while that for (d,p) is large, indicating that the state is nearly empty.

B – *The* 5/2−[512] *Orbital*

This orbital originates from a $2f7/2$ shell-model state and the 7/2 member is the only one which has a large value of C^2_{jl}. Thus, the 7/2 state is predicted to be strongly populated while the 5/2, 9/2 and 11/2 levels are not. This distribution among the four states is seen experimentally by the (d,p) and (d,t) processes in Yb^{173} where this orbital appears as the ground state. Peaks due to all four members of this band can also be seen in the proton spectra of Yb^{171} and Yb^{169}, and in the triton spectra of Yb^{175} and Yb^{171}. In the remaining spectra some of the weaker peaks are too small to be observed. Table 12 shows a comparison of the predicted relative intensities and C^2_{jl} values with those determined experimentally. Figure 18 shows a plot of the (d,p) and (d,t) cross sections for the 7/2 5/2−[512] state at $\theta = 90°$ as a function of mass number. The Q-value dependence

TABLE 8. Neutron Separation Energies for Yb Nuclei.

Mass A	$Q(d,t)$ A→A−1 Mev	$Q(d,p)$ A−1→A Mev	S_n(A) from $Q(d,t)$ Mev	S_n(A) from $Q(d,p)$ Mev	S_n(A) from Mass Tables[16]) Mev
168	−2.797 ± 0.012	—	9.055 ± 0.012	—	8.980 ± 1.010
169	—	4.636 ± 0.012	—	6.861 ± 0.012	6.790 ± 1.010
170	−2.211 ± 0.012	—	8.469 ± 0.012	—	8.550 ± 1.000
171	−0.359 ± 0.012	4.390 ± 0.012	6.617 ± 0.012	6.615 ± 0.012	6.760 ± 0.070
172	−1.772 ± 0.012	5.797 ± 0.012	8.030 ± 0.012	8.022 ± 0.012	8.140 ± 0.080
173	−0.114 ± 0.012	4.145 ± 0.012	6.372 ± 0.012	6.370 ± 0.012	6.480 ± 0.060
174	−1.218 ± 0.012	5.239 ± 0.012	7.476 ± 0.012	7.464 ± 0.012	7.440 ± 0.070
175	—	3.595 ± 0.012	—	5.820 ± 0.012	5.840 ± 0.080
176	−0.621 ± 0.012	—	6.879 ± 0.012	—	6.640 ± 0.080
177	—	3.337 ± 0.012	—	5.562 ± 0.012	5.530 ± 0.110

has been removed from these values as for the 1/2 1/2−[521] case. It is seen that this orbital appears to be half-filled at a neutron number two units greater than for the 1/2−[521] state. This is reasonable as it is the ground state of Yb^{173}, which is two units heavier than Yb^{171}.

For several cases where the above two orbitals were hole states, identification of the weak peaks in the proton spectra was possible only because the excitation energies of the levels were known from assignments made on the basis of the triton spectra. This is one of the advantages of using the two complementary reaction processes in conjunction with each other for such studies.

C – *The* 1/2−[510] *Orbital*

The 1/2−[510] orbital has been found previously[6]) in a study of Yb^{177} levels by means of the (d,p) reaction. It is characterized by large cross sections to several members of the band, an inertial parameter of $\hbar^2/2\Im$ = 12.2 kev and a decoupling parameter a = 0.22. This band is also seen in Figure 10 of the present work. Anomalous rotational bands with similar intensity patterns are also found in the proton spectra of Yb^{175} and Yb^{173} and have been assigned to the 1/2−[510] orbital. The spin 1/2 member of this band is populated rather weakly and in Yb^{175} is not resolved from the larger 13/2 9/2+[624] peak. Relative intensities and relative values of C_{jl}^2 for the various states observed in this band in Yb^{177}, Yb^{175} and Yb^{173} are shown in Table 13, where the theoretical values are included for comparison. As the 11/2 state was not observed, its value of C_{jl}^2 cannot be determined.

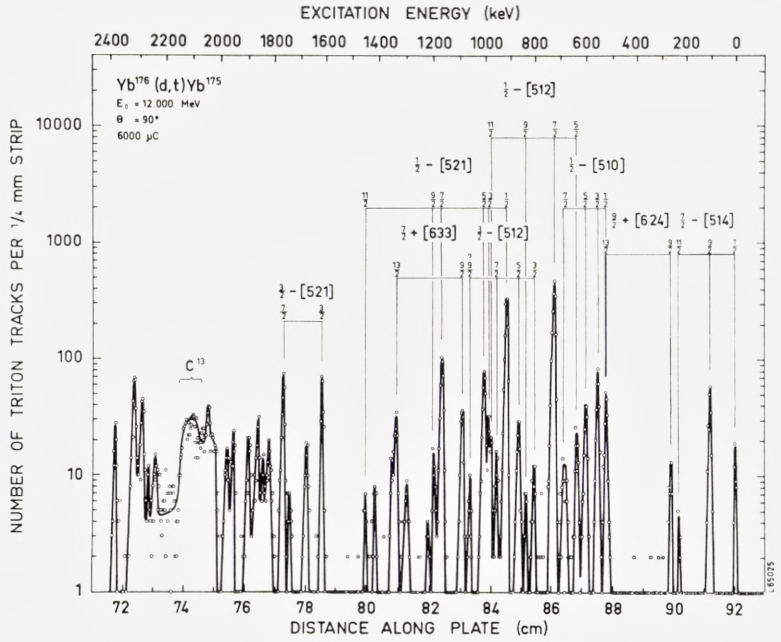

Figure 8. Triton spectrum for the reaction $Yb^{176}(d,t)Yb^{175}$ at $\theta = 90°$.

In Yb^{173} and Yb^{175}, an upper limit of ~ 0.15 can be given for the C_{jl}^2 of this state. From Table 13 it is seen that this quantity is expected to be very small and thus the values of C_{jl}^2 are normalized such that those of the observed states add to unity. This normalization should not be more than 15 % different from that which would have been obtained if all the members of the band had been observed.

Although this band would be expected to have an excitation energy slightly greater than one Mev in Yb^{171}, there is no peak in Figure 5 below two and one-half Mev excitation which has a cross section as large as that expected for the 3/2 1/2−[510] state. The most intense peak in the region of 1 Mev appears to be the spin 3/2 member of a $K = 1/2$ band which has an intensity distribution among the various spin members similar to that of the 1/2−[510] orbital. However, the absolute intensities are only about 60 % of what would be expected for this orbital on the basis of the intensities in Yb^{173} and Yb^{175}, after making allowance for the difference in Q-value. The decoupling parameter is also smaller than in the heavier Yb isotopes (see Table 11). This behaviour is ascribed to mixing between the single-particle states and vibrational states and will be discussed in a later section.

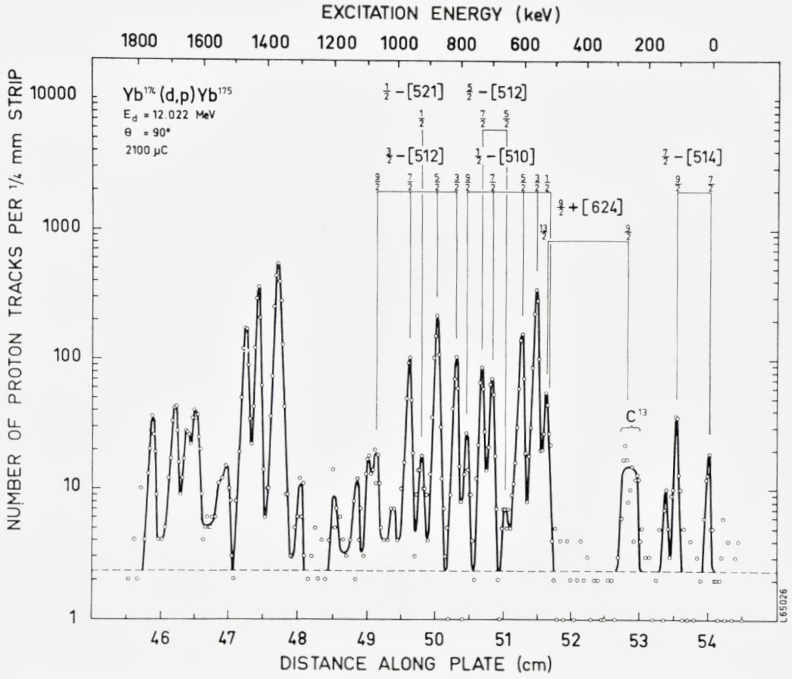

Figure 9. Proton spectrum for the reaction $Yb^{174}(d,p)Yb^{175}$ at $\theta = 90°$.

The relative intensities of states in this band have been included in Table 13 to show how the intensity pattern resembles that of the 1/2−[510] band.

A similar phenomenon appears to take place in the Yb^{169} spectrum of Figure 3, except that in this case two bands with relative intensities similar to those of the 1/2−[510] orbital are found. The absolute intensities of these are about 40 % and 45 % of that which would be expected for the pure band. It is clear that this behaviour is more complicated than that seen for the same orbital in Yb^{173}, Yb^{175} and Yb^{177} and for the 1/2−[521] and 5/2−[512] orbitals discussed above. Consequently, the interpretation is more difficult and less certain. The variation of the cross section of the strongly populated 3/2 1/2−[510] state with target mass is shown in Figure 19. As this orbital should be the ground state of Yb^{179}, comparison with Figure 18 shows that the (d,p) cross section into Yb^{177} is less than that into Yb^{173} and Yb^{175} because the U^2 is smaller. The weaker bands mentioned above are also included in this diagram.

The 1/2−[510] orbital provides a sensitive means for assessing the importance of the two-step process of rotational excitation and stripping. The

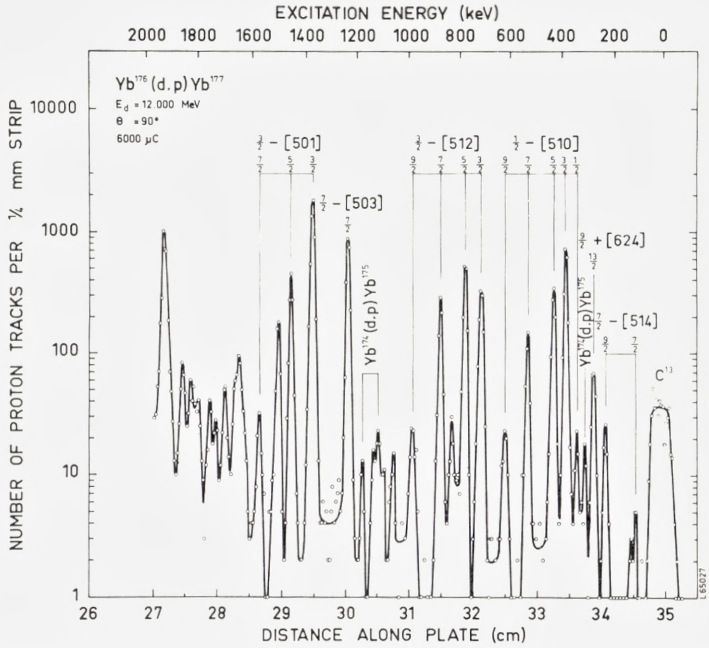

Figure 10. Proton spectrum for the reaction $Yb^{176}(d,p)Yb^{177}$ at $\theta = 90°$.

theoretical spectroscopic factor for the 3/2 member is 40 times that of the 1/2 member for the direct process. With rotational excitation and stripping, the strong $j = 3/2$ transition may contribute to formation of the 1/2 state. An enhancement of the 1/2 cross section by maybe a factor of 3 is obtained from a qualitative estimate based upon the cross section for inelastic deuteron scattering to the 2+ state. The measured spectroscopic factor for the 1/2 state relative to that of the 3/2 state is only about 30 % to 50 % larger than theoretically calculated and, in fact, constitutes excellent agreement for a state with such a small spectroscopic factor. Since we do not observe a contribution from rotational excitation and stripping in a particularly favourable reaction where even a small admixture would have easily observable effects, we conclude that it is reasonable to disregard the process. A similar conclusion has recently been reached for (d, p) reactions on W isotopes.[7].

D – *The* 3/2–[512] *Orbital*

This is another strongly populated band which has been classified[6] in Yb^{177}. In the present study, similar patterns of strong peaks have also been

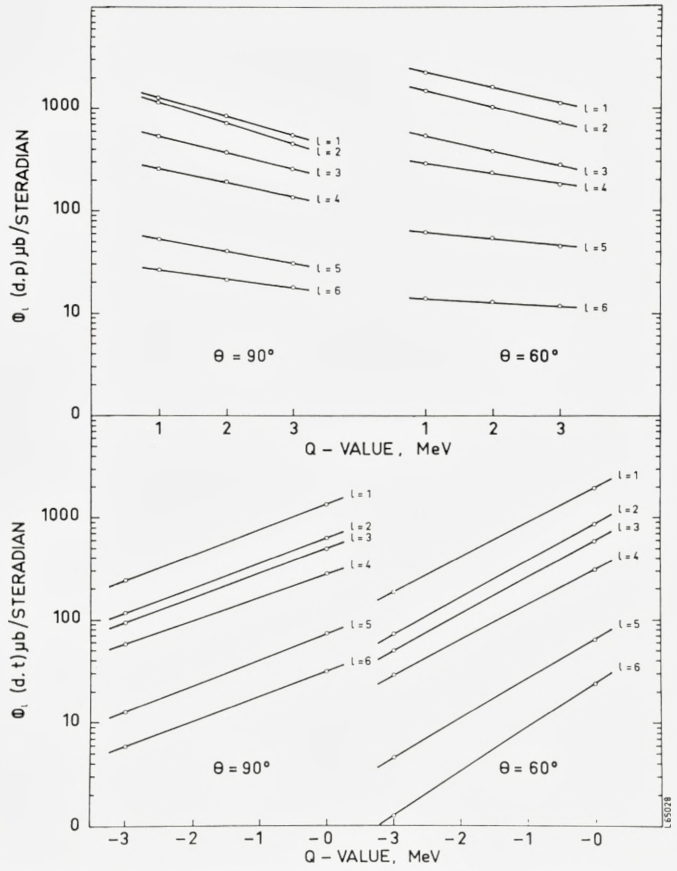

Figure 11. Typical values of the single-particle cross sections φ_l, obtained by SATCHLER[17]) who has performed a DWBA calculation with reasonable values for the optical parameters. The points in this figure are calculated values and the solid lines show the interpolation used in the present work. The (d,t) values given in the lower part of the figure are by mistake too high by a factor of 1.5.

found in the proton spectra of Yb^{173} and Yb^{175} and assigned to this orbital. The relative intensities at $\theta = 90°$ and relative values of C^2_{jl} for these three nuclei are shown in Table 14 where also theoretical values are given. Again the proton group corresponding to the spin 11/2 state was too weak to be seen, and thus the values of C^2_{jl} are normalized such that the sum for the observed states is unity.

The discrepancies between experiment and theory are greater for this orbital than for the ones discussed above. In all cases, the 7/2 and 9/2 states are more strongly populated relative to the 5/2 state than was predicted.

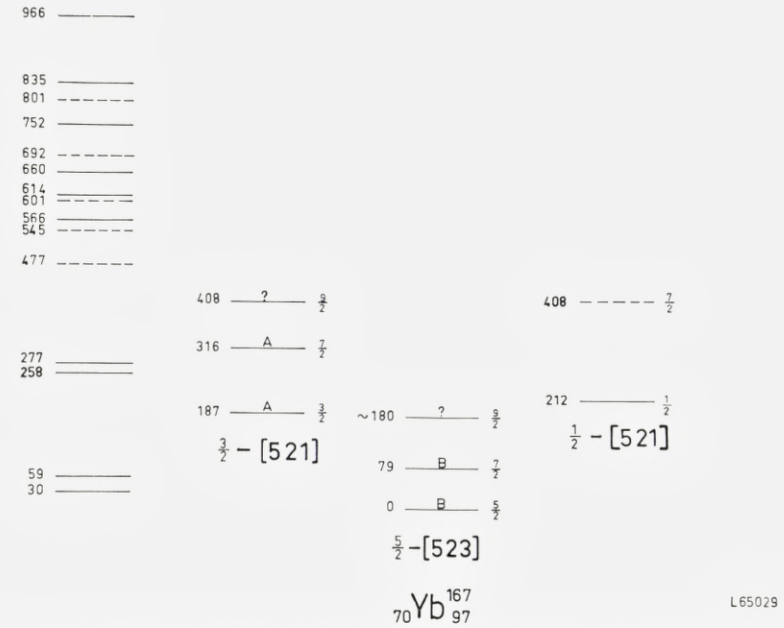

Figure 12. Level scheme for Yb^{167}. Levels shown as dashed lines were populated very weakly and may possibly be due to heavy impurities. For the meaning of A and B, see caption to Figure 13.

However, in the absence of any other similar band of comparable absolute intensity, there is no doubt as to the certainty of the assignment.

The strong peaks of both the 1/2−[510] and 3/2−[512] orbitals can also be seen weakly in the triton spectra of Yb^{173} and Yb^{175}. Needless to say, many of these peaks would not have been identified if the assignments made on the basis of the proton spectra had not been available.

E – *The* 7/2+[633] *Orbital*

From Table 9 it is seen that only the 9/2 and 13/2 spin members of this band are expected to be populated strongly enough to be detected in the present work. This is found to be the case in the nuclei where the orbital has been observed.

As the excitation energies of several members of this band were previously known in Yb^{169}, Yb^{171} and Yb^{173}, identification was no problem in these nuclei. The assignment of the states in Yb^{175} at 1088 kev and 1336 kev to the 9/2 and 13/2 spin members of this band is based mainly on the fact that these are the only two unexplained hole states with reasonable cross

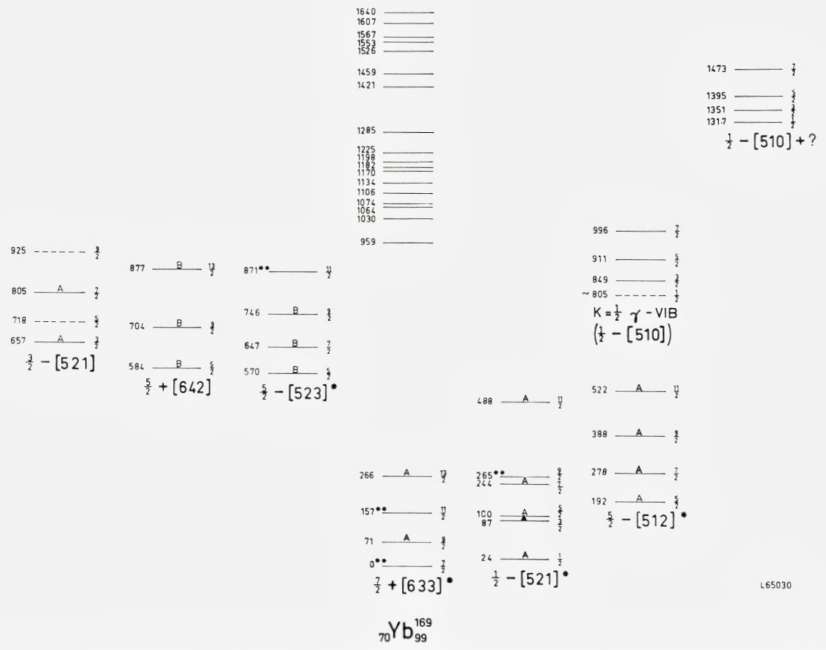

Figure 13. Level scheme for Yb^{169}. For bands labelled with an asterisk, the more precise level energies from reference 23) are shown. Individual states with two asterisks were populated too weakly to be observed, or were obscured by larger peaks, in the present work. Letter A indicates a high degree of certainty in the assignment given to a level. Letter B means that the available data suggest the quantum numbers shown, but due to the fact that the peaks are relatively weak, the assignment is considered to be somewhat tentative. For vibrational states refer to the text.

sections in the region of excitation energy where this orbital is expected to be found.

The relative intensities and relative values of C_{jl}^2 for the 9/2 and 13/2 members of this band, populated in the (d,t) process in Yb^{169}, Yb^{171} and Yb^{175}, are shown in Table 15 where they are compared with predicted values. Data for Yb^{173} are not shown because the triton group due to the 9/2 state is not resolved from the strong 1/2 1/2−[521] group. The agreement with predictions is quite good.

F – *The* 7/2−[514] *Orbital*

The position of this orbital was also known previously for Yb^{177}, Yb^{175}, Yb^{173} and Yb^{171}. As the C_{jl}^2 is large only for the spin 9/2 state, which has $l = 5$, there are no strongly populated levels in the band. However, the intensities of the proton groups in Yb^{173}, Yb^{175} and Yb^{177}, as well as the triton groups

TABLE 9. Predicted Cross-Sections for (d, t) Reactions $Q = 0$ $\theta = 90°$ $V^2 = 1$.

Orbital/Spin	1/2	3/2	5/2	7/2	9/2	11/2	13/2
3/2 + [402]	–	710	58	27	2	–	–
1/2 + [400]	1090	200	94	14	2	–	–
9/2 – [514]	–	–	–	–	1	88	–
11/2 – [505]	–	–	–	–	–	90	–
1/2 – [541]	196	250	190	26	25	13	–
1/2 – [530]	11	384	39	153	31	13	–
3/2 – [532]	–	69	140	54	51	10	–
1/2 + [660]	10	2.2	45	0.9	94	0.08	28
3/2 + [651]	–	0.7	18	1.8	75	0.4	32
3/2 – [521]	–	188	~ 0	342	23	10	–
5/2 + [642]	–	–	3.6	1.2	49	0.54	35
5/2 – [523]	–	–	49	50	71	5.4	–
1/2 – [521]	448	44	120	153	24	4.1	–
7/2 + [633]	–	–	–	0.3	25	0.62	38
5/2 –]512]	–	–	6.6	520	13	5.6	–
7/2 – [503]	–	–	–	610	5	1.9	–
7/2 – [514]	–	–	–	28	83	2.6	–
9/2 + [624]	–	–	–	–	8	0.54	40
1/2 – [510]	18	730	192	125	8	1.3	–
3/2 – [512]	–	144	420	77	13	0.11	–
3/2 – [501]	–	1380	93	50	1	~ 0	–

in Yb^{175}, are in agreement with the predicted values and can be considered to be verifications of the assignments. In Yb^{171} the spectra are quite complicated in the energy region where this orbital has previously been assigned. The data are consistent with this assignment but cannot be considered as a definite verification.

G – *The* 9/2 + [624] *Orbital*

Table 9 shows that none of the rotational members in this band should be strongly populated. Hence, in the present work it can be identified only in Yb^{177} where it is the ground-state band, and in Yb^{175} where it appears at 260 kev excitation with no other strongly populated states to interfere. It is not surprising that it cannot be found in Yb^{173} because there are many strong groups which could obscure the weak peaks.

H – *The* 3/2 – [521] *Orbital*

From Table 9 it is seen that this band should be characterized by strongly populated 3/2 and 7/2 states with only weak transitions to the other

TABLE 10. (d,t) Population of $1/2-[521]$ Band.

Spin	Relative Intensity $\theta = 90°$					Values of C^2_{jl}				
	Theory	Yb^{169}	Yb^{171}	Yb^{173}	Yb^{175}	Theory	Yb^{169}	Yb^{171}	Yb^{173}	Yb^{175}
1/2	100	100	100	100	100	0.249	0.284*	0.284	0.300	0.282
3/2	9.3	~ 5.2	24	6.3	6.5	0.024	0.015*	0.018**	0.020	0.019
5/2	26	17		17	21	0.182	0.135*	0.142**	0.142	0.165
7/2	31	31	32	27	27	0.231	0.264*	0.272	0.243	0.228
9/2	5.0	Obscured by other groups	~ 3	2.5	3.5	0.269		0.185	0.164	0.216
11/2	0.7		1.35	1.7	< 1.25	0.045		0.097	0.130	< 0.090

* Normalized such that C^2_{jl} for the spin 1/2 member is the same as that in Yb^{171}.

** Assumes that the unresolved triton groups due to the 3/2 and 5/2 spin members have an intensity ratio of 1:3 similar to that in the other isotopes.

members of the band. It is expected to be a hole state in all the Yb nuclei studied. The triton spectra of Yb^{167} and Yb^{169} each have prominent peaks which fit into bands similar to what is expected for this orbital. In each case the 3/2 and 7/2 spin members have similar intensities, which are much larger than those of other members of the band. In each of the spectra of Yb^{171}, Yb^{173} and Yb^{175} there is a pair of strong triton groups which, due to their intensity, energy spacing and excitation energy, are probably associated with the $3/2-[521]$ orbital. The variation of the absolute (d, t) cross section of the $7/2$ $3/2-[521]$ state as a function of target mass is shown in Figure 19. The decrease in intensity with increasing mass is attributed to a dilution of the state with inert components as the excitation energy becomes higher. As will be seen later, it is expected that this band will be strongly coupled with the $K = 3/2$ gamma vibration band based on the $1/2-[521]$ orbital, and thus some variations in its properties from one nucleus to another might be expected.

I – *The* $5/2-[523]$ *Orbital*

It has been suggested by JOHANSEN[23] that this orbital appears at an excitation energy of 570 kev in Yb^{169}. As it originates from the $h\,9/2$ shell-model state, the only level with a large value of C^2_{jl} is the spin 9/2 member and thus there are no strongly populated states in the band. However, it is expected that three small peaks of roughly equal intensities corresponding to the 5/2, 7/2 and 9/2 rotational states should be observed. In the triton spectrum of Yb^{169}, Figure 2, weak peaks can be seen at positions corresponding to the excitation energies reported by Johansen for the 5/2, 7/2

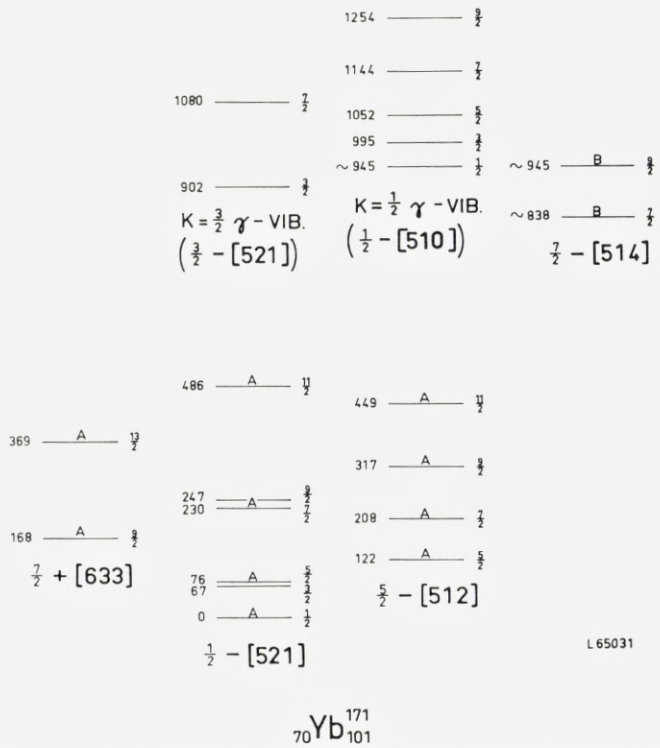

Figure 14. Level scheme for Yb^{171}. See caption to Figures 12 and 13.

and 9/2 levels. The group due to the spin 7/2 member is not completely resolved from the larger one already assigned to the 3/2 3/2−[521] state. The weak triton group observed at the position where the spin 11/2 state is expected is due largely to another state at about the same energy which is strongly populated in the (d,p) reaction.

The low log ft value for the positron decay of Yb^{167} [24, 25] suggests that the 5/2−[523] orbital is the ground state of Yb^{167}. If one assumes that the highest energy triton group in the spectrum of Figure 1 corresponds to the ground state, the level at 80 kev excitation is probably the 7/2 member of the band, and the group expected for the spin 9/2 state would be obscured by the strong 3/2 3/2−[521] peak.

J – *The* 5/2+[642] *Orbital*

There are three peaks in the triton spectrum of Yb^{169} corresponding to excitation energies of 584, 701 and 876 kev which have not yet been discussed. It is noted that, according to the Nilsson scheme, one expects the 5/2+[642]

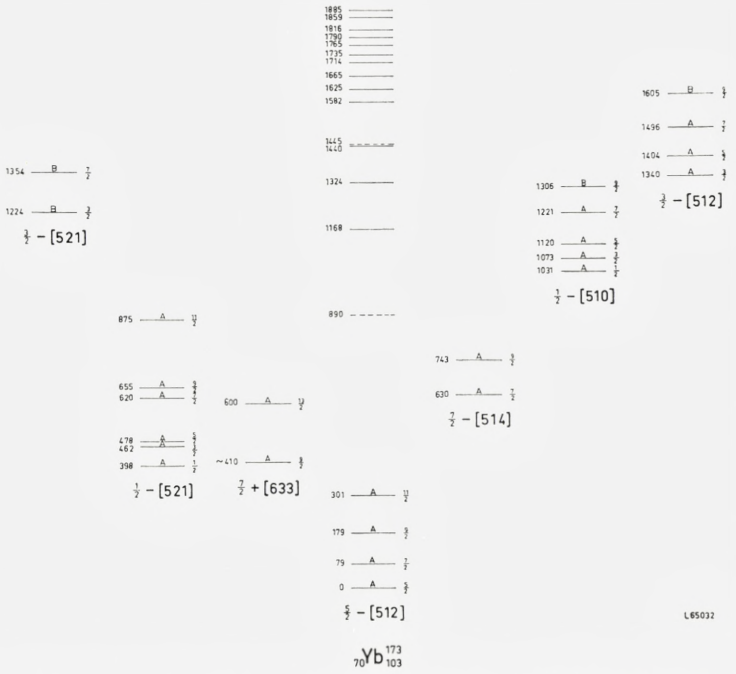

Figure 15. Level scheme for Yb^{173}. See caption to Figures 12 and 13.

state to be found close to the 5/2 − [523] and 3/2 − [521] orbitals which occur at 570 kev and 657 kev, respectively, in Yb^{169}. From a comparison of Tables 3 and 9 it is seen that the three triton groups have reasonable intensities to be the 5/2, 9/2 and 13/2 spin members of this band—the 7/2 and 11/2 spin members should be too weakly populated to be seen. This level spacing results in a rather low value of the inertial parameter $\hbar^2/2\Im = 7.3$ kev. However, this is very reasonable for the 5/2 + [642] orbital which is characterized by a large moment of inertia[2]. On the basis of the present work alone, it is not possible to distinguish between the 5/2 + [642] and 3/2 + [651] bands, as Table 9 shows that the predicted intensity patterns are almost identical, and the moments of inertia are probably similar. The choice made above is based on the fact that the 5/2 + [642] orbital appears higher in the Nilsson scheme and is known to be the ground state of Dy^{161} which has 95 neutrons.

It has been suggested[20] that the 5/2 + [642] orbital appears at an excitation of 30 kev in Yb^{167}. The spectrum of Figure 1 shows a weak group at this energy, but it seems unlikely that it can be assigned to this orbital due

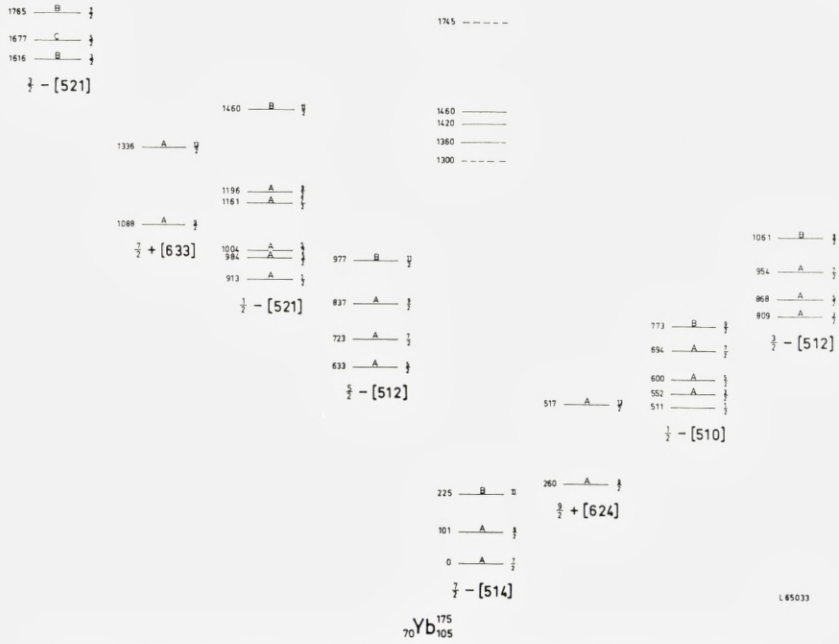

Figure 16. Level scheme for Yb^{175}. See caption to Figures 12 and 13.

to the absence of any triton group corresponding to the spin 9/2 member of the band. If one assumes a moment of inertia similar to that observed in Dy^{161} or Yb^{169}, the 9/2 state should occur at approximately 140 kev. However, there are no triton groups observed between energies corresponding to 79 and 180 kev excitation. Thus, at present there is no good explanation for the levels at 30 kev and 59 kev in Yb^{167}. It is also seen that there are many other unexplained levels in this nucleus. This is perhaps not too surprising as one expects considerable confusion to arise in this region of the Nilsson scheme. First, there should be strong interactions between the pairs of states with the same spin and parity which come from different shells, but which cannot cross each other, namely $1/2 + [660]$, $1/2 + [400]$ and $3/2 + [651]$, $3/2 + [402]$. Also there may be considerable Coriolis coupling between pairs of the above bands with K-values differing by unity.

K – *Vibrational States*

It is a typical feature of the spectra shown in Figures 1–10 that the groups at low excitation energies can be assigned to rotational bands based upon intrinsic states. The relative and absolute populations of these states are

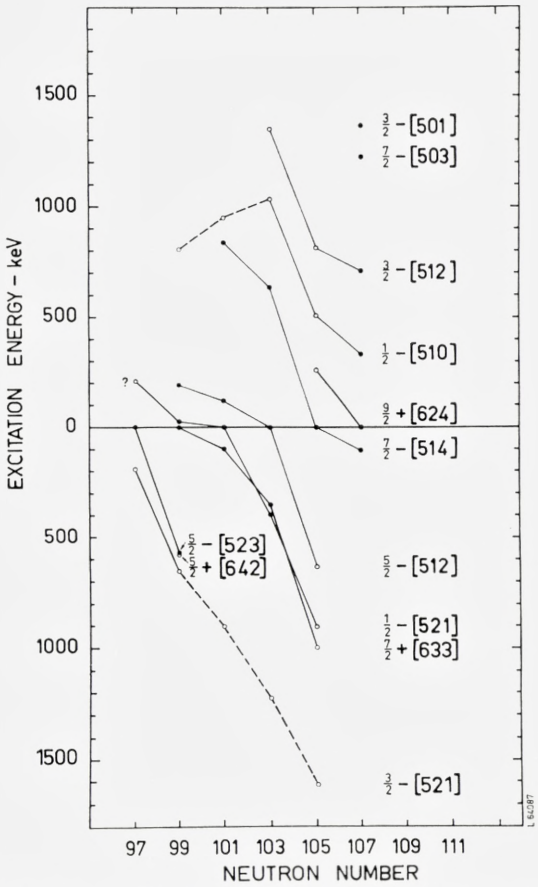

Figure 17. Plot of excitation energies for band heads of the Nilsson states observed. Points shown at negative energies indicate that the orbital is a hole state. Points connected by dashed lines only are those for which the observed cross sections were less than those expected for the pure single-particle transition. These states are interpreted as being collective. See text.

consistent with those expected on the basis of the Nilsson model with pairing effects. However, in each case it is found that the portions of the spectra corresponding to higher excitations cannot be explained in such a simple manner. There are many cases where the Nilsson model would predict the presence of a state which should be strongly populated, but the spectra show no peaks with greater than half the intensity expected for such states. On the other hand, the density of states populated is larger than expected, so that the total differential cross section per Mev of excitation is roughly as

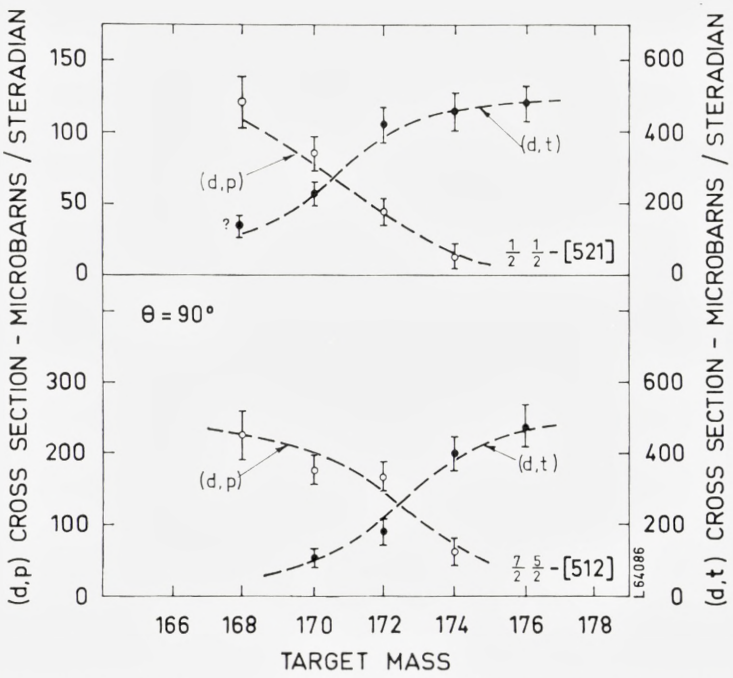

Figure 18. Cross sections for the (d,p) and (d,t) reactions of the 1/2 1/2 – [521] and 7/2 5/2 – [512] states as a function of target mass number.

calculated for the states which the Nilsson model would predict in this region. It is therefore reasonable to conclude that new modes of excitation become of significance and that the coupling of the single-particle motion to these modes gives rise to a considerable mixing so that the intensity expected for population of a given single-particle state now may be distributed over several states. In this connection it is worth remembering that several collective excitations are found at energies in the neighbourhood of 1 Mev. In the neighbouring even-even nuclei $K = 2+$, gamma vibrational states have been identified in a series of inelastic deuteron scattering experiments[10] which also have given a strong indication for low-lying octupole excitations in this region.

There is a striking correlation between the energies of the low-lying gamma vibrations and the before mentioned break-down of the pure single-particle description. This can be seen in Figure 20 which shows the energy of the most highly excited single-particle state assigned in the previous sections and the energies of the $K = 2+$ gamma-vibrational states in the neighbouring even-even nuclei. Of course it must be expected that the other

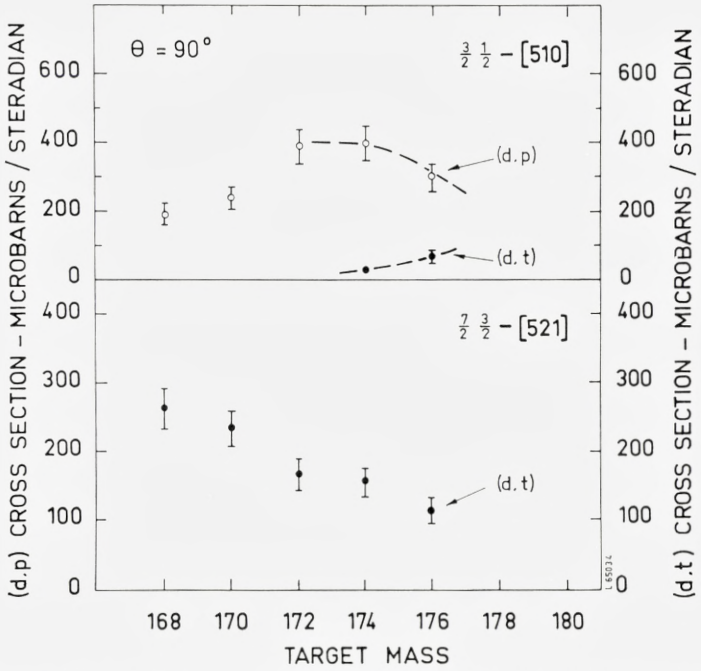

Figure 19. Cross sections for the (d,p) and (d,t) reactions of the 3/2 1/2 – [510] and 7/2 3/2 – [521] states as a function of target mass number.

TABLE 11. Inertial Parameters $\hbar^2/2\Im$ and Decoupling Parameters. Numbers in brackets are decoupling parameters for $K = 1/2$ Bands.

Orbital/Mass	167	169	171	173	175	177
3/2 – [521]	10.5	12.3	14.7	10.8	12.4	–
5/2 + [642]	–	7.4	–	–	–	–
5/2 – [523]	~ 11.3	11.0	–	–	–	–
7/2 + [633]	–	8.2	8.4	~ 7.9	10.3	–
1/2 – [521]	–	11.5	12.0	12.1	13.5	–
		(0.80)	(0.85)	(0.70)	(0.75)	
5/2 – [512]	–	12.3	12.2	11.2	12.8	–
7/2 – [514]	–	–	~ 11.5	~ 11.9	11.2	~ 12.3
9/2 + [624]	–	–	–	–	10.7	11.0
1/2 – [510]	–	13.2	12.4	11.9	11.4	12.2
		(0.08)	(0.032)	(+ 0.20)	(+ 0.20)	(+ 0.22)
3/2 – [512]	–	–	–	12.8	12.0	~ 12.9

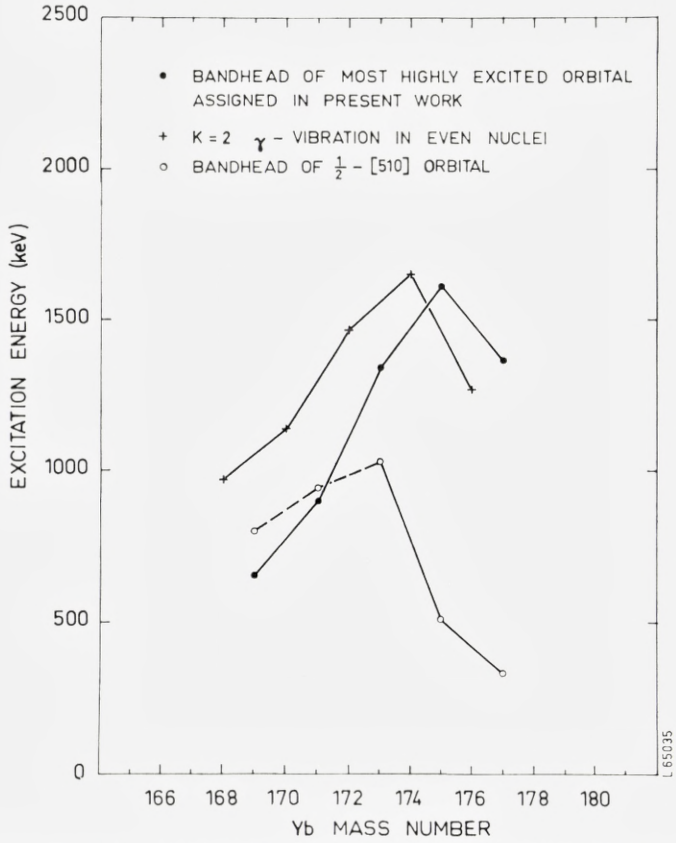

Figure 20. Plot showing the relationship between the region of excitation energy where observed states can be explained with a single-particle description and the gamma vibrational energy.

collective modes have a similar effect, but in the Yb nuclei the spacings of the single-particle states are such that levels connected by large E2-matrix elements occur separated by approximately the phonon energy (cf. Figure 17). Under such conditions a strong coupling of the particle motion to the vibrational motion is highly probable.

A qualitative understanding of some of the coupling phenomena and their significance for the observed stripping and pick-up spectra can be obtained from simple microscopic pictures of the vibrational state. The vibrational state in the even-even nucleus is a superposition of various two-quasiparticle states where the quasiparticles (in the case of the gamma vibration) have K-values differing by two units (Fig. 22). In a collective state many two-

TABLE 12A. (d,t) Population of $5/2-[512]$ Band.

Spin	Relative Intensity $\theta = 90°$				Values of C_{jl}^2			
	Theory	Yb^{171}	Yb^{173}	Yb^{175}	Theory	Yb^{171}	Yb^{173}	Yb^{175}
5/2	1.3	3.4	4.4	5.2	0.01	0.022	0.029	0.037
7/2	100	100	100	100	0.786	0.681	0.696	0.742
9/2	2.4	3.5	2.4	1.4	0.141	0.177	0.124	0.077
11/2	1.0	2.2	2.7	2.4	0.062	0.120	0.150	0.142

TABLE 12B. (d,p) Population of $5/2-[512]$ Band.

Spin	Relative Intensity $\theta = 90°$				Values of C_{jl}^2			
	Theory	Yb^{169}	Yb^{171}	Yb^{173}	Theory	Yb^{169}	Yb^{171}	Yb^{173}
5/2	1.2	2	~ 4.6	4.8	0.01	0.015	0.03	0.03
7/2	100	100	100	100	0.786	0.72	0.66	0.61
9/2	2.5	3.5	3.8	4.2	0.14	0.18	0.17	0.18
11/2	1.2	1.8	3.4	~ 4.2	0.06	0.09	0.14	0.18

quasiparticle states enter, but the major contributions come from quasiparticles near the Fermi surface. The importance of a given particle combination can be estimated on the basis of the asymptotic quantum numbers $[Nn_z\Lambda]$.

The E2-matrix element vanishes unless $\Delta N = 0$ (or ± 2), $\Delta n_z = 0$, $\Delta\Lambda = 2$ and $\Delta\Sigma = 0$. If these selection rules are fulfilled the matrix element is approximately proportional[27] to $(n+\Lambda+2)$ $(n-\Lambda)$ where $n = N - n_z$. The amplitude of a given two-quasiparticle state furthermore depends on the single-particle energies and the U and V factors for the corresponding states. Figure 21 shows for Yb^{172} the most important amplitudes in the gamma vibration[26] involving the neutron orbits of interest in this work.

In the odd nuclei one can attempt to describe the vibrational states as superpositions of one-quasiparticle and three-quasiparticle states. The three-quasiparticle states consist of the ground-state particle in the orbit K_g and (one of) the various two-quasiparticle configurations with $(K,\ K\pm 2)$ which make up the even-even gamma vibration. These states normally cannot be created from an even-nucleus ground state by the addition or subtraction of one nucleon (Fig. 22) and are therefore not populated by the (d,p) or (d,t) reactions. The components of the even vibration which involve a particle in the state $-K_g$, play a special role. In the even vibration the state

TABLE 13. (d,p) Population of $1/2-[510]$ Band.

Spin	Relative Intensities $\theta = 90°$					Relative Values of C_{jl}^2**				
	Theory	Yb^{171}	Yb^{173}	Yb^{175}	Yb^{177}	Theory	Yb^{171}	Yb^{173}	Yb^{175}	Yb^{177}
1/2	2.4	Obscured	3.3	*	3.0	0.01	–	0.01	–	0.01
3/2	100	100	100	100	100	0.40	0.34	0.31	0.31	0.32
5/2	35	43	51	45	48	0.29	0.31	0.33	0.29	0.32
7/2	25	16	25	20	19	0.19	0.10	0.15	0.12	0.12
9/2	1.36	4.4	4.2	5.5	4.5	0.09	0.24	0.21	0.28	0.23
11/2	0.24	Not Observed				0.01	–	–	–	–

* Obscured by $13/2\ 9/2+[624]$.

** The values obtained from experimental results have been normalized such that the sum of C_{jl}^2 for the observed peaks is equal to unity. The error in normalization due to inability to observe the spin 11/2 states is $< 15\,\%$ in Yb^{173} and Yb^{175}.

K_g could enter if it is connected with states $K_g \pm 2$ by large E2-matrix elements. In the odd nucleus the same matrix elements will admix the single-particle states $K_g \pm 2$ into the vibrational wave function and these components can be populated by the transfer reactions (Fig. 22). The amplitude of each component depends on the E2-matrix element connecting the states K_g and $K_g \pm 2$ and the important admixtures can therefore be localized in Figure 21. Furthermore, as pointed out, the admixtures are expected to be especially strong when the vibrational energy is close to the single-particle energies of the states $K_g \pm 2$.

Reference to Figure 21 shows that in the Yb nuclei the $5/2-[523]$ and the $3/2-[521]$ states are expected to be components of the gamma-vibrational states on the $1/2-[521]$ state. Similarly, the $1/2-[510]$ state should be a component of the $K-2$ vibration on the $5/2-[512]$ state.

Several of the experimental observations are indicative of effects of the nature discussed above. The most advantageous place to begin comparison may be Yb^{171}. This nucleus has been studied by both the (d,p) and (d,t) reactions and is furthermore a stable nucleus where additional information about the collective states can be obtained from (d,d') experiments. The vibrations based on the $1/2-[521]$ ground state have $K = 3/2$ and $5/2$. It is observed that the lowest band excited in the inelastic scattering experiments coincides in energy, within the experimental error, with the band assigned above as having a large admixture of the $3/2-[521]$ orbital. The intensity in the (d,d') spectrum to this band at $\theta = 125°$ is distributed on the 3/2, 5/2, 7/2 and 9/2 states in the ratios 5×10^{-4}, 8×10^{-4}, 2×10^{-4}, and 4×10^{-4} expressed relative to the elastic scattering intensity. For the inelastic scattering to

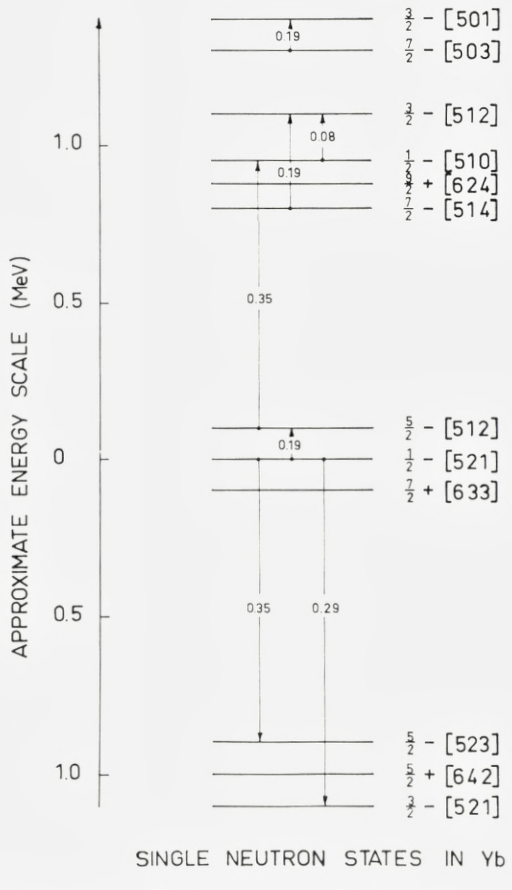

Figure 21. Approximate energy spacings and E2 matrix element strengths between Nilsson states in the Yb region.

the $2+$ and the $4+$, $K = 2$ gamma-vibrational states in Yb^{170} the ratios are 3×10^{-3} and 2×10^{-3}. The total intensity in the odd nucleus is thus approximately $40\,\%$ of that in the even nucleus, which is about as expected considering that only half the strength goes to the $K-2$ vibration and one therefore would identify the band as this component. On the other hand, the (d,t) spectrum has a strength to this band which is probably not less than $50\,\%$ of that expected for the pure single-particle state (cf. Fig. 19).

The situation is less clear with respect to the $K+2$ component of the gamma vibration. The inelastic deuteron spectrum in the neighbourhood of 1 Mev contains several peaks which could belong to this band. However,

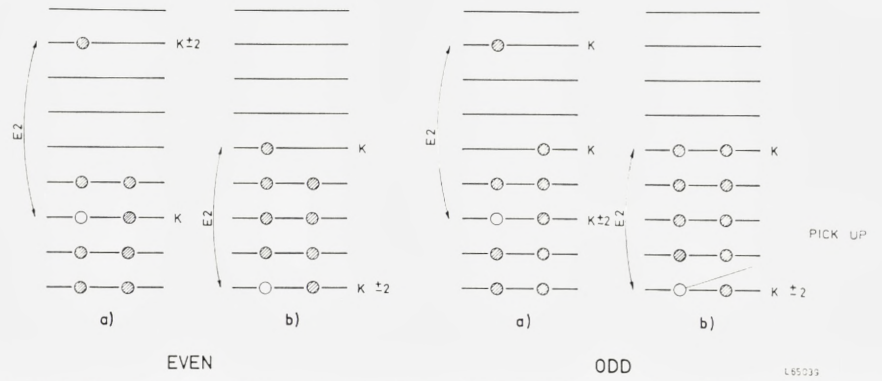

Figure 22. Independent-particle picture of the stripping reaction leading to vibrational states.

the (d,t) intensity to the expected $5/2-[523]$ admixture is weak, and it has not been possible of identify this band.

The other low-lying intrinsic state in Yb^{171} is the $5/2-[512]$ orbital. It is coupled with a strong matrix element to the $1/2-[510]$ orbital, which is a particle state and thus should be seen in the proton spectrum. The previous discussion on the $1/2-[510]$ orbital mentioned a group of levels in Yb^{171} whose intensity pattern resembled that band but whose absolute intensity was only $\sim 60\,\%$ of the expected value for that orbital. It is interesting to speculate that this might be the $K = 1/2$ gamma-vibrational band based on the $5/2-[512]$ state. It is seen from Table 11 that the decoupling parameter for this band is much smaller than the value of ~ 0.2 observed for the $1/2-[510]$ orbital in the heavier Yb nuclei. This is consistent with the fact that $K = 1/2$ vibrational states usually have small decoupling parameters.

TABLE 14. (d,p) Population of $3/2-[512]$ Band.

Spin	Relative Intensity				Relative Values of C_{jl}^2*			
	Theory	Yb^{173}	Yb^{175}	Yb^{177}	Theory	Yb^{173}	Yb^{175}	Yb^{177}
3/2	26.4	61	45	77	0.08	0.11	0.09	0.15
5/2	100	100	100	100	0.64	0.39	0.42	0.41
7/2	18.9	54	49	51	0.118	0.20	0.20	0.21
9/2	2.9	< 9.5	< 8.5	6.9	0.149	< 0.30	< 0.29	0.23
11/2	0.24	Not observed			0.012	–	–	–

* The values derived from experimental results are normalized such that the sum of C_{jl}^2 for the observed peaks is equal to unity.

Figure 20 also shows the variation of the excitation energy of the 1/2−[510] orbital with mass number. It is seen that in Yb^{173}, Yb^{175} and Yb^{177}, this state does not appear at an energy close to that which would be expected for the gamma vibration based on the 5/2−[512] orbital. This is probably the reason why the 1/2−[510] band appears as a good particle state in these nuclei. However, as one goes down in mass to Yb^{171}, the excitation energy of the 1/2−[510] orbital approaches that of the gamma vibrations and, as a result, the mixing becomes appreciable.

On the basis of these arguments, one would expect the behaviour in Yb^{169} to be similar to that in Yb^{171}. This is, in fact, seen to be the case, except that the band ascribed to the vibrational state has an intensity only $\sim 45\,\%$ of that which would be expected for the pure 1/2−[510] state. It is also interesting that another band similar in structure to the 1/2−[510] orbital, but with an intensity $\sim 40\,\%$ of that expected for the pure state, is seen at higher excitation. The lowest band has a small decoupling parameter (see Table 11) whereas the other has $a = 0.12$, a value comparable to that of the pure state in the heavier Yb nuclei.

One further observation which supports this line of reasoning concerns the results of the Dy^{164} (d,p) Dy^{165} study by Sheline et al.[22] as re-interpreted in the light of experiments by Schult et al.[28]. The latter workers have assigned a $K = 1/2$ band at excitation energy 570.25 kev to be the gamma vibration based on the 5/2−[512] orbital. The 3/2 member of this band is at 605.10 kev. In the (d,p) reaction[22], 3/2 and 5/2 states at 605 and 658 kev, respectively, are populated. Although intensity values were not given for these proton groups, the relative peak heights in the spectra shown are comparable with those found at a similar reaction angle for the analogous band discussed above in the isotone Yb^{169}. This provides the missing link which connects the bands assumed to be vibrational states in the present work with a band in Dy^{165} assigned as a gamma-vibrational band on the basis of gamma-ray studies.

In conclusion one can say that the experimental observations are in agreement with the qualitative arguments given in the introduction to this section. However, it remains to be seen whether the microscopic theories of nuclear vibrations presently in use can account for the large single-particle amplitudes determined from the observed intensities of the stripping and pick-up reactions.

5. Determination of Δ from the U^2 and V^2

The data shown in Figure 18 have been interpreted above as being an indication of the filling of the $1/2-[521]$ and $5/2-[512]$ orbitals as a function of target mass. If the portions of the curves where the (d,t) cross sections have "saturated" at maximum values are, as assumed, to correspond to V^2 almost unity, the V^2 for these states in the other isotopes can be derived from the figure. Similarly, estimates of the U^2 can be obtained from the (d,p) cross sections. Figure 19 shows, however, that this procedure cannot be applied to states which become badly mixed before the excitation energy is high enough to give the state almost pure hole or particle characteristics.

In order to obtain a value of the parameter Δ from these estimates of the U^2 and V^2, it is useful to consider the standard equations of pairing theory:

$$E_\nu = \sqrt{\Delta^2 + (\varepsilon - \lambda)^2},$$

where E_ν is the quasiparticle energy, ε is the single-particle energy without pairing, and λ is the Fermi energy.

Thus, the excitation energy of a quasiparticle level above the ground state is

$$E = \sqrt{\Delta^2 + (\varepsilon - \lambda)^2} - \sqrt{\Delta^2 + (\varepsilon_0 - \lambda)^2} = \sqrt{\Delta^2 + (\varepsilon - \lambda)^2} - E_0,$$

where ε_0 refers to the ground state. As $\varepsilon_0 - \lambda << \Delta$ the value of E_0 should be approximately equal to Δ.

If one combines the above equation with the usual expression for V^2,

$$V^2 = 1/2\left(1 - \frac{\varepsilon - \lambda}{\sqrt{\Delta^2 + (\varepsilon - \lambda)^2}}\right),$$

TABLE 15. (d,t) Population of $7/2+[633]$ Band.

Spin	Relative Intensity $\theta = 90°$				Relative Values of C_{jl}^2*			
	Theory	Yb^{169}	Yb^{171}	Yb^{175}	Theory	Yb^{169}	Yb^{171}	Yb^{175}
7/2	1.2	Not seen			0.001	–	–	–
9/2	83	~ 100	79	110	0.07	0.08	0.07	0.09
11/2	1.8	Not seen			0.015	–	–	–
13/2	100	100	100	100	0.915	0.92	0.93	0.91

* The values derived from experimental results are normalized such that the sum of C_{jl}^2 for the observed peaks is equal to unity. The error in normalization due to inability to observe the spin 7/2 and 11/2 states is less than 10 % in all cases.

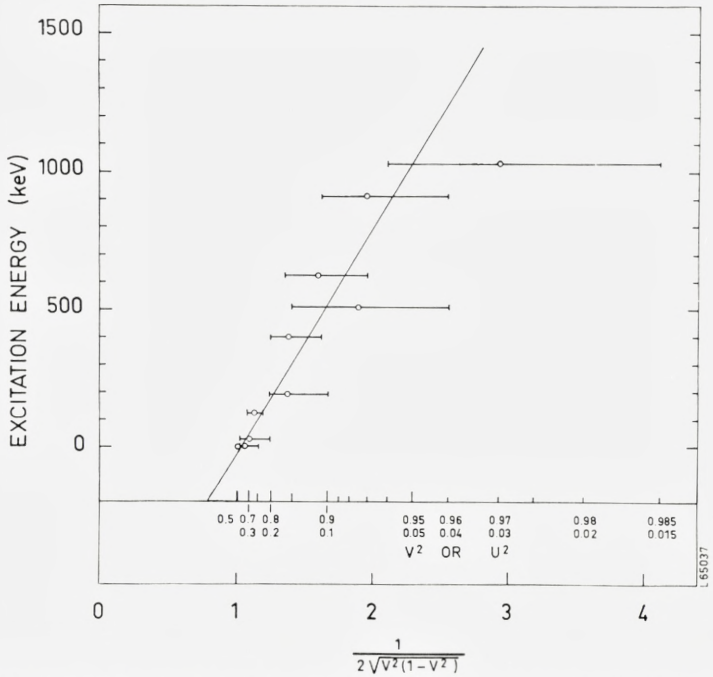

Figure 23. The relationship between the excitation energy of a state and its V^2 (or U^2). Energies are taken from odd nuclei and the values of V^2 (or U^2) were interpolated from values in neighbouring even-even nuclei. Pairing theory suggests that the points should fall on a straight line with slope Δ. The line shown in the figure has a slope of 800 ± 150 kev.

and eliminates $\varepsilon - \lambda$, it is found that

$$E = \frac{\Delta}{2\sqrt{V^2(1-V^2)}} - E_0.$$

That is, if one plots the excitation energy versus $1/2 \times (V^2(1-V^2))^{-1/2}$, the points should fall on a straight line with slope Δ and intercept $-E_0$ on the energy axis. Figure 23 shows such a plot for some of the states in the Yb nuclei. The straight line drawn through the points has a slope of 800 kev. The value of Δ thus obtained is 800 ± 150 kev, which is in good agreement with the value of 700 kev derived from the neutron separation energies in this region. It is also noted that the straight line drawn in Figure 23 passes through the point (1,0), which means that the intercept on the energy axis is approximately equal to $-\Delta$, as was to be expected.

6. Comparison of Intensities with Predicted Values

The comparisons of theoretical and experimental relative intensities given in Tables 10–15 show that the main features of the stripping and pick-up processes are described very well by the Nilsson wave functions and the distorted wave calculations. It is noted, however, that there are several cases where the relative cross section of a particular member of a band may be consistently too large or too small when compared to the predicted value. It would be interesting to look for systematic trends in these discrepancies and to try to find their origin. Also, the above discussion has been mainly concerned with relative intensities and a detailed comparison of absolute intensities with predictions has been avoided so far. Of course, in order to make an estimate of an absolute intensity, it is also necessary to have a knowledge of the quantity V^2 and, as we have seen, the purity of the state. From Figure 18, however, it is probably safe to conclude that for the $5/2-[512]$ and $1/2-[521]$ orbitals the value of V^2 is nearly unity for the Yb^{176} and Yb^{174} targets, respectively. Similarly, other cases can be found where the V^2 (or U^2) for a band can be assumed to be close to unity for the (d,t) (or (d,p)) reaction. For cases selected in this manner, Figure 24 shows the ratio of experimental to predicted differential cross section at $\theta = 90°$ plotted as a function of l-value for the (d,t) and (d,p) processes. The solid lines in this figure connect points which are obtained by geometrical averaging of all the data points for a particular l-value. It is seen that for the (d,t) case especially, the average values are dependent upon the l-value and are always greater than unity. The fact that the predictions and experiment are in better agreement for the (d,p) process is probably a reflection of the fact that the triton potentials are not as well known as the proton potentials and thus there is more uncertainty in the choice of parameters for the DWBA calculation.

It is also seen that there is a great deal of "scatter" from the average values in Figure 24. Apart from experimental inaccuracies there are various effects which could cause differences between the calculated and the observed cross sections. Several such effects can be imagined: Inelastic effects in the reaction process, a possible dependence on the quantum number j of the stripped particle, band mixing, and the fact that the Nilsson wave functions are approximations. The incoming deuteron could excite the nucleus before the stripping (or pick-up) takes place, and this could give a different distribution of intensity among the final spin states. The triton or proton resulting from the reaction could also cause similar inelastic effects as it leaves the nucleus. It is known from the inelastic deuteron spectra obtained in the present study that, at $\theta = 90°$, inelastic scattering from the first $2+$

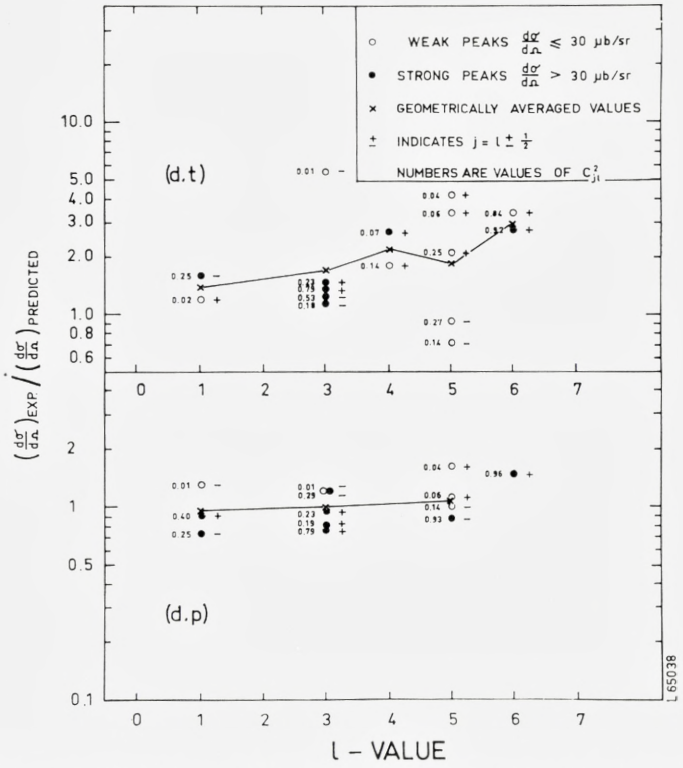

Figure 24. Ratio of experimental to theoretical cross sections for states populated by (d,p) and (d,t) reactions. See text for discussion of discrepancies between experiment and theory.

rotational state in the target nucleus occurs with a probability about 10 % of that for elastic scattering. Thus, one should expect that not more than a similar fraction of the intensity of one peak in a band would be redistributed over the other members of the band by such inelastic effects. However, many of the small peaks where discrepancies are observed have intensities from 1 % to 5 % of that of the strongest peak in the band. The net result of this type of inelastic effect would generally be an increase in intensity of the weakest peaks. Indeed, there does seem to be a slight tendency for the weakly populated states to have higher values in Figure 24 than the strongly populated ones. For the 1/2−[510] band, however, it was seen that rotational excitation and stripping lead to an overestimate of the cross section for the 1/2 state. It is therefore obvious that other effects must also be present.

In Figure 24, one can also look for indications of a j-dependence in the stripping process. If such an effect were present, one might expect a correlation between the directions of the deviations from the average values

and whether the neutron spin is parallel or antiparallel to the orbital angular momentum. The spin direction is indicated by a plus or minus sign beside each point in Figure 24. As points with both signs have random directions of deviation for any l-value, there appears to be no evidence for strong j-dependence in these stripping and pick-up reactions. Strong band mixing between the 1/2−[510] and the 3/2−[512] orbitals has been observed in the tungsten isotopes[5]. In the Yb isotopes, the larger energy differences between these orbitals reduce the mixing so that there appears to be no observable Coriolis mixing. The spacings of orbitals with $\Delta K = \pm 1$ are sufficiently large in the Yb isotopes to obviate detailed consideration of Coriolis coupling in the analysis of the data. Any other mechanism which produces band mixing is also expected to depend upon the separation of the bands. Since the separations vary with nucleus, consistent deviations from the theoretical values for the C_{jl} are probably not due to band mixing.

The Nilsson wave functions are of course approximations and some deviations between the experimental and theoretical values of C_{jl}^2 are expected. If the C_{jl}^2 for a state is large, its relative error should be small. However, if the C_{jl}^2 is small, a considerable relative error can be expected because of greater sensitivity to the choice of parameters in the Nilsson model. Thus, errors of this nature would be expected to result in larger deviations (of either sign) from the averages in Figure 21 for states with small C_{jl}^2 than for those with large C_{jl}^2. In Figure 24, the numbers shown beside the data points show the value of C_{jl}^2 for that state. It is seen that the states with small C_{jl}^2 tend to have large deviations from the average and the direction of the deviation is random. Hence, some of the discrepancies may be due to small errors in the wave functions used. A favourable opportunity for the study of such effects might be offered by the 5/2−[512] band where the 5/2 and 7/2 states have the same V^2 and l-value. The 5/2 state is expected to be populated with an intensity only about 1 % of that of the 7/2 state, but Tables 12A and 12B show that the observed population is usually about 4 %. If the discrepancy were due to inelastic effects, one would expect approximately the same amount of distortion of the intensity pattern in each nucleus where the band was observed. Table 12B indicates, however, that in Yb^{169} the intensity ratio in this band is only 2 %, and thus it is more likely that the deviation from the theoretical ratio is a nuclear effect. In this case, it is not unlikely that the theoretical value of C_{jl}^2 could be slightly in error (and could vary from one nucleus to another) as it is rather sensitive to the parameters of the Nilsson model. This is seen when one compares the value of $C_{jl}^2 = 0.01$ calculated from the Nilsson wave functions[1] with that of $C_{jl}^2 = 0.04$ calculated from the wave functions for proton states in the

$N = 5$ shell by MOTTELSON and NILSSON[2]. Although the latter value is applicable only for proton states, it does show that the small values of C^2_{jl} can be rather sensitive to the choice of parameters in the Nilsson model.

This does not mean, however, that in all cases the experimental values are more accurate than the theoretical ones. A simple test in the case of $K = 1/2$ bands is to calculate the decoupling parameter, a, from the relationship

$$a = \sum_I (-1)^{I-\frac{1}{2}}(I+\tfrac{1}{2})C^2_{Il}.$$

This is really a very severe test for the experimental data because the intensities for the invariably weak peaks corresponding to the high-spin states are weighted much more heavily than those for the low-spin states. For instance, in the 1/2−[521] band, the spin 11/2 state is populated only about 1 % as strongly as the spin 1/2 state, but its contribution in the calculation of the decoupling parameter is several times greater than that of the spin 1/2 state. When one uses the empirical values of C^2_{jl} from Table 10 in the above expression, it is found that $a = -0.1$, -0.3 and $+0.4$ in Yb^{171}, Yb^{173} and Yb^{175}, respectively. The corresponding values obtained from energy level spacings are $a = +0.87$, $+0.70$ and $+0.67$, respectively, which are in reasonable agreement with the predicted value of 0.9, obtained from the theoretical values of C^2_{jl}. Slightly better agreement can be obtained for the empirical values if correction factors for φ_l for the various l-values obtained from the curves in Figure 24 are used. This procedure should, in fact, give more realistic values for C^2_{jl} than those presented in Tables 10–15. It has not been applied to the data in these tables because the limited experimental data available do not yet give a good determination of the correction factors to be applied to the φ_l. The fact that this procedure still does not predict acceptable values for the decoupling parameter probably indicates that some small effects are present which have not been included in the description of the reaction process.

The above discussion indicates that the small discrepancies observed between experiment and theory cannot be ascribed to any single cause. The most likely causes are uncertainties in the calculated values of φ_l, uncertainties in the nuclear wave functions, and higher order effects in the reaction processes. It is to be remembered, however, that the general agreement between experiment and theory is quite good and is more than adequate to permit unambiguous assignments of bands in cases where mixing is not serious. As can be seen from Figure 24, the discrepancies are only appreciable for those cases where the intensity is less than 5–10 % of that of the strongest peaks in the spectrum.

7. Summary

In the preceding sections it has been seen that the single-nucleon transfer reactions are very useful for the assignment of levels in deformed nuclei because the relative intensities to the various rotational members of a band yield, in effect, the wave function of the intrinsic state. In the present work this technique has resulted in the classification of many previously unknown states in terms of the unified model. The combined use of stripping and pick-up reactions has been very helpful for studying the hole-particle properties of the levels and for determining the U^2 and V^2 factors for various states in the target nuclei. The distributions of neutron pairs among the orbitals near the Fermi surface were found to be in good agreement with pairing theory.

The tentative results concerning the population of vibrational states indicate that these reactions could be used for studying the compositions of such collective states, as each reaction essentially projects out one or two of the various components. This is a problem which deserves further examination and the best suitable nuclei for studies in the rare earth region would probably be the Gd, Dy or Er series. In these nuclei the gamma vibrations occur at lower excitation energies than in the Yb series and their B(E2)-values are larger. Under such conditions it is expected that many configurations contribute to the vibration and therefore the amplitude of any single component is much reduced in the total vibrational wave function.

Acknowledgments

The authors are indebted to G. R. Satchler who carried out the DWBA calculations for this work. The targets were produced by the chemistry group working with Sven Bjørnholm, except for the Yb^{168} targets which were made by G. Sørensen at the University of Aarhus mass separator. Thanks are also due to the team of plate-scanning girls for carefully counting the tracks in the emulsions and in particular to Mrs. Anna Grethe Jørgensen who counted the majority of the exposures for this work. One of the authors (D.G.B.) is grateful to the N.A.T.O. for financial support in the form of a fellowship and another (B.Z.) would like to acknowledge financial assistance from the Ford Foundation and leave of absence from the Argonne National Laboratory.

The Niels Bohr Institute
University of Copenhagen

References

1) S. G. Nilsson, Mat. Fys. Medd. Dan. Vid. Selsk. **29**, No. 16 (1955).
2) B. R. Mottelson and S. G. Nilsson, Mat. Fys. Skr. Dan. Vid. Selsk. **1**, No. 8 (1959).
3) S. A. Hjorth and B. L. Cohen, Phys. Rev. **135**, B920 (1964).
4) B. L. Cohen and R. E. Price, Phys. Rev. **121**, 1441 (1961).
5) J. R. Erskine, Phys. Rev. **138**, B66 (1965).
6) M. N. Vergnes and R. K. Sheline, Phys. Rev. **132**, 1736 (1963).
7) R. H. Siemssen and J. R. Erskine, to be published.
8) G. R. Satchler, Ann. Phys. **3**, 275 (1958).
9) R. H. Bassel, R. M. Drisko and G. R. Satchler, ORNL Report 3240 (unpublished, and G. R. Satchler, private communication.
10) D. G. Burke et al., to be published.
11) B. Elbek, Determination of Nuclear Transition Probabilities by Coulomb Excitation, (Dissertation), Ejnar Munksgaards Forlag, Copenhagen (1963).
12) Y. Yoshizawa, B. Elbek, B. Herskind and M. C. Olesen, Nucl. Phys. **73**, 273 (1965).
13) J. Borggreen, B. Elbek and L. Perch Nielsen, Nuclear Instr. and Methods **24**, 1 (1963).
14) L. Westgaard and S. Bjørnholm, to be published in Nuclear Inst. and Methods.
15) B. Elbek, M. C. Olesen and O. Skilbreid, Nucl. Phys. **10**, 294 (1959).
16) J. H. E. Mattauch, W. Thiele and A. H. Wapstra, Nucl. Phys. **67**, 32 (1965).
17) G. R. Satchler, private communication.
18) Nuclear Data Sheets, National Academy of Sciences, Washington.
19) B. S. Dzelepov, L. K. Peker and V. O. Sergeyev, Decay Schemes of Radioactive Nuclei, Moscow 1963.
20) O. Nathan and S. G. Nilsson, in Alpha-, Beta- and Gamma-Ray Spectroscopy, Vol. 1. K. Siegbahn, Editor, Amsterdam 1965.
21) C. J. Orth, M. E. Bunker and J. W. Starner, Phys. Rev. **132**, 355 (1963).
22) R. K. Sheline, W. N. Shelton, H. T. Motz and R. E. Carter, Phys. Rev. **136**, B351 (1964).
23) A. Johansen and B. Elbek, to be published.
24) T. Tamura, Nucl. Phys. **62**, 305 (1965).
25) C. Wang et al. JINR-O-1361 (1963).
26) D. R. Bés, P. Federman, E. Maqueda and A. Zuker, Nucl. Phys. **65**, 1 (1965).
27) E. R. Marshalek and J. O. Rasmussen, Nucl. Phys. **43**, 438 (1963).
28) O. W. B. Schult, B. P. Maier and U. Gruber, Z. f. Phys. **182**, 171 (1964).

Indleveret til Selskabet den 10. december 1965.
Færdig fra trykkeriet den 3. oktober 1966.

Matematisk-fysiske Meddelelser
udgivet af
Det Kongelige Danske Videnskabernes Selskab
Bind **35,** nr. 3

Mat. Fys. Medd. Dan. Vid. Selsk. **35,** no. 3 (1966)

SURVEY OF INVESTIGATIONS ON THE ENERGY-MOMENTUM COMPLEX IN GENERAL RELATIVITY

BY

C. MØLLER

København 1966
Kommissionær: Munksgaard

Synopsis

The paper contains a survey of the investigations of the last decade on the energy-momentum complex in general relativity. A comparison of the properties of the various complexes proposed in different papers is performed and their advantages and deficiencies are discussed. A satisfactory solution of the energy problem in accordance with the general principle of relativity has now been reached.

PRINTED IN DENMARK
BIANCO LUNOS BOGTRYKKERI A/S

Shortly after EINSTEIN had developed his final theory of gravitation in 1915 he also attacked the problem of energy and momentum conservation for the complete system of matter plus gravitational field. In his famous papers from the years 1915 and 1916 [1] he introduced the well-known expression for the energy-momentum complex

$$ {}_E\mathsf{T}_i^k = \mathfrak{T}_i^k + {}_E\tau_i^k \tag{1} $$

which satisfies the divergence relation

$$ {}_E\mathsf{T}_i^k{}_{,k} \equiv \frac{\partial {}_E\mathsf{T}_i^k}{\partial x^k} = 0 \tag{2} $$

as a consequence of the field equations. Here, $\mathfrak{T}_i^k$ is the matter tensor density, which appears as source of the gravitational field on the right-hand side of Einstein's field equations, while the gravitational part ${}_E\tau_i^k$ is a homogeneous quadratic expression in the first-order derivatives $g_{ik,l}$ of the metric tensor g_{ik}. In terms of the Einstein Lagrangian

$$ {}_E\mathfrak{L} = \sqrt{-g}\, g^{ik}(\Gamma_{ik}^l \Gamma_{lm}^m - \Gamma_{im}^l \Gamma_{kl}^m), \tag{3} $$

${}_E\tau_i^k$ has the canonical form

$$ {}_E\tau_i^k = \frac{1}{2\varkappa}\left(\frac{\partial {}_E\mathfrak{L}}{\partial g^{lm}{}_{,k}}\, g^{lm}{}_{,i} - \delta_i^k\, {}_E\mathfrak{L}\right) \tag{4} $$

where $\varkappa$ is Einstein's gravitational constant. ${}_E\mathfrak{L}$ is obtained from the scalar curvature density $\mathfrak{R}$ by omitting a divergence part containing the second order derivatives $g_{ik,l,m}$. It is an *affine* scalar density which is homogenously quadratic in the $g_{ik,l}$ and the expressions (1)–(4) can be obtained by the well-known method of (linear) infinitesimal coordinate transformations applied to ${}_E\mathfrak{L}$.

[1] This paper was reported at the Einstein Symposium der Deutschen Akademie der Wissenschaften, Berlin, in November 1965.

For a closed system and for a restricted class of coordinate systems the quantities obtained from ${}_E\mathfrak{T}_i^k$ by integrating over the spatial coordinates, i. e.

$$ {}_EP_i = \frac{1}{c}\int\int\int {}_E\mathsf{T}_i^4 \, dx^1 \, dx^2 \, dx^3 \tag{5} $$

have quite remarkable properties. Before stating these properties we have to specify what we mean by a *closed* system. In general, an *insular* system, i. e. a system for which $\mathfrak{T}_i^k$ is zero outside a *time-like* tube of finite spatial extension, is not closed since it may lose energy by emission of gravitational radiation. This question has been studied extensively by Bondi et al [2] and by Sachs [3], and we can now give a general definition of a non-radiative system. A system is said to be closed if it is insular and, further, if it is possible to introduce a class of coordinates

$$ x^i = \{x, y, z, ct\}, \; r = \sqrt{x^2 + y^2 + z^2} \tag{6} $$

with the following properties. Points at large spatial distances from the matter tube have large values of r, i. e. spatial infinity corresponds to $r \to \infty$. The metric is of the form

$$ g_{ik} = \eta_{ik} + \overset{(1)}{g}_{ik} \tag{7} $$

where η_{ik} is the constant Minkowski matrix and $\overset{(1)}{g}_{ik}$ and its first-order derivatives are asymptotically of the type

$$ \overset{(1)}{g}_{ik} = O_1, \quad g_{ik,l} = \overset{(1)}{g}_{ik,l} = O_2. \tag{8} $$

Here, O_n with positive integer n denotes a term for which $r^n O_n$ remains finite for $r \to \infty$. The coordinates defined by (6)–(8), the "B.S.-coordinates" for a closed system, are asymptotically Lorentzian since $g_{ik} \to \eta_{ik}$ for $r \to \infty$.

Now, by integrating (2) over a suitable cylindrical region of space-time and using Gauss's theorem one finds in a well-known way that the quantities ${}_EP_i$ have the following properties A, which are essential for the interpretation of P_i as the components of the four-momentum:

A *For a closed system and in a system of B.S.-coordinates the quantities P_i are constant in time and they transform as the components of a 4-vector under all linear transformations.*

These properties are contained in the more general statement, also following from (2), that the integrals

$$ {}_EP_i = -\frac{1}{c}\int_{\Sigma} {}_E\mathsf{T}_i^k \, dS_k \tag{9} $$

integrated over any space-like 3-dimensional hypersurface Σ of infinite extension are independent of the choice of Σ. For the validity of A it is essential that ${}_E\mathsf{T}_i^k$ is an affine tensor density of weight one and that the gravitational part ${}_E\tau_i^k$ is a homogeneous quadratic function of the $g_{ik,l}$, for this means that ${}_E\tau_i^k = O_4$ in a system of coordinates (6)–(8).

If we eliminate $\mathfrak{T}_i^k$ in (1) by means of the field equations the complex ${}_E\mathsf{T}_i^k$ appears as a function of the gravitational field variables for which the relation (2) must hold identically. This means that ${}_E\mathsf{T}_i^k$ may be written in the form

$$ {}_E\mathsf{T}_i^k = {}_E\psi_i^{kl}{}_{,l} \tag{10} $$

where $\psi_i^{kl} = -\psi_i^{lk}$, the so-called *superpotential,* is antisymmetrical in k and l. This possibility was first noted by VON FREUD [4], the explicit expression for ${}_E\psi_i^{kl}$ is [5]

$$ {}_E\psi_i^{kl} = \frac{g_{in}}{2\varkappa\sqrt{-g}}\,\mathfrak{g}^{nklm}{}_{,m} \tag{11} $$

with

$$ \mathfrak{g}^{iklm} = (-g)\,(g^{ik}\,g^{lm} - g^{il}\,g^{km}). \tag{12} $$

The latter quantity is a *true* tensor density of *weight two,* satisfying the symmetry relations

$$ \mathfrak{g}^{iklm} = -\mathfrak{g}^{ilkm} = -\mathfrak{g}^{mkli} = \mathfrak{g}^{kiml}, \tag{13} $$

while ${}_E\psi_i^{kl}$, which is a homogeneous linear function of the $g_{ik,l}$, is an *affine* tensor density of *weight one.*

By means of Stoke's theorem one gets from (9) and (10) for the four-momentum

$$ {}_EP_i = -\frac{1}{2c}\int_{\Phi} {}_E\psi_i^{kl}\,dS_{kl} \tag{14} $$

where the integration is extended over the 2-dimensional boundary surface Φ of Σ corresponding to a large constant value r_1 of the "radius" r (strictly speaking one has to take the limit $r_1 \to \infty$). Thus, ${}_EP_i$ depends only on the asymptotic values of the metric and it is, therefore, invariant under all coordinate transformations which preserve the asymptotic form of g_{ik}.

By means of (1) the equations (10) may be written

$$ {}_E\psi_i^{kl}{}_{,l} - {}_E\tau_i^k = \mathfrak{T}_i^k \tag{15} $$

which obviously is a special form of Einstein's field equations. If we raise the index i by means of the metric tensor g^{ik} these equations can also be brought into the form

$$ {}_B\psi^{ikl}{}_{,l} - {}_B\tau^{ik} = \mathfrak{T}^{ik} \tag{16} $$

where

$$ {}_B\psi^{ikl} \equiv \frac{1}{2\varkappa\sqrt{-g}}\,\mathfrak{g}^{iklm}{}_{,m} = -\,{}_B\psi^{ilk} \tag{17} $$

and ${}_B\tau^{ik}$ again is a homogeneous quadratic function of the $g_{ik,l}$. In this way we arrive at the complex first given by BERGMANN and THOMSON [6].

$$ {}_B\mathfrak{T}^{ik} \equiv \mathfrak{T}_i^{\,k} + {}_B\tau^{ik} = {}_B\psi^{ikl}{}_{,l}. \tag{18} $$

The integrated quantities ${}_BP^i$ obtained from this complex in a similar way as ${}_EP_i$ in (5) or (9) also have the properties *A*. Moreover, in any system of B.S.-coordinates we have simply

$$ {}_EP_i = \eta_{ik}\,{}_BP^k \tag{19} $$

i. e. the two different complexes give the same values for the total momentum and energy in such coordinates.

Similar properties has the following complex given by LANDAU and LIFSHITZ [6]:

$$ {}_L\mathfrak{T}^{ik} = {}_L\psi^{ikl}{}_{,l} \tag{20} $$

$$ {}_L\psi^{ikl} = \frac{1}{2\varkappa}\,\mathfrak{g}^{iklm}{}_{,m}\,. \tag{21} $$

From (16)–(21) it follows that

$$ {}_L\mathfrak{T}^{ik} = \sqrt{-g}\,(\mathfrak{T}^{ik} + {}_L\tau^{ik}) \tag{22} $$

where ${}_L\tau^{ik}$ like ${}_B\tau^{ik}$ is an affine tensor density of weight one, which is a homogeneous quadratic function of the $g_{ik,l}$. Consequently ${}_L\mathfrak{T}^{ik}$ is an affine tensor density of weight two, which means that ${}_LP^i$ is a 4-vector under Lorentz transformations only. On the other hand ${}_L\mathfrak{T}^{ik}$ has the advantage of being symmetrical in i and k as is seen at once from (20), (21) and (13). In any system of B.S.-coordinates we have

$$ {}_LP^i = {}_BP^i = \eta^{ik}\,{}_EP_k \tag{23} $$

so that the three different complexes are equally suited for the calculation of the four-momentum in such coordinates. However, in more general systems of coordinates the application of these complexes leads to meaningless results. From the point of view of general relativity this is not satisfactory and in

the past this has caused some doubts about the applicability of these complexes at all. As a matter of fact we must require of a truly generally relativistic expression for the four-momentum that it satisfies the following condition:

B For a closed physical system the total four-momentum is a free 4-vector under arbitrary space-time transformations.

The necessity for this requirement is seen at once if we go to the limit of spatially very small systems, for in this case our system is effectively a particle which, according to basic assumptions of general relativity, certainly should have a four-momentum with this property.

A somewhat weaker requirement contained in B is the condition that

B′ the fourth component of the four-momentum must be invariant under purely spatial transformations

$$x'^{\iota} = f^{\iota}(x^{\varkappa}), \quad x'^{4} = x^{4} \tag{24}$$

i. e.

$$P'_4 = P_4 \tag{25}$$

which expresses the physically evident fact that the total energy is invariant under such transformations.

Now, none of the forementioned complexes satisfy even this rather weak and triviel condition. In the case of the Einstein complex this was pointed out first by BAUER [7] who remarked that in a completely empty space Einstein's expression for the total energy gives the correct value zero in a Cartesian system of coordinates, but the meaningless value $-\infty$ when calculated in polar coordinates. For this reason the whole question of the energy in gravitational fields was taken up again in 1958 [5], and it was shown that it is possible to define a complex

$$\left.\begin{aligned} \Theta_i^{\,k} &= \mathfrak{T}_i^{\,k} + \vartheta_i^{\,k} = \chi_i^{\,kl}{}_{,l} \\ \chi_i^{\,kl} &= \frac{\sqrt{-g}}{\varkappa}\,(g_{in,\,m} - g_{im,\,n})\, g^{km} g^{ln} \end{aligned}\right\} \tag{26}$$

which satisfies the condition B'. In fact it follows from (26) that $\Theta_4{}^4$ is a scalar density under purely spatial transformations which means that the Bauer difficulty does not arise with this complex. Further, it seemed that this complex made it possible to give an unambiguous meaning to the distribution of the energy throughout space-time. Similarly as the Einstein

expression is obtained from the Lagrangian ${}_E\mathfrak{L}$, the complex (26) follows by the method of infinitesimal coordinate transformations applied to the complete scalar curvature density $\mathfrak{R}$ [8]. However, a closer consideration showed that the complex (26) does not satisfy the condition *A*. This is connected with the fact that ϑ_i^k besides the $g_{ik,l}$ also contains the second-order derivatives $g_{ik,l,m}$. Furthermore, it is not sufficient to consider the energy only, i. e. besides the condition B' we have to require the full condition *B* to be satisfied and this is not the case either for the complex (26). In fact the applicability of the latter complex is even more restricted than the three former complexes.

In a recent paper, which will appear in the Report of the Conference on Elementary Particles held in Kyoto in September 1965, the question was discussed what properties of the energy-momentum complex T_i^k are necessary and sufficient in order that the integrated quantities P_i have all the properties *A* and *B*. The result was the following:

1.
$$\mathsf{T}_i^k = \mathfrak{T}_i^k + \tau_i^k \tag{27}$$

is an affine tensor density of weight one satisfying the relation

$$\mathsf{T}_i^k{}_{,k} = 0\,. \tag{28}$$

in every system of space-time coordinates.

2. τ_i^k *is a function of the gravitational field variables which, in a B.S.-system of coordinates* (6)–(8) *for a closed system, satisfies the relation*

$$r^3\,\tau_i^k \to 0 \quad \text{for} \quad r \to \infty\,. \tag{29}$$

3. The superpotential $\mathfrak{U}_i^{kl} = -\mathfrak{U}_i^{lk}$, *which expresses* T_i^k *in the form*

$$\mathsf{T}_i^k = \mathfrak{U}_i^{kl}{}_{,l} \tag{30}$$

is a true tensor density depending on the gravitational field variables and their first-order derivatives only.

The conditions *1* and *2* ensure that the integrated quantities

$$P_i = \frac{1}{c}\int\int\int \mathsf{T}_i^4\,dx^1\,dx^2\,dx^3 = -\frac{1}{c}\int\limits_{\Sigma} \mathsf{T}_i^k\,dS_k = -\frac{1}{2\,c}\int\limits_{\Phi} \mathfrak{U}_i^{kl}\,dS_{kl} \tag{31}$$

have the properties *A*. Further, with the assumption *3.* the quantity $dA_i = \mathfrak{U}_i^{kl}\,dS_{kl}$ is a true 4-vector on Φ. Therefore, since space-time for a closed

system can be treated as flat on and outside Φ the vectors dA_i can in a unique way be parallel-displaced to a common point P on or outside Φ so as to form a true 4-vector at the point P. Thus P_i is a true free 4-vector. It should be noted that, for a system with sufficiently small spatial extension say an atomic system, "spatial infinity" is practically reached already at very small distances, so that the "radius" r_1 of Φ in such cases may even be taken microscopically small.

None of the complexes mentioned so far satisfy the condition *3*. In fact it is evident that no complex containing the metric tensor only can satisfy this condition, for it is impossible to construct a true tensor density $\mathfrak{U}_i^{kl}$ out of g_{ik} and its first-order derivatives. This shows that one has to introduce a new element into the space-time manifold of general relativity and this can be done in different ways.

Following ideas of ROSEN [9], CORNISH [10] introduces a flat space metric $\overset{(o)}{g}_{ik}$ which asymptotically for large spatial distances agrees with g_{ik}. The mapping of the real space-time with metric g_{ik} on the imaginary flat space-time with the metric $\overset{(o)}{g}_{ik}$ may for instance be performed by assuming that $\overset{(o)}{g}_{ik}$ in a *definite* B.S.-system of coordinates (6)–(8) has components $\overset{(o)}{g}_{ik} = \eta_{ik}$ throughout space-time. In any other system of coordinates obtained by a non-linear transformation the components of $\overset{(o)}{g}_{ik}$ are then not constant although, of course, the curvature tensor corresponding to the metric $\overset{(o)}{g}_{ik}$ vanishes in all systems. Now, if the covariant derivative of a tensor A_{ik} corresponding to the metric $\overset{(o)}{g}_{ik}$ is denoted by $A_{ik/l}$ one may, starting from ${}_E\psi_i^{kl}$ in (11), define a superpotential

$$ {}_C\mathfrak{U}_i^{kl} = \frac{g_{in}}{2\varkappa\sqrt{-g}}\mathfrak{g}^{nklm}{}_{/m} \tag{32} $$

which obviously is a tensor density under arbitrary space-time transformations. Then, the complex

$$ {}_C\mathfrak{T}_i^{k} = {}_C\mathfrak{U}_i^{kl}{}_{,l} \tag{33} $$

satisfies all the conditions *1–3* and the corresponding integrated quantities ${}_CP_i$ will have all the properties *A* and *B*. In a similar way one could start from the superpotentials ${}_B\psi^{ikl}$ and ${}_L\psi^{ikl}$ and construct true tensor densities by means of the flat space metric $\overset{(o)}{g}_{ik}$. In this way one would arrive at two other expressions for the total four-mementum which are numerically identical with the one following from (32), (33).

However, this method of obtaining true tensor densities by introducing an unobservable metric does not seem to me quite satisfactory. Apart from the arbitrariness in the mapping of the real space-time on the imaginary flat space-time which perhaps is not so serious since it does not effect the values of the total four-momentum, the introduction of a metric $\overset{(o)}{g}_{ik}$ which to a large extent is independent of the observable metric g_{ik} makes the covariance obtained rather formal and deprives the general principle of relativity of its physical content. If one introduces unobservable quantities, they should rather be of a similar type as the potentials in electrodynamics from which the observable quantities, in our case the g_{ik}, can be calculated uniquely. As was shown in a series of recent papers [11–13] it is, in fact, possible to obtain a satisfactory expression for the energy-momentum complex, satisfying all requirements, if one describes the gravitational field by means of tetrads $h_i^{(a)}$ which uniquely determine the metric tensor by the equations

$$g_{ik} = h_i^{(a)} h_{(a)k} . \tag{34}$$

Here, the index (a), which is raised and lowered by means of the constant Minkowski matrix $\eta_{(ab)} = \eta^{(ab)}$ numbers the four tetrad vectors $h_i^{(a)}(x)$ at the arbitrary point (x). The use of tetrads to describe the gravitational field is by no means new. In fact, tetrads enter as an essential element in the generally relativistic formulation of the Dirac equations for Fermion fields.

If one eliminates g_{ik} in the expression for the scalar curvature density $\mathfrak{R}$, by means of (34), $\mathfrak{R}$ appears as the sum of a divergence part and a new Lagrangian $\mathfrak{L}$ which is a homogeneous quadratic expression in the first-order derivatives $h_{i,k}^{(a)}$ of the tetrad variables. The explicit expression is [11]

$$\mathfrak{L} = \sqrt{-g}\,[\gamma_{rst}\,\gamma^{tsr} - \Phi_r\,\Phi^r] \tag{35}$$

where γ_{ikl} and Φ_k are the following true tensor and vector, respectively,

$$\gamma_{ikl} = h_i^{(a)}\,h_{(a)k;l}, \quad \Phi_k = \gamma^i{}_{ki} \tag{36}$$

Here, the semicolon means covariant derivation corresponding to the real observable metric g_{ik}. Thus, in contrast to the Einstein Lagrangian $\mathfrak{L}$ in (3) the Lagrangian $\mathfrak{L}$ is a true scalar density. If we apply the method of arbitrary infinitesimal coordinate transformations to this Lagrangian $\mathfrak{L}$ we get an energy-momentum complex (27) satisfying the condition *1.* Further

$$\tau_i^{\ k} = \frac{1}{2\varkappa}\left[\frac{\partial \mathfrak{L}}{\partial h^{(a)}_{l,k}} h^{(a)}_{l,i} - \delta_i^{\ k}\mathfrak{L}\right] \tag{37^1}$$

is a homogeneous quadratic function of the $h^{(a)}_{i,k}$ which is essential for the validity of *2*. The corresponding superpotential is

$$\mathfrak{U}_i^{\ kl} = -\mathfrak{U}_i^{\ lk} = \frac{\sqrt{-g}}{\varkappa}[\gamma^{kl}{}_i - \delta_i^k \Phi^l + \delta_i^l \Phi^k] \tag{37}$$

which shows that also the condition *3*. is satisfied. Thus, the complex following from (37) by (30) satisfies all the conditions *1–3* and our problem seems to be solved.

However, the tetrad field $h_i^{(a)}$ is not determined uniquely by (34) for a given metric field g_{ik}. In fact, any Lorentz rotation of the tetrads,

$$\check{h}_i^{(a)} = \Omega^{(a)}{}_{(b)}(x)\, h_i^{(b)} \tag{38}$$

leaves the right-hand side of (34) unchanged. Here, the rotation coefficients $\Omega^{(a)}{}_{(b)}(x)$ may be any scalar functions of (x) which satisfy the orthogonality relations at each point, and the complex $\mathfrak{T}_i^{\ k}$ obtained from the superpotential (37) is *not* invariant under the "gauge" transformations (38), except if the rotation coefficients are constants throughout space-time. For an arbitrary physical system there are no physically convincing arguments for fixing the gauge so as to make $\mathfrak{T}_i^{\ k}(x)$ a unique function of the space-time coordinates, but in the case of a completely empty flat space there is no doubt about the choice of the tetrads. In order to avoid the forementioned Bauer difficulty it is necessary in that case to require that the tetrad field forms a system of mutually parallel tetrads throughout space-time, i. e. we must have everywhere

$$h^{(a)}_{i;k} = 0\,. \tag{39}$$

Further, for an insular system, where space-time is asymptotically flat we must require that the tetrad fields at least *asymptotically* form a system of parallel vectors. This suggests that the tetrads in a system of B.S.-coordinates must satisfy the same boundary conditions as the metric at large spatial distances. For a closed system this would mean relations analogous to (7), (8), i. e.

$$\left.\begin{aligned} h_{(a)i} &= \eta_{ai} + \overset{(1)}{h}_{ai} \\ \overset{(1)}{h}_{ai} &= O_1\,,\ \overset{(1)}{h}_{ai,k} = O_2 \end{aligned}\right\} \tag{40}$$

Then, as was shown in reference [12] for an even more general system emitting gravitational radiation, the total four-momentum P_i is invariant under all gauge transformations (38) which respect the boundary conditions. Besides, of course, P_i is invariant under all Lorentz rotations of the tetrads with constant rotation coefficients $\Omega^{(a)}{}_{(b)}$. On the other hand, the complex T_i^k itself is invariant only under the latter type of gauge transformations. Therefore, unless one can find a good physical argument for fixing the gauge throughout the system, it has no physical meaning to speak about the energy distribution inside the system. This would be in complete agreement with Einstein's own point of view. Actually nobody has so far been able to give a prescription for measuring the energy of the gravitational field in a small region, in contrast to the total energy for which such prescriptions are easily given [13].

In any system of B.S.-coordinates, the values of P_i obtained from the tetrad complex (37) are the same as those obtained from the metric complexes (11), (17), (21) of EINSTEIN, BERGMANN and LANDAU. Therefore, once the generally covariant expression of P_i has been established by way of the tetrad formalism, we may forget about the tetrads and perform the calculation of P_i in a system of coordinates in which the purely metric-dependent complexes are known to be valid. Then, the values of P_i in an arbitrary system of coordinates can be obtained by using the law of transformation of a 4-vector.

Anyhow, the tetrad formulation has given us more confidence in the application of the energy-momentum complexes which for many years by many physicists have been regarded as not quite respectable quantities. We are also encouraged to apply them to more general physical systems. Up till now we have only considered the case where space time far away from our system is flat. What about a system in a permanent external gravitational field, for instance a planet in the field of a heavy central body like the sun? If the external gravitational field is practically constant over a region of extension l large compared with the dimensions of the planet the preceding considerations are easily generalized. We have only to choose the tetrads of the external field so that the equation (39) is satisfied at each point of the time-track of the planet. This can always be obtained by a suitable transformation (38). In a system of Fermi-coordinates where the external metric has vanishing first-order derivatives at all points of the time-track of the planet we then get by integrating T_i^4 over a sphere enclosing the planet but with a radius smaller than l a four-momentum P_i^{pl} for the planet which is a 4-vector in the space-time with the external metric.

The energy-momentum complexes can also be used for calculating the total energy and momentum for systems which emit gravitational radiation in which case these quantities are not constant of course. Also the amount of energy and momentum emitted in different directions can be calculated. Such calculations were performed in reference [12]. As regards the total energy and its variation in time the results obtained are in agreement with and corroborate earlier results of BONDI [2] and SACHS [3].

The Niels Bohr Institute and
NORDITA Copenhagen

References

1. A. Einstein, Berl. Ber. 778 (1915); 1115 (1916). Ann. d. Phys. **49**, 769 (1916).
2. H. Bondi, M. G. Van der Burg and A. W. K. Metzner, Proc. Roy. Soc. A **269**, 21 (1962).
3. R. K. Sachs, Proc. Roy. Soc A **270**, 103 (1962).
4. Ph. von Freud, Am. Math. Journ. **40**, 417 (1939).
5. C. Møller, Ann. of Phys. **4**, 347 (1958).
6. P. G. Bergmann and R. Thomson, Phys. Rev. **89**, 400 (1953).
   L. Landau and E. Lifshitz, The Classical Theory of Fields, Addison-Wessley Press, Inc., Cambridge Mass. (1951).
7. H. Bauer, Phys. Zt. **19**, 163 (1918).
8. C. Møller, Mat. Fys. Medd. Dan. Vid. Selsk. **31**, no 14 (1959).
9. N. Rosen, Phys. Rev. **57**, 147 (1940); Ann. of Phys. **22**, 1 (1963).
10. F. H. J. Cornish, Proc. Roy. Soc. A **282**, 358 (1964); 372 (1964).
11. C. Møller, Mat. Fys. Skr. Dan. Vid. Selsk. **1**, no. 10 (1961).
12. C. Møller, Mat. Fys. Medd. Dan. Vid. Selsk. **34**, no. 3 (1964); Report Conference "Galilean Days" in Firenze 1964, Edition Barbèra Firenze (1965).
13. C. Møller, Nuclear Phys. **57**, 330 (1964); Report Conference Elementary Particles, Kyoto (1965).

Indleveret til Selskabet den 4. februar 1966.
Færdig fra trykkeriet den 22. juli 1966.

Matematisk-fysiske Meddelelser
udgivet af
Det Kongelige Danske Videnskabernes Selskab
Bind **35,** nr. 4

Mat. Fys. Medd. Dan. Vid. Selsk. **35,** no. 4 (1966)

STOPPING POWER OF ALUMINIUM FOR 5-12 MeV PROTONS AND DEUTERONS

BY

H. H. ANDERSEN, A. F. GARFINKEL,
C. C. HANKE, AND H. SØRENSEN

København 1966
Kommissionær: Munksgaard

CONTENTS

		Page
I.	Introduction	3
II.	Experimental Procedure	4
	A. Energy Losses	4
	B. Energy	8
	C. Foil Thickness	10
III.	Data Treatment	11
IV.	Outline of Theory	15
V.	Results and Discussion	16
Acknowledgment		18
Appendix A: Coulomb Scattering in the Foil		19
Appendix B: Corrections Due to x-Rays and δ-Rays		21
References		23

Synopsis

The stopping power of aluminium for 5–12 MeV protons and deuterons has been measured by a thermometric compensation technique working at liquid helium temperature. The experimental method is described and the standard deviation of the results is found to be 0.3 %. In order to obtain this accuracy one has to apply theoretical corrections for the influence of Coulomb scattering, x-rays and δ-rays. Other possible corrections are discussed, but are found to be negligible for this combination of projectiles, energies and target material. The results agree with published experimental results as well as with Bichsel's semiempirical tables.

PRINTED IN DENMARK
BIANCO LUNOS BOGTRYKKERI A/S

I. Introduction

The measurement of energy losses and ranges of protons and deuterons is an old topic in atomic physics, and a vast amount of data has been collected during the years. BICHSEL has recently tried to present a detailed comparison between experimental material and theory (BICHSEL 1961, 1963, 1964). It turned out, however, that the accuracy of the existing data was not high enough to yield unambigous results for the so-called "shell-corrections" and there is thus a need for more accurate data. Until now methods utilizing nuclear instrumentation have been used and the best results obtained was 0.5 % for range (BICHSEL et al. 1957, BICHSEL 1958) and 1–2 % for stopping power measurements (NIELSEN 1961). To obtain more accurate results it is either necessary to build expensive energy analysing systems or to use new principles. The latter has, e.g., been tried by KALIL et al. (1959) and ZIEMER et al. (1959) who measured energy losses in thin foils directly by calorimetric methods. The accuracies obtained could compete with those of conventional techniques only in the special case of very low energy electrons. The idea to make a direct measurement of the energy loss has also been used in the present investigation. Our method utilizes a thermometric compensation technique working at liquid helium temperature, and avoids the conflict between target size and resolution of the analysing system. It is thus possible to measure stopping powers of thin metal foils accurately in spite of unavoidable inhomogenities in foil thicknesses.

The measurements were done at the tandem van de Graff laboratory of the Niels Bohr Institute, the University of Copenhagen. The projectiles were 5–12 MeV protons and deuterons. As a target aluminium was first chosen since this material has often been used as a sort of standard for relative stopping power measurements.

II. Experimental Procedure

A. Energy Losses

A determination of stopping power from a measurement on a thin foil requires a determination of three different quantities: the energy of the incoming particle, the energy loss in the foil, and the thickness of the foil. Since the measurement of energy and foil thickness only involves standard techniques we will first discuss the measurement of the energy loss.

The principle is shown in fig. 1. The target foil and a block thicker than the range of the projectiles are connected to a heat sink through thermal resistances W_F and W_B. The beam passes through the foil and is stopped in the block. It causes a heating of foil and block giving temperature rises measured with the thermometers R_F and R_B. The beam is then switched off, and electrical powers P_F and P_B are fed to heaters thermally connected to foil and block until the same temperature rises are obtained. A particle having energy E_0 immediately in front of the foil will suffer an energy loss ΔE in the foil given by the relation

$$\Delta E = E_0 \frac{P_F}{P_F + P_B}. \tag{2.1}$$

The requirement for obtaining a good determination of the above power ratio is that the conditions corresponding to heating by the beam are well reproduced by the electrical heaters. This is fulfilled if both systems, foil and block, are isolated to the extent that they can only interact thermally with the heat sink, and that these interactions only take place through their thermal resistances. Especially should there be no mutual thermal interaction between block and foil.

The actual experiment is performed with a liquid helium bath as heat sink. The system is placed in vacuum and surrounded by a thermal shield at liquid helium temperature. The low temperature guaranties that interactions by thermal radiation will be very small, and it is also easy to obtain such a good vacuum that heat transfer through the residual gas is negligible. Furthermore, the absolute sensitivity of thermometers is greater at lower temperatures so that a smaller temperature rise is necessary to obtain a given accuracy. This factor, small temperature rises, also reduces the radiation interactions. Finally, in order to make the system able to respond quickly to changes in beam current or electrical power, the thermal time constants of the two systems should be small. This is most easily obtained

at low temperatures, where heat capacities are small and thermal conductivities high.

If the foil itself has poor heat conductivity, the center of the spot hit by the beam may become very hot, and thermal radiation will be important. Both to avoid this, and to keep the thermal time constants low, it is necessary to work with targets having good heat conductivity at liquid helium temper-

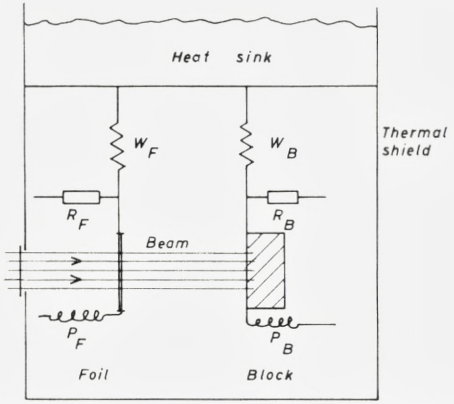

Figure 1. Diagram of stopping power measuring system. W_F and W_B are thermal resistances, R_F and R_B thermometers, and P_F and P_B electrical heaters.

atures. This means that the method is only applicable to pure metals in its present form.

The measurements are made using a commercial liquid helium irradiation cryostat (Hofmann Inc.). The measuring equipment is fastened to the bottom of the cryostat as shown in fig. 2. The helium cryostat is cut open, and the radiation shields at liquid nitrogen and liquid helium temperature (77°K and 4.2°K) are not shown. Beneath the cryostat the target foil is seen. It is soldered to a frame of well annealed very pure copper, and the heater is wound around the frame near the soldering point. The frame is mechanically fastened to the cryostat by insulating pins, and the heat path is provided by a copper wire. The length and thickness of the copper wire, and thus the thermal resistance, may easily be varied. The thermometer is an ordinary 0.1 Watt carbon resistor. The resistance of the thermometer is 68 Ω at room temperature, 290 Ω at 10°K and 850 Ω at 4.2°K, giving enormous sensitivity in the lower temperature range. The thermometer is fastened near the end of the thermal resistance.

The stopping block is shown behind the foil. It is an aluminium case

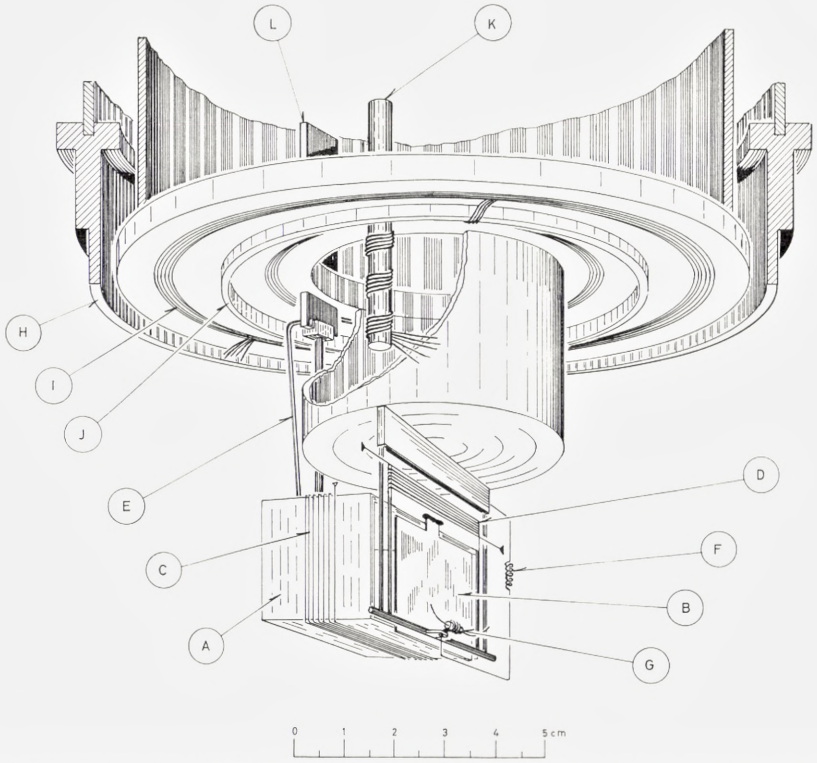

Figure 2. The set-up for stopping power measurements, showing the lower part of the helium Dewar (cut open), the measuring equipment, and the nitrogen temperature shield. A. Stopping block. B. Target foil. C. and D. Heaters. E. and F. Heat paths with resistances. G. Foil thermometer. H. Nitrogen temperature shield. I. Electrical connections laquered to the bottom of the helium Dewar. J. Copper edge to which helium temperature radiation shield is fastened. K. and L. Thermal connections to helium bath. Note that the electrical connections from the bottom of the Dewar to block and foil are not shown.

open in the side facing the foil. The opposite side, where the beam is stopped, is made from a 0.3 mm gold plate, this particular metal being chosen to reduce the influence of nuclear reactions. This shape has been chosen partly to ensure that particles have to be Coulomb scattered in the foil by more than $\pi/2$ to avoid hitting the block, and partly to ensure that most x-rays emitted from the gold surface are reabsorbed by the block and not by the foil. Heater, thermal resistance, and thermometer are placed in ways similar to those on the foil. The electrical connections to both heaters are made by superconducting Nb_3Zr wire, which has small thermal conductivity. Further details of the construction are given by ANDERSEN (1965) where the characteristics of the system are also discussed.

The usable temperature range is determined by the thermometers. Their sensivity drops off nearly exponentially with increasing temperature, which means that the temperature increase should be kept reasonably low. We also need a fairly big temperature increase to be able to measure it accurately. These competing factors give the sensitivity of the system a broad maximum between 6 and 10°K. The temperature rise of each system can then be varied a factor of three without affecting the accuracy, meaning that power ratio variations within a factor of nine are permissible.

It has, until now, been assumed that the intensity of the accelerator beam is stable, and that this defines one temperature rise for each of the systems. This is, unfortunately, not the case. Two temperature intervals rather than two temperatures are thus defined. The calibration with the electrical heaters should cover the same temperature intervals, and three calibration points are made for each system. Large variation in beam current will reduce the accuracy of the measurement and calibration, and variations larger than 10 % are normally not accepted.

The temperatures of block and foil should follow the beam current variations reasonably well, and small time constants are thus very important for the method. The time constants are 3–7 seconds for the foil and 0.5–1.5 seconds for the block, increasing with increasing temperature. This is satisfactory, although a smaller time constant for the foil would be advantageous.

The fluctuating temperatures are measured continuously and simultaneously. This is done with Wheatstone bridges, one for each system, the bridges being set at suitable values in order to give signals varying around zero. The signals are amplified and fed into recorders. It is then possible to select corresponding points on the two recorder curves. The method used for the evaluation of energy losses from recorder readings will be described later.

The determination of the energy loss has been tested in different ways. Two of these tests will be described here. They are both concerned with the problem, whether we really measure all the heat dissipated in the foil and the block. (The problem whether all the dissipated energy appears as heat or not is treated later). The compensation technique may be erroneous either if there are radiation losses or if the heat dissipated by the beam does not choose the same heat paths to reach the reservoir as that supplied by the heaters. If either of these is the case, measurements with different beam intensities will yield different results. This has been tested with 6 MeV protons in aluminium. The result is shown in fig. 3. There is no trend in the results – all agree with each other within 0.1 %.

To check the internal consistency of the calibrations we have done

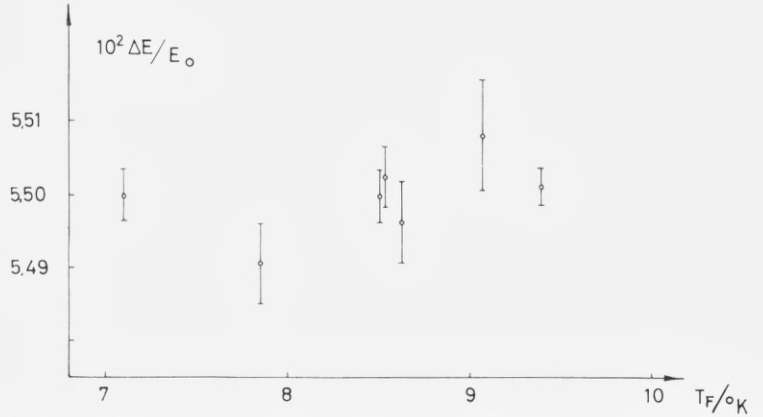

Figure 3. Relative energy loss for 6 MeV protons in an aluminium foil. The beam intensity is varied by a factor of two, and no significant variation with intensity is observed.

measurements with superposed power on the block heater. This test has been done twice with aluminium and twice with copper. When the known power is subtracted afterwards it is possible to evaluate the stopping power. The added power is chosen to have the same magnitude as that provided by the beam. These results, compared with others obtained without superposed power, are given in table 1. Again no trend is seen, and we conclude that we measure the power ratio to within $0.1\,^0/_0$.

TABLE 1. The influence of superposing the beam with power on the block heater.

Target	Proton energy (MeV)	Relative energy loss ($^0/_0$)	
		without overlapping power	with overlapping power
Al	5.001	7.635 ± 0.007	7.648 ± 0.006
Al	5.504	6.421 ± 0.004	6.422 ± 0.003
Cu	6.008	12.435 ± 0.010	12.413 ± 0.011
Cu	6.512	10.763 ± 0.008	10.780 ± 0.008

B. Energy

In the measurements ΔE is obtained from E_0 through (2.1). Stopping power formulas yield roughly $\Delta E \propto 1/E$ (4.2). Thus it is possible and quite convenient in the following graphs and tables of ΔE (or dE/dx) versus

energy to assume the energy to be a precise number and to attribute to ΔE twice the relative uncertainty in the actual measured value of E_0. An uncertainty of $0.1\,\%$ in the energy determination will then give $0.2\,\%$ for our stopping power.

The energy E_0 is determined from the field in a 90° deflection magnet. The calibration tables were prepared for a magnet similar in design to the one being used here, (p, n) threshold reactions being utilized. It was assumed that the energy was known within an accuracy of 10 keV through the whole energy range. This yields a relative accuracy of $0.2\,\%$ at 5 MeV giving an uncertainty in the stopping power of $0.4\,\%$ at that energy. This was considered unsatisfactory compared with the other uncertainties involved in the method, and the following calibration programme was therefore carried out. The particles were elastically back-scattered from a thin, heavy-mass target into a heavy-particle spectrograph. The spectrograph was calibrated using α-particles of known energy. The reproducibility of measurements made with different magnetic fields in the spectrograph indicates that it is possible to bring the uncertainty in the energy calibration down by a factor of two, to $0.1\,\%$, by this procedure. As will be seen below this is still our main source of uncertainty, and improved calibration methods are under investigation.

The energy defined by the analysing magnet is, however, not the energy of the particles hitting the foil. Six meters in front of the cryostat are placed a number of 150 $\mu g/cm^2$ gold foils, which may be inserted into the beam. The particles undergo multiple scattering in these foils, and the beam is thus spread out, ensuring a homogeneous irradiation of the target foil. Furthermore, the particles pass through 150 $\mu g/cm^2$ gold windows in the nitrogen and helium temperature radiation shields. The energy loss suffered in all foils will never exceeded $0.5\,\%$. The resulting energy degradation may be calculated accurately enough not to affect our accuracy.

Particles scattered from collimator edges will have a lower energy than the rest of the beam and will cause the measured stopping powers to be too high. This possibility was tested by varying the number of multiple scattering foils. Inserting more foils will cause a greater relative number of the particles to hit collimator edges and thus give an apparent rise in stopping power greater than the trivial one caused by the change in mean energy. This anomalous rise had a mean value of $0.05\,\%$ in nine experiments with 10–12 MeV deuterons. In each test a measurement was done with 1, 3 and 4 scattering foils, where 3 or 4 are usually used. It was concluded that this is not an appreciable error source and that the total uncertainty in the energy is the calibration error being $0.1\,\%$.

C. Foil Thickness

When we know the energy loss, the stopping power is given by

$$S(E') = \left(\frac{dE}{dx}\right)_{E=E'} = -\frac{\Delta E}{t} \tag{2.2}$$

where $E'(< E_0)$ is defined in part III, and t is the foil thickness. The thickness is determined in the following way. A piece, 6×13 mm, is cut from the foil with a very accurately machined punching tool. Care is taken to ensure that it is the same part of the foil as that irradiated during the energy loss measurements. The area of this piece, and of the hole left in the foil, is measured in a Zeiss Abbe comparator. The mean value is taken as the area, and half the difference as the uncertainty of the area measurement. The weight of the piece is found with a Cahn electrobalance. The total error in the weight per area determination is estimated to be 0.1–0.15 %. In this way we have determined the mean thickness of the same part of the foil as that over which the mean energy loss was measured. For a completely uniform irradiation of this area thickness inhomogeneities of the foil will have very small influence, and one of the main errors in stopping power experiments is thus eliminated. In practice, the number of scattering foils is chosen so that the intensity is not more than 10 % lower at the edges than at the center. Errors due to inhomogeneities will, nevertheless, at least be reduced by a factor of twenty and are insignificant.

The foil is aligned optically to be perpendicular to the beam direction within 2 degrees. We have checked that the foil does not turn or bend while being cooled. Furthermore, the foils contract during cooling, the change in weight/area being twice the linear thermal expansion between 4.2°K and room temperature. The correction is less than 1 % for most metals. Condensation on the target during the measurement can change the apparent thickness in accelerator experiments, especially with cold targets. In our experiment, condensation is not a serious problem because there exists no direct path from the accelerator to the target, and an eventual condensation will take place on the radiation shields and gold windows rather than on the target. Nevertheless, there is sometimes found a small drift which may be detected over long measuring periods. The drift is attributed to condensation of hydrogen or deuterium originating from the ion source. These particles will not condense on the nitrogen shield and only partially on the helium one. The maximum drift found corresponds to about 10 μg aluminium/cm^2 in 12 hours or about 0.2 μg/cm^2/hour of hydrogen.

III. Data Treatment

As mentioned in section II. A, the raw data consist of the power calibrations and the recorder strips showing the off-balance signals from the Wheatstone bridges. The recordings are scanned by eye to obtain corresponding points for the foil and the block. Usually there are no difficulties, but care must be taken to ensure that the systems are in thermal equilibrium at the chosen points. From these pairs of signals corresponding pairs (R_F, R_B) for the resistance of the thermometers are found, and using the power calibrations the sets of corresponding powers (P_F, P_B) are calculated. Equation (2.1) is utilized to calculate the energy loss for each point evaluated. For each energy 15–20 points are used, and the mean value is found together with the standard deviation. There are, apart from this, some systematic errors involved, since any errors in the calibrations are smoothed out and do not show up fully in the fluctuations. Usually the total standard error is below 0.1 % of the mean value (see fig. 3). The entire procedure is very simple, but the numerical work involved is great and has therefore been coded for the GIER computer at Risø.

Equation (2.2) gives the stopping power $S(E')$, which we attribute to the energy E'. To first order in $\Delta E/E$ we have

$$E' = E_0 - \frac{\Delta E}{2}. \tag{3.1}$$

An expansion of $S(E')$ in powers of $\Delta E/E$ gives a quadratic correction term

$$\frac{S_2}{S} = \frac{\Delta E^2}{12}\left(\frac{S'^2}{S^2} - \frac{S''}{S}\right) \tag{3.2}$$

where $S = S(E')$, $S' = \frac{dS}{dE}$, and $S'' = \frac{d^2S}{dE^2}$ (both at E'). Using the nonrelativistic form of the Bethe formula (4.1) and neglecting shell corrections we find

$$\frac{S_2}{S} = \frac{1}{12}\left(\frac{\Delta E}{E}\right)^2\left(\frac{2 - \ln\frac{2mv^2}{I}}{2\left(\ln\frac{2mv^2}{I}\right)^2}\right) \tag{3.3}$$

where m is the electron mass, v the velocity of the projectile and I the mean ionization potential for the target material (see part IV). As the relative

energy loss never exceeds 20 % this correction is always smaller than 0.05 % and is omitted. These results are not identical with those given by ANDERSEN (1965) (p. 35), the latter being wrong due to a calculation error.

A further assumption entering (2.2) is that the trajectory of the projectile through the target is a straight line perpendicular to the foil. This is not the case. Every particle will be Coulomb-scattered through small angles a number of times (multiple scattering). This broadens the angular distribution of the beam as it penetrates into the foil, and the mean distance the particles travel through the foil is thus slightly greater than the foil thickness. Also a small number of particles will be Coulomb-scattered through wide angles and lose nearly all their energy in the foil. Corrections due to these effects are of minor importance for aluminium except for the very thickest targets used, but the corrections are appreciable for heavy targets. The calculation of the corrections is outlined in appendix A and more detailed calculations have been presented by ANDERSEN (1965).

The characteristic angle which separates the two cases is

$$\Theta_1^2 = Nt\frac{\pi e^4 Z^2}{E^2} \tag{3.4}$$

where N is the concentration of target atoms, e is the electronic charge, and Z the atomic number of the target. The relative correction due to multiple scattering is then (see e.g. BETHE and ASHKIN (1953))

$$\frac{\delta_{\text{m.s.}}}{\Delta E} \simeq \Theta_1^2 \cdot f\left(\frac{Z^{2/3} \cdot A}{t}\right). \tag{3.5}$$

A is the atomic mass of the target and f is a slowly varying function nearly equal to two. The correction is of no importance in aluminium, but will, as an example, be 0.18 % for gold with $t = 20$ mg/cm² and $E' = 5$ MeV.

The single scattering term is of more importance. Again, using Θ_1 (3.4) this contribution is

$$\frac{\delta_{\text{s.s.}}}{\Delta E} = \frac{\Theta_1^2}{4}\left[2 + \ln\frac{8}{\Theta_1^2} + 2\ln\frac{E}{\Delta E}\right]. \tag{3.6}$$

This term will exceed 0.1 % for the thickest Al target used (22 mg/cm²). For the above-mentioned case in gold it will be about 0.3 %. The Coulomb corrections are roughly proportional to t, Z and E^{-2}. If the method is extended to other energy regions than those used here, and if one wants the

same relative energy loss as in the present measurements, the thickness must be changed proportionally to E^2. The importance of Coulomb corrections will thus be roughly the same in all energy regions, but for a fixed foil it will be most important for the lowest energy used.

Also the possible influence of the crystal lattice on the results has to be considered. A number of authors have recently found that the stopping power for high-energy particles is lowered appreciably when they move in open directions of the crystal lattice. (Dearnaley, 1964; Dearnaley and Sattler, 1964, 1965; Erginsoy et al., 1964, and Datz et al., 1965). It may, however, be shown theoretically that this will not influence the stopping power of a polycrystalline sample (Lindhard, 1965). There is still the possibility that our samples, which are cut from rolled foils, have a strong crystalline texture, and that some preferred low-indexed crystalline direction accidentally coincide with the beam direction. Whether this is the case or not may be tested experimentally. The concept involved is the following: If a particle hits the foil in a direction which coincides with a low-indexed direction within a certain critical angle, it will be trapped in regions with lower stopping power than the mean value for the material. These critical angles are, in heavy targets, of the order of 0.1° for the energies involved here. In aluminium they will be appreciably smaller (see Lindhard 1964, 1965). They depend only on the energy and charge of the particle, not on its mass, i.e. they are the same for protons and deuterons having the same energy. The critical angles decrease with increasing energy. The foil is not flat within better than 1°, and the total area of the foil perpendicular to the beam direction within the critical angle will thus also decrease with increasing energy. This decrease goes as E^{-1} for trapping along low-indexed directions (the so-called string effect) and as $E^{-1/2}$ for trapping between planes. As is shown below (5.1), protons and deuterons with the same velocity have the same stopping power in an amorphous material, but the deuterons have, in this case, twice the energy of the protons, and the possible influence of a crystal lattice will thus be smaller for the deuterons. We may now compare the measured stopping powers of protons and deuterons with the same velocity. If the deuteron stopping powers are not higher, the crystal lattice has no measurable influence.

Apart from the corrections discussed previously, which have to be applied for all stopping power experiments, there also occur some corrections which are rather specific for the measuring technique used here. We have, until now, assumed that all energy dissipated by the particles in the foil and the block will appear as heat. There is a number of processes

which can occur so that this assumption is not entirely true. The corrections due to this have been discussed in detail by ANDERSEN (1965). We will here summarize the results. The important steps in the calculation of the significant corrections are given in Appendix B.

A certain part of the energy given to the foil may escape through x-rays. A number of processes are competing. One must first calculate the fraction of the energy loss stored in vacancies in inner electron shells. Some of these vacancies are filled in such a way that the liberated energy appears as an Auger-electron and not as an x-ray quantum. The so-called fluorescence yield is the relative number of vacancies in a given shell filled under emission of x-rays. This yield is very low for low Z and for outer shells. Furthermore some of the x-rays will be reabsorbed in the foil. The product of these factors determines the correction. It is insignificant for light elements, but the corrections may be as high as $0.4\,\%$ for thin targets of heavy elements. The evaluation is summarized in Appendix B.

Furthermore, nuclear reactions in the foil and the block will give errors. They are insignificant in our energy range. If we assume the cross-sections to stay roughly constant when the projectile energy is high enough to penetrate the Coulomb barrier, the contribution from these processes will be proportional to the foil thickness and to the particle range in the block. As the range is approximately proportional to E^2, the contribution from nuclear reactions in the block will also increase in proportion to E^2. The errors introduced may be calculated for some elements, but will in all cases be a significant and not too well known correction at high energies.

The usual secondary electron spectrum will have a vanishing influence, but some electrons might get high energies (δ-rays) and introduce an error. It is a surface effect and nearly proportional to E'. (For details see Appendix B). When the proton energy varies from 5 to 12 MeV, the error in the measured energy loss will vary from 500 to 1000 eV. For thin foils and high energies the relative correction will be as high as $0.5\,\%$. The variation with Z is small. Assuming the usual variation of foil thickness for other energy ranges, the importance will decrease as we go to higher energy ranges.

Finally, we have considered the problems of sputtering of foil atoms and of energy stored in point defects in the block. Both are related to the elastic energy transfer to target atoms and are negligible. The effect might be of importance at lower energies.

IV. Outline of Theory

We will give a compressed summary of the theory for stopping power in the energy region of interest here. We are primarily interested in using the theory to find a convenient way of presenting our measured data. An up-to-date review of the present state of the theory has been given by FANO (1963). The theory originating from BETHE yields

$$-\frac{dE}{dx} = \frac{4\pi e^4 z^2}{mc^2\beta^2}\frac{N_0 Z}{A}\left[\ln\left(\frac{2mc^2\beta^2}{1-\beta^2}\right) - \beta^2 - \ln I - \frac{\Sigma C_i}{Z}\right] \tag{4.1}$$

where x is the foil thickness measured in grams/cm^2, N_0 is Avogadro's number, and A is the atomic weight of stopping material in grams. z is the charge of the projectile with velocity $v = \beta c$, Z is the atomic number of the target, and I its mean ionization potential. C_i represents the so-called shell corrections. They are deviations from the simple theory and have been evaluated for the K- and the L-shell by WALSKE (1952 and 1956). The main theoretical interest lies in the calculation of the inner shell corrections from the measurements, their comparison to the WALSKE theory, and the possible experimental evaluation of outer shell corrections for which no theoretical predictions exist.

We see from (4.1) that for a given combination of projectile and target we may write

$$-\frac{dE}{dx} = \frac{a}{E}\ln\frac{E}{b} \tag{4.2}$$

where a and b are energy-independent constants and shell corrections and relativistic effects are neglected. We see then that variation of the energy by a factor of two will also cause dE/dx to vary nearly by the same factor. It is thus not possible to represent our dE/dx-values for the whole energy range in a plot, where we at the same time may see the fluctuations. The most obvious thing to do would be to plot $E \cdot dE/dx$ rather than dE/dx, but this is still not sufficient. We have therefore chosen to use the reduced variable given by BICHSEL (1964). If we define

$$K(\beta) = 4\pi e^4 N_0/mc^2\beta^2 \tag{4.3}$$

and

$$f(\beta) = \ln(2mc^2\beta^2/(1-\beta^2)) - \beta^2 \tag{4.4}$$

we will compute

$$X = f(\beta) + \frac{A}{ZK(\beta)} \left(\frac{dE}{dx} \right)_{\text{exp}} . \tag{4.5}$$

This is in fact an experimental determination of $\ln I + \Sigma C_i/Z$ in eq. (4.1). Theoretically, the shell corrections are found to be positive in our energy range. At very high energies they are zero, and X will then be energy independent and equal to $\ln I$.

V. Results and Discussion

Results will be presented here for measurements with 5–12 MeV protons and deuterons in aluminium. The samples were cut from rolled foils supplied by the United Mineral and Chemical Co., Inc. The purity of the samples as stated by this company was 99.999 %. No corrections for impurities were thus necessary. Measurements have been made on samples with approximate thicknesses of 6, 11, and 22 mg/cm². The thinnest sample is thick enough that no correction is necessary for the unavoidable oxide layer on the aluminium surfaces. The relative energy loss varied from 2 % at high energies in thin foils to 16 % at low energies in thick foils.

The results are presented in fig. 4 in the X-variable defined by eq. (4.5). Note that dE/dx is negative. Thus higher values of X mean numerically lower values for the stopping power. At both ends of the figure is indicated the change, a 1 % change in dE/dx would give in X at that energy. Both proton and deuteron measurements are shown in the reduced energy scale $E \cdot M_p/M$, where M is the mass of the projectile and M_p the proton mass. The deuteron values are therefore indicated at the energy which a proton would have if its velocity were equal to that of the deuteron. The figure contains points measured over a long period of time. During this time significant changes occurred in the energy calibration of the accelerator, and the scatter in the points will therefore reflect the total uncertainty for each point including the calibration uncertainty in E_0. A smooth curve has been fitted by eye through the measured points. The values defined by this curve are listed in table 2. Combination of the errors listed in the preceeding paragraphs yields a total standard deviation in the tabulated values of 0.3 %. As judged from fig. 4 this does not seem to be too optimistic.

It is seen that the proton and deuteron points do not fall together as theory predicts that they should (part IV); we must, however, remember that the proton and the deuteron energy calibrations are made independently

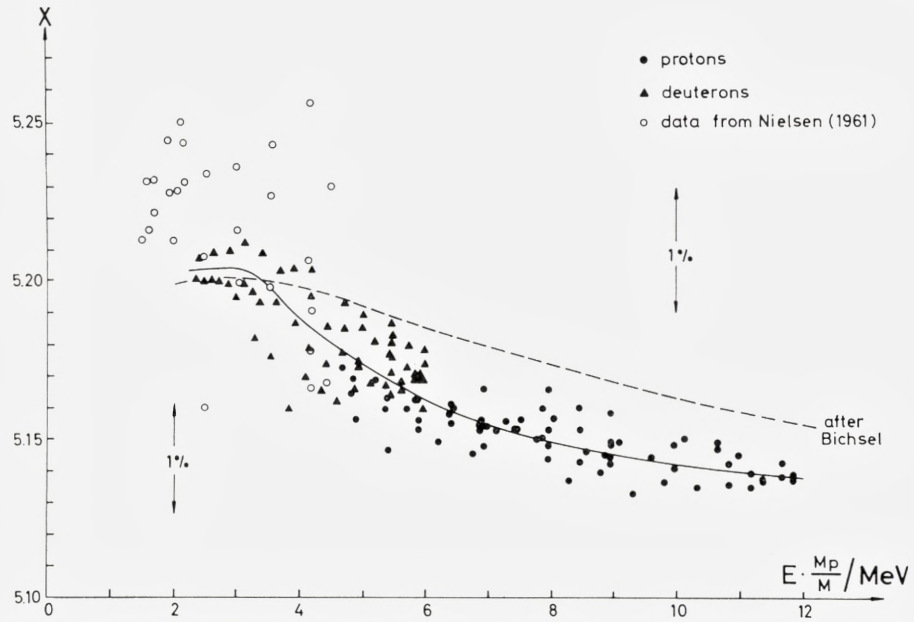

Figure 4. Measured stopping powers for aluminium in reduced variables defined by eq. (4.5). The height of the arrows indicates the change in X caused by a 1 % change in dE/dx. Open circles are measurements by Nielsen (1961) and the broken line tabulated values by Bichsel (1963 b). The full line is fitted to our experimental points by eye. $\frac{M_p}{M}$ = ratio between proton mass and mass of incident particle.

of each other (part II. B), and, in comparing, the combined uncertainty of the two calibrations has to be taken into account. The deviation is found not to be significant. It is, furthermore, certainly not due to crystallographic effects (part III) as this would introduce errors of the opposite sign.

There does not exist much other experimental information in this energy range with which it is possible to compare our results. The only relevant measurements are those of Nielsen (1961). Her points are shown as open circles. The results agree within her accuracy. It is also possible to compare our results with the tabulated values given by Bichsel (1963b). They are obtained by fitting the total amount of available data for aluminium, up to that time, to the expression (4.1) – including shell corrections. The fit is claimed to be good to 1 %, and the agreement is seen to be better than that. A very extensive table has also recently been published by Barkas and Berger (1964). The overall agreement with these tables is only good to about 2 %. Within the energies contained in fig. 4, the X-values computed

TABLE 2. Smoothed values of measured stopping powers for protons in aluminium obtained from the full line in fig. 4.
Experimental standard error ± 0.3 %

Energy MeV	$-dE/dx$ keV/mg cm^{-2}	Energy MeV	$-dE/dx$ keV/mg cm^{-2}
2.25	101.92	5.75	51.93
2.50	94.68	6.00	50.31
2.75	88.52	6.50	47.38
3.00	83.19	7.00	44.81
3.25	78.56	7.50	42.52
3.50	74.51	8.00	40.47
3.75	70.94	8.50	38.64
4.00	67.76	9.00	36.97
4.25	64.85	9.50	35.46
4.50	62.21	10.00	34.08
4.75	59.80	10.50	32.82
5.00	57.59	11.00	31.66
5.25	55.56	11.50	30.58
5.50	53.68	12.00	29.58

from their tables show such large fluctuations that they could not be contained in the figure.

We conclude that the accuracy of the tabulated data is within 0.3 %, and that the data agree with existing stopping power and range results within their estimated errors.

Acknowledgment

Special thanks are due to the Niels Bohr Institute, the University of Copenhagen, for letting us use a beam tube at the tandem accelerator. B. ELBEK and M. OLESEN from this institution gave us much advice concerning problems connected with the use of the accelerator. B. BORDRUP, G. DALSGAARD and A. NORDSKOV NIELSEN built the mechanical and electrical equipment with great care. P. VAJDA joined the group during the measurements and has taken part in the evaluation of some of the data presented here. Great stimulation came from the continuous interest of professors O. KOFOED-HANSEN and J. LINDHARD.

Appendix A

Coulomb Scattering in the Foil

The projectiles will have a longer path than the foil thickness because they are Coulomb-scattered by the target atoms. All particles undergo many small-angle scatterings while passing through the foil causing the beam to be gradually spread out, and a few particles are scattered through large angles thus travelling very much longer paths in the foil.

To be able to treat these two cases separately, we define an angle Θ_1 given by

$$Nt \int_{\Theta_1}^{\pi} \sigma(\Theta) d\Theta = 1 \tag{A 1}$$

where $\sigma(\Theta)$ is the differential Rutherford scattering cross section, i.e. Θ_1 is defined in such a way that particles passing through the foil will, in the mean, be scattered once through an angle Θ_1 or greater. We obtain

$$\Theta_1^2 = Nt \frac{\pi e^4 Z^2}{E^2} \tag{A 2}$$

by assuming $\Theta_1 \ll 1$ and substituting Z for $Z+1$. Scattering through angles smaller than Θ_1 is treated using multiple scattering theory and scattering through angles greater than Θ_1 by use of the Rutherford cross section.

If the beam has a mean square angular deviation Θ^2 from the normal, the relative correction to the energy loss will be

$$\frac{\delta(\Delta E)}{\Delta E} = \frac{\langle \Theta^2 \rangle}{2} \qquad \Theta^2 \ll 1. \tag{A 3}$$

Bethe and Ashkin (1953, p. 285) calculate Θ^2 to be

$$\langle \Theta \rangle^2 = \Theta_1^2 \ln \frac{\Theta_1^2}{\Theta_{\min}^2} \tag{A 4}$$

where $\Theta_{\min}$ is a minimum scattering angle given by the screening of the Coulomb interaction. This yields

$$\frac{\delta(\Delta E)_{\text{m.s.}}}{\Delta E} \simeq \frac{\langle \Theta^2 \rangle}{4} = \Theta_1^2 \cdot f\left(\frac{Z^{2/3} A}{t}\right) \tag{A 5}$$

provided $\langle\Theta^2\rangle \gg \Theta_1^2 \gg \Theta_{\min}^2$. f varies from 1.8 to 2.2 for all materials and thicknesses of interest to us.

To calculate the single-scattering correction the following model is assumed. The particles penetrate the foil with a constant energy E_0 to the point, where they are scattered. From this point they are assumed to lose energy at a rate given by the relation $R = c_2 \cdot E^2$ where R is the range of a particle with energy E and c_2 is an energy-independent constant, depending on projectile and target. This is a fairly good approximation corresponding to $dE/dx \propto 1/E$. The constant c_2 is eliminated from the final result.

We first calculate the energy of particles scattered in a thin layer dx situated the distance x beneath the back of the foil, $E'(E_0, \Theta, x)$. The total energy of all particles scattered through angles greater than Θ_1 leaving the foil will then be

$$E'(E_0, x)dx = dx \int_{\Theta_1}^{\pi} E'(E_0, \Theta, x)\sigma(\Theta)d\Theta. \tag{A 6}$$

If the particles were not scattered, they would leave the foil with energy $E(E_0, x)$, and the correction is

$$\delta_{\text{s.s.}}(E_0) = \int_0^t [E(E_0,x) - E'(E_0,x)]dx. \tag{A 7}$$

Performing the integration (A 6) we find

$$\left.\begin{aligned} E'_A(E_0,x) = &- c_1\sqrt{E_0^2 - x/c_2}\left[-\frac{4}{\Theta_1^2} + \frac{5}{3} + \frac{x/c_2}{E_0^2 - x/c_2}\right] - \\ &- \frac{c_1 x}{c_2\sqrt{E_0^2 - x/c_2}} \ln\left[\frac{8}{\Theta_1^2}\frac{c_2}{x}\left(E_0^2 - \frac{x}{c_2}\right)\right] \end{aligned}\right\} \tag{A 8}$$

and

$$\left.\begin{aligned} E'_C(E_0,x) = &\; c_1\sqrt{E_0^2 + \frac{x-t}{c_2}} + \\ &+ \frac{c_1(x-t)}{c_2\sqrt{E_0^2 + \frac{x-t}{c_2}}} \ln \frac{E_0^2 + \sqrt{E_0^4 - \left(\frac{x-t}{c_2}\right)^2}}{\frac{t-x}{c_2}} \end{aligned}\right\} \tag{A 9}$$

E_A refers to particles leaving the back of the foil, and E_C to those leaving the front. c_1 is the angularly independent factor in the Rutherford cross section. The integration (A 7) is carried through to second order in $\Delta E/E_0$. The relative single scattering correction is then found to be

$$\frac{\delta_{\text{s.s.}}}{\Delta E} = \frac{\Theta_1^2}{4}\left[2 + \ln\frac{8}{\Theta_1^2} + 2\ln\frac{E}{\Delta E}\right]. \tag{A 10}$$

Further details are given by ANDERSEN (1965).

Appendix B

Corrections Due to *x*-Rays and δ-Rays

Neglecting relativistic effects, (4.1) is written in the form

$$-\frac{dE}{dx} = \frac{4\pi e^4 Z^2}{mv^2}\frac{N_0}{A}\Sigma B_i \tag{B 1}$$

where

$$B_i = Z_i \ln\left(\frac{2mv^2}{I_i}\right). \tag{B 2}$$

The contributions have been split up for the different shells. Z_i is the number of electrons in the i^{th} shell, and I_i the ionization potential for this shell. Where necessary, the corrections due to WALSKE (1952, 1956) to (B 2) have been used. The fraction of the total energy loss due to the i^{th} shell is then

$$R_i = \frac{B_i}{\Sigma B_i}. \tag{B 3}$$

Some of this energy goes into kinetic energy of the expelled electron. If the fraction not doing so is f_i, the total energy stored in vacancies in the i^{th} shell will be $R_i \cdot f_i$. Due to the Auger effect only a fraction ω_i of this will appear as x-rays, and the total correction due to x-rays from the i^{th} shell and from a very thin foil is then

$$\frac{\delta_i}{\Delta E} = \omega_i f_i R_i \tag{B 4}$$

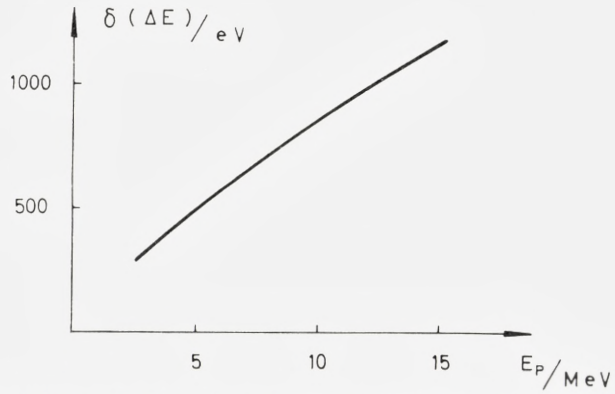

Figure 5. Energy being emitted as δ-rays from an aluminium foil traversed by a proton of energy E_p as calculated from (B 8).

This has a maximum for the K-shell of aluminium in our energy range of about $0.2\,\%$. For the L-shell in some of the heavier elements it might rise to $1.5\,\%$. Fortunately a good many of the x-rays are reabsorbed in the foil. If the absorption coefficient for a particular group of x-rays is μ, the self-absorption is a function only of the dimensionless quantity $a = \mu \cdot t$. The fraction escaping is

$$F(a) = \tfrac{1}{2}\left[\frac{1}{a} - \frac{e^{-a}}{a} + e^{-a} + a\mathrm{Ei}(-a)\right], \tag{B 5}$$

where $\mathrm{Ei}(a)$ is the Eire-function. This will usually reduce the correction by at least a factor of 3.

The δ-rays are energetic electrons emitted mainly in the forward direction. The electrons in the material are assumed to be free, and the energy distribution of the electrons is calculated by the Rutherford cross section, i.e. classically.

The probability that a single charged particle with velocity v will eject an electron with an energy in the interval Q to $Q + dQ$ from a slab with thickness dx is then

$$d\Sigma = \frac{N_0 Z}{A}\frac{2\pi e^4}{mv^2}\frac{dQ}{Q^2}\,dx = k \cdot \frac{dQ}{Q^2}\,dx. \tag{B 6}$$

These electrons are assumed to lose energy at a rate governed by a relation $R = c_2 \cdot E^2$ as in appendix A. If the slab is situated the distance x beneath the surface, the energy leaving the surface from this slab will be

$$E(x)dx = k \cdot dx \int_{\sqrt{T^2 + \frac{x}{c_2}\sqrt{\frac{T_m}{T}}}}^{T_m} \frac{1}{Q^2} \sqrt{Q^2 - \frac{x}{c_2}\sqrt{\frac{T_m}{Q}}}\, dQ \qquad \text{(B 7)}$$

where T_m is the maximum possible energy transfer. The total correction is then

$$\delta(E) = \int_0^{T_m} E(x)dx = \frac{N_0 Z}{A} \cdot c_2 \cdot \frac{\pi e^4 M}{m E_0} f(E) \qquad \text{(B 8)}$$

where $f(E)$ is a function only dependent on E, which has been found by numerical integration. The result for aluminium is shown in fig. 5.

Physics Department
Atomic Energy Commission
Research Establishment Risö
Roskilde, Denmark

A. F. Garfinkel
now at University of Wisconsin,
Madison, Wisconsin

References

H. H. Andersen (1965). A Low-Temperature Technique for Measurement of Heavy Particle Stopping Powers of Metals. Risø Report No. 93.

W. H. Barkas and M. J. Berger (1964). Tables of Energy Losses and Ranges of Heavy Charged Particles, in Studies in Penetration of Charged Particles in Matter. Publication 1133. National Academy of Science, Washington D.C.

H. A. Bethe and J. Ashkin (1953). Passage of Radiations through Matter, in E. Segre (edt.), Experimental Nuclear Physics, Wiley, N.Y.

H. Bichsel (1958). Experimental Range of Protons in Al. Phys. Rev. **112**, 1089.

H. Bichsel (1961 and 1963 a). Higher Shell Corrections in Stopping Power, and Appendix. Linear Accelerator Group. University of Southern California. Technical Report TR-3. (Unpublished).

H. Bichsel (1963 b). Passage of Charged Particles through Matter. American Institute of Physics Handbook. Second Edt. McGraw-Hill, N.Y.

H. Bichsel (1964). A Critical Review of Experimental Stopping Power and Range Data, in Studies in Penetration of Charged Particles in Matter. Publication 1133. National Academy of Science. Washington D.C.

H. Bichsel, W. Mozley and W. A. Aron (1957), Range of 6- to 18-MeV Protons in Be, Al, Cu, Ag and Au. Phys. Rev. **105**, 1788.

S. Datz, T. S. Noggle and C. D. Moak (1965), Anisotropic Energy Losses in a Face-Centered-Cubic Crystal for High-Energy ^{79}Br and ^{127}I Ions. Phys. Rev. Letters **15**, 254.

G. Dearnaley (1964), The Channeling of Ions through Silicon Detectors. IEEE Trans. Nucl. Sci. NS**11**, 249.

G. Dearnaley and A. R. Sattler (1964), Channeling of Ions through Single-Crystal Silicon Lattices. Bull. Am. Phys. Soc. **9**, 656.

G. Dearnaley and A. R. Sattler (1965), Channeling of Protons as a Function of Incident Angle in the ⟨110⟩ Plane in Silicon and Germanium. Bull. Am. Phys. Soc. **10**, 515.

C. Erginsoy, H. E. Wegner and W. M. Gibson (1964), Anisotropic Energy Loss of Light Particles of MeV Energies in Thin Silicon Single Crystals. Phys. Rev. Letters **13**, 530.

U. Fano (1963), Penetration of Protons, Alpha Particles, and Mesons. Ann. Rev. Nucl. Sci. **13**, 1.

F. Kalil, W. G. Stone, H. H. Hubbell and R. D. Birkhoff (1959), Stopping Power of Thin Aluminium Foils for 12 to 127 keV Electrons. ORNL 2731.

J. Lindhard (1964), Motion of Swift Charged Particles as Influenced by Strings of Atoms in Crystals. Phys. Letters **12**, 126.

J. Lindhard (1965), Influence of Crystal Lattice on Motion of Energetic Charged Particles. Mat. Fys. Medd. Dan. Vid. Selsk. **34**, No. 14.

L. P. Nielsen (1961), Energy Loss and Straggling of Protons and Deuterons. Mat. Fys. Medd. Dan. Vid. Selsk. **33**, No. 6.

M. C. Walske (1952), The Stopping Power of K-Electrons. Phys. Rev. **88**, 1283.

M. C. Walske (1957), Stopping Power of L-Electrons. Phys. Rev. **101**, 940.

P. L. Ziemer, R. M. Johnson and R. D. Birkhoff (1959), Measurement of Stopping Power of Copper by a Calorimetric Method. ORNL 2775.

Indleveret til Selskabet den 13. januar 1966.
Færdig fra trykkeriet den 25. juli 1966.

Matematisk-fysiske Meddelelser
udgivet af
Det Kongelige Danske Videnskabernes Selskab
Bind **35,** nr. 5

Mat. Fys. Medd. Dan. Vid. Selsk. **35,** no. 5 (1966)

1.
THE STRUCTURE OF WHITE CESIUM LEAD(II) BROMIDE, $CsPbBr_3$

BY

ASTRID MARSTRANDER AND
CHRISTIAN KNAKKERGÅRD MØLLER

København 1966
Kommissionær: Munksgaard

Synopsis

Crystals of the white modification of $CsPbBr_3$ – contaminated with orange crystals of the same composition – can be obtained from aqueous solutions of CsBr and $PbBr_2$. The white crystals appear to be only slightly less stable than the orange ones. They are needle-shaped with γ' parallel with the needle axis and they undergo a phase transition to the orange modification at 130°C. The X-ray analysis shows that the white crystals are orthorhombic belonging to space group no. 62 Pmnb, and $a = 4.597$ Å, $b = 9.72$ Å, $c = 16.81$ Å. The structure is quite analogous to that of the yellow $CsPbI_3$. Distorted $PbBr_6$-octahedra sharing Br-atoms form chain-like, polynuclear ions $(PbBr_3^-)_n$ running parallel with the a-axis. The Pb-Br-distances vary from 2.82 Å to 3.29 Å.

PRINTED IN DENMARK
BIANCO LUNOS BOGTRYKKERI A/S

Introduction

It has been shown previously that $CsPbI_3$ exists in two modifications, a black metastable form with perovskite structure and a yellow orthorhombic form which is stable under ordinary conditions[1]. $CsPbBr_3$ apparently also exists in two forms, an orange-coloured form with perovskite structure, which already has been investigated[2], and the supposed analogue of the yellow orthorhombic $CsPbI_3$, which has been prepared by WELLS and co-workers[3].

Although a fairly complete *X*-ray analysis has been done on the orthorhombic $CsPbI_3$, it seemed worth while to make an independent investigation of the white $CsPbBr_3$ in order to check the irregular octahedral coordination of the halogen atoms around the lead atoms which was found in the former compound. Also, in the previous investigation no distinction could be made between the halogen atoms and the cesium atoms because of their equal scattering powers. And finally, it might be interesting to see if the atomic parameters would be the same as in $CsPbI_3$ in spite of differences in absorption and dispersion effects.

Preparation and properties of the white $CsPbBr_3$-crystals

We have obtained the white modification of $CsPbBr_3$ in the following way. First CsBr was prepared from Cs_2CO_3 and an aqueous solution of HBr. $PbBr_2$ was precipitated from aqueous solutions of $Pb(NO_3)_2$ and HBr, recrystallized a few times in hot water. All the chemicals were Riedel-de Haën pro analysi.

Aqueous solutions with well-defined concentrations of CsBr were next prepared and saturated with $PbBr_2$ by boiling. Undissolved $PbBr_2$ was separated from the still hot solutions. On addition of an amount of hot or cold water to each solution so that the CsBr-concentrations as well as the

[1] C. K. MØLLER, The Structure of $CsPbI_3$. Mat. Fys. Medd. Dan. Vid. Selsk. **32** No. 1 (1959).
[2] C. K. MØLLER, The Structure of Perovskite-like Cæsium Plumbo Trihalides. Mat. Fys. Medd. Dan. Vid. Selsk. **32** No. 2 (1959).
[3] H. L. WELLS, Z. anorg. Chem. **3**, 195 (1893).

temperatures were kept within a certain range a precipitation of crystals usually resulted.

White needle-shaped crystals were obtained when the final concentration of CsBr was in the range 23.5–27.5 g CsBr/100 g H_2O, and the temperature at which they appeared was usually 23–25°C; but they were always contaminated with orange crystals, and sometimes also with thin flaky crystals (of $CsPb_2Br_5$?), the latter ones, however, disappearing after some time.

To avoid the formation of basic salts the solutions were mostly kept acid with pH = 1–3. Higher pH-values seemed to change the conditions for precipitation of the white crystals of $CsPbBr_3$ in the direction of higher CsBr-concentrations. Supersaturated solutions easily resulted so that seeding often was necessary.

Sometimes very thin needles of white crystals $\frac{1}{2}$ – 1 cm long were obtained. Apparently they grew very quickly under special conditions.

Only by hand-sorting under a microscope was it possible to obtain a pure product of white crystals—free from orange-coloured contaminations.

Under the polarizing microscope these crystals showed extinction parallel with and perpendicular to the needle-axis. When heated under the microscope on a hot stage the white crystals changed irreversibly into the orange modification at 130°C—this temperature being about 10°C lower than that mentioned by Wells[1].

The *X*-ray work to be mentioned shows that the crystals have the stoichiometric composition $CsPbBr_3$ as found by Wells et al[1].

Stability of the white $CsPbBr_3$-crystals

From the observation that the white needle-shaped crystals and the orange crystals could co-exist at room temperature (18–20°C) for months in aqueous solutions of CsBr with concentrations as mentioned above, it would appear that there can be only a small difference in free energy between the two forms. The white crystals eventually slowly disappeared and only orange-coloured crystals were left. With crystals of the same composition the CsBr-concentration of the solution would not be expected to influence the relative stability of the two forms, and hence it is concluded that the orange crystals are slightly more stable than the white ones. When dry, the white crystals can be kept at room temperature indefinitely.

An attempt was made to measure the difference in free energy between the two modifications. Electrochemical cells of the following type were constructed:

$$Pt\,|\,Pb(Hg)\,|\,CsPbBr_3(orange)\,|\,solution\ 27\,g\ CsBr/100\,g\ H_2O\,|\,CsPbBr_3(white)\,|\,Pb(Hg)\,|\,Pt.$$

They were kept at temperatures 19.5°C or 22.5°C. However, it was difficult to obtain reliable values for the emf.'s of the cells. Shortly after assemblage the cell had an emf. of 2–3 mv, but then drifted slowly towards lower values. Only on one occasion did the emf. stay within the interval 2.5–3.0 mv the first 24 hours after construction of the cell.

The electrode with the white $CsPbBr_3$-crystals was the positive electrode, suggesting the electrode processes:

$$2\,e^- + CsPbBr_3\,(white) \rightarrow Cs^+ + 3\,Br^- + Pb$$

$$Cs^+ + 3\,Br^- + Pb \rightarrow CsPbBr_3\,(orange) + 2\,e^-$$

Hence the white crystals are less stable than the orange ones. If a value of c. 3 mv for the emf. is accepted as being significant, the corresponding difference in free energy is $\Delta G = 3 \cdot 10^{-3} \cdot 96000 \cdot 2 \sim 600$ Joule or 140 cal/mole, which is quite small.

X-ray investigation

Oscillation and Weissenberg diagrams of single crystals of the white $CsPbBr_3$-compound showed that they had orthorhombic symmetry, and preliminary values for the crystal axes were determined from these photographs. Refined values were obtained from powder photographs in a Guinier type focusing camera as previously described[1], and Table 1 shows a comparison of the observed $\sin^2\theta$-values with those calculated from the finally accepted unit cell axes:

$$a = 4.597 \pm 0.005\,\text{Å},\quad b = 9.72 \pm 0.01\,\text{Å},\quad c = 16.81 \pm 0.02\,\text{Å}.$$

From the similarity of the powder patterns of the yellow $CsPbI_3$ and of the white $CsPbBr_3$ it is concluded that the two compounds are isomorphous with the same number of molecules in the unit cell, i. e. 4. On this basis and with the unit cell axes given above the molar volume for white $CsPbBr_3$ is 113.7 cc. This may be compared with the molar volume 120.5 cc for the orange modification and a value of 103.0 calculated from the molar volumes of CsBr and $PbBr_2$. We thus find the same trend as for the analogous iodides[4].

[4] C. K. Møller, The Structure of Cæsium Hexahalogeno-Plumbates(II). Mat. Fys. Medd. Dan. Vid. Selsk. **32** No. 3, p. 6 (1960).

TABLE 1. Observed and calculated $\sin^2\theta$-values for white $CsPbBr_3$. CuK_α-radiation.

Indices	Estimated intensity	$10^4\times \sin^2\theta_{obs}$	$10^4\times \sin^2\theta_{calc}$	Indices	Estimated intensity	$10^4\times \sin^2\theta_{obs}$	$10^4\times \sin^2\theta_{calc}$
011	m-w	0083	0084	032	vw	0653	0651
002			0084	123	vw	0721	0722
012	w	0148	0147	105	m	0809	0807
020	w	0252	0252	016	vw	0820	0820
013			0252	115	vw	0869	0870
021	m-w	0272	0273	124			0869
111	s	0364	0365	131			0869
014	m	0401	0399	132	w	0932	0932
112	m-w	0426	0428	200	m-w	1125	1125
023	w	0441	0441	134	w	1187	1184
120	m-w	0532	0533	212	vw	1270	1272
113				126	w	1294	1290
121	m	0555	0554	117	s	1377	1375
015	w	0589	0589	213			1377
024			0588	220			1377
031			0588	224	vw	1716	1713
122	s	0616	0617	215			1714

TABLE 2. Atomic parameters in white $CsPbBr_3$.

All the atoms are in the special positions:

$$\frac{1}{4}\,yz;\quad \frac{3}{4}\,\bar{y}\bar{z};\quad \frac{3}{4}\,\frac{1}{2}-y\;\frac{1}{2}+z;\quad \frac{1}{4}\,\frac{1}{2}+y\;\frac{1}{2}-z$$

and for

Cs	$x=\frac{1}{4}$	$y=0.089$	$z=0.329$
Pb	$x=\frac{3}{4}$	$y=0.163$	$z=0.063$
Br′	$x=\frac{1}{4}$	$y=0.335$	$z=0.000$
Br″	$x=\frac{3}{4}$	$y=0.028$	$z=\overline{0.116}$
Br‴	$x=\frac{3}{4}$	$y=0.302$	$z=0.211$

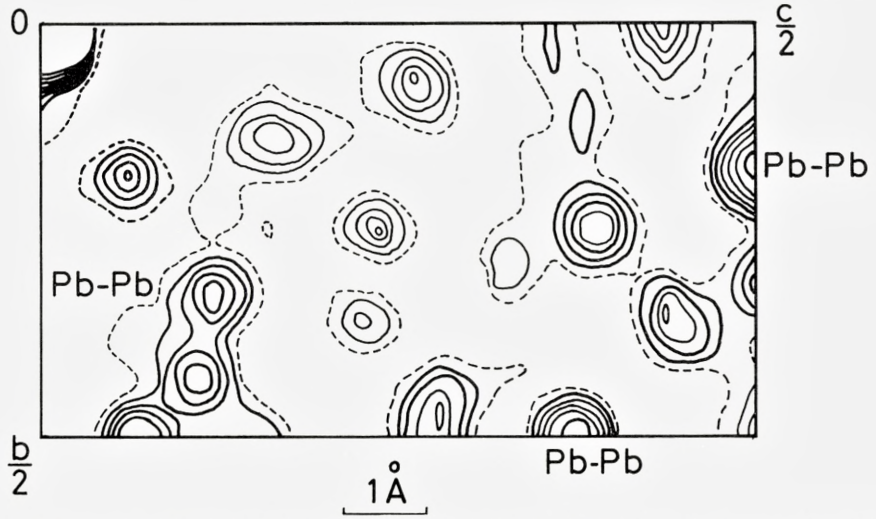

Fig. 1. Patterson projection of the white $CsPbBr_3$ on (100). Contours are drawn at the relative densities 0 (dashed), 25, 50, 75, 100, 150 and 200.

In order to see if there should be any relation between lattice planes in the orange and the white modifications of $CsPbBr_3$, oscillation diagrams were taken of a single crystal of white $CsPbBr_3$. Then the crystal was heated in a controlled flow of hot N_2-gas and thus partly converted to the orange modification while another oscillation diagram was taken. The latter shows a powder pattern superimposed on an oscillation diagram of white $CsPbBr_3$, but apparently there is no simple connection between "old" and "new" *X*-ray reflections, and it appears that the crystal is converted into a disordered powder of orange $CsPbBr_3$ within the boundary of the original crystal.

With CuK_α-radiation intensities were obtained from Weissenberg exposures by a multiple film technique as previously described[1]. The crystal was rotated about the *a*-axis—which is also the needle axis. Its length was 0.42 mm and the cross section of the crystal 0.035×0.010 mm^2.

Reflections of the type h0l were absent for h+l odd and hk0 were absent for k odd. No other systematic absences were observed, but I(0kl) and I(2kl) appeared to be equal for all values of k and l. As these rules are exactly the same as for yellow $CsPbI_3$, it is inferred that the space group is also the the same, no. 62 Pmnb.

The procedure and the arguments for determining the atomic arrangement from the observed intensities were from now exactly the same as described

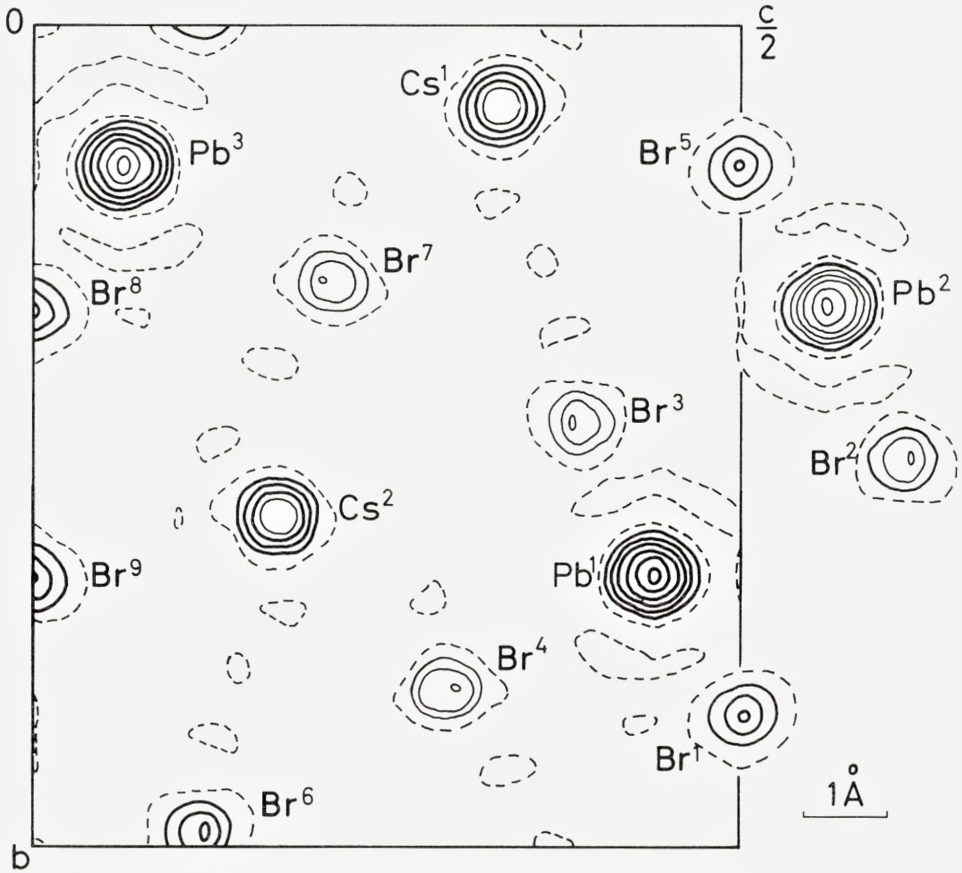

Fig. 2. Electron projection of the white $CsPbBr_3$ on (100). Contours are drawn at the relative densities 0 (dashed), 100, 200, 300, 400, 600 and 800.

for $CsPbI_3$[1] and no detailed account of it will be given. Suffice it to say that the structure of white $CsPbBr_3$ was solved independently of that of the analogous iodide and hence both Patterson and electron projections as well as difference maps were evaluated (figs. 1 and 2). The Fourier syntheses and the structure factors were calculated on a GIER electronic computer using programmes which had originally been worked out by J. Danielsen[5], and atomic scattering factors from Forsyth and Wells' paper[6].

[5] J. Danielsen, Acta Cryst. **16** Suppl. A 171 (1963).
[6] J. B. Forsyth and M. Wells, Acta Cryst. **12**, 412 (1959).

TABLE 3. Comparison of calculated and observed structure factors for white $CsPbBr_3$ (brought on the same relative scale).

$h\,k\,l$	$\lvert F_{obs}\rvert$	F_{calc}	$h\,k\,l$	$\lvert F_{obs}\rvert$	F_{calc}	$h\,k\,l$	$\lvert F_{obs}\rvert$	F_{calc}
0 0 2	105	+ 85	0 2 15	46	+ 47	0 5 1	79	+ 83
0 0 4	27	− 10	0 2 19	65	− 76	0 5 2	139	+ 164
0 0 6	41	+ 31	0 2 20	23	− 32	0 5 3	74	− 74
0 0 8	144	− 129	0 2 21	10	− 12	0 5 4	108	+ 102
0 010	22	+ 10	0 3 1	22	− 19	0 5 5	77	− 69
0 012	45	+ 46	0 3 2	121	+ 147	0 5 6	58	+ 50
0 014	79	+ 65	0 3 3	84	− 79	0 5 7	12	+ 13
0 016	85	+ 102	0 3 4	128	− 137	0 5 9	122	− 128
0 018	99	+ 130	0 3 5	133	− 138	0 5 10	67	− 66
0 020	16	− 23	0 3 7	149	+ 166	0 5 11	31	+ 26
0 1 1	49	+ 54				0 5 12	65	− 58
0 1 2	85	− 85	0 3 8	31	+ 27	0 5 14	53	− 50
0 1 3	96	+ 77	0 3 9	199	+ 225	0 5 15	39	− 40
0 1 4	166	− 155	0 3 10	40	− 36	0 5 17	75	+ 76
0 1 5	201	− 227	0 3 11	70	+ 62	0 5 18	48	+ 51
0 1 6	170	− 164	0 3 12	40	+ 38	0 6 0	117	+ 133
0 1 7	118	− 94	0 3 13	43	− 39	0 6 1	97	+ 93
0 1 8	108	+ 92	0 3 15	42	− 39	0 6 2	137	+ 165
0 1 9	25	+ 21	0 3 16	41	− 48	0 6 4	68	+ 60
0 1 10	24	+ 17	0 3 17	28	− 25	0 6 6	120	− 118
0 1 11	94	− 94	0 3 19	18	+ 29	0 6 9	35	− 21
0 1 12	115	+ 119	0 3 20	21	+ 31	0 6 11	33	+ 36
0 1 13	42	− 40	0 4 0	114	− 128	0 6 12	41	− 35
0 1 14	79	+ 77	0 4 1	54	− 57			
0 1 15	57	+ 62	0 4 2	77	− 72	0 6 13	26	− 25
0 1 16	51	− 58	0 4 3	161	+ 204	0 6 14	104	+ 114
0 1 17	14	+ 17	0 4 4	47	− 42	0 6 16	84	+ 83
0 1 20	43	− 51	0 4 5	130	+ 133	0 6 18	33	+ 30
0 2 0	59	− 59	0 4 6	52	− 42	0 7 1	82	+ 83
0 2 1	87	− 104	0 4 7	68	− 67	0 7 2	75	− 77
0 2 2	63	− 66	0 4 8	115	+ 108	0 7 3	82	− 77
0 2 3	130	− 155	0 4 10	67	+ 55	0 7 6	122	− 115
0 2 4	138	− 156	0 4 11	56	− 53	0 7 7	89	− 82
0 2 5	72	− 54	0 4 12	90	− 90	0 7 9	77	− 76
0 2 6	63	+ 54	0 4 13	76	− 78	0 7 10	96	+ 95
0 2 7	149	− 148	0 4 14	39	− 34	0 7 12	71	+ 63
0 2 8	93	+ 76	0 4 15	47	− 42	0 7 17	30	+ 30
0 2 9	73	+ 58	0 4 16	50	− 44	0 8 0	92	− 87
0 2 10	12	+ 1	0 4 17	42	+ 51	0 8 1	35	+ 25
0 2 11	162	+ 181	0 4 18	33	− 37	0 8 3	48	− 45
0 2 14	104	− 117	0 4 19	23	+ 26	0 8 4	33	− 29

TABLE 3 (continued)

$h\,k\,l$	$\lvert F_{obs}\rvert$	F_{calc}	$h\,k\,l$	$\lvert F_{obs}\rvert$	F_{calc}	$h\,k\,l$	$\lvert F_{obs}\rvert$	F_{calc}
0 8 5	131	− 141	1 1 2	77	+ 76	1 3 8	28	− 21
0 8 7	24	− 7	1 1 3	153	− 144	1 3 9	90	− 94
0 8 8	43	+ 37	1 1 5	43	− 33	1 3 10	91	+ 94
0 8 9	39	+ 34	1 1 6	133	+ 122	1 3 11	61	+ 61
0 8 11	57	+ 43	1 1 7	213	− 230	1 3 12	73	+ 80
0 8 13	98	+ 97	1 1 8	123	+ 105	1 3 14	68	+ 70
0 8 14	33	− 35	1 1 9	160	− 160	1 3 15	50	− 60
0 8 15	24	− 28	1 1 10	164	− 183	1 3 16	38	+ 38
0 9 1	63	− 53	1 1 11	77	− 63	1 3 17	55	+ 74
0 9 3	20	+ 22	1 1 12	76	− 64	1 3 18	77	− 88
0 9 5	44	+ 44	1 1 14	31	+ 30	1 3 20	44	− 58
0 9 7	97	+ 92	1 1 15	38	+ 34	1 4 0	133	− 176
0 9 8	64	− 65	1 1 16	19	− 27	1 4 2	130	− 154
0 9 9	93	+ 90	1 1 17	40	+ 38	1 4 3	129	− 146
0 9 10	80	+ 82	1 1 18	41	+ 44	1 4 4	33	− 23
0 9 14	32	− 31	1 1 19	26	+ 18	1 4 5	103	− 103
010 1	59	+ 60	1 1 20	16	+ 19	1 4 6	58	− 52
010 2	96	− 90	1 1 21	41	− 80	1 4 7	74	+ 67
010 3	74	+ 66	1 2 0	87	+ 106	1 4 8	114	+ 125
010 6	57	+ 48	1 2 1	132	− 204	1 4 10	92	+ 90
010 10	20	+ 19	1 2 2	200	+ 304	1 4 12	118	− 146
011 1	23	− 21	1 2 3	91	− 91	1 4 13	77	+ 80
011 2	58	+ 46	1 2 4	63	+ 56	1 4 14	35	− 31
011 3	52	+ 47	1 2 5	31	− 20	1 4 15	30	+ 30
011 4	80	+ 79	1 2 6	158	− 155	1 4 16	79	− 92
011 5	35	− 39	1 2 7	31	− 23	1 4 17	34	− 35
011 7	25	− 27	1 2 9	59	+ 52	1 4 18	53	− 65
011 10	25	− 25	1 2 10	41	− 30	1 4 19	21	− 25
012 0	67	+ 74	1 2 13	52	+ 46	1 5 1	34	− 26
012 2	43	+ 45	1 2 14	97	+ 117	1 5 2	100	− 99
			1 2 15	31	+ 33	1 5 3	57	− 55
1 0 1	21	− 18	1 2 16	102	+ 125	1 5 4	150	+ 178
1 0 3	103	+ 67	1 2 18	27	+ 29	1 5 5	77	+ 81
1 0 5	291	+ 332	1 2 19	54	− 71	1 5 7	152	+ 179
1 0 7	46	+ 24	1 2 20	26	+ 40	1 5 9	128	+ 139
1 0 9	99	− 89	1 3 1	80	+ 86	1 5 11	76	+ 77
1 0 11	76	− 69	1 3 2	141	− 175	1 5 12	66	− 68
1 0 13	171	− 210	1 3 3	105	− 111	1 5 13	38	− 30
1 0 15	55	+ 65	1 3 4	176	− 222	1 5 14	36	− 29
1 0 17	55	+ 58	1 3 5	18	− 2	1 5 15	64	− 60
1 0 21	43	+ 73	1 3 6	14	− 7	1 5 16	32	+ 42
1 1 1	98	+ 154	1 3 7	66	+ 64	1 6 1	111	+ 131

TABLE 3 (continued)

$h\,k\,l$	$\lvert F_{obs}\rvert$	F_{calc}	$h\,k\,l$	$\lvert F_{obs}\rvert$	F_{calc}	$h\,k\,l$	$\lvert F_{obs}\rvert$	F_{calc}
1 6 2	27	+ 21	1 7 15	59	+ 64	1 9 13	21	− 24
1 6 3	79	+ 80	1 7 16	46	+ 53	1 9 14	38	+ 44
1 6 4	80	− 75	1 7 17	10	+ 6	1 10 1	24	− 24
1 6 5	74	+ 66	1 8 0	208	+ 258	1 10 2	80	− 81
1 6 7	123	+ 132	1 8 1	43	− 35	1 10 3	63	− 61
1 6 8	54	+ 48	1 8 2	60	+ 53	1 10 4	62	− 60
1 6 9	72	− 76	1 8 5	57	− 50	1 10 6	37	+ 38
1 6 11	119	− 133	1 8 8	72	− 68	1 10 7	52	− 51
1 6 13	36	− 29	1 8 12	35	+ 39	1 10 8	38	+ 38
1 6 14	66	− 62	1 8 13	48	+ 53	1 10 9	23	+ 14
1 7 1	62	− 62	1 8 14	29	+ 28	1 10 10	27	+ 19
1 7 4	94	+ 90	1 9 2	49	− 50	1 10 11	74	+ 82
1 7 5	103	− 109	1 9 3	62	+ 62	1 11 2	56	+ 55
1 7 6	85	+ 79	1 9 4	98	− 95	1 11 3	30	− 23
1 7 7	121	− 132	1 9 5	98	− 101	1 11 5	41	+ 44
1 7 8	61	− 58	1 9 6	59	− 58	1 11 7	56	+ 61
1 7 11	86	− 90	1 9 9	38	+ 35	1 11 8	29	+ 33
1 7 12	67	− 73	1 9 10	33	+ 34	1 11 9	69	+ 107
1 7 13	33	− 30	1 9 11	24	− 33	1 12 0	37	− 30
1 7 14	44	− 49	1 9 12	66	+ 68	1 12 3	56	+ 74

TABLE 4. Interatomic distances in white $CsPbBr_3$.

Distance	From this investigation	From Pauling's ionic radii	From Goldschmidt's radii
Pb^1-Br^1	3.04 Å	3.16 Å	3.28 Å
Pb^1-Br^2	3.29 -		
Pb^1-Br^3	3.08 -		
Pb^1-Br^4	2.82 -		
Pb^1-Pb^2	4.46 -		
Pb-Cs	5.08 -		
Cs^1-Br^5	3.76 -	3.64 -	3.63 -
Cs^1-Br^1	3.79 -		
Cs^1-Br^6	3.75 -		
Cs^1-Br^3	3.84 -		
Cs^1-Br^4	3.67 -		
Cs^1-Br^7	3.67 -		
Br^1-Br^1	4.60 -		
Br^1-Br^2	4.24 -		
Br^1-Br^3	4.03 -		
Br^1-Br^4	4.24 -		

Structure factors which have been calculated from the atomic parameters in Table 2 are compared with the observed values in Table 3 after they have been brought on the same relative scale. Interatomic distances obtained with these parameters are given in Table 4.

Conclusion

The structure of the white $CsPbBr_3$ as determined from the present work is in complete analogy with that of the yellow $CsPbI_3$ and exhibits the same kind of irregular octahedral coordination of the halogen atoms around the lead atoms. In both structures catena-ions $(PbX_3^-)_n$ are parallel to the a-axis and the Cs-ions are held between these chain-like ions. One of the lead-halogen distances is considerably shorter than the others and also shorter than the sum of the corresponding ionic radii or Slater atomic radii: 2.82 Å against 3.16 Å or 2.95 Å, respectively. This might indicate a stronger bonding between lead and this particular halogen atom.

The variations of the interatomic distances in the two analogous crystals are also quite similar although the dispersion effects have not been considered in case of the bromide. One might, therefore, be tempted to conclude that if an uncertainty of 0.05 Å on the interatomic distances can be tolerated, the influence of dispersion may be neglected.

Acknowledgements

One of us (A.M.) is much indebted to the Carlsberg Foundation for financial support during this investigation. We are very grateful to cand. mag. E. Bang and cand. mag. B. Svejgård, lecturer in mathematics at the University of Copenhagen, for their continual help and guidance in computational matters in connection with this work.

[7] J. C. Slater, J. Chem. Phys. **41**, 3199 (1964).

Chemistry Department I, Inorganic Chemistry,
The H. C. Ørsted Institute,
University of Copenhagen, Denmark

Matematisk-fysiske Meddelelser
udgivet af
Det Kongelige Danske Videnskabernes Selskab
Bind **35,** nr. 5

Mat. Fys. Medd. Dan. Vid. Selsk. **35,** no. 5 (1966)

2.

THE STRUCTURE OF LEAD(II) HYDROXY-BROMIDE

BY

CHRISTIAN KNAKKERGÅRD MØLLER

København 1966
Kommissionær: Munksgaard

Synopsis

Pb(OH)Br can be prepared from aqueous solutions of lead bromide with an excess of bromide at elevated temperatures, or by mixing aqueous solutions of sodium hydroxide and lead bromide. By the former method the compound is obtained as white needles, birefringent with γ' parallel with the needle axis. The X-ray analysis shows that they are orthorhombic belonging to space group no. 62 Pmnb with $a = 4.089$ Å, $b = 7.384$ Å and $c = 10.010$ Å. It appears that the lead atoms and the hydroxyl groups form chainlike poly-ions, $(Pb(OH)^+)_n$ running parallel with the a-axis. The halogen atoms are distributed between the poly-ions. The compound is isostructural with SbSBr.

Introduction

In order to find the conditions under which the white $CsPbBr_3$ mentioned in the previous paper could be prepared, aqueous solutions with varying concentrations of CsBr were saturated with $PbBr_2$. A few drops of the solutions were placed in a hollow microscope slide on a hot stage and watched through a microscope. After heating to 70–80°C for some time it was often observed that thin white crystals began to grow from the edge of the solution. In the hope that they were the wanted white crystals of $CsPbBr_3$, some of them were isolated and examined optically and by *X*-rays. It turned out that the crystals did not undergo a phase transition to the yellow $CsPbBr_3$ at 140°C as described by WELLS[1] so that it seemed doubtful from the very beginning what they were. However, from the *X*-ray diagrams it was possible to identify them as Pb(OH)Br, a compound which may be formed under just those conditions[2].

An *X*-ray investigation of Pb(OH)Cl (laurionite) has been made by BRASSEUR[3] and of Pb(OH)I by NÄSÄNEN, MERILÄINEN, UGGLA and HYLE[4], so that it might seem rather useless to enter into a detailed investigation of Pb(OH)Br also. However, in Brasseur's work the OH-groups, and partly also the Cl-atoms, were located from space-filling considerations and no comparison is given of observed and calculated structure factors. In the other work the positions of all the atoms were obtained by the method of steepest descents, but it appears that one of the OH-I distances is unlikely short: 3.15 Å compared with the sum of the ionic (or van der Waals) radii of I and OH: 2.2 + 1.4 = 3.6 Å. Hence it was considered worth while to look more closely at the structure of Pb(OH)Br, although one could scarcely hope to localize the OH-groups. Unfortunately, no Mo *X*-ray tube was available at the time of the investigation and so the *X*-ray diagrams were taken with CuK_α-radiation, which may influence the intensities through absorption and dispersion effects.

[1] H. L. WELLS, Z. anorg. Chem. **3**, 195 (1893).

[2] "*X*-ray diffraction patterns of lead compounds" from The Shell Petroleum Company Ltd., Thornton Research Centre 1954.

[3] H. Brasseur, Bull. Soc. Roy. des Sciences de Liege No. 11, 1940.

[4] R. NÄSÄNEN, P. MERILÄINEN, R. UGGLA and M. HYLE, Suomen Kemistilehti **37** no. 4 B p. 45–46 (1964).

Preparation and properties of Pb(OH)Br

While single crystals suitable for *X*-ray work could be prepared as mentioned above, larger quantities of the compound were more easily prepared by precipitation: To a saturated solution of $PbBr_2$ in water a 0.1 molar solution of NaOH was added. A pure white precipitate was immediately formed (pH ~ 4–6). On further addition of NaOH to pH about 8 or more the precipitate turned pale yellow. The precipitates were separated from the supernatant liquid on a glass filter by suction, washed several times with water and finally with ethyl alcohol and dried at 50°C.

Both the yellowish and the white precipitate gave the same *X*-ray powder pattern in a Guinier type focusing camera. The sharpness of the powder lines indicated that the substances consisted of rather well-defined crystals.

From preliminary values of the axes in the orthorhombic unit cell as determined from oscillation and Weissenberg diagrams all the powder lines except two weak ones could be indexed, and refined values for the axes could thus be obtained:

$$a = 4.089 \pm 0.005\,\text{Å};\ b = 7.384 \pm 0.01\,\text{Å};\ c = 10.010 \pm 0.01\,\text{Å}.$$

The volume of 6.023×10^{23} unit cells is $0.6023 \times a \times b \times c \times 10^{24} = 183$ cc. The molar volumes of $PbCl_2$ and $PbBr_2$ are 47.6 cc and 55.0 cc, respectively, and if it is assumed that the molar volume of Pb(OH)Br is not too different from that of $PbCl_2$, this suggests that there are 4 molecules in the unit cell of Pb(OH)Br.

The single crystals prepared as described above were white, usually very thin and needle-shaped. Under the polarizing microscope they showed parallel extinction with γ' parallel with the needle axis, which is also the *a*-axis.

Determination of the structure

A single crystal 0.24 mm long and 0.015×0.020 mm^2 in cross section was selected for the *X*-ray work. Oscillation and Weissenberg diagrams with CuK_α-radiation were taken with the *a*-axis as rotational axis, and the intensities were visually estimated and corrected in the usual way. (For details see reference[5]). The absorption was treated as a "reversed temperature factor" which seemed legitimate considering the smallness of the crystals.

Reflections of the following types were absent: $h0l$ for $h+l$ odd and $hk0$ for k odd. Hence the space group could be either no. 62, Pmnb or no. 33, $Pbn2_1$.

[5] C. K. Møller, The structure of cæsium plumbo iodide. Mat. Fys. Medd. Dan. Vid. Selsk. **32**, No. 1 (1959).

TABLE 1. Observed and calculated $\sin^2\theta$-values for Pb(OH)Br. CuK_α-radiation.

Indices	Estimated intensity	$10^4\times \sin^2\theta_{obs}$	$10^4\times \sin^2\theta_{calc}$	Indices	Estimated intensity	$10^4\times \sin^2\theta_{obs}$	$10^4\times \sin^2\theta_{calc}$
011	w-m	0169	0168	113	vw?	0999	0998
002	w-m	0239	0239	122	vw	1029	1029
012	vs	0347	0348	031	m	1040	1038
101	vw?	0414	0414	014	m	1058	1058
020	w-m	0435	0435	032	m-w	1218	1218
?	vw	0458		123	m	1325	1324
021	m	0494	0494	131	vw?	1397	1393
111	vs	0523	0523	200	m	1423	1422
?	vw?	0553		132	vw	1572	1573
013	w	0642	0643	211	vw?	1590	1590
022	w-m	0672	0674	212	w-m, diff.	1768	1770
112	m	0703	0703	105	vw	1838	1838
120	vw	0789	0790	221	(v)w	1916	1916
121	m	0850	0849	115	w-m	1948	1947
103	m	0889	0889	213	vw	2061	2065
004	vw	0949	0949	222	(w)-m	2098	2096
023	vw	0968	0968	134	w	2283	2283

TABLE 2. Atomic parameters in Pb(OH)Br.

All the atoms are in the special positions:

$$\frac{1}{4}\,yz;\quad \frac{3}{4}\,\bar{y}\bar{z};\quad \frac{3}{4}\,\frac{1}{2}-y\,\frac{1}{2}+z;\quad \frac{1}{4}\,\frac{1}{2}+y\,\frac{1}{2}-z;$$

and for

Pb	$x=\frac{1}{4}$	$y=0.197$	$z=0.084$
Br	$x=\frac{1}{4}$	$y=0.452$	$z=0.820$
O	$x=\frac{1}{4}$	$y=0.394$	$z=0.456$

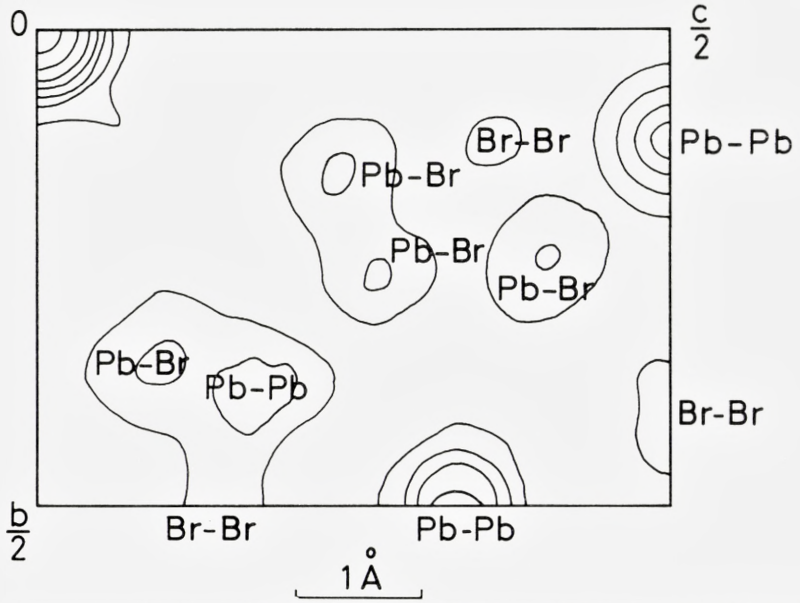

Fig. 1. Patterson projection of Pb(OH)Br on (100). Contours are drawn at the relative densities 0, 50, 100, 150, 200, 300 and 400.

Furthermore it was observed that the I($0kl$) were equal to the I($2kl$) for all k and l, thus suggesting $|F(hkl)| = |F(h+2n, k, l)|$ where n is an integer. This is the kind of relation one would expect for space group no. 62 if there are four molecules in the unit cell so that all the atoms are in the special positions:

$$\frac{1}{4}\,y\,z; \quad \frac{3}{4}\,\bar{y}\,\bar{z}; \quad \frac{3}{4}\,\frac{1}{2}-y\,\frac{1}{2}+z; \quad \frac{1}{4}\,\frac{1}{2}+y\,\frac{1}{2}-z.$$

The arguments for obtaining the atomic positions from now on are nearly the same as in reference[5]. First a Patterson projection on (100) was calculated (fig. 1), and the three strongest maxima were localized which were interrelated in the following way:

$$(2y, 2z) \quad \left(\frac{1}{2}, \frac{1}{2}-2z\right) \quad \left(\frac{1}{2}-2y, \frac{1}{2}\right).$$

They were identified as lead-lead vector maxima and the parameters (y, z) could immediately be obtained. Next an electron projection was evaluated with only those F($0kl$) whose signs could be determined from the lead

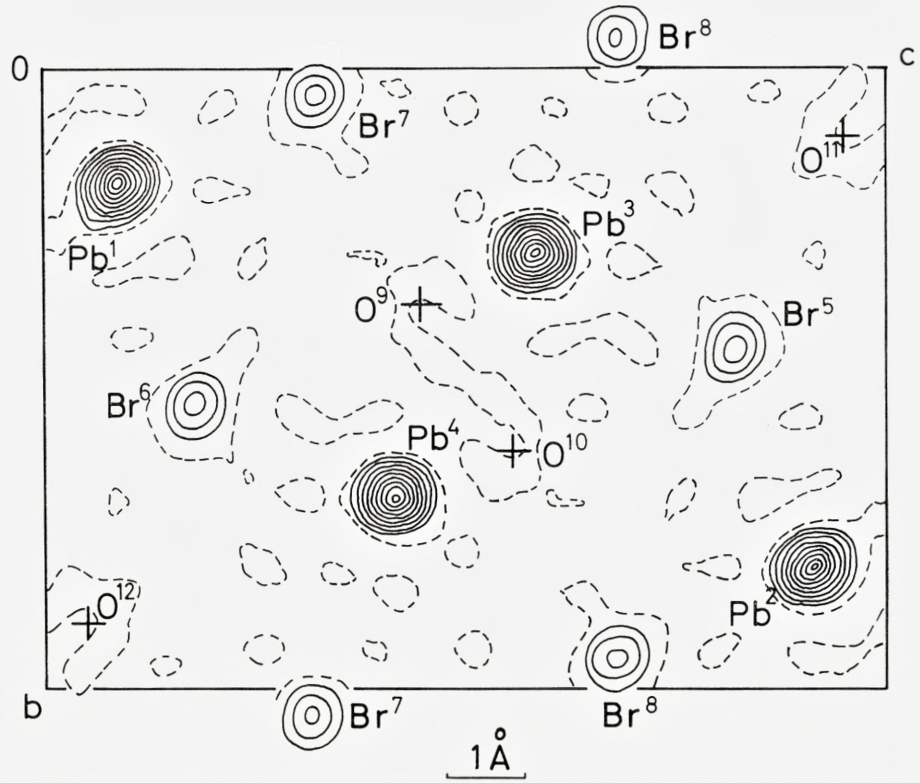

Fig. 2. Electron projection of Pb(OH)Br on (100). Contours are drawn at an interval of 50 of the relative electron density. The zero contour is dashed. The oxygen atoms (from the difference synthesis) are indicated by crosses.

contributions alone with a fair degree of certainty. The electron projection gave two possibilities for the Br-positions but comparison with the Patterson map allowed a decision to be made and in fact all the observed maxima on the Patterson projection could now be assigned to interatomic vectors. Structure factors were now calculated on a GIER-electronic computer using Danielsen's "master program" and atomic scattering factors from FORSYTH and WELLS[6, 7]. Having brought the observed and calculated structure factors on common basis, difference maps were calculated and final parameters for Pb and Br obtained in this way. The difference maps also indicated the positions of the O-atoms, although they could not be located with the same

[6] J. DANIELSEN, Acta Cryst. **16** Suppl. A 171 (1963).
[7] J. B. FORSYTH and M. WELLS, Acta Cryst. **12**, 412 (1959).

certainty as the other atoms. They are marked with crosses in the electron projection (fig. 2).

Structure factors calculated from the finally accepted atomic positions in Table 2 are compared with the observed values in Table 3.

It was also tried to find the oxygen positions from minimization of the reliability index R by systematic variation of the oxygen parameters, again using one of DANIELSEN's programs[6]. But these attempts were not successful because the minima were not well defined. Hence the determination from the difference map is considered the more reliable.

Atomic arrangement and discussion

Interatomic distances calculated on the basis of the parameters in Table 2 are given in Table 4 where a comparison is made with the distances in Pb(OH)I obtained from reference[4], and also with some of the distances in orthorhombic SbSBr. While the arrangement of the lead and the halogen atoms is very similar in the two former compounds, this cannot be said about the oxygen atoms. Although the location of the O-atoms should be taken with some reservation, their positions in Pb(OH)Br do seem more satisfactory than in Pb(OH)I where some of the OH-I-distances apparently are shorter than the sum of the ionic radii for I^- and OH^-: 3.15 Å against 3.6 Å.

Although one of the Pb-O-distances in Pb(OH)Br appears to be unusually short: 2.3 Å, this is not unlikely short. If we compare the shortest lead-halogen distances which have been found in this series of investigation: 3.01 Å in $CsPbI_3$[8], 2.82 Å in $CsPbBr_3$[9], 2.80 Å in $PbCl_2$[10] with the ionic radii of the halogens, an "ionic radius" of 0.9–1.0 Å is estimated for lead in these cases and would presumably also be expected in Pb(OH)Br. (Still shorter Pb(II)-O-distances have been found in orthorhombic PbO and in Pb_3O_4: 2.21 Å, respectively 2.15 and 2.23 Å[11]). The short bonds between the lead atoms and the hydroxyl groups produce chain-like polynuclear ions $(Pb(OH)^+)_n$ running parallel with the a-axis of the crystal. That the same kind of catena-ions occurs also in Pb(OH)I is very likely because Pb-Pb-distances of 3.90_5 Å are found in this crystal which is the same as the analogous distances of 3.93 Å in Pb(OH)Br within the uncertainty of the measurements.

[8] C. K. MØLLER, The structure of $CsPbI_3$, Mat. Fys. Medd. Dan. Vid. Selsk. **32** No. 1 (1959).
[9] A. MARSTRANDER and C. K. MØLLER, The structure of white $CsPbBr_3$. See preceding paper.
[10] R. L. SASS, E. B. BRACKETT and T. E. BRACKETT, J. Phys. Chem. **67**, 2863 (1963).
[11] See e. g. A. F. WELLS, Structural Inorganic Chemistry, 3rd ed. Oxford University Press 1962.

TABLE 3. Comparison of calculated and observed structure factors for Pb(OH)Br (brought on the same relative scale).

Indices $h\,k\,l$	F_{calc} without O	F_{calc} with O	$\lvert F_{obs}\rvert$	Indices $h\,k\,l$	F_{calc} without O	F_{calc} with O	$\lvert F_{obs}\rvert$
0 0 2	22.0	31.4	36	0 3 9	6.6	7.5	—
0 0 4	− 52.1	− 48.6	48	0 3 10	− 32.0	− 31.2	23
0 0 6	− 47.9	− 48.3	50	0 3 11	− 38.6	− 37.8	33
0 0 8	− 47.7	− 49.9	44	0 4 0	29.0	23.6	18
0 0 10	30.7	28.2	26	0 4 1	12.3	13.0	12
0 0 12	46.1	44.2	36	0 4 2	1.9	− 2.3	—
0 1 1	10.8	19.5	21	0 4 3	75.5	77.2	73
0 1 2	− 71.2	− 67.8	67	0 4 4	− 10.0	− 11.8	—
0 1 3	35.5	40.3	43	0 4 5	42.5	44.4	42
0 1 4	− 79.4	− 75.2	70	0 4 6	− 6.7	− 6.4	—
0 1 5	− 46.3	− 45.4	52	0 4 7	− 46.3	− 44.9	49
0 1 6	5.9	8.9	7	0 4 8	− 11.6	− 10.1	7
0 1 7	− 16.9	− 18.1	16	0 4 9	− 32.9	− 32.2	28
0 1 8	51.1	52.9	49	0 4 10	6.8	8.6	—
0 1 9	14.6	12.7	16	0 4 11	− 14.3	− 14.2	11
0 1 10	32.1	32.7	27	0 5 1	56.6	52.3	52
0 1 11	− 2.9	− 4.7	—	0 5 2	24.4	24.0	32
0 1 12	1.5	1.3	—	0 5 3	0.7	− 2.0	—
0 2 0	− 41.8	− 39.4	36	0 5 4	− 16.8	− 17.5	20
0 2 1	− 50.3	− 47.7	49	0 5 5	− 50.5	− 51.1	46
0 2 2	− 55.6	− 53.8	52	0 5 6	9.0	8.4	—
0 2 3	− 48.9	− 43.2	43	0 5 7	− 41.1	− 40.1	36
0 2 4	27.6	28.4	29	0 5 8	2.7	2.3	—
0 2 5	− 12.4	− 6.9	—	0 5 9	2.6	4.3	—
0 2 6	72.7	72.6	69	0 5 10	− 16.9	− 17.0	17
0 2 7	7.2	10.9	—	0 6 0	19.4	17.1	26
0 2 8	4.6	4.1	—	0 6 1	− 45.5	− 46.2	41
0 2 9	38.3	40.0	39	0 6 2	14.7	12.7	17
0 2 10	− 15.2	− 15.8	—	0 6 3	− 45.1	− 46.9	42
0 2 11	12.8	13.0	—	0 6 4	− 10.5	− 11.4	19
0 2 12	− 22.3	− 22.8	20	0 6 5	− 10.8	− 12.9	14
0 3 1	− 71.9	− 74.9	72	0 6 6	− 23.1	− 22.9	27
0 3 2	59.6	63.1	55	0 6 7	4.8	3.1	—
0 3 3	20.0	18.2	21	0 6 8	− 4.7	− 3.9	—
0 3 4	12.3	16.9	15	0 6 9	43.5	42.6	43
0 3 5	38.2	37.8	39	0 7 1	− 27.1	− 27.2	22
0 3 6	7.8	11.6	18	0 7 2	− 17.2	− 18.7	23
0 3 7	42.3	42.8	42	0 7 3	− 8.3	− 8.4	7
0 3 8	− 19.3	− 17.0	—	0 7 4	− 42.0	− 44.2	40

TABLE 3 (continued).

Indices $h\,k\,l$	F_{calc} without O	F_{calc} with O	$\lvert F_{obs}\rvert$	Indices $h\,k\,l$	F_{calc} without O	F_{calc} with O	$\lvert F_{obs}\rvert$
0 7 5	34.5	34.4	24	1 2 11	− 14.2	− 14.3	18
0 7 6	7.2	5.0	—	1 3 1	27.2	33.2	32
0 7 7	23.5	23.6	22	1 3 2	43.1	44.5	48
0 7 8	27.0	25.5	34	1 3 3	21.8	25.3	29
0 8 0	− 50.7	− 49.4	64	1 3 4	67.5	69.4	64
0 8 1	− 0.1	− 0.7	—	1 3 5	− 46.3	− 45.6	47
0 8 2	− 11.0	− 9.9	—	1 3 6	− 7.9	− 6.3	—
0 8 3	21.4	20.1	13	1 3 7	− 23.8	− 24.9	24
0 8 4	20.6	21.2	26	1 3 8	− 40.1	− 39.2	33
0 8 5	14.3	12.6	12	1 3 9	10.4	8.7	—
0 8 6	23.5	23.4	24	1 3 10	− 18.2	− 17.9	12
0 9 2	36.4	36.1	37	1 3 11	6.2	4.6	—
1 0 1	− 11.8	− 14.6	20	1 4 0	97.1	99.6	94
1 0 3	− 98.9	− 105.1	90	1 4 1	0.6	1.9	—
1 0 5	− 54.0	− 59.8	60	1 4 2	17.9	19.7	20
1 0 7	55.2	51.4	52	1 4 3	− 18.0	− 14.9	12
1 0 9	35.8	34.1	28	1 4 4	− 36.0	− 35.2	39
1 0 11	14.5	14.3	8	1 4 5	− 11.3	− 8.1	—
1 1 1	− 84.5	− 78.7	56	1 4 6	− 35.8	− 35.9	35
1 1 2	− 55.6	− 59.3	53	1 4 7	12.7	15.0	—
1 1 3	11.6	14.8	20	1 4 8	− 34.2	− 34.9	29
1 1 4	7.6	2.9	—	1 4 9	5.6	6.7	—
1 1 5	55.0	55.6	60	1 4 10	22.0	21.3	18
1 1 6	− 10.8	− 14.4	17	1 4 11	2.6	2.8	—
1 1 7	48.6	47.7	51	1 5 1	− 4.7	− 5.5	—
1 1 8	8.1	6.1	—	1 5 2	− 54.0	− 52.0	51
1 1 9	2.0	0.6	—	1 5 3	21.0	20.5	19
1 1 10	25.9	25.2	18	1 5 4	− 45.6	− 42.6	42
1 1 11	− 34.8	− 35.9	28	1 5 5	− 19.8	− 20.0	28
1 1 12	− 10.3	− 10.0	6	1 5 6	0.8	3.4	—
1 2 0	− 35.3	− 26.9	24	1 5 7	− 2.8	2.7	—
1 2 1	64.0	63.4	55	1 5 8	34.4	36.1	28
1 2 2	− 39.5	− 33.0	34	1 5 9	10.3	10.6	14
1 2 3	58.5	57.3	52	1 6 0	− 29.2	− 31.7	32
1 2 4	21.3	24.0	27	1 6 1	− 15.2	− 14.7	27
1 2 5	13.3	12.1	18	1 6 2	− 35.2	− 37.2	42
1 2 6	51.7	51.3	55	1 6 3	− 20.0	− 18.5	24
1 2 7	− 6.2	− 7.0	—	1 6 4	18.9	18.0	17
1 2 8	4.8	3.1	—	1 6 5	− 6.7	− 5.1	—
1 2 9	− 45.1	− 45.4	35	1 6 6	51.4	51.5	41
1 2 10	− 11.0	− 12.9	12	1 6 7	5.2	6.4	—

TABLE 3 (continued).

Indices $h\,k\,l$	F_{calc} without O	F_{calc} with O	$\lvert F_{obs}\rvert$	Indices $h\,k\,l$	F_{calc} without O	F_{calc} with O	$\lvert F_{obs}\rvert$
1 6 8	2.8	3.6	—	1 7 7	20.1	20.7	16
1 7 1	− 33.1	− 35.5	31	1 8 0	27.0	25.4	18
1 7 2	34.1	34.1	27	1 8 1	7.3	7.0	—
1 7 3	14.0	12.3	14	1 8 2	2.2	0.8	—
1 7 4	17.5	17.6	12	1 8 3	34.4	33.6	30
1 7 5	13.2	12.8	16	1 8 4	− 9.9	− 10.5	—
1 7 6	2.5	2.6	—	1 8 5	19.5	18.5	14

TABLE 4. Interatomic distances in Pb(OH)Br and in related compounds.

Distance	From this investigation X = Br	From reference[4] X = I	Corresponding distance in SbSBr
Pb^3-X^5	3.32 Å	3.41 Å	
Pb^3-X^6	4.43 -	4.54 -	
Pb^3-X^7	3.24 -	3.49 -	
Pb^3-X^8	3.44 -	3.70 -	2.94 Å
Pb^3-O^9	2.50 -	2.71 -	2.67 -
Pb^3-O^{10}	2.27 -	2.84 -	2.49 -
Pb^3-Pb^4	3.93 -	3.90 -	3.83 -
X^6-O^9	3.62 -	3.70 -	
X^7-O^9	3.54 -	3.15 -	
X^6-O^{12}	3.54 -	3.15 -	
X^6-X^7	4.00 -	4.15 -	
X^7-X^8	4.20 -	4.40 -	
O^9-O^{10}	2.72 -		

In this connection it is interesting that PEDERSEN[12] from pH-measurements on lead(II)nitrate solutions has obtained evidence for the formation of polynuclear ions of the type $Pb_2(OH)$ as well as $(PbOH)_4$, both of which may be regarded as fragments of the poly-ion in the crystals of Pb(OH)Br.

It seems to be a characteristic feature of many crystals containing lead (II) that the lead atoms are incorporated in some kind of polynuclear catena-ions, thus in $CsPbI_3$, $CsPbBr_3$, Pb(OH)Br and presumably also in

[12] K. J. PEDERSEN, The acid dissociation of the hydrated lead ion and the formation of polynuclear ions. Mat. Fys. Medd. Dan. Vid. Selsk. XXII No. 10 (1945).

$PbCl_2$ (though less obvious here). The existence of these chainlike poly-ions in the crystals may explain why these compounds are slightly soluble in water. It also explains why the crystals are needle-shaped and that the refractive index is highest for light vibrating parallel with the needle axis i. e. parallel with the catena-ion.

Within the mentioned poly-ions one of the lead-anion distances is usually much shorter than the others, i. e. the bonding between the lead atom and this particular anion is especially strong and may persist even after dissolution of the crystal. It is in accordance with this that aqueous solutions of the lead halogenides with an excess of halogenide ions contain a fair proportion of the lead as undissociated PbX^+-ions.

The shortest OH-OH-distance is 2.7$_2$Å, and—if reliable—might indicate hydrogen bonding between the hydroxyl groups within the $(PbOH)_n$-framework.

In both Pb(OH)Br and Pb(OH)I the lead-halogen distances are longer than the sum of the ionic radii for the halide ion and lead(II), which is 3.15 Å for Pb-Br and 3.4 Å for Pb-I. The halogen atoms in these crystals may be considered to exist as anions held in positions between the positively charged poly-ions by mere electrostatic forces. Pictorially, one could say that the halogen ions form a system of parallel "tubes", one around each poly-ion.

Finally, it should be pointed out that the structure deduced for Pb(OH)Br is very similar to that found for SbSBr by Christofferson and McCullough[13]. In fact, the two compounds are isostructural; to the chain-like $(PbOH^+)_n$-ion in the former corresponds the poly-ion $(SbS^+)_n$ in the latter, and the Sb-S distances, 2.49 Å and 2.67 Å, are analogous to the Pb-OH distances which have been discussed above (see Table 4).

An unambiguous determination of the oxygen positions in Pb(OH)Br could presumably be made only by neutron diffraction, which might also reveal the hydrogen atoms. This would require bigger crystals than used for the *X*-ray work, and it could perhaps be done more easily on Pb(OH)Cl which occurs as the mineral laurionite.

[13] G. D. Christofferson and J. D. McCullough, Acta Cryst. **12**, 14 (1959).

Acknowledgements

It is a special pleasure for the author to thank cand. mag. B. SVEJGAARD, lecturer in mathematics at the University of Copenhagen, for the programs used for electronic computation of the Fourier syntheses as well as for the program for drawing Fourier maps.

I am also very indebted to Mrs. A. MARSTRANDER who has calculated some of the structure factors and difference maps, and to cand. mag. Mrs. E. BANG for many instructive discussions and for the loan of several special programs.

Chemistry Department I, Inorganic Chemistry,
The H. C. Ørsted Institute,
University of Copenhagen, Denmark.

Indleveret til Selskabet den 28. januar 1966.
Færdig fra trykkeriet den 22. oktober 1966.

Matematisk-fysiske Meddelelser
udgivet af
Det Kongelige Danske Videnskabernes Selskab
Bind **35,** nr. 6

Mat. Fys. Medd. Dan. Vid. Selsk. **35,** no. 6 (1966)

STUDIES ON FUSED SYSTEMS CONTAINING THE 1,4-DIAZEPINE NUCLEUS

BY

STIG VEIBEL AND J. ILUM NIELSEN

København 1966
Kommissionær: Munksgaard

Synopsis

The benzo[*b*]1,4-diazepines formed when β-diketones condense with *o*-phenylenediamine have been studied.

A spectrophotometric method for determination of the basic strength of the diazepines has been elaborated.

The structure of a substituted ethyl pyruvate formed by Claisen-condensation of diethyl oxalate with 5-methyl-7-phenylbenzo[*b*]1,4-diazepine has been established.

Some derivatives of partially hydrogenated 4,8-diazaazulenes have been prepared. The dehydrogenation of these compounds to 4,8-diazaazulenes was not possible.

PRINTED IN DENMARK
BIANCO LUNOS BOGTRYKKERI A/S

I. Structure of 5,7-disubstituted benzo[*b*]1,4-diazepines

THIELE and coworkers[1, 2] found that *o*-phenylenediamine is able to condense with β-dicarbonyl compounds, basic substances showing marked halochromism being formed in the reaction. For the structure of the condensation products two possibilities exist, a symmetrical (I) and an unsymmetrical (II):

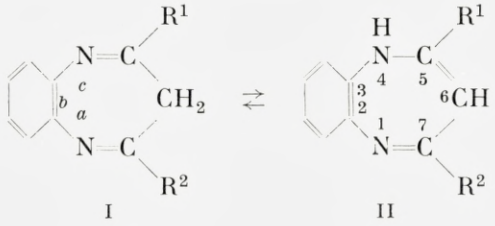

I ⇄ II

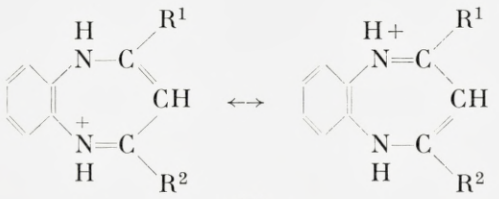

III

Different authors[1–6] have studied the reaction and it is generally accepted that the coloured salts are derived from II, the cation III being stabilised by resonance between several structures, two of which are shown. For the colourless bases the symmetrical structure I is assumed.

According to this assumption the presence of at least one hydrogen atom at C^6 is a condition for obtaining coloured salts of the benzo[*b*]1,4-diazepines.

Several attempts[3, 7] have been made to condense *o*-phenylenediamine with 3,3-dimethylpentane-2,4-dione (3,3-dimethylacetylacetone) but without

success. One reason may be that the presence of at least one hydrogen atom at C^3 in the substituted acetylacetone is necessary for the condensation. This is the opinion of CROMWELL[8], who considers the enolised form of the diketone as the one able to condense with the diamine. Another reason for the inactivity of 3,3-dimethylacetylacetone may be the steric conditions. Thus HALFORD and FITCH[7] point out that if the 5,6,6,7-tetramethylbenzo[*b*]1,4-diazepine were formed, one of the methyl groups on C^6 would have to interfere with the π-orbital of the benzene nucleus, thereby causing such a strain in the diazepine nucleus that the gain in energy obtained by the condensation would not be sufficient to counterbalance the strain established.

BARLTHROP *et al.*[6] claim to have obtained the introduction of a substituent for both of the hydrogen atoms at C^6 in 5,7-dimethylbenzo[*b*]1,4-diazepine by base-catalysed condensation of this substance with one (formula IX below) or two molecules of piperonal. It had been found previously that all benzo[*b*]1,4-diazepines with at least one hydrogen atom at C^6 in acid solution show a lowintensity absorption in the region of 5000 Å. The UV-spectra of the condensation products obtained by BARLTHROP *et al.* showed no such absorption and therefore the English authors are of the opinion that the first molecule of piperonal will condense on the methylene group, the next molecule of piperonal then attacking one of the methyl groups at C^5 and C^7. In both condensation products the C^6-atom should thus be sp^2-hybridized and the substances should, as the 6,6-disubstituted substance, be without the hydrogen atom necessary for the formation of the unsymmetrical structure.

We have repeated BARLTHROPS experiments but we cannot confirm that the condensation takes place on the methylene group. On the contrary, by examining the IR-spectra we have found that the aldehyde reacts only with the methyl group(s), thereby forming 5-mono- or 5,7-di-(3,4-methylenedioxystyryl)benzo[*b*]1,4-diazepines, the first one corresponding to formula IV below ($R^1 = CH_2O_2C_6H_3CH{=}CH-$). The evidence for this formulation is:

The substance containing one piperonylidene residue shows absorption at 1427 cm^{-1} and at 1364 cm^{-1}, corresponding to the absorption of a methyl group, but these absorptions are not found in the substance containing two piperonylidene residues. Otherwise the spectra of the two compounds are very much alike. They have an absorption at 960 cm^{-1} which we ascribe to the $-CH{=}CH-$ (trans) out-of-plane vibration. If the methylene group had reacted a $>C{=}CH-$ out-of-plane vibration should be expected to appear near 800 cm^{-1}.

Our formulation explains better than BARLTHROP's the products which he found by hydrolysis of the substance formulated by him as 5,7-dimethyl-3-piperonylidene-benzo[*b*]1,4-diazepine.

By hydrolysis of benzo[*b*]1,4-diazepines a (substituted) benzimidazole and a ketone are formed. With different substituents at C^5, C^6 and C^7 two different benzimidazoles and two different ketones may be formed (see formulas IV–VIII). According to generally accepted views the first step in

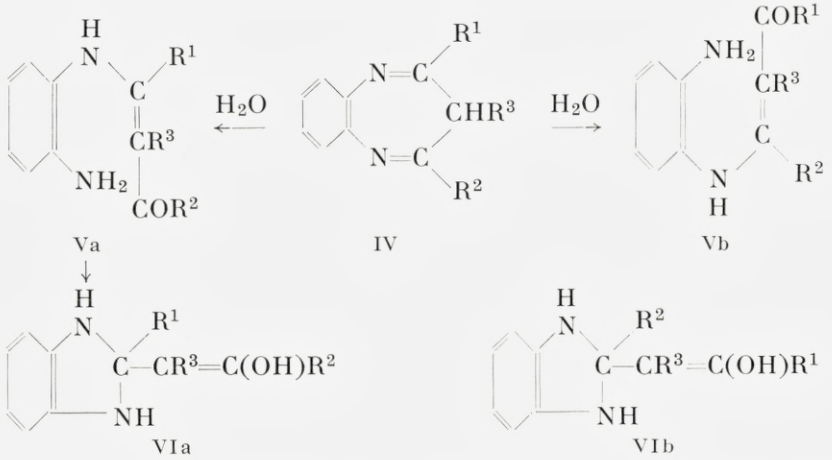

the hydrolysis is the formation of an anil which tautomerises to an α,β-unsaturated ketone (IV → Va or Vb). The next step is a 1,4-addition of the free amino group to the system of conjugated double bonds, and finally a stabilisation is obtained by the formation of benzimidazole and ketone (VIa → VII or VIb → VIII):

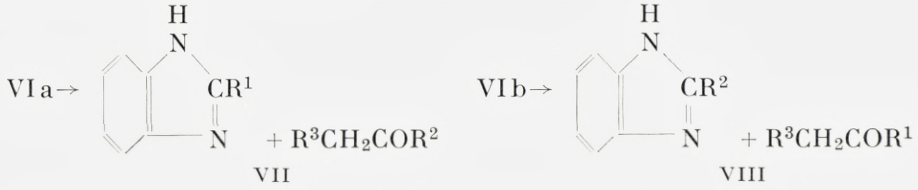

If, however, R^1 and R^2 are both CH_3 and R^3 is linked to C^6 by a double bond the first product of hydrolysis becomes the real anil, no hydrogen atom being present at C^6 to allow the formation of an α,β-unsaturated ketone able to be the precursor of benzimidazole-formation. Instead, an addition of the amino group over the –N=C-double bond might take place, fol-

lowed by a stabilisation to 2-methylbenzimidazole and piperonylideneacetone (IX–XIII; R = $CH_2O_2C_6H_3$–):

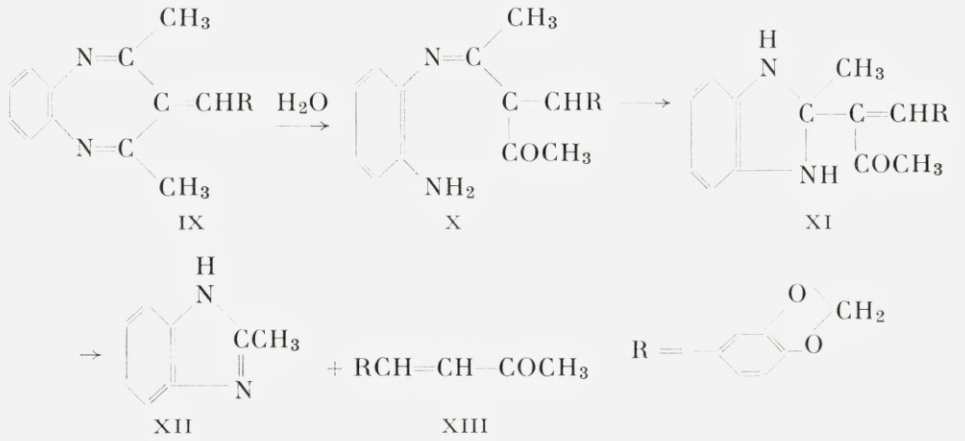

Barlthrop found these two products of hydrolysis and besides 2-(3,4-methylenedioxystyryl)benzimidazole (XVI) which cannot possibly be formed by simple hydrolysis of the 6-piperonylidene-substituted benzo-diazepine, whereas all 3 products of hydrolysis can be explained if the piperonal has reacted with one of the methyl groups instead of with the methylene group (XIV–XVI):

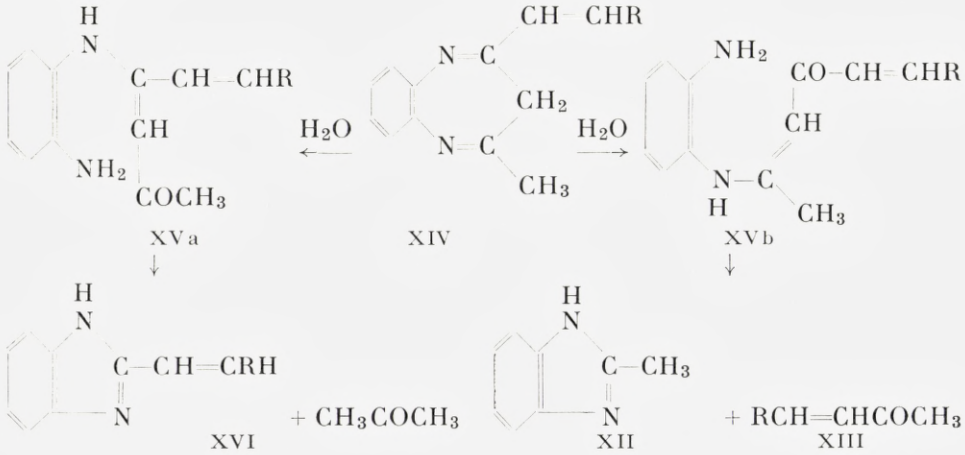

Of these products of hydrolysis only acetone, which may easily have escaped during the hydrolysis, has not been isolated, and we therefore

regard the condensation of the aldehyde on the methyl group more likely than the condensation on the methylene group.

The reaction of aromatic aldehydes with 5,7-disubstituted benzo[*b*]-1,4-diazepines is a base-catalysed reaction, and as shown is the methyl groups at C^5 and C^7 more reactive than the C^6-methylene group. Simple base-catalysed alkylation (*e.g.* with methyl iodide), on the other hand, leads to alkylation at C^6. In both instances it is the C=N-double bonds in the symmetrical structure I which activate a hydrogen atom in the methyl- or the methylene group, the anion left after elimination of a proton from the diazepine existing in tautomeric structures XVII and XVIII:

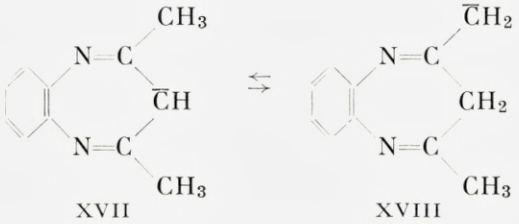

XVII XVIII

N-Methylsubstituted benzo[*b*]1,4-diazepines have been prepared from *N*-methyl-*o*-phenylenediamine and *β*-diketones[9]. They form, as the 6-unsubstituted or monosubstituted, *N*-unsubstituted benzo[*b*]1,4-diazepines, intensely coloured salts with acids, corresponding to the structure III.

Contrary to the base-catalysed substitution acid-catalysed electrophilic attack will take place at N^1 or at C^6.

Substances for which the symmetrical structure I for the benzo[*b*]1,4-diazepine system is assumed are colourless with the exception of the 6-bromo-, 6-phenyl- and the 6-nitroderivatives, all of which are red coloured substances with high melting points (184°, 268° and 361°, respectively). The colour is, however, according to Ruske and Hüfner[10], not due to an unsymmetrical structure of the ring-system, but to a "cryptoionic" arrangement XIX:

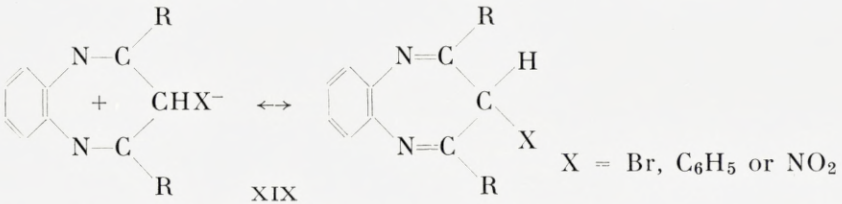

XIX X = Br, C_6H_5 or NO_2

For the two first mentioned substances Ruske and Hüfner have shown the absence of NH-groups by IR-spectroscopy. For the third a "cryptoionic"

formulation would be XX. STAFFORD, REID and BARKER[11] are, on the other hand, of the opinion that the properties of this substance are better explained by the formulation XXI:

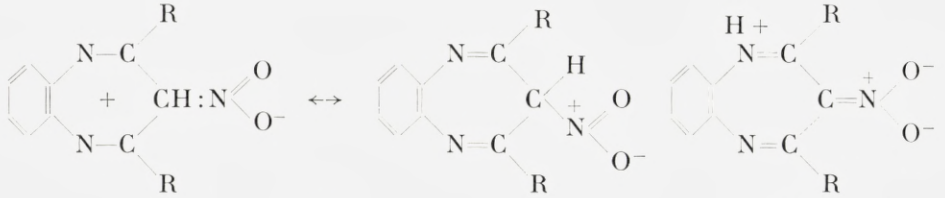

XX XXI

p-Nitrobenzenediazonium ions couple with 5,7-diphenylbenzo[*b*]1,4-diazepine at C^6 (BARLTHROP *et al.*[6]), forming a yellow *p*-nitrophenylhydrazone XXII or XXIII. By IR-spectroscopy the presence of an NH-group was established. The colour could therefore be due to the unsymmetrical diazepine ring, but as no colour shift takes place when the substance is dissolved in acid, the phenylhydrazone-structure is more likely than the azocompound-structure.

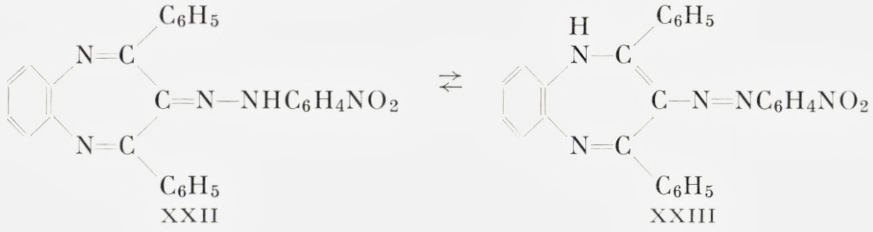

XXII XXIII

Basic strength of the benzo[*b*]1,4-diazepines

When the free benzo[*b*]1,4-diazepines are liberated from solutions of their salts by addition of a base the solution remains dark coloured for some seconds, but then colourless, crystalline substances spontaneously precipitate. When the coloured salts are treated with concentrated hydrochloric acid colourless salts with two equivalents of acid are formed. These salts are unstable in an atmosphere not saturated with hydrogen chloride, the coloured mono-salts being formed spontaneously by splitting off one molecule of hydrogen chloride from the colourless salt[2, 12].

STEIMMIG[2] and with him all later investigators (latest LLOYD *et al.*[12]) assume for the colourless substances structure I, for the coloured structure

II. I remains symmetrical and thus colourless when two protons are taken up, whereas II by addition of one proton is transformed to the resonance-stabilised, coloured cation III (see *e.g.* VAISMAN[3]).

No explanation has been given for the colour of the unsymmetrical free base II. An explanation may possibly be found, for the free base as well as for the mono-cation, when comparing their structure with the structures of the cyanine dyes XXIV and XXV[13]: For II resonance structures with separate charges as in the unsymmetrical cyanines may be written (XXVI):

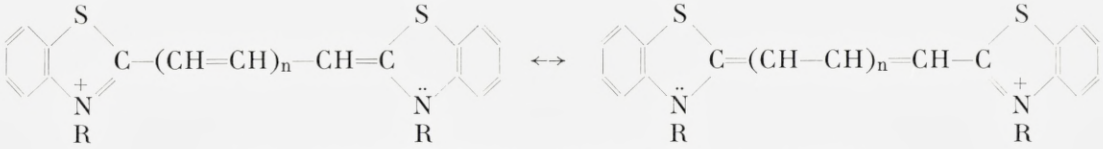

XXIV. Symmetrical cyanines, absorption for n = 0 at 4300 Å.

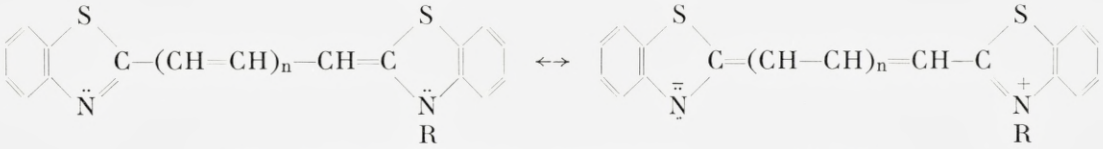

XXV. Unsymmetrical cyanines, absorption for n = 0 at 3700 Å.

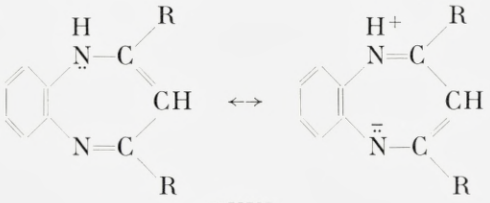

XXVI

In all three cases a double vinyl-shift of electrons will transfer one canonical structure into the other.

Of the two structures I and II the unstable, unsymmetrical structure II, according to SCHWARTZENBACH and LUTZ[4] and to LLOYD *et al.*[12], is the strongest base with a pK_a-value of 9.0 in aqueous solution, whereas pK_a for the equilibrium mixture was found to be 4.5.

The symmetrical structure I is stabilised by the two C=N double bonds in conjugation to the aromatic benzene system. For other 1,4-diazepines without annellation to an aromatic system the unsymmetrical form is the most stable, as shown *e.g.* for 2,3-dihydro-5,7-dimethyl-1,4-diazepine, XXVII and XXVIII (SCHWARTZENBACH and LUTZ[4]).

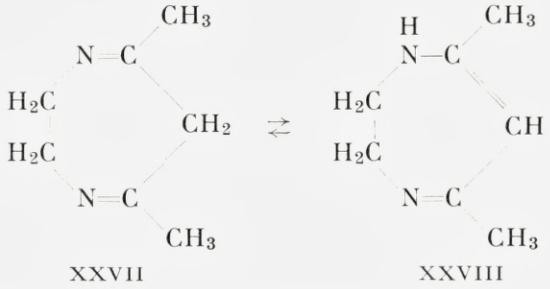

XXVII XXVIII

It is seen that XXVIII is stabilised by the $-NH-C(R)=CH-C(R)=N-$ conjugation. XXVII is a diketimine, XXVIII a monoketimine-monoenamine, and as in open-chain compounds the equilibrium diketimine $\rightleftarrows$ monoketimine-enamine is displaced still more towards monoketimine-enamine than is the displacement towards the ketone-enol structure in β-diketones, it is reasonable to assume that the unsymmetrical structure is the most stable.

This assumption has recently been confirmed by STAAB and VÖGTLE[14], using NMR-spectroscopy. The following signals were found:

$\delta = 7.76$ Integrated to one proton.
$\delta = 4.40$ Integrated to one proton.
$\delta = 3.42$ Integrated to 4 protons, corresponding to 2 methylene groups, placed nearly identically.
$\delta = 1.88$ Integrated to 6 protons, corresponding to 2 methyl groups.

Of the two signals given by single protons that at $\delta = 7.76$ corresponds to the NH-group (N^1), that at $\delta = 4.40$ to the $\rangle CH$-group (C^6).

For the benzo[*b*]1,4-diazepines STAAB and VÖGTLE found the symmetrical structure confirmed by the NMR-spectrum. No signals corresponding to NH-groups or a $\rangle CH$-group were found. A signal at $\delta = 2.70$ was integrated to two protons, corresponding to a methylene group (at C^6). As the seven-membered ring is not plane the methylene group should give rise to a doublet. At 39° a singlet is found, but at −50° the singlet is broadened, showing a slight difference between the two protons.

The monocation of this substance is of course unsymmetrical, but dissolved in concentrated sulphuric acid a symmetrical structure is again formed, the two NH^+-groups giving rise to a signal at $\delta = +13.4$. This signal disappears when an exchange of D^+ for H^+ has taken place.

We have prepared 5,7-dimethyl-2,3-dihydro-1,4-diazepines by condensation of acetylacetone with cyclopentylene-1,2-diamine and indanylene-

1,2-diamine, respectively. A study of the infrared spectrum of 5,7-dimetylcyclopenta[*b*]1,4-diazepine (XXIX) and 5,7-dimethylindano[1,2-*b*]1,4-diazepine (XXX) and the IR-spectra of a series of benzo[*b*]1,4-diazepines has confirmed that in the benzo[*b*]diazepines no absorption corresponding to a NH-stretching is found, whereas in the two "non-aromatic" diazepines an absorption at 3240–3210 cm^{-1} indicates the presence of an NH-group.

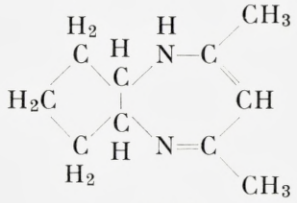

XXIX

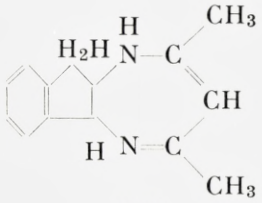

XXX

The "non-aromatic" diazepines are, therefore, considerably stronger bases than the benzo[*b*]1,4-diazepines. Schwartzenbach and Lutz[4] have determined the pK_a-value of XXVIII to 13.8, and Lloyd *et al.*[12] indicate for this substance $pK_a = 13.4$.

The existence of two tautomeric forms of 6-mono- or unsubstituted benzo[*b*]1,4-diazepines with very different basic strengths makes it difficult to determine the real pK_a-value of one of the two forms without knowledge of the equilibrium constant of the tautomeric system. Schwartzenbach and Lutz[4] have, for the above mentioned estimation of pK_a-values, used a complicated system of potentiometric measurement of pK_a immediately after the liberation of the base from its salt, *i.e.* before the establishment of the equilibrium I $\rightleftarrows$ II. They found an initial value of $pK_a = 9.0$, which dropped to $pK_a = 4.5$ when the equilibrium had been established. This means that the equilibrium in aqueous solution is nearly quantitatively displaced towards I, a result which as mentioned above has been corroborated by spectroscopic studies, both UV, IR and NMR-spectra.

We found it possible to determine the apparent pK_a-value of the equilibrium system I $\rightleftarrows$ II, using UV-spectroscopy. As mentioned above Barlthrop *et al.*[6] found that the violet benzodiazepinium ion shows a lowintensity absorption at about 5000 Å, an absorption which the neutral molecule does not show. The absorption at a given pH will therefore be dependent on the fraction of the benzodiazepine present as benzodiazepinium ion. By measuring the absorption at different pH-values and considering the benzodiazepinium ion as an acid, the free benzodiazepine molecule as the corresponding base a plot of $D = \log I_0/I = \varepsilon \cdot c \cdot l$ against pH will allow the determination

of pK_a of the system I $\rightleftarrows$ II $\underset{OH^-}{\overset{H^+}{\rightleftarrows}}$ III (D = optical density, I_0 and I = intensity of the incident and the transmitted light, c = total concentration of (protonised and unprotonised) benzodiazepine and l the path lenth of light through the solution, in cm.

In the first approximation we disregard the equilibrium I $\rightleftarrows$ II and consider only the equilibrium between III and (I + II), *i.e.* the benzo[*b*]-diazepinium ion and the "benzo[*b*]diazepine base". We then have:

(1) $pH = pK_a + \log c_b/c_a$
where c_b is the concentration of the free benzodiazepine, c_a the concentration of the benzodiazepinium ion.

(2) $c = c_b + c_a$
c being the total concentration of benzodiazepine, calculated from the amount of benzodiazepinium salt weighed out.

(3) $pH = pK_a + \log [(c - c_a)/c_a]$
which by multiplication of the logarithmic expression with ε/c gives

(4) $$pH = pK_a + \log \frac{\varepsilon - \frac{\varepsilon \cdot c_a}{c}}{\frac{\varepsilon \cdot c_a}{c}} .$$

As c_a is the concentration of the absorbing molecules we have

(5) $D = \varepsilon \cdot c_a \cdot l$ or $\varepsilon \cdot c_a/c = D/l \cdot c = \varepsilon'$,

ε' thus being the apparent molar extinction coefficient, disregarding that only a fraction of the substance present will absorb at the wavelenth considered.

By introducing (5) in (4) we get

(6) $pH = pK_a + \log [(\varepsilon - \varepsilon')/\varepsilon']$.

By measuring D at a series of known pH-values (buffer solutions) ε' can be calculated for the pH-values considered, l and c being known. The only unknown quantities in (6) are thus pK_a and ε, the molar extinction coefficient of the benzodiazepinium ion. In determining two not interdependent sets of values of pH and ε' and introducing these values in (6) 2 equations with 2 unknown quantities will allow the calculation of pK_a and ε.

The following procedure was used:

Phosphate-buffers were prepared according to BJERRUM[15]. It was planned to dissolve the benzodiazepines in these buffer-solutions to a concentration of $10^{-4} - 10^{-5}$ *M*, but some of the benzodiazepines were not sufficiently soluble in aqueous buffers with pH above 4. We therefore used an ethanol/water buffer system with 50 % (by volume) of ethanol which allowed the preparation of solutions of all the benzodiazepines investigated up to pH about 14. The pH-values in the ethanol/water system are different from those indicated by BJERRUM for aqueous solutions and had to be determined potentiometrically, using a pH-meter calibrated by means of the aqueous buffer solutions.

a. pK_a of 5-methyl-7-phenylbenzo[b]1,4-diazepinium ion.

The absorption of $10^{-4} - 10^{-5}$ *M* solutions of this compound was measured at 5060 Å at 6 different pH-values, ε' calculated for each pH (equation (5)) and plotted against pH, see table I and fig. 1.

TABLE I. Determination of ε' for the 5-methyl-7-phenyl-benzo[*b*]-1,4-diazepinium ion.

	1	2	3	4	5	6	7
pH	−0.7	0.43	1.57	3.45	4.34	5.83	6.20
ε'	1.43	1.367	1.343	1.226	0.905	0.110	0.0594

From equation (6) it is seen that this plot is a titration curve for the diazepinium ion, and pK_a is thus pH at the point of veering, 4.7.

This graphical method is, however, not sufficiently accurate. More reliable results are obtained by inserting in (6) a series of corresponding values of pH and ε', calculating the corresponding pK_a-values and ascribing each pK_a-value a weight from 1 to 6 according to how the two points are situated on the curve drawn through all the experimental points (fig. 1). The results of this calculation are given in Table II.

TABLE II. Weighted determination of pK_a for the 5-methyl-7-phenylbenzo[*b*]1,4-diazepinium ion.

Combination ...	2–5	2–6	3–5	4–5	4–6	4–7	5–6
ε	1.368	1.366	1.348	1.290	1.232	1.271	1.191
pKa	4.63	4.77	4.65	4.84	4.82	4.89	4.85
Weight.....	1	3	3	4	5	5	6

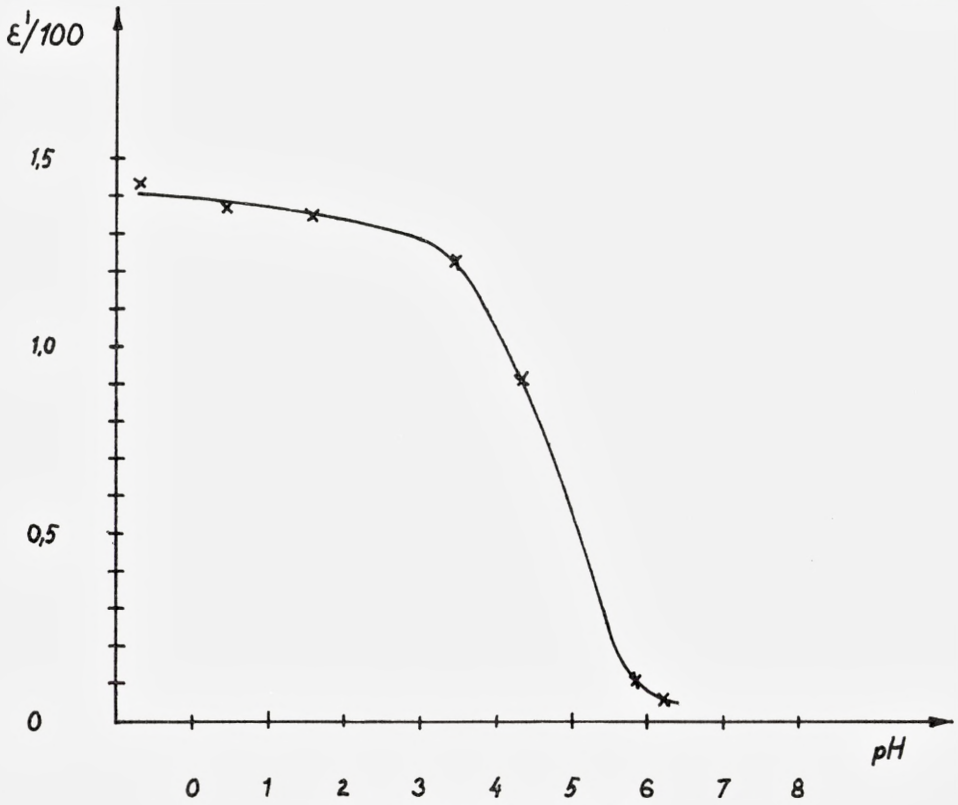

Fig. 1. Variation of ε' with pH.

The average weighted value of pK_a is 4.81, of pK_b thus 9.19.

The same procedure was followed for determining the pK_a for the 5,7-dimethylbenzo[*b*]1,4-diazepinium ion. Graphically pK_a was determined to 5.55; the weighted values were $pK_a = 5.76$, $pK_b = 8.24$.

The pK_a-value for the equilibrium mixture of 5,7-dimethylbenzo[*b*]1,4-diazepine was determined by SCHWARTZENBACH and LUTZ[4] to 4.5; for the unsymmetrical structure II the value was found to be 9.0. As it seems reasonable to locate the protolytic activity to the unsymmetrical structure, at all events in the first approximation, this means than the equilibrium constant for the equilibrium I $\rightleftarrows$ II is $10^{-4.5}/10^{-9.0} = 10^{4.5}$.

From the value 5.76 for pK_a in 50 % ethanolic solution it is seen that the equilibrium in this solvent is displaced somewhat, but not much, towards I as the equilibrium constant here is $10^{-5.8}/10^{-9.0} = 10^{3.2}$.

The spectroscopic method for determining the basic strength of the benzodiazepines is more complicated than the potentiometric titration usually applied for such determinations. The potentiometric method implies a linear dependence between the half neutralisation potentials and pK_a, which is usually found within certain limits, determined mainly by the protolytic activity of the solvent used. In order to use this linear dependence it is necessary to know the pK_a-values of at least two bases of the type considered. By plotting the half neutralisation potentials of these two bases against their pK_a-values the straight line drawn through these two points may be used for determining the basic strength of other bases of the same type, their pK_a-values being the abscissae corresponding to the half neutralisation potentials found when titrating the bases.

We have applied this method for the determination of approximative pK_a-values of the substituted benzo[*b*]1,4-diazepines listed in Table III, using the half-neutralisation potentials of the substances 3 and 6 and their pK_a-values found by the spectroscopical method for drawing the line illustrating the dependence between half neutralisation potentials and pK_a. The diazepines were dissolved in acetonitrile (0.1 millimole in 50 ml) and titrated with 0.1 *N* perchloric acid in dioxan. Table III and fig. 2 give the results.

TABLE III. Half neutralisation potentials and pK_a-values of some substituted benzo[*b*]1,4-diazepines.

Substance	Half neutralisation potential (mV)	pKa
1. 5-Methyl-7-(3,4-methylenedioxystyryl)benzo[*b*]1,4-diazepine	−134	5.2
2. 5,7-bis(3,4-methylenedioxystyryl)-benzo[*b*]1,4-diazepine ...	−230	4.4
3. 5,7-Dimethylbenzo[*b*]1,4-diazepine	− 76*	5.76*
4. 5,6,7-Trimethylbenzo[*b*]1,4-diazepine	−178	4.8
5. 5,7-Diphenylbenzo[*b*]1,4-diazepine.....	−295	3.8
6. 5.-Methyl-7-phenylbenzo[*b*]1,4-diazepine	−180*	4.81*

The points marked with an asterisk used for drawing the line.

These results are only approximate values for at least two reasons:

1). The points used for drawing the line have been fixed by using the pK_a-values found in 50 % ethanol, but the titrations were carried out in acetonitrile/dioxan where the equilibrium constant I $\rightleftarrows$ II is not known, and as shown above the equilibrium is dependent on the solvent.

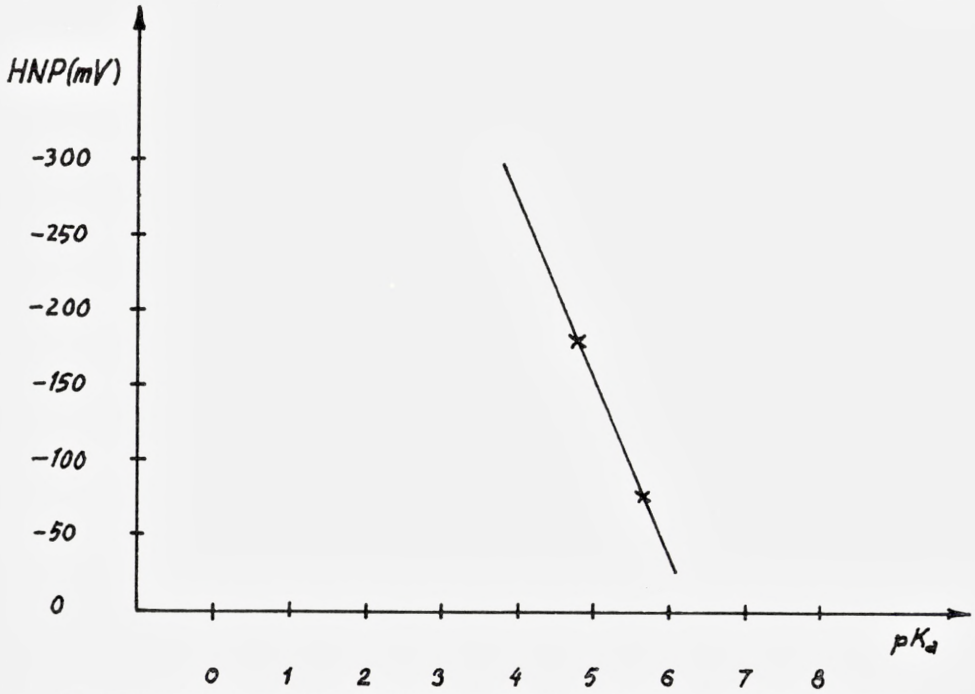

Fig. 2. Potentiometric determination of pK_a for substituted benzo[*b*]1,4-diazepines.

2). Possibly for this reason, possibly for other reasons too, the slope of the line $pK_a = f(HNP)$ is 100 mV per pK_a-unity, whereas it according to HALL[16] should be only 59 mV.

Nevertheless, we are confident that they represent the relative basic strengths of the benzodiazepines studied. The values found reflect in fact the influence expected of the electronegativity of the substituents in the seven-membered ring on the basic strength of the substances.

III. Structure of ethyl 7-phenylbenzo[*b*]1,4-diazepinyl-5-pyruvate, formed by condensation of diethyloxalate on 5-methyl-7-phenylbenzo[*b*]-1,4-diazepine

STEIMMIG[2] prepared a pyruvic ester by Claisen-condensation of diethyl oxalate on 5-methyl-7-phenylbenzo[*b*]1,4-diazepine, using sodium ethanolate as catalyst, whereas VEIBEL and HROMADKO[17] thought they obtained a substituted 5,8-diaza-benzo[*g*]azulene when potassium ethanolate was used as catalyst for the Claisen-condensation (cf. VEIBEL and ILUM NIELSEN[18]).

We have confirmed both types of condensation and have discussed the results when potassium ethanolate is used as catalyst. Here we discuss the results obtained when carrying out the condensation *ad modum* STEIMMIG, the main difference between the two *modi* being (1) that *ad modum* STEIMMIG the reaction mixture remains basic and the product obtained precipitates from the basic solution, whereas *ad modum* VEIBEL and HROMADKO the reaction mixture is acidified before isolating the precipitate. Besides, there are differences in (2) the amount of catalyst used and (3) the temperature, STEIMMIG using 1 mole of sodium ethanolate per mole of diethyl oxalate and operating at the reflux temperature of an ether/ethanol mixture 6:1 (by volume), VEIBEL and HROMADKO using 2 moles of potassium ethanolate per mole of diethyl oxalate and operating at the temperature of the ice-box (0–2°).

Operating *ad modum* STEIMMIG we obtained as he did a yellow precipitate with m.p. 150.5–151.5° in 50 % yield. This substance is the pyruvic ester. When the filtrate from this precipitate was acidified with acetic acid a red precipitate, identical with the substance isolated by VEIBEL and HROMADKO, is obtained. This red precipitate had not been described by STEIMMIG.

When water is added to the reaction mixture before filtering off the precipitate (the potassium salt of the end form of the pyruvic ester) the salt will dissolve. When the alkaline solution is left to stand for some time another substance precipitates. It was found to be the potassium salt of 3-(7-phenylbenzo[*b*]1,4-diazepinyl-5)-pyruvic acid, from which the free acid could be liberated by addition of acetic acid to an aqueous solution of the salt.

Repeating an experiment of STEIMMIG, who refluxed a methanolic solution of the yellow ester for 1 hour, we obtained, as he did, a mixture of yellow and violet crystals which could be separated by extraction with boiling ligroin, in which the yellow crystals, but not the violet, dissolved. M.p. of the violet crystals is 167.5–168.5°.

STEIMMIG assumed for the yellow ester the structure XXXI or XXXII,

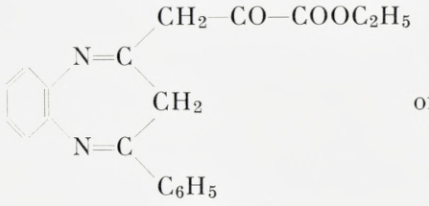

XXXI

or

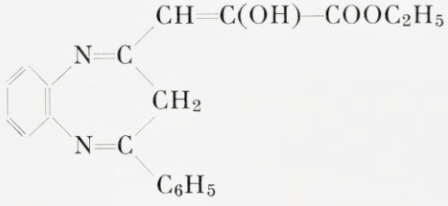

XXXII

for the violet ester the structure XXXIII or XXXIV,

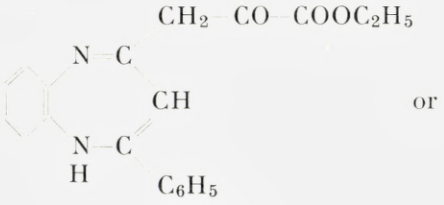

XXXIII

or

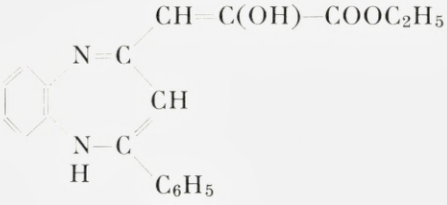

XXXIV

other possibilities, not discussed by STEIMMIG, being XXXV, XXXVI or XXXVII.

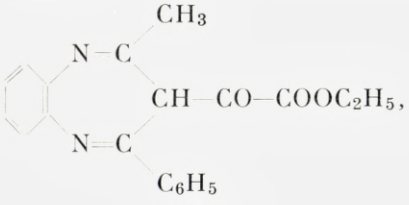

XXXV

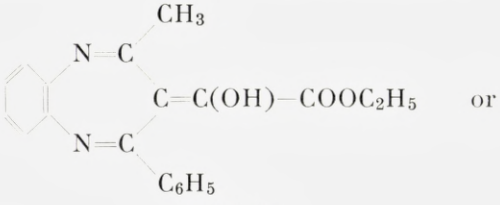

XXXVI

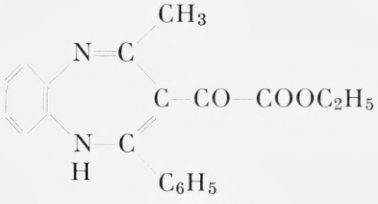

XXXVII

IR-spectra obtained using potassium bromide technique indicated that the yellow ester in the solid state, showing neither OH- nor NH-absorption, must be either XXXI or XXXV, the violet ester, showing OH- or NH-absorption, one of the other structures.

We have tried to exclude some of these possibilities by studying the NMR-spectra of the yellow substance dissolved in deuterochloroform. The following signals were observed:

1. δ = 13.2, integrated to 1 proton, not split up.
2. δ = 8.0–7.25, fixed to 9 protons, characteristic for aromatic protons in *o*- or monosubstituted benzene nuclei.
3. δ = 6.15, integrated to 1 proton, not split up.
4. δ = 4.50–4.15, integrated to 2 protons (a quadriplet, 1331).
5. δ = 3.50, integrated to 2 protons, not split up.
6. δ = 1.50–1.25, integrated to 3 protons (a triplet, 121).

Signal 1 may be OH or NH.

Signal 2 corresponds to the aromatic protons. Their number is fixed to 9, forming the basis for the calculation of the number of protons corresponding to the other signals.

Signal 3 is a single proton at a $-C=C-$ double bond. The neighbouring carbon atoms can have no protons as the signal is not split up.

Signal 4 is in the methylene region. As it is split up to a quadruplet it must be located as neighbour to a carbon atom with 3 protons.

Signal 5 is at so low a δ-value that it might be an $-OCH_3$ group but its size shows that it must be a methylene group. The neighbouring carbon atoms have no protons as the signal is not split up.

Signal 6 corresponds to the methyl group in the ethyl radical as the triplet indicates a neighbouring group with two protons.

The signals 4 and 6 together correspond to the $-COOC_2H_5$ group.

As one and only one methylene group beside the one in the ester is seen, the structures XXXI, XXXIV, XXXV, XXXVI and XXXVII must be eliminated. The structures XXXV, XXXVI and XXXVII are eliminated also because they claim the presence of a methyl group beside the one in the ester.

This leaves only the structures XXXII and XXXIII for the yellow ester dissolved in chloroform, which means that XXXI will tautomerise to XXXII or XXXIII when dissolved.

A peculiar observation was made in connection with the preparation of a perchlorate of Steimmigs ester (yellow form). The ethanolic-ethereal solution of the ester turned dark on addition of perchloric acid, but the perchlorate isolated was yellow. We therefore considered the possibility of the formation of a di-perchlorate, but elemental analysis showed the substance to be a mono-perchlorate.

The IR-spectrum showed differences from IR-spectra of the violet salts of other benzodiazepines. No absorption was found at 1460 cm^{-1} or at 1360 cm^{-1}, but an absorption due to the perchlorate ion (at about 1070 cm^{-1}) is visible. Besides, a broad absorption band is seen at about 3000 cm^{-1}.

The absorption at 1070 cm^{-1} means that the substance has taken up a proton. As this does not lead to a coloured cation the conditions for resonance must be different from those in the previously considered benzo[*b*]-1,4-diazepine cations. A structure like XXXVIII might explain both the absorption at 3000 cm^{-1} and the lack of resonance. A hydrogen bonding from the enolised carbonyl function to the N^4-nitrogen atom is sufficiently strong to prevent this atom from taking up the proton which, therefore, is

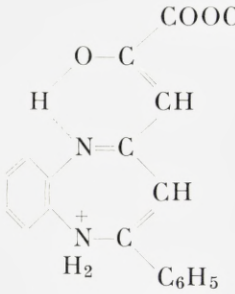

XXXVIII

taken up by the N^1-nitrogen atom, forming a grouping $-\overset{+}{N}H_2-C<$. This grouping may be responsible for the absorption at 3000 cm^{-1}, which also may include an absorption caused by the $-O-H\cdots N<$ hydrogen bond.

IV. Experiments aiming at the preparation of derivatives of 4,8-diazaazulenes

Veibel *et al.*[17, 18] having shown that derivatives of 4,9-diazabenzo[*f*]-azulene can be formed by a double Claisen-condensation of diethyl oxalate on a 5-methylsubstituted benzo[*b*]1,4-diazepine, we considered the possibility of preparing diazaazulenes not fused to a benzene nucleus by reacting a β-diketone with cyclopentylene-1,2-diamine.

Treibs and coworkers[19, 20], working on the preparation of azaazulenes with N in the 7-membered ring, arrived at the conclusion that owing to the greater electronegativity of nitrogen as compared with carbon a nitrogen in the 7-membered ring will cause a decrease in the aromaticity of the azulene system. Peters[21] has expressed a similar opinion, based on calculation of the distribution of π-electrons, using Hückels L.C.A.O. molecular orbital theory.

Treibs *et al.*[19, 20, 22] succeeded in preparing benzo-monoazaazulenes with nitrogen in the 7-membered ring. The compounds showed, as expected, considerably less aromatic character than nitrogenfree azulenes. Hafner and Kreuder[23] have prepared the unsubstituted 5-azaazulene which they describe as a substance stable dissolved in water or in organic solvents. As a solid (m.p. 35°), however, it is stable only in an inert atmosphere. It is to be expected, therefore, that 4,8-diazaazulenes will be still less aromatic and possibly not even stable.

We found it possible to prepare 5,7-dimethyl-1,2,3,3a,8,8a-hexahydro-4,8-diazaazulene or 5,7-dimethyl-2,3-dihydrocyclopenta[*b*]1,4-diazepine (XXXIX), but all attempts to dehydrogenate this compound failed.

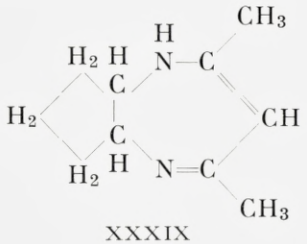

XXXIX

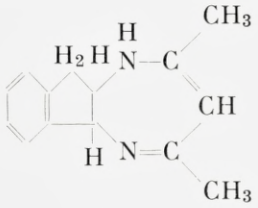

XL

We then tried to increase the tendency to create an aromatic system by fusion of the cyclopentylenediamine with a benzene nucleus, using indylene-1,2-diamine instead of cyclopentylene-1,2-diamine. Here, too, we succeeded in preparing a hydrogenated diazaazulene-derivative (XL), although in a very poor yield, but as above all attempts to dehydrogenate the compound to the fully aromaticised system failed.

The preparation of the indanylene-1,2-diamine by reduction of indane-1,2-dione dioxime or its diacetate was extremely difficult. 6 atoms of hydrogen per molecule of the dioxime diacetate were easily taken up, but then the reduction came to a standstill. We were able to prove by NMR-spectroscopy that the substance obtained after uptake of 6 atoms of hydrogen is 1,2-diacetaminoindene (XLI). Experimental details are given below, but the evidence for the structure of the compound is given here.

A solution of the substance in dimethylsulfoxide gave the following signals:

1. δ = 1.65 a double signal with 2 peaks of nearly the same size, corresponding together to 6 protons.
2. δ = 4.15 a single peak corresponding to 2 protons.
3. δ = 7.50 a single peak corresponding to 4 protons.
4. δ = 6.50 a single bond corresponding to 2 protons.

For a substance obtained from indane-1,2-dione dioxime diacetate by reduction with 6 equivalents of hydrogen the structures XLI–XLIV have to be considered.

Signal 1 corresponds to two nearly identical methyl groups without hydrogen at the neighbouring carbon atoms, *i.e.* the two CH_3CO-groups.

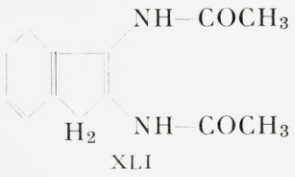

XLI

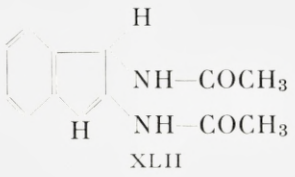

XLII

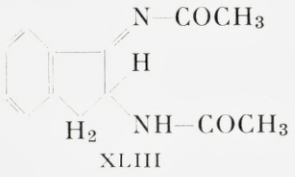

XLIII

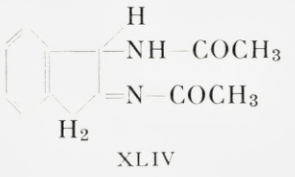

XLIV

Signal 2 corresponds in size and position to a methylene group. As it is not split up no hydrogen atom can be present at the neighbouring carbon atoms. This signal thus eliminates XLII, which contains no methylene group, and XLIII, which has a hydrogen atom at one carbon atom neighbouring the methylene group.

Signal 3 is easily interpreted as the 4 aromatic protons.

Finally, it must be concluded from signal 4, showing two nearly identical protons, that structure XLI is more likely than structure XLIV.

A substance with structure as XLI would be useful for the preparation of a diazaazulene-derivative if it could be deacetylated to the diamine. By condensation with a β-diketone this diamine should produce a 5,7-disubstituted 1,6- (or 1,4-) dihydro-benzo[*b*]-4,8-diazaazulene (XLV):

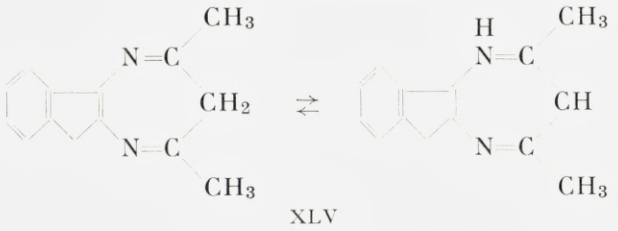

XLV

We did not succeed in isolating the indenediamine, presumably because it will immediately tautomerise to 1-iminoindane-2-amine which in acid solution easily is hydrolysed to 2-aminoindan-1-one[24]. As an α-aminoketone this substance will immediately form a pyrazine-derivative (XLVI–IL):

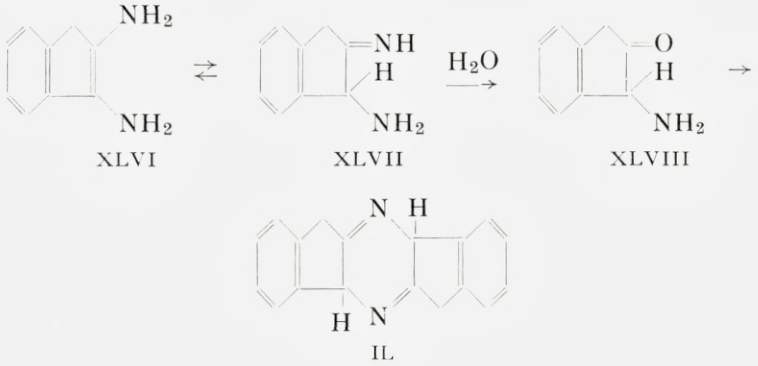

XLVI XLVII XLVIII IL

Experimental part

5,7-Dimethylbenzo[*b*]1,4-diazepine, 5-methyl-7-phenylbenzo[*b*]1,4-diazepine, 5,7-diphenylbenzo[*b*]1,4-diazepine and the corresponding hydrochlorides were prepared according to STEIMMIG[2] with mp.'s as indicated by him. 5,6,7-Trimethylbenzo[*b*]1,4-diazepine was prepared both *ad modum* BARLTHROP[6] by methylation of 5,7-dimethylbenzo[*b*]1,4-diazepine with methyl iodide and *ad modum* VAISMAN[3] by condensation of *o*-phenylenediamine with 3-methylpentane-2,4-dione, the latter method being preferable to the former.

10 g of *o*-phenylenediamine (0.0925 mole) were dissolved in a mixture of 20 ml of ethanol and 10 ml of glacial acetic acid. The solution was cooled to 0° and 12 g (0.1 mole) of 3-methylpentane-2,4-dione were added dropwise. A slight rise of temperature occurred and the solution turned cherry-red. After 5–10 minutes 50 g of water and ice were added, followed by 30 ml of concentrated hydrochloric acid in several portions. Brick-red crystals separated and were collected by suction and washed with cold dilute hydrochloric acid.

To isolate the free base the salt was dispersed in 200 ml of water and the dispersion little by little added to 200 ml of 10 % aqueous sodium hydroxide. A yellow amorphous solid separated which rapidly changed to white glimmering crystals. The crystals were filtered off, washed with water and dried. Yield 12.6 g = 73 % with m.pm 77–80° which was raised to 85–86° as indicated by VAISMAN by dissolving the base in dilute hydrochloric acid and reprecipitating it by neutralisation with base.

No doubt the yellow amorphous substance is the unsymmetrical sub-

stance corresponding to II (p. 3), the white crystals the symmetrical form corresponding to I.

Attempts to prepare 5,6,6,7-tetramethylbenzo[*b*]1,4-diazepine were all unsuccessful, 2-methylbenzimidazole being the only product isolated.

Condensation of piperonal with 5,7-dimethylbenzo[*b*]1,4-diazepine

Following the indications of Barlthrop *et al.*[6] 5.0 g (0.029 mole) of 5,7-dimethylbenzo[*b*]1,4-diazepine and 4.35 g (0.029 mole) of piperonal were dissolved in 150 ml of anhydrous ethanol containing 0.66 g (0.029 atom) of sodium. The solution was refluxed for 40 minutes. 50 ml of ethanol were then distilled off, the residue filtered when still hot, yielding 0.95 g of a substance which after recrystallisation from benzene showed m.p. 261–262°. Bartlhrop *et al.* indicate m.p. 257–258° for a bis-piperonylidene derivative of 5,7-dimethylbenzo[*b*]1,4-diazepine.

The filtrate was left for 2 days at room temperature when 2 g of a substance with m.p. 189–192° were isolated, corresponding to the mono-piperonylidene-derivative described by Barlthrop *et al.*

As indicated above (p. 4–7) we disagree with Barlthrop in considering these derivatives as the 5-methyl-7-methylenedioxystyrene-6-piperonylidene-benzo[*b*]1,4-diazepine and the 5,7-dimethyl-6-piperonylidenebenzo[*b*]1,4-diazepine respectively, the structures 5,7-bis(methylenedioxystyrene)benzo[*b*]1,4-diazepine and 5-methyl-7-(methylenedioxystyrene)benzo[*b*]-1,4-diazepine explaining better than the first mentioned the products of hydrolysis of the substances in question.

Condensation of ethyl oxalate with 5-methyl-7-phenylbenzo[*b*]1,4-diazepine

Ethyl 5-(7-phenylbenzo[*b*]1,4-diazepinyl)-3-pyruvate was prepared according to Steimmig[2]. Yellow crystals with m.p. 150.5–151.5° as indicated by Steimmig.

From the acidified filtrate a red substance precipitated. It was by closer study found to be identical with the 10-phenyl-4,9-diazabenzo[*f*]azulene described by Veibel et al.[17, 18].

300 mg of the yellow ester were refluxed for 1 hour with 5 ml of methanol. The solution turned dark and on cooling a mixture of yellow and violet crystals separated. The yellow crystals dissolved in ligroin on boiling, leaving the violet crystals undissolved. The violet crystals had m.p. 167.5–168,5° Steimmig (*l.c.*) indicates m.p. 166–167°.

The structures of these compounds are discussed p. 17–19.

The perchlorate of the yellow ester was prepared by dissolving the ester in a mixture of ethanol and ether and then adding an excess of 60 % perchloric acid. The solution turned dark but deposited yellow crystals with m.p. 224–225° (dec.).

Due to the yellow colour the possibility of an uptake of 2 protons was considered, but the elemental analysis* showed the substance to be a monoperchlorate.

		C	H	N	Cl
$C_{20}H_{19}N_2O_7Cl$	calc.	55.25	4.40	6.44	8.15
434.8	found	54.72	4.56	6.75	8.05

The structure of the cation has been discussed above, p. 19–20. The formation of the chelate prevents the N^4-nitrogen atom from taking part in the resonance stabilisation usually leading to the violet coloured benzodiazepinium cation.

Potassium salt of 3-(7-phenylbenzo[*b*]1,4-diazepinyl)-pyruvic acid and the free acid

2.4 g (0.061 mole) of potassium were dissolved in a mixture of 12.5 ml of anhydrous ethanol and 8 ml of anhydrous ether. 6 g (0.026 mole) of 5-methyl-7-phenylbenzo[*b*]1,4-diazepine were dissolved in the mixture, 4.5 g (0.031 mole) of diethyl oxalate were added at room temperature and the mixture kept the night over in the ice box. After addition of water (100 ml) a clear solution was obtained from which after some time yellow crystals precipitated. They were filtered off, washed on the filter with ice-cold water (which redissolved part of the crystals), dried and then purified by extraction with boiling benzene. After renewed filtration and drying 0.7 g with m.p. 225° remained. Elemental analysis indicated a potassium salt of the above named substituted pyruvic acid, crystallising with 1 mole of water.

		C	H	N	K	H_2O
$C_{18}H_{15}N_2O_4K$	calc.	59.65	4.17	7.73	10.79	4.97 %
362.4	found	58.50	4.27	7.60	11.00	5.09 %

Dried over phosphorus pentoxide in vacuum at 80° 5.09 % of water were removed.

From the benzene-solution 0.39 g of the original benzo[*b*]1,4-diazepine could be isolated.

* Elemental analyses here and in the following by Mr. PREBEN HANSEN, Chemical Laboratory of the University, Copenhagen.

2 g of the potassium salt were dissolved in 200 ml of water on the steam bath. 1 ml of glacial acetic acid was added. On cooling the substituted pyruvic acid precipitated. It was isolated by filtration, washed with dilute acetic acid, then with water and dried. M.p. 205°.

		C	H	N	E
$C_{18}H_{14}N_2O_3$	calc.	70.58	4.61	9.14 %	306.3
306.3	found	70.45	4.81	9.02 %	307 (titration with 0.1 *N* NaOH)

5,7-Dimethyl-2,3-dihydrocyclopenta[*b*]1,4-diazepine

This substance was prepared mainly according to LLOYD and MARSHALL[25] from cyclopentylene-1,2-diamine and acetylacetone.

For the preparation of the *diamine* cyclopentane-1,2-dione dioxime was prepared according to COPE *et al.*[26] and the dioxime reduced with sodium and anhydrous ethanol according to JAEGER and BLUMENDAL[27].

4 g (0.03 mole) of cyclopentane-1,2-dione dioxime were heated to reflux with 200 ml of anhydrous ethanol, and then 30 g of sodium, cut into small pieces, were added as fast as possible, forming a large ball of molten sodium. The solution turned very dark and remained dark when all sodium had reacted, but after addition of further 200 ml of ethanol and 20 g of sodium a clear straw-yellow coloured solution was obtained.

The diamine was isolated by steam-distillation. First the ethanol and then 1 liter of water, containing the amine, was collected. The distillate was slightly acidified with dilute hydrochloric acid (indicator methyl red) and then evaporated to dryness on a rotating vacuum-evaporator. Yield 3.82 g (71 %) with m.p. 292°. COPE[26] indicates m.p. 287–290°.

For further identification a dipicrate was prepared and recrystallised from aqueous ethanol. M.p. 250° (COPE indicates 233–233.5°). Equivalent weight (titration with perchloric acid in glacial acetic acid) 276, calculated 279.

We tried to obtain the diamine by catalytic reduction of the acetylated dioxime according to VIGNEAU[28] but the result was that ammonia was liberated (compare below, indanylidene-1,2-diamine).

5,7-Dimethyl-2,3-dihydroindano[1,2-*b*]1,4-diazepine

For the synthesis of this compound a condensation of indanylene-1,2-diamine with acetylacetone presents itself as the obvious procedure. As, however, indanylene-1,2-diamine has not, to our knowledge, been described

we had to develope a method for its preparation, and here we encountered unforeseen difficulties.

As a natural way for the synthesis we tried the nitrosation of indan-1-one, oximation of the resulting indan-1,2-dione monoxime and reduction of the dioxime to the diamine (L–LIII).

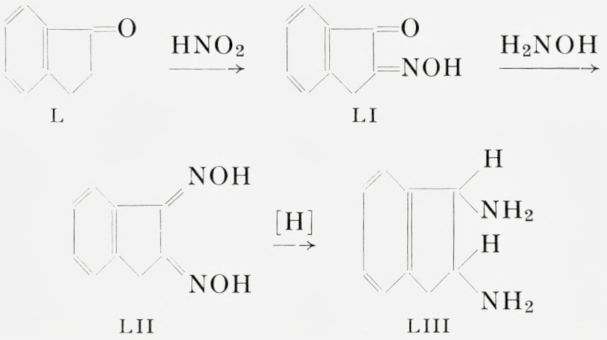

The first two steps presented no serious difficulties, but for the final reduction most of the conventional methods failed.

Indan-1-one was prepared in two different ways from β-phenylpropionic acid, *viz.* either according to AMAGAT[29] via the acid chloride, which under the influence of aluminium chloride cyclises to indan-1-one, or according to KOO[30] by direct cyclisation of the acid by heating it to 70° for 85 minutes with polyphosphoric acid. The first method resulted in an overall yield of 47–48 %, the second in a yield of 72 %.

Indane-1,2-dione-2-oxime was prepared according to LEVIN *et al.*[31] by nitrosation of indan-1-one with butyl nitrite. Yield 68.5 % of a product with m.p. 206,5–207° (dec.). LEVIN *et al.* indicate darkening at 200°.

Indane-1,2-dione dioxime. For the preparation of this compound the following procedure was worked out:

35 g (0.5 mole) of hydroxylammonium chloride were dissolved in 300 ml of ethanol. 41.3 g (0.5 mole) of anhydrous sodium acetate were added, precipitating sodium chloride. The resulting suspension was added to a solution prepared by heating 54 g (0.35 mole) of indane-1,2-dione-2-oxime with 500 ml of ethanol to 70–80° with mechanical stirring. The mixture was kept at 70–80° with mechanical stirring for 20 hours and then filtered hot. The filter-cake was washed with cold ethanol and with water, leaving 26.3 g. of a white, crystalline substance with m.p. 211.5–212° (dec.). From the filtrate crystallised on cooling 9.3 g with m.p. 204–205° (dec.); total yield

35.6 g = 61 %. After evaporation of the filtrate to 200 ml followed by addition of 500 ml of water 23.1 g of a substance with m.p. 190–191° (dec.) were obtained. It was shown by IR-spectroscopy that this compound mainly consisted of the dioxime, but it contained an impurity which was not the monoxime.

For purification of the dioxime it was treated with 2 *N* sodium carbonate which removes any monoxime present. The residue was then recrystallised from ethanol.

			C	H	N
(LII)	$C_9H_8N_2O_2$	calc.	61.36	4.58	15.90 %
	176.2	found	61.12	4.73	15.72 %

Indanylene-1,2-diamine. For the transformation of this dioxime to the diamine reduction with sodium and ethanol (see above, p. 26), with lithium aluminium hydride and with titanous chloride was tried unsuccessfully. With sodium and ethanol a small amount of a substance with m.p. about 132° (dec.) was obtained. This substance gave a picrate with m.p. 212–214° and is possibly the expected diamine (see below, p. 30).

Treated with titanous chloride an equivalent weight of, in 3 experiments, 29.9, 29.6, and 28.8, respectively, showed that only 6 equivalents of hydrogen had been taken up and not 8 as calculated for the reduction to the diamine. From the reduced solution a red coloured substance with m.p. 121–127° (dec.) not able to form a picrate, was isolated.

We then tried the method recommended by VIGNEAU[28], catalytic reduction of the diacetate of the dioxime.

In a hydrogenation apparatus for low-pressure hydrogenation 6 g (0.034 mole) of the dioxime were added little by little to 80 ml of acetic anhydride containing 2 g of anhydrous sodium acetate. The flask was heated to 50–60° for some minutes. After cooling to room temperature 2–5 g of W-2 Raney nickel were added and a hydrogen pressure of 35 cm mercury was established. After 110 minutes at room temperature 5.43 equivalents of hydrogen per mole of dioxime had been taken up, after 190 minutes 6.4 equivalents. The hydrogenation was then interrupted.

The acetic anhydride had assumed a red colour, and a colourless substance had precipitated. The colourless substance was filtered off together with the Raney-nickel, the adhering red colour removed by washing with cold ethanol and the colourless substance separated from the Raney-nickel by extraction with boiling absolute ethanol, from which 5.8 g of a substance with m.p. 233–236° separated on cooling.

The red colour was similar to the colour resulting from the reduction with titanous chloride where 6 equivalents of hydrogen were used up. If in the reduction of the acetylated dioxime the same reduction state has been reached, the reduction product has been isolated in a yield of 74 %.

		C	H	N
$C_{13}H_{14}N_2O_2$	calc.	67.81	6.13	12.16 %
230.3	found	67.60	6.07	12.07 %

We tried to remove the acetyl groups by acid hydrolysis. 0.5 g of the substance were refluxed for 20 minutes with 5 ml of concentrated hydrochloric acid. After cooling the acid mixture was extracted twice with 5 ml of chloroform to remove impurities, and then a slight excess of 50 % sodium hydroxide solution was added, producing precipitation of a red, crystalline substance which dissolved nearly colourless in chloroform but regained the red colour when the chloroform was removed by evaporation. Yield 210 mg with m.p. 122–131° (comp. p. 28, where a similar substance was isolated from the reduction of the dioxime with titanous chloride).

The IR-spectrum of the substance indicated the presence of an associated NH-group (3278 cm^{-1}), a C=O-group (1710 cm^{-1}) and a CH_2-group (1428 cm^{-1}). It might therefore be an aminoindanone, resulting from the hydrolysis of bis-acetylaminoindene, or a transformation product of the aminoindanone, comp. the discussion p. 22–23.

The red substance is insoluble in 2 *N* sodium hydroxide but dissolves without colour in 4 *N* hydrochloric acid.

We tried to purify the red substance chromatographically on an alumina column, but the compound was decomposed. From 150 mg of the substance 75 mg of a colourless substance with m.p. 151–155°, insoluble both in 2 *N* sodium hydroxide and in 4 *N* hydrochloric acid, were obtained. This compound may, too, be one of the products mentioned p. 22.

According to the discussion of the NMR-spectrum of the main product from the reduction this is considered to be the 1,2-diacetaminoindene.

Finally we tried to reduce the remaining double bond in the 5-membered ring by using a palladium/carbon catalyst as recommended by HARTUNG[32]. The catalyst was prepared as indicated in [33].

5 g (0.0217 mole) of 1,2-bis-acetaminoindene were dispersed and partially dissolved in 75 ml of anhydrous ethanol (magnetically stirred). 2 g of a 10 % palladium/carbon catalyst were added and the mixture hydrogenated at room temperature at an overpressure of hydrogen corresponding

to 50 cm of water. After 15 hours the theoretical amount of hydrogen had been taken up.

The catalyst was filtered off and washed with ethanol and water. Filtrate + washings were combined and evaporated in a rotating vacuum evaporator, leaving 4.5 g of a colourless substance with m.p. 196–201° which on recrystallisation from ethanol could be raised to 209–210°. Yield 2.75 g = 55 %.

According to the amount of hydrogen taken up the substance should be 1,2-bis-acetaminoindane, and elemental analysis was in agreement with this assumption.

		C	H	N
$C_{13}H_{16}O_2N_2$	calc.	67.21	6.94	12.06 %
232.3	found	67.05	7.06	12.23 %

Indanylene-1,2-diammonium dichloride, dipicrate and the free indanylene-1,2-diamine. 1.5 g of 1,2-bis-acetaminoindane were refluxed with concentrated hydrochloric acid for 3 hours. The solution was then evaporated to dryness in a rotating vacuum evaporator. The residue was dissolved by boiling it with 10 ml of anhydrous ethanol and precipitated after cooling by addition of ether. This procedure was repeated, but elemental analysis showed that it was not possible to isolate the pure dichloride in this way.

Hoping that it might be easier to obtain a pure dipicrate a solution of the dichloride was added to an aqueous solution of picric acid. A yellow picrate precipitated which after repeated recrystallisations from ethanol showed m.p. 215–216° (cf. the picrate mentioned p. 28). Elemental analysis could be interpreted as a not quite pure dipicrate crystallising with 3 moles of water.

		C	H	N
$C_{21}H_{24}N_8O_{17}$	calc.	38.19	3.66	16.97 %
660.5	found	39.25	3.93	16.60 %

The free diamine was liberated from an aqueous solution of 200 mg of the dichloride by adding an excess of 2 *N* sodium hydroxide, extracting the alkaline solution with ether, which removed a small quantity of a greenish substance, then with chloroform, from which after evaporation 75 mg of a nearly colourless substance were isolated, sintering at 139° and being completely molten at 153–154°.

5,7-Dimethyl-2,3-dihydro[1,2-*b*]indano-1,4-diazepinium perchlorate

We tried to prepare this compound by a method analogous to one indicated by SCHWARTZENBACH and LUTZ[34].

0.1 g of indylene-1,2-diamine (m.p. 153–154°) was heated in an oil-bath for 2 minutes with 5 drops of acetylacetone, after which, with 10 second intervals, 4 drops of glacial acetic acid were added. The heating was continued for 10 minutes.

After cooling the mixture was dissolved in 3 ml of water. On addition of 0.2 ml of 60 % aqueous perchloric acid a yellowish oil separated. The reaction mixture was shaken with 5 ml of ether which caused crystallisation of the oil. The crystals were filtered off, washed with a few ml of cold ether and dried. Yield 90 mg of a yellowish-white substance with m.p. 164–167° which after two recrystallisations from water was raised to 167–169°.

Its composition as the substance wanted was verified by elemental analysis.

		C	H	N	Cl
$C_{14}H_{17}N_2O_4Cl$	calc.	53.76	5.48	8.96	11.34 %
312.8	found	53.17	5.55	9.04	11.35 %

Aromatisation of the partially hydrogenated benzo-4,8-diazaazulene was tried, but without success. We examined all usually applied methods for dehydrogenation of partially hydrogenated azulenes or azaazulenes with *N* in the 5-membered, ring, *vic.* chloroanil[35, 36], sulphur[37], palladium (combined with cinnamic acid as hydrogen acceptor[38]), but without obtaining any indication of the formation of a 4,8-diazaazulene.

Thanks are due to cand. pharm. INGER GRETE KROGH ANDERSEN for valuable assistance in taking and discussing the IR-spectra and to The Technical University for a post-graduate grant which enabled one of us (J.I.N.) to take part in the investigation.

References

1. J. Thiele and G. Steimmig, *Ber.* 1907, **40**, 955.
2. G. Steimmig, *Thesis*, Strassbourg, 1908.
3. S. B. Vaisman, *Trans. Inst. Chem. Kharkov Univ.* **4**, no. 13 (1938), 157; *Chem. Abstr.* 1940, **34**, 5847.
4. G. Schwartzenbach and K. Lutz, *Helv. chim. Acta* 1940, **23**, 1162.
5. J. L. Finar, *J. Chem. Soc.* **1958**, 4094.
6. J. A. Barlthrop, C. G. Richards, D. M. Russell and G. Ryback, *J. Chem. Soc.* **1959**, 1132.
7. J. O. Halford and R. M. Fitch, *J. Am. chem. Soc.* 1963, **85**, 3354.
8. N. H. Cromwell, *Chem. Rev.* 1946, **38**, 83.
9. W. Ruske and G. Grimm, *J. prakt. Chem.* [4] 1962, **18**, 163.
10. W. Ruske and E. Hüfner, *J. prakt. Chem.* [4] 1962, **18**, 156.
11. W. H. Stafford, D. H. Reid and P. Barker, *Chem. and Ind.* **1956**, 765.
12. D. Lloyd, R. H. McDougall and D. R. Marshall, *J. Chem. Soc.* **1965**, 3785.
13. Houben-Weyl, *Methoden der organischen Chemie* 1955, Vol. **3/2**, 636.
14. H. A. Staab and F. Vögtle, *Chem. Ber.* 1965, **98**, 2701.
15. N. Bjerrum and A. Unmack, *Mat. Fys. Medd. Dan. Vid. Selsk.* 1929, **9**, 1 (p. 115).
16. H. K. Hall, *J. Phys. Chem.* 1956, **60**, 63.
17. S. Veibel and S. F. Hromadko, *Chem. Ber.* 1960, **93**, 2752.
18. S. Veibel and J. Ilum Nielsen, *Chem. Ber.* 1966, **99**, 2709.
19. W. Treibs and W. Schroth, *Ann. Chem.* 1961, **639**, 214.
20. W. Treibs and W. Schroth, *Angew. Chem.* 1959, **71**, 71.
21. D. Peters, *J. Chem. Soc.* 1958, 3763.
22. W. Treibs and W. Schroth, *Ann. Chem.* 1961, **642**, 108.
23. K. Hafner and M. Kreuder, *Angew. Chem.* 1961, **73**, 657.
24. F. Kröhnke and I. Vogt, *Ann. Chem.* 1954, **589**, 26.
25. D. Lloyd and D. R. Marshall, *J. Chem. Soc.* **1956**, 2597.
26. A. C. Cope, L. L. Esters, jr., J. R. Emery and A. C. Haven, jr., *J. Am. chem. Soc.* 1951, **73**, 1199.
27. F. M. Jaeger and H. B. Blumendal, *Z. Anorg. Allgem. Chem.* 1928, **175**, 161.
28. M. Vigneau, *Bull.. Soc. Chim. France* **1952**, 638.
29. P. Amagat, *Bull.. Soc. Chim. France* [4] 1927, **41**, 942.
30. J. Koo, *J. Am. Chem. Soc.* 1953, **75**, 1894.
31. N. Levin, B. E. Graham and H. G. Kolloff, *J. org. Chem.* 1944, **9**, 380.
32. W. H. Hartung, *J. Am. chem. Soc.* 1928, **50**, 3370.
33. *Organic Syntheses*, Coll. Vol. III, 686, Wiley, N.Y., 1955.
34. G. Schwartzenbach and K. Lutz, *Helv. chim. Acta* 1940, **23**, 1144.
35. W. Treibs and E. J. Poppe, *J. prakt. Chem.* [4] 1961, **13**, 331.
36. W. Treibs, R. Steinert and W. Kirchhof, *Ann. Chem.* 1953, **581**, 54.
37. P. A. Plattner, A. Fürst and M. Gordon, *Helv. chim. Acta* 1950, **33**, 1916.
38. C. O'Brien, E. M. Philbin, S. Ushioda and T. S. Wheeler, *Tetrahedron* 1963, **19**, 373.

Indleveret til Selskabet den 24. marts 1966.
Færdig fra trykkeriet den 17. oktober 1966.

Matematisk-fysiske Meddelelser
udgivet af
Det Kongelige Danske Videnskabernes Selskab
Bind **35**, nr. 7

Mat. Fys. Medd. Dan. Vid. Selsk. **35**, no. 7 (1966)

DEFORMED EXCITED STATES IN CLOSED SHELL NUCLEI

BY

JØRG EICHLER AND TOSHIO MARUMORI

København 1966
Kommissionær: Munksgaard

Synopsis

A systematic theory of treating the complex ground-state correlations for 2particle-2hole excitations is proposed. It is shown that these new ground-state correlations describe the collective predisposition of the *spherical* ground state in closed-shell nuclei to produce *deformed* excited states. The resulting deformation of the excited states incorporates the deformation of the core. These features are made evident by a self-consistent method. Formal properties of the solutions and their influence on various electromagnetic transitions are discussed.

PRINTED IN DENMARK
BIANCO LUNOS BOGTRYKKERI A/S

CONTENTS

		Page
1.	*Introduction*	5
2.	*Outline of the Theory*	8
2.1	Notation and Hamiltonian	8
2.2	The matrix elements of the interaction	9
2.3	A two-step method	11
2.4	A self-consistent approximation	13
3.	*Pair Scattering Correlations*	14
3.1	The equation of motion	14
3.2	Properties of the pair scattering modes	15
3.3	The physical meaning of the approximation	16
3.4	The expansion of physical operators	18
3.5	The expansion of the Hamiltonian	19
4.	*Interaction between Pairs*	21
4.1	The Hamiltonian in terms of pair scattering modes	21
4.2	Collective modes in the excitation of closed shells	24
5.	*Deformation of the Excited States*	26
5.1	A separable field-producing force	27
5.2	An extension of the Hartree-Fock approximation	28
5.3	The origin of the intrinsic deformation	30
	Numerical calculations for a simple model	32
5.4	A self-consistent method including the core deformation	36
5.5	Intrinsic deformations in excited 0^+ states	40
5.6	Rotational bands built on excited states	43
6.	*Electromagnetic Transitions*	44
6.1	Energy weighted sum rule	44
6.2	Transitions within rotational bands	45
6.3	E2 transitions connecting the rotational band with the ground state	46
6.4	E0 transitions from excited 0^+ states to the ground state	47
6.5	Hindrance of double gamma decay of the first excited 0^+ state	48
7.	*Conclusions*	52
	References	55

1. Introduction

For a long time it has been difficult to understand the position of low lying even parity states in closed-shell nuclei. Several years ago a clue to the solution was suggested by BOHR and MOTTELSON in connection with the "mysterious zero plus states". The suggestion (pointing out the special importance of seeing the low lying states from the stand-point of deformed excited states [1]) has been confirmed by recent experiments [2] which show that many of the low lying excited states in O^{16} and Ca^{40} can be fitted into rotational bands. Along this line, several investigations [3, 4] have been made, in particular in the interesting work af G. E. BROWN [5, 6], how to interpret the rotational band structure and in connection with it the low excitation energy of the even parity states.

As a first step, Brown considers in his model unperturbed excited states with a definite number of particles and holes. These states may be obtained [3] from a Hartree-Fock approximation*. They turn out to be deformed in a body-fixed system and thus account for the occurrence of rotational bands. The deformation then is regarded as the main reason for the low excitation energy of the first excited 0^+state in O^{16}. However, excitations consisting of pure 2particle-2hole (2p-2h) or 4particle-4hole (4p-4h) configurations would not be able to account for the observed strong electromagnetic transitions between the rotational band and the ground state. Therefore, Brown [5, 6] introduces, in a second step, a considerable mixing between a few specific unperturbed excited states and the spherical shell-model ground state. Of course, this procedure will in general destroy the rotational band structure obtained in the first step. The problem then is to find a reasonable mixing of unperturbed states, which explains both the electromagnetic transitions and at the same time preserves the rotational band structure. Because of this restriction, and in spite of the striking success of the model, it appears to us that the account for ground-state correlations is somewhat artificial and insufficient, and a refined treatment is desirable.

* Actually, in Brown's model the core deformation is taken into account phenomenologically as an important correction.

Such a refinement should be based on ground-state correlations which are known to be particularly important for collective phenomena in nuclei. We may expect that the correct ground state has a collective predisposition for collective excitations. In other words, the collective correlation which is responsible for collective excited states will also be present in the ground state as a ground-state correlation. In the phenomenological theory, the collective predisposition clearly manifests itself in the zero-point motion. Correspondingly, the success of the new Tamm-Dancoff method (NTD) or random-phase approximation (RPA) in describing collective phenomena is essentially due to the *symmetrical* treatment of correlations for both the excited states and the ground state. In this way the collective predisposition is properly incorporated in the theory. This is certainly an improvement over the Tamm-Dancoff method (TD) which asymmetrically attributes all the collectiveness exclusively to the excited states. For instance, if we just consider configurations with a definite number of particles and holes and treat them in the TD[7] or (in order to obtain a more clear-cut notion of "intrinsic deformation") in the Hartree-Fock approximation[3], the resulting collectiveness which produces the deformation is entirely ascribed to the excited states. But we have seen above that *the collectiveness should be incorporated in the ground state as a collective predisposition to produce deformed excited states.* This collective point of view has been especially stressed by BOHR and MOTTELSON*, and is the essential stand-point of the present theory. Once the corresponding ground-state correlations have been taken into account properly, the excited states will become much more "collective", and both the deformations and the level positions of the excited states will be quite different from those obtained by the TD or Hartree-Fock method. The importance of such changes for explaining the actual deformations and actual level positions has long been recognized[8]; the effect is often referred to as the "deformation of the core by the excited particle". This cooperation effect of the core is usually discussed in the single-particle picture, where it is reflected in the change of the energy difference between the highest occupied and the lowest unoccupied Nilsson level as a function of the deformation[5, 6]. Quantitatively this effect can be seen in the Volkov[9] type calculations. In O^{16}, for example, the energy necessary to excite a particle pair has a minimum for large prolate deformations. From our collective point of view, this precisely corresponds to the collective predisposition of the *spherical* ground state to produce *deformed* excited states.

* See, for instance, the discussion in Congrès International de Physique Nucléaire, Vol. I (Paris, 1964) 129.

The main purpose of this paper is to propose a theory which takes into account such a collective predisposition in the spherical ground state and to treat the cooperation effect of the core for deformations in the excited states in a self-consistent way. Of course, one might try to solve the problem by diagonalizing the Hamiltonian in a space which includes enough configurations to describe core deformation effects. However, the straightforward approach has two essential defects: (a) the rank of the matrix to be diagonalized is too large to get solutions without serious approximations; (b) even if we have the exact solution we do not gain any physical insight into the nature of excitation. In order to reach a better understanding we are forced to extract the basic physical elements from our problem. To this end it is useful to invoke the well-known notions of the *field-producing force* and the *residual interaction* as a guide. The field-producing force generates a (deformed) self-consistent field and is well accounted for in a Hartree-Fock approximation. By definition, the residual interaction cannot be incorporated in a self-consistent field. It is responsible for the pairing correlations in the superconducting state and for two-particle (or two-hole) scattering correlations in the normal (non-superconducting) state. Usually the residual interaction is considered to be unimportant for closed-shell nuclei because of the large energy spacing between occupied and unoccupied levels. However, we have discussed above that for large prolate deformations (due to the field-producing force) the occupied and unoccupied levels come quite close to each other. This means that even if the residual interaction is small, *the interplay between the residual interaction and the field-producing force will be of decisive importance.* (This is also reflected in Brown's model where the residual interaction gives rise to mixing effects). We may reformulate the statement in another way: If, for simplicity, we adopt the "pairing plus quadrupole force model", then the difference in parity between major shells prevents the quadrupole force from exciting particles from an occupied shell to the nearest unoccupied shell even if the force is strong. In fact, particles can only be excited by the *pairing force* even if its strength is weak. Once particles are excited, however, the quadrupole force will act strongly among the excited configurations and efficiently lead to deformations.

Both this picture and the aim of investigating the important interplay between field-producing forces and the residual interaction suggest the following two-step procedure: In a first step we diagonalize the residual interaction including ground-state correlations, and in a second step we diagonalize the field-producing forces. This gives rise to a new type of ground-state correlations which will be shown to exhibit the collective predisposition of

the spherical ground state for deformed excited states. The outline of this two-step method is presented in section 2 and the details of both steps in sections 3 and 4, respectively. In section 5, we extract the basic element, which produces deformations in the excited states, from the general solution of sect. 4. We show, in a succession of generalizations of the costumary Hartree-Fock approximation [3] (which leads to deformed excited states), how we can get a self-consistent method which contains the core deformation effect explicity and is an approximation for the method given in section 4. In section 6, the theory is applied to electromagnetic transitions in which the interplay between the field-producing force and the residual interaction plays a decisive role. In section 7, finally, we indicate the application of our theory to other problems and summarize our results.

2. Outline of the Theory

It is the purpose of the present section to give a first understanding of and additional motivation for our theory. For clarity, we will not use here a decomposition of the interaction into a field-producing force and a residual interaction, as discussed in the introduction, but rather use a closely related subdivision which characterizes various parts of the Hamiltonian by Feynman diagrams. The original point of view will be taken up in section 5.

2.1. Notation and Hamiltonian

Let us consider a closed-shell nucleus and assume its ground state to be spherical and normal (i.e., non-superconducting). Adopting the *j-j* coupling shell model for the zero-order states, we can define the particle- and hole creation and annihilation operators as

$$\left.\begin{aligned} c_\alpha^+ &= (1-\theta_\alpha)c_\alpha^+ + \theta_\alpha c_\alpha^+ = a_\alpha^+ + b_\alpha \\ c_\alpha &= (1-\theta_\alpha)c_\alpha + \theta_\alpha c_\alpha = a_\alpha + b_\alpha^+ \end{aligned}\right\} \quad (2.1)$$

where α denotes the complete set of quantum numbers $\alpha \equiv \{n,l,j,m,\tau\}$, and $a = \{n,l,j\}$ denotes the same set except for the projection quantum numbers.
Furthermore,

$$\theta_\alpha = \left\{\begin{aligned} &1 \text{ for levels occupied in the free ground state} \\ &0 \text{ for levels unoccupied in the free ground state} \end{aligned}\right\} \quad (2.2)$$

where the free (unperturbed) ground state $|\Phi_0\rangle$ is defined by $a_\alpha|\Phi_0\rangle = b_\alpha|\Phi_0\rangle = 0$. For a basis of stationary states it is possible to build the entire treatment on real quantities if the phase convention is suitably chosen. In the following, we always assume this to be the case. The Hamiltonian can be written as

$$\left.\begin{aligned} H &= H_0 + H_{\text{int}} \\ H_0 &= \sum_\alpha (\varepsilon_\alpha^{(0)} - \lambda) : c_\alpha^+ c_\alpha : = \sum_\alpha \varepsilon_\alpha : c_\alpha^+ c_\alpha : \\ &= \sum_\alpha \varepsilon_\alpha (a_\alpha^+ a_\alpha - b_\alpha^+ b_\alpha) \\ H_{\text{int}} &= \sum_{\alpha\beta\gamma\delta} v_{\alpha\beta\gamma\delta} : c_\alpha^+ c_\beta^+ c_\delta c_\gamma : \end{aligned}\right\} \quad (2.3)$$

where the symbol : : denotes the normal product with respect to particles and holes, and λ is the chemical potential. The potential matrix element has the symmetry properties

$$v_{\alpha\beta\gamma\delta} = -v_{\beta\alpha\gamma\delta} = -v_{\alpha\beta\delta\gamma} = v_{\gamma\delta\alpha\beta}. \quad (2.4)$$

2.2 The Matrix Elements of the Interaction

In order to discuss the various parts of the interaction H_{int} we divide the Hamiltonian (2.3) in the following way:

$$H = H_0 + H_{pp} + H_{hh} + H_{ph} + H_V + H_Y, \quad (2.5)$$

where

$$\left.\begin{aligned} H_{pp} &= \sum_{\alpha\beta\gamma\delta} v_{\alpha\beta\gamma\delta} a_\alpha^+ a_\beta^+ a_\delta a_\gamma \\ H_{hh} &= \sum_{\alpha\beta\gamma\delta} v_{\alpha\beta\gamma\delta} b_\alpha^+ b_\beta^+ b_\delta b_\gamma \\ H_{ph} &= 4 \sum_{\alpha\beta\gamma\delta} v_{\alpha\beta\gamma\delta} a_\alpha^+ b_\delta^+ a_\gamma b_\beta \\ H_V &= \sum_{\alpha\beta\gamma\delta} v_{\alpha\beta\gamma\delta} (a_\alpha^+ a_\beta^+ b_\delta^+ b_\gamma^+ + a_\alpha a_\beta b_\delta b_\gamma) \\ H_Y &= 2 \sum_{\alpha\beta\gamma\delta} v_{\alpha\beta\gamma\delta} (a_\alpha^+ a_\beta^+ b_\delta^+ a_\gamma + a_\alpha^+ b_\beta a_\delta a_\gamma \\ &\qquad + a_\alpha^+ b_\delta^+ b_\gamma^+ b_\beta + b_\delta^+ b_\alpha b_\beta a_\gamma). \end{aligned}\right\} \quad (2.6)$$

Each matrix element is represented by one of the diagrams in fig. 1. The first three parts, H_{pp}, H_{hh} and H_{hp}, conserve the number of particles and holes and therefore are the only ones considered in the Tamm-Dancoff

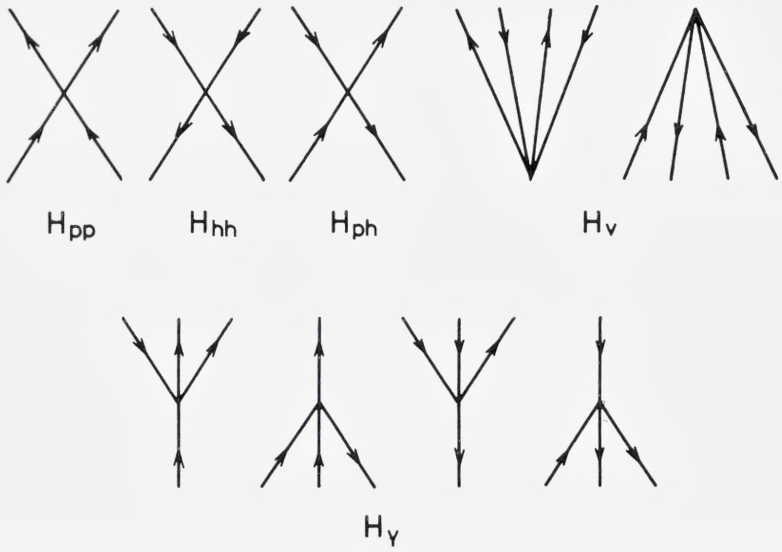

Fig. 1. Graphic representation of the matrix elements of the interaction. Lines with arrows pointing upwards indicate particles, lines with arrows pointing downwards indicate holes. Each diagram includes both the "direct" term and the "exchange" term.

calculation or the Hartree-Fock approximation [3] for a fixed number of particles and holes. The part, H_V, introduces ground-state correlations and is discussed in the following subsection. Finally, the part H_Y will be neglected in our treatment. This is equivalent to the assumption that *only the excitations with an even number of particles and even number of holes are important for a description of low lying even parity states in closed-shell nuclei.* The assumption may be justified by the following arguments. (a) Among the 2 $\hbar\omega$ excitations the 2p-2h configurations offer by far more coupling possibilities than the 1p-1h configurations. Since a strong collectiveness is necessary to produce the deformed excited states, the space of all 2p-2h configurations will be of main importance. (b) Calculations [7, 10] for O^{16}, using the Tamm-Dancoff approximation for 1p-1h and 2p-2h configurations, have failed to explain the electromagnetic transitions between the lowest excited states of even parity and the ground state. The calculated transition probabilities are by orders of magnitude too small. This means that the effect of 1p-1h configurations would be of less importance compared with the effect of ground-state correlations for the low lying even parity states in O^{16}.

2.3 A Two-Step Method

As has been indicated in the introduction, it is our aim to take the ground-state correlations properly into account and to investigate the important interplay between the field-producing force and the residual interaction. This has to be done in two distinct steps. G. E. Brown, in his model [5, 6], *first* treats the effects of the field-producing force on the excited states and afterwards incorporates, to some extent, effects of the residual interaction in the mixing of the deformed states. Such a procedure deals with the effects in the order of their importance; however, it encounters two intrinsic difficulties. (a) The unperturbed states obtained in the first step by a Hartree-Fock method will belong to different deformations. Thus (unless one uses the SU_3 model instead of the Hartree-Fock procedure), the unperturbed (deformed) states will not form an orthogonal set which, however, is required in order to treat the collective ground-state correlations properly. (b) Even if the problem of orthogonality did not arise, the incorporation of the residual interaction would destroy the rotational band structure obtained previously. To avoid such difficulties, we start from the excitation mechanism and treat the effects of the *residual interaction* in the *first step*. For a normal ground state in closed-shell nuclei, these effects will lead to 2-particle (or 2-hole) scattering correlations described by the following linearized relations:

$$[H, a_\alpha^+ a_\beta^+] = \sum_{\gamma\delta} (M_{\alpha\beta\gamma\delta} a_\gamma^+ a_\delta^+ + M'_{\alpha\beta\gamma\delta} b_\delta b_\gamma) \tag{2.7a}$$

$$[H, b_\alpha^+ b_\beta^+] = \sum_{\gamma\delta} (M_{\alpha\beta\gamma\delta} b_\gamma^+ b_\delta^+ + M'_{\alpha\beta\gamma\delta} a_\delta a_\gamma), \tag{2.7b}$$

where the coefficients M and M' depend only on the part $H_0 + H_{pp} + H_{hh} + H_V$ of the Hamiltonian (2.5). The equation of motion corresponding to the approximation (2.7) is solved by introducing certain eigenmodes (or elementary excitations) which consist of a correlated particle pair, A^+, or a correlated hole pair B^+. The correlated pairs (virtual Cooper pairs if $J = 0$) are represented schematically in fig. 2 together with the corresponding ground-state correlations. It is important to note that in constructing the pair scattering modes we have taken into account the interaction H_V at a stage where it is still easy to handle without severely reducing the dimension of the space in which the interaction is diagonalized as it is done in Brown's model.

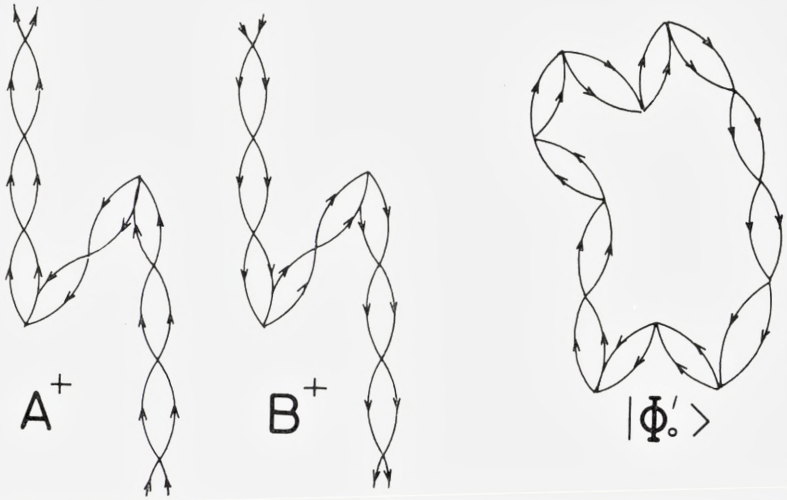

Fig. 2. Schematic representation of pair scattering modes for a particle pair A^+ and a hole pair B^+. To the right: the corresponding ground-state correlations for the ground state $|\Phi'_0>$. The states $A^+ B^+ |\Phi'_0>$ will, in the following, often be called "2p-2h" states where the quotation marks indicate that also 4p-4h, 6p-6h, ... amplitudes (in the sense of the TD method) are admixed. The correlations will be called "pair scattering ground-state correlations" due to the residual interaction.

In the *second step* we diagonalize the particle-hole interaction* $H_{p\hbar}$ by using another linearized relation

$$[H, A^+_\mu B^+_\nu] = \sum_{\varrho\sigma} (N_{\mu\nu\varrho\sigma} A^+_\varrho B^+_\sigma + N'_{\mu\nu\varrho\sigma} A_\varrho B_\sigma) \tag{2.8}$$

which gives us new and very complex correlations. They are indicated in fig. 3 with broken lines symbolizing correlated pairs of the type shown in fig. 2. The formal resemblance with the correlations known from the ordinary RPA for the "1p-1h" problem suggests the appearance of new collective effects. The new ground-state correlations may be called *ground-state correlations due to the field producing* force. They exhibit the collective predisposition of the ground state for deformed excited states.

It should not be concealed here that these results can be derived only

* The main source of deformation in the excited states of closed-shell nuclei will be the repulsive particle-hole interaction (corresponding to an attractive particle-core interaction). This interaction forces, for example, the particles to the poles of the core if the holes are concentrated in the equatorial plane, so that particles and holes contribute to the deformation with equal sign. In the SU_3 model, this corresponds to the fact that the lowest 2p-2h states in O^{16} are those with maximum weight, namely with the SU_3 representation (42). These states have the particles along one axis and the holes in the plane vertical to this axis. For details, see the discussion at the end of sect. 4.1.

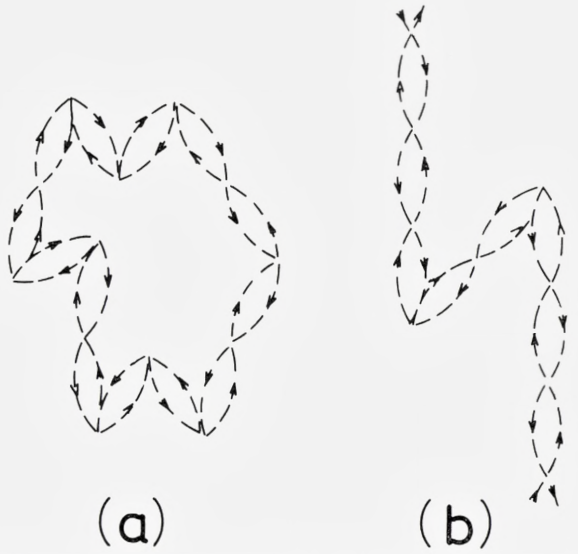

Fig. 3. Correlations introduced by the particle-hole interaction H_{ph} or by the field-producing force. The broken lines represent pair scattering modes: for a "particle pair" A^+ if the arrow points upwards, for a "hole pair" B^+ if the arrow points downwards. The diagram (a) is a typical graph taken into account in the ground state, the diagram (b) is typical of the graphs included in the description of a "dressed 2p-2h" system.

at the expense of giving up the Pauli principle between particles and holes belonging to different correlated pairs. Still, the Pauli principle is accurately taken into account as long as we are dealing with a 2p-2h system in the sense of the TD method. (For details, see section 3.3). In this respect our approximation is superior to the case in which the "*particle-hole*" *pair* is coupled to a *unit*, so that the Pauli principle is neglected even for a 2p-2h system in the sense of the TD method.

2.4 A Self-Consistent Approximation

In order to show that the solutions of our two-step procedure describe indeed deformed excited states, we propose a new self-consistent approximation which treats the cooperation effect of the core deformation in a self-consistent way. The conventional Hartree-Fock approximation for the excited states [3] is obtained as a special case of our generalized self-consistent method if we neglect ground-state correlations and thus the effect of the core deformation.

3. Pair Scattering Correlations

In the preceding section we have shown that it is convenient to treat the particle pair (and hole pair) scattering correlation before entering the full complexity of "2p-2h" (in the NTD sense) or even higher excitations. In the present section we turn to the construction of these pair scattering modes and to the discussion of their properties.

3.1 The Equation of Motion

We define the operators for pair scattering eigenmodes by

$$C_\mu^+ = \sum_{\alpha\beta}(\psi_\mu(\alpha\beta)a_\alpha^+ a_\beta^+ + \varphi_\mu(\alpha\beta)b_\alpha b_\beta) \tag{3.1}$$

with

$$\psi_\mu(\alpha\beta) = -\psi_\mu(\beta\alpha) \quad \text{and} \quad \varphi_\mu(\alpha\beta) = -\varphi_\mu(\beta\alpha), \tag{3.2}$$

where

$$\mu = \{N, JM, TZ\}, \quad m = \{N, J, T\}$$

characterize the pair by the angular momentum J and its projection M, the isospin T and its projection Z, and a set of additional quantum numbers N. We start with the following linearized relation in the NTD approximation:

$$\left.\begin{aligned}[H, a_\alpha^+ a_\beta^+] &= \sum_{\gamma\delta}(M_{\alpha\beta\gamma\delta}a_\gamma^+ a_\delta^+ + M'_{\alpha\beta\gamma\delta}b_\delta b_\gamma) \\ [H, b_\alpha^+ b_\beta^+] &= \sum_{\gamma\delta}(M_{\alpha\beta\gamma\delta}b_\gamma^+ b_\delta^+ + M'_{\alpha\beta\gamma\delta}a_\delta a_\gamma).\end{aligned}\right\} \tag{3.3}$$

The matrices M and M' are obtained by taking the appropriate matrix elements of eq. (3.3) with respect to the unperturbed ground state and 2p-2h states. It is clear that only H_0, H_{pp}, H_{hh} and H_V out of the Hamiltonian (2.5) contribute to the matrix elements M and M'. The correlation amplitudes $\psi_\mu(\alpha\beta)$ and $\varphi_\mu(\alpha\beta)$ (taken as real) are now determined as the solutions of the equation of motion

$$[H, C_\mu^+] = \omega_m C_\mu^+. \tag{3.4}$$

Using eq. (3.3) one obtains two coupled eigenvalue equations for ψ and φ which can be written in the compact form

$$\omega_m \Psi_\mu(\alpha\beta) = \sum_{\gamma\delta}\{(|\varepsilon_a| + |\varepsilon_b|)\delta_{\alpha\gamma}\delta_{\beta\delta} + 2v_{\alpha\beta\gamma\delta}\}(1 - \theta_c - \theta_d)\Psi_\mu(\gamma\delta) \tag{3.5}$$

by using the convenient notation

$$\left.\begin{aligned} \psi_\mu(\alpha\beta) &= (1-\theta_a)(1-\theta_b)\Psi_\mu(\alpha\beta) \\ \psi_\mu(\alpha\beta) &= \theta_a\theta_b \Psi_\mu(\alpha\beta), \end{aligned}\right\} \quad (3.6)$$

where θ_a is defined in eq. (2.2).

The vanishing of one of the eigenvalues ω_m would indicate an instability* of the normal ground state [11], but according to our assumption of a normal ground state we neglect this possibility. Equations of the structure (3.5) have been discussed previously in connection with the "independent pair model including the hole motion" [12] and (for the special case of $J = 0$) in connection with the "pairing vibration" [13, 14].

3.2 Properties of the Pair Scattering Modes

The secular matrix of eq. (3.5) can formally be considered as Hermitian provided we adopt an indefinite metric expressed by the following orthonormality relation [12, 13]:

$$\sum_{\alpha\beta} \Psi_\mu(\alpha\beta)(1-\theta_a-\theta_b)\Psi_\nu(\alpha\beta) = \tfrac{1}{2} s_\mu \cdot \delta_{\mu\nu}, \quad (3.7)$$

where the sign function s_μ is defined by

$$s_\mu = \left\{\begin{aligned} 1 \quad &\text{if} \quad \omega_m > 0 \\ -1 \quad &\text{if} \quad \omega_m < 0. \end{aligned}\right. \quad (3.8)$$

If none of the eigenvalues ω_m vanishes we also have the completeness relation

$$\sum_\mu \Psi_\mu(\alpha\beta) s_\mu \Psi(\gamma\delta) = \tfrac{1}{4}(\delta_{\alpha\gamma}\delta_{\beta\delta} - \delta_{\alpha\delta}\delta_{\beta\gamma})(1-\theta_a-\theta_b). \quad (3.9)$$

It is now convenient to distinguish the operators of the pair scattering eigenmodes according to the sign s_μ of the corresponding energy eigenvalue. Therefore we define, in formal analogy to eq. (2.1) for the fermion operators, the pair operators

* In that case we have a superconducting ground state so that we should make the Bogoliubov transformation.

$$\left.\begin{aligned} C_\mu^+ &= \begin{cases} A_\mu^+ & \text{if} \quad \omega_m > 0 \\ B_\mu & \text{if} \quad \omega_m < 0 \end{cases} \\ C_\mu &= \begin{cases} A_\mu & \text{if} \quad \omega_m > 0 \\ B_\mu^+ & \text{if} \quad \omega_m < 0. \end{cases} \end{aligned}\right\} \tag{3.10}$$

The physical interpretation of the operators defined in eq. (3.10) is the following. The operator A_μ^+ is the creation operator for a correlated particle pair: This means A_μ^+ creates two particles with the large amplitudes $\psi_\mu(\alpha\beta)$ $\{\text{for } \omega_m > 0\}$ and annihilates two holes with the small amplitudes $\varphi_\mu(\alpha\beta)$ $\{\text{for } \omega_m > 0\}$. The operator B_μ^+ is the creation operator for a correlated hole pair. This means that B_μ^+ creates two holes with the large amplitudes $\varphi_\mu(\alpha\beta)$ $\{\text{for } \omega_m < 0\}$ and annihilates two particles with the small amplitudes $\psi_\mu(\alpha\beta)$ $\{\text{for } \omega_m < 0\}$. In the absence of ground-state correlations, A_μ^+ and B_μ^+ are identical with the operators which create an exact 2-particle eigenstate and 2-hole eigenstate in the TD method.

The definition and physical interpretation of the creation (annihilation) operators $A_\mu^+(A_\mu)$ and $B_\mu^+(B_\mu)$ for correlated pairs enable us to define a new ground state $|\Phi_0'>$ by requiring

$$A_\mu|\Phi_0'> = B_\mu|\Phi_0'> = 0. \tag{3.11}$$

Clearly the new ground state now contains correlations due to the interactions H_{pp}, H_{hh} and H_V. It is a mixture of 0p-0h, 2p-2h, 4p-4h, etc. excitations in the sense of the TD method. Thus the diagrams considered in the ground state and the "2p-2h" excited states (in the NTD sense) are all diagrams of the type given in fig. 2.

3.3 The Physical Meaning of the Approximation

We want to use the pair scattering modes as a new basis of the theory and so it is necessary to discuss the physical implications of our approximations. For definiteness, we restrict ourselves in the following to a "2p-2h" problem* (in the sense of the NTD method, thus including 4p-4h, 6p-6h excitations, etc). The New Tamm-Dancoff method on which the present theory is built and which allows to describe the collective predisposition of the ground state has two important consequences.

* It is in principle possible([15]), however, to extend the theory to a "4p-4h" problem if it should turn out that a simple "2p-2h" description is not adequate for O^{16}.

(a) The Pauli principle is violated between identical fermions belonging to different 2p-2h pairs. Writing down the linearized relation (3.3) implies, for consistency, that the commutation relations for fermion pairs reduce to Bose commutation rules. In other words, the 2-particle pairs $a_\alpha^+ a_\beta^+$ and 2-hole pairs $b_\gamma^+ b_\delta^+$ are approximated by quasi-boson operators

$$\left.\begin{aligned} a_\alpha^+ a_\beta^+ &\to \mathfrak{A}_{\alpha\beta}^+ \quad \text{with} \quad \mathfrak{A}_{\alpha\beta}^+ = -\mathfrak{A}_{\beta\alpha}^+ \\ b_\gamma^+ b_\delta^+ &\to \mathfrak{B}_{\gamma\delta}^+ \quad \text{with} \quad \mathfrak{B}_{\gamma\delta}^+ = -\mathfrak{B}_{\delta\gamma}^+ \end{aligned}\right\} \tag{3.12}$$

which satisfy the boson commutation relations

$$\left.\begin{aligned} [\mathfrak{A}_{\alpha_1\beta_1}, \mathfrak{A}_{\alpha_2\beta_2}^+] &= \delta_{\alpha_1\alpha_2}\delta_{\beta_1\beta_2} - \delta_{\alpha_1\beta_2}\delta_{\alpha_2\beta_1} \\ [\mathfrak{B}_{\gamma_1\delta_1}, \mathfrak{B}_{\gamma_2\delta_2}^+] &= \delta_{\gamma_1\gamma_2}\delta_{\delta_1\delta_2} - \delta_{\gamma_1\delta_2}\delta_{\gamma_2\delta_1} \\ [\mathfrak{A}_{\alpha\beta}^+, \mathfrak{B}_{\gamma\delta}^+] &= [\mathfrak{A}_{\alpha\beta}^+, \mathfrak{B}_{\gamma\delta}] = 0. \end{aligned}\right\} \tag{3.13a}$$

Due to eqs. (3.1) and (3.10) these relations are equivalent to the well-known boson commutation relation for the correlated pair operators A_μ^+ and B_μ^+

$$\left.\begin{aligned} [A_\mu, A_\nu^+] &= \delta_{\mu\nu}, \quad [B_\mu, B_\nu^+] = \delta_{\mu\nu} \\ [A_\mu^+, B_\nu^+] &= [A_\mu^+, B_\nu] = 0. \end{aligned}\right\} \tag{3.13b}$$

Now it is clear that, within the subspace S composed of the unperturbed ground state and all unperturbed 2p-2h excited states in the TD sense, there exists the following one-to-one correspondence between the fermion space and the boson space:

$$|\Phi_0\rangle \leftrightarrow |\Phi_0\rangle\rangle$$

and

$$a_\alpha^+ a_\beta^+ b_\gamma^+ b_\delta^+ |\Phi_0\rangle \equiv |\alpha\beta\gamma\delta\rangle \leftrightarrow \mathfrak{A}_{\alpha\beta}^+ \mathfrak{B}_{\gamma\delta}^+ |\Phi_0\rangle\rangle \equiv |\alpha\beta\gamma\delta\rangle\rangle,$$

where $|\Phi_0\rangle\rangle$ is the unperturbed ground state in the boson space defined by $\mathfrak{A}_{\alpha\beta}|\Phi_0\rangle\rangle = \mathfrak{B}_{\gamma\delta}|\Phi_0\rangle\rangle = 0$. Thus it is easily seen from eq. (3.12) that the Pauli principle is rigorously satisfied in a 2particle-2hole system even though it is treated in the boson space.

(b) As a second consequence of our NTD method (to keep the consistency with the determination of the matrix elements M and M' in (3.3)), we observe that all occurring matrix elements of physical one-body or two-body operators T are entirely restricted to matrix elements taken within a subspace composed of the unperturbed ground state and the unperturbed 2p-2h states. This, however, is just the subspace S in which the Pauli principle is *not* violated by the use of eqs. (3.13).

Thus it is possible to give a rule how to transcribe any physical operator T given in the fermion space into an operator $\mathring{T}$ defined in the boson space [15]. The new operator $\mathring{T}$ has to be constructed such that within the subspace S

$$\left.\begin{aligned} \langle\langle \alpha_1\beta_1\gamma_1\delta_1|\mathring{T}|\alpha_2\beta_2\gamma_2\delta_2\rangle\rangle &= \langle \alpha_1\beta_1\gamma_1\delta_1|T|\alpha_2\beta_2\gamma_2\delta_2\rangle \\ \langle\langle \Phi_0|\mathring{T}|\alpha\beta\gamma\delta\rangle\rangle &= \langle \Phi_0|T|\alpha\beta\gamma\delta\rangle \\ \langle\langle \alpha\beta\gamma\delta|\mathring{T}|\Phi_0\rangle\rangle &= \langle \alpha\beta\gamma\delta|T|\Phi_0\rangle. \end{aligned}\right\} \tag{3.14}$$

Since all matrix elements which occur in the NTD method are taken with respect to states belonging to the subspace S, we can regard the operators $\mathring{T}$ as the *effective physical operators* in our NTD method. Clearly, if we neglect ground-state correlations, then, according to construction, all results obtained with the operator $\mathring{T}$ in the NTD method are identical to the results obtained with the operator T in the TD method.

3.4 The Expansion of Physical Operators

The preceding subsection provides us with a firm basis for expanding various physical operators in terms of pair scattering modes. The first task is to express the creation operator for two uncorrelated particles or holes in terms of pair scattering modes. This is easily achieved with the help of the completeness relation (3.9), and the result is

$$\left.\begin{aligned} a_\alpha^+ a_\beta^+ \to \mathfrak{A}_{\alpha\beta}^+ &= 2(1-\theta_a-\theta_b)\sum_\mu \Psi_\mu(\alpha\beta)(A_\mu^+ - B_\mu) \\ b_\alpha b_\beta \to \mathfrak{B}_{\beta\alpha} &= 2(1-\theta_a-\theta_b)\sum_\mu \Psi_\mu(\alpha\beta)s_\mu C_\mu^+. \end{aligned}\right\} \tag{3.15}$$

The next problem is to find the effective physical operators which are consistent with our NTD approximation. As an example, let us consider a physical one-body operator $\mathfrak{O}$:

$$\mathfrak{O} = \sum_{\alpha\beta}\mathfrak{O}_{\alpha\beta}{:}c_\alpha^+ c_\beta{:} = \sum_{\alpha\beta}\mathfrak{O}_{\alpha\beta}(a_\alpha^+ a_\beta - b_\beta^+ b_\alpha + a_\alpha^+ b_\beta^+ - a_\beta b_\alpha). \tag{3.16}$$

Then, the rule (3.14) easily gives us the transcribed operator

$$\mathring{\mathfrak{O}} = \sum_{\alpha\beta}\sum_\gamma \mathfrak{O}_{\alpha\beta}\{\mathfrak{A}_{\alpha\gamma}^+\mathfrak{A}_{\beta\gamma} - \mathfrak{B}_{\beta\gamma}^+\mathfrak{B}_{\alpha\gamma}\}, \tag{3.17}$$

which is equivalent to the replacement

$$a_\alpha^+ a_\beta \to \sum_\gamma \mathfrak{A}_{\alpha\gamma}^+\mathfrak{A}_{\beta\gamma} \quad \text{and} \quad b_\beta^+ b_\alpha \to \sum_\gamma \mathfrak{B}_{\beta\gamma}^+\mathfrak{B}_{\alpha\gamma}. \tag{3.18}$$

In order to get the expansion of one-body operators (3.16) in terms of pair scattering modes C^+ and C, we have now only to insert (3.15) into (3.17). As an application of the resulting expansion, one can easily find that the total number operator of our system

$$\mathfrak{N} = \sum_{\alpha} c_{\alpha}^{+} c_{\alpha} = \sum_{\alpha} (a_{\alpha}^{+} a_{\alpha} - b_{\alpha}^{+} b_{\alpha}) + \text{total number of particles in the system} \quad (3.19)$$

is expanded as

$$\mathring{\mathfrak{N}} = 2 \sum_{\mu} (A_{\mu}^{+} A_{\mu} - B_{\mu}^{+} B_{\mu}) + \text{total number of particles in the system.} \quad (3.20)$$

Similarly, the μ-component of the angular momentum operator

$$J_{\mu} = \sum_{\alpha\beta} \langle \alpha | J_{\mu} | \beta \rangle \delta_{ab} \delta_{\tau_{\alpha} \tau_{\beta}} : c_{\alpha}^{+} c_{\beta} : \quad (3.21)$$

with

$$\langle \alpha | J_{\mu} | \beta \rangle \delta_{ab} = \langle j_b 1 m_{\beta} \mu | j_a m_{\alpha} \rangle \sqrt{j_a (j_a + 1)}\, \delta_{ab}$$

is expanded as

$$\mathring{J}_{\mu} = \sum_{\varrho\sigma} \langle \varrho | J_{\mu} | \sigma \rangle \delta_{rs} \delta_{Z_{\varrho} Z_{\sigma}} (A_{\varrho}^{+} A_{\sigma} - B_{\varrho}^{+} B_{\sigma}) \quad (3.22)$$

with

$$\langle \varrho | J_{\mu} | \sigma \rangle \delta_{rs} = \langle J_s 1 M_{\sigma} \mu | J_r M_{\varrho} \rangle \sqrt{J_r (J_r + 1)}\, \delta_{rs}.$$

The formal analogy to the usual expressions in the fermion space indicates the usefulness and, in fact, the simplicity of the expansion in terms of pair scattering modes.

3.5 The Expansion of the Hamiltonian

The rule (3.14) also enables us to expand the Hamiltonian in terms of pair scattering modes. Each term (2.6) in the decomposition (2.5) of the Hamiltonian can be transcribed into the boson space. The result is

$$H_0 \to \mathring{H}_0 = \tfrac{1}{2} \sum_{\alpha\beta} (\varepsilon_a + \varepsilon_b)(\mathfrak{A}_{\alpha\beta}^{+} \mathfrak{A}_{\alpha\beta} - \mathfrak{B}_{\alpha\beta}^{+} \mathfrak{B}_{\alpha\beta}) \quad (3.23\,\text{a})$$

$$H_{pp} \to \mathring{H}_{pp} = \sum_{\alpha\beta\gamma\delta} v_{\alpha\beta\gamma\delta} \mathfrak{A}_{\alpha\beta}^{+} \mathfrak{A}_{\gamma\delta} \quad (3.23\,\text{b})$$

$$H_{hh} \to \mathring{H}_{hh} = \sum_{\alpha\beta\gamma\delta} v_{\alpha\beta\gamma\delta} \mathfrak{B}_{\alpha\beta}^{+} \mathfrak{B}_{\gamma\delta} \quad (3.23\,\text{c})$$

$$H_V \to \mathring{H}_V = \sum_{\alpha\beta\gamma\delta} v_{\alpha\beta\gamma\delta} (\mathfrak{A}_{\alpha\beta}^{+} \mathfrak{B}_{\delta\gamma}^{+} + \mathfrak{A}_{\alpha\beta} \mathfrak{B}_{\delta\gamma}) \quad (3.23\,\text{d})$$

$$H_{ph} \to \mathring{H}_{ph} = -4 \sum_{\alpha\beta\gamma\delta} v_{\alpha\beta\gamma\delta} \sum_{\varepsilon} \mathfrak{A}^{+}_{\alpha\varepsilon} \mathfrak{A}_{\gamma\varepsilon} \sum_{\varphi} \mathfrak{B}^{+}_{\delta\varphi} \mathfrak{B}_{\beta\varphi} \tag{3.23e}$$

$$H_Y \to 0. \tag{3.23f}$$

As has been discussed in section 2.1, the operator H_Y does not contribute in our approximation where only states with an even number of particles and holes are considered. This is shown once more in eq. (3.23f).

Remembering that the pair scattering modes were constructed to take into account the interaction terms H_{pp}, H_{hh} and H_V, we calculate the commutators

$$[\mathfrak{H}_0, \mathfrak{A}^{+}_{\alpha\beta}] \quad \text{and} \quad [\mathfrak{H}_0, \mathfrak{B}^{+}_{\alpha\beta}]$$

where

$$\mathfrak{H}_0 = \mathring{H}_0 + \mathring{H}_{pp} + \mathring{H}_{hh} + \mathring{H}_V. \tag{3.24}$$

Using eqs. (3.13) and (3.23) we regain the equations (3.3) which had been the starting point in constructing the pair scattering modes. Correspondingly one obtains for $\mathfrak{H}_0$ the expansion

$$\mathfrak{H}_0 = \sum_{\mu} \omega_m (A^{+}_{\mu} A_{\mu} - B^{+}_{\mu} B_{\mu}). \tag{3.25}$$

This confirms once more the internal consistency of the transcription rule (3.14) with the linearization approximation (3.3).

So far the particle-hole interaction has not been considered at all. But, in the following section, it will be of great importance as the source of new ground-state correlations which reflect the collective predisposition of the ground state for deformed excited states. The desired expansion in terms of pair scattering modes is obtained by inserting (3.15) into (3.23e). This leads to

$$\mathring{H}_{ph} = \sum_{\mu\nu\varrho\sigma} V_{\mu\nu\varrho\sigma} C^{+}_{\mu} C_{\varrho} C_{\sigma} C^{+}_{\nu}. \tag{3.26}$$

Now it is convenient to rewrite $\mathring{H}_{ph}$ as a normal product (symbolized by $\vdots\,\vdots$) with respect to the operators A^{+} and B^{+}. The necessary contractions give us a renormalization of the single-pair energies ω_m which should be determined in a self-consistent way. Here we assume for simplicity that the renormalization is already incorporated in the definition of ω_m. So we can write

$$\mathring{H}_{ph} = \sum_{\mu\nu\varrho\sigma} V_{\mu\nu\varrho\sigma} \vdots C^{+}_{\mu} C^{+}_{\nu} C_{\sigma} C_{\varrho} \vdots \tag{3.27}$$

where the transformed potential matrix element has the symmetry

$$V_{\mu\nu\varrho\sigma} = V_{\varrho\sigma\mu\nu} \tag{3.28}$$

and is explicitly defined by

$$\left.\begin{aligned} V_{\mu\nu\varrho\sigma} = -64 \sum_{\alpha\beta\gamma\delta}{}' \sum_{\varepsilon\varphi}{}' v_{\alpha\beta\gamma\delta} s_\mu s_\nu s_\varrho s_\sigma \Psi_\mu(\alpha\varepsilon)\Psi_\varrho(\gamma\varepsilon)\Psi_\nu(\beta\varphi)\Psi_\sigma(\delta\varphi) \\ \text{with} \quad \left.\begin{matrix} \theta_a = \theta_c = \theta_e = 0 \\ \theta_b = \theta_d = \theta_f = 1 \end{matrix}\right\}. \end{aligned}\right\} \tag{3.29}$$

4. Interaction Between Pairs

In the preceding section, a new basis system has been constructed which consists of pair scattering modes for particles and holes. The properties of these modes have been investigated, and it has been shown how to express all operators of physical interest on the new basis. After this preparation we can turn to the proper aim of the present work, namely the collective description of even parity states in closed-shell nuclei. The present section, therefore, is devoted to the formal solution of the problem, whereas the following section will show where the deformations in the excited states come in.

4.1 The Hamiltonian in Terms of Pair Scattering Modes

Using the expansions (3.25) and (3.27), we can write the Hamiltonian of our system in the form

$$\mathring{H} = \mathfrak{H}_0 + \mathring{H}_{ph} = \sum_\mu \omega_m (A_\mu^+ A_\mu - B_\mu^+ B_\mu) + \sum_{\mu\nu\varrho\sigma} V_{\mu\nu\varrho\sigma} {:} C_\mu^+ C_\nu^+ C_\sigma C_\varrho {:}. \tag{4.1}$$

In analogy to the procedure of section 2.2 we now decompose the Hamiltonian in various terms

$$\mathring{H} = \mathfrak{H}_0 + \mathfrak{H}_{pp} + \mathfrak{H}_{hh} + \mathfrak{H}_{ph} + \mathfrak{H}_V + \mathfrak{H}_Y, \tag{4.2}$$

where $\mathfrak{H}_0$ is given in eq. (3.25) and

$$\mathfrak{H}_{pp} = \sum_{\mu\nu\varrho\sigma} V_{\mu\nu\varrho\sigma} A_\mu^+ A_\nu^+ A_\sigma A_\varrho \tag{4.3a}$$

$$\mathfrak{H}_{hh} = \sum_{\mu\nu\varrho\sigma} V_{\mu\nu\varrho\sigma} B_\mu^+ B_\nu^+ B_\sigma B_\varrho \tag{4.3b}$$

$$\mathfrak{H}_{ph} = \sum_{\mu\nu\varrho\sigma} V_{\mu\nu\varrho\sigma} \{A_\mu^+ B_\sigma^+ A_\varrho B_\nu + A_\mu^+ B_\varrho^+ A_\sigma B_\nu + A_\nu^+ B_\sigma^+ A_\varrho B_\mu + A_\nu^+ B_\varrho^+ A_\sigma B_\mu\} \tag{4.3c}$$

$$\mathfrak{H}_V = \sum_{\mu\nu\varrho\sigma} V_{\mu\nu\varrho\sigma} \{A_\mu^+ A_\nu^+ B_\sigma^+ B_\varrho^+ + A_\mu A_\nu B_\sigma B_\varrho\}. \tag{4.3d}$$

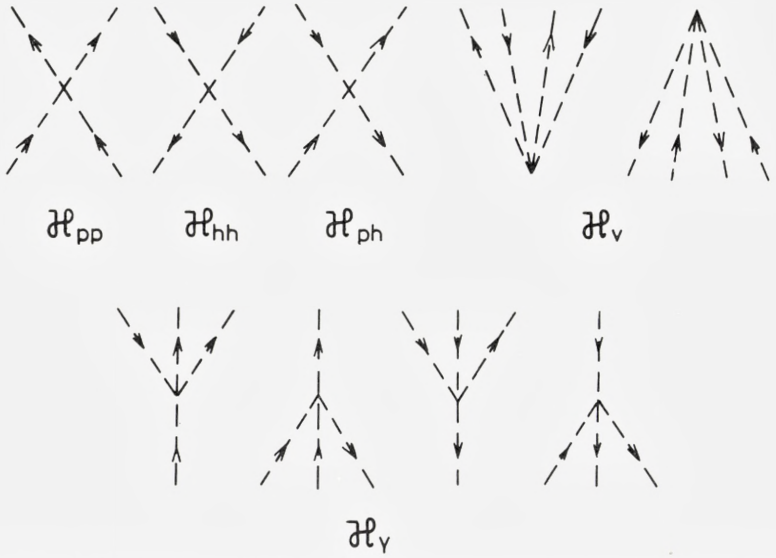

Fig. 4. Graphic representation of the matrix elements arising from the particle-hole interaction or the field-producing force. The broken lines indicate pair scattering modes, for a "particle pair" if the arrow points upwards, for a "hole pair", if the arrow points downwards.

Finally, $\mathfrak{H}_Y$ contains all possible matrix elements analogous to H_Y in (2.6). If we graphically symbolize a correlated pair by a broken line, we can depict in fig. 4 the matrix elements of each part of the particle-hole interaction $\mathring{H}_{p\hbar}$ by diagrams which are formally similar to those of fig. 1. In order to illustrate the physical meaning of these new diagrams, typical graphs contributing to $\mathfrak{H}_{p\hbar}$ and $\mathfrak{H}_V$ are shown in fig. 5 in the conventional representation. From the structure of $V_{\mu\nu\varrho\sigma}$ defined in eq. (3.29) *it is seen that, in the absence of ground-state correlations due to pair scattering* (see fig. 2), *only the first term in* (4.3c) *survives* among all the terms occurring in (4.3). This term is represented in fig. 5(a). Its significance will be discussed in section 5 in connection with deformations for the excited states. The appearance of diagrams of the type $\mathfrak{H}_V$ indicates that the interaction between pairs introduces a new kind of ground-state correlations, which will be shown later to describe the collective predisposition of the ground state for deformed excited states.

Here, it should be pointed out that the interplay between the effect of the field-producing force and the effect of the residual interaction is especially important in producing this new type of ground-state correlations. This

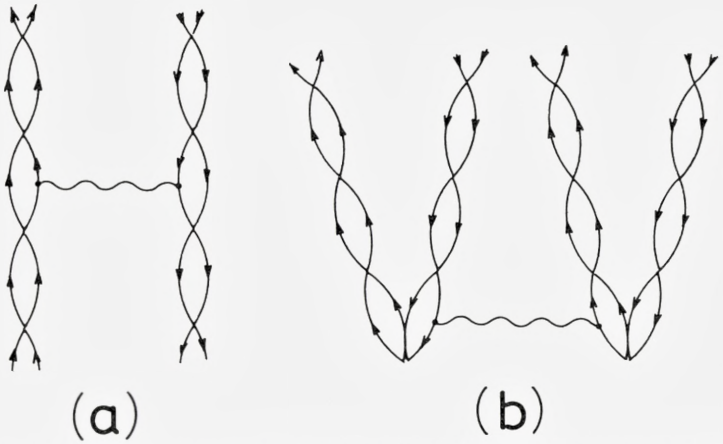

Fig. 5. Typical diagrams in the conventional fermion representation which contribute to the, term $\mathring{H}_{ph}$ decomposed in fig. 4. The diagram (a) occurs, for example, in $\mathfrak{H}_{ph}$, and (b), for example, in $\mathfrak{H}_V$.

is most obvious in the limit where the pair scattering ground-state correlation due to the residual interaction vanishes. Then the new correlations due to the field-producing force, H_{ph}, vanish as well.

At this point it might be appropriate to discuss a shortcoming of the present treatment in the two-step method. With the aim of taking into account the "residual interaction effect" in the first step, we have split the Hamiltonian into $H_{pp}+H_{hh}+H_V$ and H_{ph}, and then have diagonalized $H_{pp}+H_{hh}+H_V$ *only* in the subspace of two particles and in the subspace of two holes (including pair scattering ground-state correlations). In the second step, H_{ph} was taken as the field-producing part of the interaction, which acts between *different* pairs. As a result, those parts of H_{pp} and H_{hh} which act between *different* pairs have been neglected. Physically, this means that the neglected field-producing (i.e., long range) parts of H_{pp} and H_{hh} are assumed to be unimportant compared to H_{ph}. Indeed, if we considered a "2particle-2hole" system (in the NTD sense), the parts discarded in H_{pp} and H_{hh} would enter only via *ground-state correlations*, in contrast to H_{ph}. Thus, their influence* would presumably be very small compared with the influence of H_{ph}. Moreover, the main source of deformations in the excited states of closed-shell nuclei will be the repulsive particle-hole interaction (corresponding to an attractive particle-core interaction). This interaction forces, for example,

* In model calculations it turned out that the interaction $H_{pp}(H_{hh})$ between particles (holes) belonging to different pairs was not at all important for the deformation obtained. See also the arguments at the end of sect. 5.3.

the particles to the poles of the core if the holes are concentrated in the equatorial plane, so that particles and holes contribute with equal sign to the deformation.

To avoid the above shortcoming of our treatment, it is useful to divide the interaction into the residual interaction (with a short range) and the field-producing part (with a long range). In this case, the first step of our treatment corresponds to the diagonalization of the short range force, and the long range force then gives rise to the deformations in the excited states and, at the same time, to the collective ground-state correlations discussed above. The only formal change which results from this decomposition of the Hamiltonian is to modify the definition of the interaction matrix elements $V_{\mu\nu\varrho\sigma}$ in (3.29) by dropping the restriction on the summation, i.e.,

$$V_{\mu\nu\varrho\sigma} = -64 \sum_{\alpha\beta\gamma\delta} \sum_{\varepsilon\varphi} v_{\alpha\beta\gamma\delta} s_\mu s_\nu s_\varrho s_\sigma \Psi_\mu(\alpha\varepsilon)\Psi_\varrho(\gamma\varepsilon)\Psi_\nu(\beta\varphi)\Psi_\sigma(\delta\varphi). \tag{4.4}$$

Thus, the field-producing parts of H_{pp} and H_{hh} are fully included in the Hamiltonian (4.2). It is unnecessary to say that the original division (2.5) of the Hamiltonian has been chosen simply because it is more clear-cut from the formal point of view.

4.2 Collective Modes in the Excitation of Closed Shells

In order to investigate the collective modes due to the field-producing force we start from the following linearized relation:

$$[\mathring{H}, A_\mu^+ B_\nu^+] = \sum_{\varrho\sigma} (N_{\mu\nu\varrho\sigma} A_\varrho^+ B_\sigma^+ + N'_{\mu\nu\varrho\sigma} A_\varrho B_\sigma). \tag{4.5}$$

By taking the appropriate matrix elements of eq. (4.5) with respect to the (unperturbed) eigenstates of $\mathfrak{H}_0$, it is seen that the coefficients N and N' contain only matrix elements of $\mathfrak{H}_0$, $\mathfrak{H}_{ph}$ and $\mathfrak{H}_V$. In this approximation we can define the creation operators of eigenmodes (or "phonons") for even parity excited states of closed-shell nuclei as solutions of the following equation of motion:

$$[\mathring{H}, X_\lambda^+] = \Omega_l X_\lambda^+ \quad \text{with} \quad \Omega_l > 0, \tag{4.6}$$

where

$$X_\lambda^+ = \sum_{\mu\nu} \{\xi_\lambda(\mu\nu) A_\mu^+ B_\nu^+ + \eta_\lambda(\mu\nu) A_\mu B_\nu\} \tag{4.7}$$

with

$$\lambda \equiv \{L, IM, TZ\}, \quad l \equiv \{L, I, T\}. \tag{4.8}$$

Here, λ means the set of quantum numbers composed of the angular momentum I and its projection M, the isospin T and its projection Z and, finally, a set of additional quantum numbers L necessary for a complete specification of the "phonon". Correspondingly, l stands for the set λ with the exclusion of the projection quantum numbers M and Z. From eq. (4.5) one obtains the eigenvalue equation for the functions $\xi_\lambda(\mu\nu)$ and $\eta_\lambda(\mu\nu)$ (taken as real):

$$\left.\begin{aligned} \Omega_l \xi_\lambda(\mu\nu) &= \sum_{\varrho\sigma} \{N_{\varrho\sigma\mu\nu}\, \xi_\lambda(\varrho\sigma) - N'_{\varrho\sigma\mu\nu}\, \eta_\lambda(\varrho\sigma)\} \\ \Omega_l \eta_\lambda(\mu\nu) &= -\sum_{\varrho\sigma} \{N_{\varrho\sigma\mu\nu}\, \eta_\lambda(\varrho\sigma) - N'_{\varrho\sigma\mu\nu}\, \xi_\lambda(\varrho\sigma)\}. \end{aligned}\right\} \tag{4.9}$$

Eq. (4.9) has the same structure as the well-known equations for "1 particle-1 hole" excited states in the RPA, and thus we have the usual orthogonality and completeness relations

$$\sum_{\mu\nu} \{\xi_{\lambda_1}(\mu\nu)\xi_{\lambda_2}(\mu\nu) - \eta_{\lambda_1}(\mu\nu)\eta_{\lambda_2}(\mu\nu)\} = \delta_{\lambda_1\lambda_2} \tag{4.10a}$$

$$\left.\begin{aligned} \sum_{\lambda} \{\xi_\lambda(\mu\nu)\xi_\lambda(\varrho\sigma) - \eta_\lambda(\mu\nu)\eta_\lambda(\varrho\sigma)\} &= \delta_{\mu\varrho}\delta_{\nu\sigma} \\ \sum_{\lambda} \{\xi_\lambda(\mu\nu)\eta_\lambda(\varrho\sigma) - \eta_\lambda(\mu\nu)\xi_\lambda(\varrho\sigma)\} &= 0 \end{aligned}\right\} \tag{4.10b}$$

with

$$\Omega_l > 0.$$

From these relations we get immediately the inverse expansion to eq. (4.7)

$$A^+_\mu B^+_\nu = \sum_{\lambda} (\xi_\lambda(\mu\nu) X^+_\lambda - \eta_\lambda(\mu\nu) X_\lambda). \tag{4.11}$$

We are now in a position to define the new ground state $|\Psi_0\rangle$ for closed-shell nuclei by

$$X_\lambda |\Psi_0\rangle = 0 \tag{4.12}$$

and similarly the excited even parity states $|\Psi_\lambda\rangle$ of closed-shell nuclei by

$$|\Psi_\lambda\rangle = X^+_\lambda |\Psi_0\rangle. \tag{4.13}$$

It is clear from these definitions that both ground state and excited states contain very complex correlations, namely all diagrams of the type indicated in figs. (3a) and (3b).

In order to understand the physical significance of these ground-state correlations, let us first see what happens if we neglect them. (This also means that we neglect the ground-state correlations due to the residual interaction). In that case the linearized equation (4.5) reduces to the equation of the TD method for a 2p-2h system. As an approximation to the TD method one may use the Hartree-Fock approach [3] which is known to yield intrinsically deformed 2p-2h states and a spherical ground state. Let us now gradually switch on the ground-state correlations and correspondingly treat the problem in our NTD method. This procedure will gradually decrease the energy of the excited states. At the same time it will leave the excited states deformed and the ground state spherical, until, with increasing interaction strength, the smallest excitation energy (i.e., the lowest Ω_l) passes through zero. Then the spherical ground state becomes unstable and undergoes a phase transition into a deformed state.

Although the physical ground state is spherical, it has a collective predisposition to produce deformed excited states due to the symmetrical treatment of ground state and excited states in our NTD method. This is in contrast to the "1p-1h" problem in the usual RPA, where a spherical (deformed) ground state is always associated with a spherical (deformed) excited state. The difference is that a pure 2p-2h excitation is intrinsically deformed by itself. The bare deformation of the 2p-2h excitation has a further consequence: Due to the ground-state correlations the "dressed 2p-2h" excited states defined by (4.13) possess a "dressed" deformation which includes, and is amplified by, the cooperation effect of the core deformation.

5. Deformation of the Excited States

In the preceding section, general solutions were obtained in a spherical representation, so that the deformation of the excited states would only manifest itself in a rotational band structure. In this section, however, we want to set the deformation into evidence more directly, using a sequence of successively generalized self-consistent field methods. For simplicity, we adopt a separable field-producing force. Starting from the conventional Hartree-Fock approximation [3], we easily see how to generalize the method in order to take into account the residual interaction. A final generalization treats the full core polarization due to the collective ground-state correlations in a self-consistent way. This turns out to be an approximation to the general solutions of section 4, thus explicitly demonstrating their deformed nature.

5.1 A Separable Field-Producing Force

In order to see the origin of the deformation in the excited state more clearly, it is convenient to divide the interaction into the field-producing (long-range) part and the residual interaction (short-range part). For simplicity, we furthermore assume the field-producing force to be separable:

$$H_f = -\tfrac{1}{2}\sum_{LM}\chi_L : Q_{LM}Q_{LM}^{+} :, \tag{5.1}$$

where Q_{LM} is given by

$$Q_{LM} = \sum_{\alpha\beta} r\langle\alpha|r^L Y_{LM}(\theta\varphi)|\beta\rangle : c_\alpha^{+} c_\beta :. \tag{5.2}$$

With the aid of the rule (3.14) and eq. (3.15), the operator Q_{LM} is expanded in terms of pair scattering modes as

$$\mathring{Q}_{LM} = \sum_{\mu\nu}(\mu|Q_{LM}|\nu) : C_\mu^{+} C_\nu :, \tag{5.3}$$

where

$$(\mu|Q_{LM}|r) = 4\sum_{\alpha\beta\gamma}\langle\alpha|r^L Y_{LM}(\theta\varphi)|\beta\rangle s_\mu \Psi_\mu(\alpha\gamma)(1-\theta_a-\theta_c)s_\nu\Psi_\nu(\beta\gamma). \tag{5.4}$$

Thus, one may write down the field-producing force in terms of the pair-scattering modes in the following form:

$$\mathring{H}_f = -\tfrac{1}{2}\sum_{LM}\chi_L : \mathring{Q}_{LM}\mathring{Q}_{LM}^{+} :. \tag{5.5}$$

For later discussions it is convenient to divide $\mathring{Q}_{LM}$ and $\mathring{H}_f$ into the following parts:

$$\mathring{Q}_{LM} = \mathring{Q}_{LM}^{(1)} + \mathring{Q}_{LM}^{(2)}, \tag{5.6}$$

$$\left.\begin{aligned} \mathring{H}_f &= \mathfrak{H}^{(1)} + \mathfrak{H}^{(2)} + \mathfrak{H}^{(3)}, \\ \mathfrak{H}^{(1)} &= -\tfrac{1}{2}\sum_{LM}\chi_L : \mathring{Q}_{LM}^{(1)}\mathring{Q}_{LM}^{(1)+} : \\ \mathfrak{H}^{(2)} &= -\tfrac{1}{2}\sum_{LM}\chi_L : \mathring{Q}_{LM}^{(2)}\mathring{Q}_{LM}^{(2)+} : \\ \mathfrak{H}^{(3)} &= -\sum_{LM}\chi_L : \mathring{Q}_{LM}^{(1)}\mathring{Q}_{LM}^{(2)+} : \end{aligned}\right\} \tag{5.7}$$

where

$$\left.\begin{aligned} \mathring{Q}_{LM}^{(1)} &= \sum_{\mu\nu}(\mu|Q_{LM}|\nu)(A_\mu^{+}A_\nu + B_\nu^{+}B_\mu) \\ \mathring{Q}_{LM}^{(2)} &= \sum_{\mu\nu}(\mu|Q_{LM}|\nu)(A_\mu^{+}B_\nu^{+} + A_\nu B_\mu). \end{aligned}\right\} \tag{5.8}$$

The term $\mathfrak{H}^{(3)}$ in eq. (5.7) corresponds to $\mathfrak{H}_Y$ in eq. (4.2) which has played no role in constructing the collective excited states discussed in sec. 4. For consistency, we therefore discard $\mathfrak{H}^{(3)}$ in the following. It should be noted that, in the absence of pair-scattering ground-state correlations, only $\mathring{Q}^{(1)}_{LM}$ and $\mathfrak{H}^{(1)}$ survive. This is easily seen from the structure of $(\mu|Q_{LM}|\nu)$ in eq. (5.4).

5.2 An Extension of the Hartree-Fock Approximation

The origin of the deformation in the excited states can be traced most clearly using the self-consistent field method which leads to the notion of an *intrinsic deformation* in a natural way. In this subsection we investigate the mechanism which leads to intrinsic deformations in the excited states in the case without ground-state correlations.

In this case, the exact 2p-2h eigenstates are given by

$$|\Phi_\lambda\rangle = X^{(TD)+}_\lambda|\Phi_0\rangle, \quad (a_\alpha|\Phi_0\rangle = b_\alpha|\Phi_0\rangle = 0) \tag{5.9}$$

with their creation operators

$$X^{(TD)+}_\lambda = \sum_{\alpha\beta\gamma\delta} f_\lambda(\alpha\beta\gamma\delta) a^+_\alpha a^+_\beta b^+_\gamma b^+_\delta . \tag{5.10}$$

The function f_λ (taken as real) satisfies the eigenvalue equation

$$\Omega^{(TD)}_l f_\lambda(\alpha_1\beta_1\gamma_1\delta_1) = \sum_{\alpha_2\beta_2\gamma_2\delta_2} L_{\alpha_2\beta_2\gamma_2\delta_2,\,\alpha_1\beta_1\gamma_1\delta_1} f_\lambda(\alpha_2\beta_2\gamma_2\delta_2), \tag{5.11}$$

where the coefficients L are defined by the usual linearized relation characterizing the TD method:

$$[H, a^+_{\alpha_1} a^+_{\beta_1} b^+_{\gamma_1} b^+_{\delta_1}] = \sum_{\alpha_2\beta_2\gamma_2\delta_2} L_{\alpha_1\beta_1\gamma_1\delta_1,\,\alpha_2\beta_2\gamma_2\delta_2} a^+_{\alpha_2} a^+_{\beta_2} b^+_{\gamma_2} b^+_{\delta_2}. \tag{5.12}$$

It is known that the eigenvalue equation eq. (5.11) can also be obtained from the variational principle

$$\delta\left\{\langle\Phi_0|X^{(TD)}_\lambda, HX^{(TD)+}_\lambda|\Phi_0\rangle - \Omega^{(TD)}_l\langle\Phi_0|X^{(TD)}_\lambda, X^{(TD)+}_\lambda|\Phi_0\rangle\right\} = 0. \tag{5.13}$$

The intrinsic deformation of a state $|\Phi_{\lambda_0}\rangle$ in eq. (5.9) with $J = 0$ will manifest itself in a Hartree-Fock approximation [3, 4] in which the trial function for $f_{\lambda_0}(\alpha\beta\gamma\delta)$ is taken as

$$f_{\lambda_0}(\alpha\beta\gamma\delta) \approx f_{k_0 l_0 m_0 n_0}(\alpha\beta\gamma\delta) = \tfrac{1}{4}\,\mathfrak{A}\{\psi_{k_0}(\alpha)\psi_{l_0}(\beta)\}\,\mathfrak{A}\{\varphi_{m_0}(\gamma)\varphi_{n_0}(\delta)\}. \tag{5.14}$$

($\mathfrak{A}$: the antisymmetrization operator)

with separate orthonormality conditions among the ψ and φ. The variational principle leads to the well-known single-particle problem in a self-consistent field, whose deviation from the spherical shape defines the intrinsic deformation of the state $|\Phi_{\lambda_0}\rangle$ with $J = 0$.

In the above Hartree-Fock approximation, the residual interaction is completely discarded, as is clear from its definition, and only the field-producing force is taken into account. To overcome this shortcoming we can use the following procedure:

(a) In a first step we diagonalize the residual interaction. The operators of pair scattering eigenmodes are then of the form

$$\hat{A}_\mu^+ = \sum_{\alpha\beta} \psi_\mu^{(TD)}(\alpha\beta) a_\alpha^+ a_\beta^+, \quad \hat{B}_\nu^+ = \sum_{\gamma\delta} \varphi_\nu^{(TD)}(\gamma\delta) b_\delta^+ b_\gamma^+ \tag{5.15}$$

to which the operators of the pair scattering eigenmodes defined in eq. (3.1) are reduced when the ground-state correlations are neglected. Within the subspace of 2p-2h excitations the Hamiltonian can thus be written

$$H^{(TD)} = \sum_\mu \omega_m^{(TD)} \hat{A}_\mu^+ \hat{A}_\mu - \sum_\nu \omega_n^{(TD)} B_\nu^+ \hat{B}_\nu - \tfrac{1}{2} \sum_{LM} \chi_L : Q_{LM}^{(1)(TD)} Q_{LM}^{(1)(TD)+} : . \tag{5.16}$$

Here, $Q_{LM}^{(1)(TD)}$ is given by

$$Q_{LM}^{(1)(TD)} = \sum_{\mu_1\mu_2} (\mu_1 | Q_{LM} | \mu_2)_{TD} \hat{A}_{\mu_1}^+ \hat{A}_{\mu_2} + \sum_{\nu_1\nu_2} (\nu_1 | Q_{LM} | \nu_2)_{TD} \hat{B}_{\nu_2}^+ \hat{B}_{\nu_1}, \tag{5.17}$$

to which $\mathring{Q}_{LM}$ defined by eq. (5.6) is reduced in the absence of ground-state correlations.

(b) In the next step, we use a variational approach, taking a trial state vector for $|\Phi_{\lambda_0}\rangle$ with $J = 0$ as follows:

$$|\Phi_{\lambda_0}\rangle \approx |\Phi_{i_0 j_0}\rangle = \hat{A}_{i_0}^+ \hat{B}_{j_0}^+ |\Phi_0\rangle, \quad (\hat{A}_\mu |\Phi_0\rangle = \hat{B}_\nu |\Phi_0\rangle = 0) \tag{5.18}$$

with

$$\left.\begin{aligned} \hat{A}_{i_0}^+ &= \sum_\mu u_{i_0}(\mu) \hat{A}_\mu^+, \quad \hat{B}_{j_0}^+ = \sum_\nu v_{j_0}(\nu) \hat{B}_\nu^+, \\ \sum_\mu u_{i_0}^2(\mu) &= 1, \qquad \sum_\nu v_{j_0}^2(\nu) = 1. \end{aligned}\right\} \tag{5.19}$$

The variational principle for the Hamiltonian (5.16) gives the following self-consistent eigenvalue equations with $\Omega_{i_0}^{(TD)} = W_{i_0}^{(TD)} - W_{j_0}^{(TD)}$:

$$\left.\begin{aligned} W_{i_0}^{(TD)} u_{i_0}(\mu_1) &= \omega_{m_1}^{(TD)} u_{i_0}(\mu_1) + \sum_{\mu_2} U_{\mu_1\mu_2}^{[h]} u_{i_0}(\mu_2), \\ W_{j_0}^{(TD)} v_{j_0}(\nu_1) &= \omega_{n_1}^{(TD)} v_{j_0}(\nu_1) - \sum_{\nu_2} U_{\nu_1\nu_2}^{[p]} v_{j_0}(\nu_2) \end{aligned}\right\} \tag{5.20}$$

where

$$\left.\begin{aligned} U^{[h]}_{\mu_1\mu_2} &= -\sum_{LM} \chi_L (-)^M (\mu_1 | Q_{L-M} | \mu_2)_{TD} \cdot \alpha^{(h)}_{LM} \\ U^{[p]}_{\nu_1\nu_2} &= -\sum_{LM} \chi_L (-)^M (\nu_1 | Q_{L-M} | \nu_2)_{TD} \cdot \alpha^{(p)}_{LM}, \end{aligned}\right\} \tag{5.21 a}$$

$$\left.\begin{aligned} \alpha^{(h)}_{LM} &= \sum_{\nu_1\nu_2} (\nu_1 | Q_{LM} | \nu_2)_{TD} v_{j_0}(\nu_1) v_{j_0}(\nu_2) \\ \alpha^{(p)}_{LM} &= \sum_{\mu_1\mu_2} (\mu_1 | Q_{LM} | \mu_2)_{TD} u_{i_0}(\mu_1) u_{i_0}(\mu_2). \end{aligned}\right\} \tag{5.21 b}$$

The eqs. (5.20) constitute a self-consistent field problem for a single pair of two particles or two holes. The particle pair is moving in the field $U^{[h]}$ generated by the hole pair, and vice versa. Thus, the intrinsic deformation of the state $|\Phi_{\lambda_0}\rangle$ with $J = 0$ is given by

$$\langle \Phi_{i_0 j_0} | Q_{LM} | \Phi_{i_0 j_0} \rangle = \alpha^{(p)}_{LM} + \alpha^{(h)}_{LM} \equiv \alpha_{LM}. \tag{5.22}$$

The situation obtained by solving (5.20) is illustrated in fig. 6 for a simple model.

In order to see the connection with the Hartree-Fock approximation (5.14), it is noted that the derivation of eqs. (5.20) is essentially equivalent to a variational approach with the following choice of the trial function for $f_{\lambda_0}(\alpha\beta\gamma\delta)$ in eq. (5.10):

$$f_{\lambda_0}(\alpha\beta\gamma\delta) \approx f_{i_0 j_0}(\alpha\beta\gamma\delta) = f_{i_0}(\alpha\beta) f_{j_0}(\gamma\delta) \tag{5.23}$$

with

$$f_{i_0}(\alpha\beta) = -f_{i_0}(\beta\alpha), \quad f_{j_0}(\gamma\delta) = -f_{j_0}(\delta\gamma).$$

In this procedure the Pauli principle is taken properly into account, as was pointed out in section 3.3. The two steps used in deriving eqs. (5.20) are just a convenient but unessential decomposition of f_{i_0} and f_{j_0} into

$$f_{i_0}(\alpha\beta) = \sum_{\mu} u_{i_0}(\mu) \psi^{(TD)}_{\mu}(\alpha\beta) \quad \text{and} \quad f_{j_0}(\gamma\delta) = \sum_{\nu} v_{j_0}(\nu) \varphi^{(TD)}_{\nu}(\delta\gamma).$$

From the variational point of view, therefore, the procedure is simply a generalization of the Hartree-Fock approximation with the purpose of taking the residual interaction properly into account.

5.3 The Origin of the Intrinsic Deformation

So far we have considered the simplified case in which the ground-state correlations are completely discarded. However, the formal extension of

the treatment given in the previous subsection to the case in which the pair scattering ground-state correlations are taken into account is straightforward. We only have to consider the Hamiltonian

$$\mathring{H}' = \sum_{\mu} \omega_m A_\mu^+ A_\mu - \sum_{\nu} \omega_n B_\nu^+ B_\nu + \mathfrak{H}^{(1)}. \tag{5.24}$$

where $\mathfrak{H}^{(1)}$ is defined in (5.7). Then we construct the eigenstates of correlated "2p-2h" excitations

$$|\Phi'_\lambda\rangle = \sum_{\mu\nu} \tilde{\xi}_\lambda(\mu\nu) A_\mu^+ B_\nu^+ |\Phi'_0\rangle, \qquad (A_\mu|\Phi'_0\rangle = B_\nu|\Phi'_0\rangle = 0), \tag{5.25}$$

with the aim of diagonalizing the Hamiltonian (5.24) within the subspace composed of the unperturbed states $A_\mu^+ B_\nu^+ |\Phi'_0\rangle$. Instead of solving the eigenvalue equation for $\tilde{\xi}_\lambda(\mu\nu)$ directly, we use a similar variational approach as in section 5.2. To this end we assume for an eigenstate (5.25), $|\Phi'_{\lambda_0}\rangle$ with $J = 0$, the following trial form

$$|\Phi'_{\lambda_0}\rangle \approx |\Phi'_{i_0 j_0}\rangle = A_{i_0}^+ B_{j_0}^+ |\Phi'_0\rangle \tag{5.26}$$

with

$$\left.\begin{aligned} A_{i_0}^+ &= \sum_{\mu} u_{i_0}(\mu) A_\mu^+, \qquad B_{j_0}^+ = \sum_{\nu} v_{j_0}(\nu) B_\nu^+ \\ \sum_{\mu} u_{i_0}^2(\mu) &= 1, \qquad\qquad \sum_{\nu} v_{j_0}^2(\nu) = 1. \end{aligned}\right\} \tag{5.27}$$

The variational principle with the Hamiltonian (5.24) leads to self-consistent eigenvalue equations which are identical with eqs. (5.20), except that the label (TD) has to be dropped everywhere. For the sake of later reference, we just write down the coupled equations

$$\left.\begin{aligned} W_{i_0} u_{i_0}(\mu_1) &= \omega_{m_1} u_{i_0}(\mu_1) + \sum_{\mu_2} U^{[\hbar]}_{\mu_1\mu_2} u_{i_0}(\mu_2) \\ W_{j_0} v_{j_0}(\nu_1) &= \omega_{n_1} v_{j_0}(\nu_1) - \sum_{\nu_2} U^{[p]}_{\nu_1\nu_2} v_{j_0}(\nu_2). \end{aligned}\right\} \tag{5.28}$$

All quantities here are defined by eqs. (5.21) if the index (TD) is disregarded. The intrinsic deformation for the state $|\Phi'_{\lambda_0}\rangle$ with $J = 0$ is given by

$$\langle \Phi'_{i_0 j_0}|\mathring{Q}_{LM}|\Phi'_{i_0 j_0}\rangle = \langle \Phi'_{i_0 j_0}|\mathring{Q}^{(1)}_{LM}|\Phi'_{i_0 j_0}\rangle \equiv \alpha_{LM}, \tag{5.29}$$

where $\mathring{Q}_{LM}$ is defined by eq. (5.6) and we have used the result $\langle \Phi'_{i_0 j_0}|\mathring{Q}^{(2)}_{LM}|\Phi'_{i_0 j_0}\rangle = 0$. In contrast to eq. (5.22) the new equation (5.29) now defines an intrinsic deformation α_{LM} which contains the core polarization

effect due to the pair scattering ground-state correlations. This situation is illustrated in fig. 7 for a simplified model.

Now the origin of the intrinsic deformation in the excited states is obvious. The essential part of the field-producing force responsible for the deformations in the excited states is just the interaction $\mathfrak{H}^{(1)}$. The interaction $\mathfrak{H}^{(1)}$ survives in the absence of ground-state correlations, and can be visualized physically as the repulsive particle-hole interaction as follows: Let us decompose $\mathfrak{H}^{(1)}$ into

$$\mathfrak{H}^{(1)} = \mathfrak{H}^{(1)}_{ph} + \mathfrak{H}^{(1)}_{pp} + \mathfrak{H}^{(1)}_{hh} \tag{5.30}$$

where $\mathfrak{H}^{(1)}_{pp}$ and $\mathfrak{H}^{(1)}_{hh}$ have the same structure as eqs. (4.3a) and (4.3b), respectively, and

$$\mathfrak{H}^{(1)}_{ph} = -\sum_{LM} \chi_L (-)^M \sum_{\mu_1 \nu_1} \sum_{\mu_2 \nu_2} (\mu_1 | Q_{LM} | \nu_1)(\mu_2 | Q_{L-M} | \nu_2) \{ A^+_{\mu_1} A_{\nu_1} B^+_{\nu_2} B_{\mu_2} \}. \tag{5.31}$$

We can see that only $\mathfrak{H}^{(1)}_{ph}$, which arises mainly* from the particle-hole interaction, contributes in the "2p-2h" problem since the expectation values of $\mathfrak{H}^{(1)}_{pp}$ and $\mathfrak{H}^{(1)}_{hh}$ with respect to $|\Phi'_{\lambda_0}\rangle$ are zero.

On the other hand, the interaction $\mathfrak{H}^{(2)}$ vanishes in the absence of ground-state correlations and will become important for constructing collective ground-state correlations due to the field-producing force. This will be elucidated in section 5.4.

Numerical Calculations for a Simple Model

The coupled self-consistent equations (5.28) describe a correlated particle pair moving in the field produced by a correlated hole pair, and vice versa. In order to investigate the deformation-producing mechanism, we adopted a simplified model and solved eqs. (5.28) self-consistently. In zeroth order, the model consisted in one occupied level with angular momentum j_h and one unoccupied level with angular momentum j_p. The spacing of these levels was taken to be $2\varepsilon_0$, with ε_0 serving as an energy unit. The interaction was taken to be composed of the conventional pairing force with the strength G_0 and the conventional quadrupole force with the strength χ (both measured in units of ε_0). This system was found to have the following properties:

* This is easily seen by neglecting the pair scattering ground-state correlations. In this case, only the particle-hole interaction H_{ph} contributes to $\mathfrak{H}^{(1)}_{ph}$. Correspondingly, $\mathfrak{H}^{(1)}_{pp}$ and $\mathfrak{H}^{(1)}_{hh}$ are just reduced to the field-producing (i.e., long range) parts of H_{pp} and H_{hh} that have been discussed in section 4.1.

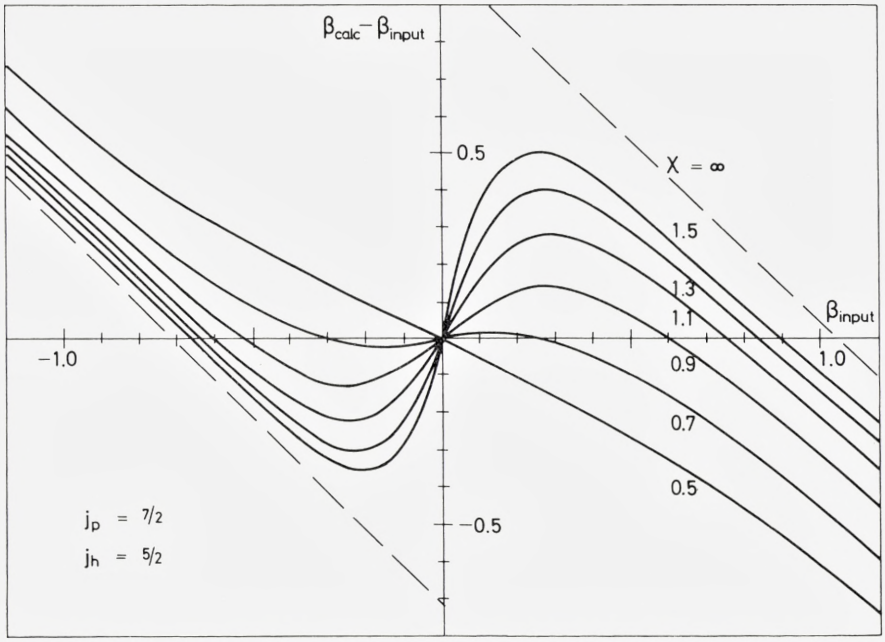

Fig. 6. Illustration showing the instability of a spherical 2p-2h excitation with respect to deformation. Details are explained in the text.

(a) Defining the deformation $\beta = \beta_p + \beta_h$ as the dimensionless *angular* part of α_{20} in eq. (5.29), the following dependence on the parameters χ and G_0 was obtained. For a fixed strength of the pairing force, the spherical shape, $\beta = 0$, is stable as long as the quadrupole force is sufficiently weak. For increasing χ the spherical shape becomes unstable, and two stable deformed solutions emerge, one with a positive and the other with a negative deformation. For large χ the deformation tends to a saturation value. The energy is lowered roughly linearly with χ, starting from the point at which the system becomes deformed. For reasonably weak pairing forces ($G_0 < 0.15$) the results are not very sensitive to G_0. Therefore we illustrate the stability situation in fig. 6 for $G_0 = 0$, choosing $j_p = 7/2$ and $j_h = 5/2$. For simplicity, we restrict ourselves in fig. 6 to particle pairs and hole pairs with $J = 0$ and $J = 2$, measuring χ in units of the arbitrarily fixed energy splitting between these levels. Inclusion of all possible values of J changes the result by less than 10 percent. In fig. 6 we use $\beta_h = \beta_{\text{input}}$ as an input parameter and plot the difference $(\beta_{\text{calc}} - \beta_{\text{input}})$ of the hole deformation (calculated according to eq. (5.28)) and the input deformation as a function of β_{input}.

Evidently, self-consistency is obtained for $(\beta_{\text{calc}}\text{-}\beta_{\text{input}}) = 0$, but the solution is stable only if the derivative $d(\beta_{\text{calc}}\text{-}\beta_{\text{input}})/d\beta_{\text{input}} < 0$. It is seen that the spherical solution becomes unstable between $\chi = 0.6$ and $\chi = 0.7$.

(b) In all calculations with an attractive quadrupole force ($\chi > 0$) the particle deformation, β_p, turned out to have the same sign as the hole deformation β_h. This feature is decisive for obtaining stable deformations and is due to the mutual repulsion of particles and holes for $\chi = 0$ (see also footnote on p. 12).

(c) *For a fixed value of* χ the deformation decreases with increasing G_0, for small G_0 slowly, for large G_0 more rapidly. The reason is the following: Increasing G_0 enlarges the energy splitting between the particle (hole) pair states with $J = 0$ and $J \neq 0$, thus diminishing the ability of the quadrupole force to mix the levels and to produce deformations.

(d) In our model the pairing force introduces ground-state correlations and consequently an admixture of 4p-4h, 6p-6h, . . . to the dominant 2p-2h configurations. That is, the pairing force leads in a natural way to core excitations. In order to investigate the effect of continuously increasing core excitations we used in fig. 7 a fixed spectrum for the pair scattering modes, unaffected by the pairing force and simulating an "experimental" spectrum. The energies of the particle (hole) pair scattering modes were arbitrarily assumed to be $E_J/\varepsilon_0 = \pm(1.5 + 0.1 \cdot J)$ for $J = 0, 2, \ldots, 8$. Fig. 7 shows how the pairing force in this case *increases* the deformation, and decreases the energy by admixing 4p-4h, 6p-6h, . . . configurations. The vertical line indicates the phase transition to superconductivity. When approaching this point, the deformation becomes much larger than the limiting deformation which can be obtained for a pure 2p-2h excitation. Thus the pairing force, by introducing ground-state correlations, softens the core so that the quadrupole force can efficiently produce deformations. However, since we disregard the effect of the pairing force which *stabilizes the spherical shape* as discussed under (c), the deformation plotted in fig. 7 gives us only a measure of the "triggering effect" for deformations. The actual deformations are mainly due to the core deformation effect which enters through the collective ground-state correlations discussed in sect. 4. *Thus, the core deformation effect due to the field-producing force is triggered by the core softening effect due to the pairing force.*

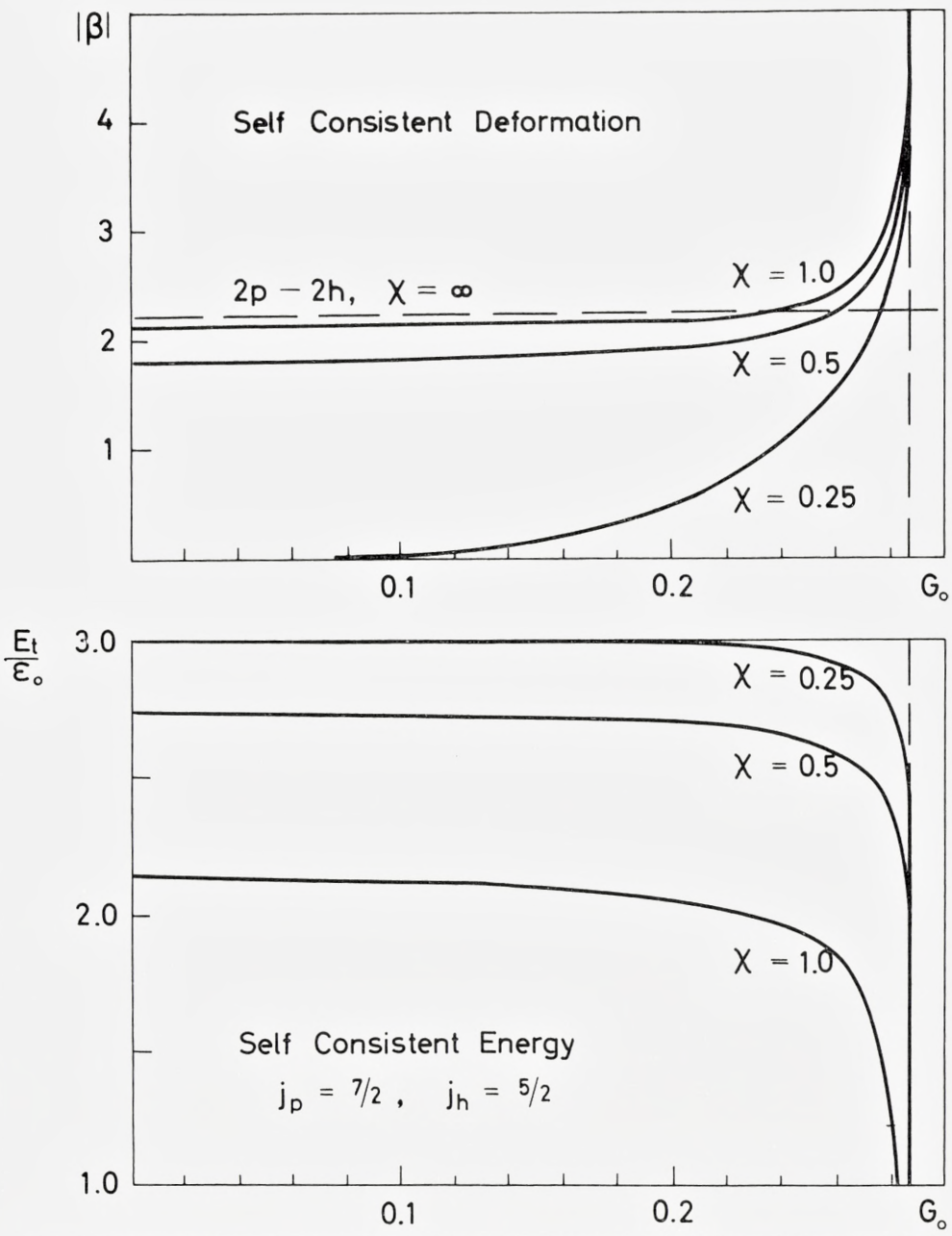

Fig. 7. Self-consistent deformation and self-consistent energy as functions of the strength G_0 of the pairing force for various strength parameters χ of the quadrupole force. Details are explained in the text.

5.4. A Self-Consistent Method Including the Core Deformation

In the preceding subsection we have traced the origin of the intrinsic deformation in excited states. Now we are in a position to present a method which demonstrates explicitly the intrinsic deformation of a "dressed 2p-2h" state containing the collective ground-state correlations. To do this, it is useful to note that the eigenvalue equation (5.28) can also be obtained from the following procedure.

(a) In a first step we introduce the approximation

$$\left.\begin{aligned} \mathfrak{H}_{ph}^{(1)} \approx & -\sum_{LM}\chi_L(-)^M\sum_{\mu\nu}(\mu|Q_{L-M}|\nu)B_\nu^+B_\mu\cdot\alpha_{LM}^{(p)} \\ & -\sum_{LM}\chi_L(-)^M\sum_{\mu\nu}(\mu|Q_{L-M}|\nu)A_\mu^+A_\nu\cdot\alpha_{LM}^{(h)} \\ & +\text{const}\Big(\sum_{LM}\chi_L(-)^M\alpha_{LM}^{(p)}\alpha_{L-M}^{(h)}\Big) \equiv \mathfrak{H}_{ph}^{(1)}(\alpha) \end{aligned}\right\} \quad (5.32)$$

with

$$\left.\begin{aligned} \alpha_{LM}^{(p)} &= \sum_{\mu\nu}(\mu|Q_{LM}|\nu)\langle A_\mu^+A_\nu\rangle \\ \alpha_{LM}^{(h)} &= \sum_{\mu\nu}(\mu|Q_{LM}|\nu)\langle B_\nu^+B_\mu\rangle \end{aligned}\right\} \quad (5.33)$$

where $\langle A_\mu^+A_\nu\rangle$ and $\langle B_\nu^+B_\mu\rangle$ are expectation values which will be determined later in a self-consistent way.

(b) As the next step we construct the eigenstate

$$|\Phi'_{ij}\rangle = \sum_{\mu\nu}\tilde{\xi}_{ij}(\mu\nu)A_\mu^+B_\nu^+|\Phi'_0\rangle \quad (5.34)$$

with the aim of diagonalizing the following Hamiltonian within the subspace composed of the unperturbed states $A_\mu^+B_\nu^+|\Phi'_0\rangle$:

$$\mathring{H}'(\alpha) = \sum_\mu\omega_mA_\mu^+A_\mu - \sum_\nu\omega_nB_\nu^+B_\nu + \mathfrak{H}_{ph}^{(1)}(\alpha). \quad (5.35)$$

(c) The expectation values $\langle A_\mu^+A_\nu\rangle$ and $\langle B_\nu^+B_\mu\rangle$ are determined self-consistently by the condition

$$\left.\begin{aligned} \langle\Phi'_{ij}|A_\mu^+A_\nu|\Phi'_{ij}\rangle &= \langle A_\mu^+A_\nu\rangle \\ \langle\Phi'_{ij}|B_\nu^+B_\mu|\Phi'_{ij}\rangle &= \langle B_\nu^+B_\mu\rangle. \end{aligned}\right\} \quad (5.36)$$

We can easily see that the eigenvalue equation for $\tilde{\xi}_{ij}(\mu\nu)$ defined by eq. (5.34) is identical to the equation obtained by the variational approach which is described by eqs. (5.26) and (5.27) and yields $\tilde{\xi}_{ij}(\mu\nu) = u_i(\mu)v_j(\nu)$.

This equivalence leads immediately to a self-consistent method which demonstrates explicitly the intrinsic deformation in the "dressed 2p-2h"

states subject to the cooperation effect of the core deformation. This method consists of the following operations: With the Hamiltonian

$$\mathring{H}(\alpha) = \sum_{\mu} \omega_m A_\mu^+ A_\mu - \sum_{\nu} \omega_n B_\nu^+ B_\nu + \{\mathfrak{H}_{ph}^{(1)}(\alpha) + \mathfrak{H}_{hh}^{(1)} + \mathfrak{H}_{pp}^{(1)}\} + \mathfrak{H}^{(2)}, \tag{5.37}$$

we start from a linearized relation similar to eq. (4.5)

$$[\mathring{H}(\alpha), A_\mu^+ B_\nu^+] = \sum_{\varrho\sigma} \{N_{\mu\nu\varrho\sigma}(\alpha) A_\varrho^+ B_\sigma^+ + N'_{\mu\nu\varrho\sigma} A_\varrho B_\sigma\}, \tag{5.38}$$

where the coefficients $N(\alpha)$ are now functions of all $\alpha_{LM}^{(p)}$ and $\alpha_{LM}^{(h)}$. The creation operator of the eigenmode, which satisfies the relation

$$[\mathring{H}(\alpha), X_\gamma^+] = \Omega_\gamma X_\gamma^+ \quad \text{with} \quad \Omega_\gamma > 0, \tag{5.39}$$

is then given by

$$X_\gamma^+ = \sum_{\mu\nu} \{\xi_\gamma(\mu\nu) A_\mu^+ B_\nu^+ + \eta_\gamma(\mu\nu) A_\mu B_\nu\}. \tag{5.40}$$

Here, γ is a set of quantum numbers specifying the excited state under consideration

$$|\Psi_\gamma\rangle = X_\gamma^+ |\Psi_0\rangle, \; (X_\gamma |\Psi_0\rangle = 0). \tag{5.41}$$

With the aid of eq. (5.38) the functions $\xi_\gamma(\mu\nu)$ and $\eta_\gamma(\mu\nu)$ are seen to obey the eigenvalue equations

$$\left.\begin{aligned} \Omega_\gamma \xi_\gamma(\mu\nu) &= \sum_{\varrho\sigma} \{N_{\varrho\sigma\mu\nu}(\alpha) \xi_\gamma(\varrho\sigma) - N'_{\varrho\sigma\mu\nu} \eta_\gamma(\varrho\sigma)\} \\ \Omega_\gamma \eta_\gamma(\mu\nu) &= -\sum_{\varrho\sigma} \{N_{\varrho\sigma\mu\nu}(\alpha) \eta_\gamma(\varrho\sigma) - N'_{\varrho\sigma\mu\nu} \xi_\gamma(\varrho\sigma)\}. \end{aligned}\right\} \tag{5.42}$$

The orthogonality and completeness relations of $\xi_\gamma(\mu\nu)$ and $\eta_\gamma(\mu\nu)$ are of the same form as eq. (4.10).

The quantities $\alpha_{LM}^{(p)}$ and $\alpha_{LM}^{(h)}$ are determined self-consistently by

$$\left.\begin{aligned} \alpha_{LM}^{(p)} &= \sum_{\mu\nu} (\mu | Q_{LM} | \nu) \langle \Psi_\gamma | A_\mu^+ A_\nu | \Psi_\gamma \rangle \\ \alpha_{LM}^{(h)} &= \sum_{\mu\nu} (\mu | Q_{LM} | \nu) \langle \Psi_\gamma | B_\nu^+ B_\mu | \Psi_\gamma \rangle. \end{aligned}\right\} \tag{5.43}$$

Now it is clear that the eigenvalue equation (5.42) with the self-consistency condition (5.43) is simply a generalization of eq. (5.20) with eq. (5.21) for the purpose of taking the cooperation effect of the core deformation into

account. The intrinsic deformation of the "dressed 2p-2h" states associated with the core deformation is now given by

$$\alpha_{LM} \equiv \langle \Psi_\gamma | \mathring{Q}_{LM} | \Psi_\gamma \rangle = \langle \Psi_\gamma | \mathring{Q}^{(1)}_{LM} | \Psi_\gamma \rangle = \alpha^{(p)}_{LM} + \alpha^{(h)}_{LM}. \tag{5.44}$$

Here we have used the result $\langle \Psi_\gamma | \mathring{Q}^{(2)}_{LM} | \Psi_\gamma \rangle = 0$, which follows immediately from eq. (4.11). The operators $\mathring{Q}^{(1)}_{LM}$ and $\mathring{Q}^{(2)}_{LM}$ are defined by eq. (5.8).

Obviously the eigenvalue equation (5.42) is an approximation to our general equation (4.9), thus demonstrating explicitly the deformed nature of the excited states obtained as solutions of (4.9). The ground state defined by (4.12), however, is spherical, and only if eq. (4.9) had a zero-energy solution, it would be really deformed. This has been discussed in section 4.2. Correspondingly, the ground state defined by eq. (5.41) will be "spherical" unless the eigenvalue equation (5.42) has a zero-energy solution.

We now want to solve the eigenvalue equation (5.42) in a way which explicitly traces the effect of $\mathfrak{H}^{(1)}_{ph}(\alpha)$ responsible for the intrinsic deformation. For this purpose we divide the Hamiltonian (5.37) into two parts:

$$\left.\begin{aligned} \mathring{H}(\alpha) &= \mathring{H}_0 + \mathfrak{H}^{(1)}_{ph}(\alpha), \\ \mathring{H}_0 &= \sum_\mu \omega_m A^+_\mu A_\mu - \sum_\nu \omega_n B^+_\nu B_\nu + \mathfrak{H}^{(1)}_{pp} + \mathfrak{H}^{(1)}_{hh} + \mathfrak{H}^{(2)}, \end{aligned}\right\} \tag{5.45}$$

and introduce the eigenmode creation operator with respect to $\mathring{H}_0$:

$$X^{(0)+}_\lambda = \sum_{\mu\nu} \{ \xi^{(0)}_\lambda(\mu\nu) A^+_\mu B^+_\nu + \eta^{(0)}_\lambda(\mu\nu) A_\mu B_\nu \} \tag{5.46}$$

which satisfies

$$[\mathring{H}_0, X^{(0)+}_\lambda] = \Omega^{(0)}_l X^{(0)+}_\lambda \quad \text{with} \quad \Omega^{(0)}_l > 0. \tag{5.47}$$

The functions $\xi^{(0)}_\lambda(\mu\nu)$ and $\eta^{(0)}_\lambda(\mu\nu)$ clearly satisfy the eigenvalue equation (5.42) with $\alpha^{(p)}_{LM} = \alpha^{(h)}_{LM} = 0$. Similarly as in the usual RPA for "1p-1h" excitations, we then obtain the well-known formulae*

$$\frac{1}{2\chi_{L=I_l}} = \sum_{\substack{\mu\nu \\ \binom{s_\mu = +1}{s_\nu = -1}}} \frac{|(\mu| Q_{I_l M_\lambda} |\nu)|^2 (\omega_m - \omega_n)}{(\omega_m - \omega_n)^2 - \Omega^{(0)2}_l}, \tag{5.48}$$

* Eqs. (5.48) and (5.49) are valid for $T_l = 0$ only, since Q_{LM} has been taken to be a scalar in isospace. For $T_l \neq 0$, eq. (5.46) becomes simply

$$X^{(0)+}_\lambda = \sum_{\mu\nu} (-)^{J_n - M_\nu} (-)^{T_n - Z_\nu} \langle J_m J_n M_\mu M_\nu | I_l M_l \rangle \langle T_m T_n Z_\mu - Z_\nu | T_l Z_l \rangle A^+_\mu B^+_\nu.$$

$$\xi_\lambda^{(0)}(\mu\nu) = \frac{N_l(\mu|Q_{I_l M_\lambda}|\nu)}{(\omega_m - \omega_n) - \Omega_l^{(0)}}, \quad \eta_\lambda^{(0)}(\mu\nu) = \frac{-N_l(\nu|Q_{I_l M_\lambda}|\mu)}{(\omega_m - \omega_n) + \Omega_l^{(0)}}, \tag{5.49}$$

where N_l is the normalization constant determined by eq. (4.10a). States like those created by the operators $X_\lambda^{(0)+}$ are conventionally called spherical, similarly as the "1p-1h" states in spherical nuclei known from the usual RPA. This is consistent with our definition of the intrinsic deformation α_{LM} and reconfirms the conclusion of the preceding subsection that $\mathfrak{H}_{ph}^{(1)}(\alpha)$ is the origin of the intrinsic deformation in the excited states of closed-shell nuclei.

Using $X_\lambda^{(0)+}$, we now can write the creation operator X_λ^+ in eq. (5.40) for a deformed excited state as

$$\left.\begin{aligned} X_\lambda^+ &= \sum_\lambda U_\gamma(\lambda) X_\lambda^{(0)+} + \sum_\lambda V_\gamma(\lambda) X_\lambda^{(0)} \\ &= \sum_{\mu\nu} \{\sum_\lambda U_\gamma(\lambda)\xi_\lambda^{(0)}(\mu\nu) + \sum_\lambda V_\gamma(\lambda)\eta_\lambda^{(0)}(\mu\nu)\} A_\mu^+ B_\nu^+ \\ &+ \sum_{\mu\nu} \{\sum_\lambda U_\gamma(\lambda)\eta_\lambda^{(0)}(\mu\nu) + \sum_\lambda V_\gamma(\lambda)\xi_\lambda^{(0)}(\mu\nu)\} A_\mu B_\nu . \end{aligned}\right\} \tag{5.50}$$

Then eq. (5.42) simply becomes a self-consistent equation for U_γ and V_γ. The functions U_γ and V_γ describe the effect of $\mathfrak{H}_{ph}^{(1)}(\alpha)$: if $\alpha_{LM}^{(p)} = \alpha_{LM}^{(h)} = 0$, then $V_\gamma(\lambda) = 0$ and $U_\gamma(\lambda) = \delta_{\gamma\lambda}$. The requirement that the operators X_γ^+ and $X_\lambda^{(0)+}$ each form a set of boson operators entails the orthogonality relations

$$\left.\begin{aligned} \sum_\lambda \{U_{\gamma_1}(\lambda)U_{\gamma_2}(\lambda) - V_{\gamma_1}(\lambda)V_{\gamma_2}(\lambda)\} &= \delta_{\gamma_1\gamma_2} \\ \sum_\lambda \{U_{\gamma_1}(\lambda)V_{\gamma_2}(\lambda) - V_{\gamma_1}(\lambda)U_{\gamma_2}(\lambda)\} &= 0, \\ \sum_\gamma \{U_\gamma(\lambda_1)U_\gamma(\lambda_2) - V_\gamma(\lambda_1)V_\gamma(\lambda_2)\} &= \delta_{\lambda_1\lambda_2} \\ \sum_\gamma \{U_\gamma(\lambda_1)V_\gamma(\lambda_2) - V_\gamma(\lambda_1)U_\gamma(\lambda_2)\} &= 0, \end{aligned}\right\} \tag{5.51}$$

and the inverse relation to eq. (5.50)

$$X_\lambda^{(0)+} = \sum_\gamma U_\gamma(\lambda) X_\gamma^+ - \sum_\gamma V_\gamma(\lambda) X_\gamma . \tag{5.52}$$

5.5 Intrinsic Deformations in Excited 0^+ States

In this subsection we restrict ourselves, for simplicity, entirely to quadrupole deformations. This corresponds to taking up only the $L = 2$ part* in the expansion (5.32) of $\mathfrak{H}^{(1)}_{ph}(\alpha)$. If the excited 0^+ state $|\Psi_{\gamma_0}\rangle$ defined by eq. (5.41) has an intrinsic quadrupole deformation (i.e. $\alpha_{2M} \neq 0$), then the solution must have the appropriate degeneracy to contain all possible orientations of the "excited deformed nucleus" in space. Without loss of generality we therefore can choose the axes of the intrinsic deformation as coordinate axes, so that $\alpha_{2,M=1} = \alpha_{2,M=-1} = 0$ and $\alpha_{2,M=2} = \alpha_{2,M=-2}$. Furthermore we assume, for simplicity, that the intrinsic deformation in the excited 0^+ state is axially symmetric, so that $\alpha_{2,M=2} = \alpha_{2,M=-2} = 0$. In this case, the intrinsic deformation is characterized by one quantity

$$\alpha_{2M=0} \equiv \beta. \tag{5.53}$$

The projection K_γ of the intrinsic angular momentum on the symmetry axis now is a constant of the motion, so that $K_{\gamma_0} = 0$ for our excited 0^+ state. We need not say that eq. (5.42) gives us the information about the *intrinsic excitations* in the body-fixed coordinate system and eq. (5.37) provides the *intrinsic* Hamiltonian of our system.

The excited 0^+ state under consideration, $|\Psi_{\gamma_0}\rangle$ with $K_{\gamma_0} = 0$, in eq. (5.41) is given by

$$|\Psi_{\gamma_0}\rangle = X^+_{\gamma_0}|\Psi_0\rangle$$

with

$$X^+_{\gamma_0} = \sum_\lambda U_{\gamma_0}(\lambda)X^{(0)+}_\lambda + \sum_\lambda V_{\gamma_0}(\lambda)X^{(0)}_\lambda. \tag{5.54}$$

Thus the eigenvalue equation (5.42) for this state becomes a self-consistent eigenvalue equation for U_{γ_0} and V_{γ_0}:

$$\left.\begin{aligned}
(\Omega_{\gamma_0} - \Omega^{(0)}_{l_1})U_{\gamma_0}(\lambda_1) &= -\chi\sum_{\lambda_2}(F^{(1)}_{\lambda_1\lambda_2}\beta^{(p)} + F^{(2)}_{\lambda_1\lambda_2}\beta^{(h)})U_{\gamma_0}(\lambda_2) \\
&\quad -\chi\sum_{\lambda_2}(G^{(1)}_{\lambda_1\lambda_2}\beta^{(p)} + G^{(2)}_{\lambda_1\lambda_2}\beta^{(h)})V_{\gamma_0}(\lambda_2), \\
(\Omega_{\gamma_0} + \Omega^{(0)}_{l_1})V_{\gamma_0}(\lambda_1) &= +\chi\sum_{\lambda_2}(F^{(1)}_{\lambda_1\lambda_2}\beta^{(p)} + F^{(2)}_{\lambda_1\lambda_2}\beta^{(h)})V_{\gamma_0}(\lambda_2) \\
&\quad +\chi\sum_{\lambda_2}(G^{(1)}_{\lambda_1\lambda_2}\beta^{(p)} + G^{(2)}_{\lambda_1\lambda_2}\beta^{(h)})U_{\lambda_0}(\lambda_2)
\end{aligned}\right\} \tag{5.55}$$

* Of course, the $L = 0$ part in $\mathfrak{H}^{(1)}_{ph}(\alpha)$ will contribute even under this restriction. However, the effect of this term is only a renormalization of the single pair energy ω_m for $J_m = 0$. In the following we assume, for simplicity, that the renormalization has already been carried out.

where $\chi \equiv \chi_{L=2}$ and

$$\left.\begin{aligned}
F^{(1)}_{\lambda_1\lambda_2} &= \sum_{\substack{\varrho\sigma \\ (s_\varrho = s_\sigma = -1)}} (\varrho|Q_{20}|\sigma) \sum_{\substack{\mu \\ (s_\mu = +1)}} \{\xi^{(0)}_{\lambda_1}(\mu\varrho)\xi^{(0)}_{\lambda_2}(\mu\sigma) + \eta^{(0)}_{\lambda_1}(\mu\sigma)\eta^{(0)}_{\lambda_2}(\mu\varrho)\} \\
F^{(2)}_{\lambda_1\lambda_2} &= \sum_{\substack{\mu\nu \\ (s_\mu = s_\nu = +1)}} (\mu|Q_{20}|\nu) \sum_{\substack{\varrho \\ (s_\varrho = -1)}} \{\xi^{(0)}_{\lambda_1}(\nu\varrho)\xi^{(0)}_{\lambda_2}(\mu\varrho) + \eta^{(0)}_{\lambda_1}(\mu\varrho)\eta^{(0)}_{\lambda_2}(\nu\varrho)\} \\
G^{(1)}_{\lambda_1\lambda_2} &= \sum_{\substack{\varrho\sigma \\ (s_\varrho = s_\sigma = -1)}} (\varrho|Q_{20}|\sigma) \sum_{\substack{\mu \\ (s_\mu = +1)}} \{\xi^{(0)}_{\lambda_1}(\mu\varrho)\eta^{(0)}_{\lambda_2}(\mu\sigma) + \eta^{(0)}_{\lambda_1}(\mu\sigma)\xi^{(0)}_{\lambda_2}(\mu\varrho)\} \\
G^{(2)}_{\lambda_1\lambda_2} &= \sum_{\substack{\mu\nu \\ (s_\mu = s_\nu = +1)}} (\mu|Q_{20}|\nu) \sum_{\substack{\varrho \\ (s_\varrho = -1)}} \{\xi^{(0)}_{\lambda_1}(\nu\varrho)\eta^{(0)}_{\lambda_2}(\mu\varrho) + \eta^{(0)}_{\lambda_1}(\mu\varrho)\xi^{(0)}_{\lambda_2}(\nu\varrho)\}.
\end{aligned}\right\} \quad (5.56)$$

The quantities $\beta^{(p)}$ and $\beta^{(h)}$ are determined self-consistently by

$$\left.\begin{aligned}
\beta^{(p)} &= \sum_{\mu\nu}(\mu|Q_{20}|\nu)\langle\Psi_{\gamma_0}|A^+_\mu A_\nu|\Psi_{\gamma_0}\rangle \\
\beta^{(h)} &= \sum_{\varrho\sigma}(\varrho|Q_{20}|\sigma)\langle\Psi_{\gamma_0}|B^+_\sigma B_\varrho|\Psi_{\gamma_0}\rangle.
\end{aligned}\right\} \quad (5.57)$$

To evaluate eq. (5.57), we first note that the operators

$$\sum_{\mu\nu}(\mu|Q_{20}|\nu)A^+_\mu A_\nu \quad \text{and} \quad \sum_{\varrho\sigma}(\varrho|Q_{20}|\sigma)B^+_\sigma B_\varrho$$

can be expanded in terms of the operators $X^{(0)+}_\lambda$ as follows:

$$\left.\begin{aligned}
\sum_{\mu\nu}(\mu|Q_{20}|\nu)A^+_\mu A_\nu &= \sum_{\lambda_1\lambda_2} F^{(2)}_{\lambda_2\lambda_1}\cdot X^{(0)+}_{\lambda_1}X^{(0)}_{\lambda_2} \\
&- \sum_{\lambda_1\lambda_2}\sum_{\mu\nu}(\mu|Q_{20}|\nu)[\sum_\varrho \xi^{(0)}_{\lambda_1}(\mu\varrho)\eta^{(0)}_{\lambda_2}(\nu\varrho)X^{(0)+}_{\lambda_1}X^{(0)+}_{\lambda_2} + \sum_\varrho \eta^{(0)}_{\lambda_1}(\mu\varrho)\xi^{(0)}_{\lambda_2}(\nu\varrho)X^{(0)}_{\lambda_1}X^{(0)}_{\lambda_2}], \\
\sum_{\varrho\sigma}(\varrho|Q_{20}|\sigma)B^+_\sigma B_\varrho &= \sum_{\lambda_1\lambda_2} F^{(1)}_{\lambda_2\lambda_1}\cdot X^{(0)+}_{\lambda_1}X^{(0)}_{\lambda_2} \\
&- \sum_{\lambda_1\lambda_2}\sum_{\varrho\sigma}(\varrho|Q_{20}|\sigma)[\sum_\mu \xi^{(0)}_{\lambda_1}(\mu\sigma)\eta^{(0)}_{\lambda_2}(\mu\varrho)X^{(0)+}_{\lambda_1}X^{(0)+}_{\lambda_2} + \sum_\mu \eta^{(0)}_{\lambda_1}(\mu\sigma)\xi^{(0)}_{\lambda_2}(\mu\varrho)X^{(0)}_{\lambda_1}X^{(0)}_{\lambda_2}].
\end{aligned}\right\} \quad (5.58)$$

In obtaining eq. (5.58), we have used a transcription rule similar to eq. (3.14), and then have employed the relation (4.11) with respect to $X^{(0)+}_\lambda$. Finally, by inserting eq. (5.52) into eq. (5.58), we get the deformations

$$\left.\begin{aligned}
\beta^{(p)} &= \sum_{\lambda_1\lambda_2} F^{(2)}_{\lambda_1\lambda_2}\{U_{\gamma_0}(\lambda_1)U_{\gamma_0}(\lambda_2) + V_{\gamma_0}(\lambda_1)V_{\gamma_0}(\lambda_2)\} \\
&+ \sum_{\lambda_1\lambda_2} G^{(2)}_{\lambda_1\lambda_2}\{U_{\gamma_0}(\lambda_1)V_{\gamma_0}(\lambda_2) + V_{\gamma_0}(\lambda_1)U_{\gamma_0}(\lambda_2)\},
\end{aligned}\right\} \quad (5.59a)$$

$$\left.\begin{aligned}\beta^{(h)} &= \sum_{\lambda_1\lambda_2} F^{(1)}_{\lambda_1\lambda_2}\{U_{\gamma_0}(\lambda_1)U_{\gamma_0}(\lambda_2) + V_{\gamma_0}(\lambda_1)V_{\gamma_0}(\lambda_2)\} \\ &+ \sum_{\lambda_1\lambda_2} G^{(1)}_{\lambda_1\lambda_2}\{U_{\gamma_0}(\lambda_1)V_{\gamma_0}(\lambda_2) + V_{\gamma_0}(\lambda_1)U_{\gamma_0}(\lambda_2)\}.\end{aligned}\right\} \quad (5.59\,\mathrm{b})$$

In the expressions (5.59a) and (5.59b) we have already dropped the following terms, respectively:

$$\left.\begin{aligned}&\sum_{\lambda_1\lambda_2} F^{(2)}_{\lambda_1\lambda_2}\cdot\sum_{\gamma} V_{\gamma}(\lambda_1)V_{\gamma}(\lambda_2) + \sum_{\lambda_1\lambda_2} G^{(2)}_{\lambda_1\lambda_2}\cdot\sum_{\gamma} U_{\gamma}(\lambda_1)V_{\gamma}(\lambda_2) \quad \text{(from (5.59a))}, \\ &\sum_{\lambda_1\lambda_2} F^{(1)}_{\lambda_1\lambda_2}\cdot\sum_{\gamma} V_{\gamma}(\lambda_1)V_{\gamma}(\lambda_2) + \sum_{\lambda_1\lambda_2} G^{(1)}_{\lambda_1\lambda_2}\cdot\sum_{\gamma} U_{\gamma}(\lambda_1)V_{\gamma}(\lambda_2) \quad \text{(from (5.59b))}.\end{aligned}\right\} \quad (5.60)$$

These terms occur not only in the excited 0^+ states $|\Psi_{\gamma_0}\rangle$ in which we are interested, but they are also common to all other excited states $|\Psi_{\gamma}\rangle$. The sum of both terms can thus be interpreted as an "unphysical deformation" of the spherical ground state $|\Psi_0\rangle$ (defined by eq. (5.41)) given by

$$\left.\begin{aligned}\langle\Psi_0|\mathring{Q}_{20}|\Psi_0\rangle &= \sum_{\lambda_1\lambda_2}(F^{(1)}_{\lambda_1\lambda_2} + F^{(2)}_{\lambda_1\lambda_2})\cdot\sum_{\gamma} V_{\gamma}(\lambda_1)V_{\gamma}(\lambda_2) \\ &+ \sum_{\lambda_1\lambda_2}(G^{(1)}_{\lambda_1\lambda_2} + G^{(2)}_{\lambda_1\lambda_2})\cdot\sum_{\gamma} U_{\gamma}(\lambda_1)V_{\gamma}(\lambda_2).\end{aligned}\right\} \quad (5.61)$$

We are now in a position to write down the final result for the intrinsic deformation β of the excited 0^+ state. The result is

$$\left.\begin{aligned}\beta &= \langle\Psi_{\gamma_0}|\mathring{Q}_{20}|\Psi_{\gamma_0}\rangle = \langle\Psi_{\gamma_0}|\mathring{Q}^{(1)}_{20}|\Psi_{\gamma_0}\rangle = \beta^{(p)} + \beta^{(h)} \\ &= \sum_{\lambda_1\lambda_2}(F^{(1)}_{\lambda_1\lambda_2} + F^{(2)}_{\lambda_1\lambda_2})\{U_{\gamma_0}(\lambda_1)U_{\gamma_0}(\lambda_2) + V_{\gamma_0}(\lambda_1)V_{\gamma_0}(\lambda_2)\} \\ &+ \sum_{\lambda_1\lambda_2}(G^{(1)}_{\lambda_1\lambda_2} + G^{(2)}_{\lambda_1\lambda_2})\{U_{\gamma_0}(\lambda_1)V_{\gamma_0}(\lambda_2) + V_{\gamma_0}(\lambda_1)U_{\gamma_0}(\lambda_2)\}.\end{aligned}\right\} \quad (5.62)$$

Here we have used the fact that $\langle\Psi_{\gamma_0}|\mathring{Q}^{(2)}_{20}|\Psi_{\gamma_0}\rangle = 0$, which follows from a relation analogous to eq. (4.11). The operators $\mathring{Q}^{(1)}_{20}$ and $\mathring{Q}^{(2)}_{20}$ are defined by eq. (5.8). From the definition (5.56) of F and G, it is obvious that in the absence of ground-state correlations due to the field-producing force (that is, if $\eta^{(0)}_{\lambda}(\mu\nu) = 0$ and $V_{\gamma_0}(\lambda) = 0$, (see eq. (5.50)) only the first term in eq. (5.62) contributes to the deformation. Thus the expression (5.62) allows us to identify clearly that part of the deformation in the excited state which arises from the cooperation effect of the core deformation.

5.6 Rotational Bands Built on Excited States

The basic equation (5.42) of our self-consistent method describes the intrinsic excitation in the body-fixed coordinate system associated with the intrinsic deformation of each excited state. Thus the state vector $|\Psi_\gamma\rangle$ in eq. (5.41), describing the intrinsic excited state, has no definite angular momentum. The proper eigenfunctions with definite angular momenta are then obtained by the usual projection operation [16], which also yields the rotational band structure belonging to the intrinsic excited state $|\Psi_\gamma\rangle$.

To avoid the problem of computing overlap integrals in this method, we may apply the conventional Bohr-Mottelson description to our problem. Then our system is described by the following effective Hamiltonian:

$$\boldsymbol{H} = \sum_{\varkappa=1}^{3} \frac{\hbar^2}{2\mathfrak{J}_\varkappa(\alpha)} \boldsymbol{R}_\varkappa^2 + \mathring{H}(\alpha), \tag{5.63}$$

where $\mathring{H}(\alpha)$ is given by eq. (5.37) and $\boldsymbol{R}_\varkappa$ is the component of the "collective" angular momentum in the direction of the $\varkappa$-axis of the body-fixed coordinate system, and the quantities $\mathfrak{J}_\varkappa$ are the principal moments of inertia.

The physical interpretation of eq. (5.63) is the following: A specific intrinsic excited state $|\Psi_\gamma\rangle$ defined by eq. (5.41) is created by applying the operator X_γ^+ to the spherical ground state of the closed-shell nucleus. Once the state is excited, we can choose the body-fixed coordinate system determined by the axes of the intrinsic quadrupole deformation of this excited state. The corresponding moments of inertia of the state $|\Psi_\gamma\rangle$ can be calculated. With these moments of inertia the intrinsic excited state performs a rotational motion which gives rise to a rotational band belonging to this specific state $|\Psi_\gamma\rangle$. The explicit calculation of the moments of inertia for the state $|\Psi_\gamma\rangle$ is possible by applying the conventional Lagrange multiplier method to our self-consistent approach developed in section 5.4. However, we do not want to go into further details in the present work. With the approximation (5.63), the rotational states belonging to the excited 0^+ state discussed in section 5.5 are of the usual form

$$\left.\begin{aligned} |IM;\gamma_0 K_{\gamma_0} = 0) &= \left[\frac{2I+1}{8\pi}\right]^{1/2} D^I_{MK_{\gamma_0}=0}(\theta_i)|\Psi_{\gamma_0}\rangle \\ \text{with} \qquad I^\pi &= 0^+, 2^+, 4^+, 6^+ \ldots . \end{aligned}\right\} \tag{5.64}$$

Here $|\Psi_{\gamma_0}\rangle$ is defined by eq. (5.54), and the effect of the well-known symmetry restrictions are taken into account in limiting the allowed values of I.

6. Electromagnetic Transitions

In this section we discuss various electromagnetic transitions involving even parity states (with $T = 0$) in closed-shell nuclei. Electromagnetic transitions are a crucial test of the theory, more than energies, in particular they are shown to be decisively influenced by the interplay between the residual interaction and the field-producing force. The essential differences between G. E. Brown's and our theory are pointed out.

6.1 Energy-Weighted Sum Rule

As a preparation we wish to show that, for a general one-body boson operator defined by

$$\mathring{\mathfrak{O}} = \sum_{\mu\nu} (\mu|\mathfrak{O}|\nu) : C_\mu^+ C_\nu : , \tag{6.1}$$

the following sum rule holds within our approximation (4.5)

$$\sum_\lambda |\langle \Psi_0|\mathring{\mathfrak{O}}|\Psi_\lambda\rangle|^2 (E_l - E_0) = \tfrac{1}{2}\langle \Phi_0'|[\mathring{\mathfrak{O}}[\mathring{H},\mathring{\mathfrak{O}}]]|\Phi_0'\rangle. \tag{6.2}$$

Here the unperturbed ground state $|\Phi_0'\rangle$ is defined by eq. (3.11), $|\Psi_0\rangle$ and $|\Psi_\lambda\rangle$ are defined by eqs. (4.12) and (4.13), respectively, and $(E_l - E_0) \equiv \Omega_l$ are the eigenvalues of eq. (4.9).

With the aid of eqs. (4.11), (4, 9) and the completeness relation (4.10b) we can rewrite the left hand side of (6.2) as

$$\left.\begin{aligned} \sum_\lambda |\langle \Psi_0|\mathring{\mathfrak{O}}|\Psi_\lambda\rangle|^2 (E_l - E_0) &= \sum_\lambda [\sum_{\mu\nu} (\mu|\mathfrak{O}|\nu)\{\xi_\lambda(\mu\nu) - \eta_\lambda(\mu\nu)\}]^2 \Omega_l \\ &= \sum_{\mu\nu\varrho\sigma} (\mu|\mathfrak{O}|\nu)(\varrho|\mathfrak{O}|\sigma)(N_{\mu\nu\varrho\sigma} - N'_{\mu\nu\varrho\sigma}). \end{aligned}\right\} \tag{6.3}$$

On the other hand, we obtain directly

$$\tfrac{1}{2}\langle \Phi_0'|[\mathring{\mathfrak{O}}[\mathring{H},\mathring{\mathfrak{O}}]]|\Phi_0'\rangle = \sum_{\mu\nu\varrho\sigma} (\mu|\mathfrak{O}|\nu)(\varrho|\mathfrak{O}|\sigma)(N_{\mu\nu\varrho\sigma} - N'_{\mu\nu\varrho\sigma}). \tag{6.4}$$

Comparison of eq. (6.3) and eq. (6.4) proves the sum rule (6.2). An analogous rule is known [17] for "1p-1h" excitations described by the conventional RPA.

Now we observe that in our theory all operators for electromagnetic transitions can be written as one-body boson operators of the form (6.1) by inserting (3.15) into eq. (3.17). Consequently, the usual energy-weighted sum rule for electromagnetic transitions holds in our approximation. This is in contrast to the mixing model [5, 6] in which there is no guarantee that the sum rule might not be violated.

6.2 Transitions Within Rotational Bands

For simplicity we confine ourselves to the rotational band belonging to the excited 0^+ state discussed in sect. 5.5; in the following we work with the wave functions (5.64). Furthermore it is convenient to refer the mass quadrupole moment operator $\mathring{Q}_{2M}$ (defined by eq. (5.3) with $L = 2$) to the body-fixed coordinate axes which are chosen to be the axes of the intrinsic quadrupole deformation of the excited 0^+ state. This is achieved in the usual way by writing

$$\mathring{Q}_{2M} = \sum_K D^{I=2}_{MK}(\theta_i)\mathring{Q}_{2K}, \quad (K = 0, \pm 2). \tag{6.5}$$

Now the $E2$ transition matrix element between an initial state $|I_i, M_i; \gamma_0 K_{\gamma_0} = 0)$ and a final state $|I_f M_f; \gamma_0 K_{\gamma_0} = 0)$ is given by

$$\left.\begin{aligned}(I_f M_f; \gamma_0 K_{\gamma_0} = 0 | \mathfrak{M}(E2, M) | I_i M_i, \gamma_0 K_{\gamma_0} = 0) \\ = \tfrac{1}{2} e (I_f M_f; \gamma_0 K_{\gamma_0} = 0 | \mathring{Q}_{2M} | I_i M_i; \gamma_0 K_{\gamma_0} = 0).\end{aligned}\right\} \tag{6.6}$$

Here we are considering only $T = 0$ states. With the aid of eqs. (6.5), (5.64) and (5.62), we then obtain the result

$$\left.\begin{aligned}(I_f M_f; \gamma_0 K_{\gamma_0} = 0 | \mathfrak{M}(E2, M) | I_i M_i; \gamma_0 K_{\gamma_0} = 0) \\ = \tfrac{1}{2} e \left[\frac{2I_i + 1}{2I_f + 1}\right]^{1/2} \langle I_i 2 M_i M | I_f M_f \rangle \langle I_i 200 | I_f 0 \rangle \cdot \beta,\end{aligned}\right\} \tag{6.7}$$

$$B(E2; I_i \to I_f) = \tfrac{1}{4} e^2 \langle I_i 200 | I_f 0 \rangle^2 \cdot \beta^2. \tag{6.8}$$

Eq. (6.8) shows the well-known dependence of the $E2$ transition probabilities within a band on the intrinsic deformation, β, defined by eq. (5.62) characteristic of this specific band.

6.3 E2 Transitions Connecting the Rotational Band with the Ground State

Here we consider the $E2$ transition from the 2^+ state in the rotational band belonging to the excited 0^+ state discussed in sect. 5.5 to the ground state. In this case, the $E2$ transition matrix element connecting the 2^+ state $|I_i = 2, M_i; \gamma_0 K_{\gamma_0} = 0)$ and the ground state, $|0_1)$, is given by

$$\left.\begin{aligned}(0_1,|\mathfrak{M}(E2,M)|I_i = 2, M_i; \gamma_0 K_{\gamma_0} = 0) \\ = \tfrac{1}{2} e\langle 22 M_i M|00\rangle \langle \Psi_0|\mathring{Q}_{2,K=0}|\Psi_{\gamma_0}\rangle\end{aligned}\right\} \tag{6.9}$$

and so we have

$$B(E2, 2_1^+ \to 0_1^+) = \tfrac{1}{20} e^2 |\langle \Psi_0|\mathring{Q}_{2K=0}|\Psi_{\gamma_0}\rangle|^2, \tag{6.10}$$

where $|\Psi_0\rangle$ and $|\Psi_{\gamma_0}\rangle$ are given in eq. (5.54) or eq. (5.40).

In evaluating $\langle \Psi_0|\mathring{Q}_{2,K=0}|\Psi_{\gamma_0}\rangle$ we first observe that $\langle \Psi_0|\mathring{Q}^{(1)}_{2,K=0}|\Psi_{\gamma}\rangle = 0$. This result is obtained with the use of the definition (5.8) of $\mathring{Q}^{(1)}_{2,K=0}$ and by inserting eq. (5.52) into eq. (5.58). Then, using eq. (4.11) with respect to X^+_γ, we have

$$\left.\begin{aligned}\langle \Psi_0|\mathring{Q}_{2,K=0}|\Psi_{\gamma_0}\rangle &= \langle \Psi_0|\mathring{Q}^{(2)}_{2,K=0}|\Psi_{\gamma_0}\rangle \\ &= \sum_{\mu\nu}(\mu|Q_{20}|\nu)\{\xi_{\gamma_0}(\mu\nu) - \eta_{\gamma_0}(\mu\nu)\},\end{aligned}\right\} \tag{6.11}$$

where $\xi_{\gamma_0}(\mu\nu)$ and $\eta_{\gamma_0}(\mu\nu)$ are defined through eq. (5.40) and are written with the help of eq. (5.50) as

$$\left.\begin{aligned}\xi_{\gamma_0}(\mu\nu) &= \sum_\lambda \{U_{\gamma_0}(\lambda)\xi^{(0)}_\lambda(\mu\nu) + V_{\gamma_0}(\lambda)\eta^{(0)}_\lambda(\mu\nu)\} \\ \eta_{\gamma_0}(\mu\nu) &= \sum_\lambda \{U_{\gamma_0}(\lambda)\eta^{(0)}_\lambda(\mu\nu) + V_{\gamma_0}(\lambda)\xi^{(0)}_\lambda(\mu\nu)\}.\end{aligned}\right\} \tag{6.12}$$

With eq. (6.11), eq. (6.10) becomes

$$B(E2; 2_1^+ \to 0_1^+) = \tfrac{1}{20} e^2 [\sum_{\mu\nu}(\mu|Q_{20}|\nu)\{\xi_{\gamma_0}(\mu\nu) - \eta_{\gamma_0}(\mu\nu)\}]^2. \tag{6.13}$$

It is interesting to observe that formally eq. (6.13) has precisely the same structure as the corresponding equation obtained by the conventional RPA for "1p-1h" problems. For the $E2$ transition from the "dressed 2p-2h" excited 2^+ state to the ground state, we will therefore expect the well-known enhancement associated with the structure of eq. (6.13). In particular we will have the usual relation: the stronger the field-producing force, the larger the B(E2) value. Such an enhancement, caused by the collective ground-state correlations due to the field-producing force, is a direct and natural

consequence of the present theory. The enhancement is needed to explain the large measured transition rate in O^{16} namely $B(E2; 2_1^+ \to 0_1^+) = 5e^2 fm^4$. An interesting feature of the electromagnetic transitions is the importance of the interplay between the residual interaction and the field-producing force. It becomes most obvious if we neglect altogether the ground-state correlations due to the residual interaction. Then, from the definition (5.4) we have

$$(\mu|Q_{20}|\nu)_{TD} = 0 \quad \text{for} \quad s_\mu = 1, \quad s_\nu = -1,$$

and thus there are no E2 transitions from the 2^+ state to the ground state. But the residual interaction need not be strong either. Even a weak residual interaction may provide a sufficient basis for strong collective ground-state correlations (due to the field-producing force).

6.4 E0 Transitions from Excited 0^+ States to the Ground State

Throughout this subsection we are again considering the excited 0^+ state, $|0_2^+) \equiv |I = 0, M = 0; \gamma_0 K_{\gamma_0} = 0)$, discussed in sect. 5.5. The effective operator for the decay of the state $|0_2^+)$ to the ground state $|0_1^+)$ by electron-positron pair emission or internal conversion is given by

$$P_0 = e \sum_{\alpha\beta} \langle\alpha| \frac{1+\tau_3}{2} r^2 |\beta\rangle : c_\alpha^+ c_\beta : . \tag{6.14}$$

With the help of the rule (3.14) and eq. (3.13), we can expand the operator in terms of pair scattering modes as

$$\mathring{P}_0 = \sum_{\mu\nu} (\mu|P_0|\nu) : C_\mu^+ C_\nu : , \tag{6.15}$$

where

$$(\mu|P_0|\nu) = 4e \sum_{\alpha\beta\gamma} \langle\alpha| \frac{1+\tau_3}{2} r^2 |\beta\rangle s_\mu \Psi_\mu(\alpha\gamma)(1 - \theta_a - \theta_c) s_\nu \Psi_\nu(\beta\gamma). \tag{6.16}$$

Thus, in the same way as in the preceding subsection, we obtain the matrix element for pair emission as

$$(0_1^+|P_0|0_2^+) = \sum_{\mu\nu} (\mu|P_0|\nu)\{\xi_{\gamma_0}(\mu\nu) - \eta_{\gamma_0}(\mu\nu)\}. \tag{6.17}$$

As in the preceding subsection, we may expect from the structure of eq. (6.17) an enhancement of the pair emission rate, possibly sufficient to account for the large experimental value in O^{16}, namely $(0_2^+|P_0|0_1^+) \approx 0.4 e R_0^2$

(R_0 = nuclear radius). Furthermore, the arguments given in the preceding subsection for the importance of the interplay between residual interactions and the field-producing force are equally applicable here. The influence of the intrinsic deformation of the state $|0_2^+\rangle$ on the pair emission rate becomes evident if we insert eq. (6.12) into eq. (6.17) and then trace the role of the functions U_{γ_0} and V_{γ_0}.

6.5 Hindrance of Double Gamma Decay of the First Excited 0^+ State

In discussions of the properties of the first excited 0^+ states in closed-shell nuclei, an instructive piece of data has often been neglected, namely the absence of observed $\gamma\gamma$-decays of these states. Usually the first excited 0^+ state $|0_2^+\rangle \equiv |\Psi_{\lambda_0}\rangle$ decays to the ground state $|0_1^+\rangle \equiv |\Psi_0\rangle$ by the E0 transition discussed in the preceding subsection. However, the two-photon emission [18, 19] may also contribute to the decay. In this case, the total energy $E_{\lambda_0} - E_0 \equiv \Omega_{l_0} = \hbar(\omega + \omega')$ is split up between two photons with energies $\hbar\omega$ and $\hbar\omega'$. The most probable decay mode will consist in the emission of two dipole quanta. Then the total transition probability is given by [18, 19]

$$\left.\begin{aligned} W_{\gamma\gamma} &= \frac{2}{105\pi}\frac{1}{(\hbar c)^6}(E_{\lambda_0} - E_0)^7\left(\frac{4\pi}{3}\right)^2 \\ &\times \left|\sum_n \frac{(0_1^+|\mathfrak{M}(E1,0)|n)(n|\mathfrak{M}(E1,0)|0_2^+)}{E_n - E_0}\right|^2 \end{aligned}\right\} \quad (6.18)$$

where

$$\mathfrak{M}(E1,0) = e\sum_{\alpha\beta}\langle\alpha|\frac{1+\tau_3}{2} r Y_{10}(\theta\varphi)|\beta\rangle : c_\alpha^+ c_\beta :$$

is the electric dipole operator. In the sum over the intermediate states $|n)$ in eq. (6.18), the most important contribution will come from the giant dipole resonance, so that $E_n - E_{\lambda_0} \gg \hbar\omega$ or $\hbar\omega'$. This fact has been used to drop the terms $\hbar\omega$ and $\hbar\omega'$ in the energy denominator of eq. (6.18).

In trying to evaluate eq. (6.18) it is necessary to relate $W_{\gamma\gamma}$ to other independent observable quantities in an unambiguous way. This is best done by introducing [19] a parameter η through the definition

$$\left.\begin{aligned} &\sum_n \frac{1}{E_n - E_0}(0_1^+|\mathfrak{M}(E1,0)|n)(n|\mathfrak{M}(E1,0)|0_2^+) \\ &\equiv \eta \sum_n \frac{1}{E_n - E_0}(0_1^+|\mathfrak{M}(E1,0)|n)(n|\mathfrak{M}(E1,0)|0_1^+). \end{aligned}\right\} \quad (6.19)$$

The sum of the right-hand side is closely related to the (-2)-moment of the photonuclear absorption cross section [20]

$$\left.\begin{aligned} \sigma_{-2} &\equiv \int \frac{\sigma(E)}{E^2}\, dE \\ &= \frac{16}{3}\frac{\pi^3}{\hbar c}\sum_n \frac{1}{E_n - E_0}\,(0_1^+|\mathfrak{M}(E1,0)|n)(n|\mathfrak{M}(E1,0|0_1^+), \end{aligned}\right\} \tag{6.20}$$

which is known to be a smooth function of the mass number A for most nuclei. The parameter η is a well-defined quantity and can be obtained from the experimental upper limits for $W_{\gamma\gamma}/W(E0)$, from $W(E0)$, and eqs. (6.18) to (6.20). The result of such an evaluation is presented in table I.

TABLE I. Hindrance of Double Gamma Decays

	E [MeV]	$W_{\exp}(E0)$ [a] [$\sec^{-1}$]	$W_{\gamma\gamma}/W_{\exp}$ $(E0)$	σ_{-2} used [d] [μb/MeV]	$W_{\gamma\gamma}$ (calc) [$\sec^{-1}$]	η^2
O^{16}	6.05	$1.4\cdot10^{10}$	$< 1.1\cdot10^{-4}$ [b]	$7\ A^{5/3}$	$5.8\cdot10^{9}\ \eta^2$	$< 2.6\cdot10^{-4}$
Ca^{40}	3.35	$2.9\cdot10^{8}$	$\leqslant 4\ \cdot10^{-4}$ [c]	$(2.6 \pm 0.5)\cdot10^{3}$	$1.2\cdot10^{8}\ \eta^2$	$< 0.95\cdot10^{-4}$
Ge^{72}	0.69	$3.4\cdot10^{6}$		$3.5\ A^{5/3}$	$5.6\cdot10^{4}\ \eta^2$	
Zr^{90}	1.75	$1.1\cdot10^{7}$	$\leqslant 1.8\cdot10^{-4}$ [c]	$3.5\ A^{5/3}$	$8.1\cdot10^{7}\ \eta^2$	$< 0.25\cdot10^{-4}$

a) see the first of refs. 19.
b) see ref. 23.
c) see ref. 24 and compare the still lower limit given in ref. 25.
d) for Ca^{40}, see ref. 26, for the other nuclei ref. 20.

Replacing in eq. (6.19) the main resonance region by a single representative state $|n_0)$, the "dipole state", we may take* η as a measure for the ratio of matrix elements

$$|\eta| \approx \left|\frac{\langle 0_2^+|\mathfrak{M}(E1,0)|n_0\rangle}{\langle 0_1^+|\mathfrak{M}(E1,0)|n_0\rangle}\right|. \tag{6.21}$$

If the two states $|0_1^+)$ and $|0_2^+)$ were of a very similar structure then η should be of the order one. Table I shows, however, that in all measured cases η must be a very small quantity, indicating, quite systematically, that the first excited 0^+ states seem to have no appreciable coupling to the giant dipole resonance.

* This replacement is possible unless there are considerable cancellations in the left hand sum of eq. (6.19) due to fluctuations in the sign of $(n|\mathfrak{M}(E1,0)|0_2^+)/(n|\mathfrak{M}(E1,0)|0_1^+)$. It is known, however, that the giant dipole resonance behaves like a single coherent state, the dipole state, so that strong cancellations are not to be expected.

Similarly the coupling of the first excited O^+ state in 0^{16} with other 1^- states which are normally described as "1p-1h" excitations seems also to be small [21, 22]

$$\left.\begin{aligned} B(E1;1^-(7.12) \to 0_2^+)/B(E1,1^-(7.12) \to 0_1^+) &< 10^{-2} \\ B(E1;1^-(13.1) \to 0_2^+)/B(E1,1^-(13.1) \to 0_1^+) &< 10^{-2}. \end{aligned}\right\} \tag{6.22}$$

Here, it should be noted that the first transition occurs only through isospin impurities. The limits are not as low as those for η; on the other hand, the interpretation is unambiguous.

As has been realized long ago [10], it will be very difficult to explain the experimental limits (6.22) in a model [5] in which both $|0_1^+)$ and $|0_2^+)$ are described as a mixture of spherical and deformed states with roughly equal amplitudes. It may be even harder to account for the smallness of $|\eta|$ without simultaneously destroying the strong $E0$ and $E2$ transitions between the rotational band and the ground state of O^{16}. On the other hand, we wish to show that the present theory does not encounter such difficulties.

Suppose that the states $|n)$ are well described as "1p-1h" states in the conventional RPA:

$$|n) = D_n^+|0_1^+) \tag{6.23}$$

with the creation operators

$$D_n^+ = \sum_{\alpha\beta}(R_n(\alpha\beta)a_\alpha^+ b_\beta^+ + S_n(\alpha\beta)b_\beta a_\alpha). \tag{6.24}$$

Then, with the aid of the inverse relation to eq. (6.24),

$$a_\alpha^+ b_\beta^+ = \sum_n (R_n(\alpha\beta)D_n^+ - S_n(\alpha\beta)D_n), \tag{6.25}$$

the denominator of eq. (6.21) is written in the usual form

$$(0_1^+|\mathfrak{M}(E1,0)|n_0) = e\sum_{\alpha\beta}\langle\alpha|\frac{1+\tau_3}{2}rY_{10}(\theta\varphi)|\beta\rangle\{R_{n_0}(\alpha\beta) - S_{n_0}(\alpha\beta)\}. \tag{6.26}$$

In the same approximation in which eq. (6.26) has been obtained, the numerator in eq. (6.21) becomes

$$\left.\begin{aligned} (0_2^+|\mathfrak{M}(E1,0)|n_0) &= e\sum_n\sum_{\alpha\beta}\langle\alpha|\frac{1+\tau_3}{2}rY_{10}(\theta\varphi)|\beta\rangle\{R_n(\alpha\beta) - S_n(\alpha\beta)\} \\ &\quad \times (0_2^+|\tilde{\mathfrak{D}}_{nn_0}|0_1^+) \\ &= \sum_n (0_1^+|\mathfrak{M}(E1,0)|n)(0_2^+|\tilde{\mathfrak{D}}_{nn_0}|0_1^+), \end{aligned}\right\} \tag{6.27}$$

where the operator $\tilde{\mathfrak{D}}_{nn_0}$ is defined by

$$\left.\begin{aligned}\tilde{\mathfrak{D}}_{nn_0} = &-\sum_{\alpha_1\beta_1}\sum_{\alpha_2\beta_2} R_n(\alpha_1\beta_1)R_{n_0}(\alpha_2\beta_2)a^+_{\alpha_1}a^+_{\alpha_2}b^+_{\beta_1}b^+_{\beta_2}\\ &-\sum_{\alpha_1\beta_1}\sum_{\alpha_2\beta_2} S_n(\alpha_1\beta_1)S_{n_0}(\alpha_2\beta_2)a_{\alpha_1}a_{\alpha_2}b_{\beta_1}b_{\beta_2}.\end{aligned}\right\} \tag{6.28}$$

To get a rough estimate for the order of $|\eta|$, we assume that we can replace the sum over intermediate states by the "dipole state" $|n_0)$. From eq. (6.26) and eq. (6.27) we get for the order of $|\eta|$ the result

$$\mathrm{O}(|\eta|) \approx (0_2^+|\tilde{\mathfrak{D}}_{n_0n_0}|0_1^+)|. \tag{6.29}$$

Expanding the operator $\tilde{\mathfrak{D}}_{n_0n_0}$ in terms of the pair scattering modes with the aid of eqs. (3.15) and (4.11), we have

$$\left.\begin{aligned}\mathrm{O}(|\eta|) &\approx |\langle\Psi_{\gamma_0}|\tilde{\mathfrak{D}}_{n_0n_0}|\Psi_0\rangle|\\ &= \Big|4\sum_{\alpha_1\alpha_2}\sum_{\beta_1\beta_2}(1-\theta_{a_1}-\theta_{a_2})(1-\theta_{b_1}-\theta_{b_2})R_{n_0}(\alpha_1\beta_1)R_{n_0}(\alpha_2\beta_2)\\ &\times\sum_{\substack{\mu\nu\\ s_\mu=1,\ s_\nu=-1}}[\xi_{\lambda_0}(\mu\nu)\Psi_\mu(\alpha_1\alpha_2)\Psi_\nu(\beta_1\beta_2)-\eta_{\lambda_0}(\mu\nu)\Psi_\mu(\beta_1\beta_2)\Psi_\nu(\alpha_1\alpha_2)]\\ &+4\sum_{\alpha_1\alpha_2}\sum_{\beta_1\beta_2}(1-\theta_{a_1}-\theta_{a_2})(1-\theta_{b_1}-\theta_{b_2})S_{n_0}(\alpha_1\beta_1)S_{n_0}(\alpha_2\beta_2)\\ &\times\sum_{\substack{\mu\nu\\ s_\mu=1,\ s_\nu=-1}}[\xi_{\lambda_0}(\mu\nu)\Psi_\mu(\beta_1\beta_2)\Psi_\nu(\alpha_1\alpha_2)-\eta_{\lambda_0}(\mu\nu)\Psi_\mu(\alpha_1\alpha_2)\Psi_\nu(\beta_2\beta_2)]\Big|,\end{aligned}\right\} \tag{6.30}$$

in which the leading terms are

$$\left.\begin{aligned}&\Big|4\sum_{\alpha_1\alpha_2}\sum_{\beta_1\beta_2}(1-\theta_{a_1}-\theta_{a_2})(1-\theta_{b_1}-\theta_{b_2})R_{n_0}(\alpha_1\beta_1)R_{n_0}(\alpha_2\beta_2)\\ &\qquad\times\sum_{\substack{s_\mu=1\\ s_\nu=-1}}\xi_{\lambda_0}(\mu\nu)\Psi_\mu(\alpha_1\alpha_2)\Psi_\nu(\beta_1\beta_2)\Big|\end{aligned}\right\} \tag{6.31}$$

According to the present theory, the hindrance of the double gamma decay comes from the extreme smallness of the overlap in eq. (6.31) between the "1p-1h" correlation functions $R_{n_0}(\alpha_1\beta_1)$ and $R_{n_0}(\alpha_2\beta_2)$ for the giant resonance and the "2p-2h" correlation function, $\sum_{\mu\nu}\xi_{\lambda_0}(\mu\nu)\Psi_\mu(\alpha_1\alpha_2)\Psi_\nu(\beta_1\beta_2)$, for the first excited 0^+ state. One reason for this smallness is simply the angular momentum recoupling which is sufficient to explain the limits (6.22). In the case of the dipole resonance, we have an additional effect: The largest components of $R_{n_0}(\alpha\beta)$ for the giant resonance state come from the highest

particle levels α and the lowest hole levels β, while the largest components of $\sum_{\mu\nu}^{\xi} \xi_{\lambda_0}(\mu\nu)\Psi_\mu(\alpha_1\alpha_2)\Psi_\nu(\beta_1\beta_2)$ for the first excited 0^+ state come from the lowest particle levels α and the highest hole level β. A rough estimate with simplifying assumptions seems to be in agreement with the experimental limits on $|\eta|$.

7. Conclusions

In the last few years, the RPA describing "1p-1h" excitations has found a wide field of application, particularly in explaining collective phenomena in nuclei. Essentially, however, this approach is exhausted and its limitations are known. In the present work we have attempted to construct a systematic theory for "2p-2h" excitations. Clearly, this problem is next in simplicity after the "1p-1h" excitations, and yet it yields a wealth of new collective phenomena. In constructing the present theory some approximations are necessary, of course. One of the important approximations is the two-step method and the other is the neglect of interaction matrix elements involving an odd number of fermions or fermion pairs (i.e., HY and $\mathfrak{H}Y$, respectively). This shortcoming may partly be compensated by a proper choice of the effective interaction. Similarly as in the conventional RPA we also were forced to renounce the Pauli principle to some extent. As far as the Pauli principle is concerned, our NTD method is constructed in such a way that, in the limiting case of a pure 2p-2h system (without ground-state correlations), all our results are exact.

The starting point of our work was the problem of O^{16} and Ca^{40}. It was felt that existing theories and models were unsatisfactory and not entirely adequate to cope with the situation. The reason why the collective ground-state correlations introduced in our NTD method should become particularly important for closed shell nuclei is obvious: These ground-state correlations carry the decisive interplay between field-producing forces and the residual interaction. Even a weak residual interaction may provide a sufficient basis for strong collective ground-state correlations (due to the field-producing force).

In a pictorial language, the residual interactions are indispensable for softening the core, so that the strong field-producing forces are able to deform it. All these effects are included in the "collective predisposition" of the *spherical* ground state for *deformed* excited states.

Although in the present work our NTD method was primarily designed for closed-shell nuclei, a wide field of applications suggests itself. The next objects of interest will be nuclei which differ by two nucleons from closed-

shell nuclei, like O^{18} and Ca^{42}. Here, certain excited states will be described by a "2p-2h phonon", X_λ^+, coupled to a correlated pair A_μ^+. The presently neglected interaction $\mathfrak{H}Y$ will become important for the coupling. Similarly it will be possible to describe certain excited states in nuclei like O^{17} and F^{17} by coupling a fermion to a "2p-2h phonon", where HY might be expected to play an important role. Since the excitation from a spherical ground state to a deformed excited state is definitely due to an anharmonic effect, we might also expect our NTD method to be useful in describing anharmonic effects in the second excited states ($J^\pi = 0^+, 2^+, 4^+$) in spherical even nuclei.

Before entering on such problems, we duly turn back our attention to the starting point O^{16} and Ca^{40}. It is true that we are not yet able to present any numbers: a quantitative discussion will be the subject of a later publication. But, fortunately, the measured properties of O^{16} and Ca^{40} are so striking that a natural *simultaneous* explanation of the various phenomena has a certain conclusive value even though it is only qualitative.

We believe that we easily can account for the strong collective lowering (with respect to the unperturbed positions) of first excited even parity states. It is due mainly to the deformation, but "triggered" by the residual interaction. Since the excited state with a definite intrinsic deformation contains the ground-state correlations properly, there is no difficulty in simultaneously understanding both the rotational band structure and the $E2$ transition to the ground state. In other words, although the ground state is *spherical* and the excited states are *deformed*, we may expect strong electromagnetic transitions between the rotational band and the ground state. This is borne out both by the validity of the energy weighted sum rule and the expression given explicitly for the transition probabilities. Formally, the expression has a very close resemblance to the corresponding expression for the strong collective transition probabilities described by the conventional RPA. Finally, the collective nature of the first excited 0^+ state in O^{16} and Ca^{40} makes it easy to understand the strong hindrance of the double gamma decays. Thus, we feel that, in principle, all the striking and not easily unifiable features of O^{16} and Ca^{40} can be well accommodated in our theory without depending on a very critical choice of some parameters.

It is sometimes argued that any theory which tries to describe the lowest excited even parity states in O^{16} as consisting mainly of 2p-2h excitations is doomed to fail from the outset. The arguments are usually based on the fact that Hartree-Fock calculations [3] for O^{16}, with certain restrictions and confined to a space of *pure* 2p-2h or alternatively *pure* 4p-4h configurations, might give a lower energy for 4p-4h excitations*. From our point of

view, such arguments are not necessarily conclusive. In spite of the result of reference 3, we still tend towards the orthodox belief that the shell-model configuration with the lowest zero-order energy should be of some importance. Furthermore, we feel that taking into account the collective ground-state correlations might change the ordering of the "2p-2h" and "4p-4h" states. The reason is that only the 2p-2h states couple directly to the shell-model ground state (provided that only conventional two-body interactions are considered). Thus, it seems to us that the question of whether the "2p-2h" or the "4p-4h" configurations win the competition of being mainly responsible for the first excited 0^+ state in O^{16} cannot be decided before quantitative calculations in the framework of the present theory are performed.

Whatever the outcome may be, certainly there *will* be states to which our approach is applicable and there may be use for it in other problems.

Acknowledgements

The authors wish to express their gratitude to Professors AAGE BOHR and AAGE WINTHER for their warm hospitality at the Niels Bohr Institute whose unique atmosphere formed the indispensable background for this work. The authors are greatly indebted to Professors A. BOHR and B. R. MOTTELSON for their helpful criticism, stimulating discussions and suggestions without which this work would never have been completed. Finally, they would like to thank Dr. J. GUNN for his advice in computer programming and to acknowledge research grants from the Ford Foundation.

* For Ca^{40} the situation would be different from the situation in O^{16}. The uppermost occupied level is a $d_{3/2}$ level in Ca^{40}, but a $p_{1/2}$ level in O^{16}. Thus, the shell in Ca^{40} is not exhausted with four holes.

From
The Niels Bohr Institute
University of Copenhagen.

First author's permanent address:
Hahn-Meitner Institut für Kernforschung
Berlin, Germany.

Second author's permanent address:
Department of Physics, Kyoto University
Kyoto, Japan.

References

1) H. Morinaga, Phys. Rev. **101** (1956) 254.
2) E. B. Carter, G. E. Mitchell and R. H. Davis, Phys. Rev. **133** B (1964) 1421, 1434.
R. W. Bauer, A. M. Bernstein, G. Heymann, E. P. Lippincott and N. S. Wall, Phys. Letters **14** (1965) 129.
3) W. H. Bassichis and G. Ripka, Phys. Letters **15** (1965) 320.
4) T. Engeland, Nuclear Phys. **72** (1965) 68.
I. Kelson, Phys. Letters **16** (1965) 143,
P. Federman and I. Talmi, Phys. Letters **15** (1965) 165.
5) G. E. Brown, Congrès International de Physique Nucléaire, Vol. I (Paris, 1964) 129.
6) G. E. Brown and A. M. Green, Nuclear Phys. **75** (1966) 401.
7) J. Borysowicz and R. K. Sheline, Phys. Letters **12** (1964) 219.
J. M. Eisenberg, B. M. Spicer and M. E. Rose, Nuclear Phys. **71** (1965) 273.
J. B. Seaborn and J. M. Eisenberg, Nuclear Phys., to be published.
8) B. R. Mottelson, Cours de l'Ecole d'Eté de Physique Théorique des Houches (Dunod, Paris, 1959).
9) A. B. Volkov, Phys. Letters **12** (1964) 118; Nuclear Phys. **74** (1965) 33.
10) N. Vinh Mau and G. E. Brown, Phys. Letters **1** (1962) 36.
11) K. Sawada and N. Fukuda, Progr. Theor. Phys. **25** (1961) 658.
12) K. Sawada, Phys. Rev. **119** (1960) 2090.
F. Iwamoto, Progr. Theor. Phys. **23** (1960) 871.
T. Marumori, T. Murota, S. Takagi, H. Tanaka and M. Yasuno, Progr. Theor. Phys. **25** (1961) 1035.
13) H. Schmidt, Z. Physik **181** (1964) 532.
14) D. R. Bès and R. A. Broglia, Nuclear Phys. **80** (1966) 289.
15) T. Marumori, M. Yamamura and A. Tokunaga, Progr. Theor. Phys. **31** (1964) 1009.
T. Marumori, M. Yamamura, A. Tokunaga, and K. Takada, Progr. Theor. Phys. **32** (1964) 726.
16) R. P. Peierls and J. Yoccoz, Proc. Phys. Soc. London, *AFO* (1957) 381.
J. Yoccoz, Proc. Phys. Soc. London, *AFO* (1957) 388.
R. P. Peierls and J. D. Thouless, Nuclear Phys. **29** (1962) 87.
17) J. D. Thouless, Nuclear Phys. **22** (1961) 78.
18) J. Eichler and G. Jacob, Z. Physik **157** (1959) 286.

19) B. Margolis, Nuclear Phys. **28** (1961) 524.
J. Eichler, Phys. Rev. **133** B (1964) 1162.
20) J. S. Levinger, Nuclear Photo-Disintegration (Oxford University Press, New York, 1960).
21) S. Gorodetzky et al., Phys. Letters **1** (1962) 14.
22) G. Goldring and B. Rosner, Phys. Letters **1** (1962) 9.
23) D. E. Alburger and P. D. Parker, Phys. Rev. **135** B (1964) 294.
24) P. Harihar and C. S. Wu, Bull. Am. Phys. Soc. **9** (1964) 457, and private communication by C. S. Wu.
25) J. C. Vanderleeden and P. S. Jastram, Phys. Letters **19** (1965) 27.
26) B. S. Dolbilkin et al., Phys. Letters **17** (1965) 49.

Indleveret til Selskabet den 26. marts 1966.
Færdig fra trykkeriet den 31. december 1966.

Matematisk-fysiske Meddelelser
udgivet af
Det Kongelige Danske Videnskabernes Selskab
Bind **35,** nr. 8

Mat. Fys. Medd. Dan. Vid. Selsk. **35,** no. 8 (1966)

SOME ACCURATE HALF-LIFE DETERMINATIONS

BY

V. MIDDELBOE

København 1966
Kommissionær: Munksgaard

Synopsis

The rate of decay of three short-lived nuclides has been re-investigated and improved half-life values have been found. The results are as follows: Ba^{137m} 153.46 ± 0.20 s, Ag^{109m} 39.80 ± 0.18 s, and Rh^{106} 30.35 ± 0.15 s. The standard deviations include the uncertainties involved in the investigations of radioactive impurities.

Some measurements in 1960–61 by the author on the half-life of Ba^{137m} seemed to indicate that the current standard value, 2.60 ± 0.05 minutes, is about two per cent too high, and through personal communication the following comment on some below-mentioned biological work was received: "... our half-lives seem to run about 2.5 minutes from those tissues which gave the best measurements. However, we do not feel that these measurements are particularly precise, ..."

A meticulous re-determination of the half-life of Ba^{137m} was then commenced, serious consideration being given to objective evaluation of impurity bias and natural uncertainty. Improved values for the half-lives of Ag^{109m} and Rh^{106} were subsequently obtained by applying the methodology developed for Ba^{137m}.

PRINTED IN DENMARK
BIANCO LUNOS BOGTRYKKERI A/S

Introduction

Three short-lived radioactive nuclides have been re-investigated and in each case a more accurate half-life value has been determined. The test nuclides were selected with a view to objective evaluation of the radio-purity of the sample and the natural uncertainty of the result.

In principle, a half-life value is found by isolating a sample of the test nuclide and measuring its rate of decay. However, the result may be biased by a radioactive impurity in the sample, and this type of uncertainty is hard to evaluate. On the other hand, the uncertainty of the result due to the random nature of radioactive decay is easy to evaluate when the well-known ratio method of half-life measurement is applicable.

In 1959, it was found that the half-life of biologically separated Ba^{137m} was slightly smaller than the value currently accepted by physicists. This apparent discrepancy could perhaps have been due to a difference in the radio-purity of the differently separated samples. Certainly, a better standard value for the physical half-life of Ba^{137m} is needed, since agreement between the observed and the standard $t_{\frac{1}{2}}$ value is used as a means of checking consistency in the type of biological work referred to here[1].

Methodology

Method of Measurement

Since the half-lives of the selected nuclides range from 0.5 to 2.5 minutes, the ratio method of measurement is practicable. In this method the investigator observes the ratio between the amount of test nuclide remaining in a sample after a period of decay and the amount initially present. Below, the following inverse ratio, the fall-off factor, is used:

$$F = \frac{N_0}{N_T}$$

where N_0 = number of test nuclei at zero time
N_T = number of test nuclei T minutes later.

When an F,T set has been observed, the corresponding value for the half-life of the test nuclide is found by use of the equation

$$t_{\frac{1}{2}} = T\frac{ln2}{lnF}. \tag{1}$$

Equation (1) is a simple transcription of Rutherford's law, $-dN = \lambda N dt$, in the integrated form $lnF = \lambda T$.

A fall-off factor is measured in the following way. A sample of test nuclide is placed near a radiation detector and pulse counting is started simultaneously with timing. The counts are summed continuously throughout a period of time, θ, of sufficient duration for virtually all the test nuclei to decay, and an observation is made of the total sum-count, Σ', thus accumulated. Also, an observation of the sum-count, S', and the corresponding counting time, T, is made (without stopping the counter) fairly early in the course of the total period of time, θ. Finally, the background radiation is assayed by counting the decayed sample for a period of time, for instance equal to θ, and observing the background sum-count, B, thus accumulated.

The value of the fall-off factor, that corresponds to the observations described above, is found by use of the simple equation

$$F = \frac{\Sigma}{\Sigma - S} \tag{2}$$

where $\Sigma = \Sigma' - B$ counts

$$S = S' - B\frac{T}{\theta} \text{ counts.}$$

Equation (2) rests on the assumption, that the counting efficiency remains constant throughout the entire 2θ period of observation.

Natural Uncertainty

The statistical fluctuation of replicate $t_{\frac{1}{2}}$ values is mainly due to the natural randomness inherent in the emission and absorption of radiation. When the ratio method of $t_{\frac{1}{2}}$ measurement is used, the natural standard deviation of the observed $t_{\frac{1}{2}}$ value can be closely approximated by the expression

$$\frac{\sigma_{\text{nat}}[t_{\frac{1}{2}}]}{t_{\frac{1}{2}}} = \frac{1}{\sqrt{\Sigma \ln F}} \sqrt{F - 1 + 2(F-1)^2\beta/\Sigma} \qquad (3)$$

where $\beta = B(\theta - T)/\theta$.

If β is completely insignificant in comparison with Σ, equation (3) indicates that $\sigma_{\text{nat}}[t_{\frac{1}{2}}]$ is minimal for $F = 5$, which is identical to the finding of PEIERLS[2]. If β is, say, one tenth of Σ, then $F = 3$ actually minimizes $\sigma_{\text{nat}}[t_{\frac{1}{2}}]$ according to equation (3), but $\sigma_{\text{nat}}[t_{\frac{1}{2}}]$ is still only ten per cent above minimum for $F = 5$.

For typical experimental values such as $\beta = 10^4$ counts, $\Sigma = 10^5$ counts and $F = 4$, equation (3) gives $\sigma_{\text{nat}}[t_{\frac{1}{2}}] = 0.005 \cdot t_{\frac{1}{2}}$, in which case the natural standard deviation of the mean of 25 replicate measurements is one part in a thousand.

Dead-Time Correction

Loss of counts at high counting rates tends to bias the observed half-life value upwards. Using the available apparatus and a fixed F value, the observed $t_{\frac{1}{2}}$ should be expected to increase linearly with the initial counting rate, R_0, and this is also in agreement with experimental observations up to almost 200 kc/min. (kilocounts per minute). Consequently, any dead-time bias on $t_{\frac{1}{2}}$ is eliminated conveniently by linear extrapolation of $t_{\frac{1}{2}}$ as a function of R_0 to the point at which $R_0 = 0$.

The dead-time loss on the counting rate, R, at any moment, t, may be theoretically approximated by

$$-\tau R^2 = -\tau R_0^2 \cdot e^{-2\lambda t}$$

where τ = dead-time.

From which we find (assuming the initial rate is less than 200 kc/min.)

$$\text{bias}_\tau[\Sigma] = -\tfrac{1}{2}\tau R_0 \Sigma, \quad \text{and} \quad \text{bias}_\tau[\Sigma - S] = -\tfrac{1}{2}\tau R_T(\Sigma - S)$$

so, since $F = \Sigma/(\Sigma - S)$, and considering equation (1),

$$\frac{\text{bias}_\tau[F]}{F} = -\tfrac{1}{2}\tau(R_0 - R_T), \quad \text{and} \quad \frac{\text{bias}_\tau[t_{\frac{1}{2}}]}{t_{\frac{1}{2}}} = \tfrac{1}{2}\tau(R_0 - R_T)/\ln F.$$

Finally, since $R_T = R_0/F$, we may write

$$\frac{\text{bias}_\tau[t_{\frac{1}{2}}]}{t_{\frac{1}{2}}} = \tfrac{1}{2}\tau \frac{F-1}{F \cdot \ln F} R_0. \qquad (4)$$

Time-Keeping

The author measures the critical period of time, T, by an eye-and-hand method, i.e., a stop-watch is started at counting time zero and stopped by hand as the eye sees the sum-count pass through an appropriate round number. This operation is analogous to timing a runner in athletics, which is known to be reproducible to 0.1 second (or 0.002 minute) by a trained time-keeper.

When all the timing is done by one and the same investigator, the possibility of a systematic error in timing becomes serious. The following control experiment was therefore designed. Three determinations of the half-life of Ba^{137m} are carried out with T equal to 0.5, 6.5 and 16 minutes, respectively, and R_0 equal to 40, 80 and 160 kc/min., respectively. The dead-time bias on the half-life value is then the same in each of the three determinations (cf. eq. (4) and Table 1). However, a small systematic error in timing must bias the first half-life determination relatively strongly and the other two only slightly.

TABLE 1. Data for control experiment on time-keeping. $F = 2^{T/t_{\frac{1}{2}}}$.

$\frac{T}{t_{\frac{1}{2}}}$	$\frac{F-1}{F \cdot lnF}$	R_0 (rel.)
0.19	0.94	1
2.5	0.47	2
6	0.24	4

Each of the three determinations comprised 25 single half-life measurements and the mean values obtained were 2.558 ± 0.004, 2.560 ± 0.001 and 2.560 ± 0.002 minutes, the stated figure of uncertainty being in each case the root-mean-square deviation

$$\sigma_{\text{rms}}[\bar{t}_{\frac{1}{2}}] = \sqrt{\frac{\sum(t_{\frac{1}{2}} - \bar{t}_{\frac{1}{2}})^2}{n(n-1)}}$$

where $t_{\frac{1}{2}}$ = single observation
$\bar{t}_{\frac{1}{2}}$ = mean observation
n = number of replicates.

The $\bar{t}_{\frac{1}{2}}$ value obtained with $T = 0.5$ minute, namely 2.558 ± 0.004, is apparently unbiased in comparison with the other two $\bar{t}_{\frac{1}{2}}$ values. This indicates a null systematic timing error with an uncertainty of about ± 0.001

minute, since a systematic timing error of 0.001 minute on T would bias the 2.558-minute value by 0.005 minute (cf. eq. (1)), which is of the same magnitude as the σ_{rms} of this value and would therefore not normally be detected by the control experiment performed.

Thus we may conclude, that under the prevailing conditions of measurement the uncertainty due to the possibility of a systematic error in timing, (below the sensitivity of the control experiment) contributes in general

$$\left(\frac{t_{\frac{1}{2}}}{T}\,0.001 \text{ minute}\right)^2 \tag{5}$$

to the overall variance of $\bar{t}_{\frac{1}{2}}$.

Radio-Purity Investigation

Consider two samples, identical in test nuclide content, which contain an alien radio-nuclide in the relative amounts $X{:}1$. To a first order approximation the impurity bias on the one sample's $t_{\frac{1}{2}}$ value is then X times that on the other. Consequently, the sum of the two impurity biases and the difference between them stand in the ratio of $(X+1){:}(X-1)$, and the following equation is applicable:

$$\frac{\bar{b}^*}{\frac{1}{2}\Delta} = \frac{X+1}{X-1} \tag{6}$$

where $\bar{b}^*$ = impurity bias on the mean of the two $t_{\frac{1}{2}}$ values
Δ = difference between the two $t_{\frac{1}{2}}$ values.

Two samples possessing the above properties can be produced experimentally as follows. Take one sample, the measurement of which is started immediately, and another sample composed of 2^N of the first kind, the measurement of which is started after a delay of $N \cdot t_{\frac{1}{2}}$ minutes. In comparison with the immediate content of radio-impurity in the first sample, the content in the second sample at the end of the delay period is different by a factor of

$$X = 2^{N - N^*} \tag{7}$$

where

$$N^* = (N \cdot t_{\frac{1}{2}})/t^*_{\frac{1}{2}} \tag{8}$$

$t^*_{\frac{1}{2}}$ representing the half-life of the alien radio-nuclide.

Half-life measurements based on the two types of sample described above may be termed immediate and delayed, respectively. When the average difference, Δ, between n_1 immediate and n_2 delayed measurements is found to be less than or about equal to the root-mean-square deviation of this difference, $\sigma_{\mathrm{rms}}[\Delta]$, then no significant impurity has been detected and the measured $t_{\frac{1}{2}}$ values possess a null impurity bias. The best result obtainable in this case is the mean, $\bar{t}_{\frac{1}{2}}$, of all $n_1 + n_2$ measurements, but this result is of course no more reliable than the null value of its impority bias, $\bar{b}^*$, of which the uncertainty is (cf. eqq. (6) and (7))

$$\sigma_{\mathrm{rms}}[\bar{b}^*] = \left| \frac{2^{N-N^*}+1}{2^{N-N^*}-1} \right| \tfrac{1}{2}\, \sigma_{\mathrm{rms}}[\Delta]. \tag{9}$$

Equation (9) shows clearly that the above-mentioned delay method of checking radio-purity is most uncertain when $t_{\frac{1}{2}}^*$ is close to $t_{\frac{1}{2}}$ (i.e., N^* close to N). Fortunately, however, the amount of impurity required to induce a significant bias on the observed half-life value increases rapidly as $t_{\frac{1}{2}}^*$ approaches $t_{\frac{1}{2}}$, which means that the delay method can be supplemented by a direct search for impurities with half-lives near that of the test nuclide.

Arbitrarily, we will restrict $\sigma_{\mathrm{rms}}[\bar{b}^*]$ to $1.5 \cdot \sigma_{\mathrm{rms}}[\Delta]$. The lower limit of $|N - N^*|$ is then 1 (cf. eq. (9)) and the half-lives of the potential impurities, that we will attempt to check by the delay method, are restricted to the following "wing-intervals" (cf. eq. (8)):

$$t_{\frac{1}{2}}^* \leqslant \frac{N}{N+1}\, t_{\frac{1}{2}} \quad \text{and} \quad t_{\frac{1}{2}}^* \geqslant \frac{N}{N-1}\, t_{\frac{1}{2}}. \tag{10}$$

In other words, the delay method is considered unacceptable for investigating potential impurities belonging to the "centre-interval"

$$\frac{N}{N+1}\, t_{\frac{1}{2}} < t_{\frac{1}{2}}^* < \frac{N}{N-1}\, t_{\frac{1}{2}}. \tag{11}$$

It is worth noting, that a null Δ value conveys sample purity with respect to any number or combination of (genetically unrelated) impurities belonging to either or both wing-intervals (10), because the apparent half-life of a sample containing a radio-impurity increases with time irrespective of whether $t_{\frac{1}{2}}^*$ is greater or less than $t_{\frac{1}{2}}$, and two or more (independant) Δ contributions will therefore always enhance one another.

Let the fall-off factor, 2^N, of the test nuclide during the delay period be, e.g., six. The centre-interval (11) is then given by $0.7 < t_{\frac{1}{2}}^{*}/t_{\frac{1}{2}} < 1.7$ and, in principle, every radio-nuclide that satisfies this condition must be looked for directly in samples of the test nuclide. Table 2 indicates the relative amount of any such nuclide required to induce a bias of one part in a thousand on the apparent half-life of the test nuclide (when F is also 6).

The relative bias on an observed $t_{\frac{1}{2}}$ due to an alien radio-nuclide, c^{*}, belonging to the centre-interval $0.7 < t_{\frac{1}{2}}^{*}/t_{\frac{1}{2}} < 1.7$, is

$$\frac{\text{bias}_{c^*}[t_{\frac{1}{2}}]}{t_{\frac{1}{2}}} = \frac{F^{1-t_{\frac{1}{2}}/t_{\frac{1}{2}}^{*}} - 1}{lnF} \cdot \frac{\Sigma^{*}}{\Sigma} \tag{12}$$

where Σ^{*} = sum-count of impurity at counting time θ.

TABLE 2. The percentage of centre-interval impurity that biases the half-life of the test nuclide by one part in a thousand, when $F = 6$. Calculated by use of equation (12).

BIAS OF −1 PER MILLE ON $t_{\frac{1}{2}}$		BIAS OF +1 PER MILLE ON $t_{\frac{1}{2}}$	
$t_{\frac{1}{2}}^{*}/t_{\frac{1}{2}}$	Σ^{*}/Σ %	$t_{\frac{1}{2}}^{*}/t_{\frac{1}{2}}$	Σ^{*}/Σ %
0.7	0.3	1.1	1.0
0.75	0.4	1.2	0.5
0.8	0.5	1.3	0.4
0.85	0.6	1.4	0.3
0.9	0.9	1.5	0.2
—	—	1.7	0.2

Finally, the presence of an unfortunate combination of genetically related and unrelated impurities might bias $t_{\frac{1}{2}}$ significantly and yet produce a zero Δ value. However, in the work presented here the only nuclides that could conceivably be the cause of such a chain effect are given in Table 3.

TABLE 3. Genetically related nuclides, two or more of which might contribute to a significant chain effect.

Ra-224	Th-234	Rn-222	Th-227	Ra-225
Rn-220	Pa-234m	Po-218	Ra-223	Ac-225
Pb-212		Pb-214	Rn-219	Fr-221
Bi-212		Bi-214	Pb-211	Bi-213
Tl-208			Bi-211	Tl-209
			Tl-207	Pb-209

A special case of genetical contamination is of course the presence of some of the test nuclide's parent in the sample. This does not bias the half-life of the sample significantly when the parent nuclide is very long-lived relative to the daughter, but it does increase the radiation background, B, and thereby the natural uncertainty of the observed half-life value as expressed in equation (3).

Barium 137 m

Previous Results

Several nuclear properties of Ba^{137m} were published in 1949 by MITCHELL and PEACOCK[3]. Their half-life value was 156 ± 3 sec. which corresponds to 2.60 ± 0.05 min.

In 1948, TOWNSEND, CLELAND and HUGHES[4] found the value 2.63 ± 0.08 min. They added sulphate ions to a solution containing Cs^{137}–Ba^{137m}. This solution was brought into contact with a piece of solid $BaSO_4$ which was subsequently washed, dried and counted. The initial counting rate was 12 kc/min.

Also in 1948, ENGELKEMEIER[5] reported the value 2.5 min.

Separation Technique

Ba^{137m} is easily separated from Cs^{137} by elution with basic EDTA from Cs^{137} absorbed on a conventional cation exchange column. The total number, Σ, of Ba^{137m} counts in the sample can be pre-determined by counting the drops of eluate included in the sample.

Present Result

240 half-life measurements were made (with $F = 6$) using a NaI crystal and counting all the pulses above the input bias voltage. The main values that were found are given in Table 4.

The 110 measurements at $R_0 = 27$ kc/min. comprise 55 immediate measurements averaging $2.558_5 \pm 0.001_5$ min. and 55 delayed measurements (with $2^N = 6$) averaging $2.558_0 \pm 0.001_5$ min. The difference, Δ, is nil and, consequently, no wing-interval impurity was present in the samples. The uncertainty of this conclusion imposes $\pm 1.5 \cdot \sigma_{\text{rms}}[\Delta] = \pm 0.0032$ min. on the mean of the 110 measurements (see page 8); and the extrapolated value of $t_{\frac{1}{2}}$ must also carry this standard deviation.

TABLE 4. 240 measurements of the half-life of Ba^{137m}.

Number of replicates (n)	Initial count-rate (R_0) kc/min.	Mean value observed ($\bar{t}_{\frac{1}{2}}$) min.	Precision of mean value ($\sigma_{rms}[\bar{t}_{\frac{1}{2}}]$) min.
55	160	2.559	0.001
50	80	2.560	0.001
25	40	2.558	0.002
110	27	2.558	0.001
	(0	2.558*	0.001)

* by extrapolation

A previous determination of the half-life of Ba^{137m} had been made using a well-crystal detector which was connected to a scaler with a dead-time of about 10^{-7} min. 110 measurements were carried out utilizing F values which were proportional to R_0, so that the counting rate at the stop watch moment, T, was the same in all the measurements. However, a variation in the dead-time bias of the measured $t_{\frac{1}{2}}$ values was attained (cf. eq. (4)), making it possible to extrapolate to zero dead-time bias. The main values that were found are given in Table 5.

TABLE 5. 110 measurements of the half-life of Ba^{137m}.

Number of replicates (n)	Rel. dead-time correction* $\left(\frac{F-1}{2F\ln F} R_0\right)$ x $10^3\tau$	Mean value observed ($\bar{t}_{\frac{1}{2}}$) min.	Precision of mean value ($\sigma_{rms}[\bar{t}_{\frac{1}{2}}]$) min.
15	−38	2.573	0.002
15	−23	2.565	0.002
50	−15	2.564	0.001
30	−10	2.560	0.002
	(0	2.557**	0.001_5)

* confer equation (4)
** by extrapolation

The two independent determinations of the half-life of Ba^{137m} agree well (compare Tables 4 and 5) and the weighted grand mean is 2.5577 ± 0.0008 min. or 153.46 ± 0.05 sec., where the standard deviation given does not include radio-purital uncertainty. The systematic timing error, according

to expression (5), is less than or about equal to 0.0004 min., which may be disregarded.

The previously mentioned centre-interval, $0.7 < t_{\frac{1}{2}}^{*}/t_{\frac{1}{2}} < 1.7$, corresponds to 1.8 min. $< t_{\frac{1}{2}}^{*} <$ 4.4 min. in the case of Ba^{137m}. Since the stock solution of Cs^{137} had been aged for over a year before the half-life of Ba^{137m} was measured, an alien radio-nuclide belonging to this centre-interval could not have existed unless it sprang from a parent or forefather with a half-life of at least a month. An investigation of all known[16] radionuclides and their properties showed that only Tl^{208}, Tl^{209} and Bi^{211} could have been of significance as centre-interval impurities. These three possibilities were investigated as follows.

Tl^{208} and Tl^{209} emit photons of 2.6 and 1.6 MeV, respectively, whereas Ba^{137m} emits 0.7 MeV photons. In an analysis using a 1-channel γ-spectrometer no 2.6 or 1.6 MeV photons were detected in the radiation from Ba^{137m} samples. The limit of detection (i.e., $\sigma_{\Sigma *}$) was less than 0.02 per cent of the total sum-count Σ, and the limit of the bias on $t_{\frac{1}{2}}$ therefore less than 0.1 part in a thousand (cf. Table 2).

Bi^{211} emits 5–6 times as many α-particles as γ-photons, yet nuclear emulsions that were impregnated with drops of Ba^{137m} sample showed no α-tracks above background after an exposure period equal to θ. This investigation also established a limit for the possible amount of chain-contamination (cf. Table 3). By calibration with drops of uranium solution and by some conservative assumptions, the uncertainty of $t_{\frac{1}{2}}$ due to the possibility of chain-contamination below the limit of detection was evaluated at 0.25 per mille, which is negligible compared to the above-mentioned ± 0.0032 min. due to the uncertainty involved in the investigation of wing-interval impurities.

The final result is thus 2.5577 ± 0.0032 min., or

$$t_{\frac{1}{2}}[\mathrm{Ba-137\ m}] = 153.46 \pm 0.20 \text{ seconds.}$$

Silver 109m

Previous Results

In 1941, Helmholz[6] observed that the process Ag(d,2n)Cd lead to the production of a long-lived radio-isotope of cadmium (besides the already known 7-hour isotope), and a daughter of the long-lived isotope was found to have a half-life of 40 ± 3 sec.

Wiedenbeck[7] reported in 1945 that silver nuclei excited by X-rays had a half-life of 40.4 ± 0.2 sec. due to either Ag^{107m} or Ag^{109m}. The same

year, BRADT et al.[8] separated radio-silver from some aged radioactive cadmium, which had been produced by the process Ag(p,n)Cd, and found a $t_{\frac{1}{2}}$ value of 40.5 ± 0.7 sec., this was corrected the following year to 39.2 ± 0.2–0.3 sec.[9].

In 1947 BRADT et al.[10] announced that it had become possible, unequivocally, to attribute the $t_{\frac{1}{2}}$ values 44 and 39 sec. to Ag^{107m} and Ag^{109m}, respectively, since HELMHOLZ[11] shortly before had made use of separated Cd^{106} and Cd^{108} that were irradiated with thermal neutrons.

Finally, in 1951, WOLICKI, WALDMAN and MILLER[12] excited a sample of highly purified Ag^{109} and measured the decay rate of the Ag^{109m} by photographing the sum-count and the clock every 5 sec. for 5 min. Their $t_{\frac{1}{2}}$ value was graphically evaluated at 40.0 ± 1.0 sec.

Separation Technique

AgCl was electroplated onto a disc of platinum gauze by the method of SUNDERMAN[13], and Ag^{109m} in solution was separated from its parent, Cd^{109}, by exchange with some of the inactive silver ions in the net of AgCl.

Present Result

74 half-life measurements were made (with $F = 6$) using one of the previous counters reinforced by the linear amplifier of the γ-spectrometer in order to register the 22 keV X-rays from Ag^{109}. The dead-time of the set-up was about 10 μsec. The main values that were found are given in Table 6.

TABLE 6. 74 measurements of the half-life of Ag^{109m}.

Number of replicates (n)	Total sum-count ($\Sigma = R_0/\lambda$) kc.	Mean value observed ($\bar{t}_{\frac{1}{2}}$) sec.	Precision of mean value ($\sigma_{rms}[\bar{t}_{\frac{1}{2}}]$) sec.
25	150	40.08	0.04
49	25	39.85	0.05
	(0	39.80*	0.06)

* by extrapolation

The 49 measurements at $\Sigma = 25$ kc. comprise 25 immediate measurements averaging 39.89 ± 0.07 sec. and 24 delayed measurements (with

$2^N = 6$) averaging 39.80 ± 0.09 sec. The difference between the immediate and the delayed series (i.e., $\Delta = 0.09$ sec.) is insignificant, since $\sigma_{\text{rms}}[\Delta] = 0.12$ sec., and in consequence no wing-interval impurity was present in the samples. The uncertainty of this conclusion corresponds to $\pm 1.5 \cdot \sigma_{\text{rms}}[\Delta] = \pm 0.18$ sec. on the $t_{\frac{1}{2}}$ values (see page 8), and the final result is thus (cf. Table 6).

$$t_{\frac{1}{2}}[\text{Ag–109m}] = 39.80 \pm 0.18 \text{ seconds}$$

pending the investigation of other possible impurities.

Since the Cd^{109} stock was aged for 9 months prior to the $t_{\frac{1}{2}}$ measurements on the daughter, the only known[16] nuclide that could have been of significance as a centre-interval impurity was 30-sec. Rh^{106}, that emits $10\,^0/_0$ 0.5–3 MeV γ-photons. Making use of the 1-channel analyzer, the Rh^{106} content in the Ag^{109m} samples was found to be less than or about equal to 0.01 per cent which corresponds to a bias of less than 0.1 part in a thousand on $t_{\frac{1}{2}}$ (cf. Table 2).

Finally, Cd^{109} is cyclotron produced, as opposed to Cs^{137} which is a fission product, so an investigation of chain-contamination was considered unnecessary in this case (cf. Table 3).

Rhodium 106

Previous Results

In 1946, Seelmann-Eggebert[14] discovered a new radioisotope of ruthenium with a half-life of about 12 months. The emission of energetic β-particles suggested the existence of a short-lived daughter nuclide, and true enough a radio-isotope of rhodium with a half-life of about 40 sec. was found.

In 1951, Glendenin and Steinberg[15] separated aged Ru^{106} from its daughter, Rh^{106}, by $HClO_4$ distillation and found the half-life of Rh^{106} to be 25–30 sec. In one run they measured the decay of Rh^{106} remaining in the distillation flask ($t_{\frac{1}{2}} = 30$ sec.), and in another run the in-growth of Rh^{106} in the distilled Ru^{106} ($t_{\frac{1}{2}} = 31$ sec.). In a third run they filtered out the β-particles and the Bremsstrahlung from the Rh^{106} radiation and measured the γ-rays ($t_{\frac{1}{2}} = 25$ sec.).

Separation Techniques

Two different separation techniques were used. The one was Glendenin's distillation procedure modified so as to trap the distilled RuO_4 in $HClO_4$,

whereby it was ready for further distillation. The second technique was the absorption of RuO_4 vapour as RuO_2 on a paper disc held close to the surface of a saturated solution of RuO_4 in $70\,^0/_0$ $HClO_4$.

Present Result

The stock of Ru^{106} was aged for 8 months prior to the measurements on the half-life of Rh^{106}. In each measurement about 2 ml of Ru-distillation residue were rapidly taken, cooled and counted in a specially constructed flat-bulbed, V-shaped pipette provided with capillary stems. This container was stood on the aluminium window above a stilbene crystal for detection

TABLE 7. 23 measurements of the half-life of Rh^{106} by decay (given in chronological order).

Background (B) kc.	Rh-106 sum-count (Σ) kc.	Average Rh-106 sum-count ($\bar{\Sigma}$) kc.	Value observed ($t_{\frac{1}{2}}$) sec.	Mean value and precision ($\bar{t}_{\frac{1}{2}} \pm \sigma_{rms}[\bar{t}_{\frac{1}{2}}]$) sec.
25	87		30.9	
9	80		30.3	
22	66		30.8	
17	118		30.7	
11	46		30.1	
5	57		30.3	
8	46		30.3	
3	97		30.4	
5	77		30.6	
9	90		30.4	
7	51		30.5	
7	50		30.5	
4	46		30.5	
1	41		30.4	
6	64		30.4	
10	37		30.3	
3	48		30.9	
2	44		30.5	
5	42		30.8	
5	46		30.1	
3	51		30.7	
8	65		30.5	
2	55	61	30.8	30.51 ± 0.05

of the β-particles from Rh^{106}. The special counting container circumvented a previously observed variation of the background counting rate due to translocation of undistilled RuO_4 within the container during counting.

During 25 consecutive hours, 25 acceptable* half-life measurements were made (with $F = 4$) on the basis of 30 distillation cycles of a single portion of Ru^{106}. Two of the acceptable* measurements were subsequently discarded, because the initial counting rate (calc. from Σ) had exceeded 200 kc/min. and the linearity of the dead-time effect was therefore in doubt. The results of the remaining 23 measurements are given in Table 7.

A linear co-variance analysis of the valus for $t_{\frac{1}{2}}$ and Σ indicates a regression coefficient of 0.0023 ± 0.0024 sec./kc. By extrapolation to $\Sigma = 0$ (i.e., $R_0 = 0$) this conveys a dead-time correction on $\bar{t}_{\frac{1}{2}}$ of -0.14 ± 0.15 sec. (cf. Table 7). Applying this correction, the resulting mean value for the half-life of Rh^{106} – as determined by decay – is 30.37 ± 0.16 sec.

Each measurement of the half-life of Rh^{106} entailed a re-distillation of the stock of parent material, yet there is no chronological trend in the observed $t_{\frac{1}{2}}$ values (cf. Table 7). In this case, radio-purital uncertainty is considered to have been insignificant in comparison with the above-mentioned uncertainty involved in the dead-time correction.

Finally, Ru^{106} was separated by the previously described paper-disc

TABLE 8. 10 measurements of the half-life of Rh^{106} by in-growth.

R_1	R_2	R_∞	F_{30}	$\bar{F}_{30} \pm \sigma_{rms}[\bar{F}_{30}]$
6.3	9.4	12.6	1.97	
6.2	9.3	12.4	2.00	
4.5	7.3	10.1	2.00	
7.2	10.3	14.0	1.89	
4.7	7.0	9.4	1.96	
4.8	7.3	10.0	1.93	
5.4	8.4	11.2	2.06	
4.0	5.9	7.9	1.95	
5.1	7.6	9.8	2.14	
8.0	11.3	14.6	2.00	1.990 ± 0.022

R_1 = number of kc. during the period from 0 to 15 sec.
R_2 = number of kc. during the period from 30 to 45 sec.
R_∞ = number of kc./10 during the period from 450 to 600 sec.
$F_{30} = (R_\infty - R_1)/(R_\infty - R_2)$.

* The rather uncontrolable amount of undistilled Ru-106 in the sample was sometimes unreasonably large. A measurement was deemed unacceptable in this respect (cf. p. 10) when the background sum-count exceeded one third of the Rh-106 sum-count.

method from the solution of RuO_4 which had been distilled 30 times, and 10 measurements on the rate of in-growth of Rh^{106} were made. In each measurement, the loaded paper disc was placed on the aluminium window of the detector and covered with an aluminium plate of the same thickness as the window. The data that were observed are given in Table 8.

The half-life of Rh^{106} – as determined by in-growth – may be calculated by use of the following equation (compare eq. (1)):

$$t_{\frac{1}{2}} = 30 \frac{\log 2}{\log F_{30}}.$$

Inserting the value of $\bar{F}_{30}$ (cf. Table 8) we find the $t_{\frac{1}{2}}$ value 30.2 ± 0.5 sec.

The weighted mean of the value obtained by in-growth and the previously mentioned value obtained by decay gives the final result:

$$t_{\frac{1}{2}}[\text{Rh-106}] = 30.35 \pm 0.15 \text{ seconds.}$$

Acknowledgement

Financial support from the STATENS ALMINDELIGE VIDENSKABSFOND and KAI HANSENS FOND is gratefully acknowledged.

Isotope Laboratory, Physics Department
Royal Veterinary and Agricultural College,
Copenhagen.

References

1. R. H. Wasserman, A. R. Twardock and C. L. Comar (1959), Science **129**, 568.
2. R. Peierls (1935), Proc. Roy. Soc. *A* **149**, 467.
3. A. C. G. Mitchell and C. L. Peacock (1949), Phys. Rev. **75**, 197.
4. J. Townsend, M. Cleland and A. L. Hughes (1948), Phys. Rev. **74**, 499.
5. D. W. Engelkemeier (1948), ANL-4139 and AECD-2125.
6. A. C. Helmholz (1941), Phys. Rev. **60**, 160.
7. M. L. Wiedenbeck (1945), Phys. Rev. **67**, 92.
8. H. Bradt, P. C. Gugelot, O. Huber, H. Medicus, P. Preiswerk und P. Scherrer (1945), Helv. Phys. Acta **18**, 256.
9. H. Bradt, P. C. Gugelot, O. Huber, H. Medicus, P. Preiswerk, P. Scherrer und R. Steffan (1946), Helv. Phys. Acta **19**, 218.
10. H. Bradt, P. C. Gugelot, O. Huber, H. Medicus, P. Preiswerk, P. Scherrer und R. Steffan (1947), Helv. Phys. Acta **20**, 153.
11. A. C. Helmholz (1946), Phys. Rev. **70**, 982.
12. E. J. Wolicki, B. Waldman and W. C. Miller (1951), Phys. Rev. **82**, 486.
13. D. N. Sunderman and C. W. Townley (1961), "The Radiochemistry of Silver", USAEC NAS-NS **3047**, 25.
14. W. Seelmann-Eggebert (1946), Naturwiss. **33**, 279.
15. L. E. Glendenin and E. P. Steinberg (1951), NNES-PRR **9**, 793.
16. "Nuklidkarte", zweite Auflage (1961), Bundesminister für Atomenergie, Bad Godesberg.

Indleveret til Selskabet den 29. marts 1966.
Færdig fra trykkeriet den 20. oktober 1966.

Matematisk-fysiske Meddelelser
udgivet af
Det Kongelige Danske Videnskabernes Selskab
Bind **35,** nr. 9

Mat. Fys. Medd. Dan. Vid. Selsk. **35,** no. 9 (1966)

RANGE-ENERGY RELATIONS FOR LOW-ENERGY IONS

BY

HANS E. SCHIØTT

København 1966
Kommissionær: Munksgaard

CONTENTS

Page

§ 1. Introduction 3
§ 2. Light Particles in Heavy Substances 6
§ 3. Length of Particle Path 12
Appendix 16
References 20

Synopsis

Projected ranges are calculated for low-energy light particles in heavy substances (e.g. 20 keV deuterons in gold), together with straggling in projected range, assuming randomness of stopping material. The projected range turns out to be considerably less than the range along the path, and the distribution in projected range is very broad. The range ratio $\bar{R}_p/\bar{R}$ as well as the relative straggling $\Delta\overline{R_p^2}/\bar{R}_p^2$, are independent of stopping substance when a reduced energy measure, ε, is used, and are not strongly dependent on the atomic number of the projectile.

As an extension of earlier work are presented range-energy tables covering a large number of combinations of incoming particle and stopping substance.

PRINTED IN DENMARK
BIANCO LUNOS BOGTRYKKERI A/S

§ 1. Introduction

The purpose of the present paper is to study in detail some aspects of range distributions and thus to supplement the results in a previous paper, "Range Concepts and Heavy Ion Ranges" (LINDHARD, SCHARFF and SCHIØTT (1963) – in the following referred to as LSS). Of the problems treated in the following, one arose from a discussion of the recent measurements by CHU and FRIEDMAN (1965), where projected ranges were observed for 20 keV deuterons in aluminium and gold. The projected ranges found by CHU and FRIEDMAN were considerably smaller than the theoretical range along the path, which was somewhat unexpected since the ranges of light particles as protons, deuterons, etc. are normally little influenced by scattering effects. In § 2, consequently, the projected range is calculated as function of energy in the case of $Z_1 \ll Z_2$, where Z_1 and Z_2 are atomic numbers of incoming particle and stopping material, respectively. It is shown that, at low energies, the projected range may become an order of magnitude less than the range along the path. Calculations giving the fluctuation in projected range are also included.

In § 3 are presented numerical calculations on range along path as function of energy, performed since the appearance of LSS.

Integral equations describing the distribution in projected range are discussed in the Appendix. It should be emphasized that calculations in LSS, as well as in the present paper, are based on the assumption of randomness in the stopping substance. Caution should therefore be observed in comparisons between these theoretical results and experimentally determined ranges in crystals, where special directional effects may come into play, cf. e.g. KORNELSEN et al. (1964), and LINDHARD (1965).

General aspects of projected range calculations

An energetic charged particle loses energy by electronic and nuclear collisions, but is deflected by nuclear collisions only (BOHR, 1948). At high particle velocities the electronic stopping is completely dominating, the

nuclear stopping being $\sim 10^3$ times smaller than electronic stopping. This picture is valid for e.g. α-particles from radioactive decay, and in general for $v > v_1 = v_0 Z_1^{2/3}$, where $v_0 = e^2/\hbar$. At lower velocities, i.e. $v < v_1$, the electronic stopping is nearly proportional to velocity (LINDHARD and SCHARFF, 1961) and may still remain dominating for $Z_1 < Z_2$. For heavy particles, and with decreasing velocity, nuclear stopping gradually takes over relative to electronic stopping to form the major part of the energy loss.

Accordingly, it is natural, when calculating projected ranges, to divide in two groups. In the first group the total range is determined by electronic stopping solely, the nuclear collisions being responsible for scattering only. This is the simplest case, the solution of which is well-known for light particles at high energies, e.g. MeV-protons, α-particles, etc. It is also the case to be discussed in the following, but for particles at low energies.

In the second group the energy loss in nuclear collisions is an essential part of the total energy loss, so that the total range is partially determined by nuclear stopping. This case, which is the more complicated except when electronic stopping is much less than nuclear stopping, was treated in LSS.

Brief review of the main features of LSS

In LSS a comprehensive theoretical treatment of range-energy relations for slow heavy ions was attempted. The treatment was based on a universal nuclear stopping cross section, S_n, calculated from a Thomas-Fermi model of the interaction between heavy ions, and an electronic stopping cross section, S_e, proportional to v, the velocity of the incoming particle.

When energy and range are measured in the dimensionless parameters ε and ϱ, where

$$\varepsilon = E \cdot \frac{aM_2}{Z_1 Z_2 e^2 (M_1 + M_2)} \quad , \tag{1}$$

$$\varrho = RNM_2 \cdot 4\pi a^2 \frac{M_1}{(M_1 + M_2)^2} \quad , \tag{2}$$

(a being the screening parameter in the Thomas-Fermi potential $a = a_0 \cdot 0.8853\,(Z_1^{2/3} + Z_2^{2/3})^{-1/2}$) the nuclear stopping power, i.e. $(d\varepsilon/d\varrho)_n$ is a function of ε only, independent of incoming particle and stopping substance (Fig. 1). In the same units the electronic stopping power is represented by $(d\varepsilon/d\varrho)_e = k\varepsilon^{1/2}$, where

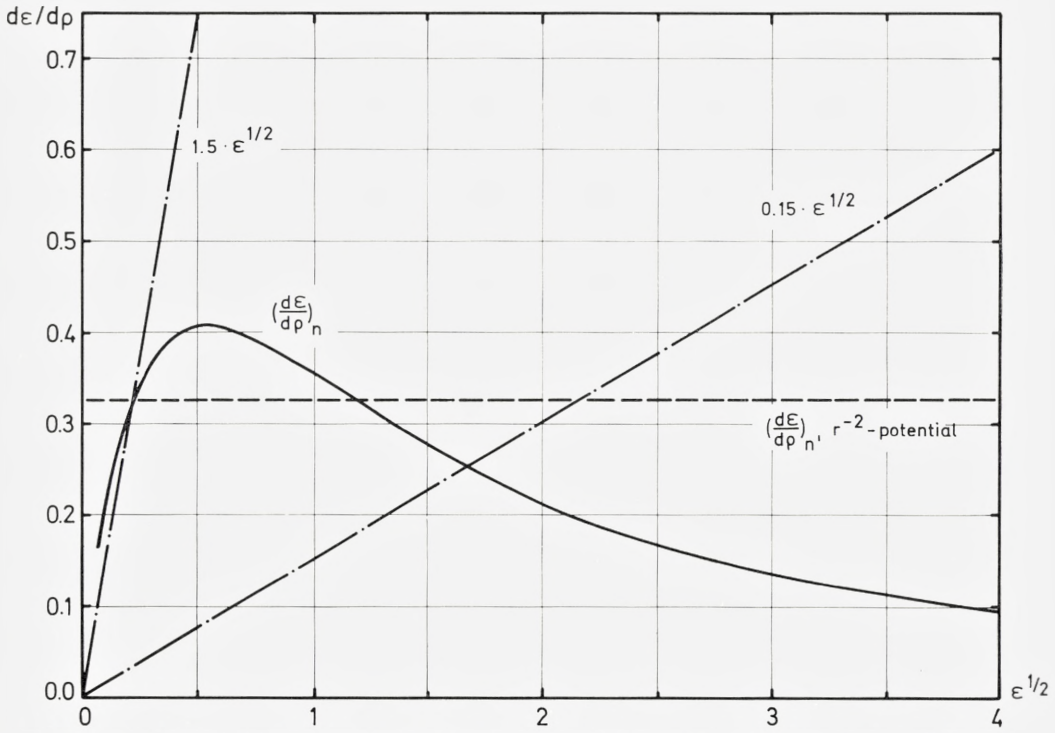

Figure 1. Nuclear and electronic stopping powers in reduced units. Full-drawn curve represents the Thomas-Fermi nuclear stopping power, the dot-and-dash lines the electronic stopping, (3), for $k = 0.15$ and $k = 1.5$.

$$k = \xi_e \cdot \frac{0.0793 \cdot Z_1^{1/2} Z_2^{1/2} (A_1 + A_2)^{3/2}}{(Z_1^{2/3} + Z_2^{2/3})^{3/4} \cdot A_1^{3/2} \cdot A_2^{1/2}}, \quad \xi_e \approx Z_1^{1/6}. \tag{3}$$

k is of order of $0.1 - 0.2$ for $Z_1 \gtrsim Z_2$, and only when $Z_1 \ll Z_2$, can k become larger than unity. The estimate, (3), of k, which is based on Thomas-Fermi arguments, gives a good over-all fit to experiments. Oscillations around the theoretical k-value, due to atomic shell effects, have been observed, especially for low atomic numbers (Ormrod and Duckworth, 1963; Fastrup, Hvelplund and Sautter, 1966). Two representative cases of electronic stopping, i.e. $k = 0.15$ and $k = 1.5$, are included in Fig. 1. The nuclear stopping power calculated from an inverse second power potential between the atoms is also included. This stopping power turns out to be constant, leading to a linear range energy relation (Bohr, 1948; Nielsen, 1956).

By numerical integration of the inverse total stopping power, $((d\varepsilon/d\varrho)_n + (d\varepsilon/d\varrho)_e)^{-1}$, for different values of the electronic stopping parameter, k, curves $\bar{\varrho} = \varrho_k(\varepsilon)$ were obtained and plotted in LSS. The range $\bar{\varrho}$ is the total length of the particle path. The penetration depth (projected range) is less than this quantity – the more so the larger the mass ratio $\mu = M_2/M_1$. The ratio $\bar{\varrho}_p/\bar{\varrho}$ was calculated by a series development to first order in μ for $\mu \ll 1$ and in a few cases for $\mu = 1$ and $\mu = 2$.

§ 2. Light Particles in Heavy Substances

Mean projected range

The equation governing the average projected range may be written down directly (cf. LSS) or may e.g. be derived from the equations describing the distribution in penetration depth, cf. Appendix. The equation is

$$1 = N \int d\sigma_{n,e}(\bar{R}_p(E) - \bar{R}_p(E - T) \cdot \cos \varphi), \tag{4}$$

where N is the number of target atoms per cm^3, $d\sigma_{n,e}$ is the differential cross section for a collision specified by energy loss T_n to the nucleus and $\sum_i T_{ei}$ to electrons, $T = T_n + \sum_i T_{ei}$, and φ is the deflection angle in the laboratory system.

Solution of equation (4) now proceeds as in LSS. The first approximation to be introduced is a series development to first order of the term $\bar{R}_p(E - T)$. Since

$$T_n < \frac{4M_1M_2}{(M_1 + M_2)^2} \cdot E = \gamma E,$$

and $\gamma \ll 1$ in the case of $4M_1 \ll M_2$, this is permissible. Moreover, the differential cross section favours strongly small energy transfers, $T_n \ll \gamma E$, and, further, energy loss to electrons in a single collision is always small compared to particle energy. Equation (4) then reads

$$1 = \bar{R}_p(E) \cdot N \int d\sigma_{n,e}(1 - \cos\varphi) + \frac{d\bar{R}_p(E)}{dE} \cdot N \int d\sigma_{n,e} \cdot T \cos\varphi. \tag{5}$$

By introducing the quantities

$$\left.\begin{aligned} \lambda_{tr}^{-1} &= N \int d\sigma_{n,e}(1 - \cos\varphi), \\ S_{tr} &= \int d\sigma_{n,e} T \cos\varphi, \end{aligned}\right\} \tag{6}$$

the solution of equation (5) may be written as

$$\bar{R}_p(E) = \int_0^E \frac{dE'}{NS_{tr}(E')} \exp\left[\int_E^{E'} \frac{dE''}{\lambda_{tr}(E'') \cdot NS_{tr}(E'')}\right]. \tag{7}$$

Equ. (7) should be a good approximation to the average projected range when γ is small.

In case of $\mu = M_2/M_1 \ll 1$ (in which case also $\gamma \ll 1$) the scattering angle φ is always very small, and $\bar{R}_p$ is not much different from $\bar{R}$. When, on the contrary, $\mu \gg 1$, there is a possibility of large scattering angles, and one cannot beforehand exclude the possibility that the projected range becomes considerably smaller than the path length.

In order to estimate λ_{tr} and S_{tr} in (6), we separate electronic and nuclear collisions, i.e. we put $d\sigma_{n,e} = d\sigma_n + d\sigma_e$, noting that $\varphi = 0$ in electronic collisions, while in nuclear collisions φ is given by

$$\cos\varphi = \left(1 - \frac{1+\mu}{2}\frac{T_n}{E}\right)\left(1 - \frac{T_n}{E}\right)^{-1/2} \cong 1 - \frac{\mu}{2}\frac{T_n}{E}, \quad \text{when } \gamma \ll 1. \tag{8}$$

We thereby obtain

$$\left.\begin{aligned} S_{tr}(E) &\cong S_e(E) + S_n(E) - \frac{\mu}{2} \cdot \frac{\Omega^2(E)}{E}, \quad \Omega^2(E) = \int T_n^2 d\sigma_n, \\ \lambda_{tr}^{-1}(E) &\cong N \cdot \frac{\mu}{2} \cdot \frac{S_n(E)}{E}. \end{aligned}\right\} \tag{9}$$

Since $k \gtrsim 1$, for $Z_1 \ll Z_2$, the electronic stopping is a major part of the energy loss even at very low energies (cf. Fig. 1). We then disregard nuclear stopping compared to electronic stopping and put $S_{tr} \cong S_e(E)$.

In actual calculations it is convenient to introduce the variables ϱ and ε given by (1) and (2). With this rescaling of units equation (7) may be written

$$\frac{\bar{\varrho}_p(\varepsilon)}{\varrho_e(\varepsilon)} = \frac{1}{\varrho_e(\varepsilon)} \int_0^{\varepsilon} \frac{d\varepsilon'}{(d\varepsilon'/d\varrho)_e} \exp\left[\int_{\varepsilon}^{\varepsilon'} \frac{d\varepsilon''(\mu/2)(d\varepsilon''/d\varrho)_n}{(d\varepsilon''/d\varrho)_e \cdot \varepsilon''} \right]. \tag{10}$$

Since we have neglected nuclear stopping compared to electronic stopping, $\bar{\varrho}_p(\varepsilon)$, given by (10), should be compared with the extrapolated electronic range, $\varrho_e(\varepsilon) = 2k^{-1}\varepsilon^{1/2}$ (cf. § 3), and although the absolute value of $\bar{\varrho}_p(\varepsilon)$ might be somewhat in error, the ratio $\bar{\varrho}_p(\varepsilon)/\varrho_e(\varepsilon)$ is expected to be rather accurate. Moreover, it may be shown that, if the nuclear stopping contributions to S_{tr} are not neglected compared to electronic stopping, the ratio between projected range and range along path is very nearly equal to $\bar{\varrho}_p(\varepsilon)/\varrho_e(\varepsilon)$, as given by equ. (10). Accordingly, we drop the subscript $_e$ in $\varrho_e(\varepsilon)$, simply writing $\bar{\varrho}_p(\varepsilon)/\bar{\varrho}(\varepsilon)$.

Inserting $(d\varepsilon/d\varrho)_e = k\varepsilon^{1/2}$ in (10), we notice that $\bar{\varrho}_p(\varepsilon)/\bar{\varrho}(\varepsilon)$ depends on the parameters μ and k through the ratio μ/k only; moreover, this ratio is very nearly independent of the target material for a specified projectile. We may then, by a single integration, calculate e.g. the projected range of protons in all heavy materials. Equ. (10) may be solved analytically if $(d\varepsilon/d\varrho)_n$ is equal to a constant, λ, corresponding to the r^{-2}-potential between atoms. One then finds

$$\frac{\bar{\varrho}_p(\varepsilon)}{\bar{\varrho}(\varepsilon)} = 1 - xe^x Ei(x), \quad x = \frac{\mu\lambda}{k\varepsilon^{1/2}} = \mu \cdot \frac{S_n}{S_e}, \tag{11}$$

where $\lambda = 0.327$ (cf. Fig. 1), and the exponential integral $Ei(x)$ is defined by

$$Ei(x) = \int_x^{\infty} \frac{e^{-t}}{t}\, dt.$$

Formula (11) is expected to be fairly accurate for ε-values less than ~ 5 (cf. Fig. 1) and to overestimate the nuclear stopping at higher energies, thereby giving too small values of $\bar{\varrho}_p/\bar{\varrho}$. For large values of x, i.e. for low energies, we may use the approximate relation

$$\frac{\bar{\varrho}_p(\varepsilon)}{\bar{\varrho}(\varepsilon)} \cong \frac{1}{x}\left(1 - \frac{2}{x}\right). \tag{12}$$

In Fig. 2 are shown $\bar{\varrho}_p/\bar{\varrho}$ given by (11) together with a numerical integration of (10) using the Thomas-Fermi nuclear stopping power. Curves are pre-

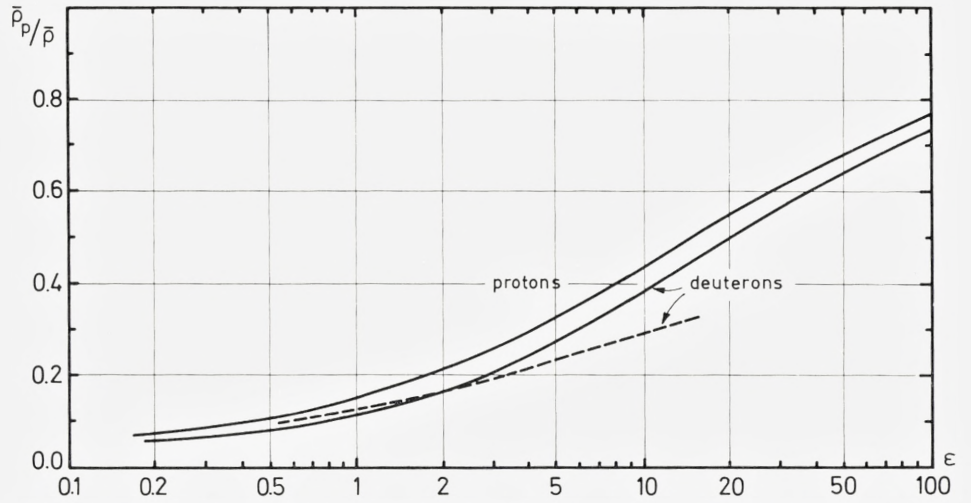

Figure 2. Projected range corrections for protons (μ/k = 13.1), and deuterons (μ/k = 18.3). Dashed curve represents the analytical solution (11) for deuterons, i.e. corresponding to constant nuclear stopping power.

sented for protons (μ/k = 13.1) and deuterons (μ/k = 18.3). It is remarkable that the dependence on μ/k is not very strong, and, moreover, that values of μ/k for other light particles fall in between those for protons and deuterons. Accordingly, an uncertainty in the theoretical estimate of k does not affect the value of $\bar{\varrho}_p/\bar{\varrho}$ in first approximation.

In case of mixed stopping substance, one may estimate the projected range by rather simple averages. If there are two elements, a and b, in the target, one finds $\bar{R}_p \approx \bar{R}_{p,a} \cdot \bar{R}_{p,b}/(x_a \cdot \bar{R}_{p,b} + (1 - x_a)\bar{R}_{p,a})$, where $\bar{R}_{p,a}$ and $\bar{R}_{p,b}$ are the projected ranges in a and b, and x_a and $1 - x_a$ are the relative abundances of a and b. The formula is valid if $\bar{R}_p$ in the pure elements of the stopping substance is proportional to a common power of E, which is the case when A_1 is much less than the mass number of both a and b. In LSS a similar formula was quoted for the range along path in a mixed substance.

It should be mentioned that we have used a velocity proportional electronic stopping power. This approximation is valid for $v \lesssim v_1 = v_0 \cdot Z_1^{2/3}$ corresponding to $E \lesssim E_1 = A_1 \cdot Z_1^{4/3} \cdot 25$ keV. Note that the corresponding maximum permissible ε-value, ε_1, for a specified particle decreases with increasing Z_2. In cases of interest it turns out that $\varepsilon_1 \lesssim 50$. For $E > E_1$, the stopping power goes through a maximum and then decreases, joining smoothly the Bethe stopping power curve. In this region the nuclear

stopping is determined by Rutherford scattering, i.e. in ε-units $(d\varepsilon/d\varrho)_n = 1/2\,\varepsilon \cdot ln\ (1.29\varepsilon)$, $(\varepsilon > 10)$. Therefore, the ratio between electronic and nuclear stopping is nearly a constant, of order of 10^3. It turns out that we can put, with close approximation for $\varepsilon \lesssim 10 \cdot \varepsilon_1$,

$$\bar{\varrho}_p(\varepsilon) = \bar{\varrho}(\varepsilon) - \bar{\varrho}(\varepsilon_1) + \bar{\varrho}_p(\varepsilon_1). \tag{13}$$

Equ. (13) leads to the familiar conclusion that scattering is a low energy phenomenon, so that the path at high energies is a straight line in first approximation. We find immediately

$$\frac{\bar{\varrho}_p(\varepsilon)}{\bar{\varrho}(\varepsilon)} = 1 - \frac{\bar{\varrho}(\varepsilon_1) - \bar{\varrho}_p(\varepsilon_1)}{\bar{\varrho}(\varepsilon)}. \tag{14}$$

From this equation it is seen that $\bar{\varrho}_p(\varepsilon)/\bar{\varrho}(\varepsilon)$ increases more rapidly for the true electronic stopping than for the velocity proportional stopping, since the former case gives a larger range than does the latter.

Formula (13) may be used in an intermediate energy region, where the correction from true to projected range still is $\gtrsim 5\,\%$. In this region it gives directly the correction to a measured projected range, namely the constant term $\bar{\varrho}(\varepsilon_1) - \bar{\varrho}_p(\varepsilon_1)$, which in actual cases may be calculated by means of Table 2 and Fig. 2. For very high energies ($\gtrsim 1$ MeV for protons e.g.) the correction $\bar{\varrho}(\varepsilon_1) - \bar{\varrho}_p(\varepsilon_1)$ is negligible, and the difference $\bar{R} - \bar{R}_p$ is determined by the small multiple scattering at high energies.

Fluctuations in projected range

A projected range becomes smaller than the corresponding true range if the particle during slowing-down undergoes numerous collisions with appreciable deflections. Because of such deflections the width of the distribution in projected range may be considerable, and it is therefore of interest to calculate e.g. the fluctuation in projected range. Equations governing fluctuations are derived in the Appendix, and it turns out to be necessary to treat simultaneously the average square of the projected range, $\overline{R_p^2}$, and of the perpendicular range $\overline{R_\perp^2}$.

The equations are of the same type as equ. (4), and may be solved by the same approximations if one knows the average projected range, which enters as a source term. In Fig. 3 are shown the results of numerical calculations for protons and deuterons. The curve illustrating the relative straggling in projected range shows that at low energies, i.e. $\varepsilon \lesssim 1$, the distribution

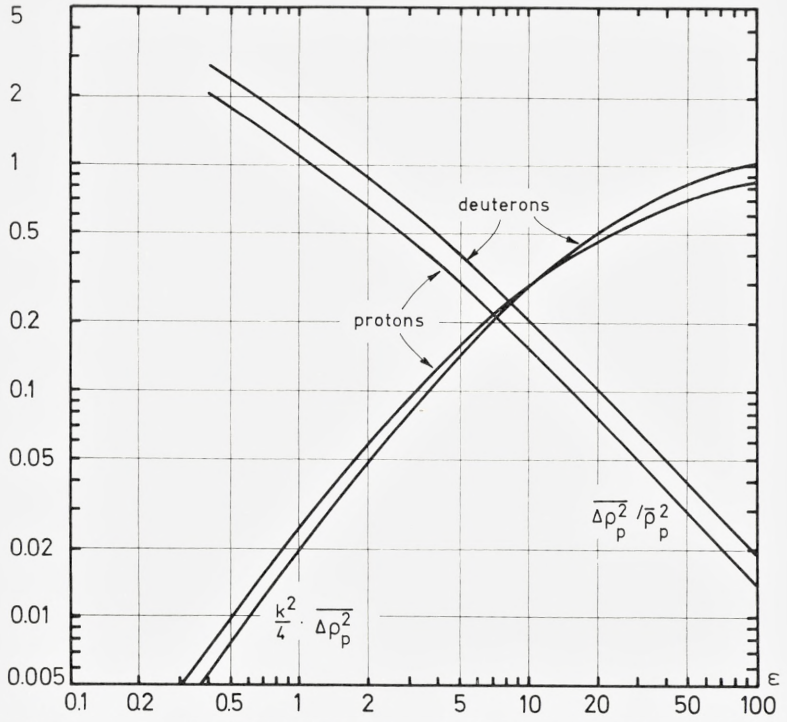

Figure 3. The square of absolute and relative straggling in projected range for protons and deuterons, calculated by means of the Thomas-Fermi nuclear stopping power (Fig. 1).

becomes very broad, actually the full width at half maximum is expected to be larger than the average value by a factor $\sim 2-3$. It is therefore expected that a fraction of the incoming particles is ejected from the target.

Comparison with experiments

The distribution in projected range of N^{15} ions ($\mu/k \approx 13.5$) with energies $0.5-6$ MeV has been measured in Au by PHILLIPS and READ (1963). The depth distribution was found by observing the yield of a resonance in the N^{15} $(p, \alpha\gamma)$ C^{12} reaction. The present theory should apply with some reservation ($k = 0.95$, so that nuclear stopping is not quite negligible), and the average projected ranges agree with theory within $\sim 10\,\%$. The theoretical straggling, $(\overline{\Delta\varrho_p^2})^{1/2}$, is larger than the experimental value found by measuring the width of the Gaussian part of the distribution by $\sim 20-50\,\%$. This result is not very surprising, since the distribution is not a Gaussian, and

a skewness in the distribution may contribute essentially to the straggling. CHU and FRIEDMAN (1965) measured, by use of the D – D fusion process, the penetration in Al and Au of 20 keV deuterons in different molecular ions (D^+, D_2^+, HD^+, etc.) and found the distribution to depend on the molecular state of the incoming deuterons. Such effects are not fully understood. Qualitatively, the average projected range and the straggling agree with theory. In both cases the velocity proportional stopping may be applied.

§ 3. Length of Particle Path

Since the appearance of LSS a large number of different range measurements have been performed, and some of the curves presented in LSS have been used in the analysis of experimental results. In order to compare more precisely theory and experiments, I have calculated several range-energy curves for k-values other than those presented in LSS.

At low energies, ($\varepsilon \lesssim 1$), and not too large values of the electronic stopping parameter, k, $k \lesssim 0.5$, the nuclear stopping is dominating. Therefore, the curves $\bar{\varrho} = \varrho_k(\varepsilon)$ for different k-values $0.1 \lesssim k \lesssim 0.5$ are closely spaced and interpolations for intermediate k-values are easily performed. At higher energies, where the electronic stopping becomes the more significant energy loss mechanism, another plot is more appropriate, cf. LSS. If nuclear stopping is disregarded, the range is given by the extrapolated electronic range

$$\varrho_e(\varepsilon) = \int_0^{\varepsilon} \left(\frac{d\varepsilon'}{d\varrho}\right)_e^{-1} d\varepsilon'. \tag{15}$$

As shown in LSS, ϱ_e is given by

$$\varrho_e(\varepsilon) = \varrho_k(\varepsilon) + A(k,\varepsilon), \tag{16}$$

where the nuclear range correction A may be calculated simply by means of the stopping powers. A is nearly constant at high energies. In case of velocity proportional electronic stopping, the extrapolated electronic range is given by $\varrho_e(\varepsilon) = 2/k \cdot \varepsilon^{1/2}$.

Values of $\varrho_k(\varepsilon)$ for $0.002 \leq \varepsilon \leq 600$ for several k-values in the interval $0.05 < k < 1.6$ are presented in Table 1. The function $(d\varepsilon/d\varrho)_n$ is also included. In Table 2 are given values of the function $(k/2) \cdot A(k,\varepsilon)$ for $1 \leq \varepsilon \leq 600$ for the same k-values. The asymptotic values of A at high

energies are shown in Fig. 4. Some of the results in Tables 1 and 2 were utilized in plotting the curves presented in LSS.

The range straggling, $\overline{\Delta\varrho_k^2}(\varepsilon)$, was also calculated in LSS for a few values of k. At low energies, where $S_e \ll S_n$, a small error in k is not significant, but at high energies it is of interest to eliminate, as far as possible,

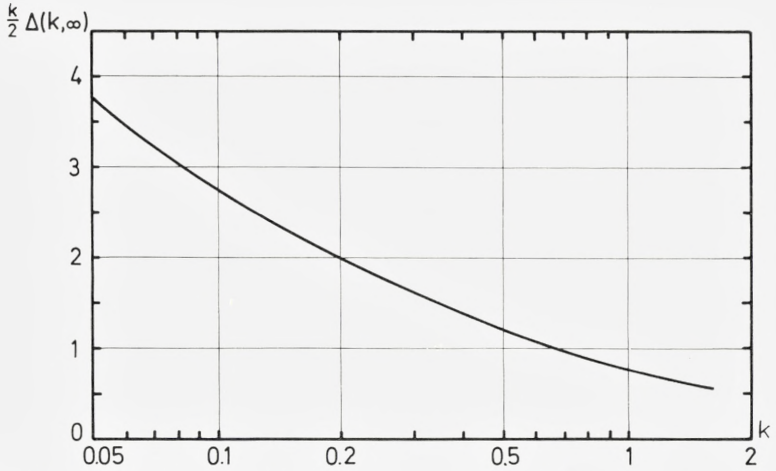

Figure 4. Asymptotic value of nuclear range correction $\Delta(k,\varepsilon)$ for large ε, cf. (16).

uncertainties in the theoretical estimate of k. It turns out that in the case of straggling the quantity $\overline{\Delta\varrho_k^2}/\varrho_k^3$ is a slowly varying function of k. Accordingly, a value of this quantity, obtained from LSS, may be compared with an experimentally determined average range to give a more precise estimate of $\overline{\Delta R^2}$.

Acknowledgments

I am much indebted to Professor J. Lindhard for his interest in the present work and his always kind advice and valuable criticism.

I want to express my thanks to P. V. Thomsen for help and criticism, and to Susann Toldi for assistance in the preparation of the manuscript.

Institute of Physics
University of Aarhus

TABLE 1.

Range along path, $\varrho_k(\varepsilon)$, for different values of electronic stopping parameter, k.

ε \ k	0.05	0.08	0.09	0.1	0.11	0.12	0.13	0.14	0.15	0.16	0.18
0.002	0.0260	0.0257	0.0256	0.0254	0.0254	0.0253	0.0252	0.0251	0.0250	0.0249	0.0248
0.004	0.0404	0.0399	0.0398	0.0395	0.0394	0.0393	0.0391	0.0390	0.0389	0.0387	0.0385
0.006	0.0522	0.0516	0.0514	0.0511	0.0509	0.0508	0.0505	0.0504	0.0503	0.0500	0.0497
0.008	0.0627	0.0619	0.0617	0.0610	0.0611	0.0609	0.0606	0.0605	0.0604	0.0600	0.0598
0.01	0.0722	0.0714	0.0711	0.0708	0.0704	0.0702	0.0699	0.0697	0.0696	0.0691	0.0689
0.02	0.114	0.112	0.111	0.111	0.110	0.110	0.109	0.109	0.109	0.108	0.107
0.04	0.181	0.178	0.177	0.176	0.175	0.175	0.174	0.173	0.172	0.171	0.170
0.06	0.241	0.236	0.235	0.234	0.232	0.231	0.230	0.229	0.228	0.227	0.225
0.08	0.296	0.290	0.288	0.287	0.285	0.284	0.282	0.281	0.279	0.278	0.275
0.1	0.348	0.341	0.339	0.337	0.335	0.333	0.331	0.330	0.328	0.326	0.323
0.2	0.592	0.578	0.574	0.570	0.566	0.562	0.558	0.555	0.551	0.547	0.540
0.4	1.06	1.02	1.01	1.00	0.995	0.986	0.977	0.969	0.960	0.952	0.936
0.6	1.52	1.46	1.45	1.43	1.42	1.41	1.39	1.37	1.36	1.34	1.32
0.8	1.99	1.91	1.88	1.86	1.84	1.82	1.79	1.77	1.75	1.73	1.69
1.0	2.47	2.36	2.33	2.29	2.26	2.24	2.20	2.17	2.14	2.12	2.07
2.0	5.09	4.75	4.65	4.56	4.46	4.38	4.29	4.20	4.13	4.05	3.91
4.0	11.1	9.94	9.61	9.38	9.02	8.77	8.52	8.28	8.07	7.87	7.49
6.0	17.7	15.4	14.7	14.3	13.6	13.1	12.7	12.3	11.9	11.5	10.9
8.0	24.5	20.8	19.7	19.1	18.0	17.3	16.7	16.0	15.5	15.0	14.0
10.0	31.5	26.1	24.6	23.6	22.3	21.4	20.5	19.6	18.9	18.2	17.0
20.0	65.6	50.6	47.0	44.3	41.4	39.2	37.1	35.3	33.7	32.2	29.6
40.0	126.0	90.9	83.4	77.4	71.8	67.2	63.2	59.7	56.6	53.7	48.9
60.0	176.0	124.0	113.0	104.0	96.3	89.8	84.1	79.2	74.8	70.8	64.2
100.0	261.0	178.0	161.0	148.0	136.0	126.0	118.0	111.0	105.0	98.4	88.7
200.0	421.0	280.0	252.0	229.0	210.0	195.0	181.0	169.0	159.0	150.0	134.0
400.0	653.0	425.0	381.0	346.0	316.0	292.0	271.0	252.0	237.0	223.0	199.0
600.0	832.0	537.0	481.0	436.0	397.0	366.0	339.0	316.0	297.0	279.0	249.0

TABLE 1 (continued).
Nuclear stopping power in reduced units, i. e. $(d\varepsilon/d\varrho)_n$ is included in the last column.

ε \ k	0.2	0.22	0.25	0.3	0.4	0.6	0.8	1.0	1.2	1.6	$(d\varepsilon/d\varrho)_n$
0.002	0.0246	0.0244	0.0242	0.0237	0.0230	0.0220	0.0210	0.0200	0.0192	0.0174	0.121
0.004	0.0419	0.0379	0.0375	0.0368	0.0357	0.0338	0.0321	0.0305	0.0291	0.0264	0.154
0.006	0.0494	0.0489	0.0484	0.0475	0.0460	0.0434	0.0411	0.0390	0.0371	0.0336	0.178
0.008	0.0593	0.0586	0.0580	0.0569	0.0551	0.0518	0.0490	0.0464	0.0441	0.0398	0.197
0.01	0.0682	0.0675	0.0668	0.0655	0.0633	0.0595	0.0562	0.0531	0.0504	0.0454	0.211
0.02	0.106	0.105	0.104	0.102	0.0983	0.0917	0.0860	0.0810	0.0765	0.0686	0.261
0.04	0.169	0.167	0.165	0.161	0.154	0.143	0.133	0.125	0.117	0.104	0.311
0.06	0.223	0.220	0.217	0.212	0.203	0.186	0.173	0.161	0.151	0.134	0.340
0.08	0.274	0.269	0.265	0.258	0.246	0.226	0.208	0.194	0.181	0.159	0.359
0.1	0.319	0.315	0.310	0.302	0.288	0.262	0.246	0.224	0.208	0.183	0.372
0.2	0.533	0.525	0.515	0.500	0.471	0.423	0.385	0.353	0.326	0.283	0.403
0.4	0.926	0.905	0.883	0.851	0.791	0.697	0.622	0.564	0.515	0.440	0.405
0.6	1.30	1.27	1.23	1.18	1.08	0.944	0.830	0.745	0.676	0.571	0.391
0.8	1.66	1.62	1.57	1.50	1.36	1.17	1.02	0.909	0.821	0.688	0.373
1.0	2.02	1.97	1.90	1.80	1.63	1.38	1.20	1.06	0.954	0.794	0.356
2.0	3.79	3.66	3.50	3.26	2.87	2.34	1.97	1.71	1.52	1.24	0.291
4.0	7.16	6.85	6.44	5.87	5.00	3.90	3.21	2.73	2.39	1.91	0.213
6.0	10.3	9.78	9.11	8.19	6.85	5.21	4.23	3.56	3.09	2.44	0.173
8.0	13.2	12.5	11.6	10.3	8.43	6.36	5.11	4.28	3.69	2.90	0.147
10.0	15.9	15.0	13.8	12.2	9.99	7.39	5.90	4.91	4.22	3.30	0.128
20.0	27.5	25.6	23.3	20.2	16.1	11.6	9.07	7.47	6.36	4.91	0.0813
40.0	44.9	41.6	37.4	32.1	25.1	17.6	13.6	11.1	9.42	7.21	0.0493
60.0	58.7	54.2	48.5	41.4	32.1	22.3	17.2	14.0	11.8	8.98	0.0362
100.0	80.8	74.3	66.3	56.2	43.3	29.8	22.8	18.5	15.5	11.8	0.0243
200.0	122.0	112.0	99.2	83.7	63.9	43.6	33.1	26.7	22.4	17.0	0.0139
400.0	180.0	165.0	146.0	123.0	93.1	63.1	47.8	38.4	32.2	24.3	0.0078
600.0	225.0	206.0	182.0	153.0	116.0	78.1	59.0	47.4	39.7	29.9	0.0056

TABLE 2.
Nuclear range correction, $k/2 \cdot \Delta(k, \varepsilon)$, cf. (16).

ε \ k	0.05	0.08	0.09	0.10	0.11	0.12	0.13	0.14	0.15	0.16	0.18
1	0.94	0.91	0.90	0.89	0.88	0.87	0.86	0.85	0.84	0.83	0.82
2	1.29	1.22	1.21	1.19	1.17	1.15	1.14	1.12	1.10	1.09	1.06
4	1.72	1.60	1.57	1.53	1.50	1.47	1.45	1.42	1.39	1.37	1.33
6	2.01	1.84	1.79	1.73	1.70	1.66	1.63	1.59	1.56	1.53	1.47
8	2.22	2.00	1.94	1.88	1.84	1.79	1.75	1.71	1.67	1.63	1.57
10	2.38	2.12	2.06	1.98	1.94	1.88	1.84	1.79	1.75	1.71	1.64
20	2.83	2.45	2.35	2.26	2.19	2.12	2.06	2.00	1.94	1.89	1.81
40	3.18	2.68	2.57	2.45	2.37	2.29	2.21	2.14	2.08	2.02	1.92
60	3.34	2.79	2.66	2.53	2.45	2.36	2.28	2.21	2.14	2.09	1.97
100	3.48	2.88	2.75	2.61	2.52	2.42	2.34	2.26	2.16	2.13	2.02
200	3.60	2.96	2.80	2.68	2.59	2.47	2.39	2.31	2.20	2.16	2.05
400	3.68	3.00	2.83	2.71	2.62	2.50	2.42	2.36	2.23	2.19	2.07
600	3.71	3.02	2.85	2.72	2.66	2.52	2.46	2.38	2.24	2.20	2.09

ε \ k	0.20	0.22	0.25	0.30	0.40	0.60	0.80	1.0	1.2	1.6
1	0.80	0.78	0.76	0.73	0.67	0.59	0.52	0.47	0.43	0.37
2	1.03	1.01	0.98	0.93	0.84	0.71	0.63	0.56	0.50	0.42
4	1.28	1.25	1.20	1.12	1.00	0.83	0.72	0.63	0.57	0.47
6	1.42	1.37	1.31	1.22	1.08	0.89	0.76	0.67	0.60	0.50
8	1.51	1.46	1.39	1.29	1.13	0.92	0.79	0.69	0.62	0.51
10	1.57	1.52	1.44	1.33	1.16	0.95	0.80	0.71	0.63	0.52
20	1.73	1.65	1.56	1.44	1.25	1.00	0.85	0.74	0.66	0.55
40	1.84	1.74	1.64	1.50	1.30	1.03	0.87	0.75	0.67	0.56
60	1.88	1.79	1.69	1.54	1.32	1.05	0.88	0.77	0.69	0.56
100	1.92	1.83	1.71	1.57	1.35	1.06	0.89	0.77	0.69	0.56
200	1.94	1.85	1.74	1.58	1.36	1.07	0.90	0.78	0.69	0.56
400	1.96	1.87	1.76	1.61	1.37	1.08	0.90	0.78	0.69	0.56
600	1.98	1.88	1.77	1.62	1.38	1.08	0.91	0.78	0.70	0.56

Appendix

Distribution in Projected Range

When a beam of particles is stopped in a substance, the individual paths of the particles are very different from each other. It is possible in principle to find the final distribution in space of the particles by means of electronic

computers, but with increasing energy of the particles and increasing number of atoms in the stopping material, such calculations become very intricate and expensive.

One may, however, derive analytical expressions governing the distribution in projected range, R_p, and in the perpendicular range, $R_\perp$. These expressions are integral equations, which are difficult to solve. Instead of attempting a direct solution, it is more fruitful to transform the distribution equation into equations describing the moments of the distribution. The latter may be solved by means of fair approximations, thereby supplying some information about the distribution functions too.

Consider a particle (Z_1, A_1) with energy E, moving in a substance (Z_2, A_2) in a direction specified by the angle ϑ with a certain direction in the substance (e.g. the surface normal), which is chosen as the z-axis. Define now a distribution function $p(E, z, \cos\vartheta)$ such that $p(E, z, \cos\vartheta)dz$ represents the probability that the final z-value comes between z and $z + dz$.

Define analogously a distribution function $q(E, r, \cos\vartheta)$ such that $q(E, r, \cos\vartheta) \cdot 2\pi r dr$ is the probability of finding the final distance from the z-axis between r and $r + dr$. The moments are given by

$$\langle z^m \rangle \equiv \langle R_p^m(E, \cos\vartheta) \rangle = \int_{-\infty}^{\infty} p(E, z, \cos\vartheta) \cdot z^m dz, \tag{A.1}$$

$$\langle r^m \rangle \equiv \langle R_\perp^m(E, \cos\vartheta) \rangle = \int_0^{\infty} q(E, r, \cos\vartheta) \cdot 2\pi r^{m+1} dr, \tag{A.2}$$

where we have introduced the expressions $R_p(E, \cos\vartheta)$ and $R_\perp(E, \cos\vartheta)$ for z and r, respectively. Clearly, $R_p(E, \cos\vartheta)$ is to be interpreted as the penetration depth of a particle originally moving in a direction specified by the angle ϑ, and $R_\perp(E, \cos\vartheta)$ is the final distance from the z-axis of the same particle.

Integral equations for $p(E, z, \cos\vartheta)$ and $q(E, r, \cos\vartheta)$ may be derived in analogy to the derivation of equation (3.1) in LSS, i.e. the equation governing the distribution in range along the path. We find readily

$$\left.\begin{aligned} &\cos\vartheta \cdot \frac{\partial p(E, z, \cos\vartheta)}{\partial z} = \\ &N \int d\sigma_{n,e} \int_0^{2\pi} \frac{d\alpha}{2\pi} \Big\{ p(E - T, z, \cos\vartheta\cos\varphi + \sin\vartheta\sin\varphi\cos\alpha) - p(E, z, \cos\vartheta) \Big\}, \end{aligned} \right\} \tag{A.3}$$

$$\left.\begin{aligned} &\sin\vartheta\cdot\frac{\partial q(E,r,\cos\vartheta)}{\partial r} = \\ &N\int d\sigma_{n,e}\int_0^{2\pi}\frac{d\alpha}{2\pi}\Big\{q(E-T,r,\cos\vartheta\cos\varphi+\sin\vartheta\sin\varphi\cos\alpha)-q(E,r,\cos\vartheta)\Big\}, \end{aligned}\right\} \quad (A.4)$$

where φ is the deflection of the incoming particle in the laboratory system, α being the azimuthal angle.

Equations (A. 3) and (A. 4) are valid under the same conditions as the corresponding equation (LSS (3.1)) describing the distribution in range along the path, i.e. the stopping substance should be a "random" system. The equation mentioned is contained in (A. 3), as may be seen by neglecting the angular dependence in (A. 3), putting $\vartheta = 0$. The same approximations as those introduced in the solution of the former equation may be employed in (A. 3) and (A. 4), i.e. we assume that the energy losses to electrons are small and separated from nuclear energy losses.

We shall not introduce the approximations at this stage, but at once turn to the moments of the distribution. Multiply (A. 3) by z^m and integrate over all z; analogously multiply (A. 4) by $2\pi r^{m+1}$ and integrate over all r, to obtain the formulae

$$\left.\begin{aligned} &-m\cdot\cos\vartheta\,\langle R_p^{m-1}(E,\cos\vartheta)\rangle \\ &= N\int d\sigma_{n,e}\int_0^{2\pi}\frac{d\alpha}{2\pi}\Big\{\langle R_p^m(E-T,\cos\vartheta\cos\varphi+\sin\vartheta\sin\varphi\cos\alpha)\rangle-\langle R_p^m(E,\cos\vartheta)\rangle\Big\}, \end{aligned}\right\} \quad (A.5)$$

$$\left.\begin{aligned} &-(m+1)\sin\vartheta\,\langle R_\perp^{m-1}(E,\cos\vartheta)\rangle \\ &= N\int d\sigma_{n,e}\int_0^{2\pi}\frac{d\alpha}{2\pi}\Big\{\langle R_\perp^m(E-T,\cos\vartheta\cos\varphi+\sin\vartheta\sin\varphi\cos\alpha)\rangle-\langle R_\perp^m(E,\cos\vartheta)\rangle\Big\}. \end{aligned}\right\} \quad (A.6)$$

The connection of the ranges $R_p(E,\cos\vartheta)$ and $R_\perp(E,\cos\vartheta)$ to the more interesting expressions $R_p(E)$ and $R_\perp(E)$, i.e. the ranges corresponding to initial angle $\vartheta = 0$, is given by Fig. 5.

$$\begin{aligned} R_p(E,\cos\vartheta) &= R_p(E)\cdot\cos\vartheta + R_\perp(E)\sin\vartheta\cdot\cos\beta, \\ R_\perp(E,\cos\vartheta) &= \Big\{\big[R_p(E)\sin\vartheta + R_\perp(E)\cos\vartheta\cos\beta\big]^2+\big[R_\perp(E)\sin\beta\big]^2\Big\}^{1/2}, \end{aligned}$$

where β is an azimuthal angle which is randomly distributed. We are interested in the case where the particle initially moves in the z-direction, i.e. we put $\vartheta = 0$ in (A. 5) and (A. 6):

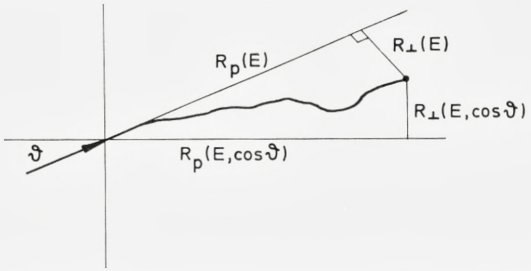

Figure 5. Illustration of connection between different range concepts.

$$m\,\langle R_p^{m-1}(E)\rangle = N\int d\sigma_{n,e}\left\{\langle R_p^m(E)\rangle - \langle R_p^m(E-T,\cos\varphi)\rangle\right\} \qquad (A.7)$$

$$0 = N\int d\sigma_{n,e}\left\{\langle R_\perp^m(E)\rangle - \langle R_\perp^m(E-T,\cos\varphi)\rangle\right\}. \qquad (A.8)$$

(A. 7) yields, for $m = 1$, the simple equation (4) for the average projected range, and $m = 2$ yields the two coupled equations

$$2\bar{R}_p(E) = N\int d\sigma_{n,e}\left\{\overline{R_p^2}(E) - \overline{R_p^2}(E-T)\cos^2\varphi - \tfrac{1}{2}\overline{R_\perp^2}(E-T)\sin^2\varphi\right\} \qquad (A.9)$$

$$0 = N\int d\sigma_{n,e}\left\{\overline{R_\perp^2}(E) - \overline{R_p^2}(E-T)\sin^2\varphi - \overline{R_\perp^2}(E-T)\cdot\frac{\cos^2\varphi+1}{2}\right\}. \qquad (A.10)$$

By introducing the ranges $\overline{R_c^2} = \overline{R_\perp^2} + \overline{R_p^2}$ and $\overline{R_r^2} = \overline{R_p^2} - \tfrac{1}{2}\overline{R_\perp^2}$, (A. 9) and (A. 10) finally read (cf. LSS)

$$2\bar{R}_p(E) = N\int d\sigma_{n,e}\left\{\overline{R_c^2}(E) - \overline{R_c^2}(E-T)\right\} \qquad (A.11)$$

$$2\bar{R}_p(E) = N\int d\sigma_{n,e}\left\{\overline{R_r^2}(E) - (1-\tfrac{3}{2}\sin^2\varphi)\overline{R_r^2}(E-T)\right\}, \qquad (A.12)$$

which equations may be solved separately if the source term $\bar{R}_p(E)$ is known, thereby giving $\overline{R_p^2}$ and $\overline{R_\perp^2}$.

References

N. Bohr, Mat. Fys. Medd. Dan. Vid. Selsk. **18**, no. 8 (1948).

Y. Y. Chu & L. Friedman, Nucl. Instr. Meth. **38**, 254 (1965).

B. Fastrup, P. Hvelplund & C. Sautter, to be published in Mat. Fys. Medd. Dan. Vid. Selsk. **35**, no. 10.

E. V. Kornelsen, F. Brown, J. A. Davies, B. Domeij & G. R. Piercy, Phys. Rev. **136**, A849 (1964).

J. Lindhard & M. Scharff, Phys. Rev. **124**, 128 (1961).

J. Lindhard, M. Scharff & H. E. Schiøtt, Mat. Fys. Medd. Dan. Vid. Selsk. **33**, no. 14 (1963).

J. Lindhard, Mat. Fys. Medd. Dan. Vid. Selsk. **34**, no. 14 (1965).

K. O. Nielsen, "Electromagnetically Enriched Isotopes and Mass Spectrometry", Butterworths, 1956.

J. H. Ormrod & H. E. Duckworth, Can. J. Phys. **41**, 1424 (1963).

W. R. Phillips & F. H. Read, Proc. Phys. Soc. **81**, 1 (1963).

Indleveret til Selskabet den 7. maj 1966.
Færdig fra trykkeriet den 28. oktober 1966.

Matematisk-fysiske Meddelelser
udgivet af
Det Kongelige Danske Videnskabernes Selskab
Bind **35,** nr. 10

Mat. Fys. Medd. Dan. Vid. Selsk. **35,** no. 10 (1966)

STOPPING CROSS SECTION IN CARBON OF 0.1-1.0 MeV ATOMS WITH $6 \leq Z_1 \leq 20$

BY

B. FASTRUP, P. HVELPLUND AND C. A. SAUTTER

København 1966
Kommissionær: Munksgaard

Synopsis

The stopping cross section, $\frac{1}{N}\frac{dE}{dx}$, in thin carbon foils has been measured for ions, $6 \leq Z_1 \leq 20$, with energies from 100 kev to 1 Mev. The experimental data have been corrected numerically for nuclear stopping to obtain the electronic stopping. The electronic stopping cross section has an oscillatory dependence on the atomic number, Z_1, for constant ion velocities. The analysis suggests that the relative amplitude of the oscillations decreases as the ion velocities increase. Apart from the oscillations, the experimental data are in reasonable agreement with the theoretical predictions. The relative accuracy of the measured data is about 2–3 per cent, and the absolute accuracy of the evaluated electronic stopping cross sections is better than 8 per cent even in the most extreme cases (low energy and high Z_1).

PRINTED IN DENMARK
BIANCO LUNOS BOGTRYKKERI A/S

Introduction

The basis for a theoretical description of the energy loss of heavy ions penetrating matter was laid by BOHR[1]. In his treatment, the stopping process is due to two distinct mechanisms: inelastic collisions with the electrons of the target atom, and elastic collisions with the target atom as a whole. The inelastic processes are dominant at high velocities, $v \gg v_0^*$, where the well-known Bethe-Bloch formula applies, while the elastic processes are almost completely responsible for the slowing-down of the ion at low velocities, $v \lesssim v_0$. However, theoretical studies of an electron gas by FERMI and TELLER[2] and by LINDHARD[3] indicate a non-vanishing electronic stopping component even at low velocity.

Unlike chemical reactions, atomic collision processes are quite violent disturbances of atoms, so the effects due to atomic shell structure, chemical properties, charge exchange, etc., should normally be of secondary importance for heavy ions. This makes it attractive to apply statistical methods as a basis for theoretical studies. FIRSOV[4] and LINDHARD and SCHARFF[5] have used Thomas-Fermi arguments to evaluate the electronic stopping cross section at low velocity, and the over-all agreement with experimental results is good.

Employing the Thomas-Fermi arguments, Lindhard and Scharff obtained for the electronic stopping cross section

$$S_e = \xi_e \frac{8\pi e^2 a_0 Z_1 Z_2}{Z} \frac{v}{v_0}, \quad (Z^{2/3} = Z_1^{2/3} + Z_2^{2/3})$$

valid for projectile velocities v less than $v_0 Z_1^{2/3}$. Here, ξ_e is a constant of order $1-2$ which may vary approximately as $Z_1^{1/6}$.

Recently, ORMROD et al.[6] have subjected the Lindhard theory of electronic stopping to a systematic experimental test in carbon and aluminum films at low energy, $E \leq 140$ kev. Although the over-all agreement with theory is reasonably good, they found a striking oscillatory behaviour of

* v_0 is the electron velocity in the first Bohr orbit of hydrogen.

S_e as a function of Z_1 for a common projectile velocity $v \sim 0.41\, v_0$. It is tempting to associate these periodic deviations with the atomic shell structure of the penetrating ions. However, quantitative theoretical calculations have not yet been made.

As the heavy-ion accelerator at the University of Aarhus[7] is well-suited for the production of ions of nearly all elements with energies up to approximately 1 Mev (doubly charged ions), it was decided to extend further the empirical information of the stopping process of heavy ions in carbon films. It was of particular interest to study the oscillation of S_e at even higher projectile velocities where it is expected that the shell structure of the ions is less important*.

Apparatus

The Aarhus 600-kv heavy-ion accelerator, provided with a universal ion source, furnished the projectiles for these experiments. By means of (p,γ) resonances in F^{19} and Al^{27} targets and a (p,α) resonance in a B^{11} target, a preliminary energy calibration was carried out.

Figure 1 shows a schematic diagram of the experimental set-up. After acceleration and deflection in the bending magnet, the ion beam is parallel-collimated by movable apertures (a) and (b) to within 1/3 degree. At the entrance and the exit ports of the target chamber, in which the films are situated, liquid-air traps are fitted to minimize the build-up of any surface contamination. The operating pressure in the target chamber is 10^{-5} Torr or less.

Attached to the target chamber is a special film holder enabling interposition of one or several (up to eight) areas of two different films in the path of the particles at the objective position of the analyzing magnet. With this device, the position of a film can be reproduced for successive ion bombardments.

The beam path in the accelerator is horizontal, whereas the plane of the deflection in the analyzer is vertical. The analyzer is a 90° sector magnet with two-directional focusing obtained by the use of inclined pole piece edges.

* Recent range studies at this Institute by J. A. Davies, L. Eriksson, and P. Jespersgaard, the results of which have been published (in part) in Nucl. Instr. Meth. *38* (1965) 245, have shown the same type of oscillations of S_e. In their experiment, an oriented tungsten monocrystal was bombarded by ions with Z_1 = 11, 15, 18, 19, 24, 29, 35, 36, 37, 54, and 55 at energies between 70 kev and 1500 kev. Due to channeling, the nuclear stopping was negligible compared with the electronic stopping.

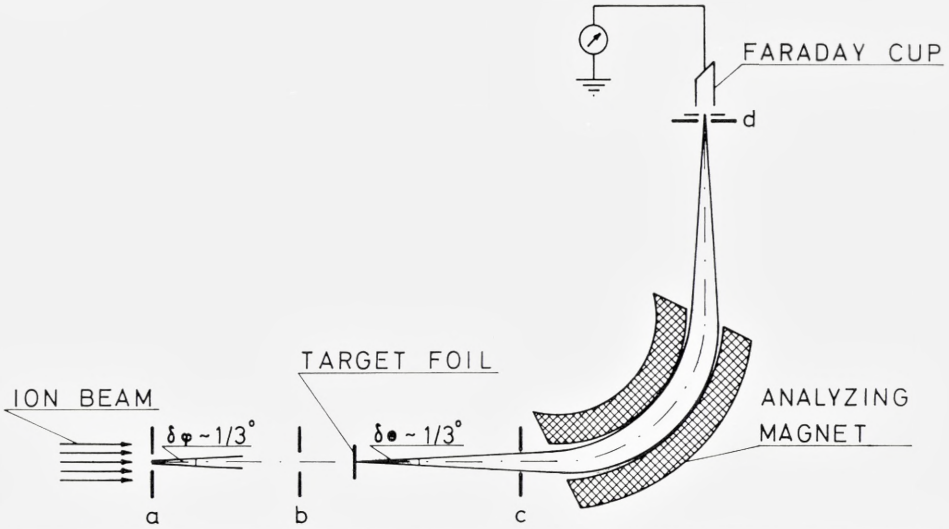

Fig. 1. The experimental arrangement. a), b), c), and d) indicate the limiting apertures in the set-up.

The entrance slit to the Faraday-cup detector at (d) is approximately 5 mm wide and perpendicular to a plane which contains the trajectories of the ions through the analyzer, providing an energy resolution $\Delta E/E$ better than 0.5 per cent.

For the measurement of the relative changes in the magnetic field of the analyzer, which we use to determine energy losses, an instrument incorporating a Hall element with linearity better than 0.2 per cent was constructed.

Experimental Method

The energy loss suffered by protons penetrating the carbon film is used to determine the film thickness. The thicknesses ranged from about $6\,\mu g/cm^2$ to $23\,\mu g/cm^2$ for the films used in the heavy-ion experiment. In order to make a preliminary calibration of this technique, two thicker films ($\sim 30\,\mu g/cm^2$) of known areas were weighed on a microbalance to about $\pm 1\,\mu g$. Subsequently, a mean energy loss was obtained for 150-kev protons for each of these two films. Energy loss measurements were made on four different areas of both films.

The 150-cm radius 75° sector bending magnet is used to define the mass of the projectiles entering the target chamber. With no film in the path of the ion beam, the projectiles are deflected by the field of the analyzing magnet into the Faraday-cup detector (refer to Fig. 1). Both with and without the film placed in the beam path, the analyzer field is adjusted for maximum response at the Faraday-cup detector with respect to the energy distribution profiles. The width of the incident beam energy profile is almost completely accounted for by the combined resolution of the analyzer and the slit at the detector.

In this experiment we measure the most probable energy loss, ΔE_0, defined as the difference between the energies of the maxima of the incident and the emerging beam profiles. The observed stopping cross section per atom, S_0, is then assumed to be given by the relation

$$S_0 = \frac{1}{N}\frac{\Delta E_0}{\Delta R}$$

at the mean energy $\bar{E} = E_i - \Delta E_0/2$, where E_i is the energy of the projectiles incident upon a film. Here, N is the number of carbon atoms per unit volume, and ΔR is the film thickness. In all cases reported here, the ratio $\Delta E_0/\Delta R$ is a good approximation to $-dE/dR$.

We determine ΔE_0 by the following technique, based on the assumption that the energy E of the beam transmitted by the magnetic analyzer is related to the field B of the analyzer, by the equation $E = kB^2$, where k is a constant. Employing this relation, we have

$$\Delta E_0 = E_i(2 - \Delta B/B_i)\Delta B/B_i,$$

where B_i is the analyzer magnetic field corresponding to the peak E_i in the energy distribution without film, and $\Delta B/B_i$ is the corresponding relative reduction in magnetic field for the transmitted beam. We then obtain

$$S_0 = \frac{A_2 E_i}{N_0 \Delta x}\frac{\Delta B}{B_i}\cdot(2 - \Delta B/B_i),$$

where N_0, Δx, and A_2 are Avogadro's number, the film surface density in grams/cm^2, and the gram-atomic weight of carbon, respectively.

Data Treatment

The electronic stopping cross section S_e is obtained by subtracting the nuclear stopping cross section S_n^* from the observed stopping cross section S_0, i.e.

$$S_e = S_0 - S_n^*.$$

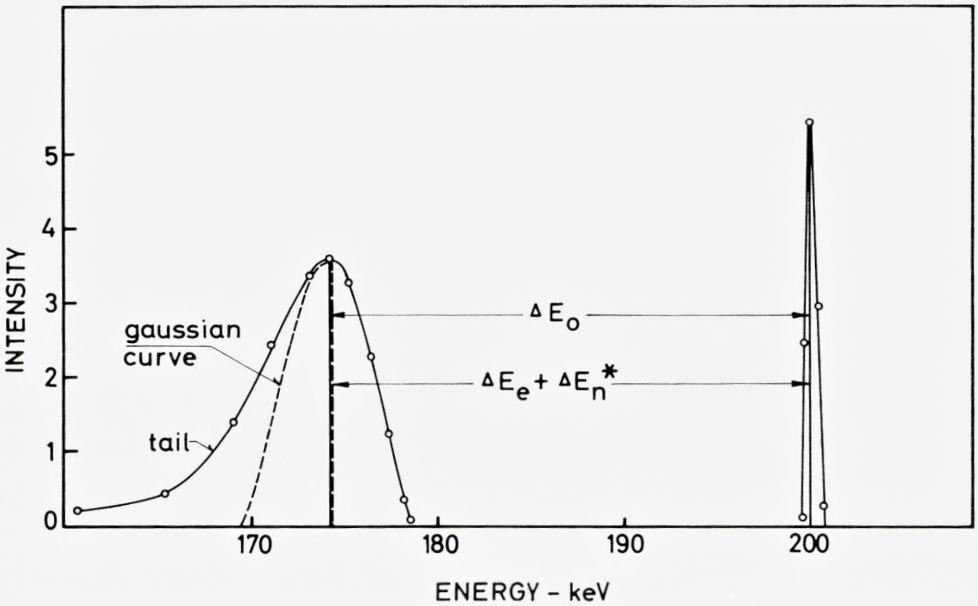

Figure 2. Energy distribution of Ar^{40} ions emerging from a 6.7 $\mu g/cm^2$ carbon film through the aperture in front of the magnet. The energy of incident ions is 200 kev.

The energy profile of the beam emerging from a foil consists of two parts: a Gaussian distribution due to soft collisions, and a tail resulting from violent ones. According to BOHR[1] and WILLIAMS[8], we may assume that the Gaussian distribution accounts almost exclusively for the peak position of the observed distribution, whereas violent collisions result in anomalously large energy losses and add to the tail only, see Fig. 2.

The most probable energy loss of the ions traversing the foil corresponds to the sum of the mean electronic energy loss, ΔE_e, and the most probable nuclear energy loss, ΔE_n^*, i.e.

$$\Delta E_0 \simeq \Delta E_e + \Delta E_n^*.$$

Here,

$$\Delta E_n^* = N\Delta R \int_0^{T_1^*} T d\sigma ,$$

where $N\Delta R$ is the number of atoms per cm^2 and $d\sigma$ is the differential cross section for an energy transfer T.

According to BOHR[1], T_1^* is roughly equal to the standard deviation of the Gaussian nuclear energy loss distribution, Ω_n^*, i.e.

$$(T_1^*)^2 \approx (\Omega_n^*)^2 \approx N\Delta R \int_0^{T_1^*} T^2 d\sigma, \text{ provided } \Delta E_0 \ll E_i .$$

As shown in the Appendix, the nuclear stopping cross section S_n^* is found to be

$$S_n^* = \int_0^{T_1^*} T d\sigma = 2.57 \cdot 10^{-16} \frac{A_1 Z_1^2 Z_2^2 \varepsilon^*}{A_2 E} I(\varepsilon^*) \text{ ev} \cdot \text{cm}^2/\text{atom},^* \qquad (1)$$

where $I(\varepsilon) = \dfrac{d\varepsilon}{d\varrho}$ (the nuclear stopping cross section in reduced units[5]), E is measured in kev, and ε^* is derived from the equation

$$F(\varepsilon^*) = \frac{\int_0^{\varepsilon^*} x^2 f(x) dx}{(\varepsilon^*)^4} = \frac{1}{N\Delta R \pi a^2}$$

The function $F(\varepsilon^*)$ has been calculated numerically by using the Thomas-Fermi differential scattering cross section[9]. The result is shown in Fig. 3.

So far, the effect of the small acceptance angle of the analyzing magnet has not been considered. The energy profile of the particles emerging from the foil within the acceptance angle is different from the energy profile of

* In the present experiment, T_1^* is always much smaller than the maximum energy transfer $T_{\max} = 4M_1M_2E/(M_1+M_2)^2$, and hence S_n^* is much smaller than the total nuclear stopping cross section $S_n = \int_0^{T_{\max}} T d\sigma$. For example, in the case of 90 kev Ar ions penetrating a 7.5 μg/cm^2 carbon foil, the ratio between T_1^* and $T_{\max}$ is approx. 0.025, and the nuclear stopping cross section, S_n^*, corresponding to the peak of the Gaussian nuclear energy loss, is only one fifth of the total nuclear stopping cross section, S_n.

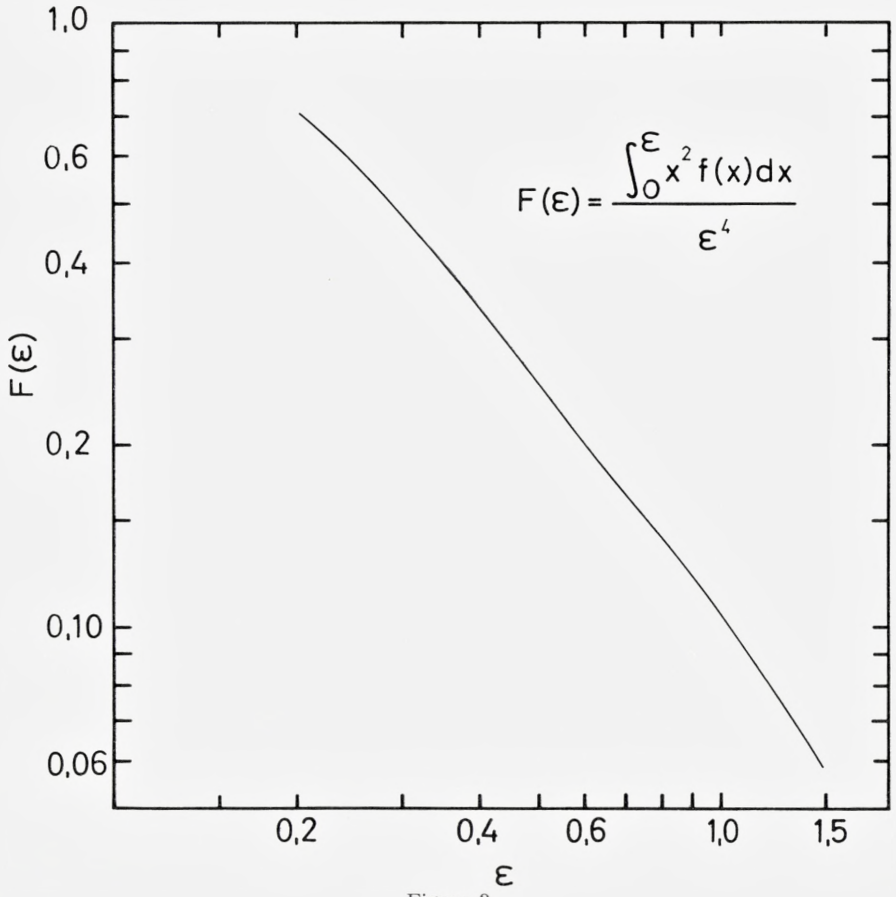

Figure 3.

all particles emerging from the foil. Particles which have experienced violent collisions with target atoms are scattered out of the acceptance angle and do not contribute to the observed energy loss distribution.

To see that the nuclear energy loss formula, eq. (1), is still valid in the case of a small acceptance angle, we must show that although the tail may be radically changed, the Gaussian nuclear energy loss distribution is unaffected.

The multiple scattering (angular) distribution of the particles emerging from the foil, see Fig. 4, is divided into a Gaussian peak and a tail. Collisions with individual deflection angles φ less than φ^* produce the Gaussian

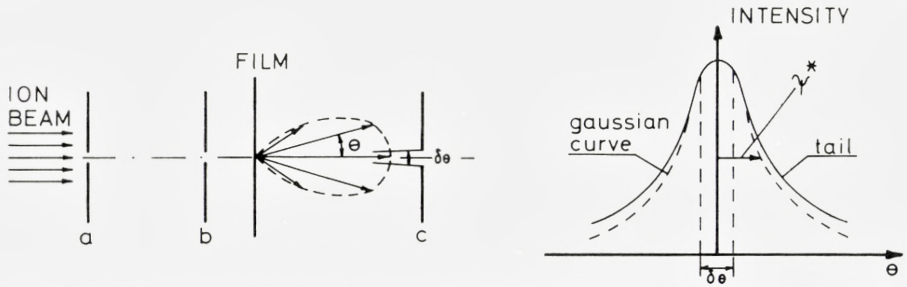

Figure 4. The angular distribution of ions emerging from the foil. $\delta\theta$ indicates the acceptance angle of the analyzing magnet.

distribution and account for the angular distribution for angles θ smaller than the half-width Ψ^* of the Gaussian distribution. Collisions with deflection angles larger than φ^* produce a tail distribution which prevails for θ larger than Ψ^*.

The acceptance angle of the analyzing magnet $\delta\theta$ is much smaller (one tenth) than the width Ψ^*.

A good first order estimate of φ^* is the half-width of the Gaussian distribution, i.e.

$$(\varphi^*)^2 \approx (\Psi^*)^2 \approx N\Delta R \int_0^{\varphi^*} \varphi^2 d\sigma, \tag{2}$$

where $d\sigma$ is the differential scattering cross section for an angular deflection φ.

For $\varphi^* \ll 1$, which is normally fulfilled, $(\varphi^*)^2 \approx A_2 T_2^*/(A_1 E)$, where T_2^* is the maximum energy transfer to the target atoms in a single collision with the ions admitted to the analyzing magnet, and A_1 and A_2 are atomic weights of the projectile and the target, respectively. In fact, T_2^* is the maximum energy transfer if the multiple scattering angle θ is smaller than approximately Ψ^*.

If, for instance, the differential scattering cross section for a THOMAS-FERMI potential[5] is used, eq. (2) may be solved with respect to φ^* and T_2^*.

In all cases reported here, it turns out that $T_2^* \gg T_1^*$; in fact $T_2^* \approx 7T_1^*$, which confirms the choice of T_1^* as the upper limit in the integral in eq. (1). This partly explains how the observed energy loss distribution may be asymmetric. Cases where the ions have experienced two or more violent collisions and reappear in the forward direction will also contribute to the tail.

From the collected data, measurements with a nuclear correction larger than 25 per cent of the observed stopping cross section have been discarded. It is believed that possible errors in the estimate of S_n^* are less than 20 per cent which result in a systematic error no greater than 4–5 per cent even in the most extreme cases (low energy and high Z_1).

The small acceptance angle eliminates possible discrepancies between projected path and actual path; hence no correction has been applied.

Results and Discussion

In the table on pp. 12–13 are given the results of the measurements, including the electronic stopping cross sections which are extracted in the manner previously described. It should be recalled that all these data are based upon a determination of the absolute stopping cross section of carbon for 150-kev protons, the result of which is

$$S_0 = S_e = 12{,}6 \times 10^{-15}\ \text{ev}\cdot\text{cm}^2/\text{atom} \pm 3 \text{ per cent.}$$

This value differs by less than 1 per cent from that obtained by SAUTTER and ZIMMERMANN[10], but is 9 per cent lower than that reported by MOORHEAD[11].

In order to adjust the measured data to each other, an intercalibration measurement was performed. At 400 kev, stopping power data were taken for all Z_1-values with two carbon films, the thicknesses of which were determined in the same run. As a result of the intercalibration, it was found that only two stopping curves had to be renormalized more than 3 per cent. In the cases of Ar^{40} and K^{39}, the original curves were raised 6 per cent and lowered 6 per cent, respectively.

The change of the film thickness during irradiation was carefully studied by comparing the energy loss of 150-kev protons before and after the irradiation. In no cases did the change exceed a few per cent.

The relative accuracy of the measured total stopping data is established within 2–3 per cent. The absolute values of the electronic stopping cross sections are estimated to be better than 8 per cent. This estimate includes errors in proton stopping values at 150 kev, and nuclear stopping corrections.

The agreement with both higher- and lower-energy empirical data is reasonably good. In all but one instance, the present data smoothly fill the intermediate energy region. In the case of C^{12}, N^{14}, O^{16}, and Ne^{20} projectiles, information is provided both by the work of PORAT and RAMAVATARAM[12] at energies above 360 kev, and of ORMROD et al.[6] at energies below

TABLE: Stopping cross sections in carbon for the atoms indicated at various energies. The foil thicknes is denoted Δx; column a) is S_n^*, the computed nuclear stopping, and column b) is the derived electronic stopping, both in units of 10^{-14} ev · cm^2/atom.

Atom	E (kev)	Δx (μg/cm^2)	a)	b)	Atom	E (kev)	Δx (μg cm^2)	a)	b)
C^{12}	82	14.7	0.12	3.89	Na^{23}	90	7.98	0.40	2.65
–	131	14.5	0.08	4.85	–	134	14.7	0.42	3.15
–	180	14.9	0.06	5.47	–	182	15.4	0.31	3.82
–	232	14.7	0.04	6.10	–	283	15.4	0.20	4.85
–	282	14.5	0.04	6.41	–	377	21.0	0.20	5.91
–	381	14.7	0.02	7.44	–	468	20.0	0.15	6.88
					–	592	9.67	0.07	8.31
N^{14}	73	22.7	0.28	3.90	–	758	19.9	0.09	9.68
–	121	22.7	0.16	4.75	–	898	6.90	0.04	10.35
–	172	21.6	0.12	5.42					
–	220	22.1	0.09	6.13	Mg^{25}	135	13.2	0.50	3.00
–	270	22.1	0.08	6.65	–	185	13.2	0.36	3.64
–	320	21.6	0.06	7.10	–	236	15.3	0.30	4.41
–	418	21.4	0.05	7.85	–	286	15.3	0.26	4.97
					–	375	22.5	0.25	5.77
O^{16}	81	15.2	0.29	3.85	–	572	21.6	0.16	7.33
–	131	14.8	0.18	4.94	–	766	21.6	0.12	9.34
–	180	15.1	0.14	5.44					
–	231	15.1	0.10	6.04	Al^{27}	88	9.12	0.70	2.78
–	282	15.2	0.08	6.38	–	140	9.34	0.47	3.53
–	330	15.2	0.07	6.96	–	182	15.4	0.48	4.10
–	380	15.1	0.06	7.42	–	292	10.0	0.24	5.52
–	430	15.1	0.06	7.82	–	464	24.1	0.25	7.21
–	479	15.1	0.05	8.27	–	563	19.5	0.18	8.17
					–	658	24.1	0.19	9.20
F^{19}	138	9.55	0.18	4.20	–	777	11.8	0.10	9.86
–	189	9.55	0.13	4.78	–	875	11.8	0.10	10.57
–	291	9.55	0.09	6.04					
–	370	23.1	0.12	6.52	Si^{28}	133	13.2	0.72	3.78
–	473	15.8	0.08	7.32	–	182	13.2	0.52	4.42
					–	288	12.0	0.31	5.94
Ne^{20}	81	18.8	0.61	2.76	–	386	12.1	0.24	6.94
–	133	14.2	0.32	3.75	–	582	13.9	0.18	8.91
–	183	16.6	0.25	4.32	–	780	13.9	0.14	10.5
–	285	15.2	0.16	5.44					
–	379	18.0	0.13	6.48	P^{31}	137	9.42	0.70	4.24
–	482	15.2	0.09	7.16	–	188	9.42	0.52	4.99
–	562	20.7	0.09	8.15	–	291	9.16	0.32	6.40
–	755	20.7	0.07	10.00	–	363	23.5	0.50	7.44
–	946	20.7	0.06	11.62	–	460	23.4	0.40	8.12

TABLE (continued).

Atom	E (kev)	Δx (μg/cm^2)	a)	b)	Atom	E (kev)	Δx (μg/cm^2)	a)	b)
P^{31}	557	19.8	0.29	9.30	Ar^{40}	394	7.28	0.36	8.42
–	654	23.8	0.28	10.09	–	492	7.75	0.29	9.12
–	849	23.7	0.22	11.58	–	593	7.75	0.24	9.98
					–	695	7.48	0.20	10.63
S^{32}	168	21.5	1.16	5.17	–	797	7.40	0.18	11.16
–	265	22.0	0.76	6.70	–	996	19.6	0.28	12.50
–	314	22.1	0.64	7.32	–	1163	19.6	0.24	13.11
–	556	22.4	0.36	9.77	–	1290	20.0	0.24	13.60
–	753	22.5	0.28	11.06					
					K^{39}	138	6.94	1.03	5.27
Cl^{35}	134	10.9	1.11	4.66	–	190	6.05	0.66	6.25
–	184	10.9	0.80	5.62	–	292	6.83	0.47	7.49
–	236	10.3	0.62	6.41	–	393	6.55	0.33	8.90
–	283	12.2	0.58	7.04	–	466	15.3	0.54	9.10
–	362	22.1	0.68	7.73	–	594	6.55	0.23	10.40
–	458	22.4	0.54	8.65	–	799	5.76	0.15	11.72
–	558	22.3	0.45	9.38	–	985	22.0	0.33	12.80
–	692	22.1	0.36	10.64	–	1138	21.8	0.28	13.60
–	989	22.0	0.24	12.50					
–	1133	22.0	0.22	13.46	Ca^{40}	191	4.67	0.56	6.00
					–	282	10.5	0.76	7.00
Ar^{40}	138	7.40	1.01	5.34	–	380	10.5	0.56	8.13
–	189	7.40	0.72	6.02	–	577	10.5	0.37	10.09
–	241	7.45	0.57	6.83	–	776	10.3	0.27	11.38
–	292	7.40	0.47	7.38	–	874	10.3	0.24	11.94

100 ~ 140 kev. For Ne^{20}, the values by Porat and Ramavataram are consistently some 20 per cent higher than the values reported here. For the remaining projectiles, no other empirical data exist in this energy range except those of ORMROD et al. which, in most cases, overlap our results at lower energies. For all projectiles except Al^{27}, our electronic stopping cross section results overlap within 10 per cent the findings of ORMROD et al. Our Al^{27} data are some 30 per cent higher. The results are shown in Fig. 5 a–5 h.

We have assumed that the electronic stopping cross sections can be fitted to an equation of the form $S_e = kE^p$. This assumption is justified by noting that in all but two instances, the log-log plot of S_e versus projectile energy yields a straight line. This type of energy dependence is predicted by theory with $p \approx 0.5$, although small deviations from $p \approx 0.5$ may occur

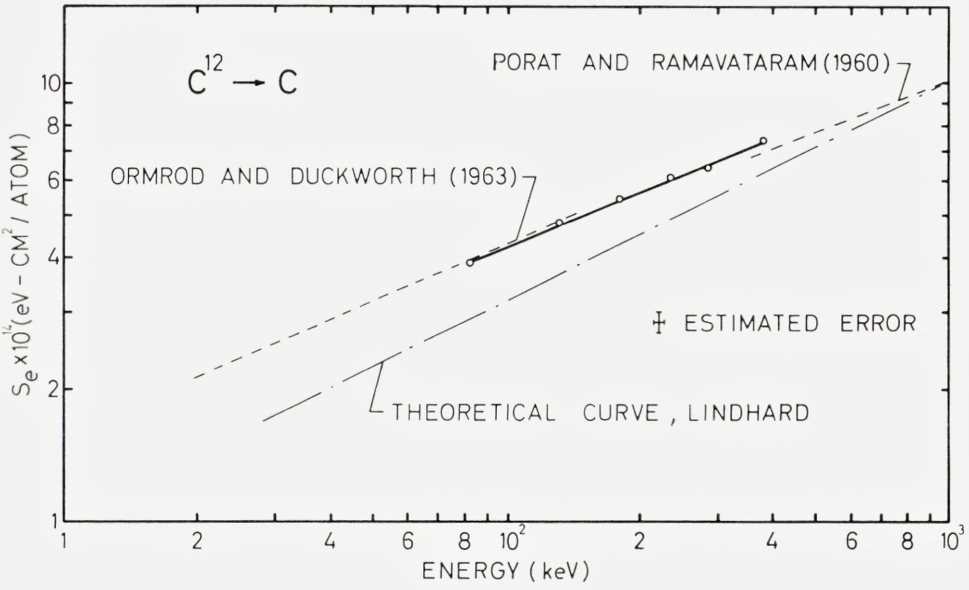

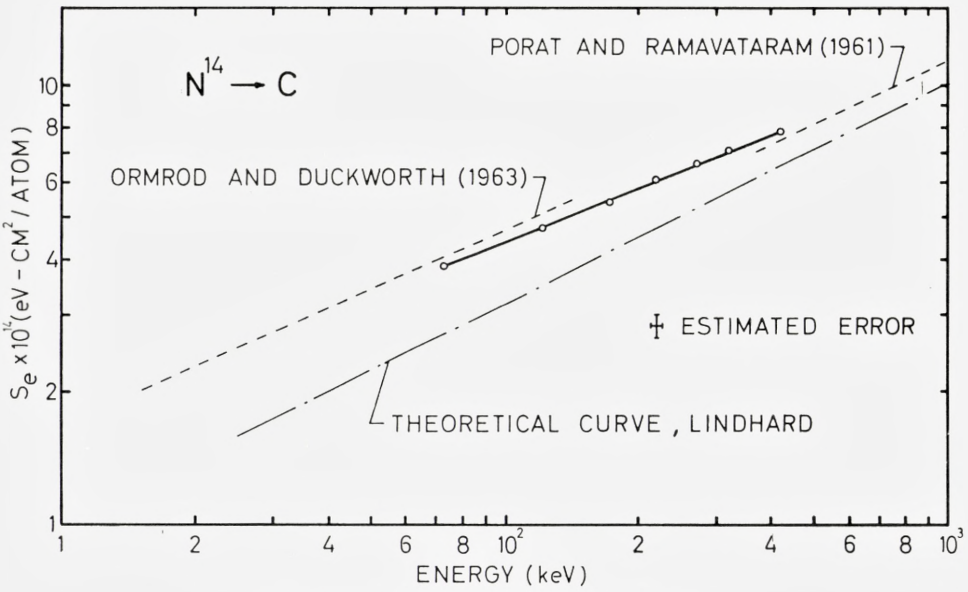

Figure 5a. Electronic stopping cross section S_e.

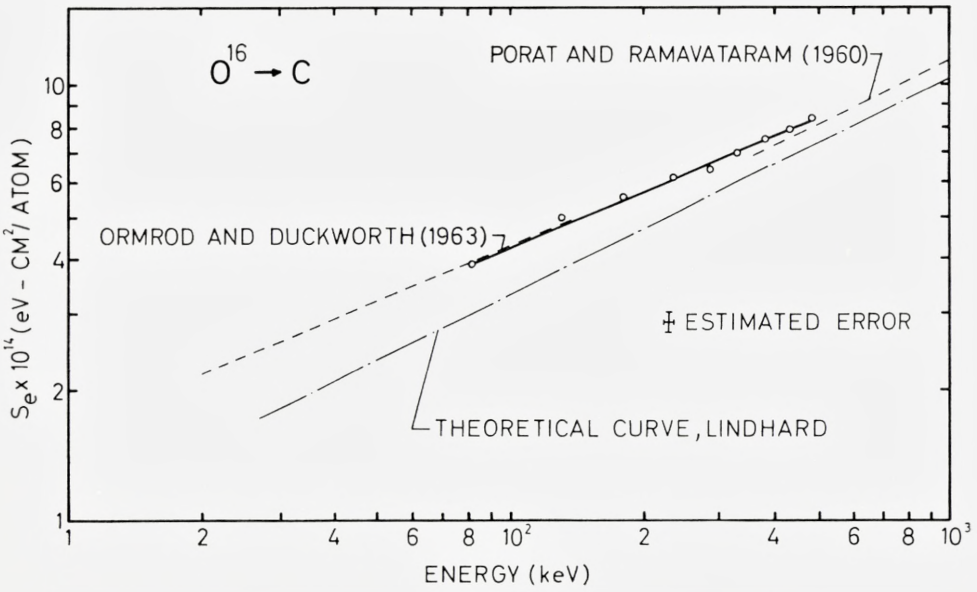

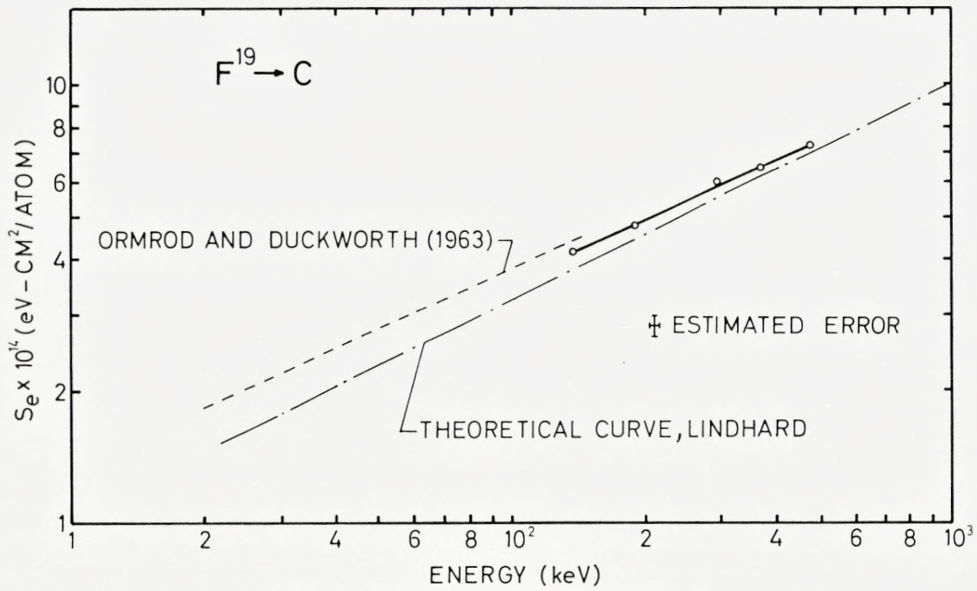

Figure 5b. Electronic stopping cross section S_e.

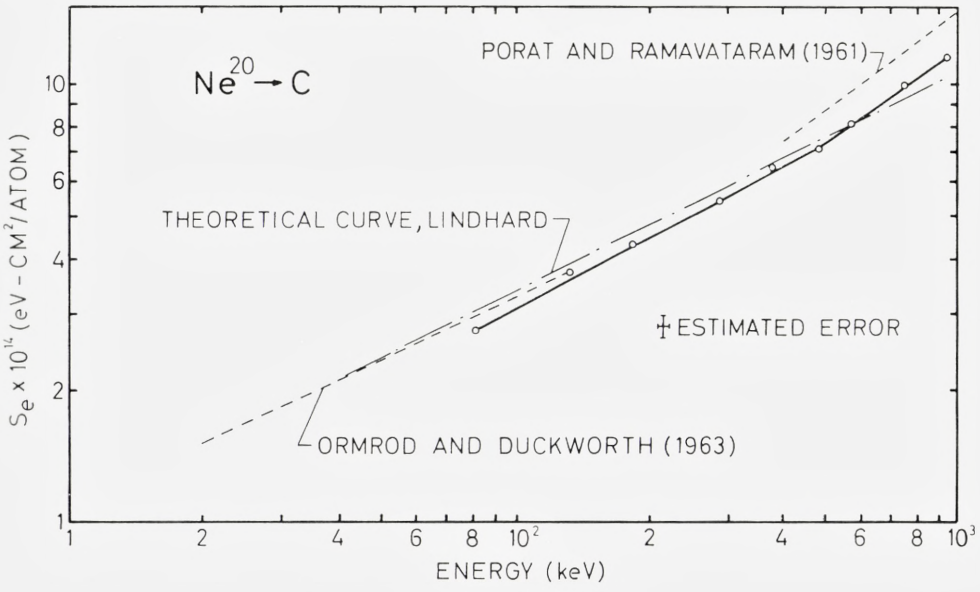

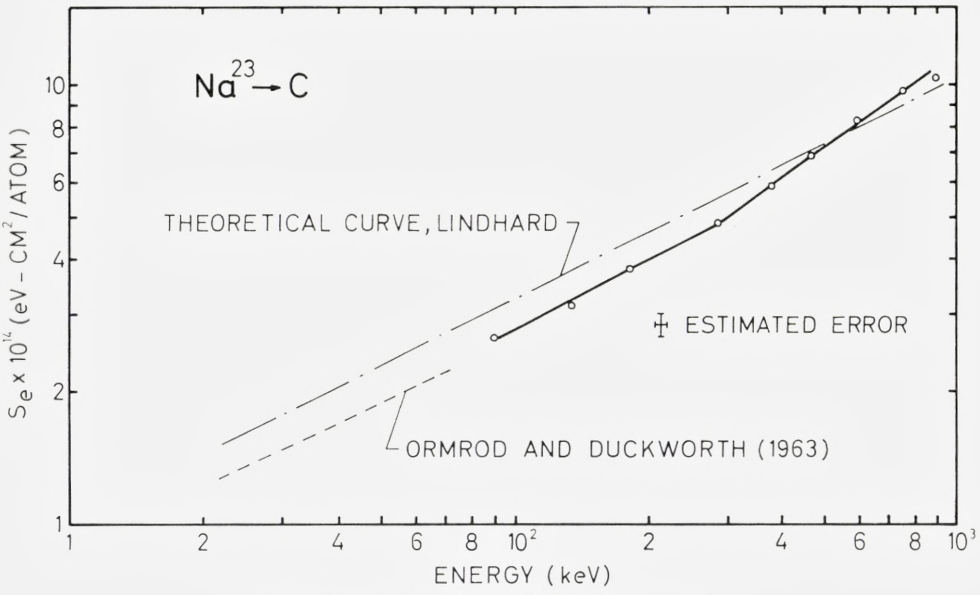

Figure 5c. Electronic stopping cross section S_e.

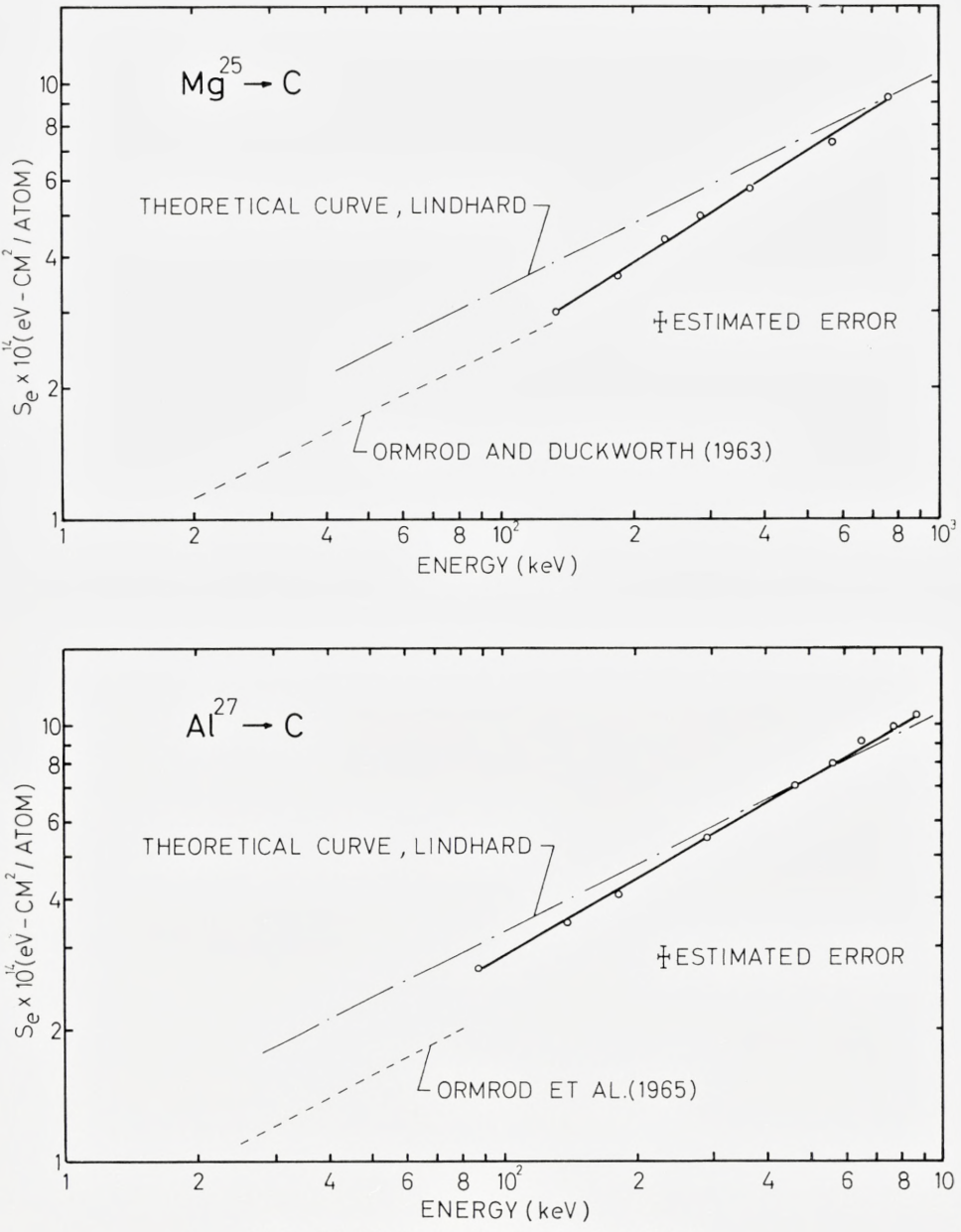

Figure 5d. Electronic stopping cross section S_e.

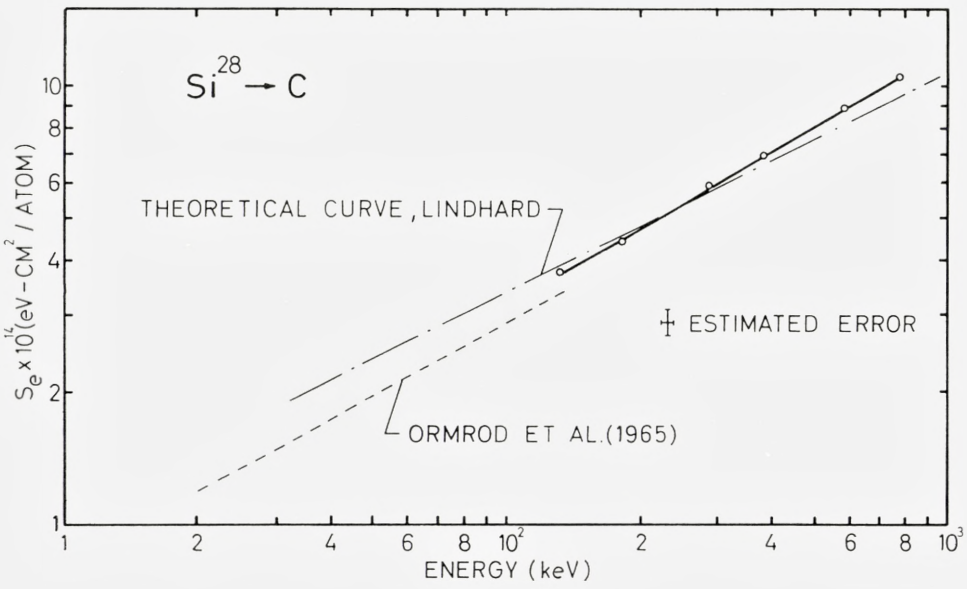

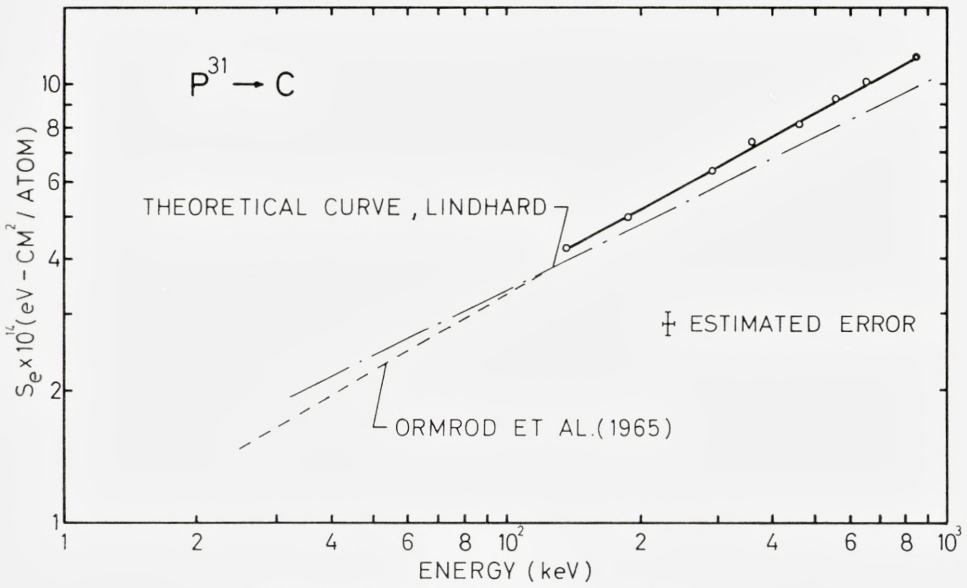

Figure 5e. Electronic stopping cross section S_e.

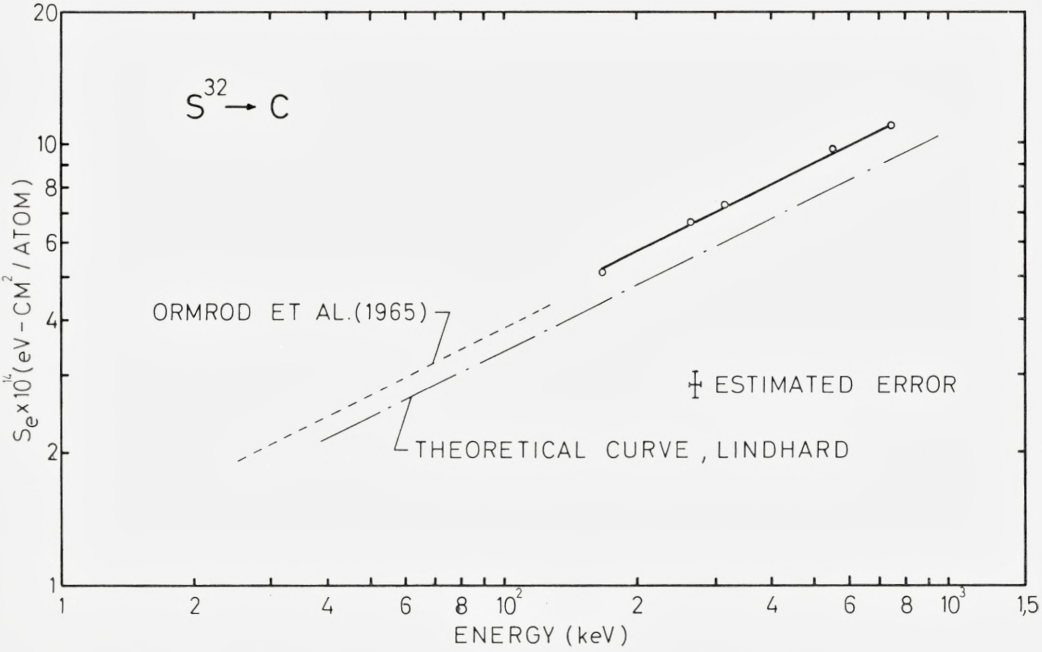

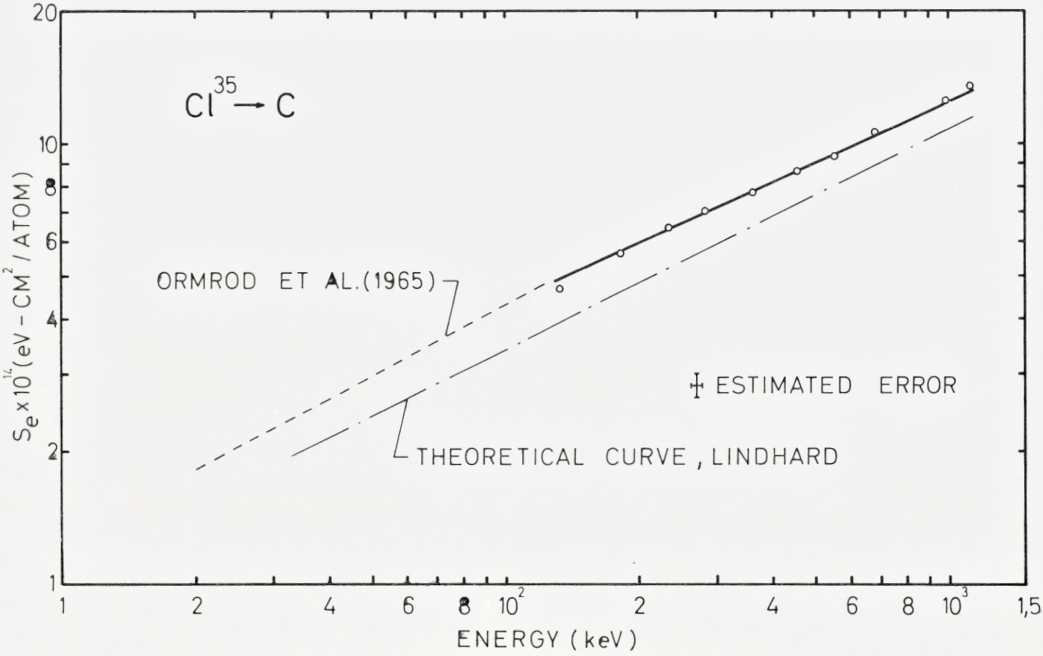

Figure 5f. Electronic stopping cross section S_e.

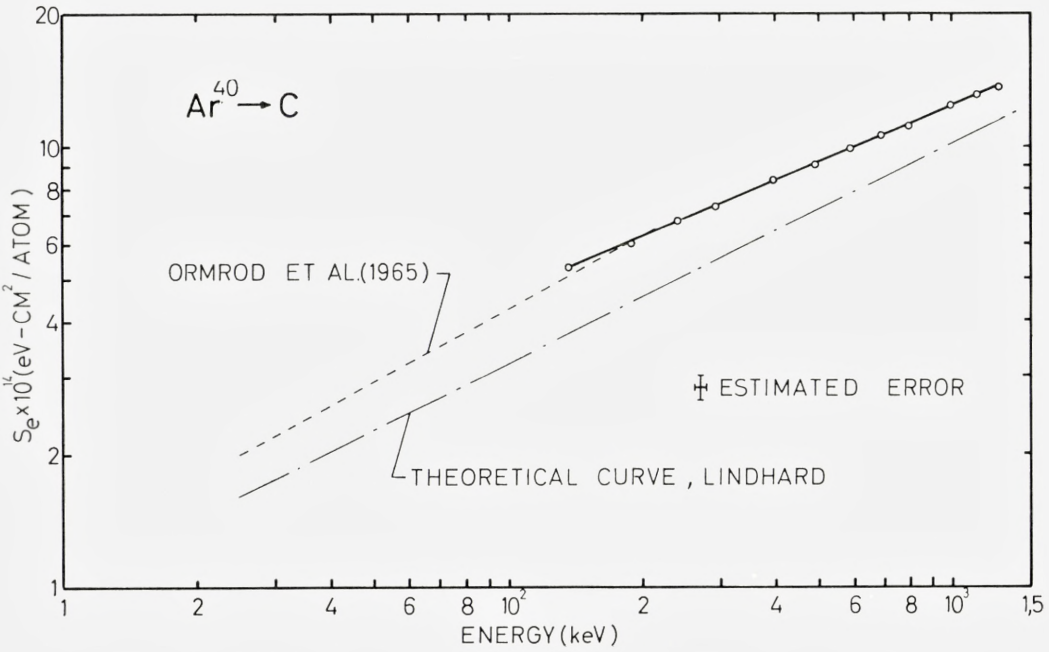

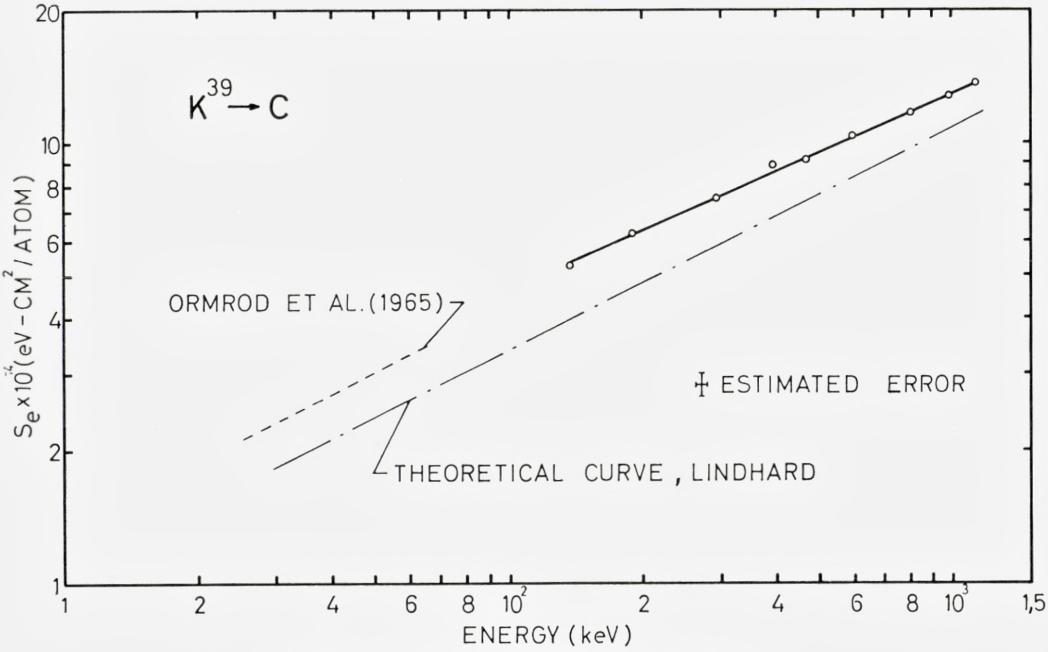

Figure 5g. Electronic stopping cross section S_e.

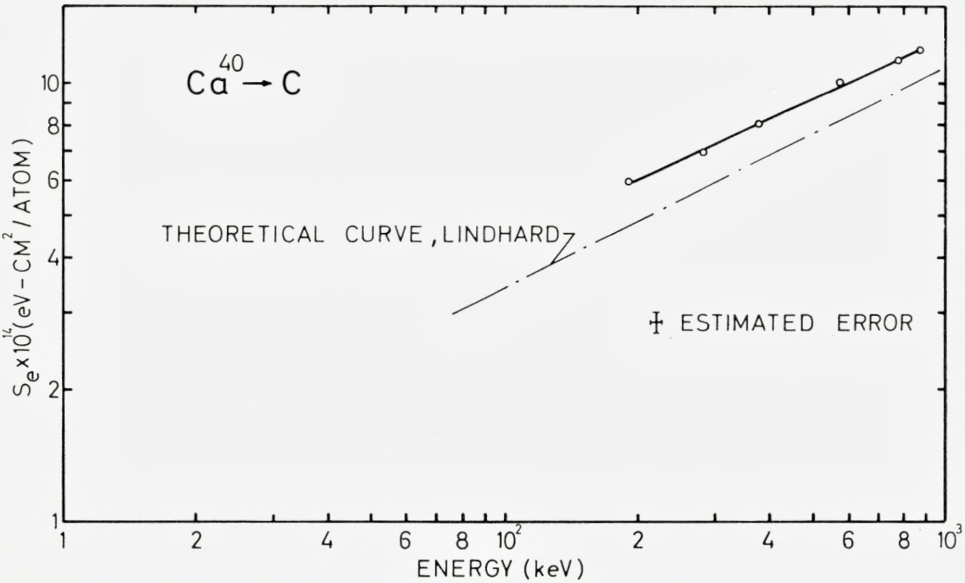

Figure 5h. Electronic stopping cross section S_e.

due to, for example, shell effects. Furthermore, in the cases where the nuclear correction S_n^* is negligible, i.e. for nearly all the data with $Z_1 < 10$, we find that the observed cross sections, $S_0 \approx S_e$, fit the above relationship. However, these remarks should not be taken as a proof that p is independent of the energy over a large energy range. In fact, our data suggest that p varies slowly with energy with an average not far from 0.5. In the cases of Ne^{20} and Na^{23}, a better fit is established by broken lines with two p-values for each element.

Plotted against Z_1 in Fig. 6 are the p-values obtained from this experiment and those found by ORMROD et al.[6] at lower energies. We have extracted p-values from PORAT and RAMAVATARAM'S[12] data in the case of $Z_1 = 6$, 7, 8, and 10. It is seen that with some correlation between adjacent elements, the empirical values exhibit an oscillation around $p = 0.5$ with an amplitude of about 0.1. As the energy ranges differ in the three experiments, differences outside those contributed by experimental errors would not be surprising.

In their treatment of their experimental data, ORMROD et al. found that, plotted against Z_1 for a constant, common projectile velocity of $v = 0.41\, v_0$, the electronic stopping cross sections exhibited a peculiar oscillation with a

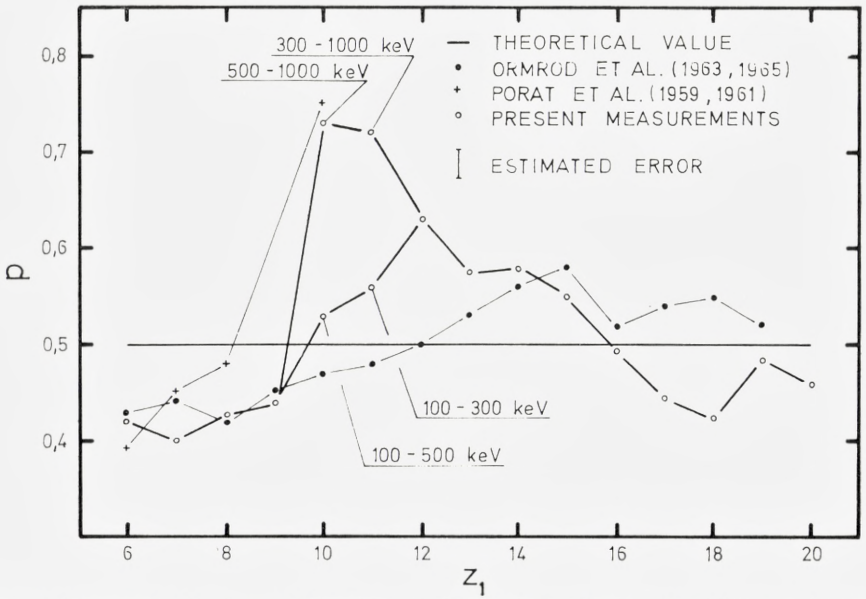

Figure 6. Exponent p in $S_e = k\,E^p$ against Z_1. The data by ORMROD et al.[6] cover the region below approx. 140 kev, the data by PORAT et al.[12] cover the region beyond 400 kev, when $Z_1 = 6$, 7, 8, and 10, and our data cover the region 100 to 500 kev when $6 \leq Z_1 \leq 9$, and 100 to 1000 kev when $10 \leq Z_1 \leq 20$. In the special cases, $Z_1 = 10$ and 11, two p-values have been displayed for each element.

long period around the curve predicted theoretically by LINDHARD and SCHARFF[5]. Due to our extended energy range, we have added three similar curves at different constant particle velocities, namely $\frac{v}{v_0} = 0.64$, 0.91, and 1.1. This makes it possible to study the periodicity in more detail. The results are displayed in Fig. 7 and compared with the theoretical curves by LINDHARD et al. The choice of a common velocity v is not strictly appropriate in the Thomas-Fermi treatment. Instead, we should have chosen a constant Thomas-Fermi velocity, i.e. constant $v \cdot Z_1^{-2/3}$. A closer examination of Fig. 7, however, shows that the qualitative features are not affected significantly if $v \cdot Z_1^{-2/3}$ is kept constant instead of v. In the same plot are also shown the theoretical stopping values by FIRSOV[4] as quoted by TEPLOVA et al.[14]. Based on a semi-classical Thomas-Fermi treatment, the results are given by

$$S_e = 5.15 \cdot 10^{-15}(Z_1 + Z_2)\frac{v}{v_0}\,\mathrm{ev} \cdot \mathrm{cm}^2/\mathrm{atom}.$$

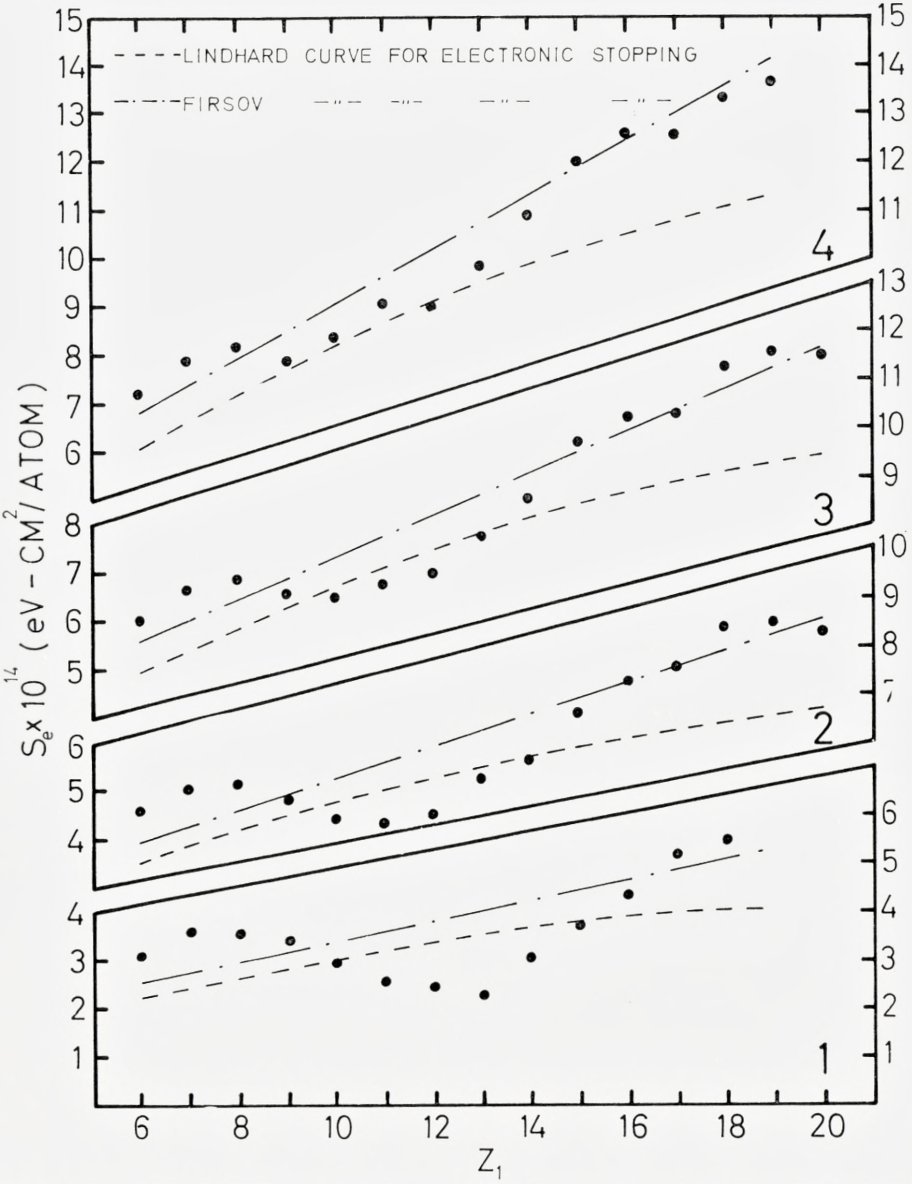

Figure 7. Electronic stopping cross section S_e versus Z_1 for constant common velocity. 1) $v = 0.41\ v_0$. 2) $v = 0.63\ v_0$. 3) $v = 0.91\ v_0$. 4) $v = 1.1\ v_0$. The data at $v = 0.41\ v_0$ are taken from Ormrod et al.[6]. Also shown are the theoretical curves by Lindhard and Scharff[5] and by Firsov[4].

Our data exhibit the same qualitative behaviour as the earlier empirical data[6]. However, a few observations can be made:

1) As would be expected, the relative amplitude of the oscillations tends to decrease with increasing particle velocity. Possible shell effects average out as a result of more close collisions where the electron clouds penetrate each other more deeply. It is observed that the simple oscillatory behaviour for small velocities is not maintained as the velocity increases. More complex structure appears.
2) The mean absolute deviation from the Lindhard theory is slightly larger at higher projectile velocities.
3) The reasonable agreement between Lindhard's and Firsov's predicted curves is partly due to the present selection of Z_1 values. Considering the functional dependence on Z_1 and Z_2 in the two theories, this is to be expected.

In the measurements, we have used singly charged ions for energies from 100 to 500 kev and doubly charged ions for energies from 500 to 1000 kev. In order to determine whether the energy loss depends on the charge state of either the incoming ions or the emerging ions from the foil, an experimental study was carried out.

a) With the analyzing magnet adjusted to one charge state, we studied the influence of the charge state of the incoming ions on the observed energy loss. We did not see any appreciable effect due to variation of the charge state of the incoming ions with the same kinetic energy. Assuming that the capture and the loss cross sections[13] in carbon for kev ions with $Z_1 < 20$ are greater than $2 \cdot 10^{-16}$ cm^2, the mean free path for obtaining charge equilibrium will be less than 0.1 μg/cm^2. This value is much smaller than the thickness of the thinnest foil (5 μg/cm^2) used in the present experiment.
b) The foil was bombarded with the same charge state ions. The dependence of the energy loss on the charge state of the emerging ions was studied. A few per cent difference between ΔE^+ and ΔE^{++} was observed where the charge index refers to the charge state of the emerging ions. The effect is of a statistical nature and partly stems from the different energy dependence of the capture and loss cross sections.

A more correct experimental procedure of taking stopping power data would be to average over the observed energy losses for different charge states of the outgoing ions, i.e.

$$\Delta E_0 = \frac{\sum_n I^{n+} \Delta E^{n+}}{\sum_n I^{n+}} ,$$

where I^{n+} is the flux of the outgoing ions in charge state $n+$.

As the charge state effect at the most is a few per cent, we have not proceeded with the more detailed measurements.

Acknowledgments

The authors wish to express their thanks to J. A. Davies and J. Lindhard for many stimulating discussions, to our colleagues, in particular to K. O. Nielsen, for their interest, to S. Olesen for his assistance in constructing the equipment, and to P. B. Kjær for operating the accelerator. This work was financially supported by the Danish State Research Foundation. One of the authors (C.A.S.) acknowledges the U.S. State Department for a Fulbright Travel Grant.

Appendix

Nuclear Stopping Correction

This appendix gives a general description of the analytical methods used for estimating the nuclear stopping contribution, S_n^*, encountered in the experiment. As previously mentioned in the Data Treatment section, it is a reasonable approximation to restrict our attention to the Gaussian-distributed nuclear collisions, i.e.

$$S_n^* = \int_0^{T^*} T d\sigma .$$

Here, T^* may be estimated from the equation

$$(T^*)^2 = (\Omega^*)^2 = N\Delta R \int_0^{T^*} T^2 d\sigma , \qquad \text{(A 1)}$$

where $N\Delta R$ is the number of atoms per cm^2, and $d\sigma$ is the differential cross section for an energy transfer T.

To solve eq. (A 1) with respect to T^*, it is convenient to introduce the reduced path length and the reduced energy, cf. LINDHARD et al.[9], ϱ and ε respectively:

$$\varrho = NRM_2 4\pi a^2 \frac{M_1}{(M_1+M_2)^2},$$

and

$$\varepsilon = E \frac{aM_2}{Z_1 Z_2 e^2 (M_1+M_2)},$$

where $a = a_0\ 0.8853(Z_1^{2/3}+Z_2^{2/3})^{-1/2}$ is the screening distance of the ion-atom potential.

If the interaction potential obeys certain similarity relations, LINDHARD et al. have shown that the differential cross sections may be written in the form

$$d\sigma = \pi a^2 \frac{dt}{2t^{3/2}} f(t^{1/2}), \tag{A 2}$$

where $t^{1/2} = \varepsilon \sin\frac{\theta}{2} = \varepsilon \sqrt{\frac{T}{T_{\max}}}$, θ is the scattering angle in the center of mass system, and $f(t^{1/2})$ depends on the chosen potential.

Equation (A 2) applies for power potentials as well as for screened potentials such as the Thomas-Fermi potential.

Combining eqs. (A 1) and (A 2), we get

$$F(\varepsilon^*) = \frac{\int_0^{\varepsilon^*} t f(t^{1/2})\, dt^{1/2}}{(\varepsilon^*)^4} = \frac{1}{N\Delta R \pi a^2}, \tag{A 3}$$

where $\varepsilon^* = \varepsilon \sqrt{\frac{T^*}{T_{\max}}}$.

Once $f(t^{1/2})$ is specified by selecting a convenient potential, ε^* and T^* may be evaluated from eq. (A 3) when the thickness of the film and the ion-atom combination (Z_1, Z_2) are known. It should be noted that ε^* does not depend on energy, while T^* is inversely proportional to the square root of energy.

Applying the relation

$$\left(\frac{d\varepsilon}{d\varrho}\right)_n^* = \int_0^{\varepsilon^*} f(t^{1/2}) \frac{1}{\varepsilon}\, dt^{1/2} = \int_0^{\varepsilon^*} f(t^{1/2}) \frac{1}{\varepsilon^*}\left(\frac{\varepsilon^*}{\varepsilon}\right) dt^{1/2},$$

the following result for the Gaussian nuclear stopping cross section is obtained:

$$S_n^* = 2.57 \cdot 10^{-16} \frac{A_1 Z_1^2 Z_2^2 \varepsilon^*}{A_2 E} I(\varepsilon^*) \text{ ev} \cdot \text{cm}^2/\text{atom}. \qquad \text{(A 4)}$$

The energy E is measured in kev, and $I(\varepsilon) = \dfrac{d\varepsilon}{d\varrho} = \displaystyle\int_0^{\varepsilon} f(t^{1/2}) \frac{1}{\varepsilon} dt^{1/2}$ is the stopping cross section in the reduced units.

Equation (A 4) exhibits some peculiar features:

(a) The Gaussian nuclear stopping cross section is inversely proportional to the energy as ε^* is independent of the energy.
(b) Change of the applied potential within the framework of eq. (A 2) alters the value of ε^* according to eq. (A 3), but does not abolish the inverse proportionality with the energy.

Strictly speaking, formula (A 1) applies only when the energy loss is much smaller than the energy of the beam, i.e. $\Delta E_0 \ll E_i$. In the case of thicker films, $\Delta E_0 \lesssim E_i$. LINDHARD and NIELSEN[15] have given a more rigorous formula.

Institute of Physics,
University of Aarhus, Denmark
B. Fastrup, P. Hvelplund,
*and C. A. Sautter**)

---

*) Present address: *Physics Department, Concordia College Moorhead, Minnesota, U.S.A.*

References

(1) N. Bohr, Phil. Mag. **25**, 10 (1913).
N. Bohr, Mat. Fys. Medd. Dan. Vid. Selsk. **18**, 8 (1948).
(2) E. Fermi and E. Teller, Phys. Rev. **72**, 399 (1947).
(3) J. Lindhard, Mat. Fys. Medd. Dan. Vid. Selsk. **28**, 8 (1954).
(4) O. B. Firsov, Soviet Phys. JETP **9**, 1076 (1959).
(5) J. Lindhard and M. Scharff, Phys. Rev. **124**, 128 (1961).
(6) J. H. Ormrod and H. E. Duckworth, Can. J. Phys. **41**, 1424 (1963).
J. H. Ormrod, J. R. Macdonald, and H. E. Duckworth, Can. J. Phys. **43**, 275 (1965).
(7) E. Bøgh, P. Dahl, H. E. Jørgensen, and K. O. Nielsen: A 600 kV Heavy Ion Accelerator with Magnet for Isotopical Separation. Preprint (1965). To be published.
(8) E. J. Williams, Proc. Roy. Soc. **A 125**, 420 (1929).
(9) J. Lindhard, M. Scharff, and H. E. Schiøtt, Mat. Fys. Medd. Dan. Vid. Selsk. **33**, 14 (1963).
(10) C. A. Sautter and E. J. Zimmermann, Phys. Rev. **140**, A 490 (1965).
(11) R. D. Moorhead, J. Appl. Phys. **36**, 391 (1965).
(12) D. I. Porat and K. Ramavataram, Proc. Roy. Soc. **A 252**, 394 (1959), Proc. Phys. Soc. **77**, 97 (1961), Proc. Phyc. Soc. **78**, 1135 (1961).
(13) V. S. Nikolaev, Soviet Phys. USPEKHI **8**, 269 (1965).
(14) Ya. A. Teplova, V. S. Nikolaev, I. S. Dmitriev, and L. N. Fateeva, Soviet Phys. JETP **15**, 31 (1962).
(15) J. Lindhard and V. Nielsen, Phys. Letters **2**, 209 (1962).

Indleveret til Selskabet den 12. maj 1966.
Færdig fra trykkeriet den 8. december 1966.

Matematisk-fysiske Meddelelser
udgivet af
Det Kongelige Danske Videnskabernes Selskab
Bind **35,** nr. 11

Mat. Fys. Medd. Dan. Vid. Selsk. **35,** no. 11 (1967)

CANONICAL QUANTUM ELECTRODYNAMICS IN COVARIANT GAUGES

BY

B. LAUTRUP

København 1967
Kommissionær: Munksgaard

Synopsis

A consistent canonical quantization procedure for electrodynamics in covariant gauges of a certain type is developed. This type comprises most of the gauges that usually are studied in the literature. In every gauge there are four photons and in the sense that the expectation value of the four-divergence of the Maxwell field is zero for all physical states, all these gauges are quantum generalizations of the classical Lorentz gauge. The quantization is carried out by means of a Lagrange multiplier field. It is shown that there exist generators for four-dimensional translations and rotations in every gauge. A peculiar aspect is that the scalar and longitudinal photons are not stationary states (except in one gauge), because the energy is not diagonalizable in general. This is connected with the necessity of introducing an indefinite metric. It is possible to connect the different gauges by operator "phase"-transformations of the electron field. The necessity of a gauge renormalization removes some difficulties with the usual formulation of quantum electrodynamics. The self-mass of the electron comes out gauge dependent by a direct calculation, but a more refined analysis shows that it actually is gauge independent.

PRINTED IN DENMARK
BIANCO LUNOS BOGTRYKKERI A/S

1. Introduction

In classical electrodynamics the free Lagrangian density of the electromagnetic potentials A_μ is

$$\mathfrak{L} = -\tfrac{1}{4} F_{\mu\nu}F^{\mu\nu}, \tag{1}$$

where $F_{\mu\nu} = \partial_\mu A_\nu - \partial_\nu A_\mu$ and we use the metric $g_{\mu\nu} = (1,-1,-1,-1)$. Variation of A_μ gives the classical equations of motion

$$\Box A_\mu + \partial_\mu \partial_\nu A^\nu = 0\,. \tag{2}$$

The freedom of gauge transformations allows us to choose both covariant and non-covariant gauge conditions, with the sole restriction that $F_{\mu\nu}$ be a covariant tensor. A typical example of a non-covariant gauge condition is $\operatorname{div} \bar{A} = 0$ (the Coulomb gauge), and typical for the covariant gauges is the condition $\partial_\mu A^\mu = 0$ (the Lorentz gauge).[1]

It has been known for more than thirty-five years[2] that difficulties are met if we attempt to quantize (2) with a covariant gauge condition, e. g. the Lorentz condition. With modern methods we can see that such difficulties arise in every covariant gauge, in other words, that the equations (2) cannot be valid in any covariant gauge. From general arguments of field theory we find that the most general vacuum representation of the field commutator must be

$$\langle o|[A_\mu(x),\ A_\nu(y)]|o\rangle = -2\pi \int dp\, \varepsilon(p)(\varrho_1(p^2)g_{\mu\nu} + \varrho_2(p^2)p_\mu p_\nu)e^{-ip\cdot(x-y)}, \tag{3}$$

where $dp = dp(2\pi)^{-4}$ and $\varrho_1(p^2)$ and $\varrho_2(p^2)$ are spectral functions. Using (2) we find $\varrho_1 = 0$ so that it follows that

$$\langle o|[F_{\mu\nu}(x),\ F_{\varrho\sigma}(y)]|o\rangle = 0\,.$$

[1] As gauge transformations and Lorentz transformations may be mixed without disturbing the tensorial character of $F_{\mu\nu}$, the phrase non-covariant is somewhat ambiguous in this connexion. Consider for instance the Coulomb gauge. If we claim that the Coulomb condition has to hold in every inertial system, then A_μ does not transform like a four-vector, but according to a combined Lorentz and gauge transformation. If we claim that A_μ is a four-vector, then the Coulomb condition is not valid in every inertial system. For the covariant gauges no such difficulty arises because it is then natural to take A_μ to be a four-vector.

[2] W. Heisenberg and W. Pauli, Zeits. f. Physik **56** (1929) 1.

Now it is generally believed that this is not true[1], so that we must give up the equations (2) in covariant gauges. In a non-covariant gauge we cannot show that the vacuum representation has the form (3) and hence we cannot prove an analogous result in this case. The Maxwell equations (2) may very well be the equations of motion for the electromagnetic field in a non-covariant gauge. Among the non-covariant gauges we can mention the Coulomb gauge[2], the axial gauge[3], and the Valatin gauge[4].

In the case of the covariant gauges the above mentioned difficulty is usually overcome by adding a term

$$-\tfrac{1}{2}(\partial_\mu A^\mu)^2$$

to the Lagrangian density (1). The "gauge" obtained in this way is called the Fermi gauge, and it is the only covariant gauge which has been formulated as a theory of canonically quantized fields[5]. A price must, however, be paid for the simplicity obtained by this trick. There will be states which are not physically realizable, in the sense that they cannot be prepared in any experiment. Some arguments may be given to show that this is probably the case in every covariant gauge. Whereas we are not able to claim that the Maxwell equations (2) are satisfied for the quantized potentials, it seems very reasonable to claim that the mean value of the potentials should be real and satisfy

$$\Box\langle A_\mu\rangle + \partial_\mu\partial_\nu\langle A^\nu\rangle = 0 \tag{4}$$

in every physically realizable state[6]. But then all states cannot be physically realizable, because this would lead us back to (2).

In quantum electrodynamics most of the gauges which usually are studied belong to a one-parameter family characterized by the photon propagator

$$D_{\mu\nu}(k) = -i\frac{g_{\mu\nu}}{k^2+i\varepsilon} + i(1-a)\frac{k_\mu k_\nu}{(k^2+i\varepsilon)^2}. \tag{5}$$

[1] R. E. Peierls, Proc. Roy. Soc. A **214** (1952) 143.
[2] L. E. Evans and T. Fulton, Nucl. Phys. **21** (1960) 492.
[3] R. L. Arnowitt and S. I. Fickler, Phys. Rev. **127** (1962) 1821.
J. Schwinger, Phys. Rev. **130** (1963) 402.
York-Peng Yao, Journ. Math. Phys. **5** (1964) 1319.
[4] J. G. Valatin, Mat. Fys. Medd. Dan. Vid. Selsk. **26** (1951) No. 13.
[5] See f. inst. G. Källén, Handbuch d. Phys. V_1 (Springer-Verlag, Berlin 1958).
[6] This is in analogy with the Ehrenfest theorem of non-relativistic quantum mechanics.

For $a = 1$ we get the Fermi gauge,
for $a = 0$ the Landau gauge[1] and
for $a = 3$ the Yennie gauge[2].

We shall show in this paper how the canonical quantization of a certain class of covariant gauges may be carried out in a systematic way. In this class we shall verify eq. (4) for the physical states. Furthermore, we shall for these gauges find

$$\partial_\mu \langle A^\mu \rangle = 0 \tag{6}$$

in every physical state, so that these gauges may all be considered as quantum generalizations of the classical Lorentz gauge. It will be shown that this class of gauges is essentially equivalent to the family given by eq. (5).

2. Quantization of the free Maxwell field

Let us begin with the study of quantum electrodynamics in the analogue of the classical Lorentz gauge, where

$$\partial_\mu A^\mu = 0 \tag{7}$$

is valid as an operator identity. Considering $A_\mu(x)$ to be generalized coordinates, we immediately see that (7) is a non-integrable relation between the generalized coordinates and velocities. This implies that quantum electrodynamics in this gauge is *non-holonomic* and hence the canonical methods cannot be expected to work at all. In classical mechanics non-holonomic systems with constraints like (7) are treated by means of Lagrange multipliers[3], and it is therefore tempting to use the same method here. Accordingly we add to the Lagrangian density (1) a term

$$-\Lambda \partial_\mu A^\mu ,$$

where Λ is the Lagrange multiplier, which in this case must be a scalar field. In the new Lagrangian density

$$\mathfrak{L} = -\tfrac{1}{4} F_{\mu\nu} F^{\mu\nu} - \Lambda \partial_\mu A^\mu \tag{8}$$

we are allowed to treat A_μ as independent coordinates, and it is immediately seen that the momentum canonically conjugate to A_0 is now $-\Lambda$,

[1] L. D. Landau, A. A. Abrikosov, and I. M. Khalatnikov, Dokl. Akad. Nauk. SSSR **95** (1954) 773; JETP **2** (1956) 69.
[2] H. M. Fried and D. R. Yennie, Phys. Rev. **112** (1958) 1391.
[3] R. Goldstein, Classical Mechanics, pp. 11, 40 (Addison-Wesley, 1959).

whereas it formerly was identically zero. It would now be possible to go on with the canonical quantization, but it is, however, convenient first to generalize (8) slightly. As variation of (8) after $\Lambda(x)$ gives us the gauge condition (7), it is seen that the Lagrange multiplier behaves like a free coordinate, with the constraint as "equation of motion". We therefore propose to change the Lagrangian density to

$$L = -\tfrac{1}{4} F_{\mu\nu}F^{\mu\nu} - \Lambda\partial_\mu A^\mu + F(\Lambda(x)) \tag{9}$$

where $F(z)$ is a holomorphic function with $F(o) = F'(o) = 0$. As this extra term not contains A_μ, it will only change the gauge condition to

$$\partial_\mu A^\mu(x) = F'(\Lambda(x)) \tag{10}$$

and should then only correspond to a gauge transformation. The equation of motion for A_μ is—independently of the function F—

$$\Box A_\mu + \partial_\mu\partial_\nu A^\nu = \partial_\mu\Lambda, \tag{11}$$

and from this we get the equation of motion for Λ

$$\Box\Lambda = 0. \tag{12}$$

From (9) we now find the momenta canonically conjugate to A_μ to be $\pi^{\mu o}$, where

$$\pi^{\mu\nu} = F^{\mu\nu} - g^{\mu\nu}\Lambda. \tag{13}$$

Canonical quantization leads to the relations

$$[A_\mu(x),\ A_\nu(y)]_{x_o = y_o} = 0, \tag{14}$$

$$[\dot{A}_i(x),\ A_\nu(y)]_{x_o = y_o} = ig_{i\nu}\delta(\bar{x} - \bar{y}), \tag{15}$$

$$[\Lambda(x),\ A_\nu(y)]_{x_o = y_o} = ig_{o\nu}\delta(\bar{x} - \bar{y}), \tag{16}$$

$$[\dot{A}_i(x),\ \dot{A}_k(y)]_{x_o = y_o} = 0, \tag{17}$$

$$[\Lambda(x),\ \dot{A}_k(y)]_{x_o = y_o} = -i\partial_k^x\delta(\bar{x} - \bar{y}), \tag{18}$$

$$[\Lambda(x),\ \Lambda(y)]_{x_o = y_o} = 0, \tag{19}$$

where the dot means differentiation with respect to time.

From (11) we find taking $\mu = 0$

$$\dot{\Lambda} = \Lambda A_o + \partial_i\dot{A} \tag{20}$$

and then by (16) and (18)

$$[\dot{\Lambda}(x),\ \Lambda(y)]_{x_0=y_0} = 0\,.$$

Integration of (12) yields for arbitrary y_0

$$\Lambda(x) = -\int d\bar{y} D(x-y) \overleftrightarrow{\partial}_{y_0} \Lambda(y),$$

where $D(x-y)$ is the well-known singular function corresponding to mass zero[1]. We furthermore use the convention $\overleftrightarrow{\partial} = \overrightarrow{\partial} - \overleftarrow{\partial}$. Hence we find that

$$[\Lambda(x),\ \Lambda(y)] = 0 \tag{21}$$

for arbitrary points x and y. Analogously we find by means of the equal-time commutation relations

$$[\Lambda(x),\ A_\mu(y)] = -i\partial_\mu^x D(x-y)\,. \tag{22}$$

Remark that the two important relations (21) and (22) both are independent of the gauge condition (10)[2]. It is possible to find one more set of relations which is independent of the gauge condition, namely the commutation relations for the field strengths $F_{\mu\nu}$. To find these we first define the transverse projection operator

$$\tau_{\mu\nu} = g_{\mu\nu} - n_\mu n_\nu + \frac{(\partial_\mu - n_\mu n\cdot\partial)(\partial_\nu - n_\nu n\cdot\partial)}{\Box + (n\cdot\partial)^2}, \tag{23}$$

where n_μ is a time-like unit vector. Here we shall always take $n_\mu = g_{\mu 0}$. Then $\tau_{\mu\nu}$ only involves spatial operations[3]. Now define the transverse field by

$$A_\mu^{Tr} = \tau_{\mu\nu} A^\nu\,. \tag{24}$$

From (11) and the well-known properties of $\tau_{\mu\nu}$ it follows that

$$\Box A_\mu^{Tr} = 0\,. \tag{25}$$

Integrating (25) and using the equal time commutation relations we find

$$[A_\mu^{Tr}(x),\ A_\nu^{Tr}(y)] = -i\tau_{\mu\nu} D(x-y), \tag{26}$$

showing that the transverse part of the Maxwell field is correctly quantized. From (20) and (23) we get[3]

[1] G. KÄLLÉN, ibid., p. 190.

[2] Equations (21) and (22) have been derived in the Fermi gauge of asymptotic quantum electrodynamics by R. E. PUGH (Ann. Phys. **30** (1964) 422).

[3] $\Delta = \Box + (n\cdot\delta)^2$ is Laplace's operator, and $1/\Delta$ may be defined as

$$\frac{1}{\Delta} f(\bar{x}) = -\int d\bar{x}' \frac{f(\bar{x}')}{4\pi|\bar{x}-\bar{x}'|}$$

$$A_\mu = A_\mu^{Tr} + \frac{n_\mu}{\Delta}\Lambda - \frac{\partial_\mu}{\Delta}\partial_i A^i$$

such that

$$F_{\mu\nu} = F_{\mu\nu}^{Tr} + \frac{\partial_\mu n_\nu - \partial_\nu n_\mu}{\Delta}\Lambda,$$

where $F_{\mu\nu}^{Tr}$ are the "transverse field strengths". Then using

$$[\Lambda(x),\ A_\mu^{Tr}(y)] = 0,$$

which follows from (22), we find

$$[F_{\mu\nu}(x),\ F_{\varrho\sigma}(y)] = i(g_{\mu\varrho}\partial_\nu\partial_\sigma - g_{\nu\varrho}\partial_\mu\partial_\sigma + g_{\nu\sigma}\partial_\mu\partial_\varrho - g_{\mu\sigma}\partial_\nu\partial_\varrho)D(x-y). \quad (27)$$

This is the most important result of this section. The quantization by means of a Lagrange multiplier method leads to the well-known commutation relations[1] for the field strengths in an arbitrary gauge of the type considered here.

In order to find the commutation relations for the potentials we shall make a special choice of gauge condition, namely

$$F(\Lambda(x)) = \frac{a}{2}\Lambda(x)^2, \quad (28)$$

where a is a real number, such that the gauge condition now reads

$$\partial_\mu A^\mu = a\Lambda. \quad (29)$$

In the appendix it is shown that this choice of gauge leads to the family of photon propagators (5). The gauge parameter a is actually identical to the mass ratio parameter in the theory of massive electrodynamics, developed by FELDMAN and MATTHEWS[2].

With the gauge condition (29) we find from (11)

$$\Box A_\mu = (1-a)\partial_\mu\Lambda. \quad (30)$$

Using (12) we get

$$\Box\Box A_\mu = 0.$$

Now it is fairly trivial to show that if a field $\varphi(x)$ satisfies the fourth order differential equation $\Box\Box\varphi(x) = 0$, then, for arbitrary y_o,

[1] R. E. PEIERLS, Proc. Roy. Soc. A **214** (1952) 143.
[2] G. FELDMAN and P. T. MATTHEWS, Phys. Rev. **130** (1963), 1633.

$$\varphi(x) = -\int d\bar{y} D(x-y) \overleftrightarrow{\partial}_{y_0} \varphi(y) - \int d\bar{y} E(x-y) \overleftrightarrow{\partial}_{y_0} \Box \varphi(y),$$

where $E(x)$ is given by

$$E(x) = 2\pi i \int đp \varepsilon(p) \delta'(p^2) e^{-ip(x-y)} = \left. \frac{\partial \Delta(x-y, \mu^2)}{\partial \mu^2} \right|_{\mu^2 = 0}.$$

The rather peculiar properties of this distribution are given in the appendix.

By means of the equal-time commutation relations and the integrated equation of motion for $A_\mu(x)$ we find after some calculation that

$$\left.\begin{aligned} [A_\mu(x), A_\nu(y)] &= -i(g_{\mu\nu}\Box + (1-\alpha)\partial_\mu\partial_\nu)E(x-y) = \\ &= -ig_{\mu\nu}D(x-y) - i(1-\alpha)\partial_\mu\partial_\nu E(x-y), \end{aligned}\right\} \tag{31}$$

where in the last line we have used the relation $\Box E(x) = D(x)$.

3. Indefinite metric

It is well known that it is necessary to introduce an indefinite metric in the Fermi gauge in order to secure the covariance of certain expression[1]. As the present theory contains the Fermi gauge as a special case, it must be expected that this will also be necessary in any covariant gauge of the type considered here.

For the moment we shall content ourselves with the following properties of the metric operator η:

$$\eta = \eta^* = \eta^{-1}, \tag{32}$$

$$\eta A_\mu^* \eta = A_\mu, \tag{33}$$

$$\eta | o > = | o >. \tag{34}$$

Equation (32) expresses the Hermiticity and unitarity of the metric operator, (33) the self-adjointness properties of A_μ with respect to η, and (34) the choice of positive norm for the vacuum. In the following section we shall fix the properties of η with respect to A_μ completely.

[1] G. KÄLLÉN ibid., p. 191, 199. Here further references can be found.

4. Fourier expansion of the field

In this section we limit ourselves to the case (29). Let us define the field

$$\chi(x) = \frac{a-1}{2}\frac{1}{\Delta}(x_o\dot{\Lambda}(x) - \tfrac{1}{2}\Lambda(x)). \tag{35}$$

From eq. (12) it then follows that

$$\Box\chi(x) = (1-a)\Lambda(x).$$

This shows that the field

$$A_\mu^F = A_\mu - \partial_\mu\chi(x) \tag{36}$$

satisfies the equation

$$\partial^\mu A_\mu^F = \Lambda, \tag{37}$$

and from (11) we find the equations of motion for A_μ^F:

$$\Box A_\mu^F = 0. \tag{38}$$

From the relation (see the appendix)

$$E(x) = \frac{1}{2\Delta}(D(x) - x_o\dot{D}(x))$$

we get using eqs. (21), (22), (31), (35), and (36)

$$[A_\mu^F(x), A_\nu^F(y)] = -ig_{\mu\nu}D(x-y). \tag{39}$$

As eqs. (38) and (39) are the equations of motion and commutation relations of the Maxwell field in the Fermi gauge we may immediately write down the usual expansion (in a periodicity volume)

$$A_\mu^F(x) = \frac{1}{\sqrt{V}}\sum_{\bar{k}\lambda}\frac{e_\mu(\bar{k}\lambda)}{\sqrt{2\omega}}(a(\bar{k}\lambda)e^{-ik\cdot x} + \tilde{a}(\bar{k}\lambda)e^{ik\cdot x}), \tag{40}$$

where $a(\bar{k}\lambda)$ and

$$\tilde{a}(\bar{k}\lambda) = \eta_\lambda a^*(\bar{k}\lambda)\eta_\lambda$$

have the usual commutation properties

$$[a(\bar{k}\lambda), \tilde{a}(\bar{k}'\lambda')] = \delta_{\bar{k}\bar{k}'}(-g_{\lambda\lambda'}),$$
$$[a(\bar{k}\lambda), a(\bar{k}'\lambda')] = 0.$$

If we therefore fix the properties of η by the relations

$$[\eta, a(\bar{k}\lambda)] = 0 \quad (\lambda = 1, 2, 3),$$
$$\{\eta, a(\bar{k}o)\} = 0,$$

we find

$$[a(\bar{k}\lambda), a^*(\bar{k}'\lambda')] = \delta_{\bar{k}\bar{k}'}\,\delta_{\lambda\lambda'}. \tag{41}$$

This permits us to interpret $a(\bar{k}\lambda)$ and $a^*(\bar{k}\lambda)$ as annihilation and creation operators for photons.

By virtue of equation (12) we may expand the A-field as

$$A(x) = \frac{i}{\sqrt{V}} \sum_{\bar{k}} \frac{\omega}{\sqrt{2\omega}} (\lambda(\bar{k}) e^{-ik\cdot x} - \tilde{\lambda}(\bar{k}) e^{ik\cdot x}), \tag{42}$$

where as above $\tilde{\lambda}(\bar{k}) = \eta\lambda^*(\bar{k})\eta$. From eqs. (37) and (40) we then find

$$\lambda(\bar{k}) = a(\bar{k}3) - a(\bar{k}o). \tag{43}$$

One may easily verify that

$$[\lambda(\bar{k}), \lambda(\bar{k}')] = [\lambda(\bar{k}), \tilde{\lambda}(\bar{k}')] = 0 \tag{44}$$

in accordance with the vanishing of the A-A commutator. Remark that (44) leans heavily on the properties of the indefinite metric.

By the expansion (42), of the A-field and by eqs. (35), (36), (40) and (43) we may now express the total field A_μ in terms of annihilation and creation operators.

As in every gauge we are able to define the creation and annihilation operators as above, the Hilbert (Fock) space will have the same structure in every gauge. Although electrodynamics in different covariant gauges must be considered as different field theories (because the gauge condition is stated before the derivation of the equations of motion), we can, however, think of these theories as formulated in the same Hilbert (Fock) space.

The transformation field $\chi(x)$, given in (35) seems to be non-covariant on account of the explicit time dependence. [If the equations of motion for A_μ are solved by Fourier transformation one finds that this time dependence essentially stems from the term $-(t/2\omega)\cos\omega t$ in the solution of differential equations of the type

$$\frac{d^2y}{dt^2} + \omega^2 y = \sin\omega t].$$

The question of the apparent non-covariance is resolved in the following way. Covariance in field theory is equivalent to showing the existence of a representation of the proper inhomogeneous Lorentz group under which the fields transform correctly, i. e. finding generators of infinitesimal translations and rotations. As we shall show in section 5 these generators exist, but are not independent of the gauge. This means that the field $A_\mu^F(x)$, which can be defined in every gauge by eq. (36), is only a four-vector in the Fermi gauge. The splitting $A_\mu = A_\mu^F + \partial_\mu \chi$ is therefore a splitting of the covariant field A_μ into two non-covariant terms in the gauge characterized by the parameter value a. An expression which is covariant in one gauge need not be so in any other gauge.

5. The energy-momentum tensor

Although it would be possible to study the general gauge condition (10) we shall here limit ourselves to the simple case (29) where the Lagrangian density is

$$\mathfrak{L} = -\tfrac{1}{4} F_{\mu\nu}F^{\mu\nu} - \Lambda \partial_\mu A^\mu + \frac{a}{2}\Lambda^2. \tag{45}$$

By straightforward calculation we find from (45) the symmetric energy-momentum tensor

$$T_{\mu\nu} = -F_{\mu\lambda}F_\nu^{\cdot\lambda} + \tfrac{1}{4} g_{\mu\nu}F_{\varrho\sigma}F^{\varrho\sigma} + A_\mu \partial_\nu \Lambda + A_\nu \partial_\mu \Lambda - g_{\mu\nu}(A_\lambda \partial^\lambda \Lambda + \frac{a}{2}\Lambda^2), \tag{46}$$

which by means of the equations of motion and the gauge condition is seen to be conserved.

By direct calculation it is possible to show that the linear and angular momentum operators P_μ and $M_{\mu\nu}$ have the correct commutation properties with respect to the Maxwell field, i. e. that they are generators of infinitesimal translations and rotations. Remark, however, that P_μ and $M_{\mu\nu}$ are not Hermitian, but self-adjoint, i. e. $\eta P_\mu^* \eta = P_\mu$ and analogously for $M_{\mu\nu}$. This has the consequence that for instance the energy H is not necessarily diagonalizable. Take for instance the model (α is real)

$$\eta = \begin{pmatrix} 1 & 0 \\ 0 & -1 \end{pmatrix}, \quad H = \begin{pmatrix} 1+\alpha & \alpha \\ -\alpha & 1-\alpha \end{pmatrix}. \tag{47}$$

This H is self-adjoint with respect to η, but it has only one eigenvector, for $\alpha \neq 0$.

Using $A_\mu = A^F_\mu + \partial_\mu \chi$ we can split the energy-momentum tensor (46) into two parts

$$T_{\mu\nu} = T^F_{\mu\nu} + T^\Lambda_{\mu\nu},$$

where the first part is what we would find in the Fermi gauge and the second is only dependent on Λ. From the usual theory of the Fermi gauge we know that (after removal of zeropoint terms)

$$P^F_\mu = \int d\bar{x}\, T^F_{\mu o} = \sum_{\bar{k}\lambda} k_\mu a^*(\bar{k}\lambda) a(\bar{k}\lambda).$$

The rest of the four-momentum

$$P^\Lambda_\mu = \int d\bar{x}\, T^\Lambda_{\mu o}$$

is now found to be

$$P^\Lambda_i = 0,$$

$$P^\Lambda_o = \int d\bar{x}\, \frac{1-a}{4}\left(\Lambda^2 - \dot{\Lambda}\frac{1}{\Lambda}\dot{\Lambda}\right) = \frac{1-a}{2}\sum_{\bar{k}} \omega \tilde{\lambda}(\bar{k})\lambda(\bar{k}).$$

Finally, we have the total momentum and energy

$$P_i = \sum_{\bar{k}\lambda} k_i a^*(\bar{k}\lambda)\, a(\bar{k}\lambda),$$

$$P_o = H = \sum_{\bar{k}\lambda} \omega a^*(\bar{k}\lambda)\, a(\bar{k}\lambda) + \frac{1-a}{2}\sum_{\bar{k}} \omega \tilde{\lambda}(\bar{k})\lambda(\bar{k}).$$

From this it follows that (in matrix notation)

$$\left[H, \begin{pmatrix} a^*(\bar{k}3) \\ a^*(\bar{k}0) \end{pmatrix}\right] = \omega \begin{pmatrix} 1 + \frac{1-a}{2} & \frac{1-a}{2} \\ -\frac{1-a}{2} & 1 - \frac{1-a}{2} \end{pmatrix} \begin{pmatrix} a^*(\bar{k}3) \\ a^*(\bar{k}0) \end{pmatrix},$$

showing—by comparison with (47)—that the energy is not diagonalizable, except in the Fermi gauge ($a = 1$). This means that the longitudinal and scalar photons are not in general stationary states, but mix with each other during time. Only one combination of scalar and longitudinal photons is stationary, namely

$$a^*(\bar{k}3) + a^*(\bar{k}0) = \tilde{\lambda}(\bar{k}).$$

Let us by a natural generalization of the definition of physical states in the Fermi gauge demand that the physical states satisfy

$$\Lambda_+(x)|\Phi> = 0, \tag{48}$$

where Λ_+ is the positive frequency part of Λ. Then it is easy to see that only the transverse photons contribute to the mean value of the energy in a physical state. Furthermore

$$<\Phi|\partial_\mu A^\mu|\Phi> = 0, \tag{6}$$

so that every gauge of the type studied here must be considered as a quantum generalization of the classical Lorentz gauge in the same sense as the Fermi gauge. (It is also seen that eq. (4) is satisfied.)

6. Quantization of the interacting fields

We shall now consider the Maxwell field in interaction with the electron field. The Lagrangian density is taken to be[1]

$$\mathfrak{L} = -\tfrac{1}{4} F_{\mu\nu}F^{\mu\nu} - \Lambda\partial_\mu A^\mu + \frac{a_o}{2}\Lambda^2 + \tfrac{1}{2}[\overline{\psi}, (i\gamma\cdot\partial - m_o)\psi] - \frac{e_o}{2}[\overline{\psi}, \gamma_\mu\psi]A^\mu, \tag{49}$$

where as before we have treated the gauge condition by means of a Λ-field. All the fields are considered to be unrenormalized, and a_o, m_o, e_o are the unrenormalized parameters of the theory. By calling the gauge parameter a_o, we have admitted the possibility of a gauge renormalization, and we have restricted ourselves to the simple gauge conditions of the type (29). The equations of motion are found to be

$$\Box A_\mu + \partial_\mu\partial_\nu A^\nu = \partial_\mu\Lambda - \frac{e_o}{2}[\overline{\psi}, \gamma_\mu\psi], \tag{50}$$

$$\partial_\mu A^\mu = a_o\Lambda, \tag{51}$$

$$(i\gamma\cdot\partial - m_o)\psi = e_o\gamma\cdot A\psi, \tag{52}$$

from which we again derive

$$\Box\Lambda = 0. \tag{53}$$

[1] We use the γ-matrices with $\{\gamma_\mu,\gamma_\nu\} = 2g_{\mu\nu}$ and $\gamma\cdot a = a_\mu\gamma_\mu$. These γ-matrices are self-adjoint, i. e. $\overline{\gamma}_\mu = \gamma_o\gamma_\mu^+\gamma_o = \gamma_\mu$.

The metric operator η, which must also be introduced in this case, with the properties given in section 3, is moreover assumed to satisfy $\overline{\psi} = \eta\psi^{+}\eta\gamma_o$.

The equal-time commutation relations for the Maxwell field and the Λ-field are found to be exactly the same as in the free case (eqs. (14)–(19)). Furthermore we have the following commutation and anticommutation relations:

$$\{\psi(x),\ \psi(y)\}_{x_o = y_o} = 0\,, \tag{54}$$

$$\{\psi(x),\ \overline{\psi}(y)\}_{x_o = y_o} = \gamma_o \delta(\bar{x} - \bar{y})\,, \tag{55}$$

$$[\psi(x),\ A_\mu(y)]_{x_o = y_o} = [\overline{\psi}(x),\ A_\mu(y)]_{x_o = y_o} = 0\,, \tag{56}$$

$$[\psi(x),\ \dot{A}_i(y)]_{x_o = y_o} = [\overline{\psi}(x),\ \dot{A}_i(y)]_{x_o = y_o} = 0\,, \tag{57}$$

$$[\psi(x),\ \Lambda(y)]_{x_o = y_o} = [\overline{\psi}(x),\ \Lambda(y)]_{x_o = y_o} = 0\,, \tag{58}$$

By methods analogous to those used in section 2 we find

$$[\Lambda(x),\ \Lambda(y)] = 0\,, \tag{59}$$

$$[\Lambda(x),\ A_\mu(y)] = -\, i\partial_\mu^x D(x - y)\,, \tag{60}$$

$$[\Lambda(x),\ \psi(y)] = e_o D(x - y)\psi(y)\,, \tag{61}$$

$$[\Lambda(x),\ \overline{\psi}(y)] = -\, e_o D(x - y)\overline{\psi}(y)\,. \tag{62}$$

These are the only integrable commutation relations in the case of the interacting fields. A consequence of the last two relations is for instance that $\Lambda(x)$ commutes with any local bilinear expression in ψ and $\overline{\psi}$, i. e.

$$[\Lambda(x),\ \psi_\alpha(y)\overline{\psi}_\beta(y)] = [\Lambda(x),\ \overline{\psi}_\beta(y)\psi_\alpha(y)] = 0\,. \tag{63}$$

7. Gauge transformation

If we had started with another value for the gauge parameter, say a'_o, then we would have arrived at a different theory of interacting fields. In the case of the free Maxwell field we have however seen that the two gauges could be connected by a gauge transformation

$$A'_\mu = A_\mu + \partial_\mu \chi \tag{64}$$

with

$$\chi(x) = \frac{a_o' - a_o}{2} \frac{1}{\Delta} (x_o \dot{A}(x) - \tfrac{1}{2} A(x)). \tag{65}$$

We shall now see that the transformation (64) with $\chi(x)$ given by (65) also carries us from the gauge a_o to the gauge a_o' in the case of interacting fields, when the electron field is subjected to the transformation

$$\psi'(x) = e^{-i\frac{e_o}{2}\chi(x)} \psi(x) e^{-i\frac{e_o}{2}\chi(x)}. \tag{66}$$

One should here remark that $\chi(x)$ is a q-number which does not commute with $\psi(x)$.

We shall now show that provided A_μ and ψ satisfy the equations of motion and commutation relations for the gauge a_o, then A_μ' and ψ' satisfy the equations of motion and commutation relations for the gauge a_o'.

From eqs. (50) and (64) we find

$$\Box A_\mu' + \partial_\mu \partial_\nu A'^\nu = \partial_\mu A - \frac{e_o}{2} [\bar{\psi}, \gamma_\mu \psi].$$

However, by (63) we have

$$[\bar{\psi}', \gamma_\mu \psi'] = [\bar{\psi}, \gamma_\mu \psi].$$

Likewise by (51), (53), (64), (65) we find

$$\partial_\mu A'^\mu = a_o' A.$$

From (52) and (66) we get

$$(i\gamma \cdot \partial - m_o)\psi' = e_o \gamma \cdot A' \psi' - i\frac{e_o^2}{2} [\chi, \gamma \cdot A] \psi' - \frac{e_o}{2} [\gamma \cdot \partial \chi, \psi'], \tag{67}$$

where we have used the fact that $[\chi(x), A_\mu(y)]$ is a c-number such that

$$e^{-i\frac{e_o}{2}\chi} A_\mu e^{+i\frac{e_o}{2}\chi} = A_\mu - \frac{ie_o}{2} [\chi, A_\mu].$$

Unless a cancellation between the singular terms on the right hand side of eq. (67) occurs, we cannot reduce it to the required form. But as we shall soon see, this cancellation actually occurs. On account of the singular character of the terms we have to treat them with some care. First we find by means of the commutation relations (61) that

$$[\gamma\cdot\partial\chi(x),\psi(y)]_{x_o=y_o} = -\frac{a_o'-a_o}{2\Delta_x}e_o\{\tfrac{1}{2}\gamma_o + x_o\gamma_i\partial_x^i\}\delta(\bar{x}-\bar{y})\psi(\bar{y},x_o),$$

while from (60)

$$[\chi(y),\gamma\cdot A(x)]_{x_o=y_o} = -i\frac{a_o'-a_o}{2\Delta_x}(\tfrac{1}{2}\gamma_o + x_o\gamma_i\partial_x^i)\delta(\bar{x}-\bar{y}).$$

Then

$$ie_o[\chi(y),\gamma\cdot A(x)]_{x_o=y_o}\psi(\bar{y},x_o) + [\gamma\cdot\partial\chi(x),\psi(y)]_{x_o=y_o} = 0.$$

Here we can take $\bar{x} = \bar{y}$ and by use of (66) we see that the last two terms in (67) actually cancel each other.

It is possible to show that the commutation relations are invariant under these finite transformations, but it must actually suffice to show that they are invariant under infinitesimal transformations with $\delta a_o = a_o' - a_o$ infinitesimal. As an example we take the anticommutator (55). Then

$$\delta\{\psi(x),\overline{\psi}(y)\}_{x_o=y_o} = -i\frac{e_o}{2}(\{\{\chi(x),\psi(x)\},\overline{\psi}(y)\}_{x_o=y_o} - \{\psi(x),\{\chi(y),\overline{\psi}(y)\}\}_{x_o=y_o}).$$

Using

$$\{A,\{B,C\}\} = [[A,B],C] + \{B,\{C,A\}\}$$

we find by means of the commutation relations

$$\delta\{\psi(x),\overline{\psi}(y)\}_{x_o=y_o} = -i\frac{e_o}{2}\Big(-\frac{\delta a_o}{2\Delta_x}x_o e_o\delta(\bar{x}-\bar{y})[\overline{\psi}(y),\psi(x)] +$$

$$+2\chi(x)\gamma_o\delta(\bar{x}-\bar{y}) - \frac{\delta a_o}{2\Delta_y}y_o e_o\delta(\bar{x}-\bar{y})[\psi(x),\overline{\psi}(y)] - 2\chi(y)\gamma_o\delta(\bar{x}-\bar{y})\Big)_{x_o=y_o} = 0.$$

The other commutation relations are shown to be invariant in an analogous manner.

It should be remarked that the A-field is not supposed to transform, in other words that it is assumed to be gauge invariant. This is also consistent with the manifestly gauge independent form of the left hand side of eq (50). *The A-field has more to do with the general mode of description (covariant gauges) than with the particular gauge in which this description is carried out.* Also the constants m_0 and e_0 must be supposed to be gauge independent.

8. Renormalization

A characteristic feature of the renormalization in the Fermi gauge is the occurrence of a term

$$-\frac{L}{1-L}\partial_\mu\partial_\nu A^\nu \tag{68}$$

in the renormalized current. This term cannot be accounted for by charge or wave function renormalization, but has to be introduced by gauge invariance arguments[1]. If the correction to the photon propagator is calculated in the lowest order in the unrenormalized theory, it is seen that starting from the Fermi gauge, one does not end up with a propagator which behaves near the mass shell like a propagator in the Fermi gauge. In the renormalized Fermi gauge the term (68) brings us back again to this form and hence the inclusion of this term must be considered as a renormalization of the gauge parameter. We shall show that this gauge renormalization comes out quite naturally in the present formulation.

Let us now introduce the renormalized mass (m), charge (e) and gauge parameter (a) by

$$m_o = m - \delta m, \tag{69}$$

$$e_o = \frac{e}{\sqrt{1-L}}, \tag{70}$$

$$a_o = (1-K)a, \tag{71}$$

where δm, L, K are renormalization constants to be determined later on. Likewise we introduce the renormalized fields $\psi^{(r)}$, $A_\mu^{(r)}$ and $\Lambda^{(r)}$ by

$$\psi = N\psi^{(r)}, \tag{72}$$

$$A_\mu = \sqrt{1-L}\,A_\mu^{(r)}, \tag{73}$$

$$\Lambda = \frac{\sqrt{1-L}}{1-K}\Lambda^{(r)} \tag{74}$$

where we have anticipated the result that the wave function renormalization constant of the Maxwell field is the same as the charge renormalization constant. The wave function renormalization constant of the Λ-field has been chosen such that the gauge condition for the renormalized fields reads

$$\partial_\mu A^{(r)\mu} = a\Lambda^{(r)}. \tag{75}$$

[1] G. KÄLLÉN, ibid., p. 346.

One might object that the Λ-field should not be renormalized as it does apparently not take part in the interaction on account of eq. (53). But a glance on eq. (61) shows that this is not true.

Leaving out the superscript (r) on the renormalized fields we now find the renormalized equations of motion

$$\Box A_\mu + \partial_\mu \partial_\nu A^\nu = \partial_\mu \Lambda - J_\mu , \tag{76}$$

$$J_\mu = \frac{eN^2}{2(1-L)} [\bar{\psi}, \gamma_\mu \psi] - \frac{K}{1-K} \partial_\mu \Lambda , \tag{77}$$

$$(i\gamma \cdot \partial - m)\psi = -f , \tag{78}$$

$$f = - e\gamma \cdot A \psi + \delta m \psi , \tag{79}$$

$$\partial_\mu A^\mu = a\Lambda . \tag{80}$$

It is seen that a term of the type (68) is now present in the renormalized current. We shall actually find in the next section that $K = L$. The commutation relations between the renormalized fields may easily be derived from the previously stated relations for the unrenormalized fields.

9. Determination of the renormalization constants

The renormalization constants are usually expressed by integrals over some spectral functions. By the well-known arguments we can write the vacuum expectation value of the current-current commutator as

$$\langle o | [J_\mu(x), J_\nu(y)] | o \rangle = - i(g_{\mu\nu}\Box + \partial_\mu \partial_\nu) \int_o^\infty d\lambda \Delta(x-y, \lambda) \Pi(\lambda) , \tag{81}$$

where $\Pi(\lambda)$ is a positive definite spectral function[1] (zero for negative λ) and

$$\Delta(x-y, \lambda) = - 2\pi i \int dp \varepsilon(p) \delta(p^2 - \lambda) e^{-ip(x-y)} \tag{82}$$

is the singular function with mass $\sqrt{\lambda}$.

In order to find the renormalization constants in terms of this spectral function the standard procedure is to integrate (81) with suitable limit conditions, which express how the interacting field asymptotically goes over

[1] As the definition (81) is obviously gauge invariant we may use the result from the Fermi gauge (G. KÄLLÉN, ibid., p. 350).

into the incoming free field. Asymptotic conditions are, however, very difficult to apply, because the limits are not well-defined. Furthermore, one finds in the conventional theory of the Fermi gauge that the matrix element of the renormalized field between vacuum and a one-photon state is different from the same matrix element of the incoming free field, because[1]

$$\langle o|A_\mu(x)|k\rangle = (g_{\mu\nu} - M\partial_\mu\partial_\nu)\langle o|A^{(in)\nu}(x)|k\rangle \tag{83}$$

where M is a non-vanishing constant. Asymptotic conditions of the conventional form[2] can therefore not be applied to quantum electrodynamics.

It is, however, possible to integrate (81) without transitions to the limit of the infinite past or future. Let us define the field

$$A_\mu^{(y_0)}(x) = -\int d\bar{y} D(x-y) \overleftrightarrow{\partial}_{y^0} A_\mu(y). \tag{84}$$

By an elementary integration by parts we find

$$A_\mu(x) = A_\mu^{(y_0)}(x) + \int_{y_0}^{x_0} dx' D(x-x') \Box A_\mu(x'). \tag{85}$$

Now from the equal-time commutation relations we find

$$[A_\mu^{(y_0)}(x), J_\nu(y)] = i\frac{K}{1-L}\partial_\mu\partial_\nu D(x-y). \tag{86}$$

Then we have

$$[A_\mu(x), J_\nu(y)] = i\frac{K}{1-L}\partial_\mu\partial_\nu D(x-y) - \int_{y_0}^{x_0} dx' D(x-x')[J_\mu(x'), J_\nu(y)],$$

where we also have used the equations of motion and the fact that the A-field commutes with the current. If we take the vacuum expectation value of this equation and insert (81) we find after some calculation

$$\left.\begin{aligned} \langle o|[A_\mu(x), J_\nu(y)]|o\rangle &= i\frac{K}{1-L}\partial_\mu\partial_\nu D(x-y) + \\ + i(g_{\mu\nu}\Box + \partial_\mu\partial_\nu)\int_0^\infty d\lambda (\Delta(x-y,\lambda) - D(x-y))\frac{\Pi(\lambda)}{\lambda} &- \\ - i(g_{\mu\nu} - g_{\mu 0}g_{\nu 0})D(x-y)\int_0^\infty d\lambda\, \Pi(\lambda), & \end{aligned}\right\} \tag{87}$$

[1] G. Källén, ibid., p. 344.
[2] H. Lehmann, K. Zymanzik, W. Zimmermann, Nuovo Cimento **1** (1955) 425.

where we have used the relation

$$\int_{y_o}^{x_o} dx' D(x-x')\Delta(x'-y,\lambda) = \frac{1}{\lambda}(\Delta(x-y,\lambda) - D(x-y)). \tag{88}$$

The last term in (87) is non-covariant and must therefore be identically zero, i. e.

$$\int_o^\infty d\lambda \Pi(\lambda) = 0. \tag{89}$$

This also follows from the application of current conservation to (87). In view of the positive definite character of $\Pi(\lambda)$ this result seems quite nonsensical. A suitable regularization procedure, however, removes this difficulty[1], and without going into details we shall in the following assume eq. (89) to be valid.

By a similar procedure we can now integrate (87) to get

$$\left.\begin{aligned} &\langle o|[A_\mu(x), A_\nu(y)]|o\rangle = \\ &= -i\left[(g_{\mu\nu}\Box + \partial_\mu\partial_\nu)\left(\frac{1}{1-L} - \overline{\Pi}(o)\right) - a\frac{1-K}{1-L}\partial_\mu\partial_\nu\right]E(x-y) - \\ &\quad - i(g_{\mu\nu}\Box + \partial_\mu\partial_\nu)\int_o^\infty d\lambda \Delta(x-y,\lambda)\left(\frac{\Pi(\lambda)}{\lambda^2} - \overline{\Pi}'(o)\delta(\lambda)\right), \end{aligned}\right\} \tag{90}$$

where

$$\overline{\Pi}(o) = \int_o^\infty d\lambda \frac{\Pi(\lambda)}{\lambda}, \tag{91}$$

$$\overline{\Pi}'(o) = \int_o^\infty d\lambda \frac{\Pi(\lambda)}{\lambda^2}, \tag{92}$$

and we have used the relation

$$\int_{y_o}^{x_o} dx' D(x-x')D(x'-y) = E(x-y).$$

which can be obtained either from (88) by letting $\lambda \to o$ or by direct calculation.

Our renormalization requirement is then that this commutator shall behave like the commutator for the free Maxwell field in the gauge a, near the mass shell. If we disregard the δ-function in the last term this gives us

[1] J. MOFFAT, Nucl. Phys. **16** (1960) 304.

$$\frac{1}{1-L} = 1 + \overline{\Pi}(o), \tag{93}$$

$$\frac{1-K}{1-L} = 1, \tag{94}$$

i. e. $K = L$.

A similar procedure may be carried out for the electron field, for which the spectral functions are defined by

$$\langle o | \{ f(x), \bar{f}(y) \} | o \rangle = -2\pi \int dp \varepsilon(p) (\Sigma_1(p^2) - (\gamma \cdot p - m) \Sigma_2(p^2)) e^{-ip\cdot(x-y)}. \tag{95}$$

The renormalization constants are then found to be given by

$$\delta m = N^2 \overline{\Sigma}_1(m^2), \tag{96}$$

$$\frac{1}{N^2} = 1 + \overline{\Sigma}_2(m^2) - 2m \overline{\Sigma}_1'(m^2), \tag{97}$$

as in the conventional theory of the Fermi gauge. We have used the notation

$$\overline{\Sigma}_i(m^2) = \int_{m^2}^{\infty} d\lambda \frac{\Sigma_i(\lambda)}{\lambda - m^2}, \tag{98}$$

$$\overline{\Sigma}_1'(m^2) = \int_{m^2}^{\infty} d\lambda \frac{\Sigma_1(\lambda)}{(\lambda - m^2)^2}. \tag{99}$$

10. Asymptotic conditions for the Maxwell field

We now assume the existence of incoming free fields $A_\mu^{(in)}$, $\Lambda^{(in)}$, such that

$$\Box A_\mu^{(in)} + \partial_\mu \partial^\nu A_\nu^{(in)} = \partial_\mu \Lambda^{(in)}, \tag{100}$$

$$\partial^\mu A_\mu^{(in)} = a \Lambda^{(in)}, \tag{101}$$

$$[A_\mu^{(in)}(x), A_\nu^{(in)}(y)] = -i(g_{\mu\nu}\Box + (1-a)\partial_\mu \partial_\nu) E(x-y). \tag{102}$$

It is then possible to show that with a suitable value for M the following asymptotic conditions are consistent:

$$\Lambda = \Lambda^{(in)}, \tag{103}$$

$$A_\mu = A_\mu^{(in)} - M\partial_\mu \Lambda + \int dx' D_R(x-x') J_\mu(x'), \tag{104}$$

where D_R is the retarted photon Green function[1]. It is quite clear that these conditions are consistent with the equations of motion. But still we have to show that for a suitable M they will also be consistent with the spectral resolution of the commutator. From a spectral analysis of $\langle o|[A_\mu(x), A_\nu^{(in)}(y)]|o\rangle$ it follows by means of the equations of motion and (103) that

$$\langle o|[J_\mu(x), A_\nu^{(in)}(y)]|o\rangle = 0. \tag{105}$$

From this we find by means of (104) that

$$\langle o|A_\mu(x)|k,in\rangle = \langle o|A_\mu^{(in)}(x)|k,in\rangle - M\partial_\mu \langle o|\Lambda(x)|k,in\rangle, \tag{106}$$

which is identical to (83) in the Fermi gauge ($a = 1$).

By a simple calculation we find by comparison with (90) that

$$2M = \overline{\Pi}'(o) = \int_o^\infty d\lambda \frac{\Pi(\lambda)}{\lambda^2}, \tag{107}$$

which also follows in the conventional theory of the Fermi gauge[2].

We are now in a position to calculate the spectral functions in the lowest order. The result is

$$\Pi^{(o)}(p^2) = \frac{e^2}{12\pi^2}\left(1 + \frac{2m^2}{p^2}\right)\sqrt{1 - \frac{4m^2}{p^2}}\,\Theta(p^2 - 4m^2), \tag{108}$$

$$\Sigma_1^{(o)}(p^2) = \frac{me^2}{16\pi^2}\left(1 - \frac{m^2}{p^2}\right)\left(3 - a\frac{m^2}{p^2}\right)\Theta(p^2 - m^2), \tag{109}$$

$$\Sigma_2^{(o)}(p^2) = a\frac{e^2}{16\pi^2}\left(1 - \left(\frac{m^2}{p^2}\right)^2\right)\Theta(p^2 - m^2). \tag{110}$$

[1] The asymptotic condition (104) has been found by ROLLNIK et al., Z. f. Phys. **159** (1960) 482, for the case of the Fermi gauge. The author is grateful to G. KÄLLÉN for calling his attention to this work and for pointing out that there may be some formal difficulties with this asymptotic condition.

[2] In order to find (107) one should use the equation

$$\langle o|[A_\mu - A_\mu^{(in)} + M\partial_\mu \Lambda, A_\nu - A_\nu^{(in)} + M\partial_\nu \Lambda]|o\rangle = \langle o|[A_\mu - A_\mu^{(in)}, A_\nu - A_\nu^{(in)}]|o\rangle,$$

and the derivation now proceeds exactly as in G. KÄLLÉN, ibid., p. 350.

For $a = 1$ these reduce to the usual Fermi gauge spectral functions. It is seen that the wave function renormalization constant $1/N^2$ is not ultraviolet divergent for $a = 0$ (the Landau gauge) and not infrared divergent for $a = 3$ (the Yennie gauge) in the lowest order. This fact has been known for some time[1]. The self-mass presents in the lowest order a special problem, which we shall discuss in the next section.

11. The gauge dependence of the self-mass of the electron

We have seen in section 7 that the bare mass of the electron is not supposed to change under gauge transformations. As the physical electron mass obviously must be gauge independent we can immediately conclude that the self-mass δm must be gauge independent.

If, however, we calculate the difference in self-mass between an arbitrary gauge and the Fermi gauge in the lowest order we find by (109)

$$\delta m^{(o)} - \delta m_F^{(o)} = \bar{\Sigma}_1^{(o)}(m^2) - \bar{\Sigma}_{1F}^{(o)}(m^2) \tag{111}$$

$$= \int_{m^2}^{\infty} d\lambda \frac{\Sigma_1^{(o)}(\lambda) - \Sigma_{1F}^{(o)}(\lambda)}{\lambda - m^2} \tag{112}$$

$$= (1 - a) \frac{me^2}{16\pi^2}, \tag{113}$$

where we have denoted quantities from the Fermi gauge ($a = 1$) with a subscript F.

Unless we can find an error in our derivation, this result shows that there is an inconsistency in the theory. The error lies, however, in the step from (111) to (112), because (111) is the difference between two infinite numbers, the value of which depends on the method we prescribe for the calculation of this difference. The result shows that the prescription (112) is not correct and we must now try to find a better way of evaluating the difference.

If we introduce a cut-off in the photon propagator the formerly infinite numbers will become finite. Hence, we get

[1] B. Zumino, Journ. Math. Phys. **1** (1960) 1.

$$D_{\mu\nu}(k) = -i\frac{g_{\mu\nu}}{k^2} + i(1-a)\frac{k_\mu k_\nu}{(k^2)^2} \to \left(-i\frac{g_{\mu\nu}}{k^2} + i(1-a)\frac{k_\mu k_\nu}{(k^2)^2}\right)\frac{-\lambda^2}{k^2-\lambda^2} =$$

$$= -i\left(\frac{1}{k^2} - \frac{1}{k^2-\lambda^2}\right)g_{\mu\nu} + i(1-a)k_\mu k_\nu \cdot \left(\frac{1}{(k^2)^2} + \frac{1}{\lambda^2}\left(\frac{1}{k^2} - \frac{1}{k^2-\lambda^2}\right)\right)$$

where λ^2 is the cut-off parameter, which is supposed to be gauge independent. In the Fourier transform of the commutator and anti-commutator the expression

$$g_{\mu\nu}\delta(k^2) + (1-a)k_\mu k_\nu \delta'(k^2)$$

must then be replaced by

$$g_{\mu\nu}(\delta(k^2) - \delta(k^2-\lambda^2)) + (1-a)k_\mu k_\nu \cdot \left(\delta'(k^2) - \frac{1}{\lambda^2}(\delta(k^2) - \delta(k^2-\lambda^2))\right).$$

This expression is now used in the calculation of the spectral functions and we find the difference

$$\left.\begin{aligned} \Sigma_1^{(o)}(p^2) - \Sigma_{1F}^{(o)}(p^2) &= \frac{me^2}{16\pi^2}(1-a)\left(1-\frac{m^2}{p^2}\right)\frac{m^2}{p^2}\Theta(p^2-m^2) - \\ &- \frac{me^2}{32\pi^2}(1-a)\frac{p^2-m^2}{\lambda^2}\left(\left(1-\frac{m^2}{p^2}\right)^2\Theta(p^2-m^2) - \right. \\ &\left. - \left(1+\frac{\lambda^2-m^2}{p^2}\right)\sqrt{\frac{\lambda(p^2,m^2,\lambda^2)}{p^2}}\,\Theta(p^2-(m+\lambda)^2)\right). \end{aligned}\right\} \quad (114)$$

Here[1]

$$\lambda(x,y,z) = x^2 + y^2 + z^2 - 2xy - 2yz - 2zx$$

is a quadratic form.

Remark that the last terms in (114) vanish for $\lambda^2 \to \infty$. If we insert (114) in (112), the integration can be performed and the result is identically zero. The original result (113) is exactly cancelled by a contribution from the last terms in (114). One should notice that the step from (111) to (112) now is perfectly allowed because both numbers in (111) are finite. Thus with this prescription the self-mass is gauge independent also in the lowest order.

[1] G. Källén, Elementary Particle Physics (Addison-Wesley, 1964).

The considerations in this section are a nice illustration of how carefully one must treat the infinite numbers met in canonical field theories of this kind.

12. Conclusions

It appears as if quantum electrodynamics in the covariant gauges of the type studied in this work is as consistent as the conventional theory of the Fermi gauge. But it is also clear that the formulation in that gauge is the simplest, not only because the photon propagator has its simplest form here, but also because the energy is not diagonalizable in any other gauge than the Fermi gauge. The transformations which connect different covariant gauges are of a rather singular nature. Although it migh be conceivable that quantum electrodynamics would only be consistent for one choice of gauge parameter, no special reasons have as yet been found which would support this possibility. One might argue that the apparently gauge dependent self-mass could be an indication of an inconsistency of quantum electrodynamics, but it is clear that this inconsistency only arises because the perturbation calculation gives rise to a divergent self-mass, and it therefore belongs to the general class of defects of the theory which are circumvented by the renormalization procedure.

Acknowledgements

The author wishes to thank Dr. K. Johnson and Professor C. Møller for helpful discussions and critical comments. In particular the author wishes to thank Professor G. Källén for his kind interest in this work and for his encouraging criticism.

APPENDIX

The distribution

$$E(x) = 2\pi i \int dp\, \varepsilon(p) \delta'(p^2) e^{-ipx} \tag{A. 1}$$

has obviously the properties

$$\Box E(x) = D(x),$$

$$E(-x) = -E(x),$$

$$E(x) = \frac{\partial}{\partial \mu^2} \Delta(x, \mu^2) \Big|_{\mu^2 = o}$$

where $\Delta(x, \mu^2)$ is the well-known singular function

$$\Delta(x, \mu^2) = -2\pi i \int dp\, \varepsilon(p) \delta(p^2 - \mu^2) e^{-ipx}. \tag{A. 2}$$

By integration over p_0 and over angles we find from (A. 1)

$$E(x) = -\int \frac{d\bar{p}}{(2\pi)^3} \frac{e^{i\bar{p}\cdot\bar{x}}}{2\omega} \frac{\partial}{\partial \omega} \left(\frac{\sin \omega x_o}{\omega} \right) \tag{A. 3}$$

$$= \frac{1}{4\pi^2} \int_o^\infty d\omega \cos \omega |\bar{x}| \frac{\sin \omega x_o}{\omega}. \tag{A. 4}$$

From this we immediately get

$$E(x) = \frac{\varepsilon(x)}{8\pi} \Theta(x^2), \tag{A. 5}$$

and from (A. 3)

$$E(\bar{x}, o) = \dot{E}(\bar{x}, o) = \ddot{E}(\bar{x}, o) = 0; \; \dddot{E}(\bar{x}, o) = \delta(\bar{x}).$$

From (A. 4) it is clear that the positive frequency part of $E(x)$ is divergent for $\omega \to 0$. But it also seems as if the positive frequency part of $\partial_\mu E(x)$

were convergent. Let us therefore study this divergence somewhat closer. We use here the well-known expansions of the singular functions

$$\Delta(x,\mu^2) = -\frac{1}{2\pi}\varepsilon(x)\delta(x^2) + \frac{\mu^2}{8\pi}\varepsilon(x)\Theta(x^2)\left(1-\frac{\mu^2}{8}x^2\right) + O(\mu^4),$$

$$\Delta^{(1)}(x,\mu^2) = -\frac{1}{2\pi^2}\frac{1}{x^2} + \frac{\mu^2}{4\pi^2}\log\frac{\gamma\mu|x|}{2} - \frac{\mu^2}{8\pi^2} +$$

$$+\frac{\mu^4 x^2}{32\pi^2}\left(\frac{5}{4} - \log\frac{\gamma\mu|x|}{2}\right) + O(\mu^4).$$

Equation (A. 5) is easily seen to follow from the first equation by differentiation after μ^2. By differentiation of the second we get

$$\frac{\partial\Delta^{(1)}(x,\mu^2)}{\partial\mu^2} = \frac{1}{4\pi^2}\log\frac{\gamma\mu|x|}{2} + \frac{\mu^2x^2}{16\pi^2}\left(\frac{5}{4} - \log\frac{\gamma\mu|x|}{2}\right) - \frac{\mu^2x^2}{64\pi^2} + O(\mu^2),$$

and this is clearly not convergent for $\mu^2 \to 0$. But the gradient of this expression is convergent in the limit

$$\partial_\lambda\frac{\partial\Delta^{(1)}(x,\mu^2)}{\partial\mu^2} = \frac{\partial}{\partial\mu^2}\partial_\lambda\Delta^{(1)}(x,\mu^2) \to \frac{1}{4\pi^2}\frac{x_\lambda}{x^2}.$$

This means that we may define the distributions

$$\partial_\lambda E^{(1)}(x) = \frac{\partial}{\partial\mu^2}\partial_\lambda\Delta^{(1)}(x,\mu^2)\Big|_{\mu^2=0},$$

$$\partial_\lambda E^{(\pm)}(x) = \frac{\partial}{\partial\mu^2}\partial_\lambda\Delta^{(\pm)}(x,\mu^2)\Big|_{\mu^2=0},$$

while the distributions $E^{(1)}$ and $E^{(\pm)}$ do not exist.

From (A. 3) it now easily follows that

$$E(x) = \frac{1}{2\Delta}(D(x) - x_0\dot{D}(x)).$$

Likewise it follows from

$$\partial_\mu E^{(1)}(x) = 2\pi i\int dk k_\mu\delta'(k^2)e^{-ik\cdot x}$$

that

$$\partial_\mu E^{(1)}(x) = \frac{1}{2\Delta}\,\partial_\mu(D^{(1)}(x) - x_0\dot{D}^{(1)}(x)), \tag{A. 6}$$

where $\frac{1}{2\Delta}$ and ∂_μ *cannot* be interchanged.

In order to find the propagator

$$D_{\mu\nu}(x-y) = \tfrac{1}{2}\langle o|\{A_\mu(x), A_\nu(y)\}|o\rangle + \tfrac{1}{2}\,\varepsilon(x-y)\langle o|[A_\mu(x), A_\nu(y)]|o\rangle \tag{A. 7}$$

we shall first calculate the vacuum expectation value of the anti-commutator. We express A_μ in terms of the Fermi field through eq. (36). Using the fact that

$$\langle o|\{A^F_\mu(x), A^F_\nu(y)\}|o\rangle = -\,g_{\mu\nu}D^{(1)}(x-y)$$

we get by means of (37)

$$\langle o|\{\Lambda(x), A^F_\nu(y)\}|o\rangle = -\,\partial^x_\nu D^{(1)}(x-y),$$

$$\langle o|\{\Lambda(x), \Lambda(y)\}|o\rangle = 0.$$

Then from these equations and eqs. (35) and (A. 6) we finally get

$$\langle o|\{A_\mu(x), A_\nu(y)\}|o\rangle = -\,g_{\mu\nu}D^{(1)}(x-y) - (1-\alpha)\partial_\mu\partial_\nu E^{(1)}(x-y).$$

From the properties of $E(x)$ it follows that

$$\varepsilon(x-y)\partial_\mu\partial_\nu E(x-y) = \partial_\mu\partial_\nu(\varepsilon(x-y)E(x-y)),$$

so that we may write the propagator in the form

$$D_{\mu\nu}(x-y) = -\,g_{\mu\nu}\left(\tfrac{1}{2}\,D^{(1)}(x-y) + \frac{i}{2}\,\varepsilon(x-y)D(x-y)\right) -$$

$$-\,(1-\alpha)\frac{\partial}{\partial\mu^2}\,\partial_\mu\partial_\nu\left(\tfrac{1}{2}\,\Delta^{(1)}(x-y,\mu^2) + \frac{i}{2}\,\varepsilon(x-y)\Delta(x-y,\mu^2)\right)\Bigg|_{\mu^2=0}.$$

In momentum space we find

$$D_{\mu\nu}(k) = -\,g_{\mu\nu}\frac{i}{k^2+i\varepsilon} + (1-\alpha)\frac{\partial}{\partial\mu^2}\,k_\mu k_\nu\,\frac{i}{k^2-\mu^2+i\varepsilon}\Bigg|_{\mu^2=0} =$$

$$= -\,i\frac{g_{\mu\nu}}{k^2+i\varepsilon} + i(1-\alpha)\frac{k_\mu k_\nu}{(k^2+i\varepsilon)^2}.$$

Indleveret til Selskabet den 22. juni 1966.
Færdig fra trykkeriet den 10. februar 1967.

Matematisk-fysiske Meddelelser
udgivet af
Det Kongelige Danske Videnskabernes Selskab
Bind **35,** nr. 12

Mat. Fys. Medd. Dan. Vid. Selsk. **35,** no. 12 (1967)

POLARIZED CRYSTAL SPECTRA OF OPTICALLY ACTIVE IONS

II. Cobalt tris ethylenediamine ion

BY

R. DINGLE and C. J. BALLHAUSEN

København 1967
Kommissionær: Munksgaard

Synopsis

The polarized absorption spectra of d,l $Coen_3Cl_3.3H_2O$, d,l $[Coen_3Cl_3]_2.NaCl.6H_2O$ and D $[Coen_3Cl_3]_2.NaCl.6H_2O$ and the deuterated species have been recorded at liquid helium temperatures. Using all of the transitions $(t_{2g})^6 \rightarrow (t_{2g})^5(e_g)$ we get $C = 3{,}925\,cm^{-1}$ and $10Dq = 25{,}275\,cm^{-1}$. At 4.2 °K a discrete vibrational structure is found in the axial, π and σ components of the $^1A_{1g} \rightarrow {}^1T_{1g}(O_h)$ transition. Since the axial and σ transverse spectra match, the transition intensity is derived via an electric dipole mechanism. The lowest line in the axial, π and σ spectrum falls at $18{,}960 \pm 2\,cm^{-1}$. At the origin the non-cubic potential field in these complexes is estimated to be $0 \pm 4\,cm^{-1}$, while at the Franck-Condon maximum extrapolation of the symmetric progression leads to a value of the "trigonal" splitting of about $10\,cm^{-1}$. Furthermore 10–15 % of the total intensity in $Co(en)_3{+}{+}{+}$ arises from electronic processes and tbe remainder from vibronic couplings. A discussion of these features leads to the result that the measured circular dicroism of a solution of optically active $Co(en)_3{+}{+}{+}$ ions is most likely to be explained by assuming two conformers to be present in solution as originally suggested by Woldbye.

PRINTED IN DENMARK
BIANCO LUNOS BOGTRYKKERI A/S

Introduction

Recently, a number of investigations that deal with the crystal absorption spectum[1][2][3] and the circular dichroism spectrum (C.D.)[2] of the tris-ethylenediamine Cobalt(III) ion, $Co(en)_3^{+3}$, have been reported. In these papers the results were analyzed assuming an effective molecular D_3 point group symmetry.

The solution absorption spectrum[4] corresponds to that expected on the basis of a simple octahedral O_h crystal field model [5] viz:

$$^1A_{1g} \rightarrow {}^1T_{1g} \quad \text{found at} \quad \sim 21{,}000 \text{ cm}^{-1}$$
$$^1A_{1g} \rightarrow {}^1T_{2g} \quad \text{found at} \quad \sim 29{,}000 \text{ cm}^{-1}$$

The broad, weak absorption at 10,000–16,000 cm^{-1} has further been associated[6] with the spin forbidden transition,

$$^1A_{1g} \rightarrow {}^3T_{1g}.$$

In the main those features were also found in the crystal spectra[1] of $Co(en)_3^{+3}$. In particular the axial spectra, reported for pure[2][8] and for dilute[3] crystals, predicted a ^1E (D_3) state in the region of the $^1T_{1g}(O_h)$ absorption. However, the almost octahedral environment made the evaluation of trigonal field parameters[3] rather hazardous. In fact, and this aspect has been largely ignored, these spectra do not give conclusive evidence that trigonal field, D_3 selection rules are adhered to in this compound. Furthermore, recent investigations of the analogous nickel (II) tris-ethylenediamine complex[7] have shown that the D_3 selection rules are not particularly well obeyed.

Much of the interest of these studies has been to characterize the trigonal field parameters, to establish the distribution of the absorption bands intensities and to elucidate the source of this spectral intensity. In some studies [2][3][8] the results have then been compared with the C.D. measurements for this ion in solution and in axial crystals.

Because the absorption bands and the C.D. curves are broad, and because the empirical parameters to be estimated are small, much un-

certainty exists with regard to some of the more fundamental quantities necessary for a succesful treatment of the problem. As a result, we have undertaken a study of the spectra in oriented crystals at 4.2 °*K* in the hope that sufficient resolution of the absorption bands will obtain and that more precise information may become available. A preliminary report of this work[9] has shown this to be the case.

Experimental

Polarized crystal spectra have been taken at ~ 300°, 80° and 4.2 °*K*. A Cary 14 spectrophotometer has been used except in cases where increased resolution has been desired and then a Zeiss 2-metre grating spectrograph (dispersion ~ 3 Å/mm in the region of interest) has been used. A microcrystal technique[10] has been used to record the total region of absorption of thin crystals (i. e. 5000–33,000 cm^{-1}). In the 4.2 °*K* spectra thicker crystals were used so that the weaker regions of absorption, which are of more concern in these spectra, show up more clearly.

Extinction coefficients in the crystal are defined as

$$\varepsilon = \frac{[\text{O.D}]\,[\text{M.W.}]}{\text{t.d } 1000}$$

where O.D. = optical density
M.W. = molecular weight
t = crystal thickness in cm
d = density in g/cc

Spectra are reported for pure single crystals, oriented and identified by means of *X*-ray techniques.

Crystal structures

d,l Co $en_3Cl_3.3H_2O$ (here after I): Trigonal[11], space group $P_{3C1}-D^4_{3d}$

a = 11.50 Å — molecular symmetry D_3

c = 15.52 Å — cobalt site symmetry C_3

z = 4

These crystals are hexagonal plates with (0001) well developed or thick hexagonal needles with $\{11\bar{2}0\}$ well developed. Axial spectra have been

taken on (0001). The unique C_3 axis of the unit cell corresponds to the C_3 axis of the molecule and both are normal to this face. Transverse spectra, with the electric vector parallel (π) or perpendicular (σ) to the C_3 axis were taken on $\{11\bar{2}0\}$ and $\{10\bar{1}0\}$.

The crystal of the other complexes studied grow in similar habits to those described above and spectra were observed in an analogous manner.

d,l $[Co\ en_3Cl_3]_2.NaCl.6H_2O$ (II): Trigonal[12], space group $P_{\bar{3}C1} - D_{3d}^2$

$a = 11.45$ Å — molecular symmetry D_3

$c = 15.68$ Å — cobalt site symmetry C_3

$z = 2$

Axial spectra were taken on (0001); transverse on $(11\bar{2}0)$

D $[Co\ en_3Cl_3]_2.NaCl.6H_2O$ (III): Trigonal[13], space group $P_3 - C_3^1$

$a = 11.47$ Å — molecular symmetry D_3

$c = 8.06$ Å — cobalt site symmetry C_3

$z = 1$

Axial spectra were taken on (0001); transverse on $\{11\bar{2}0\}$.

The deuterated species of the latter two compounds, IV and V respectively, grow in the same manner and are considered to be isomorphous and isostructural with the parent protonated species.

Results

300 °*K* spectra:

In the regions where the studies overlap, these spectra are in qualitative agreement with those reported earlier[1] [2] [3]. Since the spectra for I–V are so similar, we report details for one compound only. (II, Table 1, Figure 1).

Some care has been taken in measuring the π spectrum in the region 25,000–33,000 cm^{-1} and in all cases we confirm the earlier report[1] concerning the appearance of an absorption band in this region.

In the region 10,000–15,000 cm^{-1} there is a broad weak absorption (Figure 2), similar to that seen in solutions of $Co\ en_3^{3+}$. The absorption is not anisotropic in the crystal.

TABLE 1. Crystal Spectral Results for d,l 2[Co en_3Cl_3].NaCl.$6H_2O$ at various temperatures.

300 °K	ν_{max} cm^{-1}	$\varepsilon_{max} \pm 10\%$	$\Delta\nu_{max}(\sigma\text{-}\pi)$	$\varepsilon_\pi/\varepsilon_\sigma$	D_3 assignment	C_3 assignment
axial	21400	100	—	—	$^1E^a$	$^1E^b$
	29200	130	—	—	$^1E^b$	$^1E^b$
	~14000	1	—	—	triplet	triplet
π	21285	130	+ 140	1.30	$^1A_2$	^1A
	29650	60	− 450	0.46	$^1E^b \times \varepsilon$ or $^1A_1 \times \alpha_2$	^1A
	~14000	~1	—	~1.0	triplet	triplet
σ	21425	100	+ 140	1.30	$^1E^a$	$^1E^a$
	29200	130	− 450	0.46	$^1E^b$	$^1E^b$
	~14000	~1	—	~1.0	triplet	triplet
80 °K*						
axial, π, σ	13500	~0.5	—	1.0	$^3T_{1g}(O_h)$	—
	17750	~2.0	—	1.0	$^3T_{2g}(O_h)$	

* For spin-allowed transitions add ~300 cm^{-1} to each ν_{max} and reduce each ε_{max} by about 10—15 % to generate 80 °K results. The spectrum at 4.2 °K is very little altered to that at 80 °K if the vibrational finestructure (Table 2) is ignored.

80 °K spectra:

Compared to the above spectra these measurements show an overall shift of ν_{max} values to higher energies, a reduction in the intensity of the

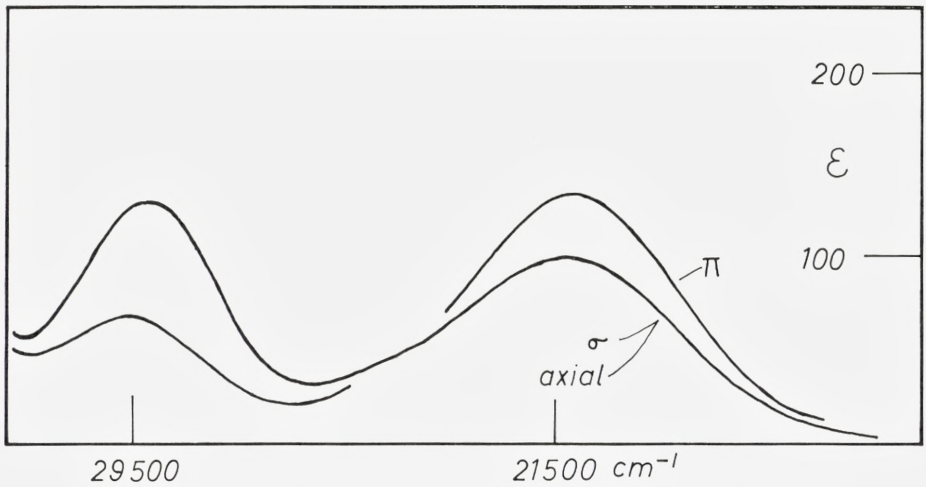

Fig. 1. The room temperature crystal spectrum of d,12 [Co en_3Cl_3].NaCl6H_2O.

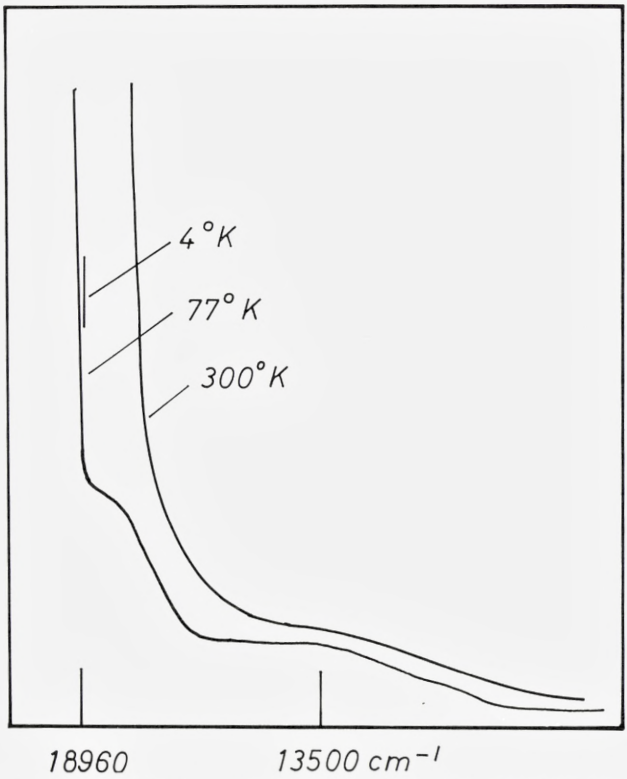

Fig. 2. The effect of temperature on the spectrum of d,1 [Co en_3Cl_3].NaCl.$6H_2O$ in the region of the spin forbidden transitions to $^3T_{1g}$ and $^3T_{2g}$.

21,500 cm^{-1} and 29,500 cm^{-1} absorption bands and the resolution of two weak absorption bands on the low energy side of 21,500 cm^{-1} (Figure 2).

4.2 °*K* spectra:

With one major exception these spectra are, in general similar to those obtained at 80 °*K*. The low frequency side of the 21,500 cm^{-1} bands develops well resolved vibrational structure, the shape and resolution of which is dependent on the particular crystal lattice under investigation. Crystals I and II are almost indistinguishable with the latter the better resolved (Figure 3). The structure in III is less obvious than in II and is also altered somewhat from that seen in Figure 3. Finally the deuterated species IV and V show frequency shifts that may be correlated with changes in zero point

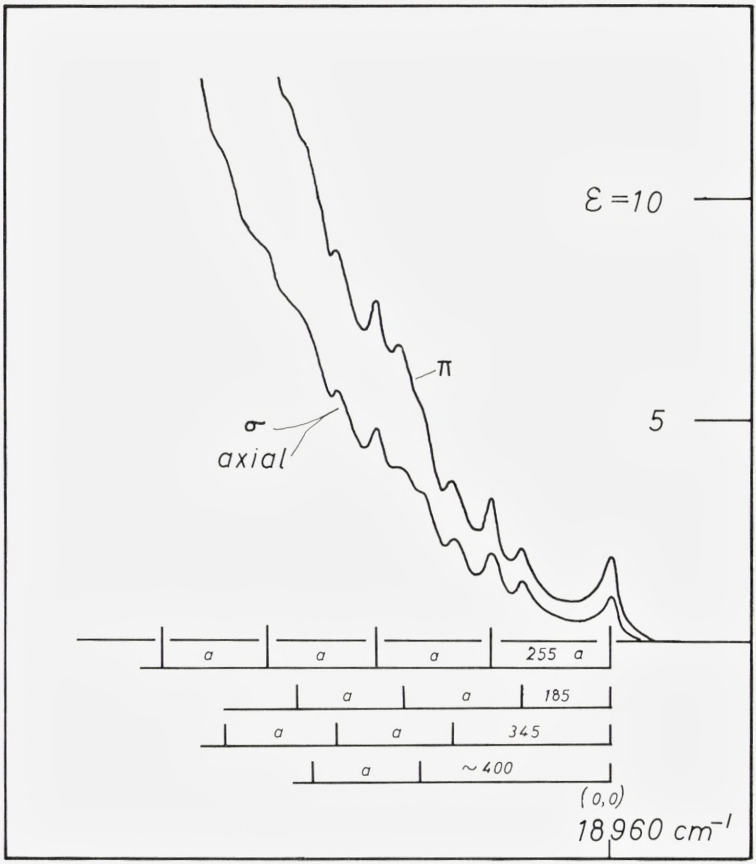

Fig. 3. Vibrational structure in the π, σ and axial spectra of d,1 2[Co en_3Cl_3].NaCl.$6H_2O$ in the region of th $^1T_{1g}(O_h)$ excited state.

energy and very minor vibrational effects that must arise from mass alterations in the vibrating systems.

For these 4.2 °K spectra the absolute frequencies are thought to be good to $\pm$ 5 cm^{-1} and the reproducibility to better than $\pm$ 2 cm^{-1}. Spectral differences greater than 3 cm^{-1} are expected to be meaningful although band width considerations apply differently to various spectra.

Assignment of spectra

(1) Ligand Field Parameters:

At 80 °*K*, the spectra show four absorption bands that may be confidently associated with singlet/tripet (13,500 cm^{-1}, 17,750 cm^{-1}) and singlet/singlet (21,500 cm^{-1}, 29,500 cm^{-1}) excitations within the *d* orbitals of the cobalt ion. Ignoring the splitting, that is apparent from polarization measurements, it is possible to calculate Dq, B and C. This is done using diagonal energy matrices and since only intensities and average energies are used the spectra are designated with O_h symbols.

$^1A_{1g} \rightarrow {}^3T_{1g}$	10 Dq − 3C	13500 ±	50 cm^{-1}
$^3T_{2g}$	10 Dq + 8B − 3C	17750 ±	50 cm^{-1}
$^1T_{1g}$	10 Dq − C	21350 ±	100 cm^{-1}
$^1T_{2g}$	10 Dq + 16B − C	29400 ±	100 cm^{-1}

$B_{singlets}$ = 503 cm^{-1}

$B_{triplets}$ = 530 cm^{-1}

$C_{^3T_{1g}/^1T_{1g}}$ = 3925 cm^{-1}

$C_{^3T_{2g}/^1T_{2g}}$ = 3815 cm^{-1}

10 Dq = 25,275 cm^{-1} when C = 3925 cm^{-1}

These data should be quite precise as a consequence of the narrowing of the bands and the observation of all four $d-d$ absorptions.

(2) 300 °*K* Spectra:

From the similarity, between Co en_3^{3+} in solutions and in crystals and $Co(NH_3)_6^{3+}$, it has been suggested[14] that the former is "almost" octahedral and that the absorption band intensity is controlled by a similar mechanism in both complexes. This is tantamount to predicting a vibronic intensity gaining mechanism and small trigonal field distortions in the former complex.

The correspondence between axial and σ spectra confirms an electric dipole mechanism in the singlet/singlet systems although no such distinction can be made for the more vulnerable singlet/triplets because the absorptions are isotropic. This is also true at lower temperatures so that no decision can be made between electric and magnetic dipole processes in these weak bands.

Assignment of the spectrum is possible in D_3 or in C_3. (Assignments Table 1). The π component at ~ 29,650 cm^{-1} deserves some comment.

Firstly, it is weaker than the other singlet/singlet transitions, thus reflecting a more forbidden character. Secondly, it falls at slightly higher energy than its σ component (^1E_b in D_3 or C_3) and finally, it should be absent if D_3 electronic selection rules are rigorously obeyed.

Thus, in D_3, a vibronic contribution is necessary to describe the absorption. It may be via either of the following mechanisms,

$$^1A_1 \rightarrow {}^1E_b \times \varepsilon \qquad xy(\sigma) \text{ and } z(\pi) \text{ polarized}$$
$$^1A_1 \rightarrow {}^1A_2 \times \alpha_2 \qquad z(\pi) \text{ polarized.}$$

If the site symmetry is included, the π intensity follows as a natural consequence of the transformational properties of the electric dipole moment operator in that symmetry

$$\text{i. e.} \quad {}^1A \rightarrow {}^1A \qquad z(\pi) \text{ polarized.}$$

From the present results alone it is seen that D_3 vibronic or C_3 electronic selection rules can give a satisfactory description of the broad band spectra. On the basis of a previous paper[7] and from the temperature dependence of the absorption band intensities (See below) it seems probable that the vibronic D_3 description is likely to dominate the spectrum. In a later section (p. 14) however, it appears that site influences are not entirely negligible.

In Table 1 ε_{max} values, ν_{max} values, $\Delta\nu_{max}$ values and polarization ratios are listed. It should be noted that these parameters are determined by vibronic contributions, by the shape of the potential surfaces of the upper states, by their relative disposition with regard to the ground state and by the associated Franck-Condon factors $|(\psi_o''|\psi_i')|^2$ occuring in the expression for the band intensity I:

$$I \propto |(\psi_o''|\psi_i')|^2 \cdot |(\psi_{e1}''|R_e|\psi_{e1}')|^2.$$

This implies that discussions relating to electronic perturbations are not necessarily valid when parameters derived from ε_{max} and $\Delta\nu_{max}$ values are utilized.

(3) 80 °*K* Spectra:

The weak bands at <18,000 cm^{-1} may reasonably be assigned as transitions to $^3T_{1g}$ and $^3T_{2g}$ (O_h). The broad room temperature absorption in this region is now accounted for. This area is further complicated by what appear to be third and fourth overtones of N-H and C-H stretching vibrations

that have almost comparable intensities to those of the singlet/triplet electronic transitions.

The intensity shifts observed by going to lower temperatures give evidence of considerable vibrational hot band contribution to the intensity of $^1T_{1g}$ and $^1T_{2g}$ of O_h. The $^1T_{1g}$ absorption edge moves 1500 cm^{-1} to higher energy on cooling to this temperature (Figure 2) and is very little affected on further cooling. Allowing for some increase in Dq on cooling this shift still corresponds to the freezing out 3 or 4 quanta of a 250–300 cm^{-1} ground state vibration. The intensity gaining efficiency of the higher members of these ground state vibrations must be strongly restricted by thermal population considerations at 300 $°K$ although it is likely that these excited ground state levels are intrinsically more potent at intensity stealing because of anharmonicity and vibrational amplitude considerations. The fact that the overall intensity decreases on cooling certainly supports this point of view as well as it does the argument that a large part of the absorption band intensity arises from vibronic processes.

(4) 4.2 $°K$ Spectra:

The important feature in these spectra is the development of discrete vibrational structure in all axial, π and σ components of the $^1A_{1g} \rightarrow {}^1T_{1g}$ (O_h) transition. Using II as model, it is possible to derive the following information (Table 2, Figure 3).

(i) The axial and σ transverse spectra correspond both in measured intensity and in quantitative matching of the vibrational structure. As a consequence the transition intensity is derived via the electric dipole mechanism (The vibronic bands in this region have $\varepsilon \sim 1-10$ so that magnetic dipole processes could have contributed considerable intensity).

(ii) The lowest line in the axial, π and σ spectrum falls at 18960 $\pm$ 2 cm^{-1}. Originally it was considered[9] that axial, π and σ could not be distinguished although measurements on a large number of crystals suggest that the axial and σ line lies at slightly lower frequency than does the π line. This difference, however, is still within the uncertainty of the measurement. In the present analysis these lines represent the (0,0) transition of the D_3 (or C_3) induced electronic* absorption system.

Thus it is possible to give a precise value for the splitting Δ of the elec-

* In this article the term "electronic" is reserved for the symmetry allowed (0,0) bands plus any associated totally symmetric vibrational progression built upon (0,0). 'Vibronic' refers to intensity arising from non-totally symmetric vibrations and their associated progressions, superimposed upon the (0,0) band.

TABLE 2. Description and Assignment of the vibrational finestructure seen in crystals II and III at 4.2 °K.

Crystal II.

axial, σ	π	$\varepsilon_\pi/\varepsilon_\sigma$	assignment
18960 ± 2 cm^{-1}	18960	2.0	(0,0)
19146	19146	1.3–1.5	+ 185
19218	19218	2.0	+ 255
19305	19306	1.3–1.5	+ 345
~19370	?	< 1.5	~ + 400
19405	19410	~ 1.4	+ 185 + 255
19470	19465	2.0	+ 2×255
19555	19550	1.3–1.6	345 + 255
19630	?	< 1.5	+ 400 + 255
19665	~19670	< 2.0	+ 185 + 2×255
19730	19740	~ 2.0	+ 3×255
~19800	—	< 2.0	+ 345 + 2×255
~20000	20000	~ 2.0	+ 4×255

Crystal III.

axial, σ	π	$\varepsilon_\pi/\varepsilon_\sigma$	assignment
(18915)	(18915)	—	(0,0)
19100 ± 5 cm^{-1}	19100 ± 5 cm^{-1}	> 1	+ 185
19158	19158	> 1	+ 255
?	?		—
?	?		—
19345	19345	> 1	+ 185 + 255
19395	19395	> 1	+ 2×255
19500	19500	> 1	+ 345 + 255 ?
—	—		—
~19600	~ 19600	—	+ 185 + 2×255
~19660	~ 19660	—	3×255
19750	19750		+ 345 + 2×255
—	—		—

These assignments are not unique, see text.

tronic energy level by the non-cubic potential field in these complexes; i. e. $\Delta = 0 \pm 4$ cm^{-1} and if the axial and σ spectra really are below the π band, $\Delta \sim 1-3$ cm^{-1}.

The intensity of these (0,0) bands is $\varepsilon \sim 1-2$ and in all cases the ratio between components is $\varepsilon_\pi/\varepsilon_\sigma = 2.0 \pm 10\ \%$.

3) A vibrational analysis of the first 12–15 lines (Figure 3) provides the following information,

(i) A progression, involving a symmetrical vibration with frequency $255 \pm 5\ cm^{-1}$ in the excited state and based on (0,0), extends some 5 or 6 numbers before it is lost in the continuous absorption that builds up very rapidly as the frequency increases. After approximate background corrections the ratio $\varepsilon_\pi/\varepsilon_\sigma$ remains near that found for (0,0). This is expected for a totally symmetrical vibration superimposed upon the (0,0) band.

(ii) A vibration of $185 \pm 5\ cm^{-1}$ adds one quantum to (0,0) and is then followed by 2 or 3 quanta of the symmetrical $255 \pm 5\ cm^{-1}$ vibration. The intensity ratio $\varepsilon_\pi/\varepsilon_\sigma$ for each member is in the range 1.3–1.6. The appearance of only one quantum of $185 \pm 5\ cm^{-1}$ plus the change in polarization ratio from that shown by (0,0) indicates that this vibration is non totally symmetrical.

(iii) A non totally symmetrical vibration with frequency $345 \pm 5\ cm^{-1}$ appears ($\varepsilon_\pi/\varepsilon_\sigma \sim 1.3$–1.5) and has several quanta of $255 \pm 5\ cm^{-1}$ built on it.

(iv) Finally the axial and σ spectra show a weakly resolved band at $(0,0) + \sim 400\ cm^{-1}$ followed by one or more quanta of $255 \pm 5\ cm^{-1}$. This vibration is not totally symmetrical.

No reliable infrared or Raman analysis is available for the Co en_3^{3+} ion. The IR spectrum shows a strong band at $\sim 250\ cm^{-1}$ and medium absorptions at 350–370 cm^{-1}, 440–470 cm^{-1} and above. It is not unreasonable to associate these values with those found in the electronic spectrum and they are quite likely to be associated with components of the $2t_{1u}$ and t_{2u} vibrations of the CoN_6 octahedron. Because of the influence of the site it is not possible to get any more information about the parentage of these vibrations.

If the D_3 assignment is preferred, these electronic transitions must be

	$^1A_1 \rightarrow {}^1A_2$	π spectrum
and	$^1A_1 \rightarrow {}^1E_a$	axial and σ spectrum

t_{1u} of O_h transforms like $a_2 + e$ and t_{2u} like $a_1 + e$ in D_3 so that if each vibration is equally efficient at gaining intensity, any vibronic contribution arising from a nearly degenerate pair a_2/e or a_1/e, will give rise, in the first quantum, to bands with composite polarizations $\varepsilon_\pi/\varepsilon_\sigma \sim 0.7$ in the former and $\varepsilon_\pi/\varepsilon_\sigma \sim 1.3$ in the latter instances. If the site symmetry is included the ration is ~ 1.3 both cases.

The discussion of a transition $(t_{2g})^6 \rightarrow (t_{2g})^5(e_g)^1$, should admit the possibility of observing a dynamic Jahn-Teller effect in the upper states.

In the present case, if the transitions may be classified in D_3 or C_3, the π spectrum is associated with a transition $^1A \rightarrow {}^1A$, and the σ spectrum with $^1A \rightarrow {}^1E_a$. The former transition should then be able to experience a pseudo Jahn-Teller effect, the latter a genuine one. The close correspondence, between the σ and π absorption in the vibrational structure as well as the position of the (0,0) band, makes it impossible to evaluate any Jahn-Teller parameters. Anyhow, the states behave as if no such effect is active.[31] [32]

Minor differences in the structure, seen in this region for other crystals, must be due to alterations in molecular and or crystal environment by crystal packing forces. Certainly, distortions of the ligand framework have been observed[3] although the molecular units still maintain D_3 symmetry and, in the cases of interest, the cobalts still occupy a site with C_3 symmetry. Because of the nature of the spectra it has not been possible to separate these various influences and the differences are loosely termed crystal effects. Even more to the point, it is still not possible to unambiguously distinguish the contributions from a vibronic D_3 mechanism and from C_3 site.

Crystal III shows some difference from II in this region. As seen earlier, the space group is altered and the packing is slightly different with small variations in the metal/chelate angles. These effects must be responsible for the changes in the details of the crystal spectrum.

Comparing with II, the spectrum of III shows an overall shift of 50–60 cm^{-1} towards lower energy, the intensity of the 255 ± 5 cm^{-1} progression is greatly reduced (including that of the origin) and the 345 ± 5 cm^{-1} progression is not clearly seen at low frequencies. When these changes are taken into account it is possible to discuss the spectrum of III in the same way as for II. The final conclusions (for III) are,

(i) The (0,0) band is very weak and is not resolved from the background.

(ii) The 255 ± 10 cm^{-1} vibration is identified and appears in several progressions, thereby confirming the previous analysis in II.

(iii) (0,0) lies at lower energy than in II and the trigonal field splitting is again very slight and less than the un-certainty of the measurements.

(iv) The correspondence between axial and σ spectra again supports the electric dipole mechanism for the intensities which, in total, are very similar to the values found in II.

The assignment of these lines (Table 2) is not unique. For instance the whole pattern could be moved 140 cm^{-1} to lower energies when the (0,0) band in II and the lowest resolved band in III would coincide. This would introduce new problems in the vibrational analysis so that the present arrangement is preferred.

The deuteration of II to give IV results in the following changes in the spectrum. The only region that appears to be affected is the low energy side of $^1T_{1g}(O_h)$. Here, the (0,0) band moves 105 ± 5 cm^{-1} to higher energy although relative intensities, within the band system, remain unaltered. This is quite in accord with similar studies on, for instance, naphathalene[15], benzene[16], acetylene[17] and the nickel (II) tris ethylenediamine ion[7].

The observed vibrational frequencies of the upper state do not seem to be influenced by the deuteration. In particular, the totally symmetrical mode, $\nu = 255 \pm 5$ cm^{-1} is not altered by as much the error of the measurements. The axial, π and σ spectra still have the same relationship to each other.

The shift in the (0,0) band position can be rationalized in terms of changes in zero point energies in the ground and excited states of the two complexes[16]. The invariance of the vibrational frequencies upon deuteration indicates very little movement of the exchanged protons in the normal modes corresponding to these frequencies.

The compounds III and V behave in an analogous manner and they will not be considered further.

(5) Intensities:

The intensities reported in this and some earlier investigations are in good agreement (Table 1).

One of the major problems, in earlier works, has been to separate the electronic intensity, f_{el} from the vibronic intensity f_{vib}. From the present measurements, especially in II, it has been possible to get reliable expressions for these two contributions.

If f_{el} arises only from (0,0) + $n\nu$, where $\nu = 255$ cm^{-1} (a lower limit to f_{el}) then in $^1A_1 \rightarrow {}^1A_2$; ^1E_a, where the total band width is 7000 cm^{-1}, $n = 28$. The (0,0) bands have $\Delta\nu_{1/2} \simeq 30$ cm^{-1} so assuming overall $\Delta\nu_{1/2} \simeq 100$ cm^{-1} and taking a mirror image about the band centre the intensity expression reduces to

$$f_{el} \simeq 4.6 \times 10^{-9} \sum_{n=1}^{28} \varepsilon_{max} \Delta\nu_{1/2} = 9.2 \times 10^{-7} \sum_{n=1}^{14} \varepsilon_{max}.$$

For the $^1A_1 \rightarrow {}^1E_a$ transition $\varepsilon_{(0,0)} = 1 \pm 10\ \%$ and assuming each line increases by one ε unit/line [reasonable, at least for $n < 5$] this leads to

$$f^E_{el} = 1.1 \times 10^{-4}; \quad f^E_{\substack{total \\ el+vib}} = 1.84 \times 10^{-3}.$$

Thus

$$f^E_{el}/f^E_{total} \simeq 6 \times 10^{-2}$$

and

$$f_{el}^{A_2}/f_{total}^{A_2} = 10 \times 10^{-2} \quad \text{since} \quad \begin{matrix} f_{el}^{A_2} = 2.2 \times 10^{-4} \\ f_{total}^{A_2} = 2.18 \times 10^{-3}. \end{matrix}$$

These estimates are probably better than order of magnitude since the lower limit is given by the bands we actually observe and this accounts for better than 10 % of the total f_{el}. Thus it is very reasonable to conclude that 10–15 % of the total intensity arises from electronic processes and the remainder from vibronic coupling.

Comparison between the solution oscillator strengths for $Co\,en_3^{3+}$ and $Co(NH_3)_6^{3+}$ lends support to this supposition. In solution the difference between the intensity in this band is

$$\Delta f_{total} \simeq 4 \times 10^{-4}$$

whereas in the crystal the electronic intensity for

$${}^1A_1 \rightarrow {}^1A_2 + {}^1E_a \quad \text{is} \quad f_{el}^{A_2,E_a} \simeq \frac{1}{3} f_{el}^{A_2} + \frac{2}{3} f_{el}^{E_a} = 1.5 \times 10^{-4}.$$

In the same way, if the π component at $\sim$ 29,650 cm^{-1} is entirely vibronic, and controlled by D_3 selection rules as opposed to C_3 site symmetry rules, then again it would indicate considerably vibronic intensity. Unfortunately, quantitative estimates based upon this absorption system are not likely to to very useful.

In III the (0,0) band is not clearly resolved and the structure is less clear than in II. Nevertheless, the correlations made in the previous section allow an estimate of f_{el} to be made. The intensity arising from (0,0) + $n\nu$ where $\nu \simeq 250$ cm^{-1} is estimated to be in the region $f_{el} \simeq 1 \times 10^{-5}$. The concomitant decrease in $f_{el}^{A_2, E_a}$ may account for the fact that, for a number of crystals, the total intensity, $f_{total}^{E_a}$ for component III seems to be 5–10 % less than that for compound II. Measured intensities in our crystals carry $\pm$ 10 % error so that this apparent difference may not be real.

(6) Distribution of intensity:

The ${}^1A_{1g} \rightarrow {}^1T_{1g}(O_h)$ absorption of II is the best example to discuss. Ignoring the differences in structure and in the distribution $f_{el}/f_{vibronic}$, the same remarks apply to the equivalent transition in III.

The (0,0) band shows $\varepsilon_{A_2}/\varepsilon_{E_a} = 2.0$ whereas the value measured at the ν_{max} position is $\varepsilon_{A_2}/\varepsilon_{E_a} = 1.3$.

This variation must arise from differing vibronic contributions in A_2 and E_a because totally symmetrical vibrations would be expected to follow the ratio given at (0,0) and there does not seem to be any reason why totally symmetrical vibrations associated with one transition should not appear in the other. Assuming that the active vibrational modes of the octahedral CoN_6 ($2t_{1u} + t_{2u}$) are equally adept at gaining intensity it is seen, that when D_3 selection rules persist and the electronic contribution arising from $(\psi'_{el}|R_e|\psi''_{el})$ is taken into account (assumed to be 2.0 in this case in favour of $^1A_2$), the expected ratio is

$$\varepsilon_{II}/\varepsilon_{\perp} = 0.9 \quad \text{(obs. 1.3)}.$$

If the site influence is included, this becomes

$$\varepsilon_{II}/\varepsilon_{\perp} = 1.3.$$

Short of actually attempting calculations of vibronic coupling intensities, these arguments are not very conclusive as concerns the D_3/C_3 symmetry question although, the predominance of polarized vibronic contributions can be rationalized in this manner.

The theoretical elucidation of the electronic intensity distribution is as usual a rather delicate matter. Compare for instance the two point groups D_3 (Symmetry elements E, $2C_3$ and $3C_2$) and C_{3v}. (Symmetry elements E, $2C_3$ and $3\sigma_v$). These two groups look very similar indeed, but a cobalt (III) complex will have quite a different intensity distribution if it belongs to the one or the other point group. The levels T_{1g} (O_h) and T_{2g} (O_h) will in *both* of the lower symmetries transform as A_2, E (T_{1g}) and A_1, E (T_{2g}). However, the electric dipole vectors transform as (A_2, E) representations in D_3 and as (A_1, E) representations in C_{3v}. Hence the 21,000 cm^{-1} band is expected to be seen in σ polarization for a D_3 molecular group and be forbidden in σ polarization assuming a C_{3v} point group, whereas the reverse is true for the 29,000 cm^{-1} band.

These general predictions are of course born out by actual calculations. Indicating the angular parts of the *molecular orbitals* in C_3 quantization, we have[18] for the pertinent molecular orbitals

$$t^+ = \sqrt{\frac{2}{3}}\,\psi_{x^2-y^2} - \sqrt{\frac{1}{3}}\,\psi_{xz}$$

$$t^- = \sqrt{\frac{2}{3}}\,\psi_{xy} + \sqrt{\frac{1}{3}}\,\psi_{yz}$$

$$t^{\circ} = \psi_{z^2}$$

$$e^{+} = \sqrt{\frac{1}{3}}\,\psi_{x^2-y^2} + \sqrt{\frac{2}{3}}\,\psi_{xz}$$

$$e^{-} = \sqrt{\frac{1}{3}}\,\psi_{xy} - \sqrt{\frac{2}{3}}\,\psi_{yz}$$

Utilizing the symmetry operations of the D_3 group ($\hat{i}$, $\hat{j}$, and $\hat{k}$ being the unit vectors) we get

$$(t^{\circ}\,|r|\,e^{+}) = o\hat{i} + \alpha\hat{j} + o\hat{k}$$
$$(t^{\circ}\,|r|\,e^{-}) = \alpha\hat{i} + o\hat{j} + o\hat{k}$$
$$(t^{+}\,|r|\,e^{+}) = o\hat{i} - \beta\hat{j} + o\hat{k}$$
$$(t^{+}\,|r|\,e^{-}) = \beta\hat{i} + o\hat{j} + \gamma\hat{k}$$
$$(t^{-}\,|r|\,e^{+}) = \beta\hat{i} + o\hat{j} - \gamma\hat{k}$$
$$(t^{-}\,|r|\,e^{-}) = o\hat{i} + \beta\hat{j} + o\hat{k}$$

where the occuring molecular integrals are

$$\alpha = (t^{\circ}\,|x|\,e^{-})$$
$$\beta = (t^{+}\,|x|\,e^{-})$$
$$\gamma = (t^{+}\,|z|\,e^{-})$$

The excited states are mainly determined by the cubic field, but are split (at least in principle) by the lower field. The following formular for the electronic dipole matrix elements are then obtained by utilizing the proper excited states functions:

$$({}^1A_1\,|R_e|\,{}^1T_2(A_1)) = 0$$
$$({}^1A_1\,|R_e|\,{}^1T_2(E^A)) = (\alpha - \sqrt{2}\beta)\hat{i}$$
$$({}^1A_1\,|R_e|\,{}^1T_2(E^B)) = (\alpha - \sqrt{2}\beta)\hat{j}$$
$$({}^1A_1\,|R_e|\,{}^1T_1(A_2)) = 2\gamma\hat{k}$$
$$({}^1A_1\,|R_e|\,{}^1T_1(E^A)) = (-\alpha - \sqrt{2}\beta)\hat{i}$$
$$({}^1A_1\,|R_e|\,{}^1T_1(E^B)) = (-\alpha - \sqrt{2}\beta)\hat{j}$$

The theoretical polarization ratio in D_3 symmetry is therefore for the "first" ($^1T_{1g}$) band

$$\frac{I_\pi}{I_\sigma} = \frac{4\gamma^2}{(\alpha + \sqrt{2}\beta)^2}$$

and for the "second" ($^1T_{2g}$) band

$$\frac{I_\pi}{I_\sigma} = \frac{0}{(\alpha - \sqrt{2}\beta)^2}.$$

These intensity ratios are completely analogous to those of McClure[19] apart of course from the fact that the levels are "reversed" and that the matrix elements α, β, and γ are different from his, due to the different symmetry elements of the group.

The actual evaluation of our matrix elements requires a detailed knowledge of the molecular orbitals, whose angular transformational properties are indicated by t^+, t^- and etc. Notice in particular that the *signs* of α, β and γ are unknown, and unrelated to each other. Since the actual intensities are rather small, the matrix elements are probably only of the order of magnitude of 10^{-10} Å. In strictly octahedral symmetry they would of course be zero. They owe their non zero value to the participation of the chelate ring orbitals in the bonding, and/or perhaps to "misdirection" of the nitrogen orbitals[20]. The fact that the σ components of the $^1T_1$ and $^1T_2$ bands have nearly the same intensity indicates that either $|\alpha| \ll |\beta|$ or $|\beta| \ll |\alpha|$.

A rather interesting sidelight are trown upon these considerations if we for a moment consider the less general model proposed by Sugano and Tanabe[21]. Their model considers explicitly the introduction of an "odd" pertubing field of the form

$$\mathcal{V}_{odd} = a \sum_i z_i + \text{higher "odd" terms.}$$

If the expansion is broken off after the first term (*assuming* this to be predominant) we get the intensity ratio for the first ($^1T_{1g}$) band $I_\pi/I_\sigma = 4/1$, but $I_\pi/I_\sigma = 0/0$ for the second ($^1T_{2g}$) band*. The experimental ratio for the "allowed" intensity of the first band is as we have seen, close to two.

(7) The Absorption Spectrum and Circular Dichroism.

The foregoing discussions have clarified some questions as to the splittings of electronic components and the influence of vibronic intensity upon the

* There appears to be a mistake in Sugano and Tanabe[21]; they get a linestrength different from zero for I_σ in the "second" band.

fine structure and the overall intensity distribution within these components. Pertinent to the question of the origin of the C.D., both in a crystal and in solution, is the ability of non-totally symmetric vibrations to contribute to the rotational power. MOFFITT and MOSCOWITZ[22] have suggested that such contributions should be very small whereas WEIGANG[23], in a series of papers, has developed the concept to the point where non totally symmetric vibrations of the excited state may contribute significantly to the C.D. From WEIGANG's treatment, it would appear that it is nearly impossible to clarify this question from the present work because the spectra are not sufficiently resolved, and the C.D. results are very broad and structureless. Yet even under these circumstances it still seems profitable to consider the more general aspects of this matter.

Absorption band maxima are often used as the measure of an electronic energy. In terms of the Franck-Condon model, and with the crystal near 0 °*K*, the absorption maximum certainly represents the (n, 0), vertical transition in a case where only one vibration may be excited. In polyatomic molecules, and especially when several vibrations of different symmetry type and of different frequency are excited, the final absorption envelope is made up from the superposition of curves obtained from several sections of what is now a (3n−6) dimensional surface. Each section may have a different potential function and the resultant band envelope, as determined by $(\psi_0''|\psi_i')^2$, may have quite a different character for each section. When the vibrational structure is resolved it is possible to estimate these various contributions. In the present case, the totally symmetric vibration, $\nu = 255$ cm^{-1} and the non totally symmetric, $\nu = 185$, 345 and ~ 400 cm^{-1} are seen only at low v' so that the estimate of their contributions are necessarily approximate. If it is assumed that each section of the P.E. surface has the same shape, it is possible to sum over these contributions by taking (0,0) + n 255 adding it at (0,0) + 185; (0,0) + 345 and (0,0) + 400 cm^{-1} with due account taken of intensities. This is shown in Figure 4. The π set gives each contribution equal intensity and results in $\nu_{max} = 21650$ cm^{-1}, $\varepsilon_{max} = 108$. The σ set halves the contribution from (0,0) + n 255 and provides $\nu_{max} = 21750$ cm^{-1} and $\varepsilon = 94$. In actual fact, the non-totally symmetric contribution in σ should be increased and hence $\Delta\nu_{max}$ should increase slightly. This procedure demonstrate the origin of the so-called "trigonal field" splitting in ν_{max}. The good agreement with experiment is probably fortuitous although it does again suggest that the major contributors to the absorption band intensity have been identified.

As we have demonstrated experimentally for most purposes the (0,0)

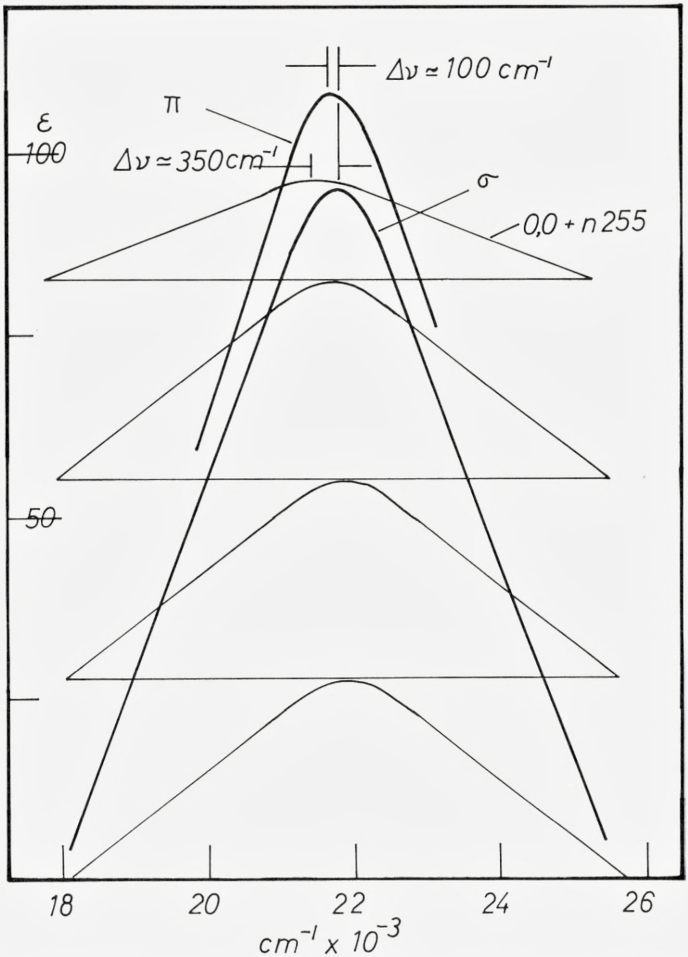

Fig. 4. Computed absorption curves for the $^1T_{1g}(O_h)$ components of II. The π and σ curves represent the absorption bands when the electronic and the three vibronic terms contribute intensity. The splitting $\Delta\nu \approx 100\ cm^{-1}$ should correspond to the measured splitting of the band maxima in absorption. The $\Delta\nu \approx 350\ cm^{-1}$ is the difference between the σ absorption maxima and the axial crystal C. D. maximum in the case that only electronic intensity contributes to the C. D.

bands in π and σ plus the first five or six members of the totally symmetric vibrational progression must be considered degenerate. Table II. If this means that $^1T_{1g}(O_h)$ is almost unaffected by non-cubic potential terms then, barring such influences as the Jahn-Teller effect, the P. E. Surfaces, for π and σ at

least at low v', must be almost, if not exactly, degenerate* for each section when the same vibration occurs in both spectra. Thus for the symmetric mode, $\nu = 255\ \mathrm{cm}^{-1}$, the splitting of the Franck-Condon maxima should be very small, and of the order of the experimental uncertaincy. We estimate this to be $\pm 10\ \mathrm{cm}^{-1}$, and this should then be the true trigonal field splitting of $^1T_{1g}$.

If the details of the analysis of II are transferred to III then the C.D. may be considered. McCaffery and Mason[2] have obtained axial absorption and C.D. corresponding to σ polarization in a crystal of III. The ν_{max} values, $\nu_{max}^{abs} = 21400\ \mathrm{cm}^{-1}$ and $\nu_{max}^{C.D.} = 21{,}050\ \mathrm{cm}^{-1}$ agree well with the simple composite curves shown in Figure 4. In the case that only the totally symmetric vibrational progression contributes to the C.D.[22]: Calculated** values $\nu_{max\,\sigma,\pi}^{0,0+n255} = 21450\ \mathrm{cm}^{-1}$, $\nu_{max\,\sigma}^{total} = 21750\ \mathrm{cm}^{-1}$. This result is suggestive that, for this case the non-totally symmetric vibrations are not very important and certainly there does not appear any change of sign in the axial σ polarized (^1E) C.D. which would have given support to the vibronic model[23].

The transition $^1A_{1g} \rightarrow {}^1T_{1g}$ is fully allowed as a magnetic dipole transition. Since the excited state to a good approximation is composed of d-orbitals, we can calculate the matrix elements of the magnetic dipole transition, assuming pure d-orbitals. We get with our chosen orientations:

$$(^1A_1\ |\vec{L}|\ {}^1T_1(A_2)) = -i\hbar\, 2\sqrt{2}\hat{k}$$
$$(^1A_1\ |\vec{L}|\ {}^1T_1(E^A)) = i\hbar\, 2\sqrt{2}\hat{i}$$
$$(^1A_1\ |\vec{L}|\ {}^1T_1(E^B)) = i\hbar\, 2\sqrt{2}\hat{j}$$

The value of $2\sqrt{2}\hbar$ should with our approximation be valid to within a few per cent. We get then for the ratio of the Rotatory Strengths $\Re = (^1A_1\ |\vec{R}|\ {}^1X)(^1X\ |\vec{L}|\ {}^1A_1)$ of the components of $^1T_{1g}$, $\Re_\pi$ and $\Re_\sigma$

$$\frac{\Re_\pi}{\Re_\sigma} = \frac{2\gamma}{\sqrt{2}\beta + \alpha} = \pm\sqrt{\frac{I_\pi}{I_\sigma}} \approx \pm\sqrt{2}$$

* The correspondence between $\nu_{0,0}$ values is necessary but not sufficient since, for some normal coordinate σ, the $\nu_{0,0}$'s may coincide but the surfaces may have minima quite removed from each other. Since $^1T_{1g}(O_h)$ in $Co(NH_3)_6^{3+}$ is at almost the same energy as the resultant π and σ states in $Co\,en_3^{3+}$ such a possibility can probably be safely neglected here.

** These are taken from 4.2 °K spectra whereas the experimental results in (2) were obtaine at ~ 300 °K. The 4.2 °K results should have 300–400 cm^{-1} subtracted from them in order to provide a result that may be compared with the results in (2).

where the value $\sqrt{2}$ is taken from our experiments. Hence

$$\Re_\pi \approx \pm \sqrt{2}\, \Re_\sigma .$$

KARIPIDES and PIPER[3] have shown that, in our notation $(\alpha + \sqrt{2}\beta) + \gamma = 0$ if in the evaluation of these molecular integrals one uses undeviated nitrogen orbitals. Our result shows clearly that this is not permissible. Indeed, it is the "misdirection" of the nitrogen orbitals[20] that leads to a breakdown of KARIPIDES and PIPER's result.

Regardless of the *sign* of the $\Re$'s we would expect the $\Re(^1A_1 \rightarrow {}^1A_2)$ to be about 1.4 as strong as the axial $\Re(^1A_1 \rightarrow {}^1E)$. The *absolute* signs of the two rotatory strengths is seen to be solely determined by the molecular integrals α, β and γ. MCCAFFERY and MASON[2] measured the C.D. of D $[Co\ en_3^{3+}]$ both in solution and axially in a single crystal. In both cases they found a positive C.D. curve centred about 20,000 cm^{-1}, however, the intensity of the solution spectrum is only 5 % of the intensity observed in the crystal. In addition a new, negative C.D. absorption appears at 23,000 cm^{-1} but *only* in solution. MCCAFFERY and MASON interpret the latter band as being due to the $^1A_1 \rightarrow {}^1A_2$ transition.

We have demonstrated that the trigonal splitting of ^1E and $^1A_2$ in the crystal of $Co(en)_3^{+++}$ does not exceed 10 cm^{-1}. This leads then to the interesting question: What is the negative C.D. at 23,000 cm^{-1} asscribed by MCCAFFERY and MASON[2] as the $^1A_2$ band due to? Even if it is true that the difference between two observed C.D. maxima by no means corresponds to the "true" electronic splitting[24] [25] we have been unable to generate on an electronic computer the observed C.D. results, assuming a splitting of *less* than $\approx$ 400 cm^{-1}.

We believe, however, to be able to solve this puzzle in the following way. We assume with WOLDBYE[26] that the complex can exist in two conformes in *solution but not in the crystal*. Now, with a negligable splitting of the electronic state we should get for the $^1T_{1g}$ band

$$\frac{\Re_{sol}}{\Re_{axial}} = \frac{\frac{1}{3}(\Re_\pi + 2\,\Re_\sigma)}{\Re_\sigma}$$

with $\Re_\pi = \pm \sqrt{2}\,\Re_\sigma$ this ratio is equal to 0.2 if the $\Re$'s have opposite sign but 1.1 if the $\Re$'s have the same sign. If a fraction of the compound should be found in a different conformation, these ratios should be multiplied with a number less than one. Anyhow, comparing these numbers with the experimental findings it is seen that it is much more likely for the two rotatory strengths to have the opposite signs.

Some authors[27] [28] have taken it for granted that $\Re_\sigma$ and $\Re_\pi$ should have opposite signs. It is true that *calculations based on a specific model* namely $d-p$ mixing[29], shows that $\Re_\sigma$ and $\Re_\pi$ here have different signs, but since this mixing is not the primary cause of optical activity in these systems[30], the appropriateness of the calculation to the sign question is rather doubtfull.

That the "other" form of Co $(en)_3^{+++}$ should possess an energy difference $\Delta E(^1A_1 - {}^1T_1)$ which is a few hundered wavenumbers larger than the "crystal form" is not unreasonable. This difference will indeed presumably mostly be found when the excited states of the two conformers are compared. These states are antibonding in nature and therefore more susceptible to changes in the molecular geometry than is the ground state. It is therefore not expected a priori that variations in the respective C.D. intensities due to small changes in temperature will occur, since the Boltzmann Distribution in the ground states may not be altered significantly, at least so long as we can still speak of solutions.

Our conclusion is therefore that the "negative" C.D. found at 23,000 cm^{-1} is due to the presence of a different conformation of Co $(en)_3^{+++}$ than that found in the crystal, and that $\Re_\pi$ and $\Re_\sigma$ have different signs.

The rotatory strength of the "second" band ($^1T_{2g}$) also presents us with a small problem. The level is not connected with the ground state by the magnetic dipole operator. Under the trigonal crystal field the two E components of T_{1g} and T_{2g} can of course mix, and we get

$$(^1E(T_1)|\mathfrak{H}_\tau^{\varrho}|^1E(T_2)) = \Delta.$$

However, by a curious coincidence, we have also that the trigonal splitting of both $^1T_1$ and $^1T_2$ is equal to Δ. Experimentally Δ is found to be arround 10 cm^{-1}. Thus in fact $^1E(T_2)$ does not "borrow" significantly amounts of angular momentum from $^1E(T_1)$ via the trigonal field. What angular momentum it carries must have been stolen from a higher excited state. Hence the two low-lying ^1E states are not coupled together.

Conclusions

The experiments show quite conclusively that the intensity in the Co en_3^{3+} ion in crystals is predominantly vibronic in origin. Furthermore these vibronic terms have been individually observed and correlated with possible IR frequencies. Deuteration of the $N-H_2$ groups in the ethylene diamine does not give rise to any large change in the spectra.

In estimation electronic splitting parameters such as the trigonal field parameter Δ, found here to be $\pm$ 10 cm^{-1}, values derived from ν_{max} positions are at the best, likely to be misleading, and are probably quite often incorrect in sign as well as magnitude.

Due to differing crystal influences the spectra of the d, l and the D crystals of 2[Co en_3Cl_3]. $NaCl.6H_2O$ are somewhat altered in finestructure. The C.D. results of McCaffery and Mason are explained assuming two conformers of $Co(en)_3^{+++}$ to be present in solution as originally suggested by Woldbye.

Acknowledgments

C. J. Ballhausen wants to thank Statens almindelige Videnskabsfond for a grant of two Helium Dewars, and we both want to thank cand. scient. O. Sonnich Mortensen for help with the electronic data computing of C.D curves.

Chemical Laboratory IV, Department for Physical Chemistry,
H. C. Ørsted Institute, The University of Copenhagen,
Copenhagen, Denmark.

References

(1) S. Yamada and R. Tsuchida: Bull. Chem. Soc. Japan **33**, 98 (1960).
(2) A. J. McCaffery and S. F. Mason: Mol. Phys. **6**, 359 (1963).
(3) A. Karipides and T. S. Piper: J. Chem. Phys. **40**, 674 (1964).
(4) C. K. Jørgensen: Acta Chem. Scand. **8**, 1495 (1954).
(5) C. J. Ballhausen: Introduction to Ligand Field Theory, McGraw-Hill Book Co., Inc. (N.Y.) (1962) p. 260.
(6) C. K. Jørgensen: Acta Chem. Scand. **8**, 1502 (1954).
(7) R. Dingle and R. A. Palmer: Theoretica Chim. Acta. **6**, 249 (1966).
(8) E. Drouard and J. P. Mathieu: Compt. rend. **236**, 2395 (1953).
(9) R. Dingle: Chem. Comm., 304 (1965).
(10) C. J. Ballhausen, N. Bjerrum, R. Dingle, K. Eriks and C. R. Hare: Inorg. Chem. **4**, 514 (1965).
(11) K. Nakatsu, Y. Saito and H. Kuroya: Bull. Chem. Soc. Japan **29**, 428 (1956).
(12) K. J. Watson: Communication (1965).
(13) K. Nakatsu, M. Shiro, Y. Saito and H. Kuroya: Bull. Chem. Soc. Japan **30**, 158 (1957).

(14) C. J. Ballhausen: Introduction to Ligand Field Theory. McGraw-Hill Book Co., Inc. (1962) p. 186, 216.
(15) D. P. Craig and J. M. Hollas: Philosophical Proceedings (London) **253 A**, 569 (1961).
(16) F. Garforth, C. K. Ingold and H. Poole: J. Chem. Soc. 508 (1948).
(17) C. K. Ingold and C. W. King: J. Chem. Soc. 2702 (1953).
(18) C. J. Ballhausen: Introduction to Ligand Field Theory. McGraw-Hill Book Co., Inc. (1962) p. 68.
(19) D. S. McClure: J. Chem. Phys. **36**, 2757 (1962).
(20) A. D. Liehr: J. Phys. Chem. **68**, 665 (1964).
(21) S. Sugano and Y. Tanabe: J. Phys. Soc. Japan **13**, 880 (1958).
(22) W. Moffitt and A. Moscowitz: J. Chem. Phys. **30**, 648 (1959).
(23) O. E. Weigang: J. Chem. Phys. **43**, 3609 (1965) and earlier papers in the series.
(24) T. Bürer: Helv. Chim. Acta **46**, 2388 (1963).
(25) K. Wellman, P. H. A. Laur, W. S. Briggs, A. Moscowitz and C. Djerassi: J. Am. Chem. Soc. **87**, 66 (1965).
(26) F. Woldbye: Record of Chemical Progress **24**, 197 (1963).
(27) N. K. Hamer: Mol. Phys. **5**, 339 (1962).
(28) M. Shinada: J. Phys. Soc. Japan **19**, 1607 (1964).
(29) T. S. Piper and A. Karipides: Mol. Phys. **5**, 475 (1962).
(30) S. Sugano: J. Chem. Phys. **33**, 1883 (1960).
(31) F. S. Ham: Phys. Rev. **138 A**, 1727 (1965).
(32) W. C. Scott and D. M. Sturge: Phys. Rev. **146**, 262 (1966).

Indleveret til Selskabet den 1. oktober 1966.
Færdig fra trykkeriet den 25. januar 1967.

Matematisk-fysiske Meddelelser
udgivet af
Det Kongelige Danske Videnskabernes Selskab
Bind **35,** nr. 13

Mat. Fys. Medd. Dan. Vid. Selsk. **35,** no. 13 (1967)

ANGULAR MOMENTUM DEPENDENT POTENTIALS

BY

C. CRONSTRÖM

København 1967
Kommissionær: Munksgaard

CONTENTS

	Page
1. Introduction	3
2. The general form of the potential	5
3. I. Basic properties of the angular momentum dependent potential	7
3. II. The partial wave equations	9
3. III. The inversion formula	11
4. The equivalence problem	13
5. The single-particle exchange potential	17
6. Numerical results and discussion	20
Appendix I: : The inversion theorem	27
Appendix II: Reduction of the Lippmann-Schwinger equation	32
References	35

Synopsis

The properties of the most general local two-body potential for elastic scattering of scalar particles are investigated. This potential is angular momentum dependent. (Arbitrarily energy dependent potentials are ruled out by general symmetry and invariance arguments.) In particular, we investigate the momentum space representation of the angular momentum dependent potential, and show that it is characterized by a particular off shell behaviour. By considering the partial wave Lippmann-Schwinger equation, we establish in a rather simple manner the existence of a p-fold class of phase equivalent potentials (containing p local, angular momentum dependent potentials), where p equals the number of bound states in the partial wave under consideration. In this connection, we show that a potential, which is defined by using a perturbative expansion of the S-matrix from field theory, can be chosen to be local and angular momentum dependent, provided the expressions representing the diagrams included in the potential satisfy simple regularity conditions. There does not, however, seem to exist any simple relation (which does not involve the inverse of the Greens function) between a given non-local potential and the corresponding phase equivalent local and angular momentum dependent potential. As an illustration, we make some numerical calculations with a non-local single-particle exchange potential. The adiabatic approximation is investigated in this case, and is shown to be quite inaccurate for a strong attractive potential.

PRINTED IN DENMARK
BIANCO LUNOS BOGTRYKKERI A/S

1. Introduction

The object of this paper is to investigate the concept of a local, angular momentum dependent potential and its relevance to the general problem of obtaining a local potential which is equivalent to a given non-local potential.

We consider only the case of scalar particles of equal mass in this paper, leaving the general case of spin-dependent potentials to a forthcoming paper[1].

From the results of the investigations of the inverse problem of scattering, one can deduce, as has been pointed out by S. OKUBO and R. E. MARSHAK[2], that if a potential is reconstructed from a given scattering matrix, it can be chosen to be a function of r^2 and $\boldsymbol{L}^2$ only, where $\boldsymbol{L}$ is the angular momentum operator.

Thus, it is in principle possible to construct a (not necessarily unique) local, angular momentum dependent potential, which is equivalent to a given non-local potential, in the sense that both potentials give identical phase shifts.

In practice, however, this problem has apparently no simple and explicit solution, since it seems to be rather difficult to obtain a simple and explicit relation between the local, angular momentum dependent potential and the class of non-local potentials, which have identical phase shifts. On the other hand, in perturbation theory, one can easily establish the explicit relation between the equivalent local potential and the corresponding non-local potentials.

Before proceeding further, we may remark that it is by no means necessary to deal with local potentials instead of non-local potentials in the scattering problem. The scattering problem is certainly more complicated with a non-local potential, since one has to solve the Schrödinger equation as an integro-differential equation, or equivalently the Lippmann-Schwinger integral equation, instead of the Schrödinger (differential) equation; but the calculations are, after all, not overwhelmingly complicated. Despite this fact, almost all the papers (known to the author at least) published on e.g. nucleon-nucleon potentials, present potentials which are local, or at

most quadratically momentum dependent. These potentials are obtained by using approximations involving expansions with respect to the inverse of the nucleon mass. The validity of approximations of this kind is quite doubtful in general.

The formalism developed in this paper may be used in practical calculations to obtain local, angular momentum dependent potentials which approximate given non-local potentials. In such an approximation we completely avoid the use of expansions with respect to the inverse of the mass of the scattered particles. As an example, we have considered a single particle exchange potential and calculated the $^1S_0$-phase shifts for the exact potential, the static approximation to it, and for our local approximation to the potential in question. The details concerning the numerical calculations are found in sections 5–6.

From our calculations we conclude that the static approximation is rather poor for attractive potentials, in particular when the mass of the exchanged particle becomes comparable to the mass of the scattered particles, whereas the phase shifts calculated with our local, angular momentum dependent potential, which approximates the non-local single particle exchange potential, agree quite well with the exact phase shifts.

There have also appeared a few papers on the problem of defining "local" potentials, in which no expansion with respect to the inverse mass is used, but where the resulting potential is energy dependent. Among these papers, we may mention one by L. A. P. Balázs[3]. In section 2 we show that the use of an energy dependent potential in an ordinary Schrödinger equation is inconsistent with fundamental symmetry and invariance requirements. This fact casts some doubt on the validity of Balázs' results in particular, and on the use of energy dependent potentials in an ordinary (time independent) Schrödinger equation in general.

In section 3, which is divided into 3 subsections, we investigate under what conditions a potential, given in the momentum representation, may be represented by a local, angular momentum dependent potential in coordinate space, and discuss the properties of such a potential both for physical (integral) values of the angular momentum and for unphysical (complex) values. Section 4 contains a discussion of the equivalence problem, i.e., the problem of obtaining a local potential, which is equivalent to a given non-local one. In section 5 we discuss the single-particle exchange potential, which is used in the numerical calculations.

Finally, in section 6, we present the results of the numerical calculations and a discussion of these results.

In an Appendix, we present a method by which the partial-wave Lippmann-Schwinger equation, which is used in the calculation with the non-local potential, can be reduced to a non-singular equation.

2. The general form of the potential

In this section we review some of the properties of a general potential, which describes the interaction between two chargeless scalar particles of equal mass, and discuss the transformation formulae from the momentum representation to coordinate space representation.

From the analysis given in an article by J. GOTO and S. MACHIDA[4], we can deduce that the most general form of a potential between two scalar particles, which fulfils natural invariance requirements, i.e. invariance with respect to coordinate space translation, Galilei transformation, the exchange of the two particles, rotation of space coordinates, space reflections, time reversal, and Hermiticity of the potential, is, in momentum representation,

$$V(\boldsymbol{q},\boldsymbol{p}) = V_0(\boldsymbol{q}^2,\boldsymbol{p}^2,(\boldsymbol{q}\times\boldsymbol{p})^2). \tag{2.1}$$

The function V_0 is a real function of its arguments, which are the three independent scalars that can be obtained from the vectors $\boldsymbol{q}$ and $\boldsymbol{p}$, which in turn are defined in terms of the centre of mass (c.m) momenta as follows, (Fig. 1)

$$\boldsymbol{q} = \boldsymbol{k} - \boldsymbol{k}', \boldsymbol{p} = \frac{1}{2}(\boldsymbol{k} + \boldsymbol{k}'). \tag{2.2}$$

Defining

$$\boldsymbol{u} = \frac{1}{2}(\boldsymbol{r} + \boldsymbol{r}'), \ \boldsymbol{v} = \boldsymbol{r} - \boldsymbol{r}' \tag{2.3}$$

we have the relation between the coordinate space potential

$$V(\boldsymbol{u},\boldsymbol{v}) \text{ and } V(\boldsymbol{q},\boldsymbol{p})$$

$$V(\boldsymbol{u},\boldsymbol{v}) = \frac{1}{(2\pi)^6}\int d^3\boldsymbol{q}\, d^3\boldsymbol{p}\, e^{i\boldsymbol{q}\cdot\boldsymbol{u}} e^{i\boldsymbol{p}\cdot\boldsymbol{v}} V(\boldsymbol{q},\boldsymbol{p}). \tag{2.4}$$

(We shall occasionally use the same symbol to denote mathematically different functions, such as $V(\boldsymbol{q},\boldsymbol{p})$ and $V(\boldsymbol{u},\boldsymbol{v})$, which should not give rise to confusion). The potential $V(\boldsymbol{u},\boldsymbol{v})$, which in general is non-local, is to be inserted in the Schrödinger equation, in the c.m system*

$$(E_{\text{cm}} + \nabla^2)\psi(\boldsymbol{r}) = \int d^3\boldsymbol{r}'\, V(\boldsymbol{u},\boldsymbol{v})\psi(\boldsymbol{r}'). \tag{2.5}$$

* We use natural units with $\hbar = c = 2M$, where M is the reduced mass.

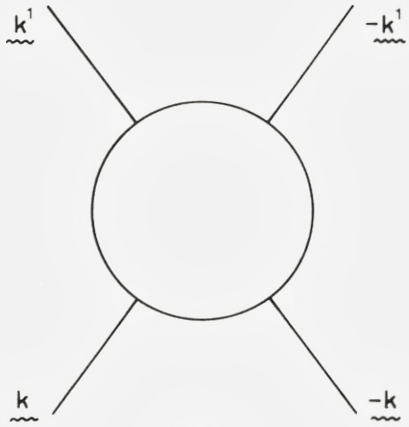

Fig. 1.

The transformation (2.4) is discussed in detail in Ref. (5), where it is shown that $V(\boldsymbol{q},\boldsymbol{p})$ may also be transformed to coordinate space by the formula

$$V(\boldsymbol{r},\hat{p}) = \frac{1}{(2\pi)^3}\int d^3\boldsymbol{q}\, e^{i\boldsymbol{q}\cdot\boldsymbol{r}} V(\boldsymbol{q},\boldsymbol{p}), \tag{2.6}$$

provided $\hat{p}$ in $V(\boldsymbol{r},\hat{p})$ is understood as $-i$ times the symmetrical gradient operator $\overleftrightarrow{\partial}$;

$$\psi^*(\boldsymbol{r})\hat{p}\psi(\boldsymbol{r}) = -\frac{i}{2}(\psi^*(\boldsymbol{r})\nabla\psi(\boldsymbol{r}) - (\nabla\psi^*(\boldsymbol{r}))\psi(\boldsymbol{r})). \tag{2.7}$$

The function $V(\boldsymbol{r},\hat{p})$ may be considered as a symbolical representation of $V(\boldsymbol{u},\boldsymbol{v})$, which in general is non-local.

Conversely, if $V(\boldsymbol{u},\boldsymbol{v})$ is given, $V(\boldsymbol{q},\boldsymbol{p})$ can be obtained by performing the inverse of the double Fourier transform (2.4). This can also be expressed in terms of $V(\boldsymbol{r},\hat{p})$ in the familiar form

$$V(\boldsymbol{q},\boldsymbol{p}) = \int d^3\boldsymbol{r}\, e^{-i\boldsymbol{k}'\cdot\boldsymbol{r}} V(\boldsymbol{r},\hat{p}) e^{i\boldsymbol{k}\cdot\boldsymbol{r}} \tag{2.8}$$

which is equivalent to the inverse of (2.4).

From the previous discussion we deduce that one can obtain a strictly local potential $V(r)$ in coordinate space from a given $V(\boldsymbol{q},\boldsymbol{p})$ only if $V(\boldsymbol{q},\boldsymbol{p})$ is independent of $\boldsymbol{p}$. If $V(\boldsymbol{q},\boldsymbol{p})$ is an arbitrary function of its arguments $\boldsymbol{q}^2,\boldsymbol{p}^2$ and $(\boldsymbol{q}\times\boldsymbol{p})^2$, the resulting coordinate space potential is completely non-local. Only in the special case when $V(\boldsymbol{q},\boldsymbol{p})$ depends quadratically $\boldsymbol{p}$,

is it possible to obtain an "effective" energy dependent potential in coordinate space from the given $V(\boldsymbol{q},\boldsymbol{p})$, in which case the resulting "effective" energy dependent potential depends linearly on the energy of the two-particle system.

We have considered the most general potential to be used in the ordinary Schrödinger equation, restricted only by the invariance and symmetry requirements stated at the beginning of this section, and shown that the potential in the coordinate space representation cannot be an arbitrary function of energy in addition to the r-dependence. We can therefore conclude that the use of an arbitrarily energy-dependent potential in an ordinary Schrödinger equation is inconsistent with the given symmetry and invariance requirements.

There is still one special case in which the potential in coordinate space is neither strictly local nor non-local. When $V(\boldsymbol{q},\boldsymbol{p})$ depends on $\boldsymbol{q}$ and $\boldsymbol{p}$ in a rather special fashion, one obtains in coordinate space a potential $V(r,\boldsymbol{L}^2)$, where $\boldsymbol{L}$ is the angular momentum operator. The next section is devoted to an investigation of this special case.

3.I. Basic properties of the angular momentum dependent potential

We now assume that the potential in momentum representation $V(\boldsymbol{q},\boldsymbol{p})$ is given, and investigate under what conditions $V(\boldsymbol{q},\boldsymbol{p})$ can be represented by a local, angular momentum dependent potential $V(r,\boldsymbol{L}^2)$ in coordinate space. If $V(\boldsymbol{q},\boldsymbol{p})$ is represented by a $V(r,\boldsymbol{L}^2)$ in coordinate space, we have the following relation (eq. (2.8)) between $V(\boldsymbol{q},\boldsymbol{p})$ and $V(r,\boldsymbol{L}^2)$

$$V(\boldsymbol{q},\boldsymbol{p}) = \int d^3\boldsymbol{r} e^{-i\boldsymbol{k}'\cdot\boldsymbol{r}} V(r,\boldsymbol{L}^2) e^{i\boldsymbol{k}\cdot\boldsymbol{r}}. \tag{3.1}$$

We now investigate the restrictive conditions implied by (3.1) for the functional dependence on $\boldsymbol{p}$ and $\boldsymbol{q}$ in $V(\boldsymbol{q},\boldsymbol{p})$ and, assuming these conditions to be fulfilled, derive the inverse of (3.1), which gives $V(r,\boldsymbol{L}^2)$ as an integral transform of $V(\boldsymbol{q},\boldsymbol{p})$.

Let us denote an eigen-state of $\boldsymbol{L}^2$ by $|L\rangle$. Then we have, formally,

$$V(r,\boldsymbol{L}^2)|L\rangle = V(r,L(L+1))|L\rangle. \tag{3.2}$$

A function of an operator can in general be defined through a series expansion in powers of the operator in question. To ensure that eq. (3.2) is valid for all physical values of L, we shall have to require that $V(r,L(L+1))$ can be expanded into a series of powers of $L(L+1)$, convergent for all

(real and complex) values of $L(L+1)$. In other words, we must require that $V(r,L(L+1))$ is an entire function of $L(L+1)$ (for fixed r). When this is the case, the action of $V(r,\boldsymbol{L}^2)$ on an eigenstate $|L\rangle$ is certainly well defined. However, despite the fact that the function $V(r,L(L+1))$ must be an entire function of $L(L+1)$, this function has a well defined meaning only for physical (integral) values of L. When we consider the Schrödinger equation with an angular momentum dependent potential for a general complex value of L, we must use an extrapolation or continuation of the potential to complex values of L, which is such that the Watson-transform[6] can be applied to the resulting scattering amplitude. It is not *a priori* certain that the entire function $V(r,L(L+1))$ offers the required extrapolation. Therefore, when we consider the angular momentum dependent potential for complex values of L, we shall mean a function which coincides with $V(r,L(L+1))$ for physical values of L, but which is extrapolated to complex values of L in such a manner that the Watson-transform can be applied to the resulting scattering amplitude. (We shall later return to this point in detail).

After these preliminaries, we consider eq. (3.1). We may now expand the plane waves in (3.1) into spherical waves and obtain a series involving $V(r,L(L+1))$ on the right hand side of (3.1). The integrations in (3.1) can now be performed term by term, provided $V(r,L(L+1))$ satisfies certain conditions, which we give below. We do not present the details of the necessary convergence proofs, which are readily obtained, using known properties of Neumann series, given e.g. in Watson's "Theory of Bessel functions"[7], (W. 526, W. 35).* The criterions which we have obtained are as follows. First, we require the existence of a fixed number $\alpha < 3$ such that

$$r^{\alpha}V(r,L(L+1)) \tag{3.3}$$

is bounded for $r \geq 0$ and for fixed L. Then we require that $V(r,L(L+1))$ be bounded by a finite power of L, for integral values of L, or more precisely, we require the existence of a fixed non-negative integer p such that

$$\sup_{r \geq 0} \frac{|r^{\alpha}V(r,L(L+1))|}{(2L+1)^{2p}} \leq A \tag{3.4}$$

where A is an absolute constant. Let N now be an arbitrary fixed positive integer. We then have to require the existence of the integrals

$$\int_0^{\infty} dr r^2 |V(r,L(L+1))| \tag{3.5}$$

* References to this work will be cited as W. followed by the appropriate page reference.

for non-negative integral values of L such that $L \leq N$, and the existence of the integrals,

$$\int_0^\infty dr r^{2+m}(2L+1)^{-2p} |V(r,L(L+1))| \tag{3.6}$$

uniformly with respect to L, for integral values of $L > N$. The number m in (3.6) takes the values $m = 0, 1, \ldots, 2p$. We understand by p the smallest non-negative integer for which the conditions (3.4) and (3.6) are fulfilled. The conditions given above are sufficient to guarantee the validity of the term by term integrations in (3.1), when the plane waves are expanded into spherical waves, and also that the resulting series is convergent, uniformly with respect to the angle between $\boldsymbol{k}$ and $\boldsymbol{k}'$, and convergent for all positive fixed values of k and k'. We may summarize the discussion as follows. If a given potential $V(r,L(L+1))$ satisfies the conditions (3.3)–(3.6), an integral transform of the form (3.1) is well defined.

3.II. The partial wave equations

We now proceed to investigate the consequences for $V(\boldsymbol{q},\boldsymbol{p})$ of the assumption that $V(\boldsymbol{q},\boldsymbol{p})$ is represented by a function $V(r,\boldsymbol{L}^2)$ in coordinate space. Let $F(\boldsymbol{k},\boldsymbol{k}')$ be a given function of $\boldsymbol{k}$ and $\boldsymbol{k}'$. We then define the partial wave projection of F as follows,

$$F_{LL'}(k,k') = \int d\Omega_k d\Omega_{k'} Y_{L'}^{m_{L'}*}(\Omega_{k'}) F(\boldsymbol{k},\boldsymbol{k}') Y_L^{m_L}(\Omega_k) \tag{3.7}$$

where the $Y_L^{m_L}$ are spherical harmonics. Taking the partial wave projection of both sides of eq. (3.1), we obtain

$$V_L(k,k') = 4\pi^2(kk')^{-\frac{1}{2}} \int_0^\infty dr r V(r,L(L+1)) J_{L+\frac{1}{2}}(kr) J_{L+\frac{1}{2}}(k'r). \tag{3.8}$$

The function $V_L(k,k')$ is given by

$$V_L(k,k') = \int_{-1}^{+1} dx P_L(x) V(\boldsymbol{q},\boldsymbol{p}), \tag{3.9}$$

where x is the cosine of the angle between $\boldsymbol{k}$ and $\boldsymbol{k}'$, and $P_L(x)$ the Legendre polynomial. The functions $J_\nu(z)$ in (3.8) are Bessel functions of the first kind.

It is clear that eq. (3.8), considered as an integral equation for $V(r,L(L+1))$, can have a solution only if the functional dependence on k and k' in $V_L(k,k')$ is rather restricted. Let us now suppose that we have obtained a solution $V(r,L(L+1))$ to eq. (3.8) ,which fulfills the conditions given earlier in section 3.I, eqns. (3.3)–(3.6). These conditions imply in particular that there should exist a fixed number $n < 2$, such that $r^n V(r,L(L+1))$ is absolutely summable in $(0,\infty)$. The eq. (3.8) is required to hold for all values of k and k' and must in particular be in force for $k = k'$. This means that $V(r,L(L+1))$ also satisfies the equation

$$kV_L(k,k) = 4\pi^2 \int_0^\infty dr r V(r,L(L+1)) J^2_{L+\frac{1}{2}}(kr). \tag{3.10}$$

Suppose now that we solve (3.10) for $V(r,L(L+1))$. The solution obtained from (3.10) can differ from the solution obtained from (3.8) only by a function which we denote by $\Delta(r,L(L+1))$, and which satisfies the equation

$$0 = \int_0^\infty dr r \Delta(r,L(L+1)) J^2_{L+\frac{1}{2}}(kr). \tag{3.11}$$

The function $\Delta(r,L(L+1))$ must also satisfy the summability condition given above and at the same time satisfy (3.11) for all values of k; $0 < k < \infty$. It is therefore clear that $\Delta(r,L(L+1))$ is a null-function, i.e., it equals zero almost everywhere in $(0,\infty)$; therefore, whenever eq. (3.8) has a solution for $V(r,L(L+1))$, this solution can be obtained from eq. (3.10) instead of eq. (3.8). Before solving eq. (3.8), we return to the problem of extrapolating $V(r,L(L+1))$ to complex values of L.

From the discussion given by L. Brown et al.[8] on the partial wave Lippmann-Schwinger (L.-S.) equation in momentum space, we may deduce that we get the "correctly" extrapolated scattering amplitude from the L.-S. equation, provided we extrapolate the potential in the L.-S. equation, which is essentially the function $V_L(k,k')$ (eq. (3.9)), in a manner which is consistent with the well known theorem of Carlson[9]. Let λ_0 be a fixed real number, and let λ denote $L+1/2$. Let $\lambda = \lambda_0 + \varrho e^{i\theta}$. The function $A(\lambda;k,k')$, which extrapolates $V_L(k,k')$, is now a function which (for k,k' fixed) (i) coincides with $V_L(k,k')$ at the non-negative integers larger than λ_0; (ii) is regular at all points inside the angle $-\alpha \leqq \theta \leqq \alpha$, where $\alpha \geqq \frac{\pi}{2}$; (iii) is bounded by $Ae^{B\varrho}$, where A and B are absolute constants and $B < \pi$, throughout the angle $-\alpha \leqslant \theta \leqslant \alpha$. If necessary, one may also allow a finite num-

ber of poles in the extrapolating function $A(\lambda;k,k')$. The coordinate space potential, corresponding to $A(\lambda;k,k')$, $W(r,\lambda)$, is now related to $A(\lambda;k,k')$ by the generalization of eq. (3.8) or equivalently eq. (3.10)

$$kA(\lambda;k,k) = 4\pi^2 \int_0^\infty drrW(r,\lambda)J_\lambda^2(kr). \tag{3.12}$$

The function $W(r,\lambda)$ defined by (3.12) coincides with $V(r,L(L+1))$ defined by (3.10) at the non-negative integers (exceeding λ_0), but is in general different for general complex values of λ.

3.III. The inversion formula

In order to solve the eqns. (3.10) and (3.12), we need the following theorem (a proof of which is given in Appendix I);

Theorem: If $xf(x,\lambda)$ is differentiable in $(0,\infty)$, and if $(xf(x,\lambda))' \equiv \frac{d}{dx}(xf(x,\lambda))$ belongs to $L^2(0,\infty)$ uniformly with respect to λ within a closed domain to the right of the line $Re(\lambda) = -\frac{1}{4}$, the equation

$$f(x,\lambda) = \int_0^\infty dyg(y,\lambda)J_\lambda^2(xy) \tag{3.13}$$

implies almost everywhere

$$g(x,\lambda) = -2\pi \frac{d}{dx}\int_0^\infty \frac{dy}{y}(yf(y,\lambda))' \int_0^{xy} duuJ_\lambda(u)Y_\lambda(u), \tag{3.14}$$

and $g(x,\lambda)$ defined for $Re(\lambda) > -\frac{1}{4}$ by (3.14) also belongs to $L^2(0,\infty)$. The function $Y_\lambda(z)$ in (3.14) is a Bessel function of the second kind.

We now assume that $(k^2A(\lambda;k,k))'$ exists and belongs to $L^2(0,\infty)$ for $Re(\lambda) \geq \lambda' \geq \lambda_0$. Then we obtain

$$rW(r,\lambda) = -\frac{1}{2\pi}\frac{d}{dr}\int_0^\infty \frac{dk}{k}(k^2A(\lambda;k,k))' \int_0^{kr} duuJ_\lambda(u)Y_\lambda(u), \tag{3.15}$$

for $Re(\lambda) \geq \max\left(\lambda', -\frac{1}{4}+\varepsilon\right)$, where ε is a fixed arbitrary positive number, however small.

We know from our inversion theorem that $rW(r,\lambda)$ defined by (3.15) belongs to $L^2(0, \infty)$. Therefore, the potential we obtain from (3.15) cannot be more singular than $o(r^{-\frac{3}{2}})$ for small values of r, in contrast to the allowed behaviour $o(r^{-3})$. However, one can probably generalize the inversion theorem to cover a class of functions which behave like $o(r^{-3})$ for small values of r.

The expression (3.15) for $W(r,\lambda)$ has been obtained by using only the on-shell part of $A(\lambda;k,k')$. As mentioned above, the function $W(r,\lambda)$, which we obtain by using only the on-shell part of $A(\lambda;k,k')$, coincides with the $W(r,\lambda)$, obtained from the original off-shell equation, whenever the latter has a solution. We can therefore conclude the following. The assumption that $V(\boldsymbol{q},\boldsymbol{p})$ is represented by a $V(r,\boldsymbol{L}^2)$ in coordinate space, implies no restrictions on the on-shell part of $V(\boldsymbol{q},\boldsymbol{p})$, (apart from the differentiability and summability condition for the class of functions considered here), but implies that $V(\boldsymbol{q},\boldsymbol{p})$ should be continued off the energy shell in a particular way.

We can formulate this condition more easily in terms of $V_L(k,k')$ as follows. In order that a $V(\boldsymbol{q},\boldsymbol{p})$ be represented by a $V(r,\boldsymbol{L}^2)$ in coordinate space, it is necessary that the partial wave projection $V_L(k,k')$ of $V(\boldsymbol{q},\boldsymbol{p})$ has a repeated integral representation of the form

$$\left.\begin{aligned} V_L(k,k') = -2\pi(kk')^{-\frac{1}{2}}\Bigg\{ & \int_0^\infty dr J_{L+\frac{1}{2}}(kr) J_{L+\frac{1}{2}}(k'r) \\ & \left(\frac{d}{dr}\int_0^\infty \frac{dz}{z}\left[\frac{d}{dz}(z^2 V_L(z,z))\right]\int_0^{zr} du u J_{L+\frac{1}{2}}(u) Y_{L+\frac{1}{2}}(u)\right)\Bigg\} \end{aligned}\right\} \tag{3.16}$$

The condition (3.16) looks rather complicated, but the content of it is clear enough, namely, that the off-shell part $V_L(k,k')$ is uniquely given by the on-shell part $V_L(k,k)$ for a potential which is represented in coordinate space by a local, angular momentum dependent potential. This is of course also true for a strictly local potential $V(r)$, as this is a special case of a local angular momentum dependent potential.

We shall now finally have to make sure that $W(r,\lambda)$, given by (3.15), actually reduces to a function $V(r,L(L+1))$ when L in λ becomes a non-negative integer, and that this $V(r,L(L+1))$ can be considered as an entire function of $L(L+1)$. When L is a non-negative integer, then we have

$$J_{L+\frac{1}{2}}(z) Y_{L+\frac{1}{2}}(z) = (-1)^{L+1} J_{L+\frac{1}{2}}(z) J_{-(L+\frac{1}{2})}(z), \tag{3.17}$$

and the right hand side of (3.17) is, apart from the factor $(-1)^{L+1}$, an entire function of $L(L+1)$ for fixed z. From (3.15) we then obtain

$$rV(r,L(L+1)) = \frac{1}{2\pi}\frac{d}{dr}\int_0^\infty \frac{dk}{k}((-1)^L k^2 V_L(k,k))' \left\{ \int_0^{kr} duuJ_{L+\frac{1}{2}}(u)J_{-(L+\frac{1}{2})}(u) \right\}. \tag{3.18}$$

From the definition of $V_L(k,k')$, eq. (3.9), we obtain

$$(-1)^L V_L(k,k) = \int_{-1}^{+1} dx P_L(-x)V(\boldsymbol{q},\boldsymbol{p}), \tag{3.19}$$

where we have used the well known symmetry property of the Legendre polynominal. (It is of course understood that we use the constraint $k = k'$ in $V(\boldsymbol{q},\boldsymbol{p})$ in (3.19)). It is known that the function $P_L(-x)$ considered as a function of $L(L+1)$ is an entire function of $L(L+1)$, when x has any assigned value, such that $-1 \leq x < 1$. The function $(-1)^L V_L(k,k)$ defined by (3.19) for general values of L will therefore be an entire function of $L(L+1)$, provided well known conditions concerning continuity and uniformity of convergence of the integral (3.19) are satisfied. The integrand in (3.18) becomes then an entire function of $L(L+1)$, which means that also $V(r,L(L+1))$, defined by (3.18), is an entire function of $L(L+1)$, provided certain standard conditions are satisfied.

It is a simple matter to show that $V(r,L(L+1))$ is bounded by a finite power of $L(L+1)$ for integral values of L, and to derive conditions for the existence of the appropriate number of absolute moments of $V(r,L(L+1))$, in accordance with the discussion in section 3.I. The proofs are neither very difficult nor very interesting, and are therefore omitted.

4. The equivalence problem

In the previous sections we have investigated in detail the properties of a local, angular momentum dependent potential, and derived the conditions under which a potential given in momentum space is represented by a local, angular momentum dependent potential in coordinate space.

Let us first discuss the definition of a potential in perturbation theory. We follow the discussion given in a paper by A. A. Logunov et al.[10]. The

authors of this paper define the potential by the requirement that, when inserted into an equation of the Lippmann-Schwinger type considered by them, it will reproduce, to each order in perturbation theory, a T-matrix on the energy shell, which is considered given through an expansion in a coupling constant. The equation in question can in fact be exactly reduced to the ordinary non-relativistic Lippmann-Schwinger equation, as we are going to show in the following subsection. The definition formulated above can symbolically be stated as follows

$$[V_2] = [T_2], [V_{2n}] = [T_{2n}] - \sum_{m=1}^{n-1} [V_{2m} \times T_{2n-2m}]. \tag{4.1}$$

Here T_2 is the second order T-matrix, and V_2 the second order potential (in momentum space) etc., and the square brackets mean a transition to the energy shell in the corresponding expressions.

Let us now discuss the meaning of eq. (4.1) more in detail. We see that the second order potential V_2 becomes fixed only on the energy shell. We can therefore continue the function V_2 off the energy shell in any (reasonable) prescribed manner. It seems therefore natural to continue V_2 off the energy shell in such a manner that V_2 becomes as simple as possible, without imposing restrictions at the same time on the resulting T-matrix by the chosen off shell continuation. This principle leads to an off shell continuation of V_2, which permits V_2 to be represented by a local, angular momentum dependent potential in coordinate space. Whatever off shell continuation we choose for V_2, we have as the result that the (new) T-matrix part corresponding to the chosen V_2 is $\bar{T}_2 = V_2$. (This fact is not indicated in eq. (24) of Logunov et al., which corresponds to our eq. (4.1)). The fourth-order potential V_4 becomes again fixed on the energy shell only, be the next equation in (4.1). However, the value of V_4 on the energy shell depends now also on the off shell continuation chosen for V_2. We can then continue V_4 off the energy shell in the same way as V_2. The new fourth order T-matrix is now $\bar{T}_4 = V_4 + V_2 \times \bar{T}_2$. It is obvious that we can continue this reasoning to any order in perturbation theory. We have thus demonstrated that there is a considerable amount of freedom in choosing the off shell continuation of a potential which is constructed to reproduce a given T-matrix on the energy shell only. This does not mean that we can add arbitrary terms vanishing on the energy shell to a given potential without affecting the resulting T-matrix on the energy shell. In particular we have shown that a potential, defined by the principle symbolically stated in eq.

(4.1), can be chosen to be local and angular momentum dependent in coordinate space.

From their eq. (24) LOGUNOV et al. conclude that the potential can be chosen to be a local, energy dependent function in coordinate space. This is inconsistent with basic symmetry and invariance requirements, as we demonstrated earlier. (Some of the equations of LOGUNOV et al. manifestly violate the necessary symmetry between in- and out-going momenta.) We note incidentally that we have also in the foregoing discussion explicitly demonstrated that it is possible to construct a local, angular momentum dependent potential, which is equivalent to a given non-local one.

It appears to be rather difficult, however, to obtain a solution to the equivalence problem without resorting to perturbation theory arguments, or without solving directly the whole scattering problem with the non-local potential. To see this clearly, let us consider the partial wave Lippmann-Schwinger equation. We define

$$U_L(k',k) = -\frac{k'}{8\pi} V_L(k',k), \tag{4.2}$$

where $V_L(k',k)$ is the partial wave projection of the potential, defined by eq. (3.9). We then have the partial wave L.-S.-equation

$$T_L(k',k) = U_L(k',k) + \frac{2}{\pi}\int_0^\infty \frac{dk'' k'' U_L(k',k'') T_L(k'',k)}{k''^2 - k^2 - i\varepsilon}, \tag{4.3}$$

where T_L is an off shell amplitude, which on the energy shell becomes

$$T_L(k,k) = e^{i\delta_L(k)} \sin(\delta_L(k)). \tag{4.4}$$

The main ambiguity in the potential is due to the fact that there exists a whole class of functions $U_L(k',k)$ which give rise to the same T_L on the energy shell, but for which T_L off the energy shell is different. This ambiguity is the one we have already discussed in the foregoing perturbation theory discussion. The other ambiguity comes from the possible existence of bound states. To see this clearly, we consider the problem of deducing $U_L(k',k)$ from a given phase shift $\delta_L(k)$, with the aid of eq. (4.3). Let us then suppose that we make an arbitrary (but sufficiently smooth) off shell continuation of the $T_L(k,k)$, which is determined by $\delta_L(k)$. The eq. (4.3) can then be considered as a singular integral equation for $U_L(k',k)$, with k' as a parameter. Consulting the literature on singular integral equations[11], we observe that

eq. (4.3) can be reduced to a Fredholm equation for $U_L(k',k)$. However, we do not in general obtain a unique solution for $U_L(k',k)$ from eq. (4.3). This ambiguity is related to the existence of linearly independent solutions to the dominant part of eq. (4.3). The theorems given in Ref. (11) state that the number of linearly independent solutions equals the index $\varkappa$ of the Hilbert problem connected to the solving of the dominant equation. The index $\varkappa$ can easily be calculated and is, in this case, given by

$$\varkappa = \frac{1}{\pi}(\delta_L(0+) - \delta_L(\infty)). \tag{4.5}$$

The index $\varkappa$ given by (4.5) is equal to the number of bound states in the L:th partial wave. We have thus obtained the result: For a given off shell continuation of T_L, we obtain $\varkappa$ independent potentials $U_L^{(1)}$, $U_L^{(2)}$, . . . , $U_L^{(\varkappa)}$, which produce the given T_L on the energy shell.

Thus, using an other off shell continuation of the T_L given on the energy shell, we can obtain $\varkappa$ different potentials $\overline{U}_L^{(1)}$, $\overline{U}_L^{(2)}$, . . . , $\overline{U}_L^{(\varkappa)}$. We can thus assert that there exists a p-fold class of potentials which produce a given phase shift, where p is the number of bound states in the partial wave under consideration.

However, we have not been able to obtain a simple and explicit relation between two members $U_L^{(i)}$ and $\overline{U}_L^{(i)}$ of this class.

We have now analysed the ambiguities inherent in a potential, which is required to produce a given T-matrix on the energy shell only. We may conclude that, although it is in principle possible to use these ambiguities in constructing a local, angular momentum dependent potential, which is equivalent to a given non-local potential, this problem has apparently no simple and practical solution.

The formalism developed in this paper may, however, be used to approximate non-local potentials by local, angular momentum dependent potentials. We conclude this section with a brief discussion of this possibility, and of the conventional methods which have been earlier used to approximate non-local potentials by local ones. Let us consider again the potential

$$V(\boldsymbol{q},\boldsymbol{p}) \tag{4.6}$$

where, as before, $\boldsymbol{q}$ is the momentum transfer and $2\boldsymbol{p}$ is the sum of the in- and outgoing momenta in the c.m. system. Let us then suppose that we can expand (4.6) in powers of $\boldsymbol{p}^2$

$$V(\boldsymbol{q},\boldsymbol{p}) = \sum_{n=0}^{\infty} v_n(\boldsymbol{q})\boldsymbol{p}^{2n} \tag{4.7}$$

The so-called static approximation means that we neglect all higher powers of $\boldsymbol{p}^2$, and use $v_0(\boldsymbol{q})$ as an approximation to $V(\boldsymbol{q},\boldsymbol{p})$. It is clear that $v_0(\boldsymbol{q})$ becomes local in coordinate space. In the next approximation we obtain a quadratically momentum dependent potential: $v_0(\boldsymbol{q}) + v(\boldsymbol{q})\boldsymbol{p}^2$. In coordinate space, this becomes of the form $\bar{v}_0(r) + \bar{v}_1(r)\hat{p}^2$, where $\hat{p}$ is the differential operator defined by eq. (2.7). It is obvious that one cannot continue this approximation method to higher order terms, since potentials of the form $\bar{v}_n(r)(\hat{p}^2)^n$ $(n > 1)$ cannot be used in the Schrödinger equation. We may remark that the potentials derived from meson theory are not entire functions of $\boldsymbol{p}^2$, so that expansions of the type (4.7) do not exist except possibly in a small region around $\boldsymbol{p}^2 = 0$. From the formal point of view, the approximations based on equations of the type (4.7) are therefore meaningless. However, if the function $V(\boldsymbol{q},\boldsymbol{p})$ is a slowly varying bounded function of $\boldsymbol{p}^2$, the static approximation need not be entirely unreliable. If this is the case, then the next approximation $v_0(\boldsymbol{q}) + v_1(\boldsymbol{q})\boldsymbol{p}^2$ is certainly very doubtful, although it might to some extent be remediable by a properly chosen cut off.

Despite the large uncertainties which inevitably are connected with the use of approximations involving expansions with respect to $\boldsymbol{p}^2$, such approximations have been used extensively e.g. in derivations of nucleon-nucleon potentials. The approximation method we suggest is rather obvious. Consider the partial wave projection $V_L(k,k')$ of the potential $V(\boldsymbol{q},\boldsymbol{p})$. We now approximate the function $V_L(k,k')$ by a function $\bar{V}_L(k,k')$, which coincides with $V_L(k,k')$ on the energy shell, but which is continued off the energy shell in the manner prescribed by eq. (3.16). The function $\bar{V}_L(k,k')$ coincides with $V_L(k,k')$ along the lines $k = 0$, $k' = 0$ and $k = k'$. Unless $V_L(k,k')$ varies violently in the sectors between these lines, we may expect that $\bar{V}_L(k,k')$ approximates $V_L(k,k')$ in an acceptable manner in the whole first quadrant of the kk'-plane. The coordinate space potential corresponding to $\bar{V}_L(k,k')$ is obtained directly by inserting $V_L(k,k)$ in the formula (3.18), or, for complex L, eq. (3.15).

5. The single-particle exchange potential

We consider an equation, recently discussed by R. Blankenbecler and R. Sugar[12],

$$M(\boldsymbol{k}',\boldsymbol{k}) = W(\boldsymbol{k}',\boldsymbol{k}) + \frac{1}{4}\int \frac{d^3\boldsymbol{k}'' W(\boldsymbol{k}',\boldsymbol{k}'') M(\boldsymbol{k}'',\boldsymbol{k})}{(2\pi)^3 \sqrt{\boldsymbol{k}''^2 + 1^1}(\boldsymbol{k}''^2 - \boldsymbol{k}^2)} \tag{5.1}$$

Here $W(\boldsymbol{k}', \boldsymbol{k})$ is the propagator for the exchange of a particle of mass m between two scalar particles of unit mass

$$W(\boldsymbol{k}', \boldsymbol{k}) = g^2(m^2 + (\boldsymbol{k} - \boldsymbol{k}')^2)^{-1}, \tag{5.2}$$

and $\boldsymbol{k}'$ and $\boldsymbol{k}$ the relative initial and final momenta, respectively, in the c.m. system. The eq. (5.1) with W given by (5.2) may be considered as an approximation to the Bethe-Salpeter equation in the ladder approximation. An equation of the type (5.1) has also been discussed earlier, e.g. in the previously mentioned article by A. A. Logunov et al. (Ref. (10)). We recall that there is a difference in normalization between the relativistic amplitude M and the amplitude T, which occurs in the ordinary non-relativistic Lippmann-Schwinger equation.

Defining

$$T(\boldsymbol{k}', \boldsymbol{k}) = -\frac{M(\boldsymbol{k}', \boldsymbol{k})}{4\sqrt[4]{\boldsymbol{k}'^2 + 1}\sqrt[4]{\boldsymbol{k}^2 + 1}}, \tag{5.3}$$

$$V(\boldsymbol{k}', \boldsymbol{k}) = -\frac{W(\boldsymbol{k}', \boldsymbol{k})}{4\sqrt[4]{\boldsymbol{k}'^2 + 1}\sqrt[4]{\boldsymbol{k}^2 + 1}}, \tag{5.4}$$

we obtain the ordinary L.-S.-equation from (5.1)

$$T(\boldsymbol{k}', \boldsymbol{k}) = V(\boldsymbol{k}', \boldsymbol{k}) + \frac{1}{(2\pi)^3}\int d^3\boldsymbol{k}'' \frac{V(\boldsymbol{k}', \boldsymbol{k}'')\, T(\boldsymbol{k}'', \boldsymbol{k})}{\boldsymbol{k}^2 - \boldsymbol{k}''^2 - i\varepsilon} \tag{5.5}$$

The function $V(\boldsymbol{k}', \boldsymbol{k})$ in (5.5) is precisely the quantity we have called a potential in momentum space, expressed as a function of the in- and outgoing momenta $\boldsymbol{k}'$ and $\boldsymbol{k}$. (Note the symmetry between $\boldsymbol{k}'$ and $\boldsymbol{k}$ in (5.4)). For later convenience, we introduce explicitly a mass M of the scattered particles in the expression (5.4), and introduce also a strength parameter $\Lambda = -g^2/16\pi$. The expression for the single-particle exchange potential is then

$$V(\boldsymbol{k} - \boldsymbol{k}', \tfrac{1}{2}(\boldsymbol{k} + \boldsymbol{k}')) = \frac{4\pi\Lambda M}{\sqrt[4]{\boldsymbol{k}^2 + M^2}\sqrt[4]{\boldsymbol{k}'^2 + M^2}((\boldsymbol{k} - \boldsymbol{k}')^2 + m^2)}. \tag{5.6}$$

We evaluate the partial wave projection of (5.6) according to eq. (3.9) and obtain

$$V_L(k,k') = \frac{4\pi\Lambda M}{kk'\sqrt[4]{k^2+M^2}\sqrt[4]{k'^2+M^2}}\, Q_L\left(\frac{k^2+k'^2+m^2}{2kk'}\right), \tag{5.7}$$

where Q_L is a Legendre function of the second kind. We can also immediately infer from the properties of the Q_L-function that the expression

$$A(\lambda;k,k') = \frac{4\pi\Lambda M}{kk'\sqrt[4]{k^2+M^2}\sqrt[4]{k'^2+M^2}}\, Q_{\lambda-\frac{1}{2}}\left(\frac{k^2+k'^2+m^2}{2kk'}\right), \tag{5.8}$$

is the correct continuation of $V_L(k,k')$.

The static approximation of (5.6) consists of replacing the factor

$$M\left(\sqrt[4]{k^2+M^2}\sqrt[4]{k'^2+M^2}\right)^{-1}$$

by unity. We then obtain, upon transision to coordinate space, the well known Yukawa potential

$$V(r) = \Lambda\frac{e^{-mr}}{r} \tag{5.9}$$

It is not difficult to see that the off shell behaviour of $V_L(k,k')$ in (5.7) does not allow $V_L(k,k')$ to be represented by a local, angular momentum dependent potential in coordinate space. In constructing the potential $W(r,\lambda)$ from $A(\lambda;k,k)$ given by (5.8), we therefore make an approximation of the kind previously discussed. We obtain, according to eq. (3.15), $\left(Re(\lambda) > -\frac{1}{4}\right)$,

$$rW(r,\lambda) = -\Lambda\int_0^\infty dk\left[\frac{d}{dk}\left(\frac{2M}{\sqrt{M^2+k^2}}\, Q_{\lambda-\frac{1}{2}}\left(1+\frac{m^2}{2k^2}\right)\right)\right]\left\{krJ_\lambda(kr)Y_\lambda(kr)\right\}. \tag{5.10}$$

We may check the integral (5.10) by putting $M(M^2+k^2)^{-\frac{1}{2}} = 1$ in the integrand. The integral can then be evaluated and becomes precisely equal to (5.9), as it should.

When L is a non-negative integer, we may use the simple analytic properties of the integrand in (5.10) to write the integral in a more convenient form. We denote by $K_{L+\frac{1}{2}}(z)$ the exponentially damped Bessel function (W. 80)

$$K_{L+\frac{1}{2}}(z) = \left(\frac{\pi}{2z}\right)^{\frac{1}{2}} e^{-z}\sum_{n=0}^{L}\frac{(L+n)!}{n!\,(L-n)!}(2z)^{-n}. \tag{5.11}$$

$$(L = 0,1,2,\ldots.)$$

Let

$$C_L(z) = \frac{d}{dz}(zK^2_{L+\frac{1}{2}}(z)). \tag{5.12}$$

After some exercises in contour integration, we obtain from (5.10)

$$\left.\begin{aligned} V(r, L(L+1)) = &-A\frac{2}{\pi}\int_{\frac{m}{2}}^{M}\frac{dyM}{\sqrt{M^2-y^2}}P_L\left(\frac{m^2}{2y^2}-1\right)C_L(yr) \\ &+A\frac{4}{\pi^2}(-1)^L\int_{M}^{\infty}\frac{dyM}{\sqrt{y^2-M^2}}Q_L\left(1-\frac{m^2}{2y^2}\right)C_L(yr) \\ &(L = 0, 1, 2, \ldots) \end{aligned}\right\} \tag{5.13}$$

It is easily seen that the local, angular momentum dependent potential (5.10) and (5.13) posesses the properties we required in section 3.I.

6. Numerical results and discussion

In this section we describe the results of the numerical calculations performed with the non-local potential (5.6) and the two approximations (5.9) and (5.13), respectively, to this non-local potential.

A calculation of phase shifts with a non-local potential in momentum space has been performed e.g. by J. Goto[13] and by P. Signell and P. S. Connors[14]. These authors restricted themselves to calculate phase shifts for a one-pion exchange potential. They also used a rather small cut off, of the order $M - 2M$, where M is the nucleon mass. This makes it difficult to compare their results directly with those obtained in the static approximation with the local potential in coordinate space.

In fact, to the best of the author's knowledge, there exists no systematic investigation of the validity of the static approximation, even for the simple case of a single-particle exchange potential. We have attempted to make such an investigation by calculating the $L = 0$ phase shifts with the potentials mentioned above, for a number of values of the strength parameter A and of the mass m of the exchanged particle. The mass M is given the value of the nucleon mass ($M = 938.5$ MeV). In order to have a physical measure of the strength of the potentials, we present below a table (Table 1), which shows the values of A, for which one and two bound S-states occur with the Yukawa potential (5.9)[15].

TABLE 1.

m(MeV)	$\Lambda(1)$	$\Lambda(2)$
140	−0.25	−0.95
280	−0.50	−1.9
400	−0.72	−2.7
700	−1.25	−4.8

(The strength of the static one-pion exchange potential in the $^1S_0$-state corresponds to $\Lambda = -0.081$.)

For positive values of Λ in the range $0 < \Lambda < 3$, there is no appreciable difference ($< 5\%$) between the phase shifts calculated with the potentials (5.6), (5.9) and (5.13), respectively, in the energy region $0 < E_{\mathrm{LAB}} < 280$ (MeV) and for the values of m, given in Table 1. For attractive potentials the situation is different. Here the static approximation yields systematically too large phase shifts. In the static approximation we replace the factor $M(M^2+k^2)^{-\frac{1}{4}}(M^2+k'^2)^{-\frac{1}{4}}$ by unity in the expression (5.6) for the potential in momentum space. The resulting coordinate space potential becomes therefore too singular near $r = 0$. When we take this factor into account in the approximation (5.13), we obtain a potential, which behaves like $O(\log^2(r))$ near $r = 0$, in contrast to the $O(r^{-1})$ behaviour of the Yukawa potential. The difference between the phase shifts in the static approximation and the phase shifts resulting from the potential (5.6) increases rapidly with increasing m and $|\Lambda|$. We give examples of this in Fig. 2–Fig. 10. The curves labeled "Exact" in Fig. 2–Fig. 10, are the $L = 0$ phase shifts, which are obtained by solving the partial wave Lippmann-Schwinger equation (see appendix II) with the potential given by (5.7). The curves labeled "Yukawa" are the phase shifts in the static approximation, obtained from the Schrödinger equation with the potential (5.9), whereas the curves labeled "Appr." are the phase shifts obtained from the Schrödinger equation with the local, angular momentum dependent potential (5.13). The phase shifts obtained from the L.S.-equation are given only in the energy region $50 < E_{\mathrm{LAB}} < 280$ (MeV). We have checked the accuracy of the phase shifts resulting from the L.S.-equation by solving also the L.S.-equation with the static approximation to (5.7). The difference between the phase shifts obtained in this way, and those obtained with the Yukawa potential (5.9), gives a measure of the accuracy achieved in solving the L.S.-equation. Table 2 shows these maximal absolute differences for the values of m and Λ given in Fig. 2–Fig. 10.

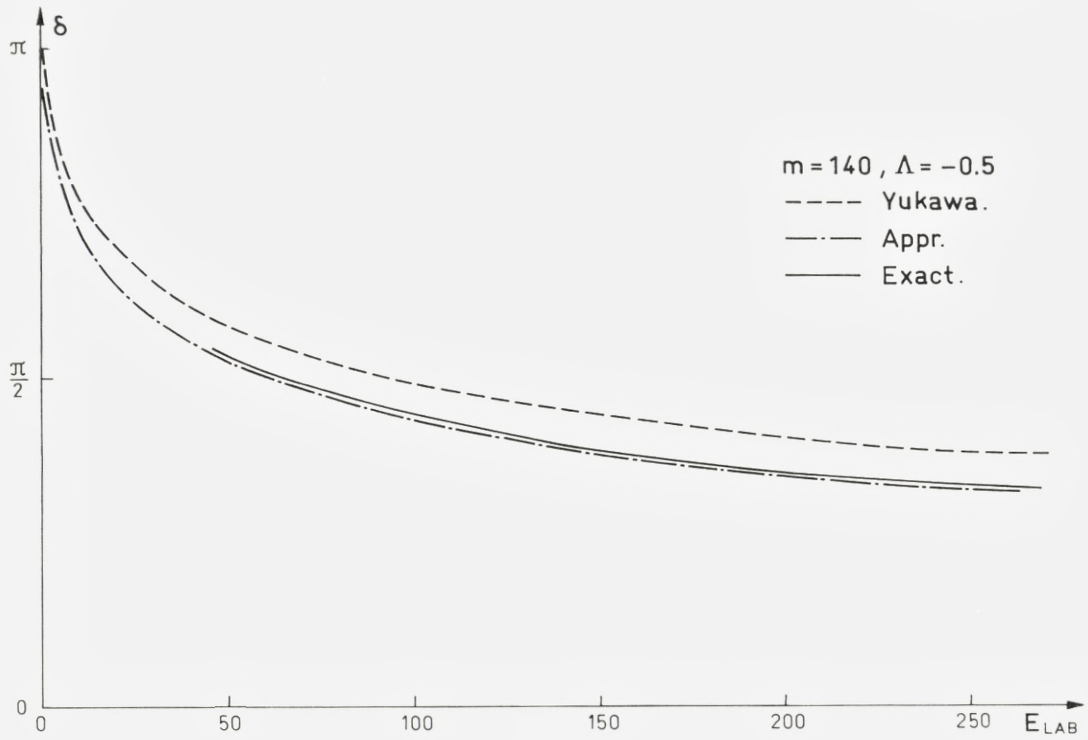

Fig. 2.

TABLE 2.

m(MeV)	Max. num. error
140	0.030
280	0.028
400	0.033
700	0.038

The numerical errors inherent in the curves labeled "Exact" in Fig. 2–Fig. 10 are therefore rather small, and can hardly produce any detectable effect in the given curves. From Fig. 2–Fig. 10, it is seen that the difference between the exact and the Yukawa phase shifts is approximately constant over the range $50 < E_{\mathrm{LAB}} < 280$ (MeV). A measure of the average error in calculating the phase shifts in the static approximation (5.9) instead of using the potential (5.7) is therefore the difference between the Yukawa phase

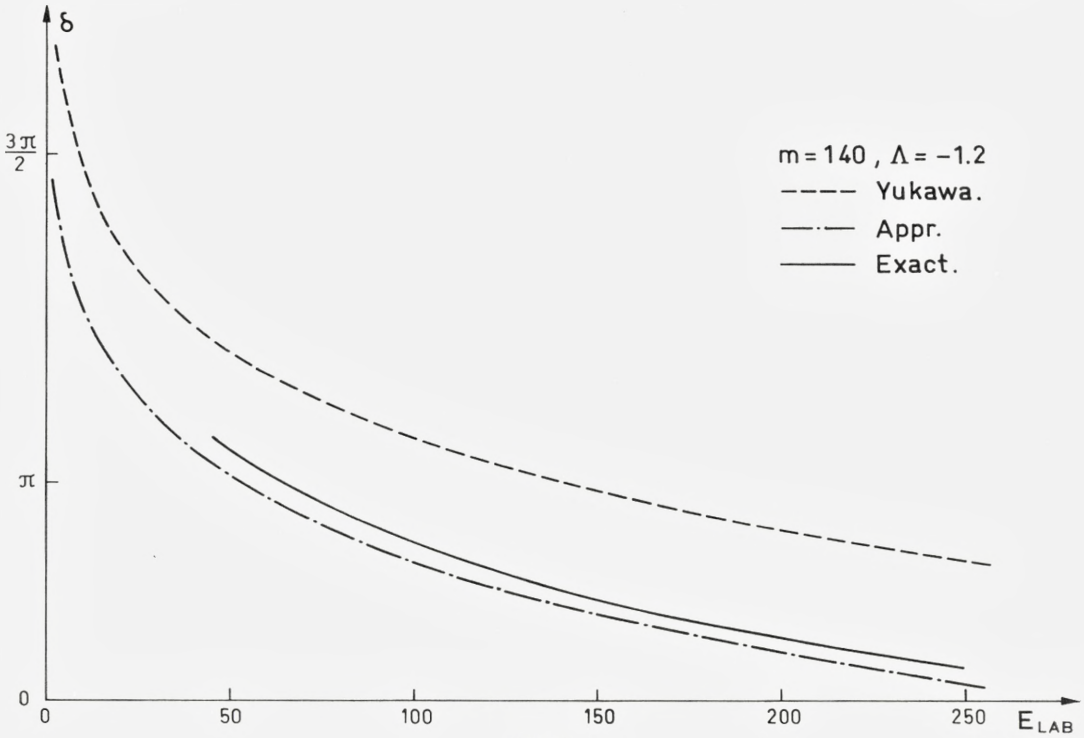

Fig. 3.

TABLE 3.

Λ	m(MeV)	D_{LOCAL} %	D_{STATIC} %
−0.5	140	—	14
−1.2	140	−2.7	20
−0.8	280	−2.7	19
−1.5	280	−2.5	24
−0.7	400	−2.1	19
−1.1	400	−3.7	24
−2.0	400	−3.9	26
−1.1	700	−4.9	32
−2.0	700	−6.5	36

shift and the exact one at 150 MeV. We give above a table (Table 3) of this difference, D STATIC, expressed in percent of the exact phase shift, and also the corresponding difference, D LOCAL, between the exact phase shift

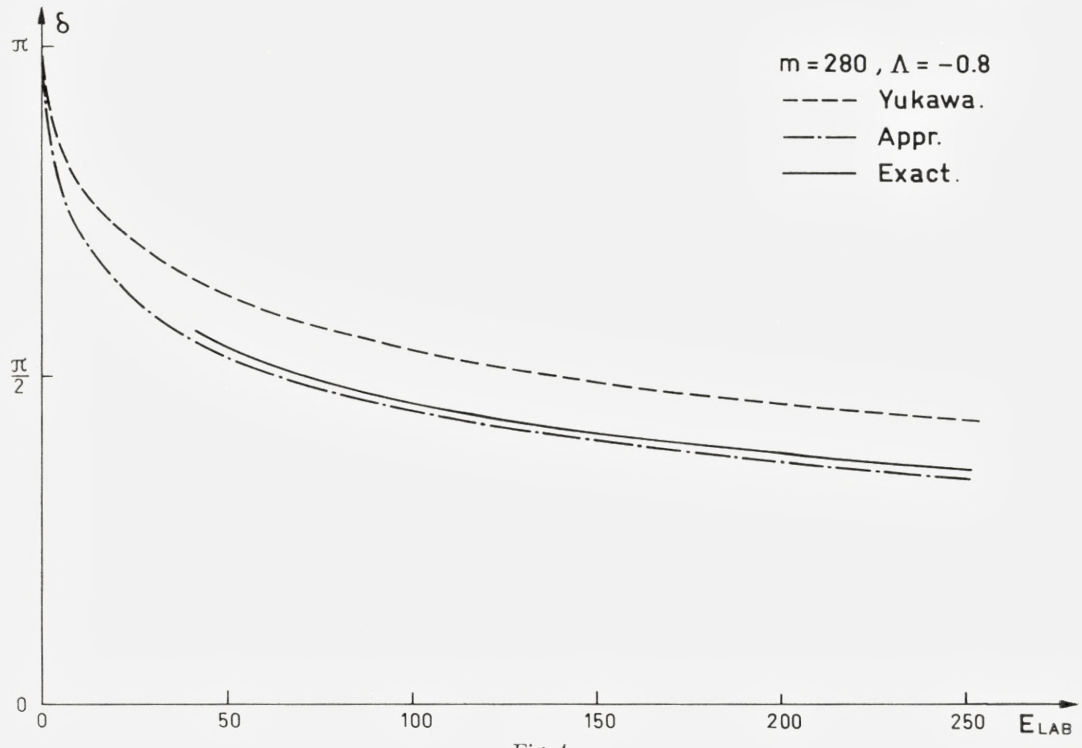

Fig. 4.

and the one obtained with the local, angular momentum dependent potential (5.13).

We have thus shown that the static approximation is quite unreliable for the attractive single-particle exchange potential, in particular when the mass of the exchanged particle becomes large, whereas the phase shifts calculated with the local, angular momentum dependent potential agree quite well with the exact phase shifts. The potential (5.6) is, of course, not exact in an absolute sense, but represents a potential which, when used in the Schrödinger equation, yields an approximation to the sum of all ladder diagrams, as previously pointed out.

In section 4 we showed explicitly that, in perturbation theory, one can choose the potential to be local and angular momentum dependent in coordinate space, since this merely corresponds to a rearrangement of the (infinite number of) equations connecting the quantities T_{2n} and V_{2n}. However, the problem of constructing a potential to all orders in perturbation

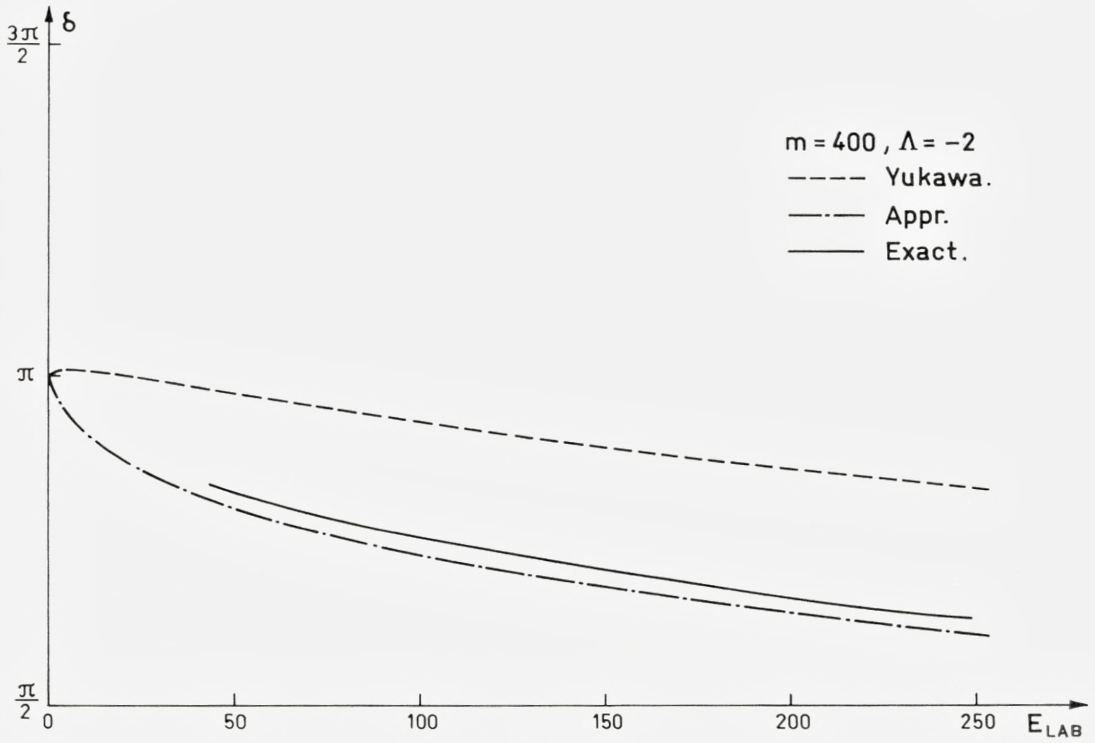

Fig. 5.

theory is, of course, highly academic since, if every T_{2n} is known, and if it is possible to sum these quantities, it is indeed unnecessary to obtain a potential V, which on insertion in a Schrödinger equation yields the known T-matrix. In practice, the potential V is constructed up to some finite (and small) order, which means that one obtains approximations to the sums of those classes of diagrams, which are the iterations of the diagrams included in V, when using this V in the Schrödinger equation. When the potential V is constructed only up to a finite order, the resulting phase shifts do indeed depend on the off shell continuation chosen for V. From the pure S-matrix point of view, the question of the off shell continuation is undecidable. However, for reasonable potentials and reasonable off shell continuations, we may expect that the resulting phase shifts do not differ much for two different off shell continuations, even when the potential is constructed up to some small order, as indicated by the numerical example considered in this section.

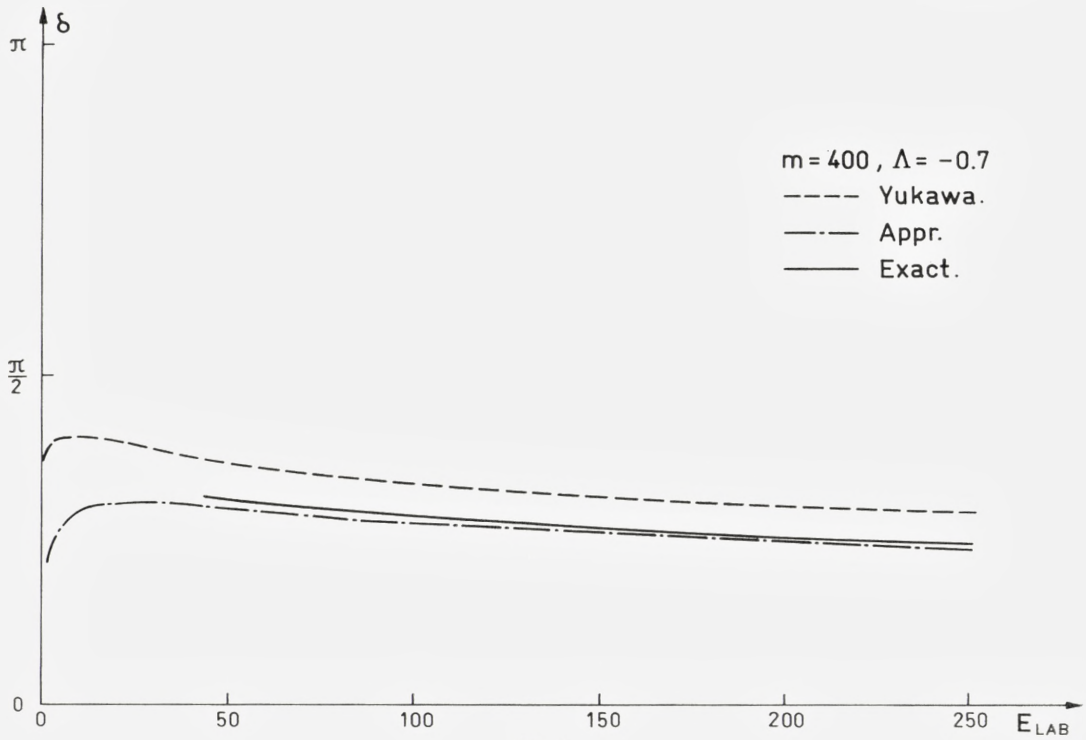

Fig. 6.

We may then assert that within a reasonable and practical perturbation-theoretic definition of a potential (not necessarily based on Feynman-Dyson expansions), it is always possible to obtain a local angular momentum dependent potential in coordinate space, provided the expressions representing the diagrams we include in the potential satisfy simple regularity (differentiability and summability) requirements of the kind given in this paper.

Acknowledgements

It is a pleasure to thank Professor T. Gustafson and Professor C. Møller for the hospitality and financial support of NORDITA. The author is also indebted to Professor L. Gårding and Professor L. Rosenfeld for inspiring discussions.

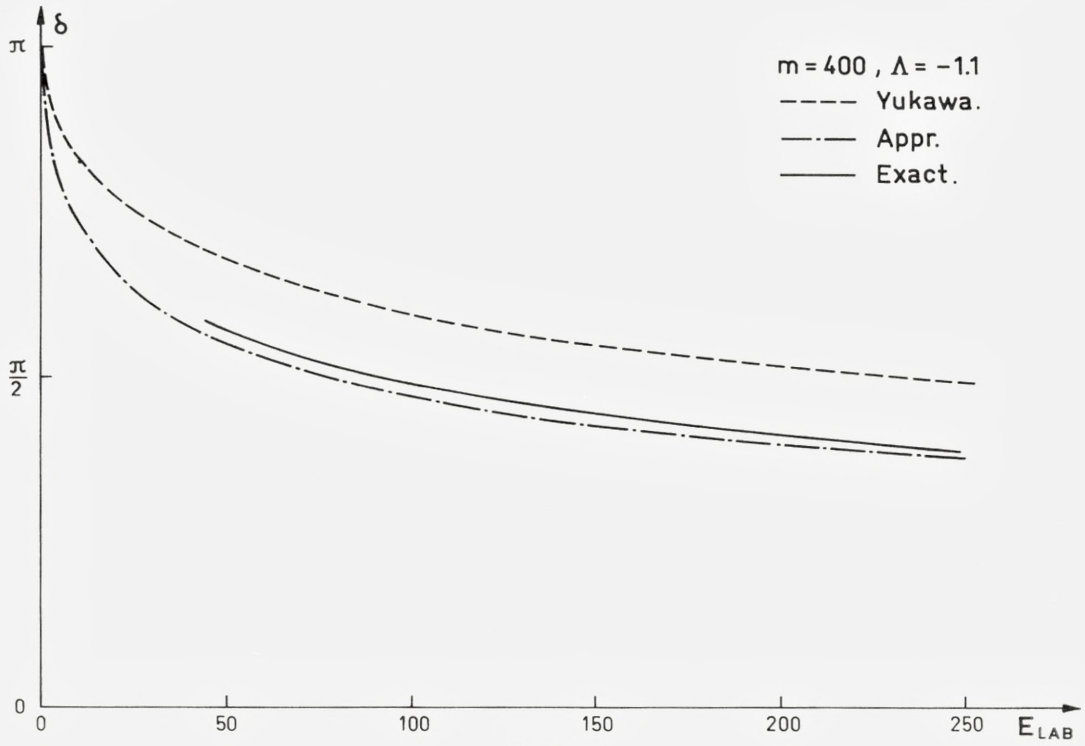

Fig 7.

Appendix I
The inversion theorem

In this Appendix we prove the inversion theorem given in section 3.III. The equation to be solved is

$$f(x,v) = \int_0^\infty dy g(y,v) J_v^2(xy). \qquad \text{(A. 1)}$$

Here $f(x,v)$ is given as a function of the real parameter x and of the parameter $v \varepsilon D$, where D is a closed domain which is subsequently determined.

In solving (A.1), we use the theory of "general transforms", an exposition of which can be found in Titchmarsh's "Theory of Fourier Integrals"[16]. We need the following theorem, which is a straightforward generalization of theorem 129 in Ref. (16).

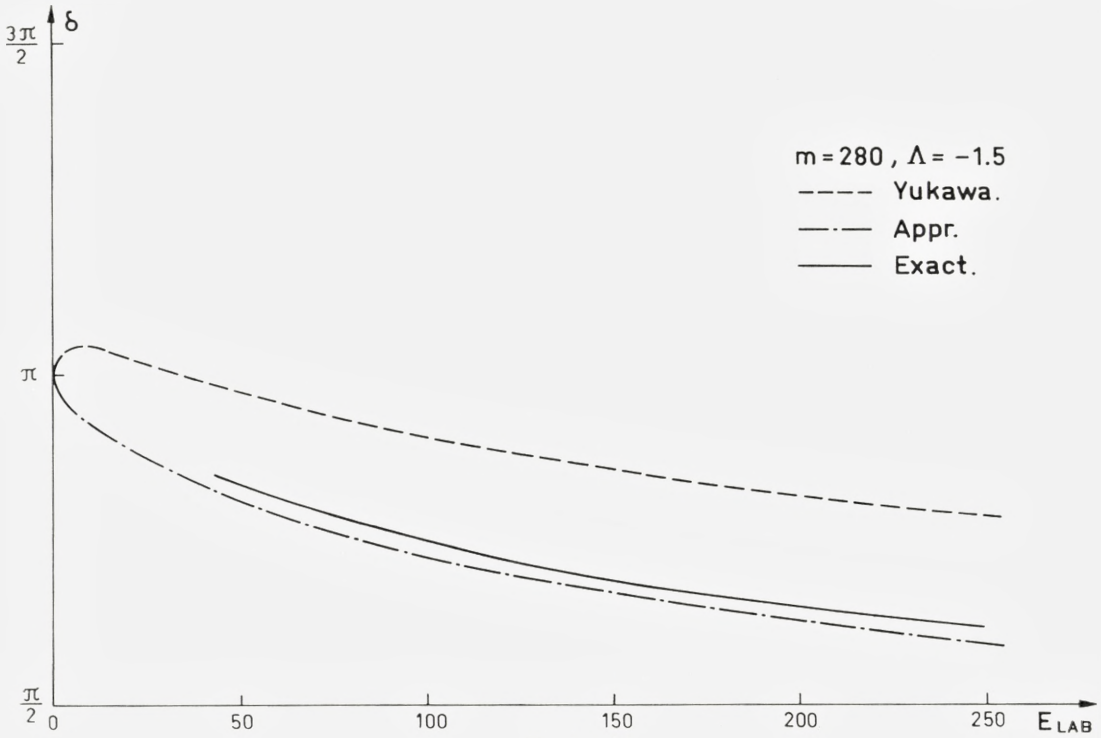

Fig. 8.

Theorem: Let $K\left(\frac{1}{2}+it\right)$ and $H\left(\frac{1}{2}+it\right)$ be any bounded functions of the real parameter t, satisfying the condition

$$K\left(\frac{1}{2}+it\right)H\left(\frac{1}{2}-it\right) = 1. \tag{A. 2}$$

Define $k(x)$ and $h(x)$ by the formulae

$$k(x) = \frac{x}{2\pi}\,\mathrm{l.i.m}_{T\to\infty}\int_{-T}^{T} dt\,\frac{K\left(\frac{1}{2}+it\right)}{\frac{1}{2}-it}\,x^{-\frac{1}{2}-it}, \tag{A. 3}$$

$$h(x) = \frac{x}{2\pi}\,\mathrm{l.i.m}_{T\to\infty}\int_{-T}^{T} dt\,\frac{H\left(\frac{1}{2}+it\right)}{\frac{1}{2}-it}\,x^{-\frac{1}{2}-it}. \tag{A. 4}$$

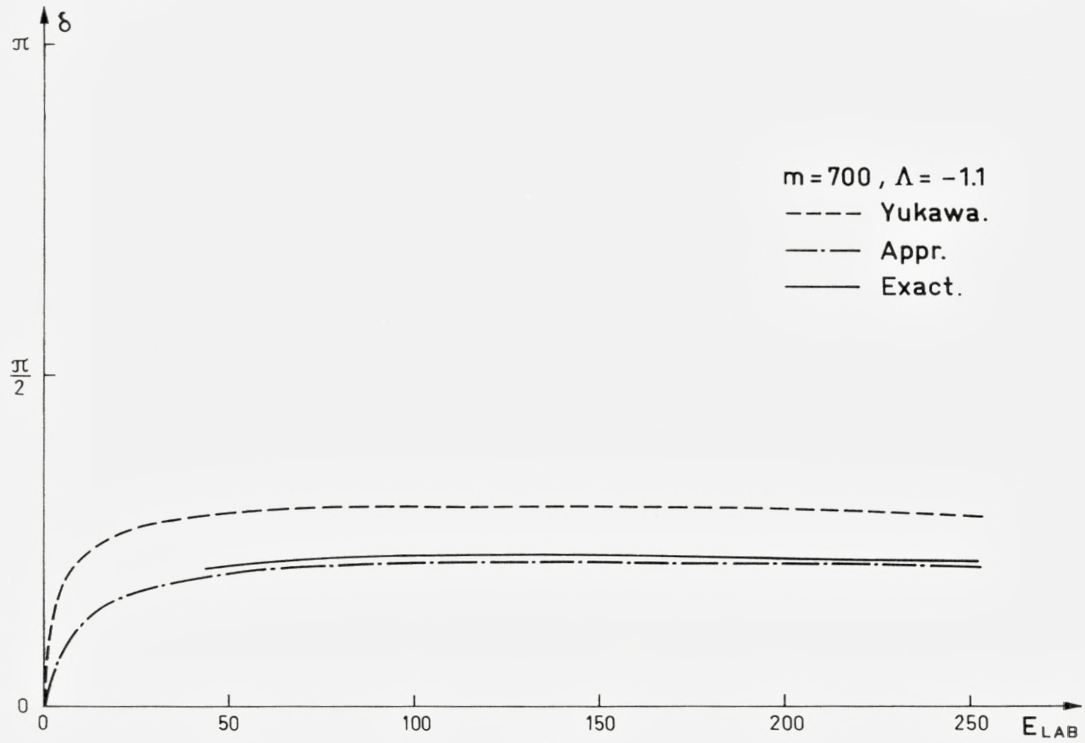

Fig. 9.

Let $f(x)\varepsilon L^2(0,\infty)$. Then the formula

$$g(x) = \frac{d}{dx}\int_0^\infty \frac{du}{u}\, k(xu)f(u) \qquad \text{(A. 5)}$$

defines almost everywhere a function $g(x)\varepsilon L^2(0,\infty)$, and the reciprocal formula

$$f(x) = \frac{d}{dx}\int_0^\infty \frac{du}{u}\, h(xu)g(u) \qquad \text{(A. 6)}$$

also holds almost everywhere.

In using this theorem for eq. (A. 1), we proceed as follows. Let $n(x)$ and $m(x)$ be two arbitrary functions of x. We multiply and divide (A. 1) by n and m

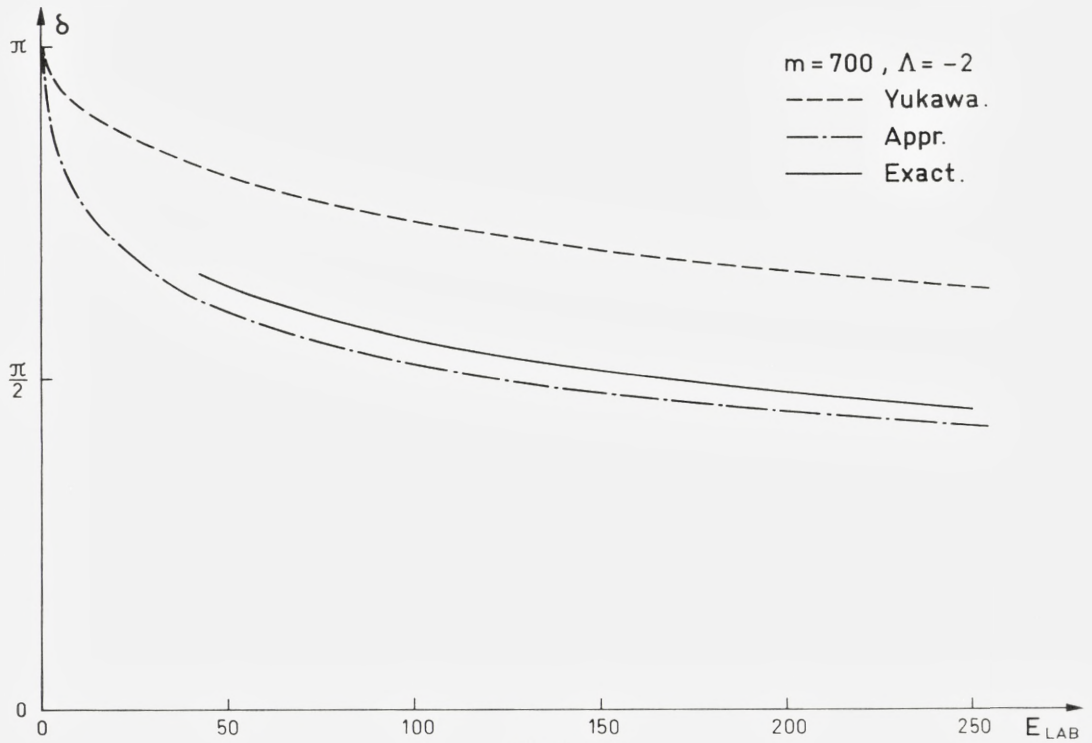

Fig. 10.

$$n(x)f(x,v) = \int_0^\infty dy m(y)g(y,v)\left[\frac{n(x)}{m(y)}J_v^2(xy)\right]. \qquad (A.7)$$

When we demand that the kernel (the term within brackets) in (A. 7) be a function of (xy), it follows

$$\frac{n(x)}{m(y)} = (xy)^a, \qquad (A.8)$$

where a is an arbitrary (real) number, which we have at our disposal. Hence $n(x) = x^a$ and $m(x) = x^{-a}$. Assume that $x^a f(x,v)$ is differentiable in $(0, \infty)$, when a has a fixed value, which we subsequently determine.

Let $f_1(x,v) = \frac{d}{dx}x^a f(x,v)$ and let $g_1(x,v) = x^{1-a}g(x,v)$. Then we get

$$f_1(x,v) = \frac{d}{dx}\int_0^\infty \frac{dy}{y} g_1(y,v)(xy)^a J_v^2(xy). \qquad (A.9)$$

We shall now have to determine the number a, so that the conditions of Theorem I are fulfilled for the kernel

$$k(x) = x^a J_v^2(x). \tag{A. 10}$$

The function $K(s)(1-s)^{-1}$ is the Mellin transform of $k(x)x^{-1}$

$$K(s)(1-s)^{-1} = \int_0^\infty dx x^{-r} J_v^2(x), \tag{A. 11}$$

where

$$r = 2 - s - a. \tag{A. 12}$$

The integral (A. 11) can readily be evaluated (W. 403)

$$K(s)(1-s)^{-1} = \frac{\Gamma(r)\Gamma\left(v + \frac{1}{2} - \frac{1}{2}r\right)}{2^r\left(\Gamma\left(\frac{1}{2} + \frac{1}{2}r\right)\right)^2 \Gamma\left(v + \frac{1}{2} + \frac{1}{2}r\right)}, \tag{A. 13}$$

provided

$$Re(r) > 0,\ Re(2v + 1 - r) > 0. \tag{A. 14}$$

The function $K(1/2 + it)$ defined by (A. 13) with $s = 1/2 + it$ is bounded and non-zero for bounded values of $|t|$. The asymptotic behaviour of $K(s)$ for large values of $t = Im(s)$ is

$$|K(s)| = |t|^{Re(s)+a-\frac{3}{2}}(1 + O(t^{-1})). \tag{A. 15}$$

Hence, in order that $K(s)$ be bounded on $Re(s) = 1/2$ for all t, we must choose

$$a = 1. \tag{A. 16}$$

As a consequence of the conditions (A. 14), we must have

$$Re(v) > -\frac{1}{4}. \tag{A. 17}$$

Defining $H(s)$ by eq. (A. 2), K(s) being given by (A. 13) with $a = 1$, and performing the integral (A. 4) we obtain

$$h(x) = -2\pi \int_0^x du u J_v(u) Y_v(u), \tag{A. 18}$$

where $Y_v(u)$ is the Bessel function of the second kind.

We have thus obtained the result;

If $xf(x,\nu)$ is differentiable in $(0, \infty)$, and if $(xf(x,\nu))' \equiv \frac{d}{dx}(xf(x,\nu)) \varepsilon L^2(0, \infty)$, uniformly with respect to ν within a closed domain to the right of the line $Re(\nu) = -\frac{1}{4}$, the equation

$$f(x,\nu) = \int_0^\infty dy g(y,\nu) J_\nu^2(xy) \tag{A. 19}$$

implies almost everywhere

$$g(x,\nu) = -2\pi \frac{d}{dx} \int_0^\infty \frac{dy}{y} (yf(y,\nu))' \int_0^{xy} du u J_\nu(u) Y_\nu(u), \tag{A. 20}$$

and $g(x,\nu)$ defined for $Re(\nu) > -\frac{1}{4}$ by (A. 20) also $\varepsilon L^2(0, \infty)$.

Appendix II
Reduction of the Lippmann-Schwinger equation

We write down the partial wave L.S.-equation, eq. (4.4)

$$T(k',k) = U(k',k) + \frac{2}{\pi} \int_0^\infty \frac{dk'' k'' U(k',k'') T(k'',k)}{k''^2 - k^2 - i\varepsilon} \tag{B. 1}$$

where for simplicity we have omitted the subscript L. We define the function

$$F(k',k) = \frac{T(k',k)}{1 + iT(k,k)} \tag{B. 2}$$

It is readily proved that for real non-negative values of k and k'

$$arg T(k',k) = arg T(k,k). \tag{B. 3}$$

The function $F(k',k)$ is therefore a real function, which on the energy shell becomes

$$F(k,k) = tan(\delta(k)). \tag{B. 4}$$

Let us then write $F(k',k)$ in the form

$$F(k',k) = \frac{N(k',k)}{D(k)}, \tag{B. 5}$$

where

$$D(k) = 1 - \frac{2}{\pi} P\int_0^\infty \frac{dk''k''H(k,k'')N(k'',k)}{k''^2 - k^2}. \tag{B. 6}$$

The function $H(k,k'')$ in (B. 6) should be chosen so that N and D in (B. 5) have convenient properties. From (B. 1), (B. 2), (B. 5) and (B. 6) we obtain the equation for $N(k',k)$

$$N(k',k) = U(k',k) + \frac{2}{\pi} P\int_0^\infty \frac{dk''k''[U(k',k'') - U(k',k)H(k,k'')]N(k'',k)}{k''^2 - k^2}. \tag{B. 7}$$

If $H(k',k)$ is chosen to be unity for $k' = k$, the kernel in (B. 7) becomes finite at $k'' = k$, provided $U(k',k)$ satisfies the appropriate Lipschitz condition. If we choose

$$H(k,k'') = \frac{U(k,k'')}{U(k,k)}, \tag{B. 8}$$

we obtain from eq. (B. 7), apart from nugatory changes in the notation, the equation recently discussed by H. P. Noyes[17]. With this choice we force the function $N(k',k)$ to have poles, as function of k, at those points where the phase shift goes through an integral multiple of π. Instead of (B. 8) we therefore take[18]

$$H(k,k'') = 1. \tag{B. 9}$$

We then have

$$N(k',k) = U(k',k) + \frac{2}{\pi}\int_0^\infty \frac{dk''k''[U(k',k'') - U(k',k)]N(k'',k)}{k''^2 - k^2} \tag{B. 10}$$

and, from (B. 4) and (B. 5),

$$\tan(\delta(k)) = \frac{N(k,k)}{1 - \frac{2}{\pi} P\int_0^\infty \frac{dk''k''N(k'',k)}{k''^2 - k^2}}. \tag{B. 11}$$

The phase shifts given in section 6 are obtained by solving a slightly modified version of eq. (B. 10), with $U(k', k)$ given by

$$U(k', k) = -\frac{\Lambda Q_0\left(\dfrac{k^2 + k'^2 + \left(\dfrac{m}{M}\right)^2}{2kk'}\right)}{2k\sqrt[4]{k^2+1}\sqrt[4]{k'^2+1}} \qquad \text{(B. 12)}$$

The method used for solving the equation is the well known matrix inversion method.

References

(1) C. Cronström, Mat.-Fys. Medd. Dan. Vid. Selsk. **35** (14) (1967).
(2) S. Okubo and R. E. Marshak, Ann. Phys. (USA) **4**, 166 (1958).
(3) L. A. P. Balázs, Phys. Rev. **137**, B 1510 (1965).
(4) J. Goto and S. Machida, Progr. Th. Phys. **25**, 64 (1961).
(5) N. Hoshizaki and S. Machida, Progr. Th. Phys. **24**, 1325 (1960).
(6) G. N. Watson, Proc. Roy. Soc. (London) **95**, 83 (1918).
V. de Alfaro and T. Regge, Potential Scattering, North Holland Publ. Comp. (1965).
(7) G. N. Watson, Theory of Bessel Functions, Second ed. Cambridge Univ. Press (1944).
(8) L. Brown, D. I. Fivel, B. W. Lee and R. F. Sawyer, Ann. Phys. (USA) **23**, 187 (1963).
(9) G. H. Hardy, Acta Math. **42**, 327 (1920).
(10) A. A. Logunov, A. N. Tavkhelidze, I. T. Todorov and O. A. Khrustalev, Nuovo Cimento, **30**, 134 (1963).
(11) N. I. Muskhelishvili, Singular Integral Equations, P. Noordhoff N.V. Groningen-Holland (1953).
(12) R. Blankenbecler and R. Sugar, Phys. Rev. **142**, 1051 (1966).
(13) J. Goto, Progr. Th. Phys. **28**, 283 (1962).
(14) P. Connors and P. Signell, Progr. Th. Phys. **26**, 757 (1961).
(15) E. M. Nyman, Nuovo Cimento **37**, 492 (1965).
(16) E. C. Titchmarsh, Theory of Fourier Integrals, Second ed. Oxford Clarendon Press (1948).
(17) H. P. Noyes, Phys. Rev. Lett. **15**, 538 (1965).
(18) M. H. Kalos and R. H. Dalitz, Phys. Rev. **100**, 1515 (1955).

Indleveret til Selskabet den 28. oktober 1966.
Færdig fra trykkeriet den 5. maj 1967.

Matematisk-fysiske Meddelelser
udgivet af
Det Kongelige Danske Videnskabernes Selskab
Bind **35,** nr. 14

Mat. Fys. Medd. Dan. Vid. Selsk. **35,** no. 14 (1967)

ANGULAR MOMENTUM DEPENDENT POTENTIALS IN NUCLEON-NUCLEON SCATTERING

BY

C. CRONSTRÖM

København 1967
Kommissionær: Munksgaard

Synopsis

We investigate the general properties of the most general local, angular momentum dependent nucleon-nucleon potential. We generalise the arguments of a previous paper on angular momentum dependent potentials, to take into account the complications which arise because of the spin of the nucleons. As an example we consider a scalar boson exchange potential, and show that the conventional approximation methods for obtaining local potentials from field theory are completely misleading in this case.

PRINTED IN DENMARK
BIANCO LUNOS BOGTRYKKERI A/S

1. Introduction

In a previous paper[1] (referred to as I hereafter) we have discussed the concept of a local, angular momentum dependent potential, and its relevance to the equivalence problem, that is, the problem of obtaining a local potential which is equivalent to a given non-local potential as far as phase shifts are concerned. We established in I that it is in principle possible to construct a local angular momentum dependent potential which is equivalent to a given non-local one. The question whether a potential is non-local or local in coordinate space depends on the off shell behaviour of the potential in momentum space. In I it was explicitly shown that in perturbation theory it is always possible to choose the off shell continuation of the potential so that the resulting coordinate space potential becomes local and angular momentum dependent, since this merely corresponds to a rearrangement of the (infinite number of) equations connecting the potentials V_{2n} to the T-matrices T_{2n} of various orders. In a practical calculation, when the potential is constructed only up to some finite (and small) order, the off shell continuation chosen for the potential will affect the resulting phase shifts. On the basis of numerical calculations performed in I for a single particle exchange potential, we may assert that the phase shift obtained with a potential which is chosen to be local and angular momentum dependent does not differ very much from a phase shift obtained with a potential which differs slightly off the energy shell from the first potential. From the practical point of view, we may therefore consider the method of constructing a local, angular momentum dependent potential as a method by which a given non-local potential can be approximated by a local one. An approximation of this kind can in general be expected to be superior to the "static" and "adiabatic" approximations which have hitherto been used.

The purpose of the present paper is to generalise the arguments given in I for interactions between spinless scalar particles to the case of interactions between nucleons in which various complications occur due to the spin of the nucleons. However, in this paper we restrict the detailed discus-

sion to only those points which cannot immediately be inferred from the discussion given in I.

Section 2 contains a discussion of the general form of a potential. In section 3 we evaluate the "spin-angle"-matrix elements of the potential in the momentum representation, which are needed in order to obtain the partial wave integral equations which connect the angular momentum dependent coordinate space potentials to the potential in momentum representation.

In section 4 we solve these integral equations, and examine briefly some of the properties of the resulting coordinate space potentials.

Section 5 contains a discussion of the scalar boson exchange potential which we use as an illustration, and in section 6 we give some concluding remarks.

2. The general form of the potential

As is shown in an article by J. Goto and S. Machida[2]), the most general form of a potential between two spin one half nucleons, which fulfils natural invariance requirements, *i.e.* invariance with respect to coordinate space translation, Galilei transformation, the exchange of the two nucleons, rotation of space coordinates, space reflections, time reversal and Hermiticity of the potential, is, in momentum space,

$$\left.\begin{aligned} V(\sigma_1,\sigma_2,\boldsymbol{q},\boldsymbol{p}) \;=\; & V_0 + V_1 i(\boldsymbol{q}\times\boldsymbol{p})\cdot\boldsymbol{S} + V_2\sigma_1\cdot\boldsymbol{q}\sigma_2\cdot\boldsymbol{q} + V_3\sigma_1\cdot\sigma_2 \\ & + V_4\sigma_1\cdot(\boldsymbol{q}\times\boldsymbol{p})\sigma_2\cdot(\boldsymbol{q}\times\boldsymbol{p}) + V_5\sigma_1\cdot\boldsymbol{p}\sigma_2\cdot\boldsymbol{p}. \end{aligned}\right\} \tag{2.1}$$

The quantities $\boldsymbol{q}$ and $\boldsymbol{p}$ are given, in terms of the centre of mass (c.m.) momenta (Fig. 1), by

$$\boldsymbol{q} = \boldsymbol{k} - \boldsymbol{k}', \qquad \boldsymbol{p} = \tfrac{1}{2}(\boldsymbol{k} + \boldsymbol{k}'). \tag{2.2}$$

The six functions V_i in (2.1) are real functions of the three independent scalars that can be formed from $\boldsymbol{q}$ and $\boldsymbol{p}$,

$$V_i = V_i(\boldsymbol{q}^2,\boldsymbol{p}^2,(\boldsymbol{q}\times\boldsymbol{p})^2). \tag{2.3}$$

Finally, σ_1 and σ_2 in (2.1) denote the spin operators for the two nucleons, and $\boldsymbol{S} = 1/2(\sigma_1 + \sigma_2)$.

When charge independence is assumed, then each function V_i can be expressed as a sum of a **1**-term and $\tau_1\cdot\tau_2$-term in iso-space, where the τ are the iso-spin operators. In what follows we shall omit the iso-spin factors, which are unessential in the discussion.

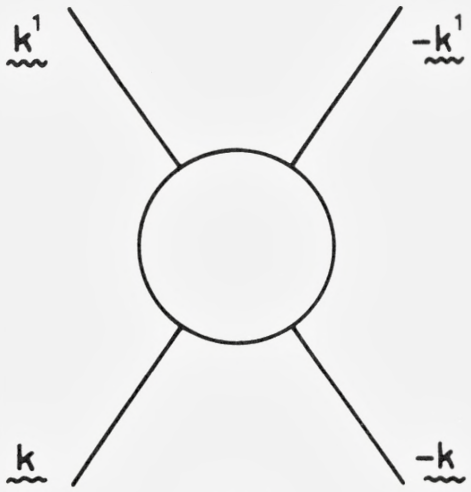

Fig. 1.

When (2.1) is transformed to coordinate space, one obtains in general a completely non-local potential.

However, in certain circumstances the resulting coordinate space potential becomes neither strictly local nor non-local, but becomes a function of r and $\boldsymbol{L}^2$, where $\boldsymbol{L}$ is the angular momentum operator. The problem of determining the form of such a potential in the two-nucleon case has been considered by S. Okubo and R. E. Marshak[3]. Their result, which is essentially based on invariance arguments, is

$$G(\sigma_1, \sigma_2, r, \boldsymbol{L}^2) = G_0 + G_1 \boldsymbol{L} \cdot \boldsymbol{S} + \tfrac{1}{2}[G_2, S_{12}]_+ + G_3 \sigma_1 \cdot \sigma_2 + G_4 L_{12}, \qquad (2.4)$$

where

$$S_{12} = 3r^{-2} \sigma_1 \cdot \boldsymbol{r} \sigma_2 \cdot \boldsymbol{r} - \sigma_1 \cdot \sigma_2, \qquad (2.5)$$

$$L_{12} = 3\sigma_1 \cdot \boldsymbol{L} \sigma_2 \cdot \boldsymbol{L} - \sigma_1 \cdot \sigma_2 \boldsymbol{L}^2. \qquad (2.6)$$

The five functions G_i in (2.4) are functions of r and $\boldsymbol{L}^2$ only. Actually (2.4) differs slightly from the expression given by Okubo and Marshak, as we have symmetrised the tensor force term, and, for reasons of convenience, changed the definition of the quadratic spin orbit operator L_{12}.

As pointed out by Okubo and Marshak, a potential of the form (2.4) is the most general local potential which can be obtained as a solution to the inverse problem of scattering.

Let us now suppose that the function V in (2.1) is properly restricted so that it has a coordinate space representation of the form (2.4). If this is the case, then we have the relation between V and G

$$V(\sigma_1, \sigma_2, \boldsymbol{q}, \boldsymbol{p}) = \langle \boldsymbol{k}' \mid G(\sigma_1, \sigma_2, r, \boldsymbol{L}^2) \mid \boldsymbol{k} \rangle \tag{2.7}$$

where

$$\langle \boldsymbol{k}' \mid G(\sigma_1, \sigma_2, r, \boldsymbol{L}^2) \mid \boldsymbol{k} \rangle = \int d^3\boldsymbol{r} e^{-i\boldsymbol{k}' \cdot \boldsymbol{r}} G(\sigma_1, \sigma_2, r, \boldsymbol{L}^2) e^{i\boldsymbol{k} \cdot \boldsymbol{r}}. \tag{2.8}$$

If the relation (2.7) holds between V and G, then it holds separately for the spin-independent, spin-linear and spin-bilinear parts of V and G respectively. We thus obtain from (2.7),

$$V_0 = \langle \boldsymbol{k}' \mid G_0 \mid \boldsymbol{k} \rangle \tag{2.9}$$

$$V_1 i(\boldsymbol{q} \times \boldsymbol{p}) \cdot \boldsymbol{S} = \langle \boldsymbol{k}' \mid G_1 \boldsymbol{L} \cdot \boldsymbol{S} \mid \boldsymbol{k} \rangle \tag{2.10}$$

$$\sum_{i=2}^{5} V_i \Omega_i = \langle \boldsymbol{k}' \mid \left\{ \tfrac{1}{2}[G_2 S_{12}]_+ + G_3 \sigma_1 \cdot \sigma_2 + G_4 L_{12} \right\} \mid \boldsymbol{k} \rangle, \tag{2.11}$$

where we have denoted by Ω_i $(i = 2, \ldots, 5)$ the four spin-bilinear expressions in (2.1).

In the first place it is clear that the relations (2.9)–(2.11) are well defined only if the functions $G_i(r, \boldsymbol{L}^2)$ satisfy certain conditions. In I we have analysed these conditions in detail for the case of a spin independent potential, which corresponds to eq. (2.9). We may summarize these conditions as follows. We require that each function $G_i\big(r, L(L+1)\big)$ for fixed $r > 0$ is an entire function of $L(L+1)$, which is bounded by a finite power of $L(L+1)$ for non-negative integral values of L. Then we require the existence of the integrals

$$\int_0^\infty dr r^2 \left| G_i\big(r, L(L+1)\big) \right| \tag{2.12}$$

for every fixed L. In addition to (2.12) we have also to require the existence of additional absolute moments of each function $G_i\big(r, L(L+1)\big)$, but on this point we refer to I for details.

Our next concern will be to invert the equations (2.9)–(2.11), that is, express the functions G_i as integral transforms of the functions V_j. At this point it is convenient to take the partial wave projection of the equations (2.9)–(2.11).

We define the partial wave projection or "spin-angle" matrix element of a given function $V(\sigma_1,\sigma_2,\boldsymbol{q},\boldsymbol{p})$ as follows:

$$V_{LL'} \equiv \langle L'|V|L\rangle = \int d\Omega_k d\Omega_{k'} Y^{M*}_{JL'S}(\Omega_{k'}) V Y^{M}_{JLS}(\Omega_k) \tag{2.13}$$

where

$$Y^{M}_{JLS}(\Omega) = \sum_{m_L,m_S} C_{LS}(J,M;m_L,m_S) Y_{L,m_L}(\Omega)\chi_S^{m_S} \tag{2.14}$$

in standard notation.

3. Matrix elements

The matrix elements of the six potential terms in (2.1) have been evaluated by GOTO and MACHIDA (Ref. (2)), but for completeness these matrix elements are also included in this paper in a more compact notation. The matrix elements we have calculated coincide with those given by GOTO and MACHIDA, except in the cases of the linear and quadratic spin orbit potential, where there is a discrepancy. We also calculate the matrix elements of the five terms in $\langle \boldsymbol{k}'|G|\boldsymbol{k}\rangle$. The evaluation of the matrix elements defined by eq. (2.13) is in principle quite straightforward, although much tedious Clebsch-Gordon algebra is required in the calculation. To simplify the notation we introduce the following abbreviations:

$$\left.\begin{aligned} A^{i(m)}_L \equiv A^{i(m)}_L(k,k') &= (1+3\delta_{i5})^{-1} \int_{-1}^{+1} dx x^m P_L(x) V_i \\ A^{i}_L(k,k') &\equiv A^{i(0)}_L(k,k'), \end{aligned}\right\} \tag{3.1}$$

and

$$G^i_L(k,k') = (2\pi)^3 (kk')^{-\frac{1}{2}} \int_0^\infty dr r G_i\big(r,L(L+1)\big) J_{L+\frac{1}{2}}(kr) J_{L+\frac{1}{2}}(k'r) \tag{3.2}$$

Here $J_\nu(z)$ is the Bessel function of the first kind, $P_L(x)$ is the Legendre polynominal and x is the cosine of the angle between $\boldsymbol{k}$ and $\boldsymbol{k}'$. Instead of *e.g.* $\langle L',\boldsymbol{k}'|G_0|\boldsymbol{k},L\rangle$ we write $\langle L'|G_0|L\rangle$ to simplify the notation. Because of the symmetry, invariance and Hermiticity requirements which we assume the potential to satisfy there will be five independent matrix elements; namely one for $S = 0$, where we have $L' = L = J$, and for $S = 1$ three matrix elements between states of equal L, where L takes the values $J-1$, J and $J+1$ respectively, and one non-diagonal element with $L' = J-1$, $L = J+1$.

For the spin-independent and spin-linear potential we readily obtain

$$\langle L'|V_0|L\rangle = 2\pi\delta_{LL'}F_L^0(k,k'), \quad F_L^0(k,k') = A_L^0, \tag{3.3}$$

$$\langle L'|G_0|L\rangle = \delta_{LL'}G_L^0(k,k'), \tag{3.4}$$

and

$$\left.\begin{aligned} &\langle L'|V_1 i(\boldsymbol{q}\times\boldsymbol{p})\cdot\boldsymbol{S}|L\rangle = \\ &\tfrac{1}{2}[J(J+1) - L(L+1) - S(S+1)]\delta_{LL'}2\pi F_L^1(k,k'), \\ &F_L^1(k,k') = kk'\left(\frac{A_{L+1}^1 - A_{L-1}^1}{2L+1}\right), \end{aligned}\right\} \tag{3.5}$$

$$\langle L'|G_1\boldsymbol{L}\cdot\boldsymbol{S}|L\rangle = \delta_{LL'}\tfrac{1}{2}[J(J+1) - L(L+1) - S(S+1)]G_L^1(k,k'). \tag{3.6}$$

The evaluation of the matrix elements of the bilinear terms requires an appreciable amount of calculation, the result of which can be expressed as follows. The four matrix elements between states of equal L of any of the functions $V_i\Omega_i (i = 2,\ldots,5)$ can be written as

$$\langle L|V_i\Omega_i|L\rangle = 2\pi F_L^{i(SP)}(k,k')\langle\sigma_1\cdot\sigma_2\rangle + 2\pi F_L^{i(QT)}(k,k')\langle S_{12}\rangle, \tag{3.7}$$

where

$$\langle\sigma_1\cdot\sigma_2\rangle = 2S(S+1) - 3, \tag{3.8}$$

and

$$\langle S_{12}\rangle = \left\{\begin{aligned} &0, && \text{for} \quad S = 0, \\ &-\frac{2(J-1)}{2J+1}, && \text{for} \quad S = 1, \quad L = J-1, \\ &2, && \text{for} \quad S = 1, \quad L = J, \\ &-\frac{2(J+2)}{2J+1}, && \text{for} \quad S = 1, \quad L = J+1. \end{aligned}\right. \tag{3.9}$$

We obtain

$$F_L^{2(SP)}(k,k') = \tfrac{1}{3}[(k^2 + k'^2)A_L^2 - 2kk'A_L^{2(1)}], \tag{3.10}$$

$$F_L^{2(QT)}(k,k') = \tfrac{1}{3}\left[(k^2 + k'^2)A_L^2 - 2kk'A_L^{2(1)} + 3kk'\left(\frac{A_{L+1}^2 - A_{L-1}^2}{2L+1}\right)\right], \tag{3.11}$$

$$F_L^{3(SP)}(k,k') = A_L^3, \tag{3.12}$$

$$F_L^{3(QT)}(k,k') = 0, \tag{3.13}$$

$$F_L^{4(SP)}(k,k') = \tfrac{1}{3}k^2k'^2[A_L^4 - A_L^{4(2)}], \tag{3.14}$$

$$F_L^{4(QT)}(k,k') = \tfrac{2}{3}k^2k'^2\left[A_L^{4(2)} - A_L^4 + \tfrac{3}{2}\left(\frac{A_{L-1}^{4(1)} - A_{L+1}^{4(1)}}{2L+1}\right)\right], \tag{3.15}$$

and

$$F_L^{5(SP)}(k,k') = \tfrac{1}{3}[(k^2 + k'^2)A_L^5 + 2kk'A_L^{5(1)}], \tag{3.16}$$

$$F_L^{5(QT)}(k,k') = \tfrac{1}{3}\left[(k^2 + k'^2)A_L^5 + 2kk'A_L^{5(1)} - \tfrac{3}{2}\left(\frac{A_{L+1}^5 - A_{L-1}^5}{2L+1}\right)\right]. \tag{3.17}$$

The non-diagonal element can be written as

$$\langle J+1|V_i\Omega_i|J-1\rangle = \frac{6\pi(J(J+1))^{\frac{1}{2}}}{2J+1}F_J^{i(T)}(k,k'), \tag{3.18}$$

where

$$F_L^{2(T)}(k,k') = \tfrac{2}{3}(k^2A_{L-1}^2 + k'^2A_{L+1}^2 - 2kk'A_L^2), \tag{3.19}$$

$$F_L^{3(T)}(k,k') = 0, \tag{3.20}$$

$$F_L^{4(T)}(k,k') = \tfrac{2}{3}k^2k'^2[2A_L^{4(1)} - A_{L-1}^4 - A_{L+1}^4], \tag{3.21}$$

$$F_L^{5(T)}(k,k') = \tfrac{2}{3}[k'^2A_{L-1}^5 + k^2A_{L+1}^5 + 2kk'A_L^5]. \tag{3.22}$$

Hence, if

$$V = \sum_{i=2}^{5} V_i\Omega_i, \tag{3.23}$$

then

$$\langle L|V|L\rangle = 2\pi F_L^{(SP)}(k,k')\langle\sigma_1\cdot\sigma_2\rangle + 2\pi F_L^{(QT)}(k,k')\langle S_{12}\rangle, \tag{3.24}$$

and

$$\langle J+1|V|J-1\rangle = \frac{6\pi(J(J+1))^{\frac{1}{2}}}{2J+1}F_J^{(T)}(k,k'), \tag{3.25}$$

where

$$\left.\begin{aligned} F_L^{(SP)}(k,k') &= \sum_{i=2}^{5} F_L^{i(SP)}(k,k'), \\ F_L^{(QT)}(k,k') &= \sum_{i=2}^{5} F_L^{i(QT)}(k,k'), \end{aligned}\right\} \tag{3.26}$$

and

$$F_L^{(T)}(k,k') = \sum_{i=2}^{5} F_L^{i(T)}(k,k'). \tag{3.27}$$

For the matrix elements of the bilinear terms in G we obtain

$$\langle L|\tfrac{1}{2}[G_2,S_{12}]_+|L\rangle = G_L^2(k,k')\langle S_{12}\rangle, \tag{3.28}$$

and

$$\left.\begin{aligned} &\langle J+1|\tfrac{1}{2}[G_2,S_{12}]_+|J-1\rangle = \\ &-\frac{6(J(J+1))^{\frac{1}{2}}}{2J+1}\tfrac{1}{2}[G^2_{J-1,J+1}(k,k')+G^2_{J+1,J-1}(k,k')], \end{aligned}\right\} \tag{3.29}$$

where

$$\left.\begin{aligned} &G^2_{L-1,L+1}(k,k')+G^2_{L+1,L-1}(k,k') = \\ &(2\pi)^3(kk')^{-\frac{1}{2}}\int_0^\infty drr[G_2(r,(L-1)L)+G_2(r,(L+1)(L+2))] \\ &J_{L-\frac{1}{2}}(kr)J_{L+\frac{3}{2}}(k'r), \end{aligned}\right\} \tag{3.30}$$

$$\langle L'|G_3\sigma_1\cdot\sigma_2|L\rangle = \delta_{LL'}(2S(S+1)-3)G^3_L(k,k'), \tag{3.31}$$

and

$$\langle L'|G_4L_{12}|L\rangle = \delta_{LL'}\langle L_{12}\rangle G^4_L(k,k'), \tag{3.32}$$

where

$$\langle L_{12}\rangle = \left\{\begin{array}{lll} 0, & \text{for} \quad S=0, & \\ (J-1)(2J-3), & \text{for} \quad S=1, & L=J-1, \\ -(2J-1)(2J+3), & \text{for} \quad S=1, & L=J, \\ (J+2)(2J+5), & \text{for} \quad S=1, & L=J+1. \end{array}\right. \tag{3.33}$$

We observe the relation between $\langle S_{12}\rangle$ and $\langle L_{12}\rangle$

$$-2\langle L_{12}\rangle = (2L-1)(2L+3)\langle S_{12}\rangle. \tag{3.34}$$

4. The integral equations and their solutions

We can now write down the integral equations which correspond to the partial wave projections of the equations (2.9), (2.10) and (2.11) respectively. We introduce the abbreviation

$$M_{L,L'}(k,k';r) = J_{L+\frac{1}{2}}(kr)J_{L'+\frac{1}{2}}(k'r). \tag{4.1}$$

From eqs. (3.3) and (3.4) we obtain

$$(kk')^{\frac{1}{2}}F^0_L(k,k') = 4\pi^2\int_0^\infty drrG_0(r,L(L+1))M_{L,L}(k,k';r), \tag{4.2}$$

and from eqs. (3.5) and (3.6)

$$(k'k)^{\frac{1}{2}}F^1_L(k,k') = 4\pi^2\int_0^\infty drrG_1(r,L(L+1))M_{L,L}(k,k';r). \tag{4.3}$$

Let us then consider the bilinear terms in G

$$\tfrac{1}{2}[G_2, S_{12}]_+ + G_3\sigma_1 \cdot \sigma_2 + G_4 L_{12}. \tag{4.4}$$

From (3.28), (3.31) and (3.32) we obtain the expression for the matrix element of (4.4), between states of equal L,

$$G_L^2(k,k')\langle S_{12}\rangle + G_2^3(k,k')\langle \sigma_1 \cdot \sigma_2\rangle + G_L^4(k,k')\langle L_{12}\rangle. \tag{4.5}$$

A comparison of (3.24) and (4.5) gives directly

$$(kk')^{\frac{1}{2}} F_L^{(SP)}(k,k') = 4\pi^2 \int_0^\infty dr r G_3(r, L(L+1)) M_{L,L}(k,k';r), \tag{4.6}$$

and, using eq. (3.34),

$$\left.\begin{aligned} (kk')^{\frac{1}{2}} F_L^{(QT)}(k,k') &= 4\pi^2 \int_0^\infty dr r G_2(r, L(L+1)) M_{L,L}(k,k';r) \\ -\tfrac{1}{2}(2L-1)(2L+3)4\pi^2 &\int_0^\infty dr r G_4(r, L(L+1)) M_{L,L}(k,k';r). \end{aligned}\right\} \tag{4.7}$$

For the non-diagonal matrix element we obtain, from eqs. (3.25) and (3.29),

$$\left.\begin{aligned} (kk')^{\frac{1}{2}} F_L^{(T)}(k,k') &= \\ -4\pi^2 \int_0^\infty dr r [G_2(r,(L-1)L) + G_2(r,(L+1)(L+2))] &M_{L-1,L+1}(k,k';r) \end{aligned}\right\} \tag{4.8}$$

The integral equations we have obtained, eqs. (4.2), (4.3) and eqs. (4.6)–(4.8) are the consequences of the assumption that the function $V(\sigma_1,\sigma_2,\boldsymbol{q},\boldsymbol{p})$ is represented by a function $G(\sigma_1,\sigma_2,r,\boldsymbol{L}^2)$ in coordinate space.

The equation corresponding to (4.2) has been investigated in I, where it was shown that whenever the equation has a solution for $G_0(r,L(L+1))$, this solution can be obtained by solving the equation obtained from (4.2) by using the constraint, or on-shell condition, $k = k'$. This means that the assumption that a function $G(\sigma_1,\sigma_2,r,\boldsymbol{L}^2)$ is the coordinate space representation of a $V(\sigma_1,\sigma_2,\boldsymbol{q},\boldsymbol{p})$ implies restrictions on the off-shell behaviour of V, but no essential restrictions on the on-shell behaviour of V.

The equations we arrive at by using the constraint $k = k'$ are of the type

$$f(x,v) = \int_0^\infty dy g(y,v) J_v^2(xy), \tag{4.9}$$

and

$$f(x,\nu) = \int_0^\infty dy\, y g(y,\nu) J_{\nu-1}(xy) J_{\nu+1}(xy). \tag{4.10}$$

In the equations (4.9) and (4.10) $f(x,\nu)$ is a given function of a real parameter x, and of the complex parameter $\nu \varepsilon D$, where the closed domain D is determined in the process of solving the equations. In order to invert (4.9) and (4.10) we need the following theorems.

Theorem I: If $xf(x,\nu)$ is differentiable in $(0, \infty)$ and if $(xf(x,\nu))' = \frac{d}{dx}(xf(x,\nu))$ belongs to $L^2(0, \infty)$, uniformly with respect to ν within a closed domain to the right of the line $Re(\nu) = -\frac{1}{4}$, the equation

$$f(x,\nu) = \int_0^\infty dy\, y g(y,\nu) J_\nu^2(xy)$$

implies almost everywhere

$$g(x,\nu) = -2\pi \frac{d}{dx} \int_0^\infty \frac{dy}{y} (yf(y,\nu))' \int_0^{xy} du\, u J_\nu(u) Y_\nu(u),$$

and $g(x,\nu)$ also belongs to $L^2(0, \infty)$.

Theorem II: If

$$f(x,\nu) = \int_0^\infty dy\, y g(y,\nu) J_{\nu-1}(xy) J_{\nu+1}(xy),$$

then

$$g(x,\nu) = -\pi \frac{d}{dx} \int_0^\infty \frac{dy}{y} (yf(y,\nu))' \left\{ \int_0^{xy} du\, u [J_{\nu-1}(u) Y_{\nu+1}(u) + J_{\nu+1}(u) Y_{\nu-1}(u)] \right\},$$

the conditions of validity being identical to those given in Theorem I. Here $Y_\nu(u)$ denotes a Bessel function of the second kind. Theorem I was proved in I, and Theorem II is proved in exactly the same manner, so we omit the proof in this paper.

The equations (4.2), (4.3) and (4.6) are now dealt with in exactly the same manner as the equation corresponding to (4.2) which was discussed in detail in I, so we shall only consider eqs. (4.7) and (4.8) in the following. We now assume that the functions $k^2 F_L^{(QT)}(k,k)$ and $k^2 F_L^{(T)}(k,k)$ for non-

negative integral values of L have square integrable derivatives. We then obtain, in accordance with theorems I and II,

$$\left.\begin{aligned} & r(G_2(r,L(L+1)) - 2((L+\tfrac{1}{2})^2 - 1)G_4(r,L(L+1))) \\ & = \frac{(-1)^L}{2\pi}\frac{d}{dr}\int_0^\infty \frac{dk}{k}(k^2F_L^{(QT)}(k,k))' \int_0^{kr} duuJ_{L+\frac{1}{2}}(u)J_{-L-\frac{1}{2}}(u), \end{aligned}\right\} \tag{4.11}$$

and

$$\left.\begin{aligned} & r(G_2(r,(L-1)L) + G_2(r,(L+1)(L+2))) \\ & = \frac{(-1)^L}{4\pi}\frac{d}{dr}\int_0^\infty \frac{dk}{k}(k^2F_L^{(T)}(k,k))' \\ & \left\{\int_0^{kr} duu(J_{L-\frac{1}{2}}(u)J_{-L-\frac{3}{2}}(u) + J_{L+\frac{3}{2}}(u)J_{-L+\frac{1}{2}}(u)).\right\} \end{aligned}\right\} \tag{4.12}$$

(Note that L in (4.11) and (4.12) is a non-negative integer.) In writing down (4.11) and (4.12) we have anticipated a result which should be a consequence of these equations, namely that the functions $G_2(r,L(L+1))$ and $G_4(r,L(L+1))$ actually are entire functions of $L(L+1)$. Let us consider eq. (4.11). The function $J_{L+\frac{1}{2}}(u)J_{-L-\frac{1}{2}}(u)$ is, for fixed positive u, an even entire function of $L+\frac{1}{2}$ and consequently an entire function of $L(L+1)$. We shall then have to prove that $(-1)^LF_L^{(QT)}(k,k)$ can be considered as an entire function of $L(L+1)$. Let us consider the first term in $F_L^{(QT)}(k,k)$, eq. (3.11). Using the symmetry property $P_L(-x) = (-1)^LP_L(x)$ of the Legendre polynominals, we obtain

$$\left.\begin{aligned} (-1)^LF_L^{2(QT)}(k,k) &= \tfrac{2}{3}k^2\int_{-1}^{+1} dx(1-x)P_L(-x)V_2 \\ &+ 3k^2\int_{-1}^{+1} dx\left(\frac{P_{L-1}(-x) - P_{L+1}(-x)}{2L+1}\right)V_2, \end{aligned}\right\} \tag{4.13}$$

where the constraint $k = k'$ is to be used in the expression for V_2. It is known that the function $P_L(-x)$ *qua* function of the complex parameter L, is an even entire function of $L+\frac{1}{2}$, when x has any fixed value such that $-1 \leq x < 1$. The first integral in (4.13) defines therefore an entire function of $L(L+1)$, provided V_2, as a function of x, is continuous in the (open) interval $(-1,1)$, and provided the integral converges uniformly for L within any closed domain. The same reasoning can obviously be carried through for the second term in (4.13), and also for the other terms included in

$(-1)^L F_L^{(QT)}(k,k)$ whence we conclude that $(-1)^L F_L^{(QT)}(k,k)$ can be continued to complex L in such a manner that it becomes an entire function of $L(L+1)$. We may note in passing that this is in general not the continuation to use if one wishes to consider the Schrödinger equation with an angular momentum dependent potential for general complex L, as pointed out in I. The integral on the right hand side of (4.11) then also becomes an entire function of $L(L+1)$, provided the requisite conditions of continuity and uniformity of convergence are satisfied. Let us denote this integral by $I_1(r, L(L+1))$. In exactly the same manner we can prove that the integral on the right hand side of (4.12) can be continued to complex L in such a manner that it becomes an entire function of $L(L+1)$. We denote this integral by $I_2(r, L(L+1))$. We shall now have to prove that $G_2(r, L(L+1))$ and $G_4(r, L(L+1))$ separately are entire functions of $L(L+1)$. Let us for a moment consider the function $G_2(r, L(L+1))$ as a function of $L+\frac{1}{2}$. The equation (4.12) then defines $G_2(r, L(L+1))$ through a difference equation of the form

$$g(z-1) + g(z+1) = f(z), \tag{4.14}$$

where $f(z)$ is an even entire function. It is known[4] that difference equations of this kind have in general solutions; moreover, if $f(z)$ is an integral function of finite order then there exists a particular solution to (4.14) which is an integral function of finite order, as proved in Ref. (4). It is readily seen that this particular solution is even if and only if $f(z)$ is even. As a result of these considerations it is clear that eq. (4.12) defines (apart from arbitrary additive solutions to the homogeneous equation) an even entire function of $L+\frac{1}{2}$; that is, $G_2(r, L(L+1))$ is an entire function of $L(L+1)$. The function $G_4(r, L(L+1))$ defined by (4.11) is consequently regular in the whole finite $L(L+1)$-plane, except possibly for $L(L+1) = \frac{3}{4}$ where a pole can occur. In order that $G_4(r, L(L+1))$ be regular also for $L(L+1) = \frac{3}{4}$, we must have

$$rG_2(r, \tfrac{3}{4}) = I_1(r, \tfrac{3}{4}), \tag{4.15}$$

where, as before, $I_1(r, L(L+1))$ denotes the properly continued integral on the right hand side of (4.11). However, on inserting $L = -\frac{1}{2}$ in eq. (4.12) we obtain

$$2rG_2(r, \tfrac{3}{4}) = I_2(r, -\tfrac{1}{4}). \tag{4.16}$$

It is easily verified that

$$2I_1(r, \tfrac{3}{4}) = I_2(r, -\tfrac{1}{4}), \tag{4.17}$$

whence it follows that $G_4(r, L(L+1))$ is an entire function of $L(L+1)$. We may finally remark that it is not a matter of necessity to obtain the expressions for $G_2(r, L(L+1))$ and $G_4(r, L(L+1))$ separately, since they occur in the radial Schrödinger equations in precisely the combinations given in eq. (4.11) and (4.12). We may also remark that the functions $G_2(r, L(L+1))$ and $G_4(r, L(L+1))$ obtained from eqs. (4.11) and (4.12) cannot be more singular than $o(r^{-\frac{3}{2}})$ near $r = 0$, since we have only considered the class of square integrable functions in the theorems I and II. The conditions which ensure the boundedness property and existence of the absolute moments of the functions G_2 and G_4 can easily be obtained, so we omit these considerations.

We may summarize the previous discussion as follows. We have established the possibility of constructing a local, angular momentum dependent two-nucleon potential starting from the most general momentum space representation of such a potential, and derived the necessary formulae for carrying out such a programme. In order that a given momentum space potential V should correspond exactly to a local, angular momentum dependent potential in coordinate space it is necessary that this V should have an off-shell behaviour which is implicitly defined by eqs. (4.2), (4.3) and eqs. (4.6)–(4.8) once the corresponding functions $G_i(r, L(L+1))$ are obtained by using the on-shell part of these equations. On the energy shell V is only restricted by the differentiability and summability conditions which ensure that the partial wave integral equations have square integrable solutions. These conditions can probably be relaxed so that the resulting solutions can behave like $o(r^{-3})$ near $r = 0$.

5. The scalar boson exchange potential

As an illustration we shall consider the lowest order potential due to the exchange of a scalar boson with mass m and coupling constant g_s. We obtain the following expression for the potential in momentum space:

$$V = V_0 + V_1 i(\boldsymbol{q} \times \boldsymbol{p}) \cdot \boldsymbol{S} + V_4 \sigma_1 \cdot (\boldsymbol{q} \times \boldsymbol{p}) \sigma_2 \cdot (\boldsymbol{q} \times \boldsymbol{p}), \tag{5.1}$$

where

$$V_0 = -\frac{g_s^2 \omega\omega'}{4M\sqrt{EE'}} \left(1 - \frac{\boldsymbol{k} \cdot \boldsymbol{k}'}{\omega\omega'}\right)^2 \frac{1}{\boldsymbol{q}^2 + m^2}, \tag{5.2}$$

$$V_1 = -\frac{g_s^2}{2M\sqrt{EE'}} \left(1 - \frac{\boldsymbol{k} \cdot \boldsymbol{k}'}{\omega\omega'}\right) \frac{1}{\boldsymbol{q}^2 + m^2} \tag{5.3}$$

and

$$V_4 = \frac{g_s^2}{4M\sqrt{EE'\omega\omega'}} \frac{1}{\boldsymbol{q}^2 + m^2}. \tag{5.4}$$

Here we have used the abbreviations

$$\left.\begin{aligned} E &= \sqrt{M^2 + k^2}, \qquad \omega = E + M, \\ E' &= \sqrt{M^2 + k'^2}, \quad \omega' = E' + M, \end{aligned}\right\} \tag{5.5}$$

and $\boldsymbol{q}$ is, as before, the momentum transfer. It is readily seen that the potentials (5.2)–(5.4) cannot, as such, be represented by local, angular momentum dependent potentials in coordinate space. However, since the lowest order potential in principle is fixed only on the energy shell, we may use the on-shell part of the potential directly to obtain the local, angular momentum dependent coordinate space potential. We shall then have to evaluate the functions $F_L^{(O)}, \ldots, F_L^{(T)}$ according to the formulae given in section 3. Let us introduce the notation

$$kF_L^{(i)}(k,k) = f_L^{(i)}(k) + r_L^{(i)}(k), \quad (i = 0,1,SP,QT,T). \tag{5.6}$$

We then obtain, from eqs. (5.2)–5.4),

$$\left.\begin{aligned} f_L^{(0)}(k) &= -\frac{g_s^2 M}{Ek}\left(1 - \frac{m^2}{4M\omega}\right)^2 Q_L(z), \\ r_L^{(0)}(k) &= -\frac{g_s^2 k}{4ME}\left[2\left(1 - \frac{k^2}{2\omega^2}\, z\right)\delta_{L0} - \frac{k^2}{3\omega^2}\,\delta_{L1}\right] \end{aligned}\right\} \tag{5.7}$$

$$\left.\begin{aligned} f_L^{(1)}(k) &= -\frac{g_s^2 k}{E\omega}\left(1 - \frac{m^2}{4M\omega}\right)\left(\frac{Q_{L+1}(z) - Q_{L-1}(z)}{2L+1}\right), \\ r_L^{(1)}(k) &= -\frac{g_s^2 k^3}{2ME\omega^2}\left(\delta_{L0} - \tfrac{1}{3}\,\delta_{L1}\right), \end{aligned}\right\} \tag{5.8}$$

$$\left.\begin{aligned} f_L^{(SP)}(k) &= -\frac{g_s^2 m^2 k}{12ME\omega^2}\left(1 + \frac{m^2}{4k^2}\right) Q_L(z), \\ r_L^{(SP)}(k) &= \frac{g_s^2 k^3}{12ME\omega^2}\left(z\delta_{L0} + \tfrac{1}{3}\,\delta_{L1}\right), \end{aligned}\right\} \tag{5.9}$$

$$\left.\begin{aligned} f_L^{(QT)}(k) &= \frac{g_s^2 m^2 k}{6ME\omega^2}\left(1+\frac{m^2}{4k^2}\right)Q_L(z) \\ &\quad + \frac{g_s^2 k^3 z}{4ME\omega^2}\left(\frac{Q_{L+1}(z)-Q_{L-1}(z)}{2L+1}\right), \\ r_L^{(QT)}(k) &= -\frac{g_s^2 k^3}{2ME\omega^2}\left(\frac{2z+3}{6}\,\delta_{L0}+\frac{5}{18}\,\delta_{L1}\right), \end{aligned}\right\} \tag{5.10}$$

$$\left.\begin{aligned} f_L^{(T)}(k) &= -\frac{g_s^2 k^3}{6ME\omega^2}\left(Q_{L+1}(z)+Q_{L-1}(z)-2zQ_L(z)\right), \\ r_L^{(T)}(k) &= -\frac{g_s^2 k^3}{3ME\omega^2}\,\delta_{L0}. \end{aligned}\right\} \tag{5.11}$$

Here $Q_L(z)$ is the Legendre function, and

$$z = 1+\frac{m^2}{2k^2}. \tag{5.12}$$

We may remark that the formulae (5.8), (5.10) and (5.11) are valid for $L \geq 1$ only, since for $L = 0$ we have to replace the function $Q_{L+1}(z) - Q_{L-1}(z)$ by $Q_1(z) - Q_0(z)$ in accordance with the formulae given in section 3.

Let us then discuss the eq. (5.7). The first term in (5.7) corresponds in the "static" or "adiabatic" limit to the ordinary Yukawa potential. The remainder $r_L^{(0)}(k)$ in (5.7) represents a short range interaction which operates only in the states with $L = 0$ or $L = 1$. Before proceeding further we may remark that it is perhaps unreasonable to pay too much attention to the short range terms $r_L^{(i)}(k)$, since in the states with $L = 0$ and $L = 1$ there are certainly unknown short range interactions which are probably more important than the simple single particle exchange forces of the type considered here. We shall therefore for a moment omit the short range terms $r_L^{(i)}(k)$ from the discussion and consider only the functions $f_L^{(i)}(k)$. We then need the asymptotic expansion[5] of $Q_L(z)$ for large values of k,

$$Q_L(z) = \left(\log\left(\frac{2k}{m}\right) - \gamma - \psi(L+1)\right)(1+O(k^{-2})). \tag{5.13}$$

Here the function $\psi(z)$ is the logarithmic derivative of the gamma function and $\gamma = -\psi(1)$.

It is now readily seen that the function $kf_L^{(0)}(k)$ has a derivative which is square integrable, but also absolutely integrable. We can then interchange the order of differentiation and integration in the inversion formula (Theorem I) given in section 4, and obtain, for integral values of L,

$$G_0(r,L(L+1)) = -\frac{1}{2\pi}\int_0^\infty dk(kf_L^{(0)}(k))'kJ_{L+\frac{1}{2}}(kr)Y_{L+\frac{1}{2}}(kr). \qquad (5.14)$$
$$(L > 1)$$

The integral (5.14) cannot be evaluated in terms of elementary functions, but it can be transformed, by using contour integration, into a form which reveals its relationship to the ordinary Yukawa potential. We have given an example of this in I, and shall not consider the matter further in this paper. The function $kf_L^{(1)}(k)$ has also an absolutely summable derivative, so that we obtain

$$G_1(r,L(L+1)) = -\frac{1}{2\pi}\int_0^\infty dk(kf_L^{(1)}(k))'kJ_{L+\frac{1}{2}}(kr)Y_{L+\frac{1}{2}}(kr). \qquad (5.15)$$
$$(L > 1)$$

Similarly,

$$G_3(r,L(L+1)) = -\frac{1}{2\pi}\int_0^\infty dk(kf_L^{(SP)}(k))'kJ_{L+\frac{1}{2}}(kr)Y_{L+\frac{1}{2}}(kr). \qquad (5.16)$$
$$(L > 1)$$

We may remark that the functions G_0, G_1 and G_3 defined by the eqs. (5.14)–(5.16) are less singular than r^{-1} near $r = 0$.

For the remaining functions, $f_L^{(QT)}(k)$ and $f_L^{(T)}(k)$, the situation is different. We observe that these functions tend to definite (non-zero) limits when k tends to infinity:

$$\lim_{k\to\infty} f_L^{(QT)}(k) = \frac{g_s^2}{4M}\left(\frac{\psi(L-1)-\psi(L+1)}{2L+1}\right), \qquad (5.17)$$

$$\lim_{k\to\infty} f_L^{(T)}(k) = -\frac{g_s^2}{6M}(2\psi(L)-\psi(L+1)-\psi(L-1)). \qquad (5.18)$$

The functions $kf_L^{(QT)}(k)$ and $kf_L^{(T)}(k)$ do therefore not have square integrable derivatives, and the inversion theorems are not immediately applicable in these cases. This difficulty can readily be overcome. Suppose now that the principal part near $r = 0$ of the functions

$$G_2(r, L(L+1)) - \tfrac{1}{2}(2L-1)(2L+3)G_4(r, L(L+1))$$

and

$$G_2(r, (L-1)L) + G_2(r, (L+1)(L+2))$$

is of the form

$$g_{24}(L) r^{-\lambda-1}, \qquad g_{22}(L) r^{-\lambda-1} \tag{5.19}$$

respectively, where $0 < \lambda < 2$ and g_{22}, g_{24} are L-dependent constants. Recalling the formula[6]

$$\left.\begin{aligned} \int_0^\infty dr r^{-\lambda} J_\mu(kr) J_\nu(kr) &= C(\lambda,\mu,\nu) k^{\lambda-1}, \\ (\mathrm{Re}(\mu+\nu+1) &> \mathrm{Re}(\lambda) > 0) \end{aligned}\right\} \tag{5.20}$$

where

$$\left.\begin{aligned} C(\lambda,\mu,\nu) &= \\ \frac{2^{-\lambda}\Gamma(\lambda)\Gamma(\tfrac{1}{2}\mu + \tfrac{1}{2}\nu - \tfrac{1}{2}\lambda + \tfrac{1}{2})}{\Gamma(\tfrac{1}{2}\lambda + \tfrac{1}{2}\nu - \tfrac{1}{2}\mu + \tfrac{1}{2})\Gamma(\tfrac{1}{2}\lambda + \tfrac{1}{2}\mu + \tfrac{1}{2}\nu + \tfrac{1}{2})\Gamma(\tfrac{1}{2}\lambda + \tfrac{1}{2}\mu - \tfrac{1}{2}\nu + \tfrac{1}{2})}&, \end{aligned}\right\} \tag{5.21}$$

we observe, from eqs. (4.7) and (4.8), that λ in (5.19) must equal unity, and obtain the relations

$$4\pi^2 g_{24}(L) C(1, L+\tfrac{1}{2}, L+\tfrac{1}{2}) = f_L^{(QT)}(\infty), \tag{5.22}$$

$$-4\pi^2 g_{22}(L) C(1, L-\tfrac{1}{2}, L+\tfrac{3}{2}) = f_L^{(T)}(\infty), \tag{5.23}$$

where $f_L^{(QT)}(\infty)$, $f_L^{(T)}(\infty)$ denote the limits (5.17) and (5.18), respectively. We then obtain (for $L > 1$)

$$\left.\begin{aligned} &G_2(r, L(L+1)) - 2((L+\tfrac{1}{2})^2 - 1) G_4(r, L(L+1)) = \\ &\frac{g_{24}(L)}{r^2} - \frac{1}{2\pi}\int_0^\infty dk (k(f_L^{(QT)}(k) - f_L^{(QT)}(\infty)))' k J_{L+\frac{1}{2}}(kr) Y_{L+\frac{1}{2}}(kr), \end{aligned}\right\} \tag{5.24}$$

and

$$\left.\begin{aligned} &G_2(r, (L-1)L) + G_2(r, L+1)(L+2)) = \\ &\frac{g_{22}(L)}{r^2} + \frac{1}{4\pi}\int_0^\infty dk (k(f_L^{(T)}(k) - f_L^{(T)}(\infty)))' k \\ &\{J_{L-\frac{1}{2}}(kr) Y_{L+\frac{3}{2}}(kr) + J_{L+\frac{3}{2}}(kr) Y_{L-\frac{1}{2}}(kr)\}. \end{aligned}\right\} \tag{5.25}$$

As we mentioned before, it is not necessary to obtain the expressions for G_2 and G_4 separately, since these functions occur in the radial Schrödinger equations in precisely the combinations given in (5.24) and (5.25).

Let us now return to the short range terms $r_L^{i)}(k)$. It is readily seen that these terms tend to non-zero limits $r_L^{(i)}(\infty)$ when k tends to infinity. By using the same arguments as above, we conclude that these terms in coordinate space correspond to potentials which behave like $O(r^{-2})$ near $r = 0$.

We may summarize the discussion as follows. The scalar boson exchange potential (5.1) can be represented by a local, angular momentum dependent potential G in coordinate space, which contains a central .., spin-orbit, spin-spin .., quadratic spin orbit .. and tensor force potential. The three first mentioned potentials behave like $o(r^{-1})$ near $r = 0$, whereas the quadratic spin orbit .. and tensor force potentials behave like $O(r^{-2})$ near $r = 0$. In addition, there appear short range terms which operate only in the states with $L = 0$ and $L = 1$, respectively, and which behave like $O(r^{-2})$ near $r = 0$.

Let us now compare this result to the one which is obtained by using expansions with respect to $\boldsymbol{p}^2/M^2$. In the adiabatic limit[7)] the spin-bilinear terms disappear completely. The central potential becomes the ordinary Yukawa potential $Y = \dfrac{e^{-mr}}{r}$, and the spin-orbit force becomes $\dfrac{1}{r}\dfrac{d}{dr}Y(mr)$, which behaves like $O(r^{-3})$ near $r = 0$. In the next approximation, keeping terms of the order $\boldsymbol{p}^2/M^2$, one obtains[8)] a quadratically momentum dependent central potential, which in coordinate space has the form $Y(mr) - \dfrac{\hat{p}^2}{M^2}Y(mr)$, where $\hat{p}$ is the differential operator $-\dfrac{i}{2}\left(\overrightarrow{\partial} - \overleftarrow{\partial}\right)$. The resulting "effective" central potential is therefore a linearly energy dependent function which behaves like $O(r^{-3})$ near $r = 0$. The spin orbit potential is in this approximation the same as in the adiabatic limit. Also, the spin-bilinear terms are absent in this approximation. We may therefore conclude that the approximations of the above mentioned type give a both qualitatively and quantitatively misleading picture of the scalar boson exchange potential.

6. Concluding remarks

In the foregoing sections we have considered the more or less formal problem of obtaining a local, angular momentum dependent potential from a given potential in the momentum representation. The formalism outlined here might be considered complicated, but this lies in the nature of the

problem and cannot be avoided. We may note that if one wishes to solve the two-nucleon scattering problem with a non-local potential in the momentum representation by using the Lippmann-Schwinger equation, then the matrix elements evaluated in section 3 are necessary ingredients in a calculation of this kind. We have shown that a potential V in the momentum representation becomes local and angular momentum dependent in coordinate space if V has a particular off-shell behaviour, which is implicitly defined by the partial wave integral equations considered in this paper. We mentioned in the introduction that in a perturbative definition of a potential it is always possible to determine the off-shell behaviour so that the coordinate space potential becomes local and angular momentum dependent. We can in fact add an arbitrary term, vanishing on the energy shell, to the lowest order potential, provided this is compensated by adding the proper corrections to the higher order potentials. This procedure can then be repeated for the potential of next order, and so on.

It is thus possible, within a perturbative definition of the potential, to get a potential with any (reasonable) off-shell behaviour, and, in particular, the off-shell behaviour which yields a local, angular momentum dependent potential in coordinate space.

Among potentials of this kind we may mention the various one-boson-exchange potentials, which have been used extensively in numerical calculations in nucleon-nucleon (N-N) scattering. We shall not enter upon a discussion of the domain of applicability of such potentials in this paper; we merely recognize the fact that the vast majority of potentials which have been considered in N-N scattering are based more or less directly on the use of perturbation theory expansions for the S-matrix from field theory. Besides the approximations of a "physical" nature involved in calculations with such potentials, one has used approximations involving expansions with respect to the inverse of the nucleon mass, in order to obtain local or "almost local" potentials.

In I we have investigated the validity of such approximations by evaluating the phase shifts for the case of scalar particles interacting through a single particle exchange potential. It was shown that the "adiabatic" approximation can lead to quite inaccurate results for this case. The example considered in section 5 of this paper shows clearly that the approximation involving an expansion in $\boldsymbol{p}^2/M^2$ is entirely misleading.

It is of course very natural to make approximations which lead to local potentials, in order to obtain manageable equations. As we have demonstrated, this can be achieved, whithout using $\boldsymbol{p}^2/M^2$-expansions, by taking

advantage of the ambiguities inherent in any S-matrix definition of the potential, and this leads to the concept of a local, angular momentum dependent potential.

Acknowledgements

It is a pleasure to thank Professor T. Gustafson and Professor C. Møller for the hospitality and financial support of NORDITA.

The author is indebted to Professor G. E. Brown and Professor J. Hamilton for their critical reading of the first draft of the manuscript.

References

1) C. Cronström, Kgl. Danske Videnskab. Selskab, Mat.-fys. Medd. **35** (13) (1967).
2) J. Goto and S. Machida, Progr. Theor. Phys., **25**, 64 (1961).
3) S. Okubo and R. E. Marshak, Ann. Phys. (U.S.A.) **4**, 166 (1958).
4) E. W. Barnes, Proc. Lond. Math. Soc. (2), II, 438 (1904).
5) A. Erdélyi (Ed.), Higher Transcendental Functions, Vol. I, McGraw-Hill Book Company, Inc., New York (1953).
6) G. N. Watson, Theory of Bessel Functions, (2nd ed.), Cambridge University Press (1944).
7) R. A. Bryan, C. R. Dismukes, and W. Ramsay, Nucl. Phys., **45**, 353 (1963).
8) N. Hoshizaki, I. Lin and S. Machida, Progr. Theor. Phys. **26**, 680 (1961).

Indleveret til Selskabet den 28. oktober 1966.
Færdig fra trykkeriet den 5. maj 1967.

Matematisk-fysiske Meddelelser
udgivet af
Det Kongelige Danske Videnskabernes Selskab
Bind **35,** nr. 15

Mat. Fys. Medd. Dan. Vid. Selsk. **35,** no. 15 (1967)

POWDER-DIAGRAM AND SPECTROSCOPIC STUDIES OF MIXED OXIDES OF LANTHANIDES AND QUADRIVALENT METALS

BY

CHR. KLIXBÜLL JØRGENSEN

AND

ELFRIEDE RITTERSHAUS

København 1967
Kommissionær: Munksgaard

CONTENTS

		Page
1.	Miscibility and Superstructures of Fluorite	3
2.	Zirconium Oxide	4
3.	The New Type $NdYO_3$	7
4.	Mixed Lanthanum-Erbium Oxides	9
5.	Bismuth Oxide	12
6.	Thorium Oxide and the Oxidation States of Praseodymium and Terbium.	14
7.	Optical Electronegativity of Praseodymium (IV) and Terbium (IV)	18
8.	Internal f Transitions; the Nephelauxetic Effect and Intensities	24
9.	Experimental Section	32
	Acknowledgments	33
	References	34

Synopsis

Praseodymium and terbium occur predominantly as Pr(III) and Tb(III) in ZrO_2 whereas strongly coloured Pr(IV) and Tb(IV) is formed in ThO_2. The uncorrected optical electronegativities of these central atoms are 2.6 and 2.55 and found to agree with the general theory for $4f^q$. The disordered fluorites $M_{0.2}Zr_{0.8}O_{1.9}$ are studied spectroscopically and show a slightly weaker nephelauxetic effect than the C-M_2O_3. $LaErO_3$ and related materials such as $La_{0.4}Er_{0.4}Zr_{0.2}O_{1.6}$ are further investigated. The new type $NdYO_3$ is found in a large variety of mixed La-Nd-Sm-Ti-Zr oxides prepared by ignition of co-precipitated hydroxides at 1000° C. Bi_2O_3 containing small amounts of Nd(III) or Er(III) is a disordered fluorite; the relations to senarmontite-Sb_2O_3 and $M_2Bi_{24}O_{40}$ are discussed. The absorption spectrum of Ce(IV) acetylacetonate is measured. Comparisons are made with the unusual octahedral 4f group and 5f group hexahalide complexes. The variable polarizability and optical electronegativity of oxide are discussed.

PRINTED IN DENMARK
BIANCO LUNOS BOGTRYKKERI A/S

1. Miscibility and Superstructures of Fluorite

It is wellknown in geochemistry that trivalent lanthanides and certain quadrivalent metals such as thorium frequently replace each other in minerals. This is usually ascribed to comparable ionic radii and the stoichiometry is normally taken care of by charge compensation of other constituents, as is also often the case for aluminium (III) and silicon (IV) in common rocks. However, it is far more surprising that ZINTL and CROATTO [133] discovered that La_2O_3 is miscible to a large extent with CeO_2 retaining the cubic fluorite structure of the latter compound. This type of miscibility explains many tenacious impurities found in old days in rare earths, and may perhaps even explain why Urbain found traces of hafnium in fractions of Lu_2O_3 and called the new element celtium, firmly believing that it was trivalent.

From a crystallographic point of view, the miscibility may either be statistical, a surprisingly large number of oxygen vacancies (frequently above 12.5 %) being formed, or new superstructures such as the C-type M_2O_3 or the pyrochlore $A_2B_2O_7$ are generated. No case seems to be known where the number of metal atoms deviate from that found in fluorite. In other words, in the unit cell characterized by the lattice parameter a_F (having the order of magnitude 5 Å), four metal atoms occur, whereas in the superstructures having the size $2a_F$, 32 metal atoms are found. They are arranged in cubic close-packing, and hence, on a Debye-powder diagram, the lines having the index $h^2+k^2+l^2 = 3, 4, 8, 11, 12, 16, 19, 24, \ldots$ would occur anyhow, even if the oxygen atoms were neglected. In one sense, CaF_2 is a superstructure of CsCl containing half as many metal atoms, but we have found no trace of miscibility between these two types.

Small quadrivalent ions such as titanium (IV) favour distinct superstructures having the coordination number $N = 8$ for the lanthanides and $N = 6$ for Ti(IV). However, some C-oxides are miscible with TiO_2 to a certain extent [70] and $Er_{0.9}Ti_{0.1}O_{1.55}$ is distinctly C-type whereas $Dy_{0.9}Ti_{0.1}O_{1.55}$ seems to be a disordered fluorite with broadened diffraction lines. AULT and WELCH [3] found that a fluorite phase extends from $Y_{0.63}Ti_{0.37}O_{1.685}$ ($a_F = 5.135$ Å) to $Y_{0.76}Ti_{0.24}O_{1.62}$ ($a_F = 5.200$ Å) and a pyrochlore phase

from $Y_{0.45}Ti_{0.55}O_{1.775}$ ($2a_F$ = 10.088 Å) to $Y_{0.59}Ti_{0.41}O_{1.705}$ ($2a_F$ = 10.127 Å). The non-Daltonian behaviour of the pyrochlore casts a weak doubt on the stoichiometry of $ErTiO_{3.5}$ ($2a_F$ = 10.0762 Å) which has been studied very carefully by X-ray and neutron diffraction [80]. The strongly distorted octahedron Ti-6 O has the internuclear distance 1.955 Å whereas the compressed cube around erbium has two Er-O 2.1815 Å ($= \sqrt{3}a_F/4$) and six Er-O 2.471 Å. The distortions from fluorite (x = 0.375) can be expressed by the oxygen parameter x = 0.420 for $ErTiO_{3.5}$. If x were 0.4375, the octahedron Ti(IV)O_6 would be regular. These figures illustrate the extraordinary liberality of ionic radius variation allowed in the superstructures. The two short Er-O distances represent the average value for A and B in $A_2B_2O_7$, whereas Er(III) otherwise seems to have an ionic radius some 0.4 Å larger than Ti(IV). One would extrapolate a_F for a hypothetical fluorite TiO_2 to be 4.80 Å whereas the (much safer) extrapolation to fluorite ZrO_2 gives 5.10 Å. These values vary less than $(4/\sqrt{3})$times the variation of the ionic radii for 6-coordination.

2. Zirconium Oxide

Excellent reviews on mixed oxides formed with Zr(IV) are written by Madame Perez y Jorba [99], Lefèvre [84] and Möbius [93]. Whereas pure ZrO_2 is not stable as fluorite, relatively small admixtures of trivalent or divalent ions stabilize the cubic form. There is an apparent discrepancy between our previous results [70] finding disordered fluorites $MZrO_{3.5}$ (M = Nd,Sm, Eu,Dy, Ho,Er,Yb) and Collongues *et al.* [25] finding pyrochlores for M = La,Ce,Nd,Sm and Gd in agreement with Roth [109] for M = La and Nd. The French authors prepared the pyrochlores under equilibrium conditions at 1300 to 1500°C and noted that $SmZrO_{3.5}$ if heated above 2400°C or $GdZrO_{3.5}$ if heated above 1550°C transform to disordered fluorites, comparable to $DyZrO_{3.5}$ at all temperatures studied. Our technique of heating co-precipitated hydroxides for one to three hours at 1000°C produces disordered Zr-fluorites (though Ti-pyrochlores) which must be metastable according to Perez y Jorba [99]. The crystallization of the oxide formed from co-precipitated hydroxides takes place at a quite definite temperature, frequently around 500°C, whereas pure ZrO_2 is formed from the hydroxide at 370°C according to Lefèvre [84]. The additional lines for pyrochlores ($a_P = 2a_F$) have indexes 3, 11, 19, 27, 35, . . .

We continued our studies by preparing $M_{0.2}Zr_{0.8}O_{1.9}$ of most of the lanthanides M. This concentration of M is well above what is normally

Table 1.

Unit cell parameters a_F in Å observed for cubic (and in the case of $LaErO_3$, perhaps quasi-cubic) structures. F is fluorite, C the Er_2O_3 type, P pyrochlore (the actual unit cells have $a_C = a_P = 2\ a_F$). The mixed La-Er-Zr oxides marked w and w^2 have the apparent fluorite-indexes 1.5 and 2.25, respectively. The calculated values a_F^* are obtained by linear combination of the constituents, the quantities for M(III) being obtained from eq.(1). +N indicates that the sample consists of two phases, the other being $NdYO_3$ of Table 2. As discussed in the text, the observation of the line w^2 may indicate N being present well.

	Type	a_F	a_F^*	Ref.
$La_{0.55}Er_{0.45}O_{1.5}$	C+N	~5.36	5.57	—
$La_{0.5}Er_{0.5}O_{1.5}$ (1000° C)	C+N	5.29	5.55	70
$La_{0.45}Er_{0.55}O_{1.5}$	C+N	~5.35	5.53	—
$La_{0.4}Er_{0.6}O_{1.5}$	C+N	~5.41	5.51	—
$La_{0.3}Er_{0.7}O_{1.5}$	C+N	~5.33	5.48	—
$La_{0.2}Er_{0.8}O_{1.5}$	C(+N)	5.31	5.45	—
$La_{0.1}Er_{0.9}O_{1.5}$	C	5.30	5.41	—
$ErO_{1.5}$	C	5.274	5.38	—
$La_{0.5}Tm_{0.5}O_{1.5}$ (820° C)	C+N	5.36	5.53	—
$La_{0.5}Yb_{0.5}O_{1.5}$ (820° C)	C+N	5.26	5.52	—
$Dy_{0.9}Zr_{0.1}O_{1.55}$	F or C	5.32	5.39	—
$La_{0.36}Er_{0.54}Zr_{0.1}O_{1.55}$	F(w^2)	5.345	5.47	—
$La_{0.27}Er_{0.63}Zr_{0.1}O_{1.55}$	F(w,w^2)	5.29	5.44	—
$La_{0.18}Er_{0.72}Zr_{0.1}O_{1.55}$	F(w)	~5.30	5.41	—
$La_{0.09}Er_{0.81}Zr_{0.1}O_{1.55}$	F(w)	~5.28	5.38	—
$Er_{0.9}Zr_{0.1}O_{1.55}$	C	5.26	5.35	—
$Sm_{0.8}Zr_{0.2}O_{1.6}$	F	~5.40	5.44	—
$La_{0.4}Dy_{0.4}Zr_{0.2}O_{1.6}$	F+N	5.38	5.48	—
$La_{0.2}Dy_{0.6}Zr_{0.2}O_{1.6}$	F+N	5.34	5.40	—
$Dy_{0.8}Zr_{0.2}O_{1.6}$	F	5.29	5.36	—
$La_{0.4}Er_{0.4}Zr_{0.2}O_{1.6}$	F(w^2)	5.30	5.46	—
$La_{0.32}Er_{0.48}Zr_{0.2}O_{1.6}$	F(w^2)	~5.29	5.43	—
$La_{0.24}Er_{0.56}Zr_{0.2}O_{1.6}$	F(w^2)	5.275	5.41	—
$La_{0.16}Er_{0.64}Zr_{0.2}O_{1.6}$	F(w,w^2)	~5.28	5.38	—
$La_{0.08}Er_{0.72}Zr_{0.2}O_{1.6}$	F(w)	5.255	5.35	—
$Er_{0.8}Zr_{0.2}O_{1.6}$	C	5.26	5.32	70
$Nd_{0.67}Zr_{0.33}O_{1.67}$	F+N	~5.36	5.42	—
$La_{0.33}Sm_{0.33}Zr_{0.33}O_{1.67}$	F	~5.37	5.45	—
$Sm_{0.67}Zr_{0.33}O_{1.67}$	F?	—	5.38	—
$Dy_{0.67}Zr_{0.33}O_{1.67}$	F	5.26	5.32	—
$Er_{0.67}Zr_{0.33}O_{1.67}$	C	5.27	5.28	70
$La_{0.25}Nd_{0.25}Zr_{0.5}O_{1.75}$	F+N	5.31	5.38	—
$Nd_{0.5}Zr_{0.5}O_{1.75}$	P	5.324	—	109
	F	5.30	5.35	70
$La_{0.25}Sm_{0.25}Zr_{0.5}O_{1.75}$	F	~5.30	5.36	—

(contd.)

TABLE 1 (contd.)

	Type	a_F	a_F^*	Ref.
$Sm_{0.5}Zr_{0.5}O_{1.75}$	P	5.288	—	99
	F	5.27	5.32	70
$Eu_{0.5}Zr_{0.5}O_{1.75}$	F	5.23	5.30	70
$La_{0.25}Dy_{0.25}Zr_{0.5}O_{1.75}$	F+N	5.27	5.33	—
$Dy_{0.5}Zr_{0.5}O_{1.75}$	F	5.21	5.26	70
$Ho_{0.5}Zr_{0.5}O_{1.75}$	F	5.20	5.25	70
$La_{0.2}Er_{0.3}Zr_{0.5}O_{1.75}$	F	~5.24	5.31	—
$La_{0.15}Er_{0.35}Zr_{0.5}O_{1.75}$	F	5.23	5.29	—
$La_{0.1}Er_{0.4}Zr_{0.5}O_{1.75}$	F	5.22	5.27	—
$La_{0.05}Er_{0.45}Zr_{0.5}O_{1.75}$	F	5.205	5.255	—
$Er_{0.5}Zr_{0.5}O_{1.75}$	F	5.19	5.24	70
$Yb_{0.5}Zr_{0.5}O_{1.75}$	F	5.17	5.21	70
$Pr_{0.4}Zr_{0.6}O_{2-x}$	F	5.265	(IV)5.225	—
			(III)5.31	—
$Pr_{0.2}Zr_{0.8}O_{2-y}$	F	5.17	(IV)5.16	—
		to 5.25	(III)5.205	—
$Nd_{0.2}Zr_{0.8}O_{1.9}$	F	5.19	5.20	—
$Sm_{0.2}Zr_{0.8}O_{1.9}$	F	5.17	5.19	—
$Eu_{0.2}Zr_{0.8}O_{1.9}$	F	5.155	5.18	—
$Tb_{0.2}Zr_{0.8}O_{1.9}$	F	5.15	(III)5.17	—
$Dy_{0.2}Zr_{0.8}O_{1.9}$	F	5.15	5.16	—
$Ho_{0.2}Zr_{0.8}O_{1.9}$	F	5.147	5.16	—
$Er_{0.2}Zr_{0.8}O_{1.9}$	F	5.145	5.16	—
$Tm_{0.2}Zr_{0.8}O_{1.9}$	F	5.135	5.15	—
$Yb_{0.2}Zr_{0.8}O_{1.9}$	F	5.13	5.15	—

needed to induce the fluorite structure, and indeed, we find a very smooth variation of a_F as seen in Table 1. The samples form unusually large (about 1 mm^3) crystals; the spectroscopic properties are discussed in chapter 8. The behaviour of praseodymium and terbium is particularly interesting. When incorporated in CeO_2, ThO_2 and in C-oxides, these two elements readily oxidize to Pr(IV) and Tb(IV) by heating in air. However, this is not at all true in ZrO_2. The value $a_F = 5.15$ Å for M = Tb interpolates nicely in the series of the other trivalent M. An even stronger argument is the amber-yellow colour of the sample suggesting that nearly all terbium occurs as Tb(III) since we see in chapter 6 that Tb(IV) is far more intensely coloured in such lattices. The case for M = Pr is a little more complicated. The powder diagram here corresponds to a superposition of two components having $a_F = 5.25$ and 5.17 Å; and when heated in ethanol vapour, $a_F \sim 5.23$ Å

and the lines are asymmetrically broadened. The sample is yellow-brown before the reduction and turns pale grey. The black $Pr_{0.4}Zr_{0.6}O_{2-x}$ turns light olive-brown by reduction in ethanol vapour, but retains the value $a_F = 5.26_5$ Å. $Pr_{0.5}Zr_{0.5}O_{2-x}$ is black and has $a_F = 5.31$ Å. When compared with $a_F = 5.39$ Å for PrO_2 [16, 45] this indicates lattice constants some 0.05–0.07 Å above Vegard's linear rule. The most probable conclusion is that most, but not all, praseodymium occurs as Pr(III) in these samples.

We also prepared some lanthanide-rich mixtures. Several of these preparations belong to a new type described in chapter 3 and which is remarkably common for lanthanum and neodymium oxides containing some Ti(IV), Y(III) or Zr(IV). However, some disordered fluorites are also found. As seen in Table 1, lanthanum substitution $La_xEr_{1-x}ZrO_{3.5}$ increases a_F from 5.19 Å for x = 0 to 5.24 Å for x = 0.4. Three other disordered fluorites are $Nd_{0.67}Zr_{0.33}O_{1.67}$, $La_{0.33}Sm_{0.33}Zr_{0.33}O_{1.67}$ and $Dy_{0.67}Zr_{0.33}O_{1.67}$ whereas $Er_{0.67}Zr_{0.33}O_{1.67}$ previously [70] was found to be a C-oxide with slightly larger a_F. $Sm_{0.8}Zr_{0.2}O_{1.6}$ has broader diffraction lines than $Dy_{0.8}Zr_{0.2}O_{1.6}$ but both seem to be disordered fluorites, whereas $Dy_{0.9}Zr_{0.1}O_{1.55}$ shows ambiguous and $Er_{0.8}Zr_{0.2}O_{1.6}$ certain signs of being C-oxides. We discuss nine mixed La-Er-Zr oxides in chapter 4 because of the relations to the problem of $LaErO_3$.

3. The New Type $NdYO_3$

Since Goldschmidt's identification [36] of the A-, B- and C-types of the rare earths, there has been an extensive discussion of the influence of temperature and pressure on the equilibria and kinetic behaviour of the transformations (*cf.* the review by Brauer [17]). Foex and Traverse [33] have recently found two new hexagonal forms of M_2O_3 which only occur above 2000°C. Schneider and Roth [112] studied mixed lanthanide oxides prepared mainly at 1650°C and concluded in the presence of Goldschmidt's three forms and of an orthorhombic perovskite $LaYbO_3$. As we shall see in chapter 4, this is a high-temperature form. When prepared at 600° or 800°C, two other types are observed.

As seen in Table 2, our technique produced [70] $Nd_{0.5}Y_{0.5}O_{1.5}$ and $Nd_{0.2}Y_{0.8}O_{1.5}$ not having the B-type expected [112] but a rather simple powder-diagram which has also been found in a large number of mixed oxides of lighter lanthanides containing some Ti(IV) or Zr(IV). Among the pure examples of this type are $Nd_{0.9}Ti_{0.1}O_{1.55}$, $Nd_{0.8}Ti_{0.2}O_{1.6}$, $Nd_{0.67}Ti_{0.33}O_{1.67}$, $Nd_{0.8}Zr_{0.2}O_{1.6}$, $La_{0.4}Nd_{0.4}Zr_{0.2}O_{1.6}$, $La_{0.45}Sm_{0.45}Zr_{0.1}O_{1.55}$ and $La_{0.45}Dy_{0.45}Zr_{0.1}O_{1.55}$. The purpose of making the ternary mixed oxides is to

TABLE 2.

d-values in Å for diffraction lines of the new type $NdYO_3$. The normalization factor n for the unit cell is indicated. +F indicates the simultaneous presence of another, fluorite-type, phase. "v" indicates the presence of additional lines, the strongest of which has $d = 2.12$ Å, and probably corresponding to a perovskite phase.

					n	Ref.
$Nd_{0.5}Y_{0.5}O_{1.5}$	3.44	2.85	2.59	2.01	1.00	70
$Nd_{0.2}Y_{0.8}O_{1.5}$	3.42	2.82	2.57	1.98	0.99	70
$Nd_{0.9}Ti_{0.1}O_{1.55}$	3.43	2.84	2.59	2.01	1.00	70
$Nd_{0.8}Ti_{0.2}O_{1.6}$	3.45	2.84	2.59	2.01	1.00	70
$Nd_{0.67}Ti_{0.33}O_{1.66}$	3.46	2.86	2.61	2.02	1.005	70
$La_{0.45}Sm_{0.45}Zr_{0.1}O_{1.55}$	3.525	2.905	2.63	—	1.02	—
$La_{0.45}Dy_{0.45}Zr_{0.1}O_{1.55}$	3.525	2.905	2.63	2.06	1.02	—
$La_{0.4}Nd_{0.4}Zr_{0.2}O_{1.6}$	3.525	2.9	2.625	2.06	1.02	—
$La_{0.2}Nd_{0.6}Zr_{0.2}O_{1.6}$	3.505	2.875	2.62	2.04	1.015	—
$Nd_{0.8}Zr_{0.2}O_{1.6}$	3.45	2.855	2.595	2.02	1.005	—
$La_{0.4}Sm_{0.4}Zr_{0.2}O_{1.6}$	3.515	2.905	2.625	2.06	1.02	—
$La_{0.2}Sm_{0.6}Zr_{0.2}O_{1.6}$(+F)	3.505	2.885	2.615	2.04?	1.015	—
$La_{0.4}Dy_{0.4}Zr_{0.2}O_{1.6}$(+F)	3.525	2.91	—	2.06	1.02	—
$La_{0.2}Dy_{0.6}Zr_{0.2}O_{1.6}$(+F)	3.515	2.895	—	2.06	1.02	—
$La_{0.33}Nd_{0.33}Zr_{0.33}O_{1.67}$(+F)	3.515	2.885	2.625	2.05	1.015	—
$Nd_{0.67}Zr_{0.33}O_{1.67}$(+F)	3.445	2.85	2.585	—	1.00	—
$La_{0.33}Dy_{0.33}Zr_{0.33}O_{1.67}$(+F)	3.535	2.915	—	2.06	1.025	—
$La_{0.25}Nd_{0.25}Zr_{0.5}O_{1.75}$(+F)	3.525	2.915	2.635	2.06	1.02	—
$La_{0.5}Y_{0.5}O_{1.5}$(600° C)	3.535	2.915	2.64	2.065	1.025	—
$La_{0.5}Y_{0.5}O_{1.5}$(1000° C)	3.545	2.92	2.64	2.065	1.03	—
$La_{0.5}Ho_{0.5}O_{1.5}$(1000° C)	3.535	2.915	2.64	2.065	1.025	—
$La_{0.6}Er_{0.4}O_{1.5}$(+v)	3.535	2.92	2.64	2.06	1.025	—
$La_{0.55}Er_{0.45}O_{1.5}$(+v, +C)	3.525	2.90	2.63	2.06	1.02	—
$La_{0.5}Er_{0.5}O_{1.5}$(600° C)	3.54	2.92	2.645	2.065	1.03	—
— (1000° C, N-component)	3.53	2.90	—	2.055	1.02	—
$La_{0.45}Er_{0.55}O_{1.5}$(+v, +C)	3.525	2.91	~2.63	2.06	1.02	—
$La_{0.4}Er_{0.6}O_{1.5}$(+C)	3.525	2.91	~2.65	2.065	1.02	—
$La_{0.5}Tm_{0.5}O_{1.5}$ (600° C) (+C)	3.535	2.92	~2.65	2.065	1.025	—
$La_{0.5}Yb_{0.5}O_{1.5}$(600° C) (+C)	3.53	2.91	~2.64	2.065	1.02	—
— (1000° C, N-component)	3.535	2.91	—	2.06	1.025	—

investigate to what extent a mixture of two lanthanides imitates the actual lanthanide having the ionic radius equal to the average radius of the mixture. Other samples, containing heavier lanthanides such as dysprosium, or containing more zirconium, consisted of two phases, one fluorite and one $NdYO_3$ type. However, $LaYO_3$ and $LaHoO_3$ prepared at 600° or 1000°C, or $LaErO_3$ prepared at 600°C also belong to the $NdYO_3$ type.

The linear dimensions of the unit cells of the various compounds isotypic with $NdYO_3$ must be rather similar. It is seen in Table 2 that the *d*-values range from 1.025 ($La_{0.5}Y_{0.5}O_{1.5}$) to 0.99 ($Nd_{0.2}Y_{0.8}O_{1.5}$) times those characterizing $NdYO_3$. It may be noted that in addition to our type, which we also find for Nd_2TiO_5 prepared by our technique, two other types M_2TiO_5 have been described. ROTH [109] found that $La_2Ti_2O_7$ and $Nd_2Ti_2O_7$ are not cubic pyrochlores (as are $Sm_2Ti_2O_7$ and heavier compounds) but have a very complicated powder-diagram not corresponding to our type. GUILLEN and BERTAUT [38] resolved the crystal structure of their orthorhombic La_2TiO_5 containing La(III)O_7 and unusual trigonal-bipyramidic Ti(IV)O_5. QUEYROUX [103] studied Gd_2TiO_5 and Dy_2TiO_5 having essentially a fluorite structure, but an actual hexagonal unit cell with the volume $9a_F^3$. Professor E. F. Bertaut was so kind as to confirm that the powder-diagrams of these four types are all different.*

4. Mixed Lanthanum-Erbium Oxides

The C-type M_2O_3 solved by PAULING and SHAPPELL [98] is represented by a surprising variety of oxides, Sc_2O_3, In_2O_3, Tl_2O_3 in addition to rare earths (favoured by small ionic radii and low temperature). Obviously, the oxygen atoms do not contribute very strongly to the X-ray diffraction, and it is only after the refinement also using neutron diffraction [10] that it has become apparent that the M-O distances do not show as much spreading as first assumed (excepting Mn_2O_3 and the mineral bixbyite, which are rather atypical cases). Thus, 8 of the 32 indium atoms in the unit cell of In_2O_3 [88] have six oxygen neighbours at the distance 2.18 Å nicely situated at the corners of a cube lacking a bodydiagonal, whereas the 24 atoms deviate more from the idealized fluorite substructure (cube lacking a face-diagonal) by having each two distances In-O 2.13, two 2.19 and two 2.23 Å. It may be remarked that the average distance 2.183 Å is very closely that of fluorite $\sqrt{3}a_F/4 = 2.189$ Å.

Phenomenologically, the fluorite diffraction lines having the index $h^2+k^2+l^2 = 3, 4, 8, 11, 12, 16, 19, \ldots$ become 12, 16, 32, 44, 48, 64, 76, ... when the unit cell is doubled in C-oxides, and new, prominent lines have the indexes 6, 14, 18, 22, 26, 38, 46, ... It was noted [70] that samples of $LaErO_3$ and $LaYbO_3$ made at temperatures lower than 1000°C have the

* Dr. Paul Caro kindly attracted the writers' attention to the danger of forming very stable oxo-carbonates $M_2O_2(CO_3)$. However, the powder-diagrams of the two hexagonal forms M = La and Sm do not correspond to ours, and a sample of $LaYO_3$(1000°C) kept for half a year, only contains 2.6% CO_2 and not 13.75% CO_2.

powder-diagram characterizing the C-type superposed very weak lines apparently having the fractional indexes 2.25 and 8.75 besides a few lines at lower *d*-values. One explanation of this behaviour would be a very large cubic unit cell having the size $4a_F$ (~ 20 Å) and only showing appreciable diffraction intensity for the indexes 9, 24, 35, 48, 64, . . . which is not a very appealing idea. Another explanation would be an ordered distortion of the C-lattice, perhaps having a symmetry much lower than cubic, as has actually been found for Gd_2O_3, Dy_2O_3, Yb_2O_3 [99] and Sc_2O_3 [84] mixed crystals with relatively small amounts of ZrO_2. However, these types do not correspond to our observations.

Here, we continued the study, and we found the same behaviour for $LaTmO_3$ and for $La_xEr_{1-x}O_{1.5}$ with x = 0.2 to 0.55, and a rather unexpected variation of a_F as function of x, as seen in Table 1. We have adapted the suggestion by BRAUER and GRADINGER [15] to define an effective a_F^* parameter for C-oxides having the observed $a_C = 2a_F$:

$$a_F^* = a_F + 0.21295\ (5.757\ \text{Å} - a_F) \qquad (1)$$

giving the values 5.62 Å for Pr_2O_3, 5.59 Nd, 5.53 Sm, 5.50 Eu, 5.45 Tb, 5.42 Dy, 5.40 Ho, 5.38 Er, 5.35 Tm, 5.33 Yb and 5.40 Y. These values, as well as the parameter a_F^* = 5.72 Å for La_2O_3, agree with the slopes extrapolated towards 100 % lanthanide content in several oxides of quadrivalent metals. The reason why a_F is smaller than a_F^* in C-M_2O_3 (0.042 Å for M = Pr, 0.115 Å for M = Yb) is essentially the six-coordination in C-oxides. Goldschmidt argued that 8-coordination corresponds to 8 % larger ionic radii than 6-coordination, which should hence decrease a_F^* of C-Pr_2O_3 (representing $(4/\sqrt{3})$times the distance Pr-O) 0.27 Å and of Yb_2O_3 0.23 Å. Apparently $N = 6$ is unpleasantly low for lighter lanthanides, and equ. (1) corresponds to much smaller changes. POIX [100] compiled M-O distances for $N = 12$ and $N = 6$ in perovskites. Thus, $N = 12$ for Nd corresponds to 2.665 Å, whereas the observed a_F = 5.54 Å for C-Nd_2O_3 corresponds to 2.40 Å (*cf.* the discussion of In_2O_3 above). Another example [100] is $N = 6$ for Ce 2.405 Å whereas CeO_2 has the actual value (for $N = 8$) 2.338 Å showing a larger rather than a smaller value for six-coordination.

Returning to our $La_xEr_{1-x}O_{1.5}$, the values for $(a_F^* - a_F)$ are 0.11 Å for x = 0 and 0.1; 0.14 Å for 0.2; and 0.15 Å for x = 0.3. This shows that our samples are even more tightly packed than the ordinary C-oxide. For x = 0.5, this difference assumes the rather astonishing size 0.26 Å. Apparently, these very high values are not perfectly reproducible. $LaTmO_3$ has $(a_F^* - a_F)$ = 0.17 Å and $LaYbO_3$ 0.26 Å.

However, most and probably all of these observations can be explained by the presence of two phases. It turned out that $LaErO_3$ prepared at 600°C is entirely of $NdYO_3$-type (N), and that the effect of heating hence seems to be the formation of a mixture of much C- and some N at 1000°C and of perovskite at 1200°C. There are two unusual aspects of this interpretation. One is the w-line with the apparent fluorite index 9/16. Actually, it can be included in Table 2 at the position $d = n \cdot 6.7$ Å. This line is particularly strong in the mixed La-Er oxides, and it was apparently absent in several of the samples given in Table 2. However, a closer comparison showed that in all of these cases, it was due to insufficient exposure of the film. The other unexpected feature is that $LaErO_3$ prepared at 600°C has slightly larger *d*-values than $LaYO_3$ and $LaHoO_3$. Actually, n = 1.02 seems to be a lower limit for the last entries in Table 2, and the N-component of $LaYbO_3$ has a slightly *larger* value of n than the N-component of $LaErO_3$. This can be rationalized if the rearrangement typically taking place between 800 and 1000°C does not involve a complete transformation to the C-type, but that some N-phase remains containing somewhat less Yb in the former case compared to the proportion of Er in the latter case, whereas the C-type assumes a low value for a_F corresponding to less than 50% La. In many ways, the N-type assumes the same role as the B-type in SCHNEIDER and ROTH's studies [112] at 1650°C. We have found no case where the N-type survives at 1200°C.

The mixed La-Er-Zr oxides containing 10% Zr are not extremely different in behaviour. a_F for the C-type increases linearly until 18% La, whereas the samples containing 27 and 36% La also contain some N-phase. The samples containing 20% Zr tend to contain three phases, as is distinctly the case for $La_{0.48}Er_{0.32}Zr_{0.2}O_{1.6}$, *viz.* a fluorite with $a_F \sim 5.36$ Å, an N-phase and something giving sharp lines, the strongest of which at $d = 2.13$ Å. This third phase which can also be perceived in $La_{0.55}Er_{0.45}O_{1.5}$ and $La_{0.45}Er_{0.55}O_{1.5}$ prepared at 1000°C (strongest line $d = 2.12$ Å) is probably a perovskite.

Nearly all our disordered fluorites [70] $MZrO_{3.5}$ have $(a_F - a_F^*) = 0.05$ Å, and this is also true for $La_xEr_{0.5-x}Zr_{0.5}O_{1.75}$ having x = 0.05, 0.1 and 0.15. For x = 0.2, the fluorite lines are somewhat broadened and apparently, the phase breaks down by further lanthanum substitution.

The various oxides having C + N diffraction lines are all transformed irreversibly by heating for three hours to 1200°C. The powder-diagrams indicate clearly perovskites, the average cubic value for the strong multiplets of closely adjacent lines is $a_{av} = 4.23$ Å for $La_{0.4}Er_{0.6}O_{1.5}$, 4.21 Å for $La_{0.45}Er_{0.55}O_{1.5}$, 4.22 Å for $La_{0.5}Er_{0.5}O_{1.5}$, 4.22 Å for $La_{0.55}Er_{0.45}O_{1.5}$, 4.21 Å for

$La_{0.5}Tm_{0.5}O_{1.5}$ and 4.19 Å for $La_{0.5}Yb_{0.5}O_{1.5}$. It is highly probable that the homogeneity ranges for these orthorhombic perovskites are narrow, and that excess rare earth of one kind forms other phases. Thus, $La_{0.3}Er_{0.7}O_{1.5}$ when subject to 3 hours 1200°C seems to have superposed lines of a fluorite or C-oxide a_F = 5.35 Å (pure Er_2O_3 5.274 Å) and another phase. Though the perovskite $LaErO_3$ definitely is the stable thermodynamic form, the coordination number $N = 12$ for La is unusually high, and $N = 6$ for Er unusually low, and correspondingly, the value for $(a_{av}/\sqrt{2}) = 2.98$ Å is considerably larger than Poix' value [100] for La-O 2.71 Å, whereas $a_{av}/2 = 2.11$ Å is smaller than expected for Er-O. Of course, because of the orthorhombic distortions, these two expressions do not correspond exactly to the M-O distances.

5. Bismuth Oxide

C-M_2O_3 has a highly distorted 6-coordination for 24 of the 32 M atoms in the unit cell. Among the most unusual properties of this type considered as a superstructure of fluorite is that the oxygen vacancies are surrounded by four (such six-coordinated) M-atoms without any metallic properties being apparent (with the exception of Tl_2O_3 [70]). One may ask whether a cubic structure is not feasible, where all M atoms adapt the coordination (cube lacking body-diagonal) characterizing the 8 remaining M-atoms in the C-type. Actually, senarmontite, one of the modifications of Sb_2O_3, is cubic O_h^7 with $a = 11.14$ Å and isotypic with arsenolithe As_2O_3 having $a = 11.074$ Å. This type can either be considered as a lattice of individual As_4O_6 molecules or as a superstructure of fluorite, all M-atoms being of the body-diagonal-vacancy class discussed above. The choice between these two descriptions is determined by the actual extent of three M-O distances being considerably shorter than the three others. The powder diagram lines have the indexes 3, 12, 16, 19, 24, 27, 32, 35, 36, 44, 48, 51, . . . [94] which obey the same selection rules as pyrochlore. However, in actual practice, confusion between the two types rarely occurs, because the intensity distribution is very different (19 stronger than 16; 51 comparable to 44; *etc.*).

Levin and Roth [85] reviewed the many modifications reported of Bi_2O_3. The two most common forms of high purity are monoclinic α-Bi_2O_3 and tetragonal β-Bi_2O_3. Sillén [118] found a cubic form ($a = 10.08$ Å) having the composition $M_2Bi_{24}O_{40}$ where M is a quadrivalent impurity such as silicon (*e. g.* deriving from porcelain crucibles). Schumb and Rittner [113] prepared the isotypic γ-Bi_2O_3 ($a = 10.245$ Å) which is definitely not a super-

structure of fluorite (like all other cubic structures discussed here) since it contains 26 Bi atoms per unit cell which can be written $Bi_{26}O_{39}$. LEVIN and ROTH [85] prepared many more "sillenites", mixed oxides 12 Bi: 1 M, where M = Pb, Cd, Rb, V, Zn, Ti, Ge, Al, P, Ge, B, Si, presenting a-values in the range from 10.258 to 10.104 Å. The strongest lines have indexes [113] 8, 10, 12, 14, . . . , 34, 36, 38, 46, . . .

GATTOW and SCHRÖDER [34] described the (disordered) fluorite δ-Bi_2O_3 (a_F = 5.665 Å) which is only stable in the interval from 730°C to the melting point 825°C. These authors also report δ^* mixed oxides such as $Bi_{12}SiO_{20}$ not being a sillenite, but again a disordered fluorite a_F = 5.542 Å. HUND [49] found that UO_2 is completely miscible with δ-Bi_2O_3 forming red-brown $U_xBi_{1-x}O_{1.5+0.5x}$ and that ThO_2 and CeO_2 are miscible to a great extent with this fluorite.

When we melted Bi_2O_3 at 850°C for 30 minutes, the cooled product had a vitreous aspect. However, it does give a complicated powder-diagram. If oxides were carefully pre-mixed corresponding to the compositions $Nd_{0.04}Bi_{0.96}O_{1.5}$, $Nd_{0.08}Bi_{0.92}O_{1.5}$, $Ho_{0.04}Bi_{0.96}O_{1.5}$ and $Er_{0.04}Bi_{0.96}O_{1.5}$, the products have powder-diagrams exclusively corresponding to fluorites having a_F = 5.545, 5.515, 5.515 and 5.515 Å, respectively. Attempts to make $Ho_{0.08}Bi_{0.92}O_{1.5}$ produced a mixture of two phases. We conclude that these samples are essentially δ-Bi_2O_3, and that the a_F-values extrapolate towards a value for pure Bi_2O_3 a_F = 5.575 Å. It must be remembered that Gattow and Schröder's 0.09 Å higher value was obtained at 750°C.

The two groups of cubic pure and impure bismuth(III)oxides are similar to γ-Bi_2O_3 having 26 metal atoms in an unit cell with $a \sim 10.2$ Å and δ-Bi_2O_3 having 32 metal atoms in eight unit cells, $2a_F \sim 11.1$ Å. The latter group might have a relation with senarmontite, the ordering of the body-diagonal vacancies having disappeared. It is not probable that δ-Bi_2O_3 is related to C-M_2O_3 since a_F is larger than for Nd_2O_3. Thus, it is known from the discovery of europium that the (twelve-coordinated) $Bi(NO_3)_6^{-3}$ forms double salts having properties intermediate between those formed by $Sm(NO_3)_6^{-3}$ and $Eu(NO_3)_6^{-3}$, and for many other purposes, the ionic radius of Bi(III) seems to be even smaller than that of Eu(III). On the other hand, the possibility kept open in the senarmontite structure of three short and three long Bi-O distances would join other cases of strongly distorted s^2-stereochemistry [96]. It may be remarked that a_F^* of fluorite Sm_2O_3 according to equ. (1) is 5.53 Å, and that Nd(III) and Er(III) contract our δ-Bi_2O_3 strongly.

6. Thorium Oxide and the Oxidation States of Praseodymium and Terbium

Zintl and Croatto's phenomenon of introduction of large quantities of $LaO_{1.5}$ in CeO_2 was found by HUND and DÜRRWÄCHTER [47] for ThO_2 to the surprising higher limit of $La_{0.52}Th_{0.48}O_{1.74}$. Under the conditions applied by BRAUER *et al.* [15, 35] (*i. e.* equilibria at 1200 to 1500°C) the miscibility is smaller for the heavier lanthanides and attains (at 1200°C) $Eu_{0.36}Th_{0.64}O_{1.82}$ and $Yb_{0.08}Th_{0.92}O_{1.96}$. We prepared [68] $Eu_{0.5}Th_{0.5}O_{1.75}$ and a variety of $M_{0.14}Th_{0.86}O_{1.93}$ (including M = Yb) by heating the coprecipitated hydroxides to 1000°C and we found single fluorite phases. The paradox is the same as discussed above for $MZrO_{3.5}$ that such a technique frequently produces samples which would only be thermodynamically stable at a much higher temperature. GINGERICH amd BRAUER [35] report an increasing miscibility at increasing temperatures above 1200°C.

Since the spectroscopic and crystallographic behaviour of trivalent lanthanides in ThO_2 has been extensively treated, we are here going to discuss only the behaviour of praseodymium and terbium. These two elements have a far greater tendency to be oxidized to Pr(IV) and Tb(IV) in ThO_2 and CeO_2 than they have in ZrO_2, as we saw in chapter 2. MARSH [89] demonstrated this tendency by analytical methods and found that the black $Pr_xTh_{1-x}O_2$ can be reduced by H_2 to Pr(III). A most extraordinary observation was that strong ignition in hydrogen again blackened the material and apparently produced Pr(II) quantitatively. Further on, C-Y_2O_3 was shown to allow full oxidation of Pr present to Pr(IV). On the other hand, Marsh could not confirm the claims by PRANDTL and RIEDER [102] that $Pr_xY_{1-x}O_{1.5+0.5x}$ can be further oxidized to Pr(V). It is well-known by preparative rare-earth chemists that traces of Pr produce a dark-brown discoloration of C-oxides far easier than of A-oxides [131].

We observed a violet colour of $Pr_{0.0005}Th_{0.9995}O_2$ and a purple colour of $Tb_{0.001}Th_{0.999}O_2$. We are interested in the origin of these intense colours, and as we shall discuss in chapter 7, we are convinced that they are due to electron transfer from the adjacent oxide ligands to the Pr(IV) and Tb(IV) central atoms. It is not excluded that cubic oxides containing higher concentrations of Pr or Tb are black because of collective effects in mixed oxidation states, but the presence of monomeric chromophores at low concentration seems beyond doubt. The wavenumbers of these absorption bands increase slightly when the M-O distances decrease. Thus, $Pr_{0.0002}Ce_{0.9998}O_2$ is pink and $Pr_{0.01}Ce_{0.99}O_2$ brick-red [12,14] and Tb(IV) gives a

characteristic orange colour when present as traces in Y_2O_3, which is the reason why Mosander already in 1843 could indicate the existence of this rare element. The Tb-O distance is presumably even shorter in the yellow perovskite (a = 4.28 Å) $BaTbO_3$ and yellow-brown K_2TbO_3 (disordered sodium chloride, a = 5.11 Å) reported by Hoppe [44]. It may be noted that this author has reported colourless K_2CeO_3 and pale brown K_2PrO_3.

In the case of black oxides, we recommend the mineralogical technique of making coloured streaks on an unglazed tile. This has been quite informative in the study of mixed Ce-Th-U oxides.

The mixed Ce(III, IV), Pr(III, IV) and Tb(III, IV) oxides have a highly complicated crystal chemistry. The dark blue colours of $CeO_{1.65-1.81}$ [14] and $Ce_xU_{1-x}O_2$ [86] are certainly due to co-operative effects; but in the former case, a number of distinct phases such as Ce_7O_{12}, Ce_9O_{16} and $Ce_{11}O_{20}$ [11] (previously written as $Ce_{32}O_{55}$, $Ce_{32}O_{56}$ and $Ce_{32}O_{58}$) have been identified for higher oxygen content, whereas in the latter case, a fluorite smoothly changes a_F from 5.412 Å for CeO_2 to 5.469 Å for UO_2. We are not going here to discuss the fascinating uranium oxides but only mention that UO_2 is miscible with $YO_{1.5}$ having a_F^* according to equ. (1) [32]. However, such samples are rapidly oxidized in air, diminuishing a_F and turning black. The black, cubic Pr_6O_{11} (essentially fluorite with a_F = 5.468 Å, lacking 1/12 oxygen atoms and showing weak superstructure lines) [92, 39] is a well-defined, almost Daltonian, compound. An argument for the electronic ordering [definite atoms being Pr(III) and others being Pr(IV)] is Marsh' preparation of $Pr_4La_2O_{11}$ [89]. Electronic ordering has not been detected in many cases; spectroscopic studies of Sb(III) and Sb(V) in cubic crystals such as K_2SnCl_6 [27] and crystallographic investigation of K_2SbBr_6 [50] and $(NH_4)_2SbBr_6$ [83] have established the phenomenon. As one would expect, the electronic ordering is accompanied by fairly different M-X distances in the crystal.

We confirmed a_F = 5.45 Å for our sample of Pr_6O_{11}. However, a minor component corresponds to a_F = 5.39 Å and is probably PrO_2 (*cf.* Brauer and Pfeiffer [19]). Several authors [126] have expressed doubts as to whether Goldschmidt's C-Pr_2O_3 exists. Actually, as discussed in the experimental section, we reduced Pr_6O_{11} at low temperature with ethanol or octanol vapour and obtained yellow-tan materials being C-oxides with a_F = 5.57 Å. The previously reported values of this parameter are 5.570 Å [92] and 5.568 Å by Mazza and Iandelli [91] who also measured reflection spectra. Brauer and Pfeiffer [18] found complete miscibility between C-Pr_2O_3 (a_F = 5.576 Å) and C-Tb_2O_3 (a_F = 5.365 Å). However, it is highly probable that C-Pr_2O_3 is

thermodynamically unstable, relative to A-Pr_2O_3, even at room temperature.

Honig, Clifford and Faeth [43] pointed out that the distinct phases Pr_nO_{2n-2} (n = 4, 5, 6, 7, 9, 10, 11, 12) have been observed.

Terbium oxides TbO_x exist in a surprising number of distinct phases [5]. The C-type Tb_2O_3 has $a_F = 5.364$ Å. Tb_7O_{12} is a rhombohedral phase, closely related to fluorite with $a_F = 5.319$ Å and the rhombohedral unit cell having the volume $\frac{7}{4} a_F^3$ and systematically lacking one out of every seven oxygen atoms. When treated with oxygen, $Tb_{1.812}$ is obtained, presumably a triclinic structure $Tb_{16}O_{29}$, and again, on a powder diagram, the fluorite lines are very conspicuous, but are separated in narrow doublets or triplets, much in the same way as non-cubic perovskites. It is more difficult to approach TbO_2 than PrO_2; $TbO_{1.95}$ was reported [5] as a fluorite with $a_F = 5.220$ Å. Recently, Brauer and Pfeiffer [19] have succeeded in making stoichiometric TbO_2. This compound is dark red and not black as the intermediate phases. Chase [24] studied the mixed oxide Y_6UO_{12} containing U(VI); it is isostructural with Tb_7O_{12}. In this connection, it may be mentioned that Chang and Phillips [21] reported La_6WO_{12} ($2a_F = 11.18$ Å) and Sm_6WO_{12} ($2a_F = 10.80$ Å) as disordered pyrochlores.

We found, as expected, that purple $Tb_{0.001}Th_{0.999}O_2$ has a value of $a_F = 5.59$ Å which cannot be distinguished from that of ThO_2 made under the same conditions. As discussed in chapter 7, we believe that this material contains discrete Tb(IV)O_8 chromophores. Actually, Baker *et al.* [6] studied the electron spin resonance, finding a value for the gyromagnetic factor $g = 2.0146$ surprisingly different from that theoretically calculated for a free Tb^{+4} ion in the groundstate $^8S_{7/2}$ of the configuration $4f^7$, *viz.* 1.9889. The opposite sign of the deviation from the Schwinger value for the free electron is ascribed to effects of covalent bonding, which are more pronounced in the strongly oxidizing Tb(IV) than in the isoelectronic Gd(III) and Eu(II). Our black $Tb_{0.05}Th_{0.95}O_2$ and $Tb_{0.1}Th_{0.9}O_2$ have $a_F = 5.585$ and 5.57 Å, respectively. At higher terbium concentrations, some Tb(III) seems to be formed [68].

$Pr_{0.05}Th_{0.95}O_2$ was found to have $a_F = 5.59$ Å and $Pr_{0.1}Th_{0.9}O_2$ 5.57 Å. An attempt to make $Pr_2Th_4O_{11}$ by ignition of the co-precipitated hydroxides at 1000°C produced a black material with $a_F = 5.56$ Å. This must contain both Pr(III) and Pr(IV) since reduction produces a grey colour and $a_F = 5.595$ Å. Nd(III) is known to expand ThO_2 [68].

The pronounced stability of the ThO_2 lattice would not be predicted by somebody concentrating his attention on the vacancies surrounded by eight

oxygen atoms. WILLIS [130] has shown by neutron diffraction of ThO_2 and UO_2 that the oxygen atoms vibrate more strongly than the metal atoms, and as temperature rises (towards 1100°C), the oxygen atoms tend to be displaced towards these large interstitial holes (which have always been made responsible for the ionic conductance of doped ZrO_2 at higher temperature [93]). There is little doubt that disordered UO_{2+x} actually contain excess oxygen atoms at these very interstitial sites, and that O_9 clusters hence are formed. AURIVILLIUS and LUNDQVIST [4] showed that BiF_3 has the orthorhombic YF_3 structure whereas $BiO_{0.1}F_{2.8}$ is tysonite (LaF_3) which has recently been shown by MANSMANN [87] to contain very distorted chromophores La(III)F_{11} (or perhaps rather La(III)F_9, since two of the La-F distances are very long). Whereas BiOF and BiOCl are of the tetragonal PbFCl type [4] a cubic phase with a_F = 5.84 Å was found, which is cited [87] as $Bi_4O_2F_8$ having ten rather than eight anions in each fluorite unit cell. All our disordered fluorites have anion deficit rather than anion excess; but it is worth remembering that both alternatives are possible. We have not studied the mixed oxide-fluorides of compositions such as $LaO_{0.56}F_{1.88}$ [79], β-YOF [46] and $ThO_{1.6}F_{0.8}$ [28] which are fluorites, frequently with anion excess. Similar pure fluorides are known*, *e. g.* $NaCaCdYF_8$ [48] and hightemperature forms of $NaYF_4$ and $Na_5Y_9F_{32}$ [124]. One would expect such compounds to be more numerous, because the conditions for forming fluorites (and their superstructures and disordered phases) obviously are appropriate stoichiometry combined with sufficiently large ionic radii and oxidation states of the metallic atoms *relative* to the anions. This is also why only oxide and fluoride are normally found. Lanthanum(III) is one of the few central atoms which is nearly *too* large forming fluorites as can be seen from the persistence of A-La_2O_3. At this point, it is interesting that the 5f group dioxides PaO_2, UO_2, NpO_2, PuO_2, AmO_2 and CmO_2 are particularly stable, supporting Goldschmidt's ideas of "thorides".

Niobium(V) and tantalum(V) are too small to participate in disordered fluorites and favour pyrochlore formation. In the cases of $LaNbO_4$, $LaTaO_4$, $DyNbO_4$ and $DyTaO_4$, monoclinic fergusonites containing isolated groups Nb(V)O_4 and Ta(V)O_4 are even formed [107a]. Smaller quadrivalent metals such as Tc(IV) [92b], Ru(IV) and Ir(IV) [92a] form pyrochlores $A_2B_2O_7$ with the lanthanides. On the other hand, protactinium(V) is the only quinquevalent metal to form disordered fluorites. KELLER [77a] described $M_{0.5}Pa_{0.5}O_2$ of fifteen rare earths, having a_F ranging from 5.525 Å for M = La

* Thus, ZINTL and UDGÅRD [134] reported miscibilities extending approximately to YCa_2F_7, $LaSr_2F_7$ and $ThCa_3F_{10}$.

to 5.322 Å for M = Lu (and 5.257 Å for M = Sc). The value of a_F^* of eq. (1) thus obtained is 5.325 Å for Pa(V) somewhat smaller than the observed value 5.505 Å for PaO_2. KELLER [77a] also found a considerable miscibility with M_2O_3, arriving *e. g.* at $a_F = 5.53$ Å for $Nd_{0.75}Pa_{0.25}O_{1.87}$.

7. Optical Electronegativity of Praseodymium(IV) and Terbium(IV)

Most intense absorption bands of d group complexes can be ascribed to electron transfer from filled molecular orbitals (M. O.) mainly localized on the ligands to the empty or partly filled d shell [57, 60, 63, 72]. „Inverted" electron transfer from the partly or completely filled d shell to low-lying, empty M. O. on the ligands is only common when the ligands are conjugated, carbon-containing molecules [129, 59, 67]. Electron transfer spectra caused by the transfer of electrons from filled M. O. to the 4f shell were difficult to observe, but were identified in solutions of bromide and dialkyldithiocarbamate complexes in ethanol [58] and in aqueous sulphate and ethanolic chloride solutions [7]. It is possible to define [60] *optical electronegativities* x_{opt} for the central atom M and the ligand X, where the values for X:

$$F^- \ 3.9 \qquad H_2O \ 3.5 \qquad SO_4^{--} \ 3.2 \qquad Cl^- \ 3.0 \qquad Br^- \ 2.8 \qquad I^- \ 2.5 \tag{2}$$

agree with the values normally accepted on Pauling's scale, and where the central atom values for x_{opt} are corrected for spin-pairing energy in the partly filled shell. However, for our purposes, it is more convenient to consider the uncorrected electronegativities x_{uncorr} for the central atom, which are defined from the wavenumber σ of the first electron transfer band:

$$\sigma = \left[x_{opt}(X) - x_{uncorr}(M)\right] \cdot 30000 \text{ cm}^{-1} \tag{3}$$

Table 3 gives the values obtained for trivalent lanthanides.

The octahedral hexachloride and hexabromide complexes MX_6^{-3}, which are only stable in solvents such as acetonitrile [111] give values for x_{uncorr} some 0.1 to 0.2 units higher. This may be ascribed to the smaller M-X distances for $N = 6$, which seem to be further decreased in such solvents [61] besides the grouptheoretical fact that the highest filled M. O. in octahedral hexahalides have four angular node-planes (like g-orbitals) and are destabilized by ligand-ligand anti-bonding effects. Similar effects were found in the 5f by RYAN and one of the writers [110] studying U(IV), Np(IV) and Pu(IV) hexahalides. In aqueous solution, x_{uncorr} is somewhat smaller; and in

TABLE 3.

Uncorrected optical electronegativities $x_{uncorr}(M)$ for trivalent lanthanides.

Electron configuration	Sm(III) $4f^5$	Eu(III) $4f^6$	Tm(III) $4f^{12}$	Yb(III) $4f^{13}$	Ref.
MCl^{++} in ethanol	1.48	1.79	—	1.63	7
MCl_6^{-3}	1.56	1.89	—	1.78	111
MBr^{++} in ethanol	1.46	1.76	1.32	1.62	58
MBr_6^{-3}	1.63	1.98	1.51	1.83	111
MSO_4^{+} in water.....	1.60	1.81	—	1.72	7
$M(H_2O)_9^{+3}$	—	1.73	—	~1.53	65

uranyl complexes the situation is rather extreme [71]. In such anisotropic complexes, the ligands in the equatorial plane of UO_2X_4 or UO_2X_6 have so large distances U-X that the apparent x_{uncorr} of U(VI) seems to be 1.8. The analogous anisotropic neptunyl complexes indicate 2.1 for Np(VI). These values can be compared with $x_{uncorr} = 2.6$ for Np(VI) in NpF_6 [121] and 2.85 for Pu(VI) in PuF_6 [120]. It is possible to extrapolate $x_{uncorr} = 2.3$ for U(VI) in UF_6, though this means that this compound should have no electron transfer band before 48000 cm^{-1} [71, 75a].

It is now known from the spectra of $CeCl_6^{--}$ and $CeBr_6^{--}$ [111] that $x_{uncorr} = 2.1$–2.15 for Ce(IV). Previously, we measured the spectrum of the tetrakis-acetylacetonate Ce aca_4. This redbrown complex is chemically very unstable [51] but its crystal structure has recently been determined [90]. We find a shoulder at 21000 cm^{-1} ($\varepsilon \sim 700$) in the absorption spectrum. Since the ligand aca^- is known [59] to have $x_{opt} = 2.7$, this suggests $x_{uncorr} = 2.0$ for Ce(IV) in the chromophore $Ce(IV)O_8$.

Oxide is nearly the only ligand for which it has not been possible to establish a well-defined x_{opt} [60]. In the d group complexes, the main reason is the very strong π-anti-bonding effect on the partly filled d shell. This effect should be of minor importance in the 4f and 5f groups; but it is difficult to establish the value in a highly anisotropic complex such as UO_2^{++}. If $x_{uncorr} = 2.3$ for U(VI), $x_{opt} = 3.1$ for O^{--}. A more direct determination comes from Eu(III) in Y_2O_3 having an electron transfer band [12a, 22, 70] near 41000 cm^{-1}. Since most other Eu(III) compounds show $x_{uncorr} = 1.8$, this would mean $x_{opt} = 3.15$ for O^{--}. This value can be expected to vary with the circumstances; thus, the maximum in the excitation spectrum [108] of fluorescence of Eu(III) has lower wavenumbers in Gd_2O_3 (38600 cm^{-1}) and La_2O_3 (33600 cm^{-1}) suggesting $x_{opt} = 3.1$ and 3.0, respectively. Cf. also the recent studies by BLASSE and BRIL [12b].

The variation of x_{uncorr} as a function of the number q of electrons in the partly filled shell $4f^q$ is explained by a theory [58] taking into account the variation $-q(E\text{-}A)$ of the relative one-electron energies, as well as the spin-pairing energy contributing to the electron transfer $4f^q \rightarrow (\text{M. O.})^{-1}4f^{q+1}$:

$$\left.\begin{aligned} 0 < q \leqq 6\text{:}\ & -8q\,D/13 \\ 13 > q \geqq 7\text{:}\ & (8\,D) - 8q\,D/13 \end{aligned}\right\} \quad (4)$$

where the spin-pairing energy parameter D corresponds to $(9E^1/8)$ in terms of RACAH's parameters of interelectronic repulsion [104]. To this approximation, equ. (4) represents two parallel line segments jumping $8D$ at the half-filled shell $4f^7$. If other effects of interelectronic repulsion and first-order relativistic effects (spin-orbit coupling) are included [58, 110] the result is a decrease of the wavenumbers of the first electron transfer band from f^0 to f^2, a roughly invariant wavenumber f^2 to f^4, a decrease from f^4 to f^6, a steep increase from f^6 to f^7, and the zigzag curve is essentially repeated in the second half, f^{7+k} being comparable to f^k. The relative order of x_{uncorr} found for trivalent lanthanides agrees with this theory $f^6 > f^{13} > f^5 > f^{12} > \ldots$ BARNES and PINCOTT [9] have recently pointed out that the difference between Eu(III) and Yb(III) complexes varies to some extent in solids. This difference is according to our theory [58, 110]:

$$\sigma_{\text{Yb(III)}} - \sigma_{\text{Eu(III)}} = -7(E\text{-}A) + \tfrac{48}{13}D + \tfrac{3}{2}\,\zeta_{4f}\,(\text{Yb}) - 2\zeta_{4f}\,(\text{Eu}). \quad (5)$$

The observed value is roughly 5800 cm^{-1} for the aqua ions [65] and 4000 cm^{-1} for most complexes in solution. In the cyclopentadienides [97] $M(C_5H_5)_3$ it is only -500 cm^{-1}. Since D is a parameter of interelectronic repulsion, and since we know from the nephelauxetic effect to be discussed in chapter 8 that such parameters vary less than 6 percent in complexes, we can maintain a nearly constant value of $D = 6500$ cm^{-1} and ascribe the observed variation of equ. (5) to the (theoretically not very accessible) quantity $(E\text{-}A)$ increasing from 2800 cm^{-1} for the aqua ions to 3700 cm^{-1} for the cyclopentadienides. For comparison, it may be mentioned that $(E\text{-}A) = 6000$ cm^{-1} for 4d and 5d group hexahalide complexes [60, 72].

The wavenumber difference between the $4f^7$-system Tb(IV) and the 4f-system Pr(IV) should be

$$\sigma_{\text{Tb(IV)}} - \sigma_{\text{Pr(IV)}} = -6(E\text{-}A) + \tfrac{56}{13}\,D + 9E^3 - \tfrac{3}{2}\,\zeta_{4f}\,(\text{Tb}) + \zeta_{4f}\,(\text{Pr}). \quad (6)$$

Figure 1 shows the reflection spectra of very dilute solid solutions of Pr(IV) (having a pronounced shoulder at 18500 cm^{-1} and a maximum at 24300 cm^{-1})

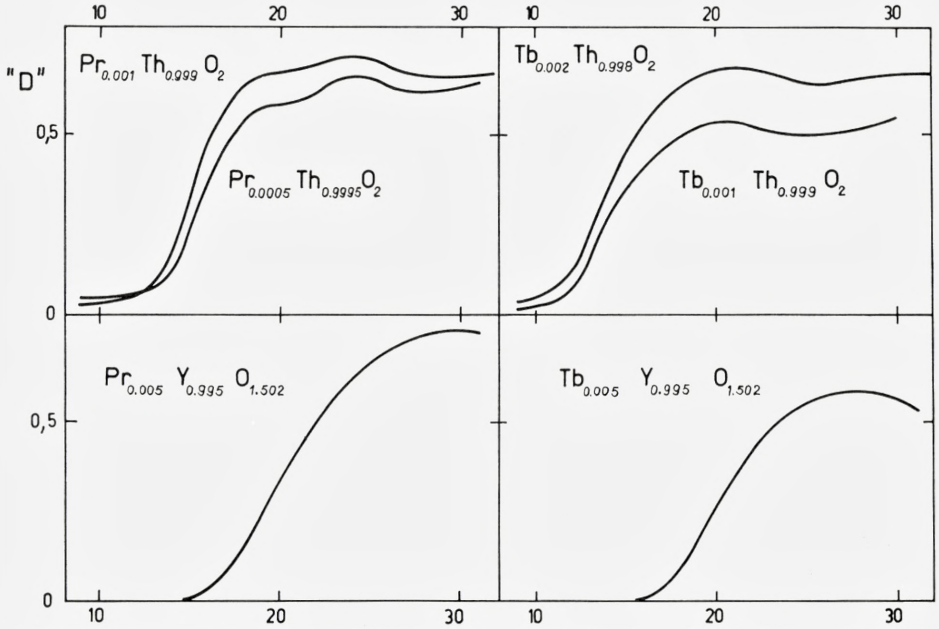

Figure 1. Reflection spectra of thorium and yttrium oxides containing minute amounts of praseodymium (IV) and terbium (IV). The optical density "D" = $\log_{10}(I_0/I)$ refers to the white reference material producing the light intensity I_0 and the compound I, and is given as a function of the wavenumber in the unit 1000 cm^{-1}.

and Tb(IV) in ThO_2 (band at 20300 cm^{-1}). The wavenumber difference of equ. (6) is 1800 cm^{-1}. It is not certain what are exactly the size of the parameters of spherical symmetry in quadrivalent as in trivalent lanthanides. At one side, it is nearly certain that gaseous M^{+4} would have D and Racah's E^3 some 20 % larger than M^{+3}, but on the other hand, the nephelauxetic effect [110] is expected to be more pronounced in M(IV) than in M(III). Reasonable values seem to be D = 7500 cm^{-1} and E^3 = 670 cm^{-1}. Hence, $(E\text{-}A)$ = 5700 cm^{-1}.

If x_{opt} = 3.2 for oxide in ThO_2, x_{uncorr} turns out to be *2.6 for Pr(IV)* and *2.55 for Tb(IV)*. Hence, one would expect Ce(IV) to have the first electron transfer band at 35000 cm^{-1} (x_{uncorr} = 2.05) quite in agreement with the very pale, lemon-yellow colour of pure CeO_2. Our results are also compatible with the only other evidence available for quadrivalent lanthanides. Professors L. B. Asprey and R. Hoppe were so kind as to inform one of the writers that Cs_3NdF_7 and Cs_3DyF_7 are orange compounds [2] both having

electron transfer bands at 26000 cm^{-1}, *i. e.* $x_{uncorr} = 3.05$. Our theory gives

$$\sigma_{Dy(IV)} - \sigma_{Nd(IV)} = -6(E\text{-}A) + \tfrac{56}{13} D + 3E^3 - \zeta_{4f}(Dy) + \tfrac{1}{2} \zeta_{4f}(Nd) \qquad (7)$$

which is -1500 cm^{-1} with our parameters, in satisfactory agreement with experience. A corollary of this result is that if Nd(IV) or Dy(IV) could be prepared in ThO_2, the first electron transfer band would occur already about 5000 cm^{-1}. This suggests that these two species cannot be prepared; though there is no absolute rule for how small a wavenumber the first electron transfer band can have in a stable species, there is not at present known any case below 9350 cm^{-1} in OsI_6^{--} [64].

The absorption bands of the oxides on Figure 1 are relatively broad. Pr(IV) shows two transitions having the distance 5800 cm^{-1} which is quite intelligible because the excited configuration (M. O.)$^{-1}4f^2$ have many adjacent energy levels. The situation is different in $4f^6$ systems such as Eu(III) or $4f^{13}$ systems such as Yb(III), where the two or three absorption bands observed [58, 97] must correspond to M. O. of differing energy.

We have disproved the hypothesis that the strong colours in ThO_2 necessarily indicate mixed oxidation states Pr(III, IV) and Tb(III, IV). The coherent description by the theory makes it highly probable that the colours are caused by monomeric $Pr(IV)O_8$ and $Tb(IV)O_8$ chromophores, and anyhow, one would have predicted the band positions observed. This does not exclude, of course, that genuine mixed-oxidation state colours are observed in CeO_x and $Ce_xU_{1-x}O_2$. It is not quite clear whether the dark blue colour in the second case is induced by the presence of Ce(III, IV) [simultaneously with U(IV, V)] or due to actual electron transfer from U(IV) to Ce(IV) comparable to the electron transfer from Ag(I) and Tl(I) to species such as $OsCl_6^{--}$ and $IrCl_6^{--}$ [63]. The prussian blue type compounds such as $K[Fe^{II}(CN)_6Fe^{III}]$ are electronically ordered according to Robin [107] (*cf.* also Shriver [117] and Braterman [13a]). Anderson [1] discussed the interesting question whether the many distinct phases in the systems CeO_x, PrO_x and TbO_x when brought to equilibrium at an appropriately low temperature, in contrast to the disordered fluorite structure of many mixed oxides containing tri- and quadrivalent metals, is not due to the fact that in the former cases, the complicated ordering is accompanied by electronic ordering of the same element, whereas in the second case, the metal atoms need to interchange their positions by diffusion; and it is known that this diffusion (as contrasted to that of oxide ions in deficient structures) needs a very high activation energy. Cf. also the review by Brauer [19a].

We discussed above the somewhat varying colours of Pr(IV) and Tb(IV) in different oxides. The pink to chamois colour of Pr(IV) in CeO_2 corresponds, according to preliminary measurements, to an almost linear increase of the optical density (as a function of wavelength) between 15000 and 18000 cm^{-1} with a very broad shoulder at 20500 cm^{-1}, and a strong cut-off of the CeO_2 matrix above 28000 cm^{-1}. Figure 1 gives the reflection spectra of the orange $Pr_{0.005}Y_{0.995}O_{1.502}$ having a weakly pronounced shoulder at 21300 cm^{-1} and a broad maximum at 29800 cm^{-1}, and of the orange $Tb_{0.005}Y_{0.995}O_{1.502}$ having a broad band at 27400 cm^{-1}. Hence, Y_2O_3 seems to be less reducing than ThO_2. If the values of $x_{uncorr} = 2.6$ for Pr(IV) and 2.55 for Tb(IV) are maintained, the first band of each sample indicate $x_{opt} = 3.3$ and 3.45, respectively, for the oxide ligands. It might seem more consistent to retain $x_{opt} = 3.2$ for oxide found from the absorption spectrum of Eu(III) in Y_2O_3 and if the main maxima are then considered, x_{uncorr} would be 2.2 for Pr(IV) and 2.3 for Tb(IV). However, this choice does not seem to be realistic. The low value for Pr(IV) would not interpolate satisfactorily between the values for Ce(IV) and Nd(IV) discussed above. Actually, one of the difficulties with these very broad absorption bands (which is accentuated in reflection spectra, relative to transmission spectra of liquid solutions) is that the position of the first electronic transition is not easily detected. The low symmetry of the two sites in Y_2O_3 may contribute to a superposition of closely adjacent bands.

It would be interesting to compare the spectra of dilute solutions of Pu(IV), Am(IV), Cm(IV), Bk(IV) and Cf(IV) in ThO_2, though, in the case of the highly radioactive isotopes, one would have to be careful with colour centres induced by radiation damage. Our results once more stress the profound difference between the 4f and the 5f groups [26, 40, 71, 77]. The values 2.6 and 2.55 found for x_{uncorr} of Pr(IV) and Tb(IV) can be compared to the values 0.9 and 0.4 extrapolated [58] for the isoelectronic species Ce(III) and Gd(III) or to 1.1 and 0.8 for the lower oxidation states Pr(III) and Tb(III) of the same elements. In other words, x_{uncorr} increases more [71] than 1.5 unit when going from M(III) to M(IV) in the 4f group. On the other hand, the values (found for hexahalide complexes) Np(VI) 2.6; Pu(VI) 2.85; Np(IV) 1.9; and Pu(IV) 2.1 indicate half the effect when going from M(IV) to M(VI) in the 5f group, changing the oxidation numbers by two units. In the 4d and 5d groups, the variation of the optical electronegativities as a function of the oxidation state is roughly the same as in the 5f group. This variation, and related problems are discussed in a recent review [75a].

8. Internal f Transitions; the Nephelauxetic Effect and Intensities

Whereas the transitions 4f → 5d correspond to rather broad and electron transfer (filled M. O.) → 4f to even broader absorption bands, the internal transitions in the configuration $4f^q$ correspond to groups of very narrow bands or absorption lines. Each such group normally represents one excited J-level of the corresponding gaseous ion M^{+3} in spherical symmetry, and the finestructure of the groups has been studied very extensively [54, 77, 132]. Originally, ligand field theory was applied in the form of BETHE's electrostatic model [41] but an alternative is the angular overlap model considering weak σ- and π-anti-bonding effects on the partly filled d or f shell [66, 74, 116].

However, there is another experimental fact about the 4f group compounds M(III) which has attracted relatively less attention. The *nephelauxetic effect* (the "cloud-expanding" effect according to a Greek word kindly suggested by Professor K. BARR) that the parameters of interelectronic repulsion are smaller in complexes than in the corresponding gaseous ions is quite conspicuous in the 3d, 4d and 5d groups [114, 62, 76]. In the 4f group, the nephelauxetic effect has been recognized early as a shift of the narrow absorption bands towards smaller wavenumbers in the relatively more covalent compounds, the least covalent being the fluorides and the aqua ions. WAEGNER [125] noted that the line groups of blue Nd_2O_3 have slightly lower wavenumbers than other pink Nd(III) compounds, and JOYE [52] made similar observations on Nd_2S_3 and anhydrous $NdCl_3$. HOFMANN and KIRMREUTHER [42] found a red-shift in Er_2O_3 compared to other Er(III) compounds and invoked Stark's valency hypothesis assuming loosened ("gelockertes") valency electrons (this remark was made three years before N. BOHR's explanation of the hydrogen spectrum). EPHRAIM and BLOCH [29] made more systematic studies of the red-shift in Pr(III) and Nd(III) compounds and established the variation $F^- > H_2O > Cl^- > Br^- > I^-$. These authors suggested that the electronic orbits are contracted in highly electrovalent salts and expanded in covalent compounds. They suggested electron jumps between orbits of different radii, whereas we consider energy differences due to differing interelectronic repulsion, the groundstate having the lowest average value of the reciprocal interelectronic distance $\langle 1/r_{12} \rangle$; the excited levels of $4f^q$ have essentially the same average radius $\langle r \rangle$ of the partly filled shell as the groundstate. We can only retain the second half of EPHRAIM and BLOCH's explanation, *viz.* the expansion, though it was first in 1965 SUGAR [122] reported the energy levels belonging to $4f^2$ of gaseous Pr^{+3} showing that even the Pr(III) aqua ion has a red-shift amounting to

some 4 percent. That the expansion is relatively the most pronounced in compounds of the most reducing anions is quite expected; but EPHRAIM [30] found that Pr_2O_3 is unexpectedly covalent on this basis, even more than anhydrous PrI_3. Similar effects have been found in d group compounds such as Cr_2O_3 [115] and in 4f group oxides studied by BOULANGER [13] and us [68, 70]. This is particularly striking when compared to the less pronounced nephelauxetic effect of oxygen-containing ligands in aqueous solution [13, 56]. On the other hand, solid sulphides, which are expected to be even more covalent, only show a nephelauxetic effect slightly stronger than the oxides [73]. EPHRAIM, JANTSCH and ZAPATA [31] noted that most Er(III) compounds show far weaker red-shifts than the analogous Pr(III), Nd(III) and Sm(III) compounds, and in a few cases, small blue-shifts are actually observed [56]. This anomaly can be explained by the term $d\sigma$ in equ. (8). Today, there is no doubt that the nephelauxetic effect occurs for all the lanthanides, though it is more pronounced in the beginning of the 4f group than for the later members such as Ho(III), Er(III) and Tm(III).

We proposed a linear relation [68, 70]:

$$\sigma_{\text{compound}} - \sigma_{\text{aqua}} = d\sigma - (d\beta)\sigma_{\text{aqua}} \qquad (8)$$

where the difference between the wavenumbers of the baricenters (ideally of the sub-levels weighted with their degeneracy number; in actual practice frequently, the centers of intensity distribution) of the J-levels of the compound considered and of the aqua ions (which have now been studied in $M(H_2O)_9(C_2H_5SO_4)_3$ at liquid helium temperature) is equalled the relative stabilization $d\sigma$ of the ground J-level of the compound (again compared with the lowest sub-level of the aqua ion) minus the relative nephelauxetic effect $(d\beta)\sigma_{\text{aqua}}$. There are several reasons why the linear relation (8) is not absolutely valid*. A closer analysis [119] of the wavenumber differences

* Recently, CHANG [23a] determined the actual positions of the baricenters of eighteen J-levels of Nd(III) in Y_2O_3. When compared with the baricenters of $Nd(H_2O)_9^{+3}$ [36a], $d\beta = 2.4\,\%$ is obtained. By the same token, KISLIUK, KRUPKE and GRUBER [78] determined sixteen J-baricenters for Er(III) in Y_2O_3. When compared to $Er(H_2O)_9^{+3}$, $d\beta$ turns out to be $0.9\,\%$. These two values are somewhat smaller than the parameters of equ. 8 ($d\beta = 3.2\,\%$ and $d\sigma = 150\ cm^{-1}$ for C-type $Nd_{0.2}Yb_{0.8}O_{1.5}$; $d\beta = 1.6\,\%$ and $d\sigma = 200\ cm^{-1}$ for Er_2O_3 [70]). This discrepancy is mainly caused by the negligible variation of the Landé parameter ζ_{4f} (the decrease relative to the aqua ions is $0.3\,\%$ for Nd(III) in Y_2O_3) whereas the parameters of interelectronic repulsion E^1 and E^3 decrease 4.4 and $3.1\,\%$, respectively. The absolute values of $d\sigma$ would be calculated from the baricenters (276–210) = $66\ cm^{-1}$ for Nd(III) and (203–147) = $56\ cm^{-1}$ for Er(III). The differences between these quantities and the values for $d\sigma$ previously determined have the same order of magnitude as $\frac{7}{2}\,\zeta_{4f}(Nd)$ $d\beta = 100\ cm^{-1}$ and $3\,\zeta_{4f}(Er)$ $d\beta = 150\ cm^{-1}$ which would represent the first-order effect of the Landé parameter not being influenced by the nephelauxetic effect.

It is excluded that the variable extent of the shift of the excited levels is caused by dispersion

between gaseous Pr^{+3} and Pr(III) in $LaCl_3$ shows that the parameters of interelectronic repulsion, and in particular Racah's E^3, are decreased more than twice as much than the Landé parameter ζ_{4f}. If the nephelauxetic effect was due to delocalization of weakly anti-bonding M. O. [66] one would expect E^k to decrease twice as much as ζ_{4f}. Empirically, one finds that certain levels, such as $^5D_0$ and $^5D_1$ of Eu(III), or $^2H_{11/2}$ of Nd(III) and Er(III), move much less than predicted by equ. (8) for the value of $d\beta$ satisfactorily describing the red-shift of most of the other band groups.

Barnes [8] performed a statistical analysis of the validity of equ. (8) and concluded that it was not possible to ascribe physical significance to the parameter $d\sigma$ obtained, and that only in the case of a few oxides (Nd_2O_3 $d\beta = 3.4 \pm 1.3\,\%$, Er_2O_3 $d\beta = 1.4 \pm 0.6\,\%$) it is possible to assign positive values of $d\beta$ at the confidence level 0.95. We do not agree that this statistical analysis indicates all the relevant aspects. If one draws best straight lines according to equ. (8) at two different occasions through the same set of experimental data, one normally has a scattering of 50 cm^{-1} in $d\sigma$ and 0.2 % in $d\beta$. It may be that the confidence level 0.95 does not represent this feature well, and in particular, the scattering of the "misbehaving" points may not at all correspond to a Gaussian error-curve. In the extreme case of half of the points being on a straight line and half being widely scattered, one would recognize the straight line very readily with a transparent rule. However, it is of course worthwhile to devote some statistical analysis to such problems.

Dr. Romano Pappalardo took spectra at liquid nitrogen temperature (or more exactly, at 100° K) of our $M_{0.2}Zr_{0.8}O_{1.9}$ under conditions similar to those previously used [68]. Surprisingly enough, these highly compressed lattices generally show a less pronounced nephelauxetic effect than the oxides M_2O_3. In order to obtain a more reliable comparison, we plotted $\sigma_{\text{mixed oxide}} - \sigma_{\text{oxide}}$ according to equ. (8) and obtained the values of $d\sigma$ and $d\beta$ (relative to aqua ions) given in Table 4. A list of baricenters of Nd(III), Ho(III), Er(III) and Tm(III) compounds are given in Table 5.

It had previously been noted [70] that pyrochlores $MTiO_{3.5}$ had a less pronounced nephelauxetic effect than our disordered fluorites $MZrO_{3.5}$. If it is argued that the extraordinary large nephelauxetic effect of oxides is mainly connected with short M-O distances [66], this phenomenon can be rationalized. One would expect four types of M sites in our mixed oxides:

effects dependent on the transition dipole moments. However, the experimental fact that the nephelauxetic effect is more pronounced for transitions in the visible than in the infra-red might be connected with second-order perturbations from continuum levels at high wavenumbers, though a more predominant factor seems to be the importance of the rather invariant Landé parameter for transitions in the infra-red.

cubic $M(III)O_8$; $M(III)O_7$ adjacent to one vacancy; $M(III)O_6$ lacking a face-diagonal like in the C-oxides; and $M(III)O_6$ lacking a body-diagonal. Of these sites, the first and the last have centres of inversion. The importance of this situation was not realized until quite recently, when octahedral MX_6^{-3} were prepared [111] and when KISLIUK, KRUPKE and GRUBER [78] after a careful study of Er(III) in Y_2O_3 were not able to detect any absorption lines originating in that quarter of the erbium atoms being on sites possessing a centre of symmetry. (However, the corresponding weak vibronic structures have recently been reported [36c]). Though the grain size of the sample and the experimental apparatus used in ref. [70] do not allow an absolute comparison of band intensities, one has the definite impression that the pyrochlores containing $M(III)O_8$ with centre of inversion have far weaker intensities than the disordered fluorites presumably containing a fair proportion of $M(III)O_7$. The reflection spectrum of the low-temperature form of $LaYbO_3$ [70] is very similar to that of C-Yb_2O_3 suggesting that the local symmetry of the sites is the same $M(III)O_6$ lacking a face-diagonal. The detailed structure of each *J*-group is also strikingly similar in $LaErO_3$ and a fairly compressed C-oxide such as $ErInO_3$.

A marked difference between cubic $M(III)O_8$ and the C-oxide site is the behaviour of the level $^7F_1$ observed in fluorescence $^5D_0 \rightarrow {}^7F_1$ of Eu(III). In ThO_2 [68], this level is not split, in accordance with the group-theoretical prediction for O_h, whereas in Y_2O_3 [23, 128] three sub-levels are observed 199, 359 and 543 cm^{-1} above the groundstate $^7F_0$. Our $Eu_{0.2}Zr_{0.8}O_{1.9}$ fluoresced with red line emission. The strongest line (measured both at 4°K and 78°K by Dr. Romano Pappalardo) occurs at 16930 cm^{-1} surrounded by weaker shoulders at 16875 and 17000 cm^{-1}. Since the $^5D_0 \rightarrow {}^7F_0$ transition is observed as a very weak line at 17260 cm^{-1}, this corresponds to three different $^7F_1$ sub-levels at 260, 330 and 385 cm^{-1}. Since the $^7F_1$ level occurs at 320 cm^{-1} in $Eu_{0.14}Th_{0.86}O_{1.93}$ [68], the 330 cm^{-1} sub-level may very well correspond to an essentially cubic $Eu(III)O_8$ site in $Eu_{0.2}Zr_{0.8}O_{1.9}$ whereas the 260 and 385 cm^{-1} sub-levels, showing a smaller spreading than Eu(III) in Y_2O_3, corresponds to $Eu(III)O_7$ involving only one vacancy. It is not understood why $^7F_0$ and $^7F_1$ have a so relatively small energy difference in cubic crystals, whereas it is 380 cm^{-1} for $Eu(H_2O)_9^{+3}$ and Eu(III) in $LaCl_3$. Our sample of $Eu_{0.2}Zr_{0.8}O_{1.9}$ shows weaker fluorescence lines at 16530 and 16370 cm^{-1}, corresponding to $^7F_2$ sub-levels at 730 and 890 cm^{-1}. This may be compared to the sub-level of symmetry type Γ_5 identified [68] at 890 cm^{-1} in ThO_2. LINARES [85a] recently identified several sites for fluorescent Eu(III) in partly charge-compensated CeO_2 and ThO_2.

The reflection spectrum of $Yb_{0.2}Zr_{0.8}O_{1.9}$ shows bands at 10300, 10360 and 10480 cm^{-1}, a shoulder about 10700 cm^{-1} and a broad asymmetric maximum at 10990 cm^{-1}. Hence, the local symmetry deviates more from cubic than $Yb_{0.5}Zr_{0.5}O_{1.75}$ [70] having a relatively narrow band at 10280 cm^{-1} and a very broad band at 10940 cm^{-1}. With regard to band positions (though not to intensities), $Yb_{0.2}Zr_{0.8}O_{1.9}$ shows certain analogies with the pyrochlore $Yb_{0.5}Ti_{0.5}O_{1.75}$ [Figure 5 of ref. 70] containing chromophores $Yb(III)O_8$ compressed along a body-diagonal but retaining a centre of inversion. According to the principle of holohedrized symmetry in the angular overlap model [116] one would expect the sub-level energy differences to have a certain similarity with those of $Yb(III)O_7$.

As discussed in chapter 1, the internuclear distances are re-distributed in pyrochlores such as $ErTiO_{3.5}$ [80] in such a way that the six Ti-O distances are much shorter than six of the eight Er-O distances, the two remaining Er-O distances being adapted to the cubic lattice parameter. In disordered fluorites such as $M_{0.2}Zr_{0.8}O_{1.9}$ or $M_{0.5}Zr_{0.5}O_{1.75}$, one might have expected that the decreasing values of a_F by introducing the small Zr(IV) would decrease the distance M-O and increase the nephelauxetic parameter $d\beta$. However, it is quite conceivable that the $M(III)O_7$ chromophores mainly responsible for the band intensities observed have longer M-O distances on the average than the Zr-O distances. $ErCl_6^{-3}$ has $d\beta = 1.2\,\%$ [111] which is larger than $0.9\,\%$ found for Er(III) in the six-coordinated YCl_3 [105] and $0.3\,\%$ characterizing Er(III) in nine-coordinated $LaCl_3$ with much larger Er-Cl distances. Hence, one would expect that one of the rare cases where $M(III)O_6$ would show a more pronounced nephelauxetic effect than in C-oxides might be the octahedral site of perovskites (*cf.* Tables 4 and 5). This has not been satisfactorily detected until now; one reason may again be the comparatively low band intensities.

The concept of hypersensitive pseudoquadrupolar transitions [69] has been much discussed recently. It is beyond any doubt that those transitions (characterized by the selection rules $J \to J - 2$ and in Russell-Saunders coupling $L \to L - 2$ and $S \to S$) which would be relatively strong as electric quadrupole transitions are very sensitive to the nature of the adjacent ligands and frequently get very high intensities. In Judd's parametrization [53] this corresponds to large matrix elements of the operator $U^{(2)}$, and the phenomenon was further studied by Carnall, Fields and Wybourne [20] and Krupke and Gruber [81]. Recently, Judd [55] and Nieuwpoort and Blasse [95] discussed the influence of linear ligand-field contributions which are group-theoretically acceptable in low symmetries such as C_s,C_n and C_{nv}

TABLE 4.

Nephelauxetic parameters from eq.(8) for mixed oxides and for various halide complexes.

	$d\sigma$ (cm^{-1})	$d\beta$ (%)	Ref.
Nd(III)$LaCl_3$	−60	0.6	70
$NdCl_6^{-3}$	+50	2.2	111
Nd_2O_3 (type A)	+200	3.6	70
$Nd_{0.1}La_{0.9}O_{1.5}$(A)	+200	3.4	70
$NdYO_3$	+250	3.5	70
$Nd_{0.2}Yb_{0.8}O_{1.5}$(C)	+150	3.2	70
$Nd_{0.1}Ce_{0.9}O_{1.95}$(F)	+300	3.7	70
$Nd_{0.14}Th_{0.86}O_{1.93}$(F)	+150	3.3	68
$Nd_{0.5}Zr_{0.5}O_{1.75}$(F)	+250	2.7	70
$Nd_{0.2}Zr_{0.8}O_{1.75}$(F)	+100	1.6	—
$BaNd_2S_4$	+250	4.2	73
Sm_2O_3 (type B)	+200	2.3	70
$Sm_{0.5}Zr_{0.5}O_{1.75}$(F)	+350	2.0	70
$Sm_{0.2}Zr_{0.8}O_{1.9}$(F)	+200	1.5	—
Dy_2O_3(C)	+500	1.8	70
$Dy_{0.5}Zr_{0.5}O_{1.75}$(F)	+500	2.0	70
$Dy_{0.2}Zr_{0.8}O_{1.9}$(F)	+500	1.9	70
$HoCl_6^{-3}$	+150	1.1	111
Ho_2O_3(C)	+450	2.5	70
$Ho_{0.5}Zr_{0.5}O_{1.75}$(F)	+500	2.3	70
$Ho_{0.2}Zr_{0.8}O_{1.9}$(F)	+450	2.0	—
Er(III)$LaCl_3$	−30	0.3	70
Er(III)YCl_3	0	0.9	105
$ErCl_6^{-3}$	+100	1.2	111
Er_2O_3(C)	+200	1.6	70
$Er_{0.5}Ti_{0.5}O_{1.75}$(P)	+250	1.3	70
$Er_{0.8}Zr_{0.2}O_{1.6}$(C)	+200	1.6	70
$Er_{0.5}Zr_{0.5}O_{1.75}$(F)	+300	1.7	70
$Er_{0.2}Zr_{0.8}O_{1.9}$(F)	+250	1.1	—
$LaErO_3$	+250	1.9	70
$La_{0.45}Er_{0.55}O_{1.5}$ (perovskite)	+200	1.7	—
$La_{0.2}Er_{0.3}Zr_{0.5}O_{1.75}$(F)	+250	1.6	—
$TmCl_6^{-3}$	+100	1.3	111
Tm_2O_3(C)	+300	1.5	—
$Tm_{0.2}Zr_{0.8}O_{1.9}$(F)	+350	1.1	—
$LaTmO_3$ (perovskite)	+350	1.7	—

but previously were rejected with (invalid) arguments about energy minima for the position of the central atom. However, we feel that a somewhat more chemical explanation may be more appropriate. Our reasons are that

TABLE 5.

Baricenters of excited J-levels evaluated from the reflection spectra of mixed oxides measured at 100° K. The absolute baricenters are known from aqua ions in salts such as $M(H_2O)_9(C_2H_5SO_4)_3$.

	$Nd(H_2O)_9^{+3}$	Nd_2O_3(A)	Nd(III)Y_2O_3[23a]	$Nd_{0.2}Zr_{0.8}O_{1.9}$
$^4I_{15/2}$	(5880)	5950	6160	5800
$^4F_{3/2}$	11580	11190	11300	11420
$^4F_{5/2}$	12620	12270	12300	12420
$^4F_{7/2}$	13580	13250	13350	13420
$^4F_{9/2}$	14840	14470	14630	14770
$^2H_{11/2}$	16030	15770	15840	—
$^4G_{5/2}$	17330	16720	16970	17150
$^4G_{7/2}$	19180	18600	18640	18940
$^4G_{9/2}$	19630	19170	19330	19530
$^2P_{1/2}$	23400	22840	22910	23150
	$Ho(H_2O)_9^{+3}$	Ho_2O_3(C)	$Ho_{0.2}Zr_{0.8}O_{1.9}$	
$^5I_7$	5030	5230	5260	
$^5I_6$	8530	8800	8850	
$^5I_5$	11140	11340	11380	
$^5F_5$	15420	15500	15650	
$^5S_2, ^5F_4$	18450	18550	18640	
$^5F_3$	20560	20530	20640	
$^3K_6, ^5F_1$	22250	22220	22270	
$^5G_5$	24030	23920	23980	
$^5G_4, ^3K_7$	26100	25970	26040	
$^5G_6$	27740	27470	27620	

	$Er(H_2O)_9^{+3}$	Er_2O_3(C)	$Er_{0.2}Zr_{0.8}O_{1.9}$	$La_{0.2}Er_{0.3}Zr_{0.5}O_{1.75}$ (F)	$LaErO_3$ (C-similar)	$La_{0.45}Er_{0.55}O_{1.5}$ (perovskite)
$^4I_{13/2}$	(6650)	6640	6640	6680	6660	6580
$^4I_{11/2}$	10220	10250	10360	10310	10270	10270
$^4F(I)_{9/2}$	12520	12480	12580	12580	12520	12480
$^4I(F)_{9/2}$	15350	15290	15380	15340	15270	15280
$^4S_{3/2}$	18480	18210	18400	18350	18280	18300
$^2H_{11/2}$	19230	19090	19270	19210	19120	19230
$^4F_{7/2}$	20600	20370	20530	20490	20410	20430
$^4F_{5/2}$	22270	22030	22220	22150	22050	22080
$^4F_{3/2}$	22610	22430	22680	22560	22510	22570
$^2H_{9/2}$	24630	24540	24570	24540	24510	24540
$^4G_{11/2}$	26490	26280	26390	26350	26230	26390

(contd.)

TABLE 5 (contd.)

	$Tm(H_2O)_9^{+3}$	Tm_2O_3(C)	Baricenters for $Tm_{0.05}Y_{0.95}O_{1.5}$(36b) ($^3H_6$ at 312 cm^{-1})	$Tm_{0.2}Zr_{0.8}O_{1.9}$	$LaTmO_3$ (perovskite)
$^3F(H)_4$	5810	5880	5960	5990	5990
$^3H_5$	8230	8370	8400	8460	8260
$^3H(F)_4$	12560	12790	12810	12800	12800
$^3F_3$	14480	14590	14660	14700	14640
$^3F_2$	15110	15210	15170	15270	(15200)
$^1G_4$	21280	21460	21640	21550	21460
$^1D_2$	27950	27740	27830	(27930)	27780

octahedral MX_6^{-3} [111] and gaseous $NdBr_3$ and NdI_3 [37] show extreme effects of hypersensitivity, and that, quite generally, conjugated ligands such as acetate and acetylacetonate have a strong effect. It is interesting that KRUPKE [82] in a quantitative study of the band intensities of M(III) in Y_2O_3 also determined considerably larger values of $U^{(2)}$ than for the aqua ions.

Several authors [127] have suggested a connection between the nephelauxetic effect and the electric polarizabilities α of the ligands. In our opinion [62] this is a somewhat secondary connection, because reducing ligands of low electronegativity, favouring M. O. delocalization, also tend to have rather large α. One might have connected the large nephelauxetic effect of oxide with high values of α. It is worth noting that though oxide(-II) does not have a sharply defined value for α (which would be infinite for gaseous O^{--}), using the cation polarizabilities determined by TESSMAN, KAHN and SHOCKLEY [123] consistently, one obtains a fairly moderate variation, α being 1.1 Å^3 for O(-II) in ClO_4^-, 1.3 Å^3 for Al_2O_3, 1.65 Å^3 for MgO and 2.1 Å^3 for BaO [75]. Anyhow, the main reason for the high nephelauxetic effect in our oxides, relative to aqua ions, must be the short M-O distances, as also discussed by POOLE [101] for Cr(III) and by REINEN [106] for Co(II), Ni(II) and other d group mixed oxides.

It is a fascinating question to what extent our oxides are covalent. The nephelauxetic effect is less informative in a numerical sense in the 4f group, where the empty 5d and 6s orbitals must be responsible for a much larger proportion of the covalent bonding than the partly filled 4f shell, than would be the case in the d groups [62, 76]. A chemical argument would be the very slow dissolution of C-oxides and fluorite-type dioxides in aqueous mineral acids, though, of course, the very large Madelung energy might

contribute to this high activation energy. What is perhaps more striking is the occurrence of O_9 clusters in UO_{2+x} as discussed at the end of chapter 6. The electronic density of the anions seems indeed to be depleted to an extent where one rather would talk about oxygen atoms than oxide ions from the point of view of fractional atomic charges [76]. Since this M. O. delocalization is connected with empty, rather than partly filled, central atom orbitals, we do not yet have sufficiently clear-cut physical methods to study the quantitative extent of covalent bonding. However, the nephelauxetic effect on the 4f shell indicates, at least indirectly, that the anhydrous halides are relatively more electrovalent than the oxides.

9. Experimental Section

The mixed oxides were prepared by ignition of co-precipitated hydroxides as discussed previously [70]. 0.5 M or 0.1 M lanthanide perchlorate solutions were prepared from 99.9 % or better purity La_2O_3, Nd_2O_3, Sm_2O_3, Eu_2O_3, Dy_2O_3, Ho_2O_3, Er_2O_3, Tm_2O_3 and Yb_2O_3 from American Potash (Lindsay Division, West Chicago) in a slight excess of 2 M Merck *p. a.* $HClO_4$ (diluted from 60 %). Pr_6O_{11} and Tb_7O_{12} from the same supplier can only be dissolved by prolonged boiling with more concentrated perchloric acid. 1 M or 0.5 M zirconyl chloride (Fluka, Buchs, S. G., Switzerland) was dissolved in 2 M HCl and filtered from a small amount of white, insoluble material. 0.5 M aqueous thorium nitrate was made from American Potash code 103 and analyzed by gravimetry of ThO_2 formed by our technique. Appropriate amounts of such stock solutions (usually containing totally 5 millimoles of metal) were mixed in beakers and diluted to 100 ml with demineralized water. Excess (1.5 times the stoichiometric amount, except when La is present, thrice the stoichiometric amount) Merck *p. a.* aqueous ammonia was rapidly added. Next day, the mixed hydroxides were washed thoroughly with water, and ignited in new porcelain crucibles, first over a Bunsen burner for a few minutes until nearly all water had left, and then in an electric furnace, usually at 1000°C for 1 hour. $LaErO_3$ was made under similar circumstances, whereas $LaTmO_3$ and $LaYbO_3$ were heated to 820°C for 1 hour. The subsequent transformation to orthorhombic perovskites took place by heating to 1200°C for 3 hours. Merck *p. a.* Bi_2O_3 was heated to 850°C for 30 minutes, pure or pre-mixed with Nd_2O_3 or Er_2O_3 as described in chapter 5. Lindsay Pr_6O_{11} was heated gently with various reducing agents in order to study the formation of Pr(III) oxide (which turned out to be well-defined C-Pr_2O_3) at as low temperature as possible.

Thus, boiling with 1-octanol (200°C) or heating the contents in a test-tube to about 300°C produced very pale yellow-green products.

Cerium(IV) acetylacetonate was, after unsuccessful attempts with $(NH_4)_2Ce(NO_3)_6$, made by shaking 2 millimoles of finely powdered, yellow $[N(CH_3)_4]_2CeCl_6$ [58] for 30 minutes in a flask (protected against light) with a solution of 8 millimoles anhydrous $N(C_2H_5)_3$ and 12 millimoles acetylacetone in 50 ml 1,2-dichloroethane. The filtered red-brown solution shows molar extinction coefficients ε at various wavelengths which decrease to the extent of some 20 % per hour.

The reflection spectra on Figure 1 were measured on the Beckman DU spectrophotometer. Y_2O_3 and $BaSO_4$ were used as references for Y- and Th-oxides, respectively. The internal $4f^q$-transitions given in Table 5 were measured at 100°K on the Cary 14 spectrophotometer with the reflection apparatus previously constructed by Dr. Romano Pappalardo [68].

The powder-diagrams were made with a Guinier-De Wolff camera (Enraf-Nonius, Delft) applying copper Kα-radiation. Silicon was used as internal standard; the three strongest lines at d = 3.135, 1.920 and 1.637 Å were invariantly found on the reading scale at 1.05 % lower d-values during the two years the measurements were performed. We did not attempt to determine lattice parameters better than one part per thousand; all our measurements were made at 20–30°C.

Acknowledgments

We would like to thank Dr. Romano Pappalardo for his kind permission to publish certain spectral data for $M_{0.2}Zr_{0.8}O_{1.9}$ and the two perovskites. We are grateful to Miss E. Viefhaus for making powder-diagrams of mixed Bi and certain mixed Pr-Zr oxides, to Miss E. Pobitschka for making powder-diagrams of oxides of La containing other lanthanides and of certain Pr-Th oxides and to Mr. B. Dusonchet for taking reflection spectra of the Pr-Th and Tb-Th oxides and for various preparative assistance. Finally, we would like to thank Professor G. Brauer, Freiburg-i-Brisgau, for information about TbO_2 and related problems, and Professor E. F. Bertaut, Grenoble, for information about the various types of M_2TiO_5.

Cyanamid European Research Institute
Cologny (Geneva), Switzerland 1223.

E.R.: Present address General Telephone and Electronics Laboratories, Bayside, N.Y. 11360.

References

1. Anderson, J. S., 1964, Proc. Chem. Soc., 166.
2. Asprey, L. B. and Cunningham, B. B., 1960, Progress Inorg. Chem. **2**, 267.
3. Ault, J. D. and Welch, A. J. E., 1966, Acta Cryst. **20**, 410.
4. Aurivillius, B. and Lundqvist, T., 1955, Acta Chem. Scand. **9**, 1209.
5. Baenziger, N. C., Eick, H. A., Schuldt, H. S. and Eyring, L., 1961, J. Amer. Chem. Soc. **83**, 2219.
6. Baker, J. M., Chadwick, J. R., Garton, G. and Harrell, J. P., 1965, Proc. Roy. Soc. (London) **286 A**, 352.
7. Barnes, J. C., 1964, J. Chem. Soc., 3880.
8. Barnes, J. C., 1966, J. Chem. Soc. **A**, 667.
9. Barnes, J. C. and Pincott, H., 1966, J. Chem. Soc. **A**, 842.
10. Betzl, M., Hase, W., Kleinstück, K. and Tobisch, J., 1963, Z. Krist. **118**, 473.
11. Bevan, D. J. M. and Kordis, J., 1964, J. Inorg. Nucl. Chem. **26**, 1509.
12. Bjørn-Andersen, H., 1933, Z. anorg. Chem. **210**, 93.

12a. Blasse, G., 1966, J. Chem. Phys. **45**, 2356.

12b. Blasse, G. and Bril, A., 1966, J. Chem. Phys. **45**, 3327.

13. Boulanger, F., 1952, Ann. chim. (Paris) [12] **7**, 732.

13a. Braterman, P. S., 1966, J. Chem. Soc. **A**, 1471.

14. Brauer, G. and Holtschmidt, U., 1951, Z. anorg. Chem. **265**, 105.
15. Brauer, G. and Gradinger, H., 1954, Z. anorg. Chem. **276**, 209.
16. Brauer, G. and Gradinger, H., 1954, Z. anorg. Chem. **277**, 89.
17. Brauer, G., 1964, Progress Science Techn. Rare Earths, **1**, 152 (Pergamon Press, Oxford).
18. Brauer, G. and Pfeiffer, B., 1965, Z. anorg. Chem. **341**, 237.
19. Brauer, G. and Pfeiffer, B., 1966, J. prakt. Chem. **34**, 23.

19a. Brauer, G., 1966, Progress Science Techn. Rare Earths, **2**, 312.

20. Carnall, W. T., Fields, P. R. and Wybourne, B. G., 1965, J. Chem. Phys. **42**, 3797.
21. Chang, L. L. Y. and Phillips, B., 1964, Inorg. Chem. **3**, 1792.
22. Chang, N. C., 1963, J. Opt. Soc. Amer. **53**, 1315.
23. Chang, N. C. and Gruber, J. B., 1964, J. Chem. Phys. **41**, 3227.

23a. Chang, N. C., 1966, J. Chem. Phys. **44**, 4044.

24. Chase, G. A., 1962, Acta Cryst. **15**, 91.
25. Collongues, R., Perez y Jorba, M. and Lefèvre, J., 1961, Bull. Soc. Chim. France 70.
26. Connick, R. E., 1949, J. Chem. Soc. **S**, 235.
27. Day, P., 1963, Inorg. Chem. **2**, 452.
28. D'Eye, R. W. M., 1958, J. Chem. Soc. 196.
29. Ephraim, F. and Bloch, R., 1926, Ber. **59**, 2692; 1928, ibid. **61**, 65 and 72.
30. Ephraim, F., 1928, Ber. **61**, 80.
31. Ephraim, F., Jantsch, G. and Zapata, C., 1933, Helv. Chim. Acta **16**, 261.
32. Ferguson, I. F. and Fogg, P. G. T., 1955, J. Chem. Soc. 3679.
33. Foex, M. and Traverse, J. P., 1966, Compt. rend. (Paris) **262 C**, 636 and 743.

34. Gattow, G. and Schröder, H., 1962, Z. anorg. Chem. **318**, 176.
35. Gingerich, K. A. and Brauer, G., 1963, Z. anorg. Chem. **324**, 48.
36. Goldschmidt, V. M., Ulrich, F. and Barth, T., 1925, Skrifter Norske Vid. Akademi I. Mat. Naturvid. Klasse, no. 5.
36a. Gruber, J. B. and Satten, R. A., 1963, J. Chem. Phys. **39**, 1455.
36b. Gruber, J. B., Krupke, W. F. and Poindexter, J. M., 1964, J. Chem. Phys. **41**, 3363.
36c. Gruber, J. B., Henderson, J. R., Muramoto, M., Rajnak, K. and Conway, J. G., 1966, J. Chem. Phys. **45**, 477.
37. Gruen, D. M. and DeKock, C. W., 1966, J. Chem. Phys. **45**, 455.
38. Guillen, M. and Bertaut, E. F., 1966, Compt. rend. (Paris) **262 B**, 962.
39. Guth, E. D., Holden, J. R., Baenziger, N. C. and Eyring, L. R., 1954, J. Amer. Chem. Soc. **76**, 5239.
40. Haïssinsky, M. and Jørgensen, C. K., 1966, J. chim. phys. **63**, 1135.
41. Hellwege, K. H., 1948, Ann. Physik [6] **4**, 95, 127, 136, 143, 150 and 357.
42. Hofmann, K. A. and Kirmreuther, H., 1910, Z. physik. Chem. **71**, 312.
43. Honig, J. M., Clifford, A. E. and Faeth, P. A., 1963, Inorg. Chem. **2**, 791.
44. Hoppe, R., 1964, Angew. Chem. **76**, 691.
45. Hughes, K. J., 1965, Dissert. Abstracts **26**, 2459.
46. Hund, F., 1951, Z. anorg. Chem. **265**, 62.
47. Hund, F. and Dürrwächter, W., 1951, Z. anorg. Chem. **265**, 67.
48. Hund, F. and Lieck, K., 1952, Z. anorg. Chem. **271**, 17.
49. Hund, F., 1964, Z. anorg. Chem. **333**, 248.
50. Jensen, A. T. and Rasmussen, S. E., 1955, Acta Chem. Scand. **9**, 708.
51. Job, A. and Goissedet, P., 1913, Compt. rend. (Paris) **157**, 50.
52. Joye, P., 1913, Archiv. sci. phys. nat. (Genève) [4] 36, 41, 113 and 431.
53. Judd, B. R., 1962, Phys. Rev. **127**, 750.
54. Judd, B. R., Operator Techniques in Atomic Spectroscopy. McGraw Hill, New York, 1963.
55. Judd, B. R., 1966, J. Chem. Phys. **44**, 839.
56. Jørgensen, C. K., 1956, Mat. Fys. Medd. Dan. Vid. Selsk. **30**, no. 22.
57. Jørgensen, C. K., 1959, Mol. Phys. **2**, 309.
58. Jørgensen, C. K., 1962, Mol. Phys. **5**, 271.
59. Jørgensen, C. K., 1962, Acta Chem. Scand. **16**, 2406.
60. Jørgensen C. K., Orbitals in Atoms and Molecules. Academic Press, London, 1962.
61. Jørgensen, C. K., 1962, J. Inorg. Nucl. Chem. **24**, 1587.
62. Jørgensen, C. K., 1962, Progress Inorg. Chem. **4**, 73.
63. Jørgensen, C. K., 1963, Acta Chem. Scand. **17**, 1034.
64. Jørgensen, C. K., 1963, Acta Chem. Scand. **17**, 1043.
65. Jørgensen, C. K. and Brinen, J. S., 1963, Mol. Phys. **6**, 629.
66. Jørgensen, C. K., Pappalardo, R. and Schmidtke, H.-H., 1963, J. Chem. Phys. **39**, 1422.
67. Jørgensen, C. K., Inorganic Complexes. Academic Press, London, 1963.
68. Jørgensen, C. K., Pappalardo, R. and Rittershaus, E., 1964, Z. Naturforsch. **19a**, 424.
69. Jørgensen, C. K. and Judd, B. R., 1964, Mol. Phys. **8**, 281.

70. Jørgensen, C. K., Pappalardo, R. and Rittershaus, E., 1965, Z. Naturforsch. **20a**, 54.
71. Jørgensen, C. K., 1965, Proceedings of Symposium on Coordination Chemistry in Tihany 1964, p. 11. Hungarian Academy of Sciences, Budapest.
72. Jørgensen, C. K. and Schwochau, K., 1965, Z. Naturforsch. **20a**, 65.
73. Jørgensen, C. K., Pappalardo, R. and Flahaut, J., 1965, J. chim. phys. **62**, 444.
74. Jørgensen, C. K., 1965, J. Physique **26**, 825.
75. Jørgensen, C. K., 1966, Structure and Bonding **1**, 234 (Springer-Verlag, Heidelberg).
75a. Jørgensen, C. K., 1966, Int. Rev. Halogen Chemistry **1**, 265 (Academic Press, London).
76. Jørgensen, C. K., 1967, Helv. Chim. Acta (Werner Commemoration Volume and Proceed. 9.ICCC) 131.
77. Jørgensen, C. K., Lanthanides and 5f Elements. Academic Press, London, 1968.
77a. Keller, C., 1964, J. inorg. nucl. Chem. **26**, 2069; *ibid.*, 1965, **27**, 797.
78. Kisliuk, P., Krupke, W. F. and Gruber, J. B., 1964, J. Chem. Phys. **40**, 3606.
79. Klemm, W. and Klein, H. A., 1941, Z. anorg. Chem. **248**, 167.
80. Knop, O., Brisse, F., Castelliz, L. and Sutarno, 1965, Canad. J. Chem. **43**, 2812.
81. Krupke, W. F. and Gruber, J. B., 1965, Phys. Rev. **139 A**, 2008.
82. Krupke, W. F., 1966, Phys. Rev. **145**, 325.
83. Lawton, S. L. and Jacobson, R. A., 1966, Inorg. Chem. **5**, 743.
84. Lefèvre, J., 1963, Ann. chim. (Paris) [13] **8**, 117.
85. Levin, E. M. and Roth, R. S., 1964, J. Res. Nat. Bur. Stand. **68 A**, 189.
85a. Linares, R. C., 1966, J. Opt. Soc. Amer. **56**, 1700.
86. Magnéli, A. and Kihlborg, L., 1951, Acta Chem. Scand. **5**, 578.
87. Mansmann, M., 1965, Z. Krist. **122**, 375.
88. Marezio, M., 1966, Acta Cryst. **20**, 723.
89. Marsh, J. K., 1946, J. Chem. Soc. 15.
90. Matković, B. and Grdenić, D., 1963, Acta Cryst. **16**, 456.
91. Mazza, L. and Iandelli, A., 1951, Atti della Accad. Ligure di Scienze e Lettere **7**, 44.
92. McCullough, J. D., 1950, J. Amer. Chem. Soc. **72**, 1386.
92a. Montmory, M. C. and Bertaut, E. F., 1961, Compt. rend. (Paris) **252**, 4171.
92b. Muller, O., White, W. B. and Roy, R., 1964, J. inorg. nucl. Chem. **26**, 2075.
93. Möbius, H. H., 1964, Z. Chem. **4**, 81.
94. National Bur. Stand. Circular No. 539 vol. **1**, 51. Washington D.C., 1953 (2. Ed. 1962).
95. Nieuwpoort, W. C. and Blasse, G., 1966, Solid State Comm. **4**, 227.
96. Orgel, L. E., 1959, J. Chem. Soc. 3815.
97. Pappalardo, R. and Jørgensen, C. K., 1967, J. Chem. Phys. **46**, 632.
98. Pauling, L. and Shappell, M. D., 1930, Z. Krist. **75**, 128.
99. Perez y Jorba, M., 1962, Ann. chim. (Paris) [13] **7**, 479.
100. Poix, P., 1965, Compt. rend. (Paris) **261**, 4761.
101. Poole, C. P., 1964, J. Phys. Chem. Solids **25**, 1169.

102. Prandtl, W. and Rieder, G., 1938, Z. anorg. Chem. **238**, 225.
103. Queyroux, F., 1964, Compt. rend. (Paris) **259**, 1527.
104. Racah, G., 1949, Phys. Rev. **76**, 1352.
105. Rakestraw, J. W. and Dieke, G. H., 1965, J. Chem. Phys. **42**, 873.
106. Reinen, D., 1964, Z. anorg. Chem. **327**, 238.
107. Robin, M. B., 1962, Inorg. Chem. **1**, 337.
107a. Rooksby, H. P. and White, E. A. D., 1963, Acta Cryst. **16**, 888.
108. Ropp, R. C., 1965, J. Electrochem. Soc. **112**, 181.
109. Roth, R. S., 1956, J. Res. Nat. Bur. Stand. **56**, 17.
110. Ryan, J. L. and Jørgensen, C. K., 1963, Mol. Phys. **7**, 17.
111. Ryan, J. L. and Jørgensen, C. K., 1966, J. Phys. Chem. **70**, 2845.
112. Schneider, S. J. and Roth, R. S., 1960, J. Res. Nat. Bur. Stand **64 A**, 317.
113. Schumb, W. C. and Rittner, E. S., 1943, J. Amer. Chem. Soc. **65**, 1055.
114. Schäffer, C. E. and Jørgensen, C. K., 1958, J. Inorg. Nucl. Chem. **8**, 143.
115. Schäffer, C. E., 1958, J. Inorg. Nucl. Chem. **8**, 149.
116. Schäffer, C. E. and Jørgensen, C. K., 1965, Mol. Phys. **9**, 401.
117. Shriver, D. F., 1966, Structure and Bonding **1**, 32 (Springer-Verlag, Heidelberg).
118. Sillén, L. G., 1937, Arkiv Kemi Min. Geol. **12 A**, no. 18.
119. Sinha, S. P. and Schmidtke, H.-H., 1965, Mol. Phys. **10**, 7.
120. Steindler, M. J. and Gunther, W. H., 1964, Spectrochim. Acta **20**, 1319.
121. Steindler, M. J. and Gerding, T. J., 1966, Spectrochim. Acta **22**, 1197.
122. Sugar, J., 1965, J. Opt. Soc. Amer. **55**, 1058.
123. Tessman, J. R., Kahn, A. H. and Shockley, W., 1953, Phys. Rev. **92**, 890.
124. Thoma, R. E., Hebert, G. M., Insley, H. and Weaver, C. F., 1963, Inorg. Chem. **2**, 1005.
125. Waegner, A., 1904, Z. anorg. Chem. **42**, 118.
126. Warshaw, I. and Roy, R., 1961, J. Phys. Chem. **65**, 2048.
127. Weakliem, H. A., 1962, J. Chem. Phys. **36**, 2117.
128. Wickersheim, K. A. and Lefever, R. A., 1964, J. Electrochem. Soc. **111**, 47.
129. Williams, R. J. P., 1955, J. Chem. Soc. 137.
130. Willis, B. T. M., 1963, Proc. Roy. Soc. (London) **A 274**, 122 and 134.
131. Wolf, L., Bärnighausen, H. and Massonne, J., 1956, J. prakt. Chem. **3**, 211.
132. Wybourne, B. G., Spectroscopic Properties of Rare Earths. Interscience (John Wiley), New York 1965.
133. Zintl, E. and Croatto, V., 1939, Z. anorg. Chem. **242**, 79.
134. Zintl, E. and Udgård, A., 1939, Z. anorg. Chem. **240**, 150.

Indleveret til Selskabet den 25. november 1966.
Færdig fra trykkeriet den 31. marts 1967.

Matematisk-fysiske Meddelelser
udgivet af
Det Kongelige Danske Videnskabernes Selskab
Bind **35,** nr. 16

Mat. Fys. Medd. Dan. Vid. Selsk. **35,** no. 16 (1967)

STRING EFFECT WITH 5 MeV PROTONS AND 20 MeV ALPHA PARTICLES ON BISMUTH

BY

CLIVE ELLEGAARD AND N. O. LASSEN

København 1967
Kommissionær: Munksgaard

Synopsis

The yield of backward elastic scattering (150°) of 5 MeV protons and 20 MeV α-particles from a single crystal of bismuth was found to depend on the orientation of the crystal with respect to the beam direction. When the latter coincides with the trigonal axis of the crystal the yield has a deep minimum, the angular width of which agrees with Lindhard's formula. Smaller and narrower minima in the yield are found when the beam is parallel to low index crystal planes. The effect is found to increase when the crystal is cooled to liquid nitrogen temperature. The string effect decreases with the depth below the surface, at the low temperature, with a factor of two in about 10 μm. The variation is found to correspond to an almost linear increase in Ω^2, the mean square angular width of the beam, which may be understood as a result of the thermal vibrations of the atoms.

PRINTED IN DENMARK
BIANCO LUNOS BOGTRYKKERI A-S

1. Introduction

As first pointed out by LINDHARD[1], when a narrow beam of charged particles enters a single crystal, the yield of nuclear reactions and scattering processes will have a minimum when a low index crystal axis is parallel to the beam direction. Looking at the crystal in the direction of the axis, one could imagine (with high! magnification) to see the end of the "strings" on which the atoms are sitting like pearls, and between the strings would be empty channels. Rather, the channels would not be completely empty; only the nuclei and some of the inner atomic electrons are located in or near the strings, whereas the outermost electrons may also be found in the channels. One could further imagine that, if charged particles were shot into the crystal in a direction almost exactly parallel to the strings, only nuclei in the front layer could be hit and the particles having passed this layer would travel along the channels without striking the nuclei. Such "channelling" effects may be present if the angle ψ between the beam direction and the axis is very small. However, LINDHARD has shown that even when particles have much larger ψ-values, for which no proper channelling takes place, the Coulomb fields around the nuclei in a string prevent the particles from striking the nuclei, provided only that ψ is smaller than a certain critical angle ψ_1. In fact, the particles cannot even come close enough to the nuclei to undergo large angle Coulomb scattering.

ψ_1 is given approximately by

$$\psi_1 \sim \sqrt{\frac{2Z_1Z_2e^2}{Ed}}, \tag{1}$$

where Z_1 and Z_2 are the charge numbers of the projectile and the target nucleus, respectively, e is the electronic charge, E the C.M. energy, and d the distance between neighbouring atoms in a string. For an incoming particle beam having an angular width smaller than ψ_1 one observes, by varying the crystal orientation, a minimum in the yield of nuclear reactions when the beam direction coincides with the string direction. This was

first demonstrated by BØGH, DAVIES and NIELSEN[2], who studied the yield of the resonant (p,γ) reaction in aluminum using protons with a kinetic energy slightly higher than the 411 keV resonance. In the (1, 1, 1) direction they found a decrease in the γ-yield to about 20 % of the normal value, the angular half width of the dip being in rough agreement with (1).

It was the purpose of the present experiments to investigate whether the string effect could be observed also in the elastic scattering with higher energy particles such as could be obtained from our cyclotron, and furthermore to look for a possible temperature effect.

Studies of the string effect have meanwhile been continued in Aarhus[3] and elsewhere. Dips in yield of γ-radiation and in Rutherford scattered particles have been observed not only for string directions, but smaller dips also when the beam is parallel to a plane in the crystal. For higher energy particles the effect has been observed with 1–2 MeV protons at the Van de Graaff of this Institute and with naturally occurring α-particles in Stockholm[4].

Particles moving parallel to string directions will tend to move at some distance from the nuclei, hence where the electron density is relatively low. Such particles will therefore have a longer range than particles moving at some angle with the crystal axis, an effect which was observed by DAVIES et al.[5] long before LINDHARD predicted the reduction in nuclear reaction yield. Even for particles which are predominantly stopped by electronic encounters, the specific energy loss will be smaller for string directions than normal, an effect which has also been directly observed[6].

2. Experimental apparatus

The arrangement is shown in fig. 1. Part of the analyzed beam from the Copenhagen cyclotron was passed through two lead stops, *Pb*1 with a 2 mm diameter hole and *Pb*2 with a 1 mm diameter hole. The two diaphragms were 420 mm apart, and thus the transmitted beam had an angular half width of 0.0036 radians or 0°.2. A small piece of a *Bi* single crystal, about 3 mm thick, was glued to a hollow copper cylinder *C* and placed close to the axis of the scattering chamber. The crystal was made by cleaving a larger single crystal cooled to liquid air temperature; the surface was parallel to the trigonal plane, as was found by *X*-ray analysis. The copper cylinder was supported by an insulating teflon holder *D* screwed to the brass ring *E*. To increase the heat insulation of the copper cylinder the two axles *F* (only one shown in the figure) were thin-walled stainless steel

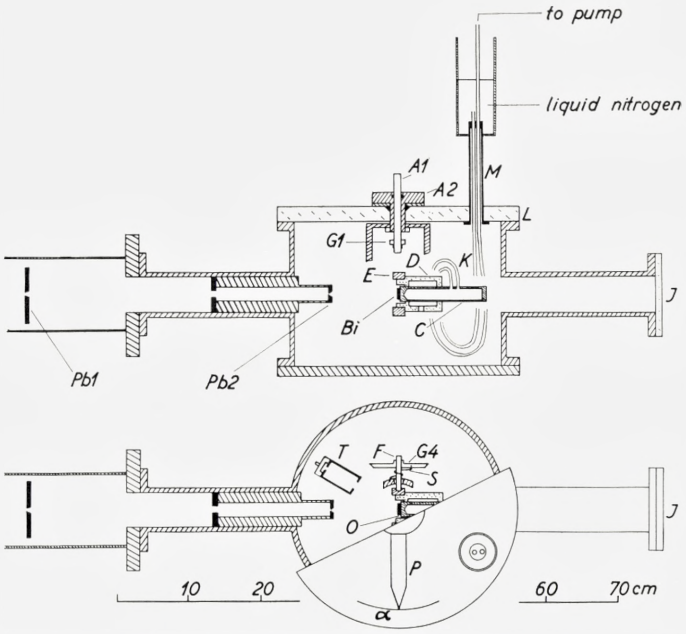

Fig. 1. Upper figure: Vertical section through scattering chamber. Lower figure: To the left, horizontal section and, to the right, top view.

tubes. By rotating the axle $A1$ the copper cylinder could be tilted about F, the connection being made through four gear wheeles, only two of which are shown ($G1$ and $G4$). The setting of the axle $A1$ was read on a duodial; one revolution = 100 divisions would produce a tilt of 12° of the copper cylinder. The axles F rotated in ball bearings and a spring S minimized the uncertainty in the tilting angle β. The holders for the ball bearings were stiffly connected to the outer axle $A2$, the setting of which could be read with an accuracy of 0°.2 on the scale α by means of the pointer P. Thus, the crystal could be rotated about a vertical axis (angle α) and a horizontal axis (angle β). By holding a small lamp at I and looking at the light reflected from the end of the copper cylinder one could predetermine the setting where the crystal surface is perpendicular to the beam with an accuracy of about one degree.

The copper cylinder could be filled with liquid nitrogen from a well-insulated reservoir (insulation not shown). The copper tubes K were thin (1.5 mm inner diameter) and long (each about 50 cm) in order not to impede the movements of the copper cylinder. A thin-walled stainless steel tube M

served to avoid cooling the lucite lid L of the scattering chamber. A copper-constantan thermo-element (not shown) measured the temperature of the copper at O.

The current to the copper cylinder was of the order of $10^{-9}A$. An integrating device determined the dose of α-particles or protons. The particles scattered at 150° were measured by a solid state counter T with an opening angle of $2 \cdot 10^{-3}$ steradians.

3. Results and discussion

In fig. 2 some proton spectra are shown. When the beam enters in a direction *not* coinciding with a string, the shape of the spectrum may be calculated. Neglecting finite energy resolution and straggling, $N(E)$ should be proportional to $\left[(E')^2 \frac{dE}{dx}\right]^{-1}$, where E' is the energy of the protons just before scattering, E is the energy of the protons when escaping from the surface of the crystal, and $\frac{dE}{dx}$ is the stopping power of the crystal for the latter energy. Using the range-energy relations for *Pb* given by WILLIAMSON and BOUJOT[7] we find that the average decrease in $N(E)$ in the range from 3 to 5 MeV is about 6 per cent per MeV, in agreement with the experimental curves.

$N(E)$ is considerably smaller when the beam is parallel to the trigonal axis. This effect is more pronounced for the cooled target; not only is the difference larger for the cold than for the warm target, but the effect also extends to larger depths in the crystal (smaller E) in the former case. For the upper curves, 4 MeV (3 MeV) corresponds to protons scattered at a depth of 17 μm (32 μm); thus, one channel roughly corresponds to one μm. For the lower curves, the relation between energy and scattering depth is not the same (and not known), since the stopping power for protons moving parallel to the trigonal axis is smaller than the normal value. Neglecting this difference, we find roughly that the string effect decreases by a factor of two in 3 μm or in 10 μm for the warm and the cold crystal, respectively. If the stopping power in the string direction has half the normal value these figures are reduced by about 25 per cent. However, it may be mentioned here that the reduced stopping power produces a change in the curve, which is not just a multiplication of the abscissae, but somewhat more complicated. For example, if a layer of the target were a perfect crystal, whereas for greater

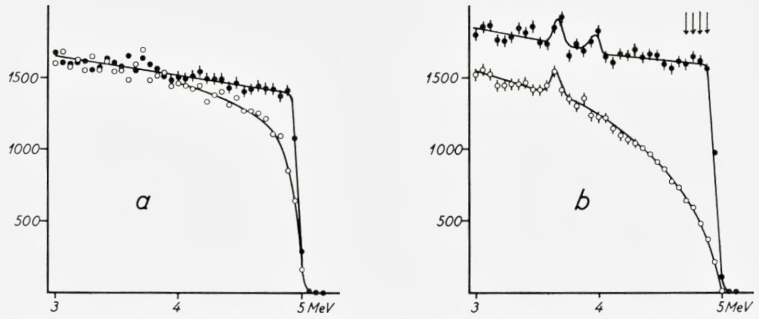

Fig. 2. Spectra of scattered protons, $\vartheta = 150°$. a) Bi-crystal at room temperature. b) Crystal at liquid nitrogen temperature. The upper curves and full circles are obtained with the incoming beam a few degrees off the (1, 1, 1) direction; the lower curves and open circles are obtained when the beam coincides with the (1, 1, 1) direction (the trigonal axis).

depths the atoms were randomly arranged, then the two curves of fig. 2a (or 2b) would never meet, but show a "string effect" for any depth, simply because the particles having passed the crystalline layer in the string direction have the higher energy.

The curves in figs. 2a and 2b correspond to the same measured dose of incoming protons. The ordinates of the two upper curves should therefore be expected to be equal. The reason for the observed difference is unknown. One possible explanation may be that the changing of surface conditions gives rise to different amounts of secondary electrons from the target and, hence, influences the beam dose measurement. There does not seem to be any connection with the thickness of the surface layer of carbon and oxygen, since the corresponding two peaks in the proton spectrum, at energies about 3.6 and 4 MeV, varied quite irregularly in intensity from day to day, whereas the yield difference between a cold and a warm target was reproducible.

Fig. 3a shows the low scattering yield for protons entering the crystal in a direction close to the trigonal axis. When the beam coincides with the axis, the yield for the cold target is reduced to less than half the normal value. A decrease in yield, though smaller, was also observed when the beam was parallel to a low index plane of the crystal (see later). When the angle β is kept constant at the proper value while the angle α is varied (open circles), the beam direction passes through the trigonal axis, but for all values of α the beam is nearly parallel to a $(0, \bar{1}, 1)$ plane, and hence the yield is low also outside the dip. When gluing the crystal to the supporting copper cylinder we aimed at such a position that the α-axis should be parallel to a $(0, \bar{1}, 1)$ plane. Since we were off by some fraction of a degree, the

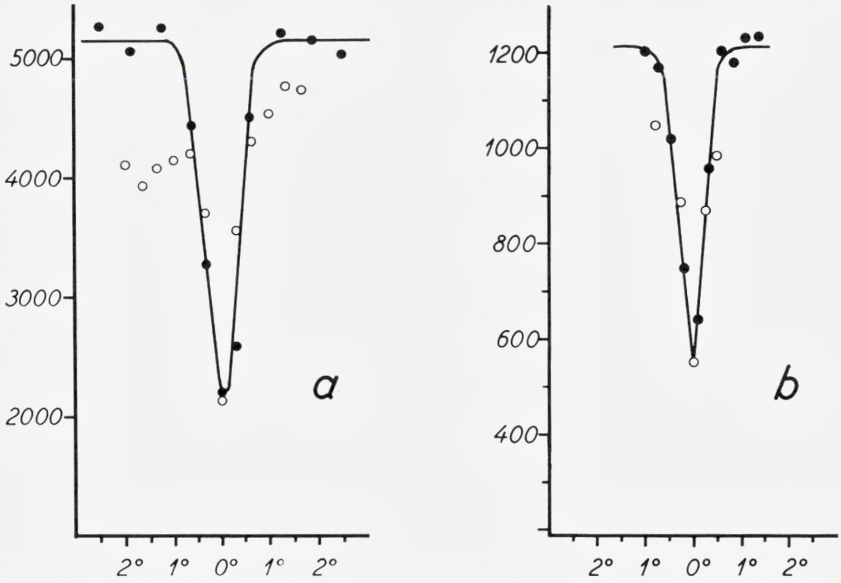

Fig. 3. a) Yield of elastic scattering of 5 MeV protons as a function of the angle between the trigonal axis and the beam direction, for a Bi-crystal at liquid nitrogen temperature. Ordinates: Number of scattered particles in four energy channels (approximately the arrow marked channels in fig. 2 b) per 200 *n*Coulomb of incoming beam. Full drawn curve and full circles correspond to tilting the crystal in the β-direction, i.e., perpendicular to a $(0, \bar{1}, 1)$ plane. Open circles correspond to a tilting in the α-direction, i.e., parallel to a $(0, \bar{1}, 1)$ plane. b) Similar curves for 20 MeV α-particles.

varying of α does not correspond exactly to travelling along the bottom of the $(0, \bar{1}, 1)$ valley, but it corresponds to a path slantingly climbing the valley side and this accounts for the lack of symmetry indicated by the open points.

In fig. 3 b, similar measurements for 20 MeV α-particles are shown. For α-particles the obtainable statistics is poor, and the attention was therefore focussed on the proton measurements.

For the full drawn curves, the angle α is kept constant and the varying of β corresponds to moving perpendicularly to the $(0, \bar{1}, 1)$ plane. As seen in the figure, the shape of the dip is nearly identical for α- and β-tilting, apart from the difference in yield outside the dip. The half widths agree roughly with the theory; the full width at half minimum depth is about 0.°8 for protons and 0.°6 for α-particles. Neglecting the finite half width (0.°2) of the beam, we find for the measured half widths Δ of the dips $\Delta = 1.3\ \psi_1$ for both α-particles and protons, where ψ_1 is given by (1).

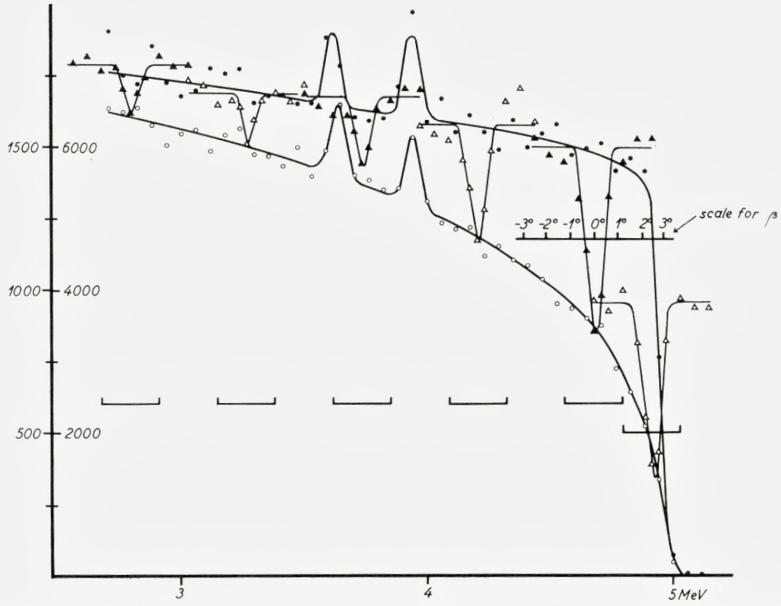

Fig. 4. Spectra of protons scattered 150° from a cold Bi-crystal with the beam coinciding with the trigonal axis (lower curve and open circles) and 2.°4 off this direction (upper curve and closed circles); scale of ordinates to the left of the axis. The variation in yield when tilting the crystal in the β-direction, i.e., perpendicular to the (0, $\bar{1}$, 1) plane, is shown for several values of the depth of the scattering layer; in each case the number of protons in four energy channels, indicated in the figure, was counted for different β-settings in the vicinity of the trigonal axis; scale of ordinate to the right of the axis.

Fig. 4 shows the result of another measurement which illustrates the declining of the string effect as the protons penetrate deeper into the crystal. Measuring the effect by the percentage decrease in cross section, we again find a reduction by a factor of two in roughly 10 μm. However, the half width of the dip is constant, $\sim$ 0.°8, at least to depths greater than 20 μm; only for the two last curves corresponding to depths of 30–40 μm the half width may be slightly smaller.

Fig. 5 illustrates some planar effects. The curve to the right shows the variation in scattering yield when the crystal is tilted in such a way that the beam direction passes normally across a (1 $\bar{1}$ 0) plane. The three biggest dips correspond to traversing planes of the same order (1 $\bar{1}$ 0), but the two outer dips are wider than the middle one, because the outer planes are crossed at angles of 60° from the normal to the planes. The half widths are 0.°5 for the middle dip, 0.°9 for the other two, the ratio thus being close to

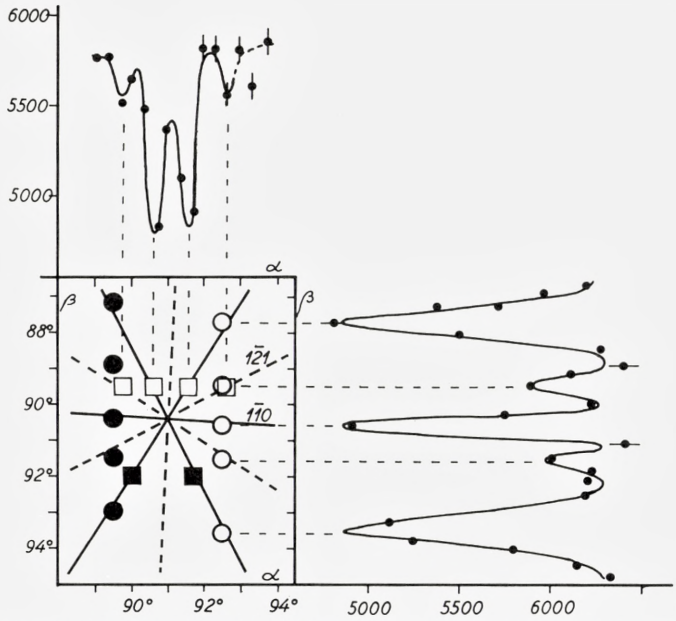

Fig. 5. Map showing positions of some relative minima in scattering yield due to plane effects. When keeping $\alpha = 92.^{\circ}5$ and varying β, we obtained a yield *vs.* β curve shown to the right, giving minima represented by the open circles in the map. The upper curve corresponds to β constant at $89^{\circ}.5$ and α being varied; the minima of this curve are represented by open squares. The size of the "points" represents the estimated uncertainty. The absolute values of the ordinates in the two graphs should not be compared, see text.

the expected value $\cos 60^{\circ}$. As can be seen, the planar dips are narrower than the string dip, in accordance with the theory. However, the ratio is not quite as high as the estimated theoretical factor[8] $2Z_2^{1/6} \approx 4$. In between the big dips are seen smaller dips corresponding to planes of order (1 $\bar{2}$ 1).

The upper curve shows the yield variation when tilting in a direction parallel to a (1, $\bar{1}$, 0) plane but 3/4 of a degree away from this plane. Again the (1, $\bar{1}$, 0) planes are clearly seen, and there are also indications of the (1, $\bar{2}$, 1) planes. At the center, for $\alpha = 91^{\circ}$, the curve does not rise to "normal" yield, because we are here on the edge of the string hole (cf. fig. 3a).

The two yield curves were not obtained on the same day and since there might be slight changes in beam energy, etc., the absolute ordinates of the two curves are not directly comparable.

Similar curves were obtained for α = const. = $89.^{\circ}5$, yielding minima shown in the map by full circles and for β = const. = 92° yielding the minima shown by full squares. When drawing straight lines in the proper way

through the minima thus located, we get a picture of the planes intersecting in the (1, 1, 1) direction.

For the plane marked (1, $\bar{1}$, 0) in the figure, the dip observed by perpendicular crossing was followed as far away ($\sim 30°$) from the string as permitted by our apparatus; no appreciable change in the dip was seen.

Each point in the curves of fig. 5 was obtained from a spectrum like those in fig. 2. From these spectra we can obtain the variation of the planar effect with the depth in the crystal in the same way as shown for the string effect in fig. 4. The planar effect decreases with depth somewhat faster than does the string effect, the half length being ~ 3.5 μm.

4. Discussion of influence of lattice vibrations

According to LINDHARD, a beam of particles entering a single crystal will be divided into a random and an aligned beam, the latter consisting of the particles having $\psi < \psi_1$ inside the crystal. Particles with $\psi < \psi_1$ entering the crystal at points far away from strings will never come closer to any string than $\sim a = a_0 \cdot 0.88\ [Z_1^{2/3} + Z_2^{2/3}]^{-\frac{1}{2}}$, which in our case is $a = 10^{-9}$ cm. When approaching a string, the particles lose part of or the whole velocity component perpendicular to the string, but after reflection ψ again obtains its original value. If all the incoming particles in the beam have $\psi < \psi_1$, only those striking the surface within the distance a from string positions will go into the random beam and have the possibility of suffering large angle scattering or initiate nuclear reactions. The yield at the dip minimum should therefore be expected to be $Nd\pi a^2 \approx 10^{-2}$ times the normal yield. We shall discuss why we do not observe so low a yield and why the minimum yield increases with depth.

Let us assume that the beam inside the target has a Gaussian shape, the angular distribution being

$$W(\theta)d\theta = \frac{2}{\Omega^2}\theta e^{-\frac{\theta^2}{\Omega^2}}d\theta. \tag{2}$$

The fraction of the particles *not* belonging to the aligned beam is—neglecting the very small contribution $Nd\pi a^2$—

$$\int_{\psi_1}^{\infty} W(\theta)d\theta = e^{-\frac{\psi_1^2}{\Omega^2}}. \tag{3}$$

Furthermore, assume that Ω^2 increases linearly with the distance z traversed, say

$$\Omega^2 = \frac{z}{L} \cdot \psi_1^2, \tag{4}$$

where L is a constant. Then, the fractional scattering yield in the dip minimum is

$$Y = e^{-\frac{L}{z}}. \tag{5a}$$

In figure 6 we have plotted experimental points obtained from the same measurements as the points in figure 2. The ordinate for a point in figure 6 is the number of protons counted in a channel when the incoming beam is parallel to the axis divided by the number counted in the same channel for a "random" crystal orientation (ratio between the two curves in, for example, fig. 2a). The errors shown are the statistical errors; no corrections have been applied for the carbon and oxygen peaks, and they are the cause for the increased scattering exhibited by the points corresponding to the cold target in the region $2.5L < z < 3.5L$.

The points for the cold target can be well fitted by a curve of the type (5a) if we put $L = L_c = 7$ channels ~ 7 μm. For reasons which will be outlined in the following, we have chosen to compare the points with a curve of the form

$$Y = S + (1 - S)e^{-L/z}, \tag{5b}$$

where $S = 0.15$, and again a good fit is obtained for $L_c = 7$ channels, as shown by the curve in figure 6.

The points for the warm target fit reasonably well to a curve of the same type (5b), but with $S = 0.50$ and $L_w \sim 1.96$ channels ~ 2 μm.

In an amorphous *Bi*-target the nuclear small angle scattering would produce an increase in Ω^2 of the order of ψ_1^2 in one μm, thus giving $L = L_0 \sim 1$ μm. The experimental value $L_c \sim 7$ μm illustrates the reduction in multiple scattering in the cold crystal. In an amorphous target, the electrons would give a negligible contribution to the multiple scattering; the length L_{0e} needed to give an increase of ψ_1^2 in Ω^2 by electronic encounters alone would be $L_{0e} \sim Z_2 L_0 \sim 80$ μm, and in the crystal the corresponding length is probably at least a factor of two larger[8]. The electronic multiple scattering is therefore insufficient to explain the increase in the minimum scattering yield with depth in the crystal.

The difference between a cold and a warm target may suggest that thermal vibrations of the atoms play some role. If, for simplicity, we assume

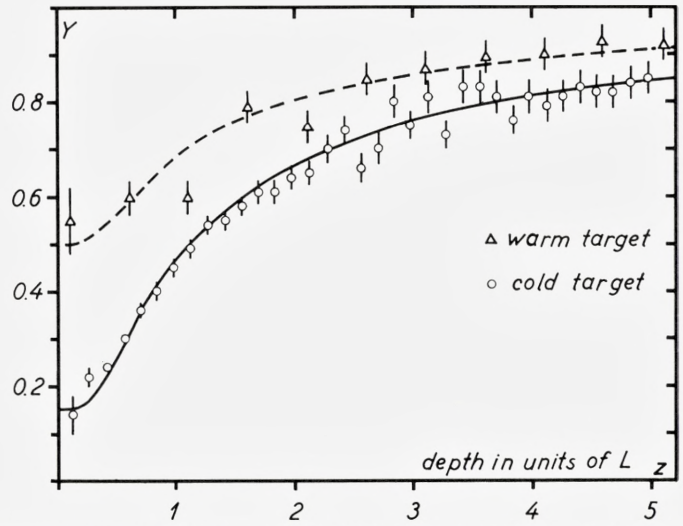

Fig. 6. Scattering yield in string direction relative to the normal yield as a function of the depth in the crystal. The circles and the full drawn curve correspond to the cold target, the triangles and the dotted curve to the crystal at room temperature. The distance between successive points is about one μm. The curves correspond to a linear increase in the mean square angular width Ω^2 of the beam.

isotropy in the oscillations, the displacements ϱ in a plane perpendicular to the string may be assumed to be normally distributed, i.e.,

$$W(\varrho)d\varrho = \frac{2}{\alpha^2}\varrho e^{-\frac{\varrho^2}{\alpha^2}}d\varrho, \tag{6}$$

where α^2 is the mean square displacement given by

$$\alpha^2 = 6T\hbar^2/(mk\theta^2) = 1.0\cdot 10^{-20}\cdot T. \tag{7}$$

Here $k = 1.38\cdot 10^{-16}$ erg/^0K is the Boltzmann constant, T is the absolute temperature, $\theta = 117$ is the Debye temperature for Bi, and m is the mass of the Bi-atom.[9)]

Again as a first crude approximation, the protons in the aligned beam passing through a layer of atoms may be assumed to be randomly distributed with respect to the location of the atoms, except that they do not come closer to any string than a. In their transverse vibrations the atoms will move far out from their equilibrium positions in the strings, and when they are displaced more than a, collisions between the atoms and the par-

ticles in the aligned beam may occur. The probability that an atom has a distance larger than a from a string is

$$S = \int_a^\infty W(\varrho)d\varrho = e^{-a^2/\alpha^2}, \tag{8}$$

and this is also the fraction, relative to an amorphous target, of collisions made by the protons in the aligned beam. Therefore, near the surface the minimum fractional scattering yield is $Y = S$ in accordance with (5b). Furthermore, $L = L_0/S$ and, according to (3), (4) and (5a) the fraction of the particles belonging to the aligned beam at the depth Z is $1 - e^{-L/z}$. At this depth we thus expect

$$Y = e^{-L/z} + S(1 - e^{-L/z}) = S + (1 - S)e^{-L/z}. \tag{5b}$$

As we have already seen, the experiments agree well with this formula, and it may be noted that also the ratio L_w/L_c agrees with theoretical expectations. From (7) and (8) we find

$$\frac{ln(1/S_w)}{ln(1/S_c)} = \frac{\alpha_c^2}{\alpha_w^2} = \frac{T_c}{T_w} \sim \frac{90}{300} = 0.3,$$

whereas the experiments give

$$\frac{lnL_w}{lnL_c} \sim \frac{ln2}{ln7} = 0.35.$$

In view of the crude procedure leading to (6), (7), (8) and (5b) it is not surprising that these formulae do not agree with the absolute experimental values of S. (7) gives $\alpha_c = 9.5 \cdot 10^{-10}$ cm and $\alpha_w = 1.7 \cdot 10^{-9}$ cm, whereas to obtain the observed S-values from (8) we must introduce the values $\alpha_c \sim 7 \cdot 10^{-10}$ cm and $\alpha_w \sim 1.4 \cdot 10^{-9}$ cm.

In an amorphous target, the Ω^2 corresponding to multiple scattering will increase somewhat faster than linearly with the distance z and, in addition, single and plural scattering will throw particles out of the beam, whose angular distribution therefore deviates slightly from a Gaussian. We may expect a similar behaviour in the crystal. Furthermore, it should be considered that the reduced stopping power in the axial direction influences the points; their ordinates are incorrect, because we compare protons with the same energy when coming out of the crystal, whereas we ought to compare protons having the same energy at the instant of scattering; the points should be corrected upwards.

Thus, although the measurements do not give the accurate yield *vs.* depth function, they do seem to show that the reduced string effect and its variation with the depth may be understood as a result of lattice vibrations. We remark that the finite energy resolution is of no significance, and that the carbon and oxygen layer on the surface also is unimportant, even if the original angular width of the beam is taken into account. Assuming a cross section of 30 times the Rutherford cross section—a value obtained by extrapolating from known data[10]—the thickness of the layer, estimated from the peaks in fig. 2, is equivalent to about 0.1 mg/cm^2 of oxygen. Such a layer will produce an increase in Ω^2 by about 0.1 ψ_1^2 by small angle scattering.

The authors wish to express their gratitude to Professor H. Højgaard Jensen, the Physical Laboratory I, H. C. Ørsted Institute, University of Copenhagen, for kindly presenting the crystal and for valuable discussions, and to Mr. P. Gregers Hansen, cand. polyt., for performing the cleaving and the X-ray analysis of the crystal. We further wish to thank the members of the cyclotron group, The Niels Bohr Institute, University of Copenhagen, for their valuable help with the experiments.

References

1. J. Lindhard: Phys. Lett. **12**, 126, 1964.
2. E. Bøgh, J. A. Davies and K. O. Nielsen: Phys. Lett. **12**, 129, 1964.
3. E. Bøgh and E. Uggerhøj: Phys. Lett. **17**, 116, 1965; Nucl. Instr. Meth. **38**, 216, 1965.
   J. U. Andersen, J. A. Davies and K. O. Nielsen: Nucl. Instr. Meth. **38**, 210, 1965.
   E. Uggerhøj: Phys. Lett. **22**, 382, 1966.
4. B. Domeij and K. Björkquist: Phys. Lett. **14**, 127, 1965.
5. J. A. Davies, F. Friesen and J. D. McIntyre: Can. J. Chem. **38**, 1526, 1960.
6. A. R. Sattler and G. Dearnaley: Phys. Rev. Lett. **15**, 59, 1965.
   C. Erginsoy, H. E. Wegner and W. M. Gibson: Phys. Rev. Lett. **13**, 530, 1964.
7. C. Williamson and J. P. Boujot: C. E. A. Report 2189.
8. J. Lindhard: Mat. Fys. Medd. Dan. Vid. Selsk. **34**, no. 14, 1965.
9. G. Leibfried in Flügge: Hdb. d. Phys. VII, **1**, pp. 260–64 (see also pp. 377 ff. loc. cit.).
10. N. Jarmil and J. O. Seagrave: Charged Particle Cross-Sections, Los Alamos, New Mexico, 1956.

Several papers dealing with various aspects of the penetration of charged particles through crystals are published in Nucl. Instr. Meth. Vol. **38**: Proc. Int. Conference on Electromagnetic Isotope Separators, Aarhus, Denmark, June 1965, Part V, pp. 207–76.

Indleveret til Selskabet den 20. januar 1967.
Færdig fra trykkeriet den 8. maj 1967.

Matematisk-fysiske Meddelelser
udgivet af
Det Kongelige Danske Videnskabernes Selskab
Bind **35,** nr. 17

Mat. Fys. Medd. Dan. Vid. Selsk. **35,** no. 17 (1967)

STOPPING OF SWIFT PROTONS EVALUATED FROM STATISTICAL ATOMIC MODEL

BY

EJVIND BONDERUP

København 1967
Kommissionær: Munksgaard

Synopsis

Calculations of electronic stopping for heavy particles with low charge number are performed down to quite low energies, e. g. for protons down to ~ 100 keV. The treatment is a refinement of a procedure suggested by LINDHARD and SCHARFF. This procedure makes extensive use of statistical models of the atom.

Stopping as a function of energy is determined by the I-value of the target material and the energy dependent "shell correction". As discussed, the shortcomings of the present statistical treatment should show up mainly in the I-values. In fact, the shell corrections obtained appear to be comparatively accurate, especially in view of the fact that previous estimates have been made by fitting parameters in semi-empirical formulas.

There is also a discussion of the possibility of determining I-values from theoretical shell correction curves and experimental stopping powers at very low energies.

PRINTED IN DENMARK
BIANCO LUNOS BOGTRYKKERI A/S

§ 1. Introduction

The present paper will be concerned with electronic stopping of a heavy particle of low charge penetrating a substance with randomly distributed atoms. In such a situation quantal perturbation theory should be applicable down to quite low energies—e.g. for protons, which will be our standard projectiles, down to $\sim$ 100 keV (cf. p. 10).

Although deflections in the screened atomic fields are of major importance in determining the scattering of the incoming particle, it is well known that the contribution to total stopping from these nuclear collisions can be neglected at the energies mentioned above[1].

§ 2. Review of Theory and Definition of Model

For electronic stopping one finds in a perturbation treatment that the specific energy loss, $(-dE/dx)_e$, suffered by a heavy incoming particle with charge $Z_1 e$, will be given by

$$(-dE/dx)_e = \frac{4\pi Z_1^2 e^4}{mv^2} N \cdot Z_2 L(v, Z_2), \tag{1}$$

m, v and N being, respectively, the electron mass, the velocity of particle 1 and the density of target atoms with atomic number Z_2. The dimensionless function $L(v, Z_2)$ is the one to be evaluated. The use of perturbation theory introduces the important simplification that the incoming particle appears in formula (1) only through the factor $(Z_1 e)^2$. Hence, the problem of evaluating the electronic stopping power is reduced to a treatment of the target material.

For v much larger than the velocities of the electrons in the stopping material $L(v, Z_2)$ is given by Bethe's expression

$$L(v, Z_2) = \sum_n f_n \log \frac{2mv^2}{\hbar\omega_n} + \log \frac{1}{1-(v/c)^2} - \left(\frac{v}{c}\right)^2, \tag{2}$$

the summation being performed over all possible transition frequencies ω_n with corresponding dipole oscillator strengths f_n ($\sum f_n = 1$). Relativistic terms enter only as the fourth and higher powers of v/c and are omitted in the following.

Before entering into actual calculations of $L(v, Z_2)$, let us briefly consider the possibility of applying similarity of the kind characteristic of the Thomas-Fermi description of the atom. The line of argument is the one given in refs. 2 and 3a.

In a dynamic Thomas-Fermi model f_n should only be a function of the one variable ω/Z_2, the frequency scale being proportional to Z_2. Moreover, denoting the dipole oscillator strength density by $g(\omega/Z_2)$* we get from (2) the asymptotic formula

$$L(v, Z_2) = \int_0^\infty g\left(\frac{\omega}{Z_2}\right) \log \frac{2mv^2}{\hbar Z_2(\omega/Z_2)}\, d\left(\frac{\omega}{Z_2}\right). \tag{3}$$

Here, L only depends on v and Z_2 in the combination v^2/Z_2. Thus, if we define a new energy measure x by[6, 2)]

$$x = \frac{v^2}{v_0^2 Z_2} \quad (v_0 = e^2/\hbar), \tag{4}$$

L can be expressed as

$$L = \log x + \log \frac{2mv_0^2}{I_0} \tag{5}$$

with I_0 given by

$$\log I_0 = \int_0^\infty g\left(\frac{\omega}{Z_2}\right) \log \hbar\left(\frac{\omega}{Z_2}\right) d\left(\frac{\omega}{Z_2}\right). \tag{6}$$

In a real atom, the distribution of oscillator strength differs somewhat from that of a Thomas-Fermi model. At intermediate values of ω/Z_2 the departure from the smoothly decreasing function $g(\omega/Z_2)$ should reflect the presence of various electronic shells and thus be of an oscillating nature. However, a more systematic deviation is expected below a frequency $\omega \sim \omega_R (\hbar\omega_R = mv_0^2/2)$, ω_R giving e.g. the order of magnitude of both the ionization frequency of an inert gas and the plasma frequency of the valence electrons in a metal. This means that the integral representing $\log I_0$ will receive only

* An evaluation of $g(\omega/Z_2)$ from a hydrodynamical type of Thomas-Fermi model was suggested by Bloch in 1933[4)] and has recently been carried through by Ball[5)].

very small contributions below a value $(\omega/Z_2)_{\text{cut-off}}$. On the whole, $(\omega/Z_2)_{\text{cut-off}}$ is proportional to Z_2^{-1}, but significant individual fluctuations exist. Hence, $g(\omega/Z_2)$ being a decreasing function, departures from the Thomas-Fermi prediction for the I_0-value should arise mainly because of deviations of the oscillator strength distribution from $g(\omega/Z_2)$ at the low frequency end of the spectrum. This observation seems essential not only for the calculation of I_0-values, but also for any attempt to continue the evaluation of $L(v, Z_2)$ down to values of v where the asymptotic formula (2) does not apply. In fact, the contribution to L from the low frequencies must remain of order of $\sum f_n \log(2mv^2/\hbar\omega_n)$, and thus the effect being responsible for the most pronounced departure from a similarity description at high energies should persist down to quite low energies.

One way of handling the many body problem involved in calculating $L(v, Z_2)$ for all values of v and Z_2 would be to solve a system of self-consistent equations for the electromagnetic field inside the target material. However, a main difficulty of such a (microscopic) dielectric treatment of an atomic system arises from the fact that the electron density varies in space. In order to avoid this difficulty, LINDHARD and WINTHER[7] considered the idealized case of a free electron gas, which, as discussed in the following, provides a good starting-point for more realistic situations. Suppose that a Fermi gas is disturbed by a charge density $\varrho_0(\vec{r}, t)$ and that this gives rise to a potential $\Phi(\vec{r}, t)$. If the disturbance can be considered as a perturbation, a linear description can be applied, and all the information about the stopping material, necessary to calculate $L(v, Z_2)$, is contained in the longitudinal dielectric constant ε^l connecting the Fourier components $\varrho_0(\vec{k}, \omega)$ and $\Phi(\vec{k}, \omega)$ of ϱ_0 and Φ. In fact, defining $\varepsilon^l(\vec{k}, \omega)$ by the equation

$$k^2 \varepsilon^l(k, \omega) \Phi(\vec{k}, \omega) \equiv 4\pi \varrho_0(\vec{k}, \omega), \tag{7}$$

one has[7]

$$L = \frac{i}{\pi \omega_0^2} \int_0^\infty \frac{dk}{k} \int_{-kv}^{kv} \omega \left\{ \frac{1}{\varepsilon^l(k, \omega)} - 1 \right\} d\omega, \tag{8}$$

ω_0 and i being, respectively, the plasma frequency $\sqrt{4\pi e^2 N \cdot Z_2/m}$ and the imaginary unit. (Because of isotropy in coordinate space, ε^l does not depend on the direction of $\vec{k}$.) From the calculations in ref. 7 several important results have emerged, especially concerning the question of the effect on the oscillator strength distribution of the polarizability of the medium.

LINDHARD and SCHARFF[6, 2] argued that even if a dielectric calculation could not be carried through for the atomic case, the picture of a polarizable electron gas should still be useful. One could try to average L for a gas of constant density over the electron cloud of the atom, thus making a statistical approach to the many body problem. However, some way or other, the effect of the electrons not beeing free, should be introduced in the expression for the stopping contribution from the various parts of the electron cloud.

From such considerations it was suggested that

$$L = \frac{1}{Z_2} \int_{r_{\min}}^{\infty} 4\pi r^2 \varrho(r) \log \frac{2mv^2}{\gamma \hbar \omega_0(r)} \, dr, \quad 2mv^2/\gamma\hbar\omega_0(r_{\min}) = 1 \tag{9}$$

could be expected to give a fair approximation even down to rather small values of v. Here, $\varrho(r)$ is the electron density in an atom of the target material, and $\omega_0(r)$ the corresponding local plasma frequency $\sqrt{4\pi e^2 \varrho(r)/m}$. For $\varrho(r)$ the densities found in for instance a Thomas-Fermi or a Hartree description could be used. Qualitative arguments were presented[6] to show that the binding forces acting on the electrons probably could be approximately accounted for by the constant γ, appearing in (9). γ was expected to be of order of $\sqrt{2}$. The values of I_0, calculated from (5) and (9), are seen to become proportional to γ, and $\gamma = \sqrt{2}$ gives fair agreement with experimentally determined mean excitation energies[2].

In the Lindhard-Scharff model a distinction was made between "outer" electrons ($2mv^2/\sqrt{2}\hbar\omega_0(r) > 1$), the contribution of which was calculated as if at rest, and "inner" electrons ($2mv^2/\sqrt{2}\hbar\omega_0(r) < 1$) that were considered to give no stopping at all. With a cut-off of this kind, L remains a function of x only, when the Thomas-Fermi expression for $\varrho(r)$ is used. If we compare with (3), an essential aspect of (9) can be expressed in the following way: L is supposed to be obtainable as an average of a function $L(\omega_0, v)$ weighted with a dipole oscillator strength density for which an ansatz has been made. The frequency $\sqrt{2}\,\omega_0$ should correspond to the density $-4\pi r^2 \varrho(r) \left.\dfrac{dr}{d\omega_0}\right|_{r = r(\omega_0)}$.

The results presented in ref. 2 were so promising, even down to energies around maximum in stopping cross section, that it might be profitable to repeat the calculations with the same ansatz for the oscillator strength distribution, but with a refined expression for $L(r, v) \equiv L(\omega_0, v)|_{\omega_0 = \omega_0(r)}$.

In their treatment of a free electron gas, LINDHARD and WINTHER[7] showed that L can be expanded in powers of $(v_F/v)^2$, v_F being the velocity of an electron at the Fermi surface. It turned out that for a gas with plasma frequency ω_0 and average kinetic energy $\langle T \rangle$ the first correction term $(\Delta L)_1$ to the asymptotic formula

$$L = \log \frac{2mv^2}{\hbar\omega_0}, \tag{10}$$

was given by

$$(\Delta L)_1 = -\frac{\langle T \rangle}{mv^2/2}. \tag{11}$$

Moreover, FANO and TURNER[3b] found this sort of expression to be of general validity in the atomic case (with $\langle T \rangle$ being the average over both coordinate and momentum space). As pointed out by LINDHARD and WINTHER[7], it would therefore seem natural to put

$$L(r,v) = \log\left(\frac{2mv^2}{\sqrt{2}\,\hbar\omega_0(r)}\right) - \frac{\langle T \rangle(r)}{mv^2/2} \tag{12}$$

for the "outer" electrons. Here, the average kinetic energy $\langle T \rangle(r)$ of a unit volume at a distance r from the nucleus should, as always in a statistical description of the atom, be obtained from $\varrho(r)$ by means of the formula

$$\langle T \rangle(r) = \frac{3}{5}\frac{\hbar^2}{2m}(3\pi^2\varrho(r))^{2/3}. \tag{13}$$

The behaviour of an electron gas is well described by a free particle model only at high densities[7], more specifically, when $\chi^2 \lesssim 1$, χ being defined by

$$\chi^2 = \frac{e^2}{\pi\hbar v_F}. \tag{14}$$

The Lenz-Jensen model of the atom[8] shows that, when $Z_2 = 10$, $\chi^2(r)$ is less than 1 for 97 % of the electrons (v_F and thus χ now being functions of r), and for higher values of Z_2 the situation is even better. A typical order of magnitude in the electron cloud is $\chi^2(r) \sim 10^{-1} - 10^{-2}$.

Let us try to find a reasonable expression for the stopping contribution from the inner electrons of an atom. From the $(k, \omega/k)$-diagrams of ref. 7 (Figs. 1 and 3) it is seen that for sufficiently large v the decisive aspect is

that for $k \to \infty$ (close collisions with single electrons), and $k \to 0$ (distant collisions) the oscillator strength is contained in a strip around the line $\omega/k = \hbar k/2m$ and in a resonance curve corresponding to $\varepsilon^l(k, \omega) = 0$, respectively. The distribution for intermediate values of k is not important as long as all the oscillator strength corresponding to a fixed value of k can be assumed to be below the line $\omega/k = v$.

However, in case the velocity of the incoming particle is small compared to orbital velocities of atomic electrons, this situation is changed fundamentally. Now it will not be sufficient to know the distribution of oscillator strength in asymptotic limits, and the oscillator strength will not be collected in resonance curves (ref. 7, Fig. 1). On the one hand, it seems difficult to tell exactly how the distribution is shifted when free electrons are replaced by bound ones, but, on the other hand, there is no evidence of systematic shifts of the kind appearing for large v. The latter shifts, which correspond to changes in the resonance frequencies, should be accounted for by the introduction of the factor $\gamma \sim \sqrt{2}$ in (9). Furthermore, the contribution to total stopping from inner electrons is known to be small, cf. also § 3. We can therefore probably give a fair account of the slowing-down due to inner electrons by just taking over the expression for the stopping of a slow particle in a free electron gas. Thus, defining $\chi^2(r)$ as in (14), we put up the following formula for $L(r, v)$ (ref. 7, formulae (12) and (15)):

$$L(r,v) = \begin{cases} \log\left(\dfrac{2mv^2}{\sqrt{2}\,\hbar\omega_0(r)}\right) - \dfrac{\langle T\rangle(r)}{mv^2/2}, & \text{if} \quad \geq 0 \quad \text{(a)} \\ \left(\dfrac{\chi^2(r)}{3}\right)^{3/4} \dfrac{1}{2}\left[\log\left(\dfrac{1}{\chi^2(r)}\right) - 1\right]\left(\dfrac{2mv^2}{\hbar\omega_0(r)}\right)^{3/2} & \text{otherwise} \quad \text{(b).} \end{cases} \tag{15}$$

Fig. 1 contains a reproduction of Fig. 5 in ref. 7, showing L as a function of $y = 2mv^2/\hbar\omega_0$ for two gas densities, $\chi^2 = 0.1$ and $\chi^2 = 0.01$. Here, the scale at the left-hand side should be used. The full drawn and dashed curves refer to numerical calculations and asymptotic expressions, respectively. With the scale to the right, the upper dashed and the dot-and-dash curves represent (a) and (b) of (15) at the same constant values of χ^2. It is noted that (b) is the result of an approximation which for high densities does not differ much from the one given in ref. 7, formula (15).

In connection with Fig. 1, two remarks should be made. First, the passage from (a) to (b) in (15) ought to occur at a value of r, where $\langle T\rangle(r) \sim 1/2\,mv^2$. This is seen to be fulfilled. Second, it would have been preferable

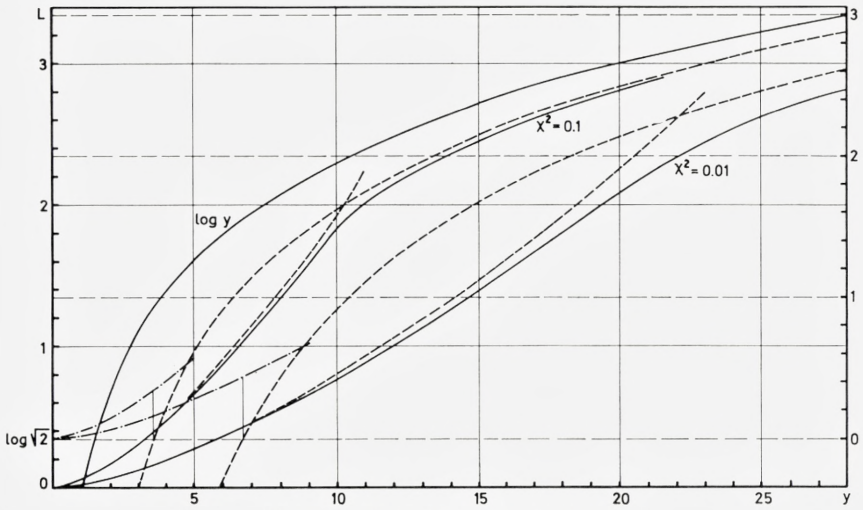

Figure 1. For explanation cf. text.

to avoid the discontinuity in $L(r, v)$, but it seemed difficult to find a simple analytic expression connecting (a) and (b) in a smooth manner. It will be shown later, however, that the discontinuity is of only little importance for the results of the calculations.

With $L(r, v)$ given by (15) the similarity as expressed by $L = L(x)$ is lost, even if $\varrho(r)$ is taken from a Thomas-Fermi model. However, as a function of (x, Z_2) the Z_2-dependence of L must still be only weak.

From the general discussion of oscillator strengths given at the beginning of this chapter it is to be expected that the detailed distribution of the outermost electrons is essential for the calculation of I_0-values. That this is so indeed, can be demonstrated by an example: Using a tabulated[9] Hartree-Fock distribution for $C(Z_2 = 6)$ I_0 was determined to 11.43 eV. By calculating the volume per atom in amorphous carbon it was found that 0.42 of the six electrons (7 %) were situated outside this volume. Smearing out these 0.42 electrons equally over the accessible space, one altered I_0 to 13.75 eV – a change of 20 %.

In order to avoid the large dependence of the calculated quantity on the details in the outermost part of the electron cloud, it was decided to look at the function C/Z_2 defined by

$$\left(-\frac{dE}{dx}\right)_e = \frac{4\pi Z_1^2 e^4}{mv^2} N \cdot Z_2 \left\{\log\left(\frac{2mv^2}{I}\right) - \frac{C(x, Z_2)}{Z_2}\right\} \quad (I = I_0 \cdot Z_2) \qquad (16)$$

rather than at $L(x, Z_2)$. This seems to be the most direct way of comparing with experiments and thereby obtaining information about the applicability of the Lindhard-Scharff ideas to such detailed calculations.

The conventional term "shell correction" for C/Z_2 is somewhat misleading in the present treatment, but will be used, nevertheless.

Before making comparisons with experimental material one question should be considered. The present procedure rests upon the outcome of a perturbation calculation for a free electron gas. To what extent can a perturbation treatment be used in our case? The electron cloud was divided into two parts: a) "outer" electrons corresponding to $v \gtrsim v_F(r)$, and b) "inner" electrons corresponding to $v \lesssim v_F(r)$. Case a) should be tractable by (quantum mechanical) perturbation theory for $\varkappa > 1$, where[3a, 10)]

$$\varkappa \equiv \frac{2Z_1 e^2}{\hbar v}, \tag{17}$$

and for case b) a perturbation calculation can be shown to be valid for comparatively high gas densities—more specifically, if $v_0 \cdot Z_1^{2/3} \lesssim v_F(r)$ (LINDHARD). For protons, the two requirements are satisfied for $v \gtrsim 2v_0$, i.e. for energies down to $\sim$ 100 keV. Although depending on the target material, 100 keV gives the order of magnitude for the energy at which the maximum in stopping power appears.

It might be mentioned that calculations for proton energies below $\sim$ 500 keV have often been considered to be doubtful due to capture and loss of electrons. However, within a self-consistent dielectric treatment of a Fermi gas the electrons provide a time-independent screening of an incoming positive particle, the screening distance being generally a function of Z_1,v and the density of the gas. Therefore, such a description includes a balance between capture and loss. The special case of a linear treatment corresponds to the situation where the screening distance does not depend on Z_1.

We now seem justified in comparing theoretical and experimental data down to $x \sim 10^{-1}$, at least for the heavier elements.

§ 3. Discussion of Results

Shell corrections and *I*-values

Let us now turn to the C/Z_2-curves that have been calculated by means of the procedure described above*. In Fig. 2 comparison is made between

* The Lenz-Jensen calculations were performed on the GIER computer at the University of Aarhus. As for the Hartree curves, the calculations were done by hand, but were much reduced through the use of unpublished numerical results from the original work by LINDHARD and SCHARFF.

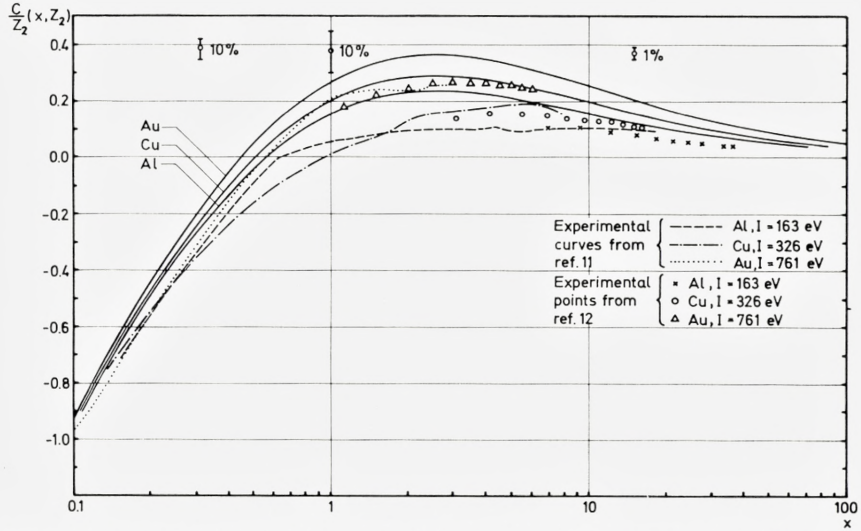

Figure 2. Comparison of experimental and theoretical shell corrections. The solid curves represent calculated values. The error bars show the approximate influence of a 10 % (1 %) uncertainty in the applied stopping power.

experimentally determined and computed shell corrections, the latter having been obtained by applying a Thomas-Fermi type of expression for $\varrho(r)$, namely the analytic first order Lenz-Jensen distribution function. The empirical curves were drawn by introducing experimental values for $(-dE/dx)_e$[11, 12] and I into (16), the I-values being those recommended in ref. 3 (I and not I_{adj} of ref. 3 should be used).

Two features are seen to be reproduced correctly by the computed shell corrections:

1) the general shape of the curves,
2) the order of magnitude of C/Z_2.

Furthermore, it seems to be in agreement with experiments that C/Z_2 should increase with increasing Z_2 (Fig. 2 and ref. 3c). However, a detailed check on this point is difficult because of the significant experimental uncertainties, especially as regards the I-values (cf. below).

Low energies

Although the difference between the calculated shell corrections for Al and Au, taken relatively to L, i.e. $\Delta(C/Z_2)/L$, amounts to about the same

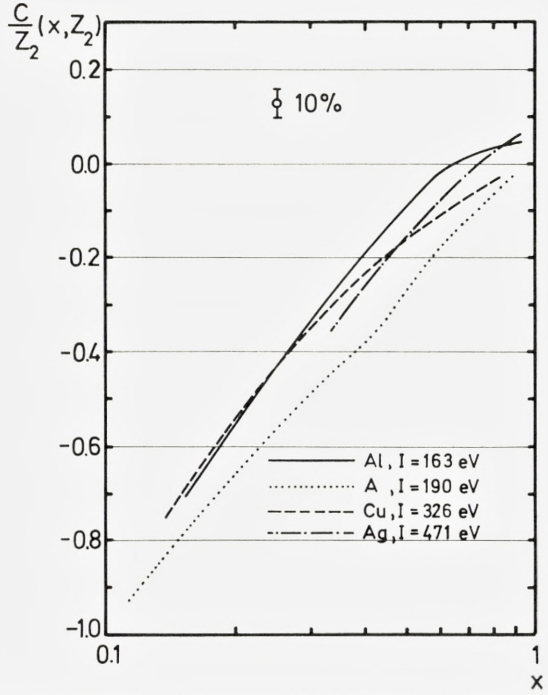

Figure 3. Shell correction curves determined from Bichsel's stopping power data and experimental I-values. The error bar shows the approximate influence of a 10 % uncertainty in the applied stopping power.

at $x = 0.1$ and $x = 1$ (8–10 %), the small difference on an absolute scale between the various C/Z_2-curves at low energies seems to be of some importance. Suppose that one wants to extract the I-value of a material from some experimentally determined stopping power and a theoretical value for the corresponding shell correction. The formula to be used is

$$L(x, Z_2)_{\text{exp}} = \log x + \log\left(\frac{2mv_0^2}{I/Z_2}\right) - \frac{C}{Z_2}(x, Z_2), \tag{18}$$

where $L(x, Z_2)_{\text{exp}}$ is found by means of (1) in an obvious way.

If L has been measured with an uncertainty ΔL and C/Z_2 is given with an error $\Delta(C/Z_2)$ one has for the maximum possible error ΔI in I:

$$\frac{\Delta I}{I} \simeq -\left[\left(\frac{\Delta L}{L}\right) \cdot L + \Delta\left(\frac{C}{Z_2}\right)\right]. \tag{19}$$

In a high energy experiment L is of order of 6–10. However, at $x = 0.1$ the L-value will be at most 0.5, which means that an uncertainty of $10\,\%$ in the measured stopping power leads to an experimental uncertainty in I of only $5\,\%$. If C/Z_2 can be calculated in such a way that $\Delta(C/Z_2) \lesssim 0.10$, say, the extracted I-value will be determined with a total uncertainty not exceeding $15\,\%$.

Admittedly, it is most pronounced for the theoretical shell corrections that the curves approach each other at low x-values (Figs. 2 and 3). Yet, it must be remembered that, firstly, the stated uncertainty of $1–10\,\%$ in the stopping powers reported by BICHSEL[11] is of some importance for the drawing of the empirical curves, and, secondly, a change of $1\,\%$ in the applied experimental I causes a parallel shift of the corresponding curve of 0.01. Therefore, even if it is true that the shell correction depends in an only weak manner on Z_2 at small x-values, it would probably be very difficult to point out such an effect from existing experimental material alone, i.e. from stopping power data at low energies and I-values determined at high energies.

TABLE 1.
Lenz-Jensen calculation for Ag. Z_2^*: number of "inner electrons". L^*: contribution to L from "inner electrons".

x	Z_2^*/Z_2	L^*	L^*/L
8.04	0.07	0.014	0.00
3.62	0.16	0.028	0.01
1.055	0.40	0.054	0.04
0.613	0.52	0.058	0.06
0.376	0.63	0.059	0.08
0.235	0.72	0.055	0.10
0.095	0.85	0.038	0.14

Before giving any examples of I-values obtained along the lines suggested above, let us make a couple of further remarks concerning the reliability of the method used for calculating shell corrections. One difficulty might seem to be that a large portion of the electron cloud is considered as belonging to "inner" electrons at small x-values, and the contribution from an inner electron was only taken care of through a rough estimate. This problem is, however, not very serious because, as shown in Table 1, the role played by these electrons in the slowing-down is very limited, both relatively and

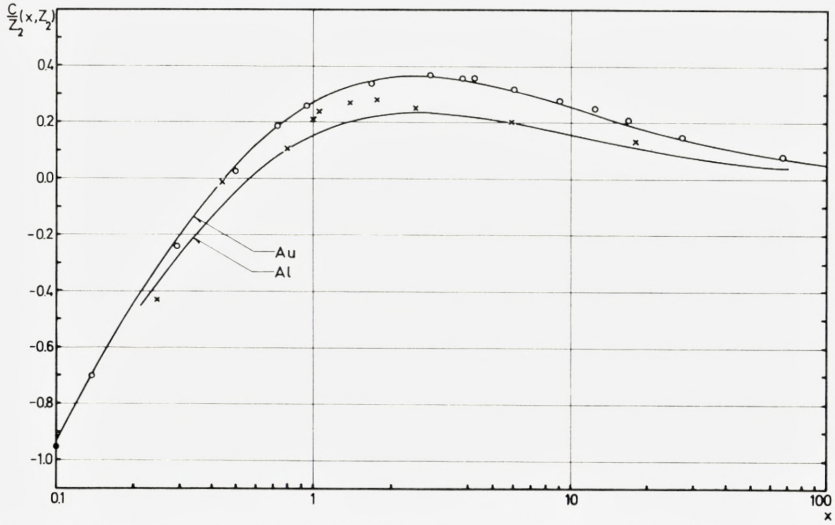

Figure 4. Solid curves represent results from Lenz-Jensen calculations. Points from corresponding Hartree models are denoted by x (Al) and o (Au).

absolutely. Moreover, Table 1 makes it very plausible that the discontinuity in the expression for $L(r, v)$ cannot be of much importance. As a matter of fact, an estimate shows that by changing $L(r, v)$ in such a way that (a) and (b) in (15) become smoothly connected, one changes C/Z_2 by less than 0.01–0.02.

The calculated shell corrections should thus depend only weakly on the detailed distribution of both inner and outermost electrons, but this is, in fact, what justifies the use of a statistical method. Especially the introduction of Hartree models for the electron clouds should for heavier materials only lead to slight deviations (oscillations) from the Lenz-Jensen results (Fig. 4).

If a common C/Z_2-curve can be drawn in a certain x-interval for two materials denoted by indices A and B, the corresponding L-values will only differ by a constant reflecting the difference in I for the two substances. More specifically, the following relation should apply:

$$I_A = I_B \frac{Z_A}{Z_B} \exp(L_B - L_A). \tag{20}$$

To test formula (20) it was decided to take Al as a standard, because this material seems to be the one with the experimentally best known I. A value

TABLE 2.

Comparison of calculated and empirical I-values. In several cases ref. 3 only gives I_{adj}. $(I_{adj} - I)$ was then found by interpolation in the table on p. 101 of the same publication. BICHSEL does not consider his value for Ag to be reliable. FANO has taken his value for Kr from BICHSEL.

Element	Z_2	x	I_{cal}(eV)	I_{exp}(eV) FANO	I_{exp}(eV) BICHSEL	I_{exp}(eV) BARKAS & BERGER	$\exp(L_B - L_A)$
C	6	0.667	70± 8	81		78	0.925
Ne	10	0.400	144± 9			131	1.146
A	18	0.308	157±15	190	184 212	210	0.696
Ni	28	0.308	296±23		307.5 310	302	0.844
Cu	29	0.308	319±23	313	326	312	0.878
Kr	36	0.308	355±30	360	360 380	377	0.787
Ag	47	0.340	433±42	471	447.5	480	0.736
Sn	50	0.320	460±43			507	0.733
Xe	54	0.308	462±45			543	0.683
Au	79	0.308	779±66	761		768	0.787
Pb	82	0.308	769±69	788		795	0.748

of 163 eV was taken from ref. 3. The stopping power measurements used for the determination of L were those cited by BICHSEL[11], the x-value always being the lowest one common to Al and the medium under consideration. However, measurements below 100 keV were not taken into account.

Table 2 shows the results from such a calculation (I_{cal}) together with empirical I-values. The uncertainty in I_{cal} corresponds to the stated maximum experimental error in the stopping power for the substance investigated (10 %). As already mentioned, the experimental I-values are often uncertain, a fact clearly demonstrated by the different numbers given for the same material by the authors of ref. 3.

For an account of how the experimental mean excitation energies were found, the reader is referred to ref. 3. Here, we merely note that the numbers given by BARKAS and BERGER[3d] for $Z_2 \geq 13$ were determined by means of a semi-empirical formula for I/Z_2, giving very closely the values quoted by FANO[3c] for Al, Cu, and Pb. Yet, in some cases, e.g. for the noble gases, an interpolation procedure of this kind may not be very reliable, since the distribution of the outermost electrons can be rather special. The last column

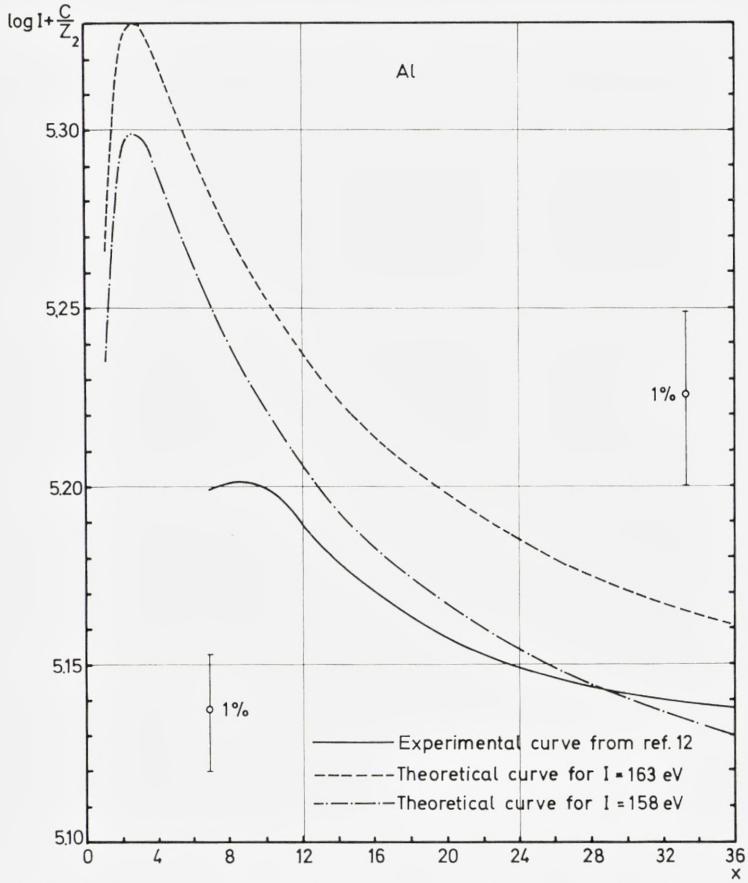

Figure 5a. The error bars show the influence of a 1 % change in the experimental stopping power (similar for Fig. 5b).

of Table 2 exhibits the factors $\exp(L_B - L_A)$ reflecting the rather large variations of I/Z_2.

The agreement with the I-values suggested in ref. 3 is rather good considering the experimental uncertainties. It seems that these have not been exaggerated by the authors. For instance, the stopping powers for protons in carbon measured recently by SAUTTER and ZIMMERMANN[13] with a reported accuracy of $\pm 1.7 - \pm 2.3$ %, are lying from 11.4 % to 15.5 % below Bichsel's values in the region of overlap (100–300 keV).

From the theoretical curves C/Z_2 was found to increase for increasing Z_2.

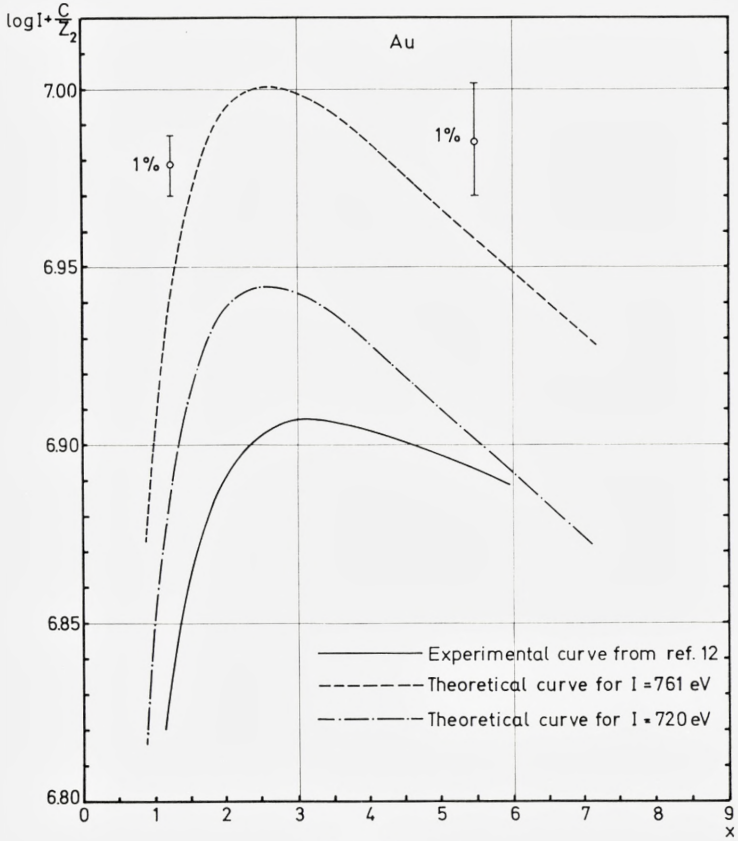

Figure 5b.

Thus, choosing an experimental shell correction curve for Al as a common standard for all materials, one should for $Z_2 > 13$ have underestimated C/Z_2 and thereby overestimated I, this being the more serious the larger the used x. However, in Table 2 the calculated I-values are not systematically larger than the corresponding experimental ones. Yet, although $I_{exp} = 163$ eV for Al may be determined with considerable accuracy, the stopping power measurements at low energies are probably not much better for Al than for most other metals. In this context it may be noted that a $10\,\%$ change in the stopping power for Al at $x = 0.308$ ($E_{proton} = 100$ keV) would correspond to a systematic change in the calculated I-values of $\pm 6\,\%$.

Intermediate energies

The above discussion of the region of small x-values originated in a general feature of the calculated shell corrections. A direct comparison between theory and experiments appeared to be difficult.

At intermediate energies the experimental situation is much more satisfying, mainly due to a new technique for measuring stopping powers developed by ANDERSEN, GARFINKEL, HANKE, SØRENSEN, and VAJDA[12]. According to these authors, the data obtained are reliable to within $\pm 0.3\,\%$. This means that a detailed comparison between, at least, the shapes of the experimental and theoretical shell correction curves can be made for the energies investigated (2–12 MeV protons).

Figs. 5a and 5b show a plot of $\log I + C/Z_2$ against x for Al and Au. For both elements, the second I-value used for the calculated curve has been chosen to avoid a parallel shift between corresponding theoretical and empirical curves rather than being in close agreement with current estimates. It is seen that the location of the maximum is accounted for fairly well, but there is a significant difference in the trend towards it, the calculated curves being much too steep.

It is not at all evident if this discrepancy can be removed within the model by some appropriate change, but it might be in place to note that the x-values in question correspond to the "bulk" of electrons passing from being counted as "outer" to being counted as "inner" electrons, i.e. the maximum of the function $4\pi r^2 \varrho(r)$ appears around the radius where one goes from (a) to (b) in (15).

§ 4. Concluding Remarks

The purpose of the present paper may be said to have been twofold. Firstly, from a theoretical point of view it seemed desirable to investigate the applicability of the Lindhard-Scharff ideas in a detailed evaluation of slowing-down problems, and, secondly, even if the results of the calculations should not be in very accurate quantitative agreement with experiments, it might well be that such a treatment of Thomas-Fermi type could give some information as to the over all dependence of fundamental quantities on the atomic number Z_2. As discussed, such information is not always easy to extract from experimental material alone.

Keeping in mind the detailed nature of any theoretical description trying to account for shell corrections, the results obtained must be interpreted as supporting the basic assumptions of the method. Furthermore, the expression

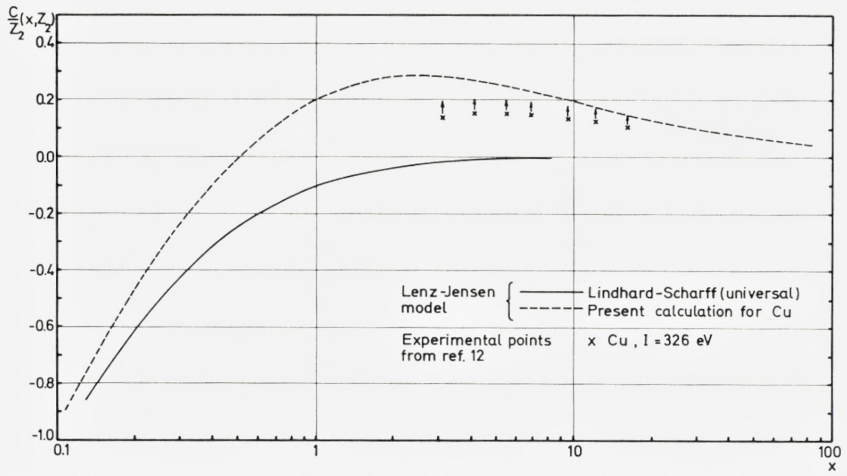

Figure 6. Comparison of Lindhard-Scharff model with present calculations. Arrows at experimental points correspond to a change of I from 326 eV to 312 eV (cf. Table 2).

chosen for $L(r, v)$ probably cannot be much in error. An indication of this is provided by a comparison of the present shell corrections with the (universal) Lenz-Jensen curve from the model used by LINDHARD and SCHARFF (Fig. 6).

Acknowledgments

The present work was undertaken at the suggestion of Professor JENS LINDHARD, and I wish to express my gratitude for the help and guidance I have received from him through numerous talks.

I want to thank H. H. ANDERSEN, C. C. HANKE, H. SØRENSEN, and P. VAJDA for communication of experimental results prior to publication, and SUSANN TOLDI for her assistance in the preparation of the manuscript.

Institute of Physics,
University of Aarhus.

References

1. J. Lindhard, M. Scharff, and H. E. Schiøtt, Mat. Fys. Medd. Dan. Vid. Selsk. **33**, no. 14 (1963).
2. J. Lindhard and M. Scharff, Report on Conference on Penetration of Atomic Particles, Gatlinburg 1958. NAS-NRC Publ. 752 (1960).
3. Studies in Penetration of Charged Particles in Matter, NAS-NRC Publ. 1133 (1964).

3a. J. Lindhard, paper no. 1 of ref. 3.
3b. U. Fano and J. E. Turner, paper no. 4 of ref. 3.
3c. U. Fano, Appendix A of ref. 3 and Ann. Rev. Nucl. Sci. **13**, 1 (1963).
3d. W. H. Barkas and M. J. Berger, paper no. 7 of ref. 3.

4. F. Bloch, Z. f. Physik **81**, 363 (1933).
5. J. A. Ball, unpublished thesis, Princeton University (1963).
6. J. Lindhard and M. Scharff, Mat. Fys. Medd. Dan. Vid. Selsk. **27**, no. 15 (1953).
7. J. Lindhard and Aa. Winther, Mat. Fys. Medd. Dan. Vid. Selsk. **34**, no. 4 (1964).
8. H. Jensen, Z. f. Physik **77**, 722 (1932).
9. A. Jucys, Proc. Roy. Soc. London **173**, 59 (1939).
10. N. Bohr, Mat. Fys. Medd. Dan. Vid. Selsk. **18**, no. 8 (1948).
11. H. Bichsel, American Institute of Physics Handbook, 2nd. ed., Sect. 8c (McGraw-Hill, New York 1963).
12. H. H. Andersen, Risö Report No. 93 (1965); H. H. Andersen, A. F. Garfinkel, C. C. Hanke, and H. Sørensen, Mat. Fys. Medd. Dan. Vid. Selsk. **35**, no. 4 (1966); H. H. Andersen, C. C. Hanke, H. Sørensen, and P. Vajda, Phys. Rev. **153**, 338 (1967).
13. C. A. Sautter and E. J. Zimmermann, Phys. Rev. **140**, A490 (1965).

Indleveret til Selskabet den 13. januar 1967.
Færdig fra trykkeriet den 8. maj 1967.